Transactions of the ASME®

Journal of Turbomachinery

Published Quarterly by The American Society of Mechanical Engineers

VOLUME 114 • NUMBER 2 • APRIL 1992

TECHNICAL PAPERS

(Contents Continued on p. 276)

Technical Editor,
G. K. SEROVY
Associate Technical Editors
Advanced Energy Systems
M. J. MORAN
Environmental Control
H. E. HESKETH
Fuels and Combustion Technologies
D. W. PACER
Gas Turbine
L. S. LANGSTON
Internal Combustion Engine
J. A. CATON
Nuclear Engineering
S. M. CHO
Power
R. W. PORTER

BOARD ON COMMUNICATIONS
Chairman and Vice-President
M. E. FRANKE

Members-at-Large
W. BEGELL
T. F. CONRY
T. DEAR
R. L. KASTOR
J. KITTO
R. MATES
W. MORGAN
E. M. PATTON
R. E. REDER
A. VAN DER SLUYS
F. M. WHITE
B. ZIELS

President, **N. H. HURT, JR.**
Executive Director,
D. L. BELDEN
Treasurer, **ROBERT A. BENNETT**

PUBLISHING STAFF
Mng. Dir., Publ.,
CHARLES W. BEARDSLEY
Managing Editor,
CORNELIA MONAHAN
Sr. Production Editor,
VALERIE WINTERS
Production Assistant,
MARISOL ANDINO

Transactions of the ASME, Journal of *Turbomachinery* *(ISSN 0889-504X) is published* quarterly (Jan., Apr., July, Oct.) for $125.00 per year by The American Society of Mechanical Engineers, 345 East 47th Street, New York, NY 10017. Second class postage paid at New York, NY and additional *mailing offices. POSTMASTER: Send address* change to Transactions of the ASME, Journal of Turbomachinery, c/o THE AMERICAN SOCIETY OF MECHANICAL ENGINEERS, 22 Law Drive, Box 2300, Fairfield, NJ *07007-2300.*

CHANGES OF ADDRESS must be received at Society headquarters seven weeks before they are to be effective. Please send old label and new address.

PRICES: To members, $36.00, annually; to nonmembers, $125.00.

Add $15.00 for postage to countries outside the United States and Canada.

STATEMENT from By-Laws. The Society shall not be responsible for statements or opinions advanced in papers or . . . printed in its publications (B 7.1, para. 3).

COPYRIGHT © **1992** by The American Society of Mechanical Engineers. Reprints from this publication may be made on condition that full credit be given the TRANSACTIONS OF THE ASME—JOURNAL OF TURBOMACHINERY, and the author, and date of publication be stated.

INDEXED by Applied Mechanics Reviews and *Engineering Information, Inc.*
Canadian Goods & Services Tax Registration #126148048

Downloaded 01 Jun 2010 to 171.66.16.52. Redistribution subject to ASME license or copyright; see http://www.asme.org/terms/Terms_Use.cfm

(Contents Continued)

ANNOUNCEMENTS

J. P. Smed
Principal.

F. A. Pisz
Principal Engineer.

J. A. Kain
Advanced Engineer.

Westinghouse Electric Corporation,
Power Generation Technology Division,
Orlando, FL 32826

N. Yamaguchi
Chief Staff Engineer.

S. Umemura
Assistant Chief Engineer.

Takasago R & D Center,
Mitsubishi Heavy Industries, Ltd.,
2-1-1, Shinhama, Hyogo 676 Japan

501F Compressor Development Program

As part of the Westinghouse-MHI 501F development program, a new 16-stage axial flow compressor has been designed. Reported here are elements of the aerodynamic and mechanical design as well as general design features. Overall performance test results are also presented, which indicate that the compressor met or exceeded all expectations amenable to measurement during the full load shop test program.

Introduction

As part of the joint Westinghouse-Mitsubishi Heavy Industries (MHI) 501F development project, Westinghouse assumed the task of designing a new, industrial, axial flow compressor. The inlet flow and pressure ratio were chosen to meet the engine requirements of 150 MW at ISO conditions [1]. The compressor flow path is shown in Fig. 1 and includes the following design and performance features:

- 16 axial stages.
- Three interstage bleeds to assist in starting and to supply bleed air for turbine hot parts cooling.
- Variable inlet guide vanes (IGVs) to assist in starting and to provide for exhaust temperature control for combined cycle or cogeneration applications.
- Casing structure utilizing blade ring concept to allow for closer tip clearance control and improved maintenance.
- Improved blade locking devices and stator vane structural design for increased reliability.
- Total to total isentropic efficiency of over 88 percent for ISO baseload operation.

The aerodynamic design of this compressor is based on current technology supported by over 20 years of successful design experience on the Westinghouse W501 and smaller CW251 combustion turbines.

The rotating and stationary blade elements were designed for mechanical integrity and long-term reliability. Again, Westinghouse experience with the W501 fleet played a large role in the design of these components.

Upon completion of the design and building phases the unit was assembled and full-load tested (water rheostat) in the MHI shop in Takasago, Japan. An important part of the test program was to determine starting, overall performance, and mechanical characteristics of the new compressor. Included in this paper are the results of this performance evaluation. For load testing purposes engine operation was limited to synchronous speed at varied IGV settings. Thus, except for a small change (13°C) in ambient temperature between runs, the testing was conducted at a single referred speed of about 3535 rpm.

No load tests were conducted at reduced referred speeds at various IGV settings to determine the position of the surge line. These results are reported and are compared to similar data for other Westinghouse-MHi engines.

As part of the starting test, rotating stall characteristics were

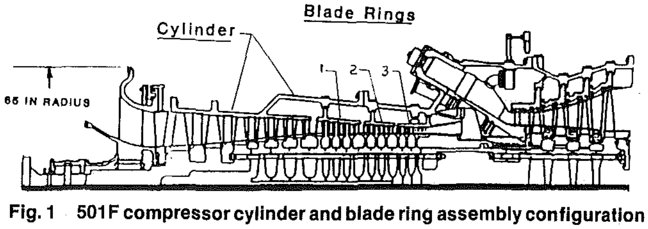

Fig. 1 501F compressor cylinder and blade ring assembly configuration

---

Contributed by the International Gas Turbine Institute and presented at the 36th International Gas Turbine and Aeroengine Congress and Exposition, Orlando, Florida, June 3-6, 1991. Manuscript received at ASME Headquarters March 4, 1991. Paper No. 91-GT-226. Associate Editor: L. A. Riekert.

Table 1 Evolution of W501 compressor

MODEL	STAGES	PR*	FLOW*	CUSTOMER	TEST DATE
501AA	17	10.04	687	Cincinnati G&E	JAN 71
501B1	17	10.32	685	Salt River Proj Glendal, AZ	JUL 74
501C	19	11.23	685	Kansas P&L	MAR 75
501D	19	12.03	722	Kansas P&L	MAR 76 and JUL 76
501D5	19	13.11	722	GSU	1st QTR 82

* NEMA Conditions

also determined. The results showed close similarity to other Westinghouse compressors, there being no stall above 2150 rpm, and will not be reported on here.

Compressor Design Background. Although new in some respects, the 501F compressor is the latest in a series of W501 compressors which have evolved since the early 1970s. As shown in Table 1, the 501F compressor is the product of 20 years of development work starting with the W501AA. The new compressor draws heavily from the W501D5, which was extensively tested at Gulf States Utility in 1982. Certain units have since logged in excess of 50,000 baseload operating hours. For the W501D5, with the exception of some lube oil fouling problems, which have been corrected, no starting or other compressor performance related incident has ever been reported.

Performance Design Specifications. To meet the overall objectives of the engine design project, the basic performance requirements were specified as:

- ISO inlet condition, 59°F and 14.696 psia
- 3600 rpm shaft speed (60 Hz)
- 16 stages
- 14:1 pressure ratio
- 912.5 lb/sec inlet flow
- Variable inlet guide vanes
- Three interstage bleeds for cooling and starting

Additional functional requirements included:

- Reference speed range of 3400-4000 rpm (−40°F to 120°F).
- Compressor designed with the objective of operating surge-free and at the highest possible efficiency.
- Besides aiding in starting the three bleeds (stages 6, 10, and 13) also supply cooling air to the hot components of turbine stages 2, 3, and 4. Bleed pressures must be sufficient to provide cooling air over the entire operating envelope.
- Variable inlet guide vanes designed to:

(*a*) Provide inlet swirl to the first rotor blade to minimize inlet relative mach numbers.

(*b*) Provide the ability at synchronous speed to reduce the inlet flow for combined cycle or cogeneration applications.

(*c*) During starting provide necessary swirl to first blade with the objective of keeping the blade out of the detrimental stall condition.

- Acceleration and line synchronization in 10 to 12 minutes.

Aerodynamics Design Method

General. The 501F compressor aerodynamic design effort was carried out using Westinghouse developed analytical procedures. The method also draws from field experience, shop and field testing, and published literature when suitable. Analysis and design procedures are performed using a series of computer codes, which allow the designer to perform a "rough cut" pitch line analysis, during the initial design phase, or the detailed final design using an axisymmetric quasi-three-D code. This analytical design process continues through a number of iterations until all aerodynamic, performance, and mechanical design requirements are judged to meet conservative design criteria. The compressor design is considered acceptable after it can be shown to meet all applicable design criteria throughout the established operating envelope.

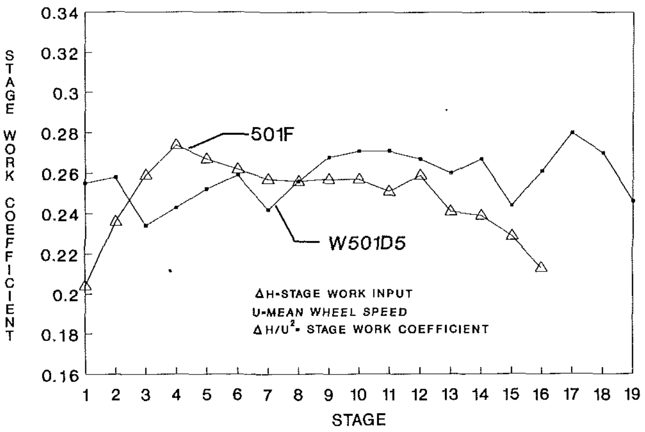

Fig. 2 501F and W501D5 stage work coefficient distribution

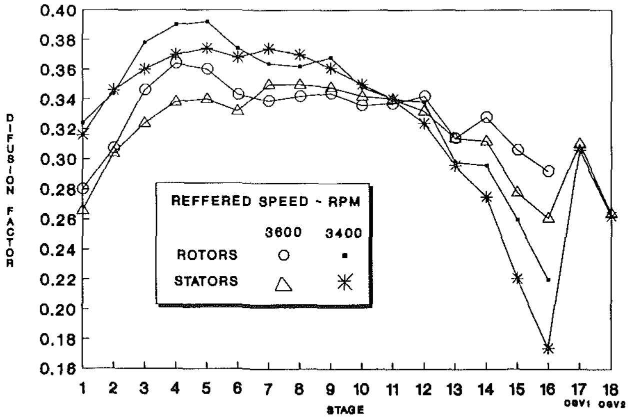

Fig. 3 W501F compressor rotor and stator mid-height diffusion factor

With the knowledge of the engine specifications firmly in hand, design choices were made concerning the various aerodynamic design parameters required to define the compressor flowpath. Selection must be made for stage work distribution, mean flow coefficient, annulus blockage factor, hub reaction, maximum allowable diffusion factor, inlet Mach number, and radial vortex pattern. Typical of these, as selected by Westinghouse, are the stage-by-stage work and diffusion factors. The 501F and 501D5 work distribution are shown in Fig. 2. By increasing the stage work in the middle stages, relative to the inlet and discharge, the goal was to make the 501F compressor even more tolerant than the 501D5 to swings in ambient temperature and engine loadings. The 501F baseload diffusion factors are shown in Fig. 3 for rotors and stators at reference speeds of 3400 rpm (120°F) and 3600 rpm (59°F).

Airfoil Design Performance. Airfoil shapes are selected with the goal of producing the desired velocity triangles with the minimum possible total pressure loss across the row. Prior to the 501F, Westinghouse used W-65[1] series airfoils in all 501 compressors. For the 501F higher than traditional inlet Mach

---

[1] W-65 series is a modified NACA-65 thickness distribution on a circular arc mean line.

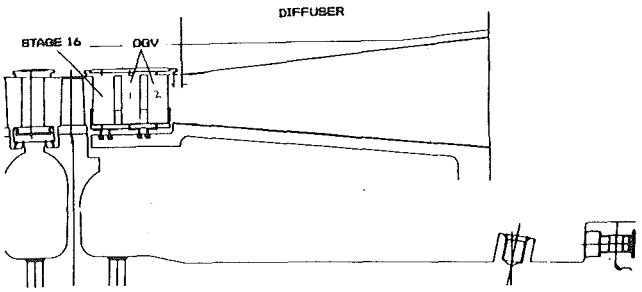

Fig. 4 OGV and diffuser arrangement

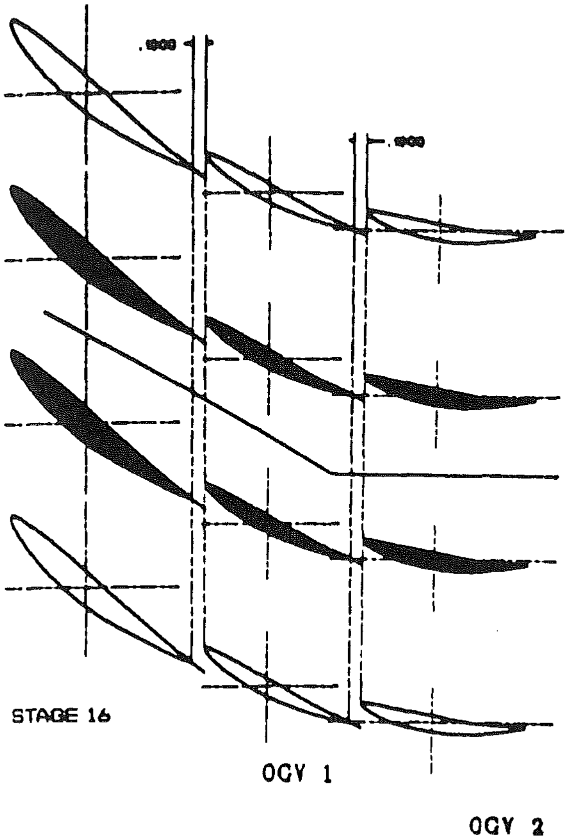

Fig. 5 Tandem OGV arrangement

numbers at stages 1-4 warranted the use of double circular arc (DCA) airfoils for rotor blades 1-4. All other rows including the outlet guide vanes (OGVs) use W-65 airfoils.

Although new to the W501 family of engines, DCA airfoils have been successfully applied to other Westinghouse-MHI designs such as the Westinghouse-Fiat TG50 and the Canadian-Westinghouse CW251B12 [2] combustion turbines.

Additional Aerodynamic Improvements. The compressor discharge diffuser and OGV configurations are shown in Figs. 4 and 5. The tandem OGV arrangement is new to Westinghouse machines, which traditionally used single OGVs. Design studies indicated that the tandem system was the most efficient way to remove the higher exit swirl of the 501F and hence to obtain the maximum amount of static pressure recovery prior to entering the exit annular diffuser.

As shown in Fig. 1, the new 501F compressor casing structure is of two-piece construction. The "blade rings" incorporated from the 7th through 16th stages have many potential advantages, including improved alignment for better clearance control and reduced tip and interstage seal clearances. Also, since they can be "rolled" out of the structure, maintenance should also be made easier when it comes to servicing the stator vanes. The risk associated with this new design was considered minimal since Westinghouse has a long successful history (dating back to the late 1960s) of incorporating blade rings into their turbine designs.

Full Load Shop Test. Upon completion of design and construction, a full-load test program was performed at the Mitsubishi shop in Takasago, Japan. An important part of the test program was the determination of overall engine performance and in particular the evaluation of the engines new compressor.

The following measurements were obtained relevant to the compressor:

- Ambient conditions
- Engine speed (3600 rpm)
- Compressor inlet temperature and pressure
- IGV position
- Interstage bleed flows
- Compressor discharge total temperature and pressures
- Rotating stall patterns
- Diaphragm (stator) frequencies at stages 4, 8, 9, and 13
- Rotor blade frequencies at stages 1, 2, 4, and 7
- No load (idle) surge point
- Starting speed versus time
- Tip clearances at rows 4, 9, 13, and 15

All steady-state performance testing was conducted at 3600 rpm. Thus, with a small variation in the ambient temperature, test data were obtained for reference speeds of 3480 and 3535 rpm only.

The performance-related measurements deserve special mention. The compressor inlet flow was measured two different ways (flow nozzle and pitot tubes). The difference was within one percent with the pilot tube result being the lower of the two. The lower flow is used throughout in evaluating the compressor performance. Discharge conditions were determined by special rakes fitted as close as possible to the compressor diffuser outlet plane. Radial distributions of total temperature and pressures across the discharged annulus were measured. These results were integrated to obtain the outlet total conditions. Other special measurements and measuring techniques included:

- Rotating stall patterns: blade path dynamic pressure transducers
- Rotor blade frequencies: optical sensors
- Stator vane frequencies: strain gages

The compressor inlet flow results for the full range or IGV settings are shown in Fig. 6. Data points include idle through baseload operation and are seen to exceed the respective design goal in each case. At the four-degree design IGV setting the inlet flow exceeds the design value by about two percent. Besides being good from the overall engine performance standpoint, the results also serve to reinforce the validity of Westinghouse's aerodynamic design procedures. Although it is advantageous to end up with slightly greater than the design flow, the ability to predict compressor performance accurately is at least as important when considered from the long-term engine development viewpoint.

The compressor temperature efficiency is displayed in Fig. 7 for pressure ratios from about 9 (no load) to over 13:1 at base load firing temperature. It should be noted that the 13:1 pressure ratio is somewhat lower than expected for the given operating conditions and is attributed to the first-stage turbine vanes (stators) being more open than expected. This situation has since been corrected by restaggering the stage 1 turbine vanes. The baseload measured efficiency is seen to be generally higher than the 88 percent design point target. It is anticipated that the goal will also be met at full design pressure ratio.

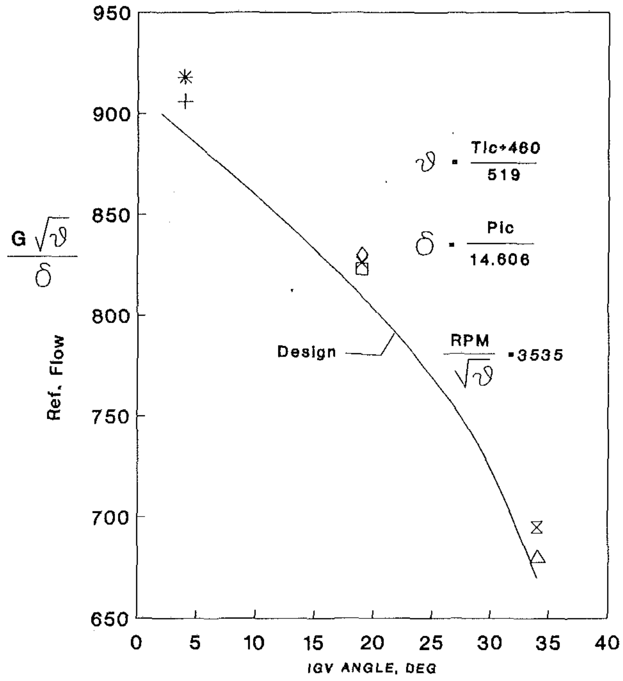

Fig. 6 Compressor flow versus IGV setting

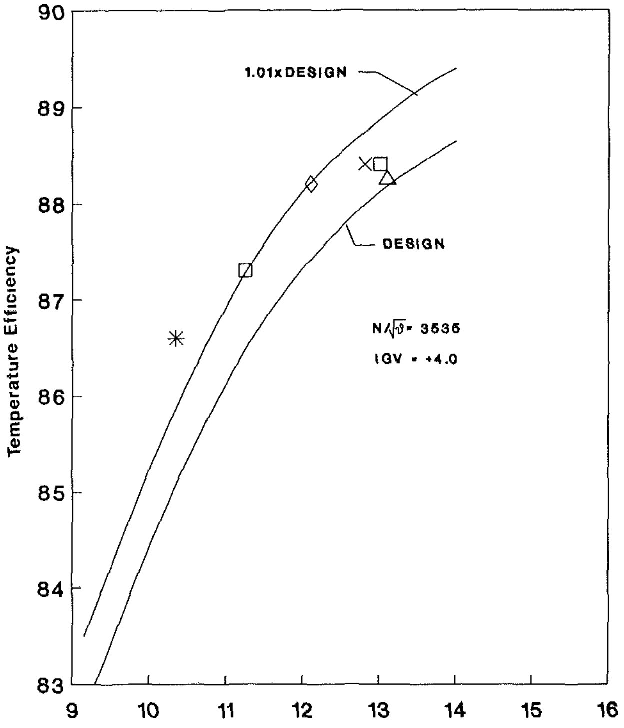

Fig. 7 Efficiency versus pressure ratio

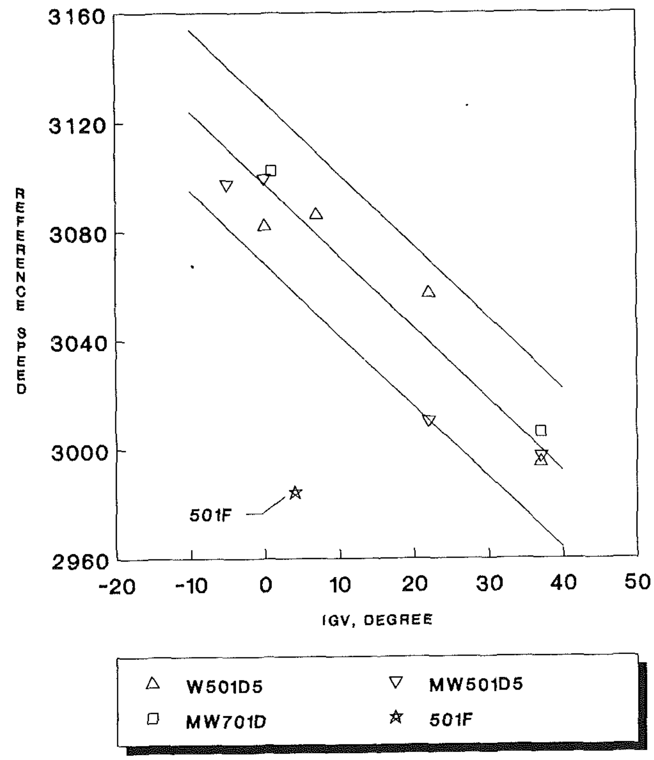

Fig. 8 Surge speed versus IGV setting

An important characteristic of all compressors is their ability to start and to operate free of surge or other instabilities while operating under load. Historically, Westinghouse has used no-load tests to establish the surge resistance of its compressor designs. The general procedure is to operate the engine at zero-load with bleed valves closed and slowly reduce the speed until surge occurs. The surge point is found at several IGV settings, including the design value, to establish the compressor surge characteristic. The speed at which surge occurs is then compared to other successful compressors, of similar designs. Results of the surge test are shown in Fig. 8. Here, the 501F is compared to the W501D5 and MW701D (3000 rpm) machines. Although neither of these machines has a surge problem, the test data clearly show the 501F to have a speed advantage of about 98rpm relative to these earlier designs. Our experience shows that improvements in the zero-load surge resistance generally translate into improved surge margin throughout the operations range.

Blading Mechanical Design

Rotating Compressor Blades. The mechanical adequacy of the 501F rotating compressor blades is defined by design criteria derived from operating experience as well as design guidelines of ASME codes. The applied criteria can be broken down into four categories: (1) For prevention of excessive elastic deformation or elastic instability, limits are placed on primary, local primary, and primary bending stresses; (2) resonant frequencies in the lower modes at running speed are tuned and regions of high potential excitation level are avoided to preclude resonant fatigue in these modes; (3) a high cycle fatigue index based on vibration theory and experience is used to promote adequate fatigue strength in off-resonant and intermediate/high mode resonant conditions; and (4) a "reduced frequency parameter" is determined and compared to a target value for flutter avoidance.

Beam theory, combined with a finite element analysis, as illustrated in Fig. 9, is used to meet the appropriate criteria during the design process. Because of the relatively low hub-to-tip ratios and small tip camber possessed by the upstream rows, even a slight untwist will have a negative impact on performance due to greater than optimum turning at the tip. Therefore, based on the results of the finite element calculations, the first four rotating compressor blade rows are pretwisted such that they revert back to an optimum performance configuration when rotating in the compressor at design speed.

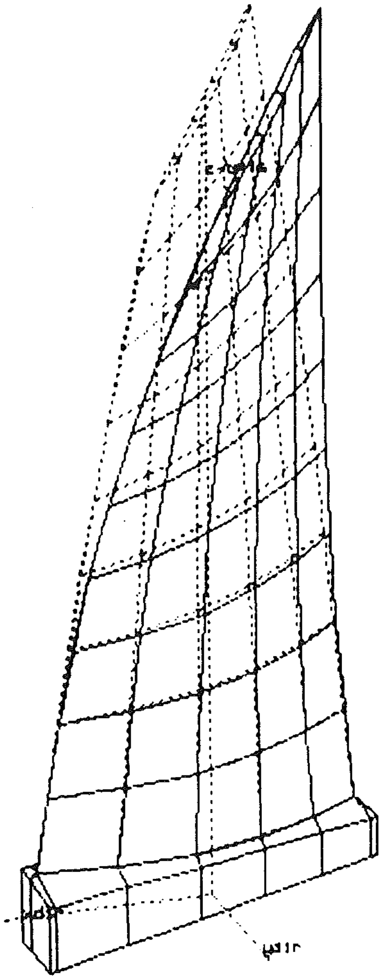

Fig. 9 Finite element model of rotating compressor blade first-mode deflection pattern

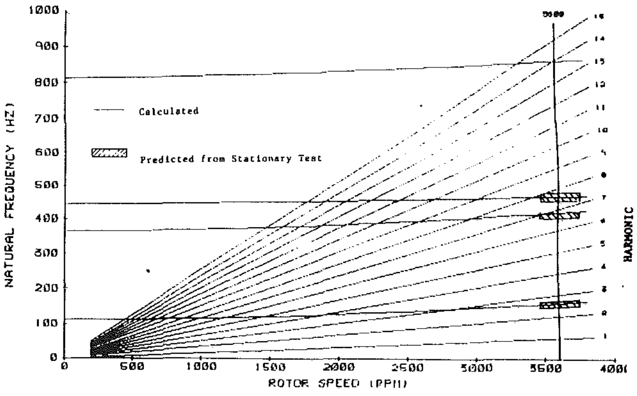

Fig. 10 Campbell diagram for typical rotating compressor blade

Due to the importance of avoiding resonance in the lower modes, the calculated frequencies are verified by test in two steps. First, a stationary frequency test is conducted, the associated rotating frequency calculated, and the blade modified as required. This is followed by a full-scale shop test for confirmation of frequency at design speed. Results of such calculations and tests are presented in the form of a Campbell diagram such as shown in Fig. 10.

Because diaphragm wake and inlet stream flow disturbances can excite the rotating compressor blades and it is not possible to "tune" the blades in the intermediate and higher modes, the finite element calculations are extended into this region. Response levels of suspect modes are monitored during shop tests and verified as being low enough to preclude fatigue failure.

Flutter, or the self-excited oscillation of an aerodynamic lifting surface, is addressed through the calculation of a dimensionless parameter called the reduced frequency [3],

$$F_R = \frac{\omega c}{V} = \frac{2\pi f}{V} \tag{1}$$

Here, f is the first flexural mode frequency of oscillation, c is the blade tip chord, and V is the relative inlet velocity of the airstream at the blade tip. This parameter appears both explicitly and implicitly in the governing equations for unsteady aerodynamics of oscillating airfoils and also plays an extremely important role in the empirical relationships associated with dynamic stall and stall flutter. A high reduced frequency is favored in avoiding flutter and a target minimum of F_R is established based on experience.

Due to stress considerations, the first seven rows of blades are manufactured from martensitic precipitation hardenable stainless steel forgings with high strength level and fatigue properties. The subsequent downstream rows, with lower strength requirements, are forged from martensitic hardenable 12 percent Cr stainless steel. The roots are of simple dovetail design, coated in the first several rows to reduce fretting potential. The blades are retained in the rotor with a new locking device, which is visibly inspectable, and which permits blade assembly/disassembly without removing the rotor from the cylinder [4].

Stator Vanes. All stator diaphragms in the 501F compressor consist of a pair of 180 deg half rings, and are of two basic design types:

- Rows 1–8 utilize fabricated diaphragm assemblies in which forged vanes, with enlarged tenons, are fastened between continuous 180 deg inner and outer shrouds. The row 16 and outlet guide vane assembly is similar to rows 1–8 except that vanes manufactured from rolled airfoil section stock are used in place of forged vanes with enlarged tenons.
- Rows 9–15 feature assemblies of individual integral vane/shroud segments, which are joined together at the inner and outer shroud joints by electron beam welding.

All diaphragm rows feature four-staged interstage seals between the inner shroud and rotor to help reduce backflow (leakage). Interstage seals on rows 4–15 are carried by a removable slide-on seal holder. This removable design facilitates direct inspection of the inner shroud joints, and also simplifies worn seal replacement.

The diaphragm designs utilized on the 501F are very similar to those being used on the latest W501D5 units. These designs have evolved through many years of experience with fabricated diaphragms. The latest Westinghouse diaphragm designs have been reconfigured to provide greater strength at the critical vane-to-shroud junctions. The vane-to-shroud junction is now continuous material with a smooth fillet radius, accomplished through the use of forged vanes with enlarged tenons, or individual integral vane/shroud segments. Weld joints have been repositioned to locations of lower stress. The combination of greater strength and a removable seal holder should reduce maintenance requirements.

501F diaphragm designs for rows 1–16 have been evaluated and accepted with respect to component mechanical criteria jointly defined by Westinghouse and MHI. These criteria include evaluation by computer analysis of diaphragm natural frequencies with respect to compressor blade wake passing frequencies. Natural frequencies have also been measured by stationary impact testing. The final phase of the design verification process was an instrumentation test of several select diaphragm rows during operation in the prototype 501F unit. All rows tested indicated favorable design results.

Conclusions

Based on the full-load shop test operating experience with the Westinghouse fleet of W501s the following conclusions regarding the 501F can be made:

1 Compressor performance (inlet flow and efficiency) was close to analytical prediction. The inlet flow exceeded the design value by about two percent and the efficiency was at least as good as predicted up to the maximum pressure ratio tested and appeared to be still climbing.

2 The surge margin appears to be superior to that of the W501D5, which has a history of surge-free operation.

3 The closeness of testing and design performance results clearly illustrates the accuracy of Westinghouse's compressor performance prediction methodology.

4 Specific problems, such as stator vane cracking and blade "walking," which have been associated with early W501s, have been addressed.

5 Addition of blade rings at stages 7-16 has improved the alignment of tip and seal clearances and should simplify maintenance by making it easier to service the stators.

Acknowledgments

In the writing of this paper, two individuals deserve special mention: first, C. A. Rohr, former (now retired) compressor designer who engineered the 501F compressor from start to finish. Without Carl's meticulous work, the writing of this paper would have been far more difficult. Special appreciation is also extended to G. S. Howard, former manager of Westinghouse performance section, for reviewing the manuscript thus helping to assure the accuracy of reported results.

References

1 Scalzo, A. J., McLavrin, L. D., Howard, G. S., Mori, Y., Hiura, H., and Sato, T., "A New 150-MW High-Efficiency Heavy-Duty Combustion Turbine," ASME *Journal of Engineering for Gas Turbines and Power*, Vol. III, pp. 211-217.

2 Marson, E., "Compressor Redesign for (CW)251BB12 Gas Turbine," ASME Paper No. 89-GT-141, 1989.

3 Scalzo, A. J., Allen, J. M., and Antos, R. J., "Analysis and Solution of a Nonsynchronous Vibration Problem in the Last Row Turbine Blade of a Large Industrial Combustion Turbine," ASME *Journal of Engineering for Gas Turbines and Power*, Vol. 108, pp. 591-598.

4 Scalzo, A. J., Antos, R. J., and Fukue, I., "Operating Experience Complements New Technology in Design of Advanced Combustion Turbine," ASME Paper No. 88-JPGC/GT-1.

Design of a High-Performance Axial Compressor for Utility Gas Turbine

A. Sehra[1]
Textron Lycoming,
Stratford, CT 06468

J. Bettner
Allison Gas Turbine Division,
Indianapolis, IN 46241

A. Cohn
Electric Power Research Institute,
Palo Alto, CA 94304

An aerodynamic design study to configure a high-efficiency industrial-size gas turbine compressor is presented. This study was conducted using an advanced aircraft engine compressor design system. Starting with an initial configuration based on conventional design practice, compressor design parameters were progressively optimized. To improve the efficiency potential of this design further, several advanced design concepts (such as stator ends bends and velocity controlled airfoils) were introduced. The projected polytropic efficiency of the final advanced concept compressor design having 19 axial stages was estimated at 92.8 percent, which is 2 to 3 percent higher than the current high-efficiency aircraft turbine engine compressors. The influence of variable geometry on the flow and efficiency (at design speed) was also investigated. Operation at 77 percent design flow with inlet guide vanes and front five variable stators is predicted to increase the compressor efficiency by 6 points as compared to conventional designs having only the inlet guide vane as variable geometry.

I Introduction

There have been great improvements in axial compressor design techniques for compressors used in aircraft gas turbine engines. In addition to increasing the efficiency, these improvements have been aimed at increasing the specific flow, the surge margin, and the pressure ratio per stage. This has allowed development of compact, lightweight high-performance compressors and engines that are of primary importance for flight economics.

The purpose of the design presented in this paper was to apply the knowledge and design techniques developed for aircraft engine axial flow compressors to the compressor for a large utility turbine engine. With weight and number of stages being of secondary importance, the goal was to develop an aerodynamic design with a level of efficiency potentially higher than that of the large utility turbine engine compressors that are now in operation.

This paper presents the results of an investigation to develop a 14:1 pressure ratio, 800 lb/sec utility compressor aerodynamic design.

The design study for this Electric Power Research Institute (EPRI) compressor was conducted in four phases. The first phase was concerned with a detailed parametric study to evaluate, with the objective of maximizing overall compressor efficiency, the influence of key aerodynamic and geometric design variables on compressor performance. Phase II refined the Phase I design to consider (1) selection of airfoil profiles, (2) off-design performance, and (3) blade and vane dynamics. Phases I and II employed conventional compressor design techniques in that circular arc and series airfoil profiles were incorporated in the design. The basic design tool used was based on the radial equilibrium with built-in semi-empirical loss-loading correlations. The Phase II design should only be viewed as an optimized detailed aerodynamic design.

Phase III examined the application of advanced blading concepts that had the potential for increasing design point efficiency. Two and three-dimensional end-wall and airfoil surface boundary layer analysis codes, along with secondary flow and blade tip clearance analysis models, were employed to develop the advanced concept airfoil design loss models. These advanced concept airfoils were then integrated into the Phase II design to produce the final advanced concept compressor.

The final phase (Phase IV) of this study was directed at investigating the influence of variable geometry on the compressor efficiency during the part-power operation of the utility turbine.

II Axial Compressor Design System

Figure 2-1 shows the overall logic of the axial compressor design system used for the design study reported in this paper. Also shown in this figure are the major computer modules used for EPRI compressor design. Several other modules specifically used for highly loaded transonic compressor stages (for example, method of characteristics code) are not included here.

The basic design philosophy centers around iteratively updating design parameters (such as work distribution) and airfoil shape until a "minimum loss" design is established. In this

---

[1] Previous address: Allison Gas Turbine Division, Indianapolis, IN 46241.

Contributed by the International Gas Turbine Institute and presented at the 36th International Gas Turbine and Aeroengine Congress and Exposition, Orlando, Florida, June 3-6, 1991. Manuscript received at ASME Headquarters February 20, 1991. Paper No. 91-GT-145. Associate Editor: L. A. Riekert.

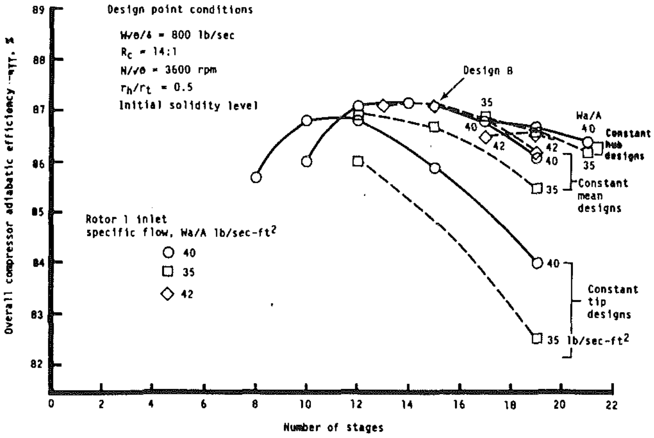

Fig. 3-1 Influence of number of stages and inlet specific flow on compressor efficiency

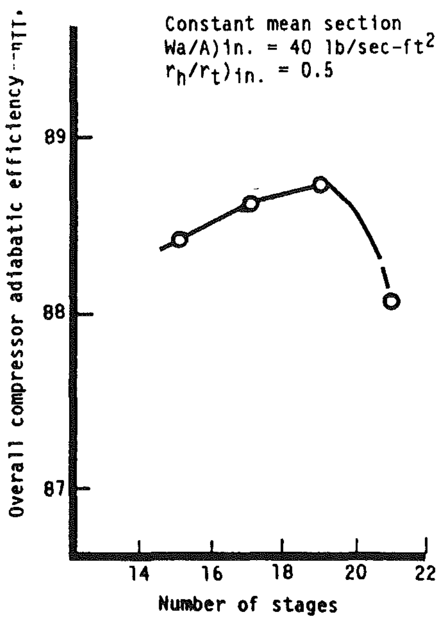

Fig. 3-2 Effect of number of stages on (constant mean section, low solidity design) compressor efficiency

As seen from Fig. 3-1, the initial screening study favors a 15-stage, constant meanline configuration with an inlet specific flow of 40 lb/sq ft-sec.

The adiabatic efficiency potential of this configuration is computed to be 87.0 percent (polytropic efficiency = 90.8 percent), which is of the same level as the GE E^3 compressor.

In the next phase of the parameteric study, a more detailed optimization was carried out with design variables extended well beyond the conventional levels used in the aircraft engine compressors. One such design variable was the tip solidity, which was progressively reduced below the conventional aircraft compressor design practices. To counter the effect of increased diffusion factor associated with reduced solidity, the stage number was increased, thereby reducing the average stage pressure ratio. Particular attention was also paid to the stagewise and spanwise distributions of work, diffusion factor, and swirl.

Results of this fine tuning indicated that the maximum efficiency potential is offered by a 19-stage configuration having a relatively high specific flow in the front stage and very low airfoil solidity. Increasing the number of stages beyond 19 causes a sudden drop in efficiency (see Fig. 3-2).

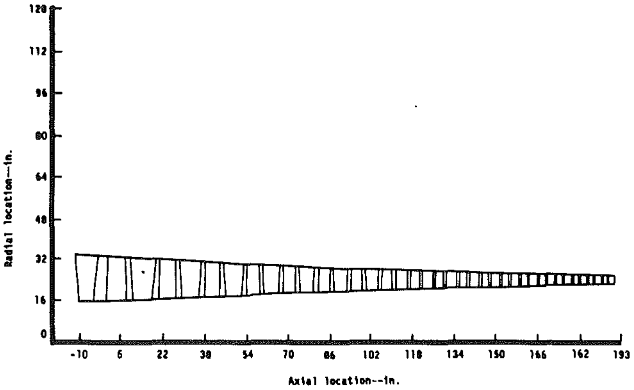

Fig. 3-3 19-stage preliminary design compressor

Preliminary Design Configuration. Based on the results of the detailed parametric study, the compressor configuration that produced maximum efficiency incorporated the following features:

- 19 stages plus IGV
- 40 lb/sec-ft^2 inlet specific flow
- 0.45 inlet hub/tip radius ratio
- Constant mean flow path
- Swirl in all stages except the last stator
- Very low solidity

It was predicted that the proposed compressor design would have the following design point performance:

- Compressor exit Mach number, M_e 0.3
- Overall adiabatic efficiency, η_{TT} 88.8 percent
- Overall polytropic efficiency, η_{poly} 92.1 percent

Figure 3-3 presents the flow path of the optimized preliminary design configuration. Important design variables for this configuration are presented in Figs. 3-4-3-7. Also shown in these figures are the corresponding design parameters of contemporary aircraft engine compressors. The compressors selected for this comparison are the T56-A427 and five other unnamed compressors. This comparison highlights the similarities and differences of the EPRI design with these existing compressors.

IV Phase II—Airfoil Geometry

Phase I of this study optimized global design parameters, using conventional design techniques, to produce a preliminary design. In Phase II, the preliminary geometry of rotor and stator airfoils was defined. This involved selection of incidence, chord, maximum thickness/chord, and interblade row gaps. The criteria were to select airfoil geometric parameters that offer the best compromise between the design and off-design performance without compromising the structural integrity of the airfoil. Some adjustment of solidity and swirl distributions were also carried out to improve stagewise and spanwise distributions of airfoil loading. No attempt was made at this point to customize the airfoil shape. All the airfoils had circular arc meanline with the exception of the first rotor multiple circular arc (MCA) configuration.

Incidence. In an effort to maximize the performance at the design point conditions by keeping the airfoil diffusion requirements reasonable and still to limit the swing in incidence angles from design point to a near-stall operating point (20 percent surge margin), near-zero incidence angles were selected for all the rotors. For stators, incidence angles were iteratively selected in the forward portion of the compressor; in the aft stages, the stator incidence angles were set at negative values. The negative incidence angles were limited to the aft stages,

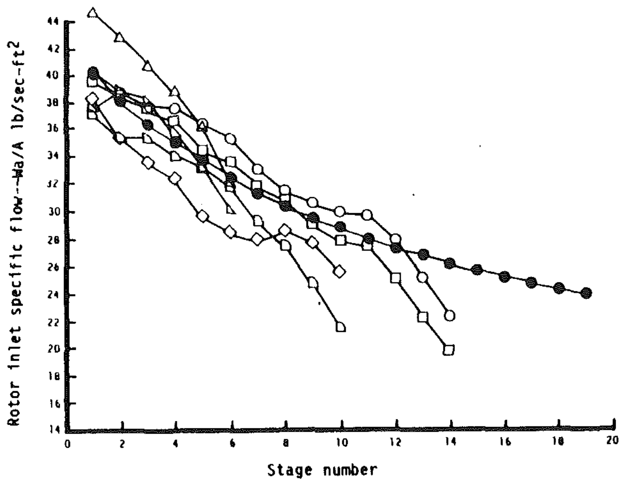

Fig. 3-4 Comparison of EPRI proposed design rotor inlet specific flow distribution with other contemporary designs

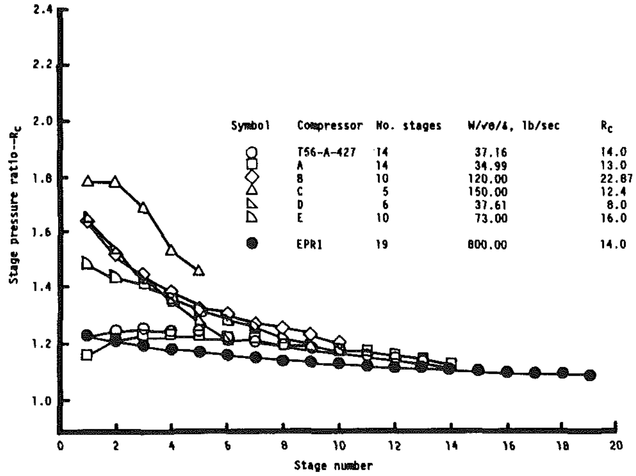

Fig. 3-5 Comparison of EPRI proposed design stage pressure ratio distribution with other contemporary designs

since in the multistage environment, it is principally the aft stages of the compressor that react to the increases in loading and incidence angle change as the compressor moves from design point operation to stall.

The design process began with the basic airfoil geometry of the preliminary design configuration whose flow path was shown in Fig. 3-3. Incidence angles were then selected based on the above criteria, and the resulting airfoils were configured for design operating point using a deviation rule based on the NASA SP36 [1] cascade correlation with corrections for end-wall effects.

A detailed blade-to-blade flow analysis was also conducted on selected rotor and stator airfoils, with the resulting surface velocity distributions, examined for possible flow separation and unacceptably large values of the equivalent diffusion parameter, D_{eq}, (suction surface $V_{\max}/V_{te}$, which is a measure of suction surface diffusion).

The criteria used during this phase of study for the prevention of incipent flow separation were to keep the value of the surface incompressible boundary layer shape factor $H_i \leq 3.0$ at the airfoil trailing edge. It is recognized that the value of $H_i = 3.0$ is somewhat higher than the more generally accepted value of $H_i > 2.2$ for incipient separation. It was anticipated that H_i could be substantially reduced later in the study when the advanced concept customized airfoil profiles would be employed in the design process.

Once the design point airfoil flow conditions were considered acceptable, an off-design model of the compressor was developed, and the above computations were repeated at the predicted 20 percent surge margin operating point. The increases in incidence angles, D_{eq}, and potential flow separation were examined at the 20 percent surge margin point. If the resulting design/off-design point results were deemed unsatisfactory, the entire process was repeated with another assumed axial/radial incidence angle distribution. This design process led to the incidence angle distributions illustrated in Figs. 4-1 and 4-2 for the rotors and stators, respectively. It can be seen that the incorporation of negative incidence angles at the design point limited the swing in incidence from about -1 to $+6$ deg for the rotors and -5 to $+6$ deg for the stators for the projected range of operation at design speed. Figure 4-3 presents the predicted design speed pressure-flow characteristic asso-

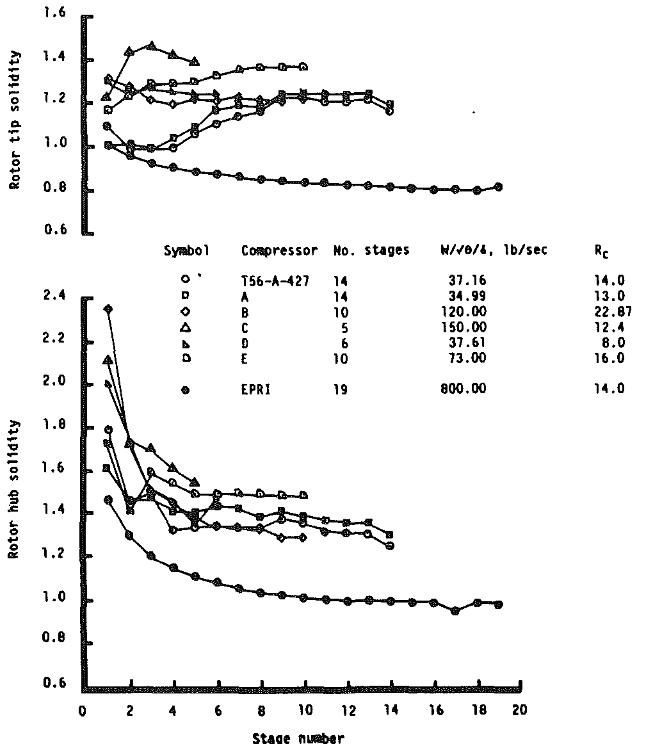

Fig. 3-6 Comparison of EPRI proposed design rotor solidity with other contemporary designs

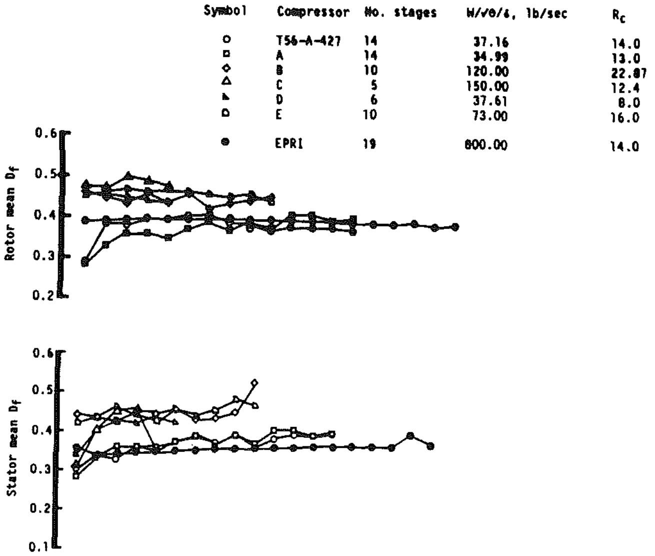

Fig. 3-7 Comparison of EPRI proposed design diffusion factors with other contemporary designs

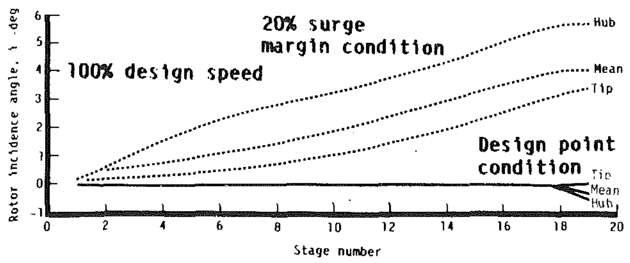

Fig. 4-1 Variation of the rotor incidence angle from design to 20 percent surge margin operating conditions

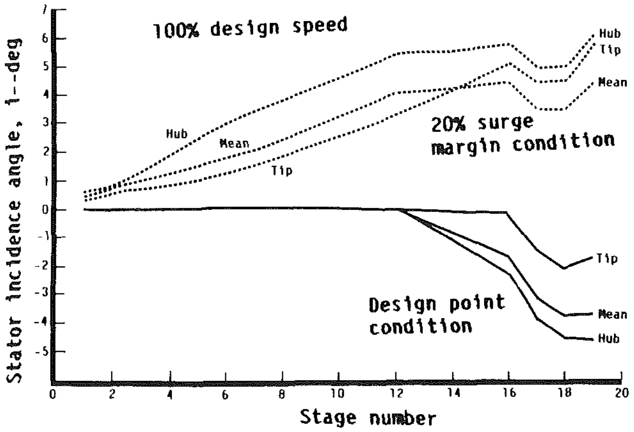

Fig. 4-2 Variation of the stator incidence angle from design to 20 percent surge margin operating conditions

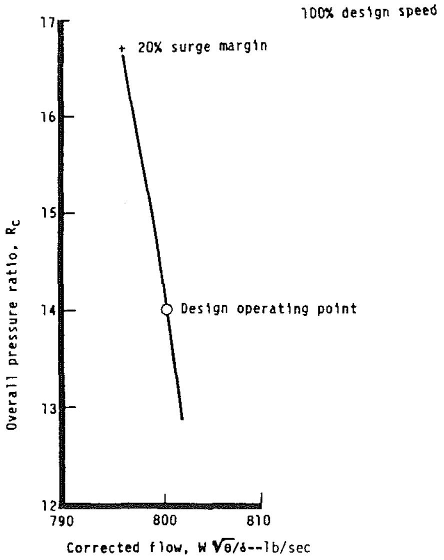

Fig. 4-3 Flow characteristics at 100 percent design speed pressure

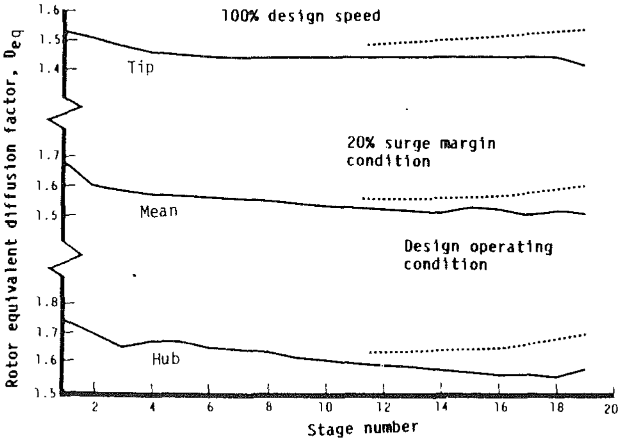

Fig. 4-4 Variation of the rotor equivalent diffusion factor from design to 20 percent surge margin operating conditions

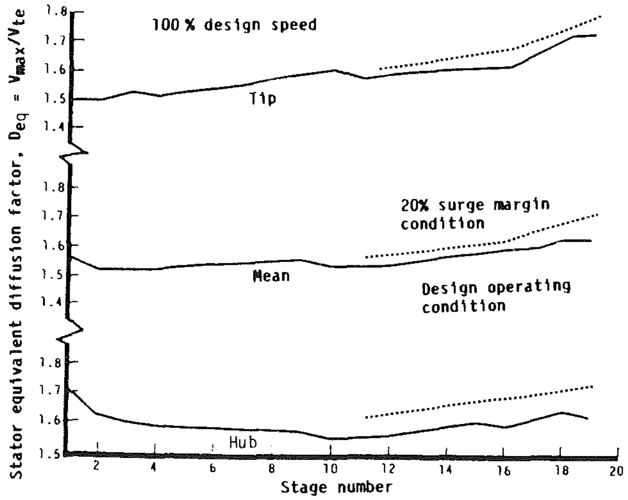

Fig. 4-5 Variation of the stator equivalent diffusion factor from design to 20 percent surge margin operating conditions

ciated with the airfoil geometry resulting from the incidence angle distributions of Figs. 4-1 and 4-2.

Figures 4-4 and 4-5 show the stagewise radial distribution of D_{eq} for the rotors and stators, respectively. Forward-stage rotor and aft-stage stator values are aggressive, but, as stated earlier, it is anticipated that these levels of high diffusion can be accommodated by customizing the airfoil contours. Also shown in Figs. 4-4 and 4-5 are the projected increased levels of D_{eq} at the 20 percent surge margin operating point. The improved diffusion capability of the customized airfoil contours will be beneficial in attaining these off-design D_{eq} levels and providing the compressor with the capability to achieve 20 percent surge margin.

Dynamic Analysis. To ensure that the detailed design configuration was structurally sound, a dynamic analysis (using the state-of-the-art finite element code) was performed on blade rows throughout the compressor. The objective was to identify the maximum airfoil aspect ratio that is acceptable from the point of view of structural integrity as well as the passage diffusion capacity. The criteria for dynamic acceptability were that all rotor first bending-mode natural frequencies be above second engine order. For stators, the criteria were that the first bending frequency not be near the first engine order. The criteria for the limiting passage diffusion capacity were similar to those presented in Koch's paper [2].

This part of the study helped to define airfoil thickness/chord ratios and the minimum acceptable length of the compressor. Minimizing the length reduces endwall skin friction drag, shafting dynamics problem, and probably, overall compressor cost. Details of this are presented in [3].

Detailed Design Configuration. Relative to the preliminary design configuration reviewed in Section III, all of the previously mentioned design refinements of airfoil incidence, thickness/chord ratio, solidity, aspect ratio, and axial gaps along with minor changes in airfoil swirl distributions, produced the detailed design configuration presented in Fig. 4-6.

Comparing the compressor flow path of the preliminary design configuration of Fig. 3-3 with that of Fig. 4-6 shows that a substantial reduction in overall compressor length has been affected in the detailed design configuration. Stagewise distributions of key design aerodynamic and geometric param-

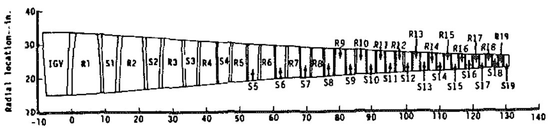

Fig. 4-6 Detailed design configuration flow path

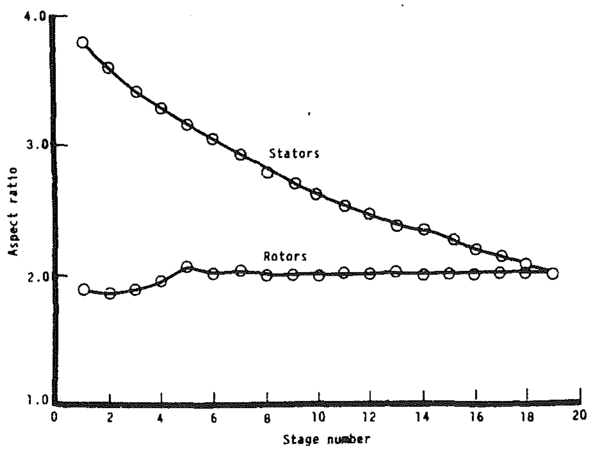

Fig. 4-7 Detailed design configuration stagewise distribution of rotor and stator aspect ratio

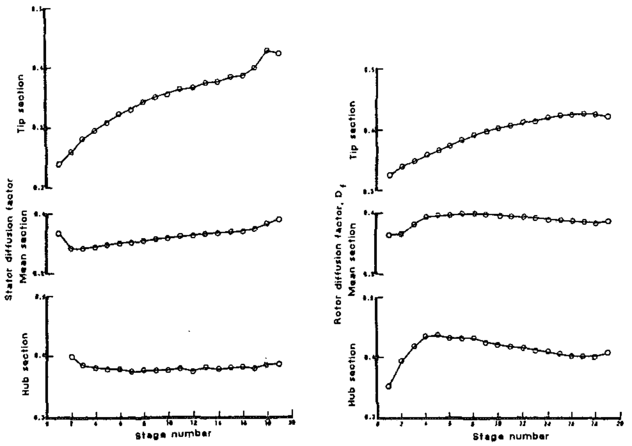

Fig. 4-8 Detailed design configuration stagewise distribution of diffusion factors

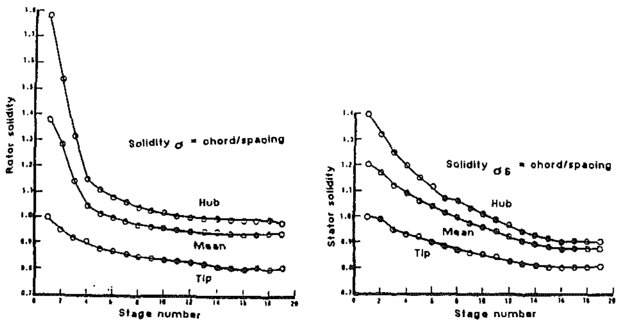

Fig. 4-9 Detailed design configuration stagewise distribution of solidity

eters for the detailed design configuration are illustrated in Figs. 4-7–4-9.

The detailed design configuration can be categorized as being a conventionally designed compressor with relatively high specific flow, subsonic, high aspect ratio, fairly lightly loaded, very low solidity design features. Results of these design studies show that the optimum values of design parameters such as stage loading, hub/tip radius ratio, and swirl are similar to industrial compressors in service today. The predicted design point performance for the detailed design configuration is:

• Overall adiabatic efficiency	88.8 percent
• Overall polytropic efficiency	92.1 percent
• Surge margin, SM	20 percent

This projected performance level is considered to be that which would result from experimental development to fine-tune stage matching, high quality airfoils, very good surface finishes, and a blade running tip clearance of 0.02 in.

V Phase III—Advanced Design Concepts

The performance results described in the previous sections have shown that if any significant improvements in efficiency are going to be realized, they are going to be the result of integration of advanced airfoil design concepts into the aerodynamic design process. In any compressor blade row design, the principal contributors in total pressure loss are the following:

- *Cascade Profile Loss*—due to viscous effects on airfoil surfaces.
- *Endwall Loss*—due to viscous three-dimensional boundary layer flows resulting in pressure loss on the endwalls, formation of energy dissipating secondary corner vortices, and high incidence on airfoil leading edges submerged within the wall boundary layer.
- *Tip Clearance Loss*—losses associated with the blade tip clearance leakage flow along with the casing boundary layer fluid contained and dissipated within the tip leakage vortex core.
- *Shock Loss*—total pressure losses associated with deceleration through a shock positioned in front of or within airfoil passage

The detailed design configuration is essentially a subsonic compressor design; consequently, the impact of shock loss on overall compressor efficiency was not a major consideration. On the other hand, the means to control or reduce profile, endwall, secondary, and tip clearance losses are a major concern if the efficiency level predicted for the EPRI detailed design configuration is to be improved.

Although several advanced airfoil concepts were reviewed (see [3]), only the the following three concepts were considered potentially beneficial for reducing aerodynamic losses:

- *Customized or Velocity-Controlled Airfoils*—These airfoil shapes minimize suction surface diffusion loss and maximize the static pressure rise capability of an airfoil.
- *Stator End Bends*—This concept has shown promise by unloading the stator endwall region and by improving the incidence on the portion of the airfoil submerged in the wall boundary layer.
- *Swept-Forward Leading Edge Stators*—This concept reduces endwall region loss by inducing a migration of high-momentum fluid to the stator endwall region.

The performance potential of velocity-controlled airfoils (VCA) and stator end bends was estimated with the aid of Allison's advanced design tools. A detailed description of the design methodology and analytical procedures adopted for incorporating the VCA and stator end bends into the detailed design configuration is presented in the following text.

Velocity-Controlled Airfoils. The VCA concept, which aims at optimizing the streamwise distribution of suction surface diffusion, was applied to the airfoil sections not subjected to strong three-dimensional effects (i.e., away from the endwall regions).

This concept could be extended to the endwall region, but that would require a fully three-dimensional viscous analysis.

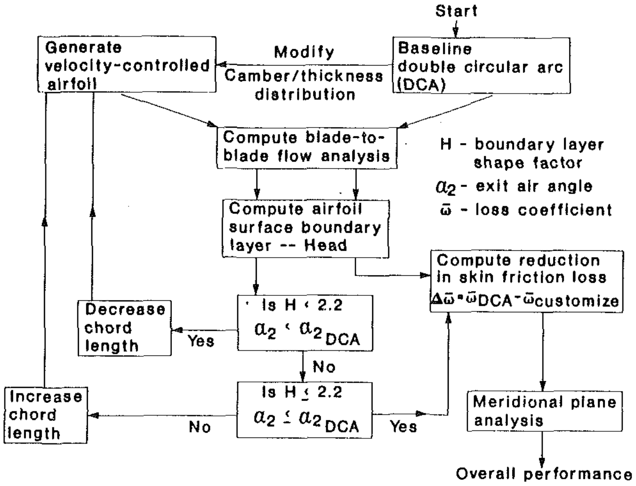

Fig. 5-1 Overall logic for optimizing airfoil geometry

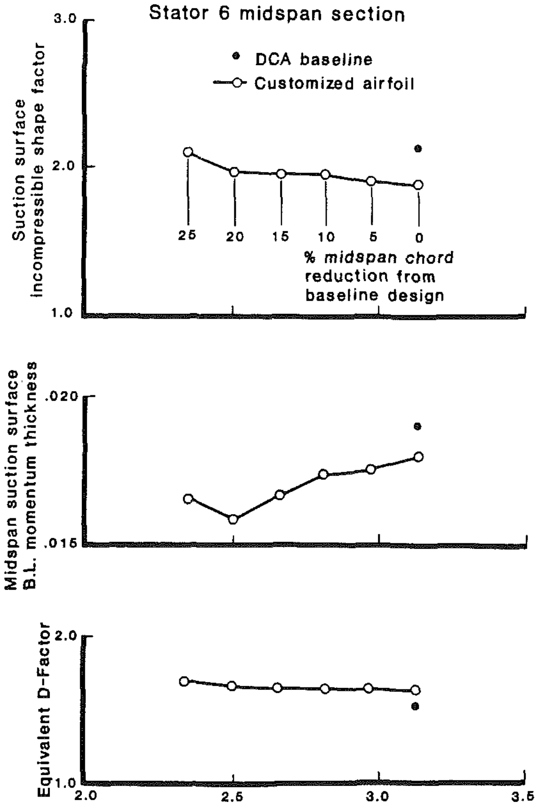

Fig. 5-2 Influence of midspan chord reduction on stator 6 customized airfoil section

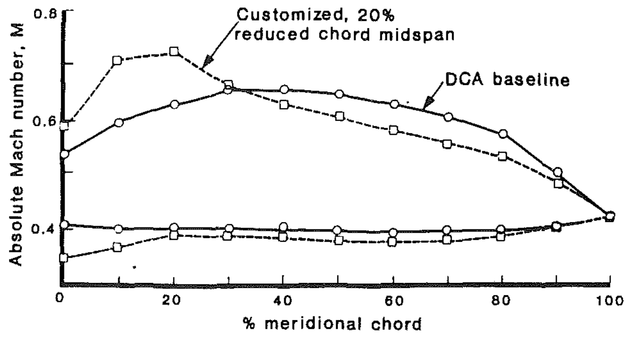

Fig. 5-3 Comparison of stator 6 surface Mach number distribution on baseline DCA and customized reduced chord midspan airfoil sections

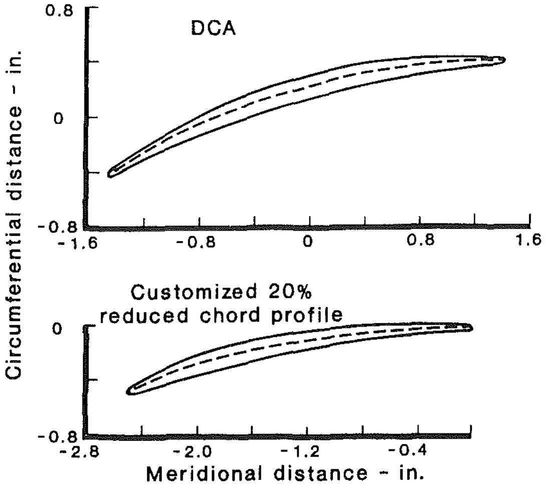

Fig. 5-4 Stator 6 midspan DCA and customized profile sections

To generate VCA sections, the customized blade generation program (CBG) was combined with two-dimensional blade-to-blade flow analysis code (BBFA) and an integral-momentum boundary layer analysis. The BBFA is a fast analysis capable of handling variation in streamtube height, boundary layer blockage, loss, and local supersonic bubbles. The scheme, based on the streamline curvature technique, has been validated against cascade data and other computational schemes and is extensively used to design axial compressor airfoils. The boundary layer analysis, which is merged with BBFA, is based on the well-known Head's momentum-integral technique [4].

The design methodology adopted for the present study involved iteratively updating the airfoil shape to minimize the boundary layer skin friction loss while ensuring that the suction surface boundary layer does not separate. The following design criteria were used:

- The trailing edge shape factor, H, is less than or equal to 2.2. This is to ensure that the boundary layer remains attached to the airfoil surface.
- The computed exit flow angle for the customized airfoil remained equal to that of the baseline circular arc meanline airfoil. This design requirement ensured that the inlet swirl to the downstream rotor would remain unchanged.

Figure 5-1 shows the overall logic employed to arrive at the optimized VCA sections.

Figure 5-2 shows, for stator 6, the impact of (1) customizing the midspan profile to optimize diffusion, and (2) the influence of chord (solidity) reduction on key boundary layer and aerodynamic parameters relative to the baseline circular arc midspan sections. These results illustrate that a 20 percent reduction in chord is possible for the customized airfoil and produces a substantial decrease in trailing edge shape factor and momentum thickness relative to the baseline midspan section. In other words, customizing has produced a lower solidity, slightly more heavily loaded airfoil that is less susceptible to flow separation and should perform more efficiently than a baseline midspan section.

Figure 5-3 shows the midspan suction surface Mach number distribution for the baseline and the customized profile with a 20 percent reduction in chord length.

Customizing moves the loading forward on the airfoil, thus effecting a more gradual diffusion to the trailing edge with attendant reduction in skin friction loss.

Midspan DCA and the 20 percent reduced chord customized sections are illustrated in Fig. 5-4.

The reduction in skin friction or profile loss resulting from the use of velocity-controlled airfoils was estimated by computing the suction and pressure surface boundary layer characteristics at the stator trailing edge. The expression, developed in [5] for this purpose, is as follows:

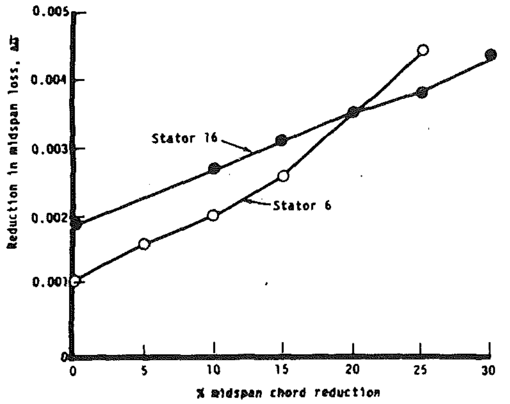

Fig. 5-5 Influence of midspan chord reduction of customized airfoils on midspan loss reduction

$$\Delta\omega = \left\{\frac{\theta}{C}\frac{\sigma}{\cos\beta}\left[\frac{\left(1+\frac{H+1}{3H-1}\right)}{\left(1-\frac{\theta}{C}\frac{\sigma H}{\cos\beta}\right)^{3}}\right]\right\}_{\text{Baseline}_{\text{DCA}}} - \left\{\frac{\theta}{C}\frac{\sigma}{\cos\beta}\left[\frac{\left(1+\frac{H+1}{3H-1}\right)}{\left(1-\frac{\theta}{C}\frac{\sigma H}{\cos\beta}\right)^{3}}\right]\right\}_{\text{Customized}_{\text{airfoil}}} \tag{5-1}$$

Results of the reduction in midspan loss computation for the customized airfoil sections (stators 6 and 16) are presented in Fig. 5-5. They show that a 20 percent reduction in chord length, relative to the baseline DCA section, produces a decrease in the midspan profile loss coefficient of 0.0035 for both stators 6 and 16.

The foregoing loss model demonstrated that a 0.0035 reduction in stator midspan loss coefficient could be realized by the implementation of reduced midspan chord customized stator airfoils. This design concept and its associated reduction in loss was applied to all stator rows.

Stator End Bends. The stator end bend configurations were evolved from an iterative computation that included a new secondary flow loss model formulation.

This subsection contains highlights of this loss model, followed by a brief description of the procedure that optimized the stator reset angle geometry.

The method adopted for computing the change in endwall losses and deviation angle resulting from the incorporation of stator end bends was based on a secondary flow analysis (SECOND) similar to the classical secondary flow theory [6]. However, unlike in [6], the analysis employed here takes into account the viscous flow effects on the development of secondary vorticity through the blade row.

An implicit finite difference scheme is used to integrate the secondary vorticity equation along an inviscid midpassage streamline passing through the edge of the boundary layer. The integration is carried out twice, once for the hub region and once for the casing region. The numerical procedure for the secondary flow computation needs the following input:

- *Inlet Boundary Layer Profile*—This is computed with the aid of Allison's three-dimensional endwall boundary layer code (SHROUD) described in [7].
- *Inviscid Blade Passage Velocity Distribution at the Edge of the Boundary Layer*—BBFA was used for this computation.
- *Spanwise Distribution of Exit Flow Angle*—This is available from the meridional plane flow analysis (MFA).

The secondary vorticity distribution computed in the exit plane of the stator was determined by solving the Poisson equation for the secondary flow stream function as formulated in [8]. By integrating secondary velocity in the circumferential direction, deviation angles associated with endwall boundary layer secondary flow can be evaluated.

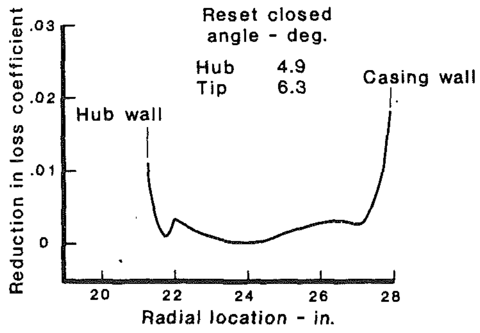

d to stator end bends.

Fig. 5-6 Stator 10 reduction in loss coefficient due to stator end bends

To compute the total pressure loss associated with the secondary flow, it was assumed that all of the secondary flow kinetic energy is dissipated and converted into total pressure loss. This heuristic assumption needs some refinement and validation for computing the secondary flow loss in a cascade; however, it is considered to provide a reasonable approximation for estimating the change in secondary flow loss between the geometries. Based on this assumption, the reduction in total pressure loss coefficient, due to the influence of reset closed stator end bends, was evaluated.

Results of the loss reduction computation for a representative stator (stator 10) are shown in Fig. 5-6. Also, for all of the geometries evaluated, the change in deviation angle was of the order of one degree. The loss computation shows a fairly large reduction in the endwall region, with levels depending on the amount of reset and where the subject stator was positioned in the compressor. Also, the region located a small distance from the hub and tip wall experienced a sizable reduction in loss coefficient.

Loss contours of the type shown in Fig. 5-6 were developed for all 19-stage stators and used in the iterative process that produced the final stator reset geometry for all stages. The following stepwise procedure was used to optimize the reset angles and define the end bend geometry to be factored into the detailed design configuration:

1 With the aid of the three-dimensional endwall boundary layer code (SHROUD) stator inlet flow angle was calculated inside the endwall boundary layer.

2 The endwall sections (hub and tip) of each stator were reset to ensure that the incidence in the endwall boundary layer is less than or equal to zero.

3 The secondary flow analysis code (SECOND) was then used to estimate the endwall secondary flow including losses and flow angles for reset and baseline blades.

4 The computed endwall region losses and exit flow angles were then input into the meridional flow analysis (MFA), and the program was run in the predict performance mode. Reduced losses for the customized stator midspan sections were also included in this calculation; thus, the results of this analysis gave the total pressure ratio and efficiency of the complete advanced concept design.

5 If the pressure ratio of advanced design was different from the design intent (14.0:1), the resets were adjusted, and steps (1)-(4) were repeated until the pressure ratio matched the design intent.

A three-dimensional view of the advanced concept compressor design final stator 6 geometry, including end bends in addition to the reduced chord velocity-controlled midspan region, is compared with the baseline DCA airfoil in Fig. 5-7.

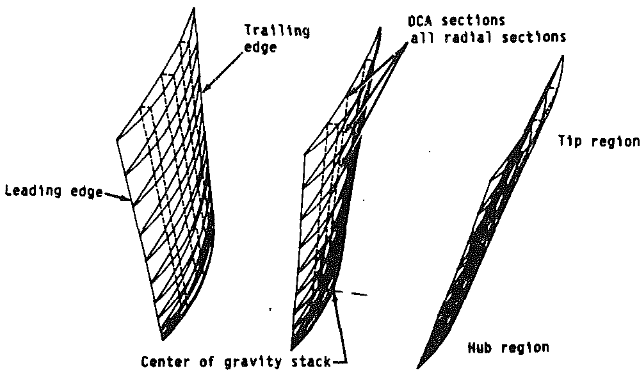

Stator 6 baseline DCA airfoils

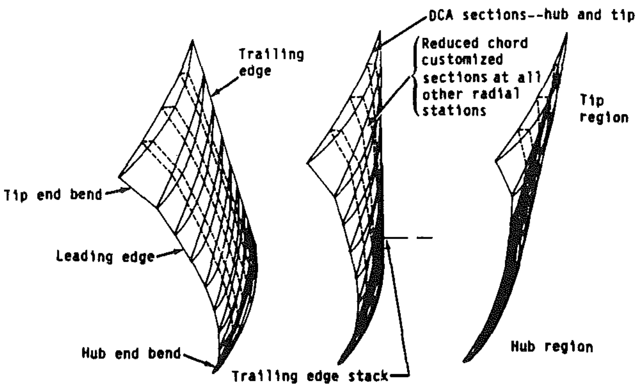

Stator 6 reduced chord, customized midspan section with hub and tip end bend airfoils

Fig. 5-7 Impact of incorporating reduced chord customized midspan sections with hub and tip end bends on stator 6 baseline DCA airfoils: advanced concept compressor design final stator 6 design

Incorporation of the airfoil reset geometry and the respective reduced loss coefficient profiles for the stator end bends and reduced chord customized midspans produced a computed overall advanced concept compressor design adiabatic efficiency of 89.3 percent.

Although no separate investigation was carried out to customize rotor airfoils in the midspan and endwall region, it is expected that incorporation of customized rotor airfoils will produce higher levels of efficiency improvements than that estimated for customized stator airfoils. This is because, for the same change in the boundary layer momentum thickness, the change in the total pressure loss is larger in a rotor than in a stator, due to the higher inlet dynamic head and exit flow angle.[2] Based on this argument, the overall adiabatic efficiency of the advanced concept compressor design is projected to be at least one percent higher than the baseline design. This translates to an adiabatic efficiency of 89.8 percent or a polytropic efficiency of 92.8 percent.

Final Advanced Concept Compressor Design. The design point projected performance of the final advanced concept compressor design is as follows:

• Corrected inlet flow, $W\sqrt{\theta}/\delta$	800 lb/sec
• Pressure ratio, R_c	14.0:1
• Corrected wheel speed, $N/\sqrt{\theta}$	3600 rpm
• Surge margin, SM	20 percent
• Adiabatic efficiency, η_{TT}	89.8 percent
• Polytropic efficiency, η_{poly}	92.8 percent

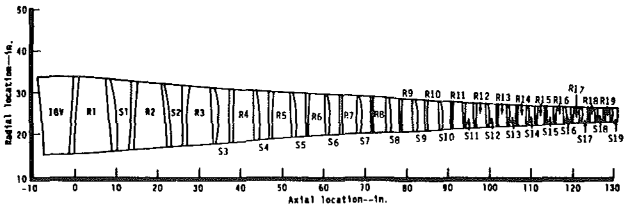

Fig. 5-8 Advanced concept compressor design configuration

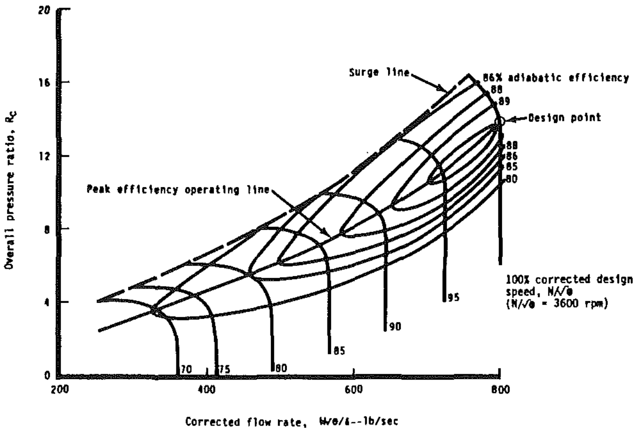

Fig. 5-9 Fixed geometry performance map for EPRI advanced concept compressor design

Figure 5-8 presents the flow path and blading of the advanced concept compressor design.

A performance map was developed for the advanced concept compressor design. The map, presented in Fig. 5-9, illustrates the impact of speed variation on overall performance. The off-design characteristics were estimated with the aid of extensive in-house data base on multistage, fixed-geometry, high-pressure ratio compressors. The EPRI compressor design presented in this paper would be more suitable for a variable-geometry design. For a fixed-geometry situation, it would have been more desirable to unload the front stages of the compressor to allow good surge margin at lower corrected speed.

VI Phase IV—Optimization of Part-Power Operation With Variable Geometry

A variable inlet guide vane (IGV) is commonly used in utility gas turbine compressors in order to (1) improve starting flexibility and (2) improve the heat rate at part-power in a combined cycle. In aircraft gas turbines, it is common to have a number of variable stator stages (in addition to the IGV) to further improve compressor operability at part-power and under changing flight conditions. In a utility gas turbine compressor, the power is reduced at the design rpm (3600) by reducing the inlet flow and pressure ratio through the closure of the IGV and stator vanes.

In order to find the possible improvement in part-flow efficiency, the following three configurations of variable geometry were considered in this study:

1. Variable IGV only.
2. Variable IGV and stators 1-5 in a ganged mode (all vanes reset same number of degrees).
3. Variable IGV and stators 1-5 in a graduated mode. (In this configuration, for each degree rest of IGV, stators 1-5 were reset 5/6, 4/6, 3/6, 2/6, and 1/6 deg, respectively.)

To do this study, the IGV reset was varied from 5 deg to 30 deg. The operating point of each reset was on a constant Rc/W line (which corresponds to constant turbine inlet tem-

---

[2] $\left(\frac{\omega \cos \beta_2}{2\sigma}\right)=\frac{\theta}{C}$, $\omega=\frac{\Delta P_T}{\frac{1}{2}\rho V^2}$.

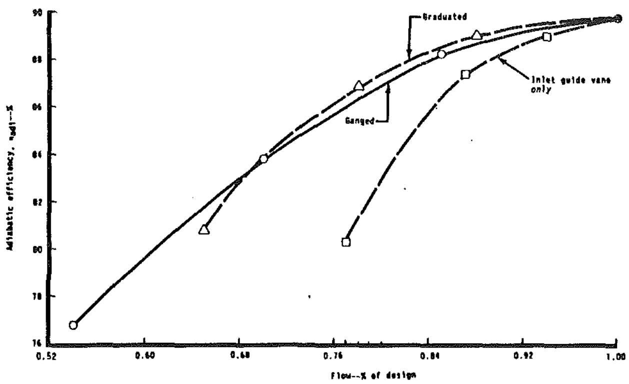

Fig. 6-1 **Efficiency decrement versus flow reduction for three variable-geometry configuration**

perature) prescribed by the design point value. An iterative procedure using the meridional flow analysis code (MFA) was adopted for estimating the mass flow and efficiency corresponding to each reset. Extra losses were added to account for separation due to high incidence; at the same time, the flow was dropped to ensure that the compressor was operating in an unchoked mode.

The primary results of this analysis are presented in Fig. 6-1, which compares the efficiency decrement as a function of flow for the above three variable geometry configurations. It may be seen that either of the two variable stator configurations is highly superior to the IGV-only configuration. At 75 percent flow, there is approximately one-third as much decrement to efficiency as for the IGV-only.

VII Conclusions

Based on the results of this three-phase design study effort to develop an aerodynamic design for a large utility gas turbine engine compressor, the following conclusions can be drawn:

1 Using conventional design techniques, a preliminary compressor design was developed and refined to produce a polytropic efficiency of 92.1 percent. This level of efficiency potential was achieved by having a large number of lightly loaded stages with low solidity airfoils.

2 Several advanced design concepts were investigated, and stator midspan velocity-controlled airfoils, stator end bends, and stator leading edge sweep were shown to hold promise for increasing overall compressor efficiency.

3 Analytical studies on the velocity-controlled stator midspan sections showed that the customized airfoils would operate with less loss and be less susceptible to flow separation, even with a 20 percent reduction in solidity, than a baseline DCA airfoil.

4 Incorporation of geometries and losses associated with stator end bends and stator customized midspan sections resulted in a 0.5 percent improvement in adiabatic efficiency. An additional improvement of 0.5 percent in adiabatic efficiency is expected to result from the customizing of rotor airfoils.

5 Estimated performance of the 800 lb/sec, 14.0:1 pressure ratio EPRI advanced concept compressor design was:

Surge margin, *SM*	>20 percent
Adiabatic efficiency, η_{TT}	89.8 percent
Polytropic efficiency, η_{poly}	92.8 percent

6 Incorporation of variable geometry in the IGV and the first five stators of the advanced concept compressor design demonstrated that the compressor flow could be reduced by 25 percent with a 4 percent efficiency penalty. The corresponding efficiency penalty for the variable IGV-only configuration was estimated to be in excess of 10.7 percent.

References

1 Johnson, I. A., Bullock, R. O., et al., "Aerodynamic Design of Axial Flow Compressors," National Aeronautics and Space Administration, NASA-SP-36, 1965.

2 Koch, C. C., "Stalling Pressure Rise Capacity of Axial Flow Compressor Stages," ASME *Journal of Engineering for Power,* Vol. 103, No. 4, 1981.

3 Bettner, J. L., and Sehra, A. K., "High Efficiency Axial Compressor," EPRI Report No. AP-4943, Dec. 1986.

4 Head, M. R., "Entrainment in the Turbulent Boundary Layer," ARC Technical Report No. RM3152.

5 Lieblein, S., and Roudebush, H., "Theoretical Loss Relationships for Low-Speed, Two-Dimensional Cascade Flow," NACA-TN-3662, Mar. 1956.

6 Squire, H. B., and Winter, K. G., "The Secondary Flow in a Cascade of Airfoils in a Nonuniform Flow," *J. Aero Sci.,* Vol. 18, 1951, pp. 271-277.

7 Bettner, J. L., and Turner, E. R., "Shroud Flow Characteristics," AF-WAL-TR-82-2038, June 1982.

8 Hawthorne, W. R., and Novak, R. A., "The Aerodynamics of Turbomachinery," *Ann. Rev. Fluid Mech.,* Vol. 1, 1969.

M. A. Cherrett

J. D. Bryce

Propulsion Department,
Royal Aerospace Establishment,
Pyestock, Farnborough,
Hants, United Kingdom

Unsteady Viscous Flow in a High-Speed Core Compressor

A probe incorporating a miniature high-frequency response pressure transducer has been traversed behind the first three stages of a high-speed multistage compressor operating at throttle settings corresponding to near choke, peak efficiency, and near surge. A novel method of compensating for transducer temperature sensitivity was employed. Consequently, time-averaged pressures derived from the transducer were found to be in good agreement with pneumatic pressure measurements. Analysis of the unsteady pressure measurements revealed both the periodic and random fluctuations in the flow field. This provided information on rotor-rotor interaction effects and the nature of viscous blade wake and secondary flows in each stage.

Introduction

Further improvements in the efficiency, stage-loading, and stable operating range of compressors rely heavily upon developing improved computational flow modeling and design methods. In turn, the improvement of computational methods requires detailed measurements to be taken in representative compressors to create data bases for code validation. A number of workers have undertaken detailed measurements of the flow in axial compressors. Ravindranath and Lakshminarayana (1980) and Lakshminarayana and Govindan (1981) investigated the characteristics of blade wake development while Dring et al. (1982), Lakshminarayana et al. (1986) and Dong et al. (1987) extended these studies to include secondary flow development in the hub and tip regions. Further, Wagner et al. (1978) and Zierke and Okiishi (1982) investigated the effects of blade row interaction. These studies have done much to improve understanding of axial compressor flows and highlighted the complex, viscous, three-dimensional, interactive, and unsteady nature of the flowfield. However, all the cited studies have been limited to low-speed research compressors. Therefore, although blade geometry and stage loading may be representative of aero-engine compressors, flow Mach numbers are not. Published measurements taken in high-speed compressors have been limited to single-stage transonic fans (Weyer and Hungenberg, 1975; Ng and Epstein, 1985; Gertz, 1986). These indicate significant flow field unsteadiness that has been attributed to shock oscillation. While the mechanism producing these unsteady effects has yet to be explained fully, it is likely that their existence, along with quasi-steady compressibility effects, have a significant influence upon the development of wake and endwall flows. Matters are further complicated by complex interaction between the stages within multistage compressors. Hence it is necessary to carry out investigations within high-speed (engine-relevant) compressors in order to improve the fundamental understanding of the phenomena involved and to explore the applicability of low-speed data for computational code validation.

The Propulsion Department of the Royal Aerospace Establishment (RAE) is engaged in a program to employ high-frequency response instrumentation to investigate unsteady viscous flow within high-speed axial compressors and fans. The work reported in this paper documents preliminary activity "piggy-backed" onto a major conventional rig measurement program reported by Ginder (1991). A single sensor probe, containing a high-frequency response pressure transducer, was used to measure the unsteady flow within the first three stages of the five-stage C147 high-speed core compressor. Errors due to temperature sensitivity of the pressure transducer were corrected using a combination of careful calibration and an expedient method of measuring transducer diaphragm temperature. This system is described, together with the data acquisition and processing techniques employed. The time-averaged pressures derived from the compensated transducer signals are compared with conventional pneumatic measurements to illustrate the success of the method. Finally, unsteady pressure measurements taken at rotor exit are presented and discussed.

Experimental Procedure

The Test Compressor. The RAE C147 research compressor is a high-speed machine representative of the rearmost stages of a military or highly loaded civil core compression system. It is of large scale, approximately 1 m in diameter, with extended axial gaps between the blade rows to allow detailed traverse measurements to be taken. To date it has been tested in two configurations. The initial build, reported by Calvert et al. (1989), was a four-stage compressor of 4.0 pressure ratio. For the second build, the blading was redesigned using the RAE S1-S2 calculation system (also described by Calvert et al., 1989) and a zero stage added. Because the second build evolved from a four-stage predecessor, the convention of referring to stages as stage 0 through to stage 4 is adopted throughout the paper. This five-stage machine was designed to deliver a pressure ratio of 6.4 at a flow rate of 49.5 kg/s and is referred to by Ginder (1991).

Contributed by the International Gas Turbine Institute and presented at the 36th International Gas Turbine and Aeroengine Congress and Exposition, Orlando, Florida, June 3-6, 1991. Manuscript received at ASME Headquarters February 19, 1991. Paper No. 91-GT-91. Associate Editor: L. A. Riekert.

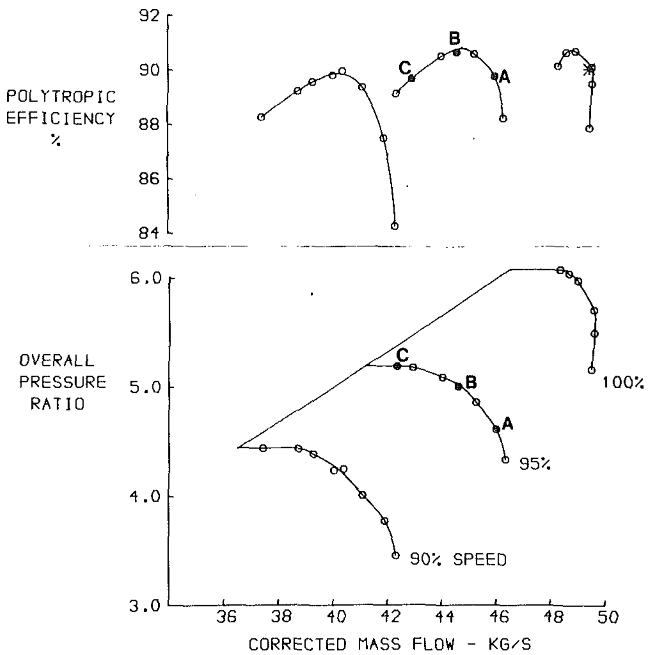

Fig. 1 The performance characteristics of C147 build 2; A, B, and C denote traverse operating points

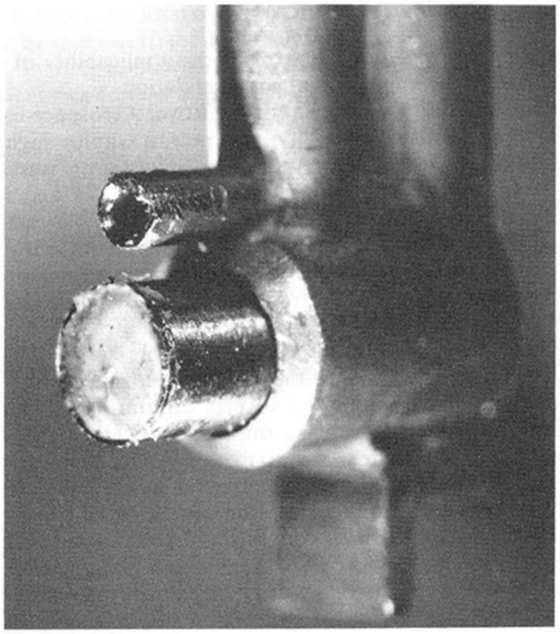

Fig. 2 The pressure probe used during the traverses

Table 1

Compressor/probe geometry			
	Rotor 0	Rotor 1	Rotor 2
Tip speed (m/s)*	313	304	299
Blade passing frequency (Hz)*	8623	10588	11680
Mean chord (m)	0.0590	0.0485	0.0440
Mean aspect ratio	1.559	1.296	1.034
Mean pitch-chord ratio	0.551	0.550	0.552
$\frac{\text{Probe diameter}}{\text{Mean pitch}}$	0.049	0.059	0.065
$\frac{X^{**}}{\text{Mean rotor chord}}$	0.154	0.195	0.208

* At 95% speed

** X = Mean streamwise distance from rotor trailing edge to the transducer diaphragm.

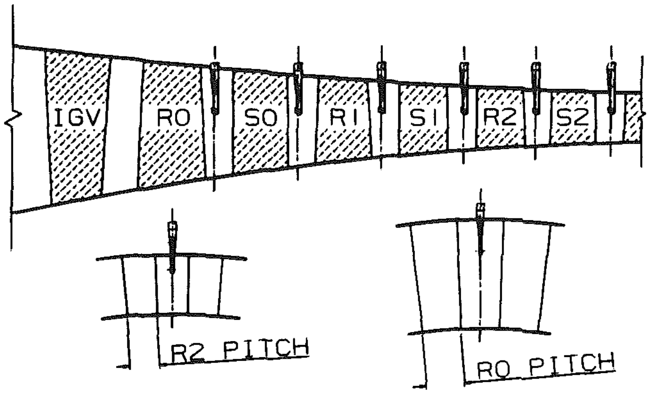

Fig. 3 The size of the traverse probe relative to the compressor

Unsteady pressure measurements were taken in the second build of C147. Radial traverses were carried out behind rotors 0, 1, and 2 while the compressor was operating at three conditions on the 95 percent speed characteristic. The operating points, defined as near choke (A), peak efficiency (B) and near surge (C), as shown in Fig. 1.

Traverse Probes. Three probes were used to take the unsteady pressure measurements. Each contained a single Kulite type XCQ-062 (344 kPa absolute) pressure transducer of 1.57 mm diameter mounted 1.65 mm below a pneumatic Pitot tube as shown in Fig. 2. Two of the transducers employed a 0.07-mm-thick coating of silastomer rubber to protect the pressure sensing diaphragm while the third utilized a perforated metal (Kulite "type B") screen for protection. The relative size of the probes to the rotor rows traversed is shown in Fig. 3 and detailed in Table 1 along with additional information concerning the blade rows.

Unpublished measurements, taken by Oxford University for RAE, show that the natural resonant frequency of the "coated" transducer diaphragm was of the order of 500 kHz. The frequency response characteristics ensured a "flat" amplitude response with negligible phase angle lag over a 100 kHz bandwidth. Frequency response of the "screened" transducer is determined by the natural resonant frequency of the screen geometry coupled to that of the cavity between the screen and the transducer diaphragm. Measurements made by Oxford University show that this is 50–60 kHz. Measurements taken behind rotor 0 in C147, with both types of transducer, indicate that both measurements were generally in good qualitative and quantitative agreement but that some attenuation of peak unsteadiness levels occurred with the screened transducer.

The sensitivity of a screened transducer probe to yaw angle was measured in an open jet wind tunnel at a Mach number of 0.7. Results showed that transducer output varied by less than 1 percent over ±10 deg range. Prior to each rotor exit traverse in C147, the probe was yawed to ensure that its axis was aligned with the mean flow at 50 percent span. Limited checks carried out at other radii indicated that deviation from the mean midspan flow angle was less than ±10 deg.

Transducer Temperature Compensation. The strain gage elements, which sense transducer diaphragm deflection, are prone to changes in resistance with temperature because of their high thermal coefficient of resistance. Consequently

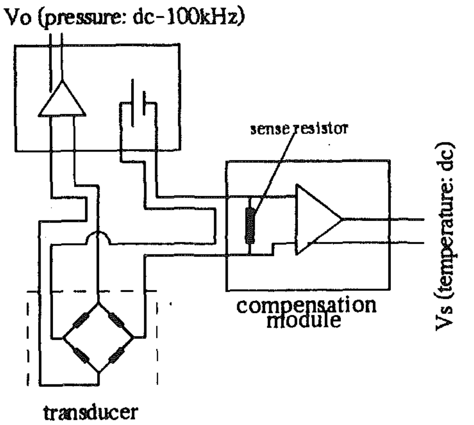

Fig. 4 *The transducer temperature error compensation system*

Table 2

Radial and circumferential extent of the rotor exit measurements

	Rotor 0	Rotor 1	Rotor 2
No. of radial measurements.	16	16	12
Measurement nearest tip (% span).	97.1	98.6	91.8
Measurement nearest hub (% span).	2.7	6.9	7.7
No. of rotor blade passages recorded.	4.3	5.4	6.0
Transducer type used	'B-screen' & silastomer coated.	Silastomer coated.	'B-screen'

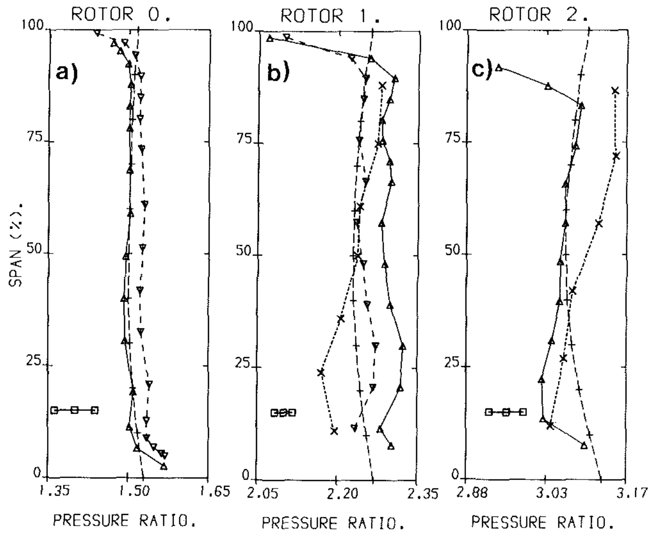

Fig. 5 **Time-averaged transducer total pressure ratio measurements taken at peak efficiency operation**

transducer pressure sensitivity and null-pressure reading (or zero-offset) change with temperature. Hence large pressure measurement errors arise if the sensitivity and zero-offset, used to convert the transducer output voltage to pressure, are not those associated with the temperature experienced by the transducer diaphragm. At RAE Bedford, Welsh and Pyne (1980) showed that if the transducer is excited with a constant voltage, changes in strain gage bridge resistance induce a change in current drawn by the bridge, which can in turn be sensed as a change in voltage across a "sense" resistor placed in series with the transducer polarizing voltage. A prototype system using this approach was produced that coupled commercially available signal conditioning amplifiers to a sense resistance monitoring module (Fig. 4). Setting-up of the system required the transducer to be immersed in a chamber where both pressure and temperature could be varied. Hence, the transducer pressure sensitivity and zero-offset were determined from the transducer output (*Vo*) for a range of constant temperatures. Similarly the sense voltage (*Vs*), which is independent of pressure, was monitored. Subsequently, the variations of *Vo* and *Vs* with temperature were coded into a data processing program. Hence, during the compressor measurements, *Vs* was used to determine transducer diaphragm temperature, which in turn was used to derive the associated pressure sensitivity and zero-offset in order to convert *Vo* to the correct absolute pressure level.

Ideally the calibrated performance of a transducer should not change significantly with time. However measurements taken at RAE have recorded transducer "calibration drift" corresponding to up to 1 percent of transducer full-scale deflection over several weeks. This calibration drift was quantified by calibrating the transducers several times during the test series. Further information concerning the compensation system and how it is implemented together with details of the transducer characteristics are reported by Cherrett (1990).

The transducer temperature compensation and signal conditioning units were installed adjacent to the compressor rig. The signals were amplified and transmitted to the data acquisition system in the facility control room.

Data Acquisition and Processing. The unsteady pressure signals were recorded on a CEL Datalab Multitrap data acquisition system. This consists of three main components: a waveform recorder, a 20 Mbyte Winchester disk, and a host Hewlett Packard HP310 microcomputer. The RAE system is capable of sampling 17 channels simultaneously at up to 1 MHz with better than 10-bit accuracy. The analogue-to-digital storage modules have a capacity of 256 K samples per channel and can be partitioned into segments that allow the capture of data sampled to a once-per-revolution trigger signal. This trigger pulse was generated using an inductive probe to monitor the passing of a ferrite-tipped rotor 2 blade. On receipt of the first pulse, the recorder is switched on to record the passing of a predetermined number of blade passages and the data stored in the first memory segment. After a complete rotor revolution, the second trigger pulse initiates sampling of the same blade passages, and the data stored in the second memory segment. This continues until the memory is full. The data are then downloaded to the microcomputer where they are processed on-line, to yield the periodic and random fluctuations within the pressure signals and subsequently stored on disk. The equations used to derive these parameters are given in the Appendix. The signals were captured at a 1 MHz sample rate, which allowed 115 samples per rotor 0 passage and 85 per rotor 2 passage. Typically records of 512 μs duration were captured on receipt of each trigger pulse and the data base built up over 128 consecutive rotor revolutions. Table 2 details the number of blade passages covered by each 512 μs data set and also indicates the radial extent of the measurements and the type of probe used (i.e., "B-screen" or silastomer rubber coated). Continuous instantaneous data records were also captured typically recording two complete rotor revolutions. These were subsequently subjected to spectral analysis.

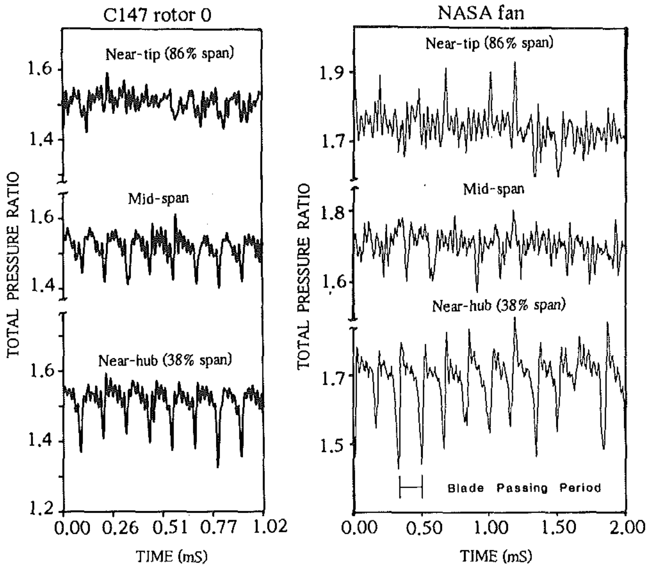

Fig. 6 Comparison of instantaneous total pressure ratio measurements taken behind C147 rotor 0 and a NASA Lewis transonic fan

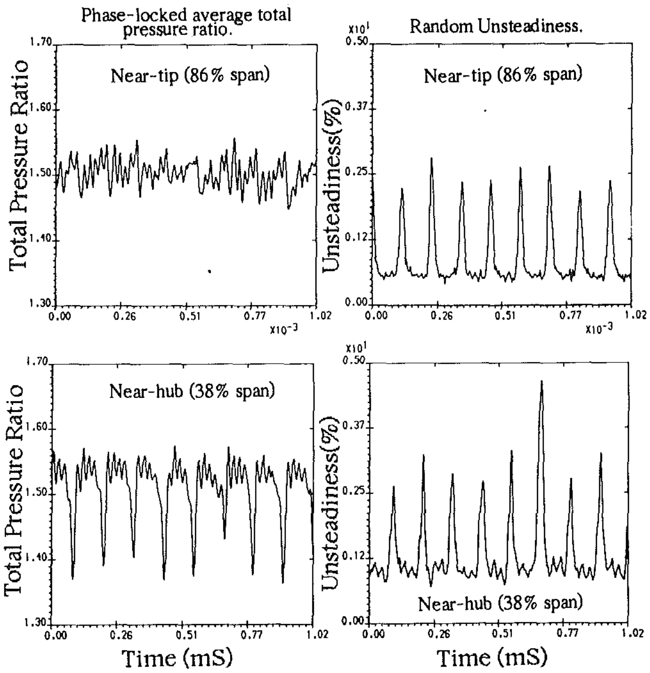

Fig. 7 Phase-locked average total pressure ratio and random unsteadiness measurements taken behind C147 rotor 0 at peak efficiency operation

Test Results

Time-Averaged Total Pressure Measurements. Figure 5 illustrates the spanwise variation of time-averaged total pressure measured at exit from rotor 0 while operating at peak efficiency (point B). The data are expressed as a ratio of total pressure at compressor inlet. The results contain an indication of the extent of absolute pressure uncertainty due to calibration drift. This corresponds to ±2.7 percent of reading behind rotor 0, ±0.8 percent behind rotor 1, and ±1.1 percent behind rotor 2. These figures could have been reduced by carrying out more frequent calibrations. Figures 5(*a*) and 5(*b*) show that agreement between the transducer and adjacent Pitot measurements is within 2 percent behind rotors 0 and 1, respectively.

In addition to this encouraging quantitative agreement, the profiles are in excellent qualitative agreement. Because the adjacent Pitot is far less sensitive to yaw angle than the transducer, it may be concluded that no significant errors were incurred in the transducer measurements through traversing at a fixed yaw angle. Unfortunately no adjacent Pitot measurements were taken at peak efficiency operation behind rotor 2. However, those taken behind rotor 2 at near choke flow and near surge were found to agree with the transducer results to within 0.5 percent. Pneumatic measurements were also taken using Pitot tubes mounted on the stator blades. At peak efficiency operation only those at rotor 1 and rotor 2 exit were available. Figures 5(*b*) and 5(*c*) show that agreement with the transducer data is less satisfactory than the adjacent Pitot measurements, especially away from midspan. However, it should be noted that these two measurements were not made in the same meridional plane and hence not in the same position relative to upstream stator wakes and other blade row interference effects. While overall agreement between the transducer and pneumatic measurements is encouraging and instils confidence in the temperature error compensation system, it must be borne in mind that the pneumatic measurements are subject to uncertainty due to possible averaging effects in the transmission lines. These are difficult to quantify accurately. Hence the transducer measurements are further compared with predictions arising from throughflow analysis. This shows that agreement to within 1.75 percent is found behind rotor 0 and rotor 2 at midspan. Agreement behind rotor 1 is within 2.75 percent.

It is interesting to note the development of the extent of the annulus wall flows. At the tip, significant total pressure deficit (associated with the endwall boundary layer and over-tip leakage flow) is noted beyond 95 percent span in the rotor 0 measurements. In the rotor 1 and 2 measurements dynamic head decrease begins at 90 and 82 percent span, respectively. At the hub however, rather than the expected fall in total pressure within the hub-annulus boundary layer, it is observed to increase. This is thought to be a consequence of kinetic energy imparted to the fluid by the rotating endwall.

Rotor Exit Unsteadiness. Figure 6 shows the instantaneous total pressure fluctuations measured behind rotor 0 at peak efficiency operation (point B). Data at three radii are illustrated, i.e., near the hub (38 percent span), at midspan (51 percent span), and near the tip (86 percent span). Included in the same figure are measurements reproduced from Ng and Epstein (1985) taken at the same spanwise stations behind a NASA Lewis transonic fan. The NASA rotor is fully transonic with inlet relative Mach numbers varying between 0.75 and 1.35 from hub-to-tip while C147 rotor 0 inlet relative Mach number varies from 0.79 at the hub to 0.94 at the tip at 95 percent speed. Despite the difference in shock system strength between the two rotors, the instantaneous pressure measurements are remarkably similar in qualitative appearance. That is, at the hub, the blade wakes are clearly visible as strong absolute total pressure deficits while their strength diminishes with increasing span. Most striking are the pressure oscillations in the inviscid core flow. These are noted in both rotor flows and are characterized by a frequency three or four times that of blade passing. Spectral analysis of the C147 rotor 0 data confirm that the oscillations are primarily second and third harmonics of rotor 0 blade passing. No frequencies that could be attributed to downstream rotors are evident. In the NASA rotor they were seen to increase in amplitude by a factor of two in moving from hub to tip. In the C147 case, although they appear more significant because of the decrease in wake total pressure deficit, the intrapassage oscillations are of similar amplitude over much of the blade span. Quantitatively the strength of the intrapassage oscillations represents 6 percent of the NASA rotor total pressure ratio at the tip and 4 percent at midspan. The C147 intrapassage oscillations represent 4–5 percent of rotor total pressure ratio.

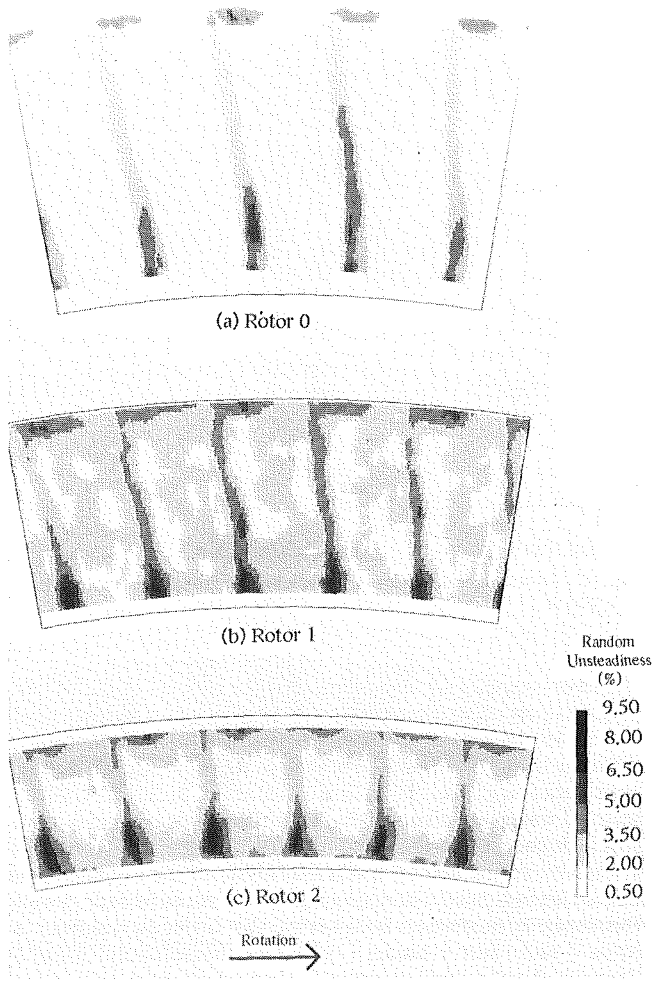

Fig. 8 Random unsteadiness measured at near choke flow (i.e., Condition A)

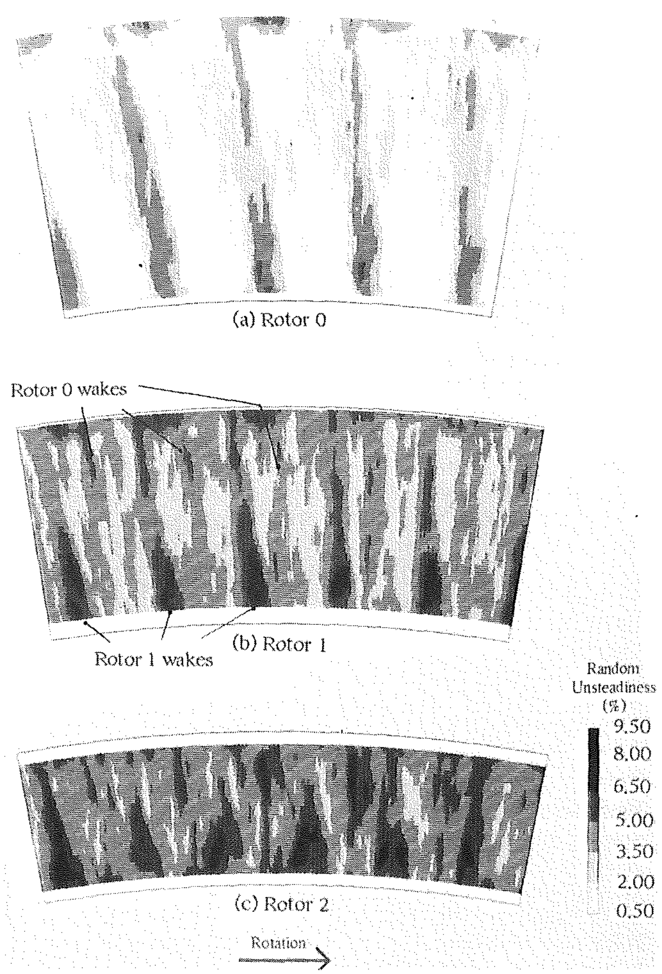

Fig. 9 Random unsteadiness measured at near-surge flow (i.e., Condition C)

Figure 7 presents the data derived from processing the 128 segments of instantaneous data sampled in response to the once-per-revolution trigger pulse. Measurements at 38 and 86 percent span taken behind C147 rotor 0 during peak efficiency operation (point B) are shown. Both periodic (or phase-locked average) pressure variations and the random unsteady pressure fluctuations are depicted. It is evident from comparison of these data with the C147 measurements in Fig. 6 that the intrapassage pressure oscillations are largely stable in the rotor relative frame and characterized by stable differences from one passage to another. These observations are in variance with the measurements of Ng and Epstein (1985) where the ensemble averaging process, to derive the phase-locked average total pressure field, obliterated much of the intrapassage oscillation amplitude for the NASA rotor. Hence Ng and Epstein (1985) and Gertz (1986), in discussion of similar findings associated with two other transonic fan rotors, concluded that the oscillations were unstable in the rotor relative frame. Ng and Epstein postulated that the intrapassage total pressure fluctuations arose from oscillation of the rotor shock system. Further, Epstein et al. (1986) suggested that the shock oscillation was driven by vortex shedding in the blade wakes. The arguments presented for shock oscillation being the primary mechanism are certainly convincing and it is difficult to imagine what other unstable system would give rise to similar results. However, as the Mach numbers associated with C147 rotor 0 are so much lower than for the transonic fans tested it is difficult to reconcile the quantitative similarity of the measurements. However, as the C147 intrapassage oscillations are stable in the rotor relative frame, while they were not in the other transonic rotors, it is conceivable that some degree of aerodynamic coupling is present in the C147 field that was not present in the other compressors.

The Effects of Compressor Operating Point and Blade-Row Interaction. In the previous discussion, the phase-locked average (i.e., periodic) and random unsteady pressure fluctuations were presented as single pressure–time traces. However, while this form of presentation lends itself to detailed consideration of the measurements, it does not provide a convenient way of assessing the overall flow field. Hence, the data have been further processed to provide a pictorial representation of the flow field variation with span. The random unsteadiness field provides a convenient tool with which to assess the salient features and spatial extent of the viscous flow field and as such will be considered first. The phase-locked average field will then be discussed. It should be noted that the phase-locked average pressure field must be interpreted carefully because the pressure variations depicted represent absolute total pressure variations while it is intuitive to think in terms of the rotor relative field during their interpretation. Consequently these data are somewhat limited in the information they can provide concerning the aerodynamic performance of the associated rotor. This underlines the need to employ probes capable of measuring unsteady flow angle variation, with which it would be possible to transpose the measurements to the rotor relative field. To this end, RAE have procured two dynamic yawmeters of the type described by Cook (1989). These will permit measurement of unsteady tangential flow angle. In addition RAE are engaged in collaborative programs to fund the development of probes capable of resolving three dimensional unsteady flow angle variation. Such probes will play an important role in future work at RAE.

The effects of compressor operating point on the viscous field, manifest in the random unsteadiness data, are shown in Figs. 8 and 9, where measurements taken at near-choke flow (A) and near surge (C) behind all three rotors are presented respectively. Data taken at peak efficiency (B) have been excluded for brevity, although it should be pointed out that these measurements bear close qualitative agreement to those at near choke flow. The random unsteady fluctuations in Figs. 8 and 9 are quantified as a percentage of local rotor exit total pressure.

It can be seen from Fig. 8 that the random unsteady flow fields recorded behind all three rotors at near-choke flow exhibit strong similarities. The flow is repeatable from one passage to another and is characterized by three regions: (1) an inviscid intrablade core flow, (2) two-dimensional-type blade wakes away from the endwalls, (3) regions of vortical activity in the hub endwall-wake area and toward the tip casing. The vortical activity toward the hub is thought to indicate separation of the suction surface/endwall boundary layer due to low-momentum fluid in the endwall boundary layer being swept into the endwall corner under the action of the cross-passage pressure gradient. The extent of these features bears close similarity to high loss regions measured behind low-speed rotors by Dring et al. (1982), Lakshminarayana et al. (1986), and Dong et al. (1987). The measurements shown in Fig. 8 indicate that these features are offset slightly to the pressure surface side of the two-dimensional wake flow; this is probably a consequence of different amounts of underturning within the endwall-corner separation relative to that in the two-dimensional wake and the fact that the measurements were taken some way downstream of the rotor trailing edge (see Table 1). It is interesting to note that the spatial extent of these features increases within successive rotors. At the blade tip, the regions of high random unsteadiness appear to be positioned toward the pressure surface side of the nearest blade wakes. However, the blade tip clearance levels measured during the test series indicated tip gaps of the order of 1 percent span, which is not consistent with the existence of large scraping vortices (Inoue and Kuroumaru, 1989). Rather, it is thought that the observed vortical flow is due to tip clearance flow and that the observed spatial position, relative to the two-dimensional-type wake, is a consequence of cross-passage migration and the fact that the measurements were taken downstream of the rotor trailing edge. Indeed, this is borne out by measurements (not presented in this paper) of the unsteady static pressure field over C147 rotor 0 in which it was possible to trace cross-passage migration of the tip clearance flow consistent with the above observations.

Attention is now turned to the near surge data (C) shown in Fig. 9. While increasing compressor pressure ratio from point A to B (not illustrated in this paper) was accompanied by very little change in the qualitative and quantitative extent of the random unsteady flow fields, the change in moving from point B to C is marked. Behind rotor 0, the previously unadulterated core flow (Figs. 8*a* and 9*a*), is now characterized by markedly higher levels of unsteadiness particularly between 50 percent span and the tip. Also, the rotor 0 blade wakes are seen to thicken (to 20–25 percent pitch compared with 10–15 percent at lower pressure ratios). In addition, the wake flow is not so readily characterized by the distinct coexistence of hub-endwall corner separation and two-dimensional-type wakes, the former being notably less in evidence. Similar behavior has been observed in measurements taken behind a low-speed compressor rotor operating at different pressure ratios by Dring et al. (1982).

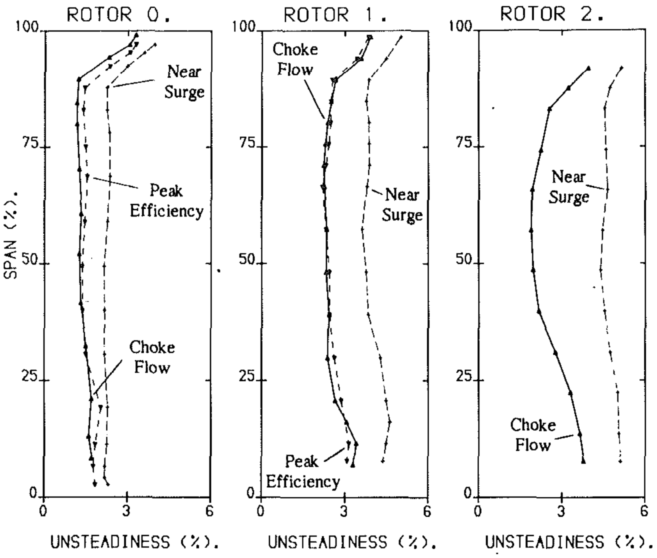

Fig. 10 Time-averaged random unsteadiness measured behind rotors 0, 1, and 2

The corresponding near-surge data for rotors 1 and 2 become progressively more complex due to the effect of upstream blade wakes. In the rotor 1 measurements (Fig. 9*b*) it is possible to attribute the most influential upstream wakes to rotor 0 through consideration of their pitch and orientation, although chopped stator 0 wakes are also visible. That the major upstream blade row influence, other than that of rotor 1, originated from rotor 0 was also confirmed by spectral analysis of the instantaneous data. This indicated a strong fundamental rotor 0 blade passing frequency component. Because of the different number of rotor 0 and rotor 1 blades (79 and 97, respectively) some of the rotor 0 wakes pass unimpeded through the rotor 1 passages whereas others impinge upon, or pass close to, the rotor 1 blades themselves. Where close proximity occurs the rotor 1 unsteadiness is augmented, particularly in the endwall corner separation. As this phenomenon is related to the number of blades in each row, a cyclic "waxing and waning" of the rotor 1 unsteadiness is set up about the annulus, which in this case is locked to the rotating reference frame. Detailed examination of the data reveals maximum endwall-corner separation unsteadiness levels are attained every 6 to 7 rotor 1 blades. This is commensurate with rotor–rotor interaction between stages 0 and 1.

Examination of the rotor 2 field (Fig. 9*c*) reveals that a number of upstream blade wakes are evident. Spectral analysis of instantaneous data reveals that the most influential upstream influences are rotor 0 and rotor 1. However, whereas it was quite possible to arrive at the same conclusion through subjective examination of the rotor 1 field, this is not possible for rotor 2 due to the complexity of the data. The progressive increase in complexity of the rotor exit field is commensurate with the attention being shifted to more embedded rotor flows. Figure 10 presents the circumferentially averaged variation of random unsteadiness with span for the rotor exit flows at the three operating points. These data reinforce the trends already noted in the discussion of Figs. 8 and 9. This is: (1) the level of random unsteadiness rises within successive rotor flows at the same operating point, (2) increasing compressor pressure ratio (i.e., rotor loading) increases the intensity of the random unsteady field. However, the increase in intensity of the random unsteady field becomes more marked as compressor surge is approached.

Attention is now turned to the a-c-coupled phase-locked average (periodic) pressure field. Qualitatively the appearance of the data did not change dramatically with operating con-

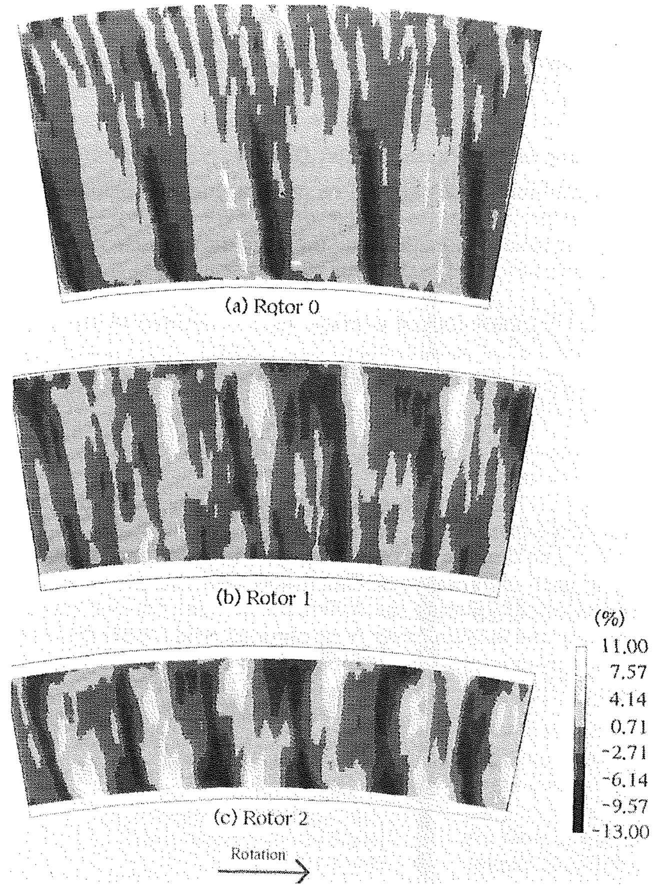

Fig. 11 AC-coupled phase-locked average total pressure expressed as a percentage of local time-averaged total pressure; all measurements were taken at near-surge operation

dition as observed for the random unsteadiness data. Hence, only the near surge (point C) data are presented in Fig. 11 where they are quantified as a percentage of local time-averaged total pressure at rotor exit. However, while the data at different operating points are qualitatively similar, their quantitative extent (particularly behind the embedded rotors) did not change.

From Fig. 11(*a*) it can be seen that the excess total pressure oscillations, noted previously in Figs. 6 and 7, dominate the rotor 0 intrapassage flow field. Further, these features are aligned radially to form coherent structures extending over much of the blade span. However, they are particularly apparent in the lower half of the annulus. The quantitative extent of the range of maximum to minimum pressures encountered in the flow field is similar at the three operating conditions. That is, for the rotor 0 measurements illustrated in Fig. 11(*a*), they range between +5.7 and −11.0 percent while figures of +6.5 to −14.1 percent and +6.8 to −10.9 percent were recorded at near maximum flow and peak efficiency operation. The rotor 1 and 2 periodic flow fields are significantly different from the rotor 0 data in their appearance. While the rotor 0 field is quantitatively repeatable from one passage to another, this is not so behind rotors 1 and 2. That is, although radially aligned intrapassage total pressure excess regions are seen behind rotors 1 and 2, the flow is dominated by localized pressure excess regions. These are found toward the tip in the rotor 1 field and at both hub and tip behind rotor 2. The strength of these features is not repeatable from one passage to another. Rather, their intensities "wax and wane" over a wavelength consistent with the rotor–rotor interaction observed in the random unsteadiness path described earlier. The peak pressures attained in these regions equate to 9.9 and 10.6 percent of the local time-averaged total pressures encountered behind rotor 1 and rotor 2, respectively. These peak pressure levels were noted to increase significantly with increasing compressor pressure ratio. That is, the peak pressure excess levels in the rotor 1 field increase by 18 percent in moving from choke flow to near surge. Similarly a 24 percent increase accompanies the movement from choke flow to near surge operation behind rotor 2. Of course in the absence of unsteady flow angle measurements it is difficult to ascertain to what extent these absolute total pressure excess regions are manifestations of relative flow angle or relative total pressure fluctuations. However, it is interesting to note that in the rotor 1 measurements the strongest total pressure excess regions in the phase-locked average field were found in the same blade passages that contained the most vigorous hub-corner vortical activity as measured in the random unsteadiness field.

Conclusions

A high-frequency response total pressure probe has been traversed behind the first three rotors of a high-speed five stage core compressor (C147). Measurements were taken at maximum flow, peak efficiency, and near surge operation at 95 percent speed. Major conclusions resulting from the work are outlined below.

1 A reliable and easily implemented approach to correcting semiconductor transducer temperature errors has been applied successfully. Comparisons between transducer time-averaged pressure measurements, and pneumatic pressure measurements show agreement within 2–3 percent. This gives confidence in the temperature compensation system but more work is required to improve accuracy.

2 In the case of the first stage rotor, strong total pressure oscillations of 3–4 times blade passing frequency were observed in the inviscid intrapassage flow. These appeared stationary in the rotor relative frame, which is at variance with measurements taken in single-stage transonic fans.

3 The random unsteady pressure flow field measured at exit from the C147 rotors showed the nature and extent of the inviscid core flow as well as the viscous wake, hub-endwall separation, and over-tip leakage flow regions. The wake and hub-endwall separation regions increased in size and level of random pressure unsteadiness as compressor pressure ratio was increased.

4 At a given compressor operating point, the tip-leakage and hub-endwall separation regions were found to grow in size, for successive downstream rotors, and hence occupy a more significant portion of the rotor exit flow.

5 In the embedded stage rotors, strong rotor–rotor interaction effects were noted. These induced waxing and waning of the size and intensity of the zones of peak unsteadiness at the hub and excess phase locked total pressure at the tip.

6 An encouraging start has been made in a continuing program of research into unsteady compressor flows at RAE Pyestock. However, single sensor probe measurements provide limited information. Two-dimensional and three-dimensional multisensor probes will be used in future compressor research at RAE.

References

Calvert, W. J., Ginder, R. B., McKenzie, I. R. I., and Way, D. J., 1989, "Performance of Highly Loaded HP Compressor," ASME Paper No. 89-GT-24.

Cherrett, M. A., 1990, "Temperature Error Compensation Applied to Pressure Measurements Taken With Miniature Semiconductor Pressure Transducers in a High-Speed Research Compressor," *Proceedings, 10th Symposium on Measuring Techniques for Transonic and Supersonic Flows in Cascades and Turbomachines*, Von Karman Inst., Brussels, Belgium.

Cook, S. C., 1989, "Development of a High Response Aerodynamic Wedge Probe and Use on a High-Speed Research Compressor," *Proceedings of the Ninth International Symposium on Air Breathing Engines*, Vol. 1, pp. 1113–1125.

Dong, Y., Gallimore, S. J., and Hodson, H. P., 1987, "Three-Dimensional Flows and Loss Reduction in Axial Compressors," ASME *Journal of Engineering for Gas Turbines and Power*, Vol. 109, pp. 354–361.

Dring, R. P., Joslyn, H. D., and Hardin, L. W., 1982, "An Investigation of Axial Compressor Aerodynamics," ASME *Journal of Engineering for Power*, Vol. 104, pp. 84–95.

Epstein, A. H., Gertz, J. B., Owen, P. R., and Giles, M. B., 1986, "Vortex Shedding in Compressor Blade Wakes," *Proceedings, Transonic and Supersonic Phenomena in Turbomachines*, AGARD-CP-401, pp. 5.1–5.13.

Gertz, J. B., 1986, "Unsteady Design-Point Flow Phenomena in Transonic Compressors," MIT Report GTL No. 188.

Ginder, R. B., 1991, "Design and Performance of Advanced Blading for a Highly-Loaded HP Compressor," ASME Paper No. 91-GT-374.

Inoue, M., and Kuroumaru, M., 1989, "Structure of Tip Clearance Flow in an Isolated Axial Compressor Rotor," ASME JOURNAL OF TURBOMACHINERY, Vol. 111, pp. 250–256.

Lakshminarayana, B., and Govindan, T. R., 1981, "Effects of Rotation and Blade Incidence on the Properties of the Turbomachinery Rotor Wake," AIAA Paper No. AIAA-81-0054.

Lakshminarayana, B., Sitaram, N., and Zhang, J., 1986, "End-Wall and Profile Losses in a Low-Speed Axial Flow Compressor Rotor," ASME *Journal of Engineering for Gas Turbines and Power*, Vol. 108, pp. 22–31.

Ng, W. F., and Epstein, A. H., 1985, "Unsteady Losses in Transonic Compressors," ASME *Journal of Engineering for Gas Turbines and Power*, Vol. 107, pp. 345–353.

Ravindranath, A., and Lakshminarayana, B., 1980, "Mean Velocity and Decay Characteristics of the Near and Far-Wake of a Compressor Rotor Blade of Moderate Loading," ASME *Journal of Engineering for Power*, Vol. 102, pp. 535–548.

Wagner, J. H., Okiishi, T. H., and Holbrook, G. J., 1978, "Periodically Unsteady Flow in an Imbedded Stage of a Multistage Axial-Flow Turbomachine," ASME Paper No. 78-GT-6.

Welsh, B., and Pyne, C. R., 1980, "A Method to Improve the Temperature Stability of Semiconductor Strain Gauge Transducers," *Journal of Physics E Science Instrumentation*, Vol. 13, pp. 816–818.

Weyer, H. B., and Hungenberg, H. G., 1975, "Analysis of Unsteady Flow in a Transonic Compressor by Means of High-Response Pressure Measuring Techniques," *Proceedings, Unsteady Phenomena in Turbomachinery*, AGARD-CP-177.

Zierke, W. C., and Okiishi, T. H., 1982, "Measurement and Analysis of Total-Pressure Unsteadiness Data From an Axial-Flow Compressor Stage," ASME *Journal of Engineering for Power*, Vol. 104, pp. 479–488.

APPENDIX

Processing of the Phase-Locked Data

The multiple instantaneous records captured in response to the once-per-revolution trigger pulse were processed in the following manner to determine the periodic (phase-locked average) and random fluctuations within the pressure transducer signals.

(*a*) The phase-locked average $V(t)$ is defined as the sum of the individual instantaneous data records meaned over the number of rotor revolutions (or instantaneous data records) recorded, i.e.,

$$V(t)=\frac{1}{N}\sum_{k=1}^{N} V_k(t)$$

where: $V_k(t)$ = instantaneous data values; N = number of rotor revolutions.

(*b*) The random unsteadiness $V_r(t)$ is determined by comparing each instantaneous data trace with the phase-locked average trace, squaring the difference between the two traces, summing and meaning over N revolutions, and finally dividing by the time-averaged d-c component of the phase-locked average $V(t)$, i.e.,

$$V_r(t)=\frac{\sqrt{\frac{1}{N}\sum_{k=1}^{N} (V_k(t)-V(t))^2}}{V(t)}$$

NASA Low-Speed Centrifugal Compressor for Three-Dimensional Viscous Code Assessment and Fundamental Flow Physics Research

M. D. Hathaway
Propulsion Directorate,
U.S. Army Aviation Systems Command,
Cleveland, OH 44135

J. R. Wood
NASA Lewis Research Center,
Cleveland, OH 44135

C. A. Wasserbauer
Sverdrup Technology, Inc.,
Lewis Research Center Group,
Cleveland, OH 44135

A low-speed centrifugal compressor facility recently built by the NASA Lewis Research Center is described. The purpose of this facility is to obtain detailed flow field measurements for computational fluid dynamic code assessment and flow physics modeling in support of Army and NASA efforts to advance small gas turbine engine technology. The facility is heavily instrumented with pressure and temperature probes, in both the stationary and rotating frames of reference, and has provisions for flow visualization and laser velocimetry. The facility will accommodate rotational speeds to 2400 rpm and is rated at pressures to 1.25 atm. The initial compressor stage being tested is geometrically and dynamically representative of modern high-performance centrifugal compressor stages with the exception of Mach number levels. Preliminary experimental investigations of inlet and exit flow uniformity and measurement repeatability are presented. These results demonstrate the high quality of the data that may be expected from this facility. The significance of synergism between computational fluid dynamic analyses and experimentation throughout the development of the low-speed centrifugal compressor facility is demonstrated.

Introduction

Centrifugal compressors are widely used in a variety of applications because of their ability to achieve high pressure ratios in a relatively short axial distance and due to their rugged construction. Centrifugal compressors are characterized by long blade channels that have complex in- and out-of-plane turns with high curvature. Due to the complex turning of the flow and rotational forces, strong secondary flows are produced. These secondary flows, along with separated flow regions, lead to strong crossflow velocity components, which transport fluid with low momentum and high total-pressure loss into the mainstream. Attempts to model the complex three-dimensional nature of the flow in centrifugal compressors have generally met with little success, although recently a number of investigators have produced numerical computations that show great promise (e.g., Moore and Moore, 1989, 1990; Hah et al., 1988, 1990; Dawes, 1988). Designers of centrifugal turbomachines have therefore had to rely heavily on empiricism. As a result, centrifugal compressors tend to have lower efficiencies than their axial-flow counterparts. For significant improvements in the aerodynamic performance of centrifugal compressors to be realized, a more detailed understanding of the fundamental flow physics is required. Synergism between experiments and computational analyses will undoubtedly play a key role in developing this understanding.

With the advent of more powerful computers and further development of three-dimensional Navier-Stokes codes, the numerical prediction of centrifugal compressor flow fields has greatly improved. However, assessment of the ability of these predictions to model accurately the fundamental physics of centrifugal compressor flow fields is largely lacking. Krain and Hoffman (1989), Eckardt (1976), Joslyn et al. (1991), Young et al. (1987), Japikse and Karon (1989), Hayami et al. (1985), and Johnson and Moore (1980, 1983) have reported measurements of flows in centrifugal compressors that have shed light on many aspects of centrifugal compressor flow physics. Most of these investigations, however, have lacked the detailed measurements required to assess the ability of three-dimensional viscous codes to model accurately the fundamental flow physics. Furthermore, none of the investigations yielded detailed information within viscous regions (i.e., blade boundary layers).

The NASA Low-Speed Centrifugal Compressor (LSCC) was designed and built in order to obtain the detailed measurements that are required to assess three-dimensional viscous codes and to develop more sophisticated models of the various physical phenomena occurring in centrifugal compressors. This paper describes the major components and instrumentation of the

---

Contributed by the International Gas Turbine Institute and presented at the 36th International Gas Turbine and Aeroengine Congress and Exposition, Orlando, Florida, June 3-6, 1991. Manuscript received at ASME Headquarters February 20, 1991. Paper No. 91-GT-140. Associate Editor: L. A. Riekert.

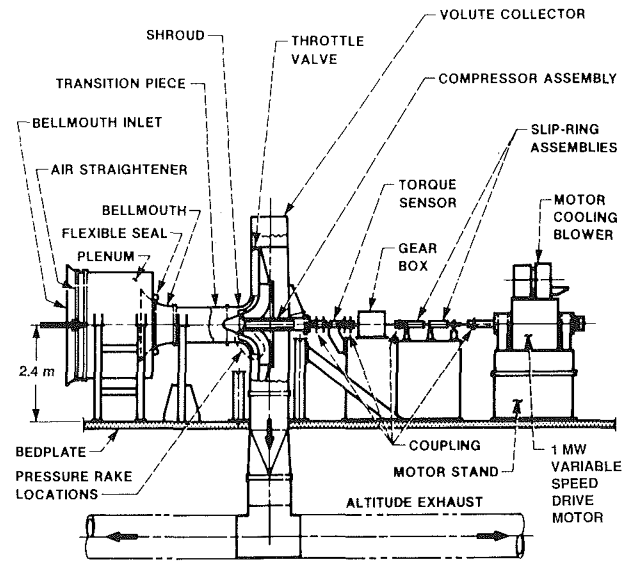

Fig. 1 Low-speed centrifugal compressor facility

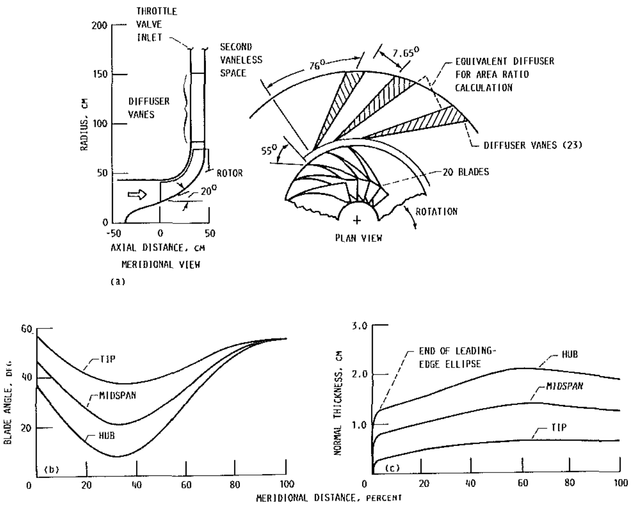

(a) MERIDIONAL AND PLAN VIEW.
(b) BLADE MEAN CAMBER LINE DISTRIBUTION FOR HUB, MIDSPAN, AND TIP.
(c) BLADE NORMAL THICKNESS DISTRIBUTION FOR HUB, MIDSPAN, AND TIP.

Fig. 2 Configuration of low-speed centrifugal compressor initial stage design

low-speed centrifugal compressor facility. Experimental investigations of inlet and exit flow uniformity, measurement repeatability, and overall performance are also presented, which demonstrate the high quality of the data that may be expected from this facility. The significance of synergism between computational fluid dynamic (CFD) analyses and experimentation throughout the development of the low-speed centrifugal facility is demonstrated.

Facility

Figure 1 depicts the major elements of the low-speed centrifugal compressor facility. Air is drawn in from a filtered vent in the roof past a bank of steam pipes and louvers designed to control the air temperature to within ±1°F for mass flows up to 45 kg/s. The flow then enters the facility room and is then drawn into the plenum through a bank of flow straighteners contained between two mesh screens. The air passes through a specially designed bellmouth with a 10:1 area contraction. The turbulence levels at the bellmouth exit are expected to be less than 1 percent, and will be measured in the near future along with the impeller inlet turbulence profile. The flow then enters the compressor and exits through a specially designed throttle valve at the entrance to the collector. The throttle valve consists of two concentric rings with overlapping holes drilled in each ring which slide relative to each other to produce a throttle. This throttle valve design was chosen to minimize circumferential asymmetry in the exit static pressure distribution such as is typically found in scroll-type collectors. The bellmouth, inlet transition piece, and shroud flow path were machined together to minimize any boundary layer disturbance due to a step in the flow path. Altitude exhaust capability of 660 mm Hg (26 in. Hg) of vacuum enables mass flow rates up to 45 kg/s. A 1.115 MW (1500 hp) electric motor and gear reducer drives the facility to a maximum speed of 2400 rpm. A complete description of the facility is provided by Wood et al. (1983).

Test Compressor

During the design of the low-speed compressor several conditions were imposed. First, the design should reflect the geometric and dynamic parameters that were deemed to be representative of modern compressors, and second, the blade lean should not be so severe that laser access would be precluded. The design parameters for the low-speed centrifugal compressor are given in Table 1 while Table 2 shows a comparison of some low-speed centrifugal compressor stage parameters with those from several high-speed centrifugal compressor stages. Meridional hub and shroud contours for the rotor and a plan view of the stage geometry are shown in Fig. 2, along with the impeller blade angle and normal thickness distributions for the hub, midspan, and tip sections.

During the same time frame that the LSCC compressor was being designed, NASA Lewis embarked on a companion program to obtain detailed internal data on a high-speed centrifugal compressor. Stage 2 in Table 2 was selected as the candidate for the high-speed tests since it has very high performance for a centrifugal compressor. Stage 2 was analyzed with a quasi-three-dimensional inviscid program, with total pressure loss through rotor specified, in order to determine the level of loading used. A loading parameter representing the cross-channel pressure gradient divided by the mean flow dynamic head was used as a measure of the tendency of the hub wall boundary layer to migrate toward the blade suction surface. The design of the low-speed centrifugal blading was set, using the above-mentioned quasi-three-dimensional code, so that a level of the loading parameter similar to that of Stage 2 would be obtained. At that time also, it was estimated that by the time the low-speed compressor facility became operational, parabolic marching codes would be available for analysis with no capability to calculate impellers with splitter blades. Conse-

Nomenclature

b = impeller exit blade height, cm
D = impeller exit tip diameter, cm
H = ideal head rise, m
N = rotational speed, rad/s
Q = volumetric flow rate, m^3/s
R = radius, cm
U = rotor blade speed, m/s
V = absolute velocity, m/s
W = relative velocity, m/s
Z = axial coordinate, cm
ν = kinematic viscosity, m^2/s

Subscripts

0 = plenum
1 = impeller inlet survey station
2 = impeller exit survey station
fs = free stream
r = radial direction
t = impeller tip
z = axial direction

quently, it was decided to design the initial impeller for less diffusion than might have been used otherwise in order to reduce the risk of streamwise separation, and with no splitter blades (although an even number of blades was selected for the impeller). This decision resulted in the absolute flow angle from the impeller being lower than the other stages as evidenced by the flow angles into the diffusers.

Although the virtues of the various types of diffusers used on centrifugal compressors—pipe, wedge, cambered vane—are extolled by various proponents, the area of basic interest is the region where the flow transitions from the somewhat axisymmetric impeller exit flow with potential perturbations from the diffuser vanes to a nearly one-dimensional flow in the diffuser channel downstream of the throat. Data obtained from the diffuser of a 4:1 pressure ratio centrifugal stage designed for automotive applications indicated that after the initial rapid adjustment of the flow around the uncovered region of the diffuser upstream of the throat, the isobars became nearly orthogonal to the diffuser channel midline. This same tendency was observed for the diffuser of Stage 1 at flow rates away from diffuser choke. The wedge diffuser of the LSCC is similar to that for Stage 2 and was designed with a throat area consistent with a pressure recovery coefficient from the impeller exit to the throat of 0.20.

Table 1 Design parameters for low-speed centrifugal compressor

Stage:	
Flow rate, kg/sec.	30
Total pressure ratio	1.166
Estimated efficiency	0.90
Rotor:	
Total pressure ratio	1.173
Estimated efficiency	0.934
Rotor speed	1920[1]
Inlet hub-tip radius ratio	0.5
Inlet span, cm	22.042
Inlet tip radius, cm	42.939
Exit radius, cm	76.200
Exit blade height, cm	13.740
Axial clearance, cm	0.5725[2]
Number of blades	20
Reynolds number, $U_t D_t/\nu_0$	16x10^6
Inlet tip relative Mach number	0.31
Exit absolute Mach number	0.29
Diffuser:	
Rotor exit/vane inlet radius ratio	1.08
Number of vanes	23
Leading-edge circle radius, cm	0.409
Pressure surface angle, deg	72
Suction surface angle, deg	80
Channel divergence, deg	7.65
Area ratio	2.9
Throat blockage, percent	2
Throat Mach number	0.263
Exit Mach number	0.08
Inlet Reynolds number, $b_t V_t/\nu_t$	10^6

[1] all testing was conducted at 1862.4 rpm (97% design speed).

[2] later reduced to 0.254 cm.

The choice of axial tip clearance reflected the previous experience obtained with small stages, such as Stage 1 in Table 2. The closest clearance tested with that stage was 3.9 percent of exit blade height, which was 0.02 cm. Also, since centrifugal stages tend to "flower" (i.e., deflect axially) significantly with rotational speed, the actual running clearance at part-speed conditions can be much more than the design value. For example, for Stage 2 the design clearance was 2.5 percent, but the clearance should be about 3.3 percent at 80 percent design speed—a speed that might be typical of a cruise condition—if the change in deflection with speed is considered. Stage 4 suffered even more axial deflection because of its higher design speed and even though it was tested at 2.4 percent clearance, the calculated value at 80 percent speed would be more like 6.1 percent clearance if active clearance control were not used. The choice of what clearance to use for the LSCC became a matter of selecting a low-clearance representative of large machines or a rather large clearance more representative of small machines (and part-speed conditions). Since it was anticipated that the duration of the test program would be long term, it was decided to provide for flexibility in varying tip clearance by selecting a large clearance for initial tests and reducing it for later tests. Obviously, adding material such as balsa wood to the impeller tips is preferable to machining a 1360 kg impeller.

Instrumentation

The facility instrumentation includes a torque meter for measuring overall work input, and standard aerodynamic probes for surveying the distributions of total pressure and temperature as well as flow pitch and swirl angle of the impeller inlet and exit stations and diffuser exit station. Information on probe locations is given in Fig. 3 and Table 3. Five-hole pressure probes (Fig. 4) are used for the aerodynamic probe surveys. The probes are controlled by a PC-based automatic positioning system capable of simultaneous control of up to 16 drive motors (typically, eight auto-yawing single-axis-positioning actuators).

Mass flow through the impeller is determined from a calibration curve of actual versus theoretical mass flows. The actual mass flow was obtained from detailed aerodynamic surveys of the bellmouth exit boundary layer. The theoretical mass flow rate is determined by averaging measurements from eight equally spaced static pressure taps around the circum-

Table 2 Comparison of low-speed centrifugal compressor to typical centrifugal compressors

Parameter	Low speed	Stage 1	Stage 2	Stage 3	Stage 4
Stage:					
Flow rate, kg/sec	30	1.05	4.5	4.5	11.4
Rotational speed, rpm	1920	68 384	21 789	36 366	23 000
Pressure ratio	1.17	6.0	4.0	8.0	8.0
Reynolds number, $U_t D_t/\nu_0$	16x10^6	6.3x10^6	15x10^6	21x10^6	33x10^6
Specific speed, $N\sqrt{Q}/H^{3/4}$	104	89	76	93	93
Rotor:					
Rotor exit tip speed, m/sec	153.2	576.4	504	612	612
Rotor inlet tip relative Mach number	0.31	1.15	0.88	1.39	1.39
Blade angle at inlet tip, deg	56.3	61.4	55.8	61.4	61.4
Blade angle at exit, deg	55	35	50	40	40
Exit blade height, cm	13.740	0.516	1.666	1.049	1.659
Ratio of exit axial clearance to exit blade height	0.042[3]	0.039	0.025	0.023	0.023
Vaneless space:					
Radius ratio	1.08	1.16	1.08	1.07	1.07
Percent contraction	0	0	1.8	7.2	7.2
Diffuser:					
Type	Wedge	Cambered Vane	Wedge	Cambered Vane	Cambered Vane
Number of vanes	23	27	24	21-21	21-21
Inlet flow angle, deg	70	73	75.1	73	73
Area ratio	2.9	2.5	2.75	1.6	1.6
Channel divergence, deg	7.65	7	7.8	6	6
Inlet Reynolds number, $V_t b_t/\nu_t$	10^6	0.3x10^6	0.6x10^6	1.6x10^6	1.6x10^6

[3] later reduced to 0.020

Table 3 Probe survey station locations

STATION	Z, cm	R, cm
0	-76.581	0.0 to 43.511
1	-20.373	13.905 to 43.511
2a	32.205 to 46.543	81.280
2b	32.205 to 46.543	95.872
3	32.205 to 46.543	167.640

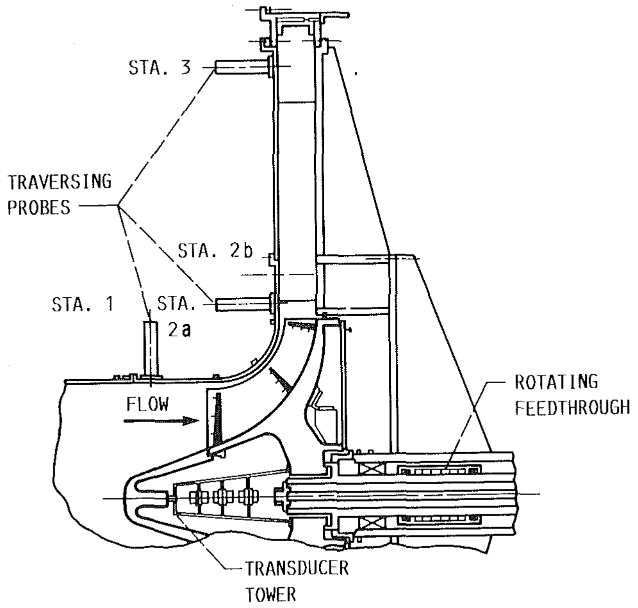

Fig. 3 Schematic of LSCC flowpath

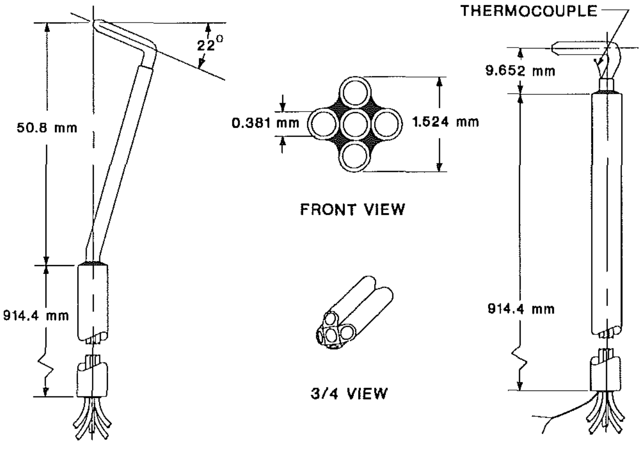

a) Inlet hub probe

b) Sensing head

c) Inlet shroud an exit probe

Fig. 4 Five-hole pressure probes

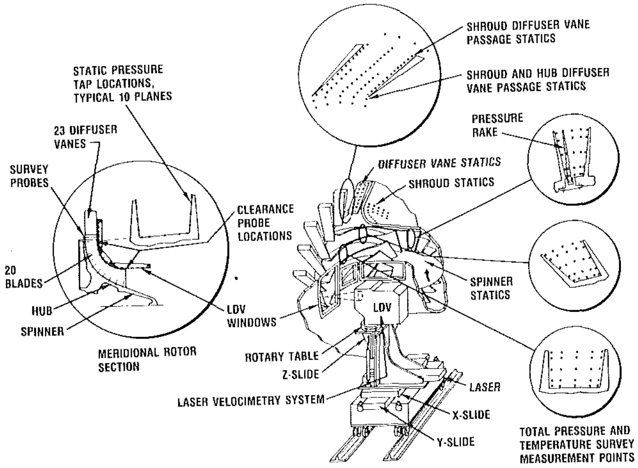

Fig. 5 Low-speed centrifugal compressor instrumentation

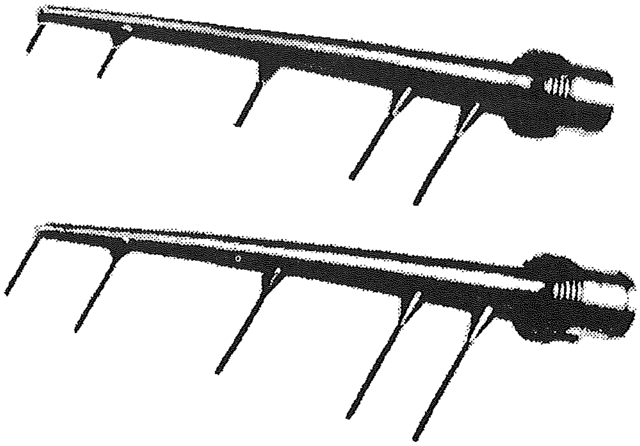

Fig. 6 Rotating frame total pressure and total temperature rakes

ference of the bellmouth throat and from the measured plenum total pressure and total temperature.

Figure 5 shows a schematic of instrumentation locations for the low-speed centrifugal compressor. Arrays of static taps are provided on the impeller blade and hub surfaces, on the diffuser hub and vane surfaces, and along the shroud surface from impeller inlet to diffuser exit. Static taps are also provided at each of the probe survey stations. Five-element (spanwise) total pressure and temperature rakes (Fig. 6) are provided at the impeller inlet, knee, and exit regions. At each rake measurement plane the total pressure and temperature rakes can be positioned at three pitchwise locations. In addition, there are total pressure tubes at five spanwise locations along both the pressure and suction surfaces at each of the rake measurement planes. The total pressure rakes and surface mounted total pressure tubes provide a 25-element grid of total pressure measurements at the three rake measurement planes through the impeller. The total temperature rakes provide a 15-element grid of total temperature at each of the three measurement planes through the impeller. The rake and surface-mounted total pressure tubes are oriented in the streamwise direction using the channel geometry for guidance and their openings are chamfered to improve flow angle insensitivity. Although all rakes can be installed at the same time, no more than one rake will be installed per blade channel for any measurement in order to minimize blockage effects and any disturbances produced on downstream elements.

All rotating frame pressures are sensed through 0.05 cm (0.020 in.) i.d. tubing by silicon pressure transducers housed in five 48-port electronic scanning pressure (ESP) modules. The ESP modules are mounted on the impeller centerline on an instrumentation tower located under the impeller nose cone (see Fig. 3). The transducer diaphragms within the ESP modules are oriented perpendicular to the centerline. The signals from the ESP modules are sent to the laboratory frame of reference via an electrical slip ring assembly. On-line calibration of the ESP modules is accomplished using a pneumatic slip ring, which supplies calibration pressures to the ESP modules. The supplied calibration pressures are measured with a SETRA transducer, which is also mounted on the instrumentation tower. The pressure tubing to the ESP modules is routed down the backface of the impeller between radial stiffening ribs. A flat plate bolted to these ribs traps a quantity of air approximately 7.6 cm (3 in.) thick over the entire back face

Table 4 Measurement uncertainties (95 percent confidence interval)

Primary measurement	Nominal value	Percent uncertainty
Pressure	101325 N/m^2	0.034
Temperature	288 °K	0.4
Swirl angle	70 deg	1.4
Pitch angle	5 deg	3.0
Position	13 cm	0.05
Calculated measurement	**Nominal value**	**Percent uncertainty**
Velocity	100 m/sec	0.25
Mass flow rate	30 kg/sec	0.3
Pressure ratio	1.13	0.042

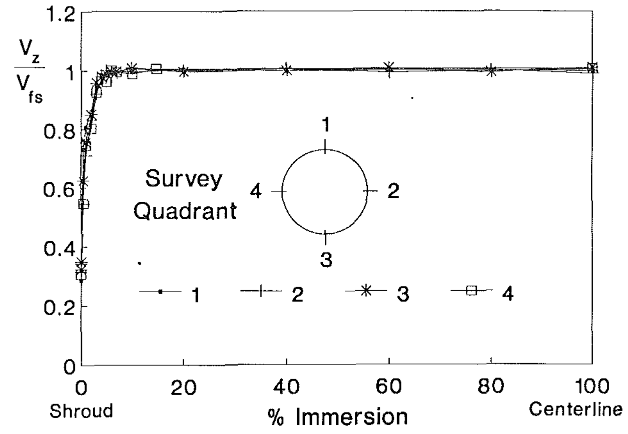

Fig. 7 Circumferential uniformity/repeatability of inlet flow field, Station 0

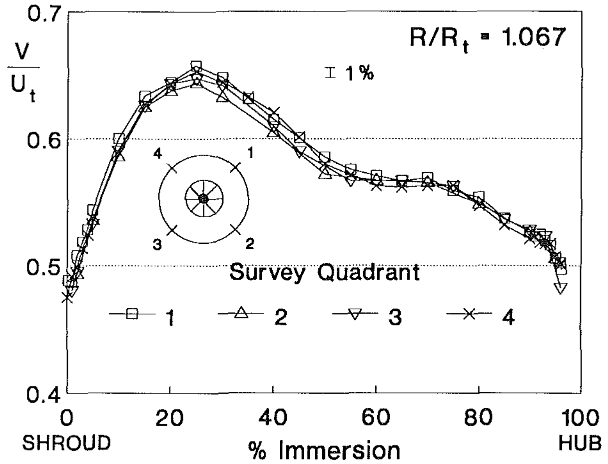

Fig. 8 Circumferential uniformity/repeatibility of impeller exit flow field, Station 2a (4 percent tip clearance)

of the impeller, which essentially bathes the pressure tubing in air undergoing solid body rotation. Since this air is undergoing solid body rotation, it's possible to calculate the air temperature distribution and compare it with thermocouple readings located at various radii along the pressure tubing. The temperature distribution along the pressure tubing is used to correct the measured pressures for the centrifugal head effects due to the fluid in the pressure tubing between the static pressure measurement location and the ESP pressure sensor port.

In addition to the above instrumentation, windows are provided over the impeller inlet, knee, and exit regions to allow for optical access to the flow field (Fig. 5). The exit window covers the rotor trailing edge, the vaneless space, and the diffuser throat region. Laser anemometry and flow visualization are therefore possible. The ammonia-ozalid flow visualization technique will be used in both the impeller and diffuser. Fluorescing oil, liquid crystal sheets, and tufts will also be used in the diffuser.

Measurement Uncertainties

Uncertainties determined for each of the primary and calculated measurements are listed in Table 4. In addition to providing uncertainty estimates for measured and calculated parameters, indications of the repeatability and circumferential uniformity of the flow field that can be expected from the low-speed centrifugal compressor are provided. The repeatibility of the data provides assessment of how well flow conditions can be matched from test to test. The degree of circumferential uniformity of the flowfield is important since most steady-flow CFD codes require axisymmetric boundary conditions. The normalized velocity profiles shown in Figs. 7 and 8 were acquired at four different circumferential locations over a one-month period. These results therefore provide an indication of the repeatability of the measurements as well as the degree of circumferential uniformity in the impeller inlet and exit flow field.

Results and Discussion

The data presented herein consist of conventional aerodynamic probe surveys upstream and downstream of the impeller, and flow visualization results from fluorescing oil (Jurkovich et al., 1984). Results of computational analyses that support the experimental data are also presented. The main emphasis of the data and computational analysis presented herein is to illustrate the impact of synergism between experiments and computational analysis on the development of the low-speed centrifugal compressor facility.

Research operating conditions selected for detailed investigations of the low-speed centrifugal compressor flow field were chosen to reflect design flow conditions (30 kg/s) as well as high (36.36 kg/s) and low (23.64 kg/s) flow conditions. Because of a problem with the facility temperature control, which has since been fixed, and limitations on the maximum physical speed of the impeller (1950 rpm), the corrected speed for all research data was set at 97 percent of design speed (1862.4 rpm). Preliminary measurements indicate that the impeller inlet boundary layer thickness measured at survey station 1 is approximately 20 percent of span (5.921 cm) on the shroud and 2 percent of span (0.592 cm) on the hub.

Impact of Experiment/CFD Synergism. The history of the development of the low-speed centrifugal compressor illustrates how synergism between computational analyses and experimentation has affected the final design of the test hardware. The first research entry into the facility occurred October 1, 1988, and due to a scheduled rehabilitation of the NASA variable-frequency control facilities, testing was concluded November 1, 1988. Since this was a new facility, the intent of the initial entry was to check out the research data acquisition system. During the one month of operation, preliminary surveys were acquired upstream and downstream of the impeller. The data were not analyzed in great detail, since the probes were uncalibrated and because several problems were uncovered with the data acquisition system.

About the same period of time, results of a computational analysis of the compressor flow field by Moore and Moore (1989, 1990) of the Virginia Polytechnic Institute became available under a NASA grant. This grant was initiated in the spirit of a cooperative effort to minimize the time typically required to develop a new facility. The Moores calculated the LSCC flow field with their Elliptic Flow Program, a three-dimensional pressure correction solution for discretized forms of the

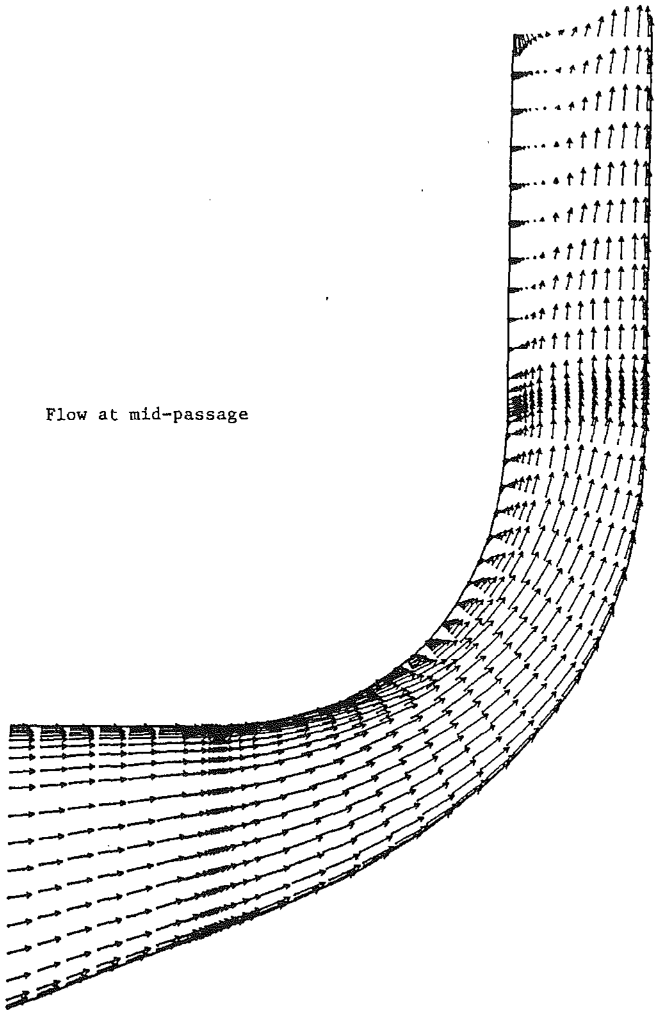

Fig. 9 Meridional view of velocity vectors from Moore's (1988) three-dimensional flow calculations of LSCC with 4 percent tip clearance and constant height vaneless diffuser

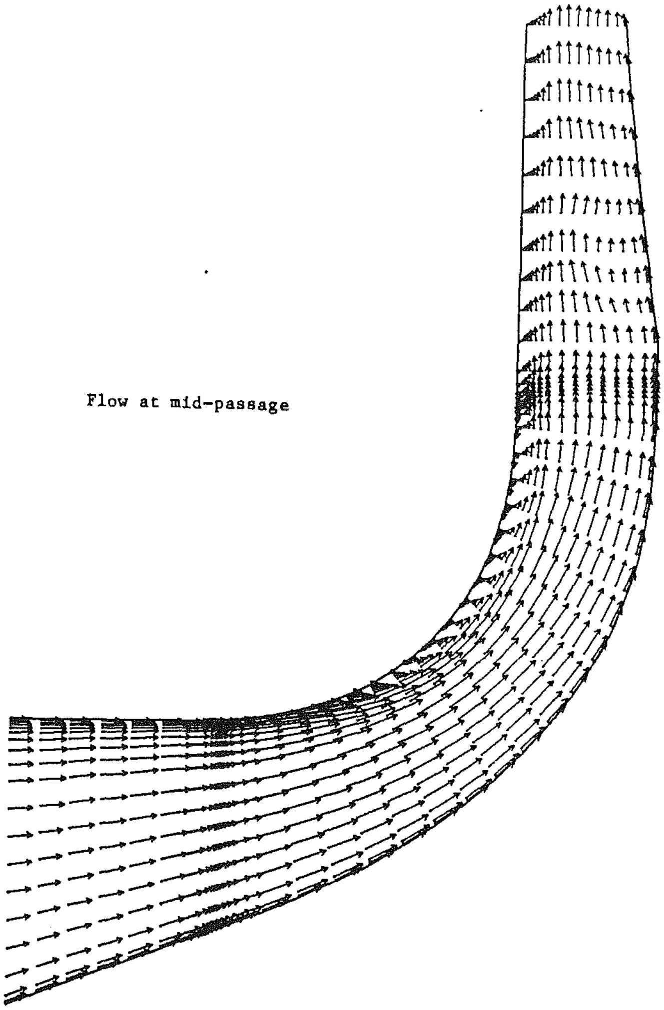

Fig. 10 Meridional view of velocity vectors from Moore and Moore's (1988) three-dimensional flow calculations of LSCC with 4 percent tip clearance and modified vaneless diffuser

Navier–Stokes equations. The three-dimensional flow through the impeller was modelled using a 53 streamwise by 22 spanwise by 21 pitchwise grid.

The Moores' CFD solution indicated separation along the impeller shroud wall near the impeller exit as shown in Fig. 9. This separation continued downstream all the way to the outflow boundary condition, which prevented the CFD solution from converging since the backflow within the separation region was bringing mass flow into the solution domain across the outflow boundary. In order to obtain a converged solution, the Moores altered the geometry in the vaneless diffuser region, as shown in Fig. 10, to force the separated flow region to close before it reached the outflow boundary.

About the same time the Moores were generating their predictions of the LSCC flow field, NASA was also generating predictions of the flow field using the three-dimensional computational analyses of Hah (1988, 1990) and Dawes (1988). These predictions also indicated that separation would occur along the impeller shroud. As a result of these CFD predictions, the previously acquired preliminary experimental results were investigated and were found to indicate a severely retarded flow region near the shroud wall as shown in Fig. 11. Although the preliminary measurements were inconclusive in substantiating the predicted shroud wall separation, the severely retarded flow region measured near the shroud wall indicated that shroud wall separation was probably imminent. Certainly, a reverse flow region within the tip clearance gap is expected, although the survey probe was not able to detect it. Since the rig was intended for fundamental flow physics research and CFD assessment, it was considered undesirable to have separation that would affect the impeller flow field and produce an undesirable downstream boundary condition for CFD analysis. Considering that the facility was shut down for a scheduled one year rehabilitation on November 1, 1988, further investigation of the predicted shroud wall separation until after the shutdown was not possible. We decided, therefore, that

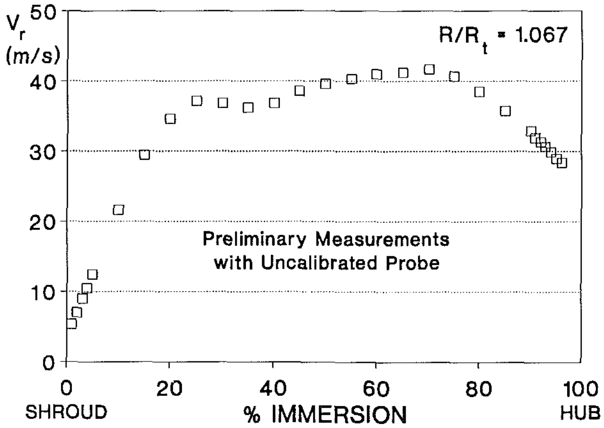

Fig. 11 Radial velocity distribution at impeller exit station 2a (4 percent tip clearance)

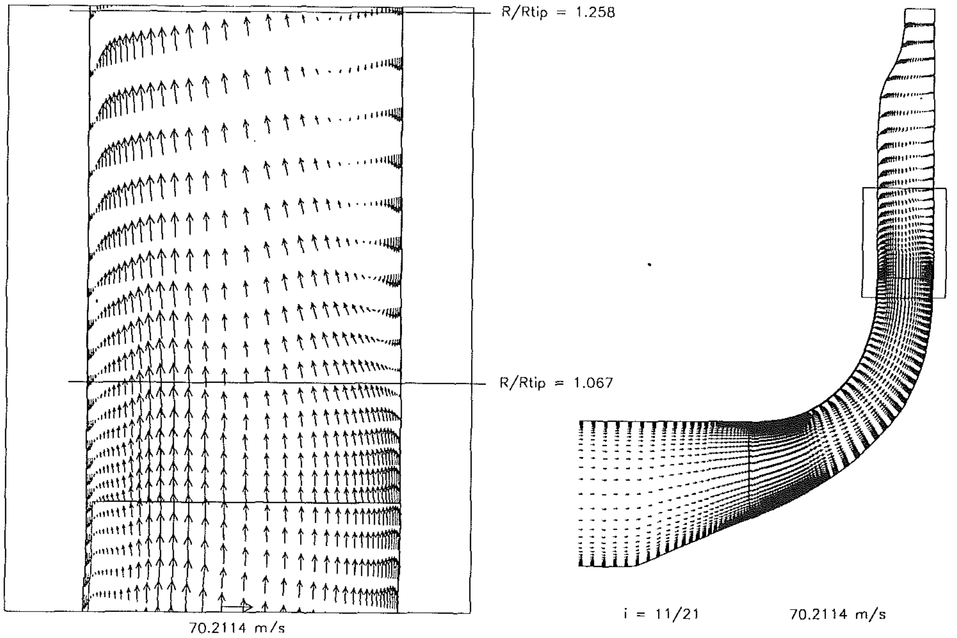

Fig. 12 Meridional view of velocity vectors predicted by the Dawes three-dimensional viscous flow calculation of the LSCC with 2 percent tip clearance

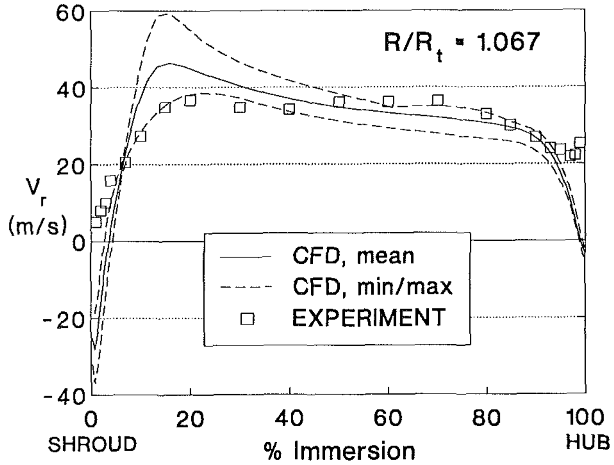

Fig. 13 Radial velocity distribution at impeller exit station 2a (2 percent tip clearance)

the best time to effect any modifications to the compressor geometry would be during the facility shutdown.

Two potential modifications to the low-speed centrifugal compressor were considered: (1) reduce the impeller exit tip clearance; (2) increase the vaneless diffuser area contraction. Reduction of the impeller tip clearance was considered appropriate since the low-speed centrifugal compressor was initially designed with a uniform 4 percent exit tip clearance, which, although not atypical of industry practice (see Table 2), was on the high side. Before reducing the tip clearance, we asked industry for an opinion as to what level of tip clearance would be most representative of typical operating conditions. Based on industry response, we reduced the tip clearance to a circumferentially uniform level from inlet to exit of 2 percent based on the impeller exit blade span by bonding balsa wood strips to the tip of the impeller. In-house CFD analysis of the low-speed centrifugal compressor with the reduced tip clearance was then initiated using the Dawes and Hah codes to determine whether a further modification to increase the vaneless diffuser area contraction was necessary. At the same time the low-speed centrifugal compressor was reinstalled in the facility and testing was initiated with the reduced tip clearance impeller. Hereafter, all references to the low-speed centrifugal compressor will be for the reduced tip clearance impeller.

Figure 12 shows a meridional view of velocity vectors at midpitch predicted by the Dawes code. The Dawes code was run with a 107 streamwise by 41 spanwise by 21 pitchwise grid with three control volumes in the clearance gap. The Dawes solution predicts separation to occur on both the shroud and hub walls. A comparison between the predicted and measured radial velocity profiles at the impeller exit survey station, STA. 2a, is shown in Fig. 13. The experimental results clearly do not indicate separation on either the hub or shroud surfaces as is predicted by the Dawes code. Since the Dawes code prediction showed that the hub separation began very close to the experimental survey station and that the shroud separation was confined to a thin layer, it seemed reasonable to expect that the survey probe might not be able to detect the separation regions. As a result, it was decided to add a new aerodynamic survey location, STA. 2b, near the point at which the hub wall separation was predicted to reach its maximum thickness (i.e., at $R/R_t = 1.258$). In addition, flow tufts were taped to the laser window covering the impeller/diffuser shroud region and to the opposite hub diffuser wall. The shroud tufts indicated that the reduced impeller tip clearance was effective in clearing up the separation on the impeller exit shroud region. However, the inner wall tufts on the hub side of the diffuser indicated that the flow was now separated beyond impeller exit survey station 2a, as predicted by the Dawes code. The shroud wall flow separation due to the 4 percent tip clearance may have produced sufficient flow blockage to prevent separation on the hub wall. Cleaning up the flow separation on the shroud wall reduced the shroud side blockage, which resulted in subsequent separation of the hub wall. The propensity for hub wall separation is a result of rapid deceleration of the flow near the hub wall as flow in the relative frame of reference leaving the impeller is brought to rest at the stationary hub wall. A comparison between the Dawes code predictions and measured radial velocity profiles at impeller exit survey station 2b is shown in Fig. 14. The experimental results clearly indicate a flow separation on the hub wall and show no indication of

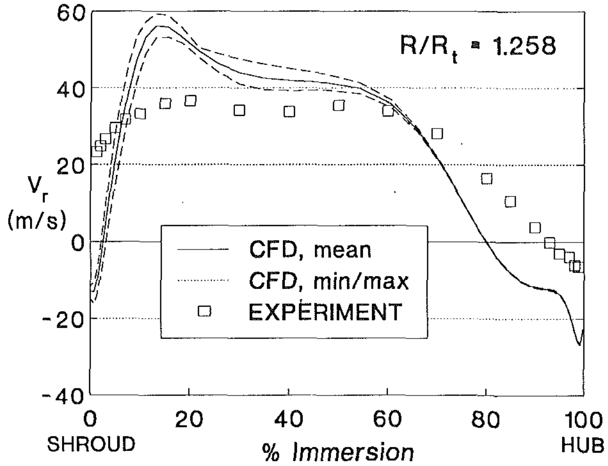

Fig. 14 Radial velocity distribution at impeller exit station 2b (2 percent tip clearance)

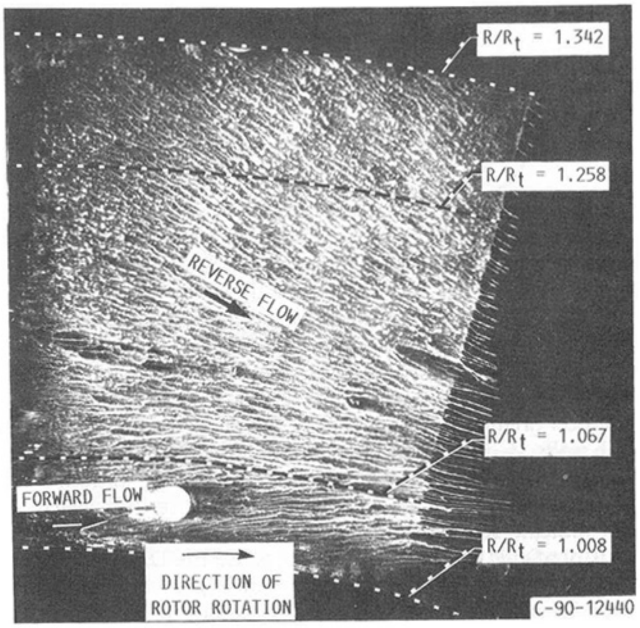

Fig. 15 Fluorescing oil flow visualization on hub surface (2 percent tip clearance)

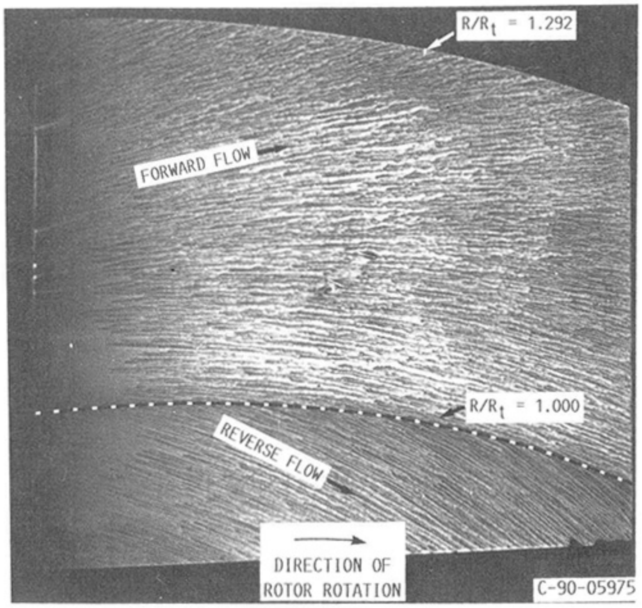

Fig. 16 Fluorescing oil flow visualization on shroud surface (2 percent tip clearance)

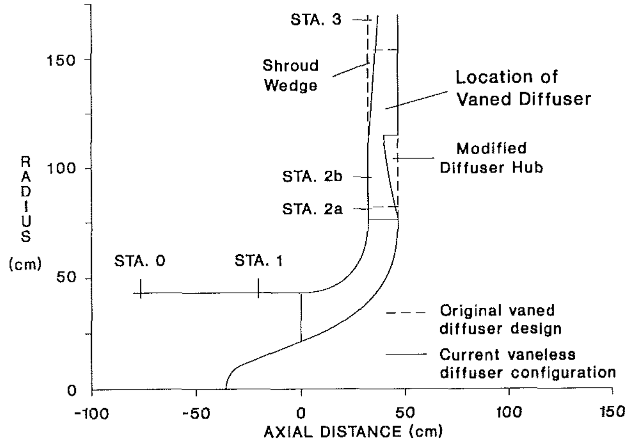

Fig. 17 Final flow path configuration showing modification to diffuser hub contour in order to eliminate separation

separation on the shroud wall, which is in agreement with the flow tufts. Another flow visualization technique using fluorescing oil was also used to indicate flow directions on the shroud and hub surfaces at the impeller exit. The fluorescing oil technique substantiated the results of the flow tufts and the flow surveys, indicating separation on the hub wall and elimination of separation on the shroud wall; see Figs. 15 and 16.

The Dawes CFD solution predicts the onset of separation on the hub wall quite well but overpredicts the spanwise extent of the separation region. However, both CFD predictions and experimental flow visualization indicate that flow along the hub wall is separating. Since the low-speed centrifugal compressor is intended for fundamental flow physics investigation and CFD code assessment, the facility was therefore modified by installing a hub wall contour in order to increase the vaneless diffuser area contraction and thereby eliminate the hub wall separation. The vaneless space between the impeller exit and vaned diffuser leading edge will also be contracted for the LSCC tests with the vaned diffuser installed in order to reduce the propensity for the flow to separate. The modified hub wall contour for the current vaneless diffuser configuration is shown in Fig. 17. It should be mentioned that the shroud wedge, also shown in Fig. 17, has been present since the initial vaneless diffuser configuration in order to reduce the flow area beyond the laser window. The shroud wedge blockage alone, however, was insufficient to prevent flow separation.

The new hub contour has been analyzed using the Dawes code. The predicted results indicate that the flow is still separated on the shroud. This separation starts near midchord and continues out into the diffuser. The shroud separation closes before the outflow boundary is reached, however, as shown in Fig. 18. There is no separation on the hub wall for flow rates that correspond to the design flow rate or higher. At flow rates near 75 percent of design flow rate or lower a small separation bubble occurs on the hub wall, but this bubble closes before reaching the outflow boundary condition. In order to enable assessment of the ability of CFD codes to capture changes in the flow field as the compressor operating condition is changed, data will be acquired for flow rates with and without flow separation on the diffuser hub wall.

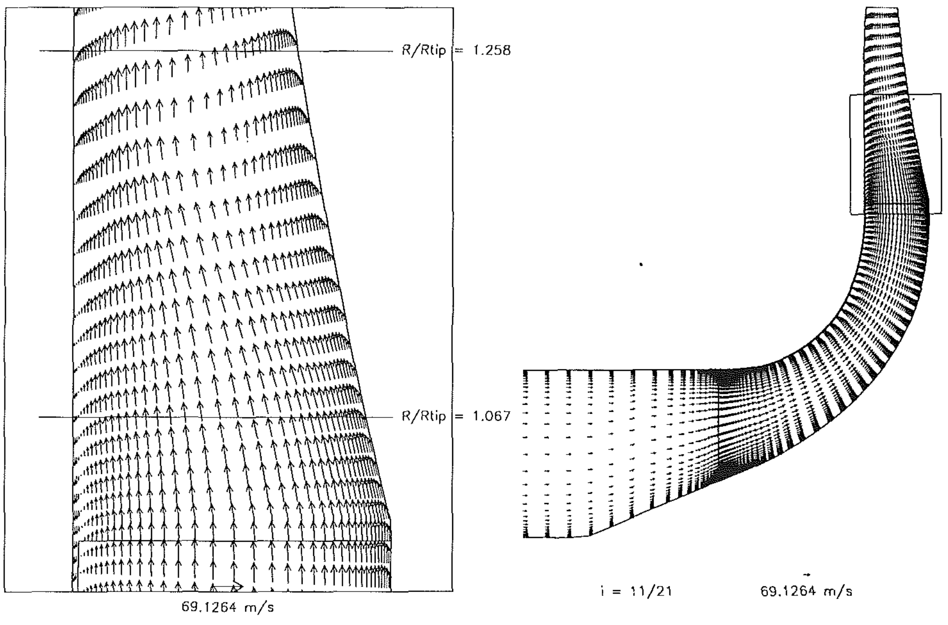

Fig. 18 Final solution of LSCC velocity field with modified diffuser hub contour and 2 percent tip clearance as predicted by Dawes three-dimensional viscous code

Summary and Conclusions

A new low-speed centrifugal compressor facility for three-dimensional viscous code assessment and fundamental flow physics research has been described. The facility is heavily instrumented with pressure and temperature probes, both in the rotating and stationary frames of reference, and has provisions for flow visualization and laser velocimetry. Preliminary measurements presented herein indicate the high quality of the data that can be expected from this facility.

The synergism between experimental data and computational analysis during the development of the LSCC has led to modifications of compressor geometry, which facilitate its use for fundamental flow physics research and computational code assessment. Although the CFD models used for analysis of the LSCC flow field may not have correctly predicted the magnitudes of the flow parameters, they have been invaluable for capturing the essential features of the flow physics. The CFD results also provided useful guidance for the experimental efforts to validate the CFD predictions.

Acknowledgments

The authors would like to thank C. Hah and K. Kirtley for their computational analyses and T. Strazisar for his helpful suggestions and assistance in preparing this paper.

References

Dawes, W. N., 1988, "Development of a 3-D Navier–Stokes Solver of Application to All Types of Turbomachinery," ASME Paper No. 88-GT-70.

Dorney, D. J., and Davis, R. L., 1990, "Centrifugal Compressor Impeller Aerodynamics (A Numerical Investigation)," ASME Paper No. 90-GT-213.

Eckardt, D., 1976, "Detailed Flow Investigations Within a High-Speed Centrifugal Compressor Impeller," ASME *Journal of Fluids Engineering*, Vol. 98, pp. 390–402.

Hah, C., Bryans, A. C., Moussa, Z., and Tomsho, M. E., 1988, "Application of Viscous Flow Computations for the Aerodynamic Performance of a Backswept Impeller at Various Operating Conditions," ASME JOURNAL OF TURBOMACHINERY, Vol. 110, pp. 303–310.

Hah, C., and Krain, H., 1990, "Secondary Flows and Vortex Motion in a High Efficiency Backswept Impeller at Design and Off-Design Conditions," ASME JOURNAL OF TURBOMACHINERY, Vol. 112, pp. 7–13.

Hayami, H., Senoo, Y., and Ueki, H., 1985, "Flow in the Inducer of a Centrifugal Compressor Measured With a Laser Velocimeter," ASME JOURNAL OF ENGINEERING FOR GAS TURBINES AND POWER, Vol. 107, pp. 534–540.

Japikse, D., and Karon, D. M., 1989, "Laser Transit Anemometry Investigation of a High Speed Centrifugal Compressor," ASME Paper No. 89-GT-155.

Johnson, M. W., and Moore, J., 1980, "The Development of Wake Flow in a Centrifugal Impeller," ASME *Journal of Engineering for Power*, Vol. 102, No. 2.

Johnson, M. W., and Moore, J., 1983, "Secondary Flow Mixing Losses in a Centrifugal Impeller," ASME *Journal of Engineering for Power*, Vol. 105, No. 1.

Joslyn, H. D., Brasz, J. J., and Dring, R. P., 1991, "Centrifugal Compressor Impeller Aerodynamics: An Experimental Investigation," ASME JOURNAL OF TURBOMACHINERY, Vol. 113, pp. 660–669.

Jurkovich, M. S., Greber, I., and Hingst, W. R., 1984, "Flow Visualization Studies of a 3-D Shock/Boundary Layer Interaction in the Presence of a Non-uniform Approach Boundary Layer," AIAA Paper No. 84-1560.

Krain, H., and Hoffman, W., 1989, "Verification of an Impeller Design by Laser Measurements and 3D-Viscous Calculations," ASME Paper No. 89-GT-159.

Moore, J., and Moore, J. G., 1989, "A Prediction of 3-D Viscous Flow and Performance of the NASA Low-Speed Centrifugal Compressor," Virginia Polytechnic Institute and State University, Mechanical Engineering Department, Turbomachinery Research Group, Report No. JM/89-1, Jan.

Moore, J., and Moore, J. G., 1990, "A Prediction of 3-D Viscous Flow and Performance of the NASA Low-Speed Centrifugal Compressor," ASME Paper No. 90-GT-234.

Wood, J. R., Adam, P. W., and Buggele, A. E., 1983, "NASA Low-Speed Centrifugal Compressor for Fundamental Research," NASA TM 83398.

Young, M. Y., Spraker, W. A., and Struble, A. G., 1987, "Laser (L2F) Measurements at the Impeller Inlet and Tip Exit of a 91 mm Turbocharger Compressor," *Third International Symposium on Laser Anemometry*, ASME, New York.

Deterministic Blade Row Interactions in a Centrifugal Compressor Stage

K. R. Kirtley

T. A. Beach

Sverdrup Technology, Inc.,
Lewis Research Center Group,
Brook Park, OH 44142

The three-dimensional viscous flow in a low-speed centrifugal compressor stage is simulated using an average passage Navier-Stokes analysis. The impeller discharge flow is of the jet/wake type with low-momentum fluid in the shroud-pressure side corner coincident with the tip leakage vortex. This nonuniformity introduces periodic unsteadiness in the vane frame of reference. The effect of such deterministic unsteadiness on the time mean is included in the analysis through the average passage stress, which allows the analysis of blade row interactions. The magnitude of the divergence of the deterministic unsteady stress is of the order of the divergence of the Reynolds stress over most of the span from the impeller trailing edge to the vane throat. Although the potential effects on the blade trailing edge from the diffuser vane are small, strong secondary flows generated by the impeller degrade the performance of the diffuser vanes.

Introduction

Recent experimental and computational studies have shed considerable light on the problem of blade row interactions in axial flow turbomachinery. However, blade row interactions in centrifugal machines have not received much attention. Many numerical simulations of isolated centrifugal impeller flows have been made, e.g., Moore and Moore (1990), Hah and Krain (1990), and Bansod and Rhie (1990), all of which show the complexity of the impeller flow as well as the inhomogeneity of the impeller discharge flow. This inhomogeneity, often referred to as the jet/wake discharge flow and nicely described by Eckardt (1976) and Krain (1988) can be a significant source of unsteadiness. Indeed, Fradin (1988) reports eight degree flow angle fluctuations and Mach number fluctuations on the order of 12 percent in the throat region of a vaned diffuser aft of a transonic impeller. In addition, Fradin showed that the time-mean flow angles do not follow the vane angles near the vane surface, a manifestation of the unsteadiness. Most of the unsteadiness is due to the periodic motion of the impeller discharge nonuniformities convected through the vane. This deterministic unsteadiness and its effect on the time mean can be studied efficiently using the average passage equations derived by Adamczyk (1985).

The average passage equations are similar to the steady Reynolds-averaged Navier-Stokes equations except that body forces, energy sources, and a metal blockage factor are included to introduce the effect of neighboring blade rows. In addition, the Reynolds stress is augmented by two additional stresses. The first additional stress includes the effect of spatial aperiodicity on the average passage flow and the second includes the effect of deterministic unsteadiness on the time-mean flow. The three stresses are collectively referred to as the average passage stress and require some modeling to close the equation system.

In this paper, the flow development in the impeller and vane passages is studied using results of a viscous, three-dimensional average passage simulation. The migration of impeller-generated secondary flow through the vane is also studied. Since the average passage stress influences flow mixing and therefore plays an important role in the development of the flow in the diffuser vanes, the magnitude of the predominant components of the average passage stress is investigated. In addition, potential interactions are studied by comparing the stage calculation to an isolated impeller calculation at the same operating point.

Method of Analysis

The three-dimensional flow in the centrifugal compressor stage was computed using the average passage Navier-Stokes equations derived by Adamczyk (1985). The numerical method used to solve the average passage equations is described by Kirtley et al. (1990) and is outlined here.

The equations are discretized using a cell-centered, finite volume scheme. The solution is advanced in time to a steady state using a four-step Runge-Kutta integration. Artificial disipation is added to ensure a unique solution but is removed inside boundary layers so as not to mask the physical dissipation. A multigrid scheme is employed to accelerate the convergence of the method. For multiple blade row calculations, the first blade row flow is calculated for a few hundred iterations. The average passage stress, blade body forces, and energy sources are computed for that blade row by comparing the three-dimensional and axisymmetric flow fields. The next blade row flow is computed using the aforementioned source

---

Contributed by the International Gas Turbine Institute and presented at the 36th International Gas Turbine and Aeroengine Congress and Exposition, Orlando, Florida, June 3-6, 1991. Manuscript received at ASME Headquarters March 4, 1991. Paper No. 91-GT-273. Associate Editor: L. A. Riekert.

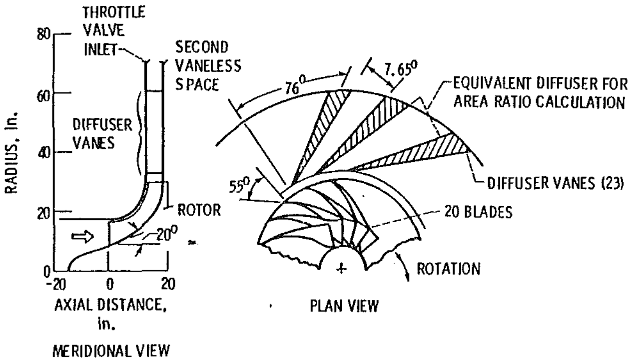

Fig. 1 Compressor stage geometry

terms to represent the influence of the upstream blade row. The average passage stress, body forces, and energy sources for the second blade row are computed and used in the calculation of the first blade row flow. The process is repeated until the axisymmetric averages of each blade row flow are identical. A common axisymmetric flow is the compatibility condition that links the individual three-dimensional average passage flow for each blade row.

The random unsteadiness, i.e., turbulence, is modeled using an algebraic eddy viscosity model based on the renormalization group (RNG) formalism. The algebraic RNG model has been used to compute the mean flow in an axial flow compressor impeller with very good accuracy (see Kirtley, 1991). The RNG model properly accounts for near-wall damping and outer flow intermittency and mimics the boundary layer transition process very well. A turbulence length scale must still be prescribed; however, constants in the model are determined analytically through the RNG procedure. The high Reynolds number limit of the model is nearly identical to all other algebraic eddy viscosity models in the literature.

The deterministic stress component of the average passage stress is assumed to be axisymmetric, which allows for direct calculation by comparing the three-dimensional flow with its axisymmetric average. Additional modeling of this stress is included, which is essentially a correction to the eddy viscosity in the wake region, in order to mix by turbulence diffusion streamwise vortical flows at a rate seen experimentally in axial flow turbomachinery. The mixing rate for radial machines is assumed to be the same since no mixing data are available to confirm or contradict it. The spatial aperiodic stress is assumed to be very small as suggested by experimental data (see Kirtley et al., 1990).

The adiabatic no-slip boundary condition is applied at solid walls. At the inlet, flow angles are fixed and total pressure and temperature distributions are held at their experimental values, which include the incoming shear layers. The axial velocity is then determined by extrapolating the upstream running Reimann invariant. At the radial outflow exit, the whirl, axial velocity, and entropy are extrapolated, as is the total enthalpy from which the exit radial velocity is determined. The boundary condition allows flow nonuniformities to pass unrestricted. The exit static pressure is constant from hub to tip far downstream and is adjusted to give the design weight flow. The periodicity condition is applied outside of the blade passages.

The computational mesh used here, generated using the interactive program of Beach (1990), contains 156 cells in the streamwise direction and 40 cells each in the spanwise and blade-to-blade directions. Eight cells are used in the tip clearance region. The mesh in the tip region is similar to that reported by Bansod and Rhie (1990). On average, the first cell from the wall lies within a y^+ of 5 and so wall functions are not required. The trailing edges of the blades and vanes are rounded to facilitate smooth meshes. To increase the Mach number and ensure attached flow at the domain exit, a small nozzle is added aft of the diffuser vanes by contouring the hub and shroud.

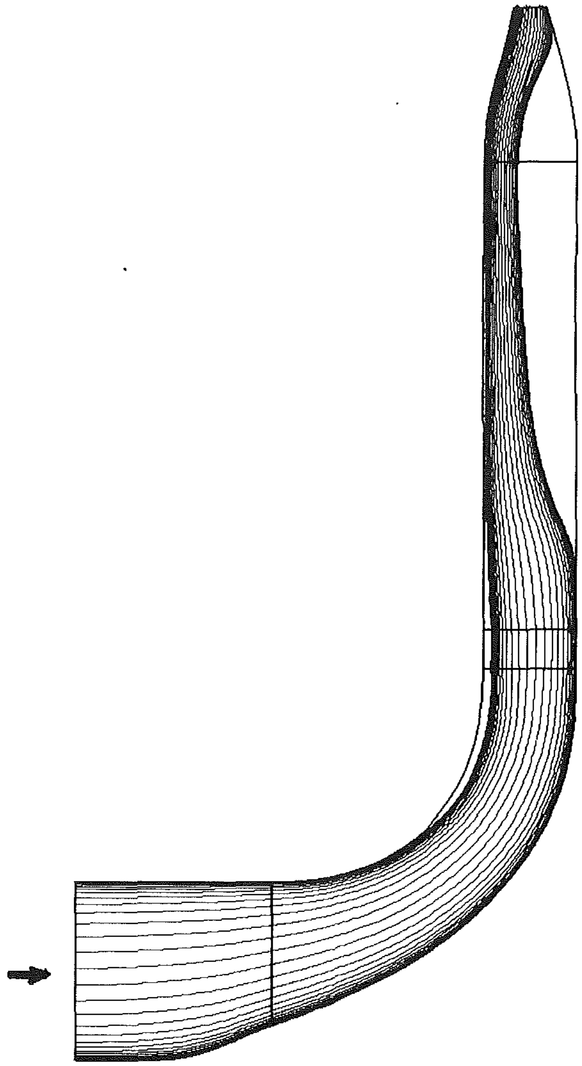

Fig. 2 Axisymmetric flow streamlines, isolated impeller build

Results and Discussion

The compressor stage studied here, the NASA Lewis Low-Speed Centrifugal Compressor described by Wood et al. (1983), is illustrated in Fig. 1. The low-speed rig is composed of a backswept impeller with 20 blades and an exit diameter of 1.524 m. The 23 wedge diffuser vanes extend to 3.048 m in diameter, with a vane inlet to impeller exit radius ratio of 1.08. The calculation was run at 97 percent design speed, i.e., 1860 rpm, and a weight flow of 30 kg/s. At 100 percent design speed, the design total pressure ratio is 1.17 and the Reynolds number based on impeller exit diameter and tip speed is roughly 16 million. The tip gap is a constant 0.254 cm.

The available experimental data are preliminary and unpublished; however, the impeller exit static to inlet total pressure ratio was measured just downstream of the impeller in the isolated impeller build and given as 1.0923 by Hathaway (1990). The computed pressure ratio is 1.0990. This agreement, along with previous experience with the flow code in multistage turbomachinery flows, gives the authors confidence in the accuracy of the present numerical results.

The calculation required 10 CPU hours on the NAS Cray YMP at NASA Ames for the isolated impeller build. The calculation was stopped after the residuals dropped four orders

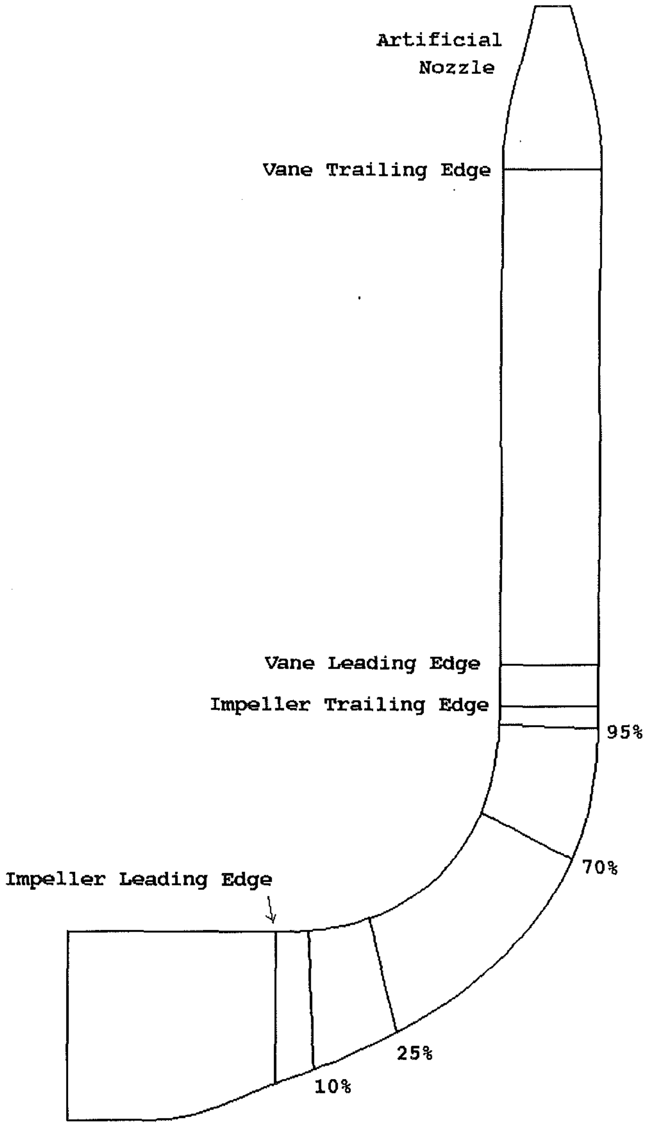

Fig. 3 Impeller reporting stations

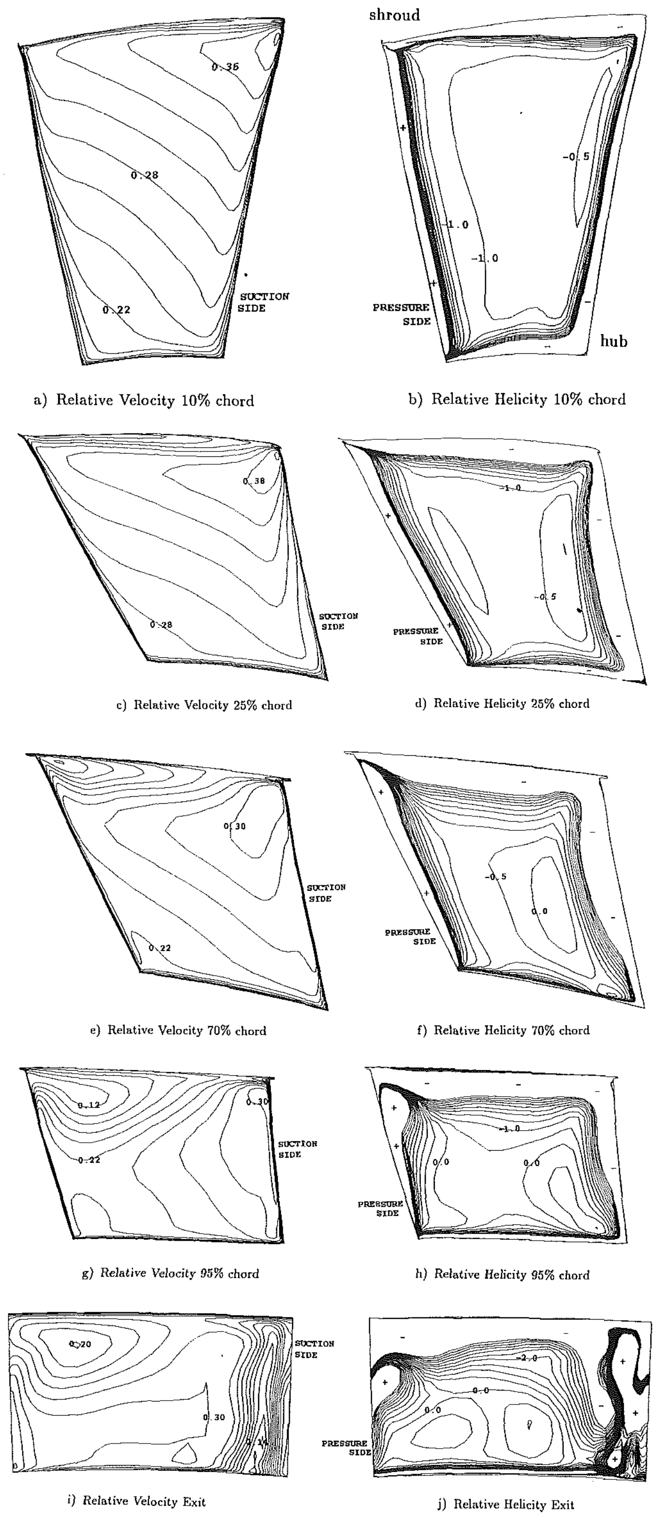

a) Relative Velocity 10% chord

b) Relative Helicity 10% chord

c) Relative Velocity 25% chord

d) Relative Helicity 25% chord

e) Relative Velocity 70% chord

f) Relative Helicity 70% chord

g) Relative Velocity 95% chord

h) Relative Helicity 95% chord

i) Relative Velocity Exit

j) Relative Helicity Exit

Fig. 4 Isolated impeller flow

of magnitude. The stage calculation was started from the isolated impeller solution and required an additional 20 CPU hours until each blade row's axisymmetric average flows was within 0.1 percent of the other.

Isolated Impeller Build

Initially, the viscous flow in the isolated impeller with a vaneless diffuser was computed. Streamlines of the axisymmetric flow are given in Fig. 2. The separated flow in the tip region of the impeller is evident. This separated flow closes in the vaneless space and a detached flow arises on the hub. The hub detachment seems to arise from a disturbance generated at the moving impeller hub/stationary diffuser wall interface. This hub separation is also seen experimentally (Hathaway, 1990).

The three-dimensional flow development is described using contours of total relative velocity and relative helicity. The relative helicity is defined as the inner product of the relative velocity and vorticity vectors normalized by the total relative velocity and is a direct measure of streamwise vorticity. All velocities presented here are nondimensionalized by the characteristic speed $\sqrt{RT_0}$ at the impeller inlet. Lengths are nondimensionalized by the impeller exit diameter. The reporting stations are shown in Fig. 3.

At 10 percent meridional chord, Figs. 4(*a*) and 4(*b*), a velocity nonuniformity has already developed with a peak velocity in the shroud–suction side corner. The development of the blade boundary layers is evident, as are a thin hub and thick shroud boundary layer, both of which are present at the inlet. The helicity indicates spanwise outward flow on both blade surfaces as well as the beginnings of a tip leakage vortex. A hub passage vortex is evident but tends to thin out along the blade passage until near the impeller exit.

At 25 percent chord, Figs. 4(*c*) and 4(*d*), the peak velocity has decreased slightly and migrated toward the middle of the passage. The helicity indicates strong spanwise outward flow

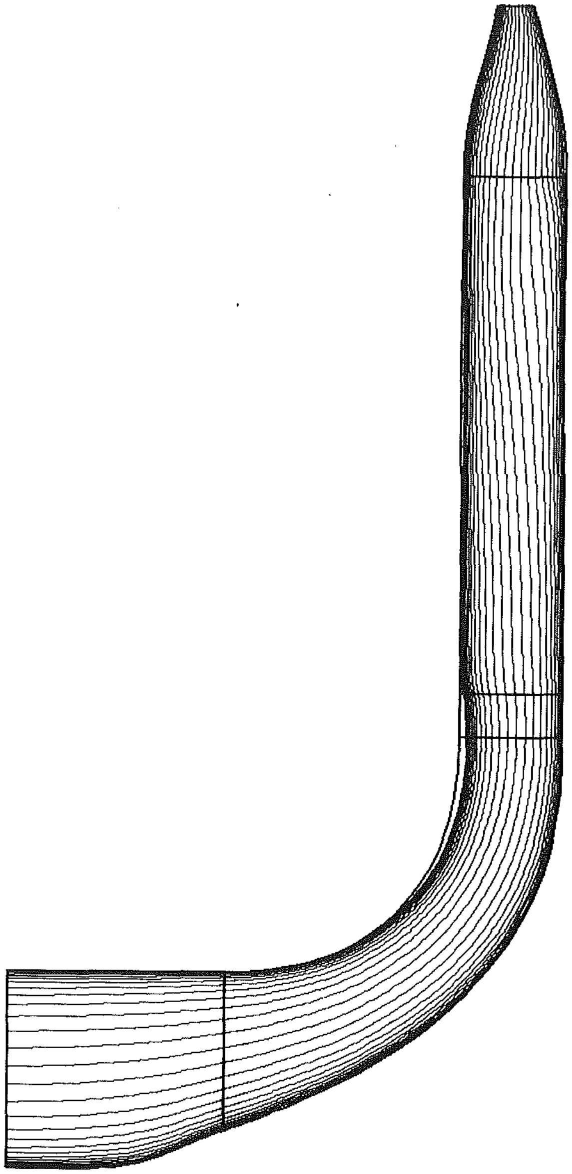

Fig. 5 Axisymmetric flow streamlines, compressor stage build

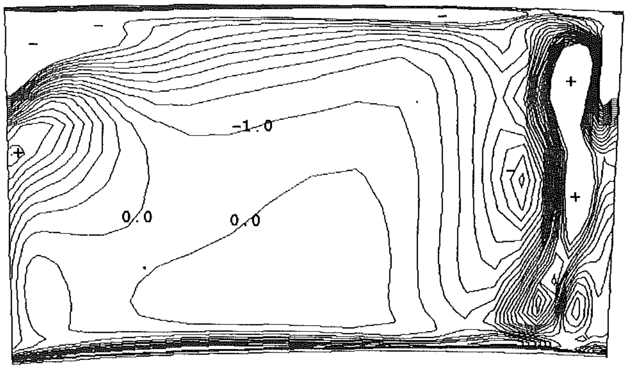

Fig. 6 Relative helicity, impeller exit stage build

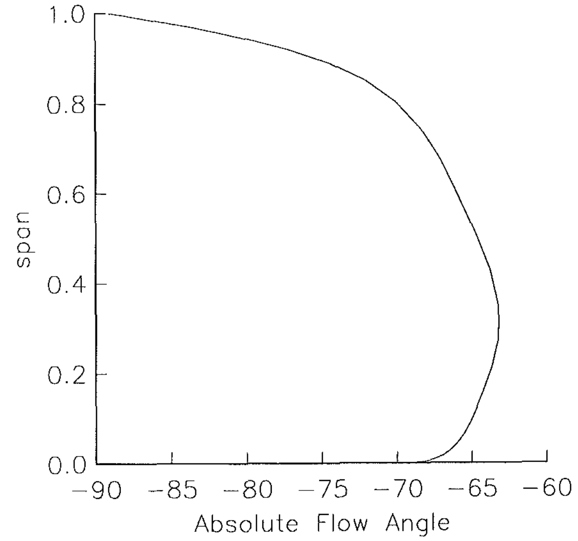

Fig. 7 Impeller exit absolute flow angle

on the suction and pressure sides. A slight radial pressure gradient and blockage from the tip leakage flow tend to move the peak velocity from the shroud region toward midspan.

A 70 percent chord, Figs. 4(*e*) and 4(*f*), the jet has diffused somewhat and remains close to the suction side. The leakage vortex has moved toward the pressure side due to the additional dragging effect of the relative motion of the shroud wall.

The helicity plot indicates that the leakage flow and the spanwise flow along the pressure side come together near 90 percent span. At this point, the surface streamlines converge and the flow detaches from the surface. A low-momentum region has developed in the shroud–pressure side corner from the leakage jet pushing the shroud boundary layer flow toward the pressure side.

The picture is similar at 95 percent chord except that the pressure side separation point has moved farther down the span in response to the strengthening leakage vortex. In addition, the low-momentum (or wake) region is more well defined and the high-momentum (or jet) region has diffused over most of the blade passage. At the impeller exit, Fig. 4(*i*) and 4(*j*), the leakage vortex is clearly visible, as is the low-momentum flow associated with it. In the actual blade wake, the shed vorticity is visible. The classical jet/wake pattern exists at the exit, and is similar to Eckardt's (1976) impeller flow except that his wake region is near the suction side. The present jet/wake development is also similar to Krain's (1988) except that the present wake region is more distinct, which will lead to higher levels of deterministic unsteadiness.

Compressor Stage Build

Streamlines for the axisymmetric flow for the stage are shown in Fig. 5. A comparison with Fig. 2 shows that the additional blockage due to the vane forces a reattachment of the shroud separated flow in the gap and prevents the hub separating flow from developing. The impeller flow is nearly identical to the isolated impeller flow except at the exit where slight differences exist. The impeller exit relative helicity is plotted in Fig. 6 for direct comparison with the isolated impeller flow in Fig. 4(*j*); the only difference is that the interaction of the leakage vortex and the spanwise outward flow on the pressure side occurs slightly farther up the span in the stage build, which is consistent with the reduced shroud separated flow evident in Fig. 5. Few other potential influences can be seen.

The absolute flow angle of the axisymmetric flow at midgap is given in Fig. 6. Remnants of an impeller hub passage vortex are visible, as is the tip leakage vortex. The thick shroud boundary layer yields a tip leakage vortex, which is of positive sense in the absolute fame. Even with the flow angle distortion, the loading distribution on the diffuser vane is essentially two-dimensional except near the tip as seen in Fig. 8. The pressure distribution in the uncovered portion of the vane varies along the span; however, aft of the throat, the spanwise variation is small. Near the tip, the suction peak is not as strong as at midspan because of of the improved incidence there. The throat location is clearly visible at the 10 percent chord location on the pressure side.

The development of flow in the vane is now described. The design flow angle at the exit of the impeller is −69.5 deg. From Fig. 7, it is clear that in the midspan region, the flow angle is roughly −65 deg but widely varying. Part of the difference in flow angle from design, roughly 1 deg, is due to running at 97 percent speed, the speed at which the experimental facility is being run. The additional increase is from the large amount of impeller-generated secondary flow, which tends to underturn the midspan flow. This increase in incidence yields a stream-tube area increase of 20 percent from design, which degrades the diffuser performance up to the throat.

Indeed, the pressure recovery coefficient:

$$C_p = \frac{p_2 - p_1}{p_{0_1} - p_1}$$

from the impeller exit to the throat is −0.46, whereas the design value is 0.2 (Wood et al., 1983). Half of this discrepancy can be rationalized based on the argument of a change in streamtube area. The rest has not been determined but may be due to the quickly growing suction side boundary layer, which further reduces the throat area. From the throat to the vane trailing edge, the design pressure recovery is 0.72 and the computed value is 0.65. Thus, the computed overall pressure recovery for the vane is roughly half of the design value. The computed efficiencies show similar disagreement with design.

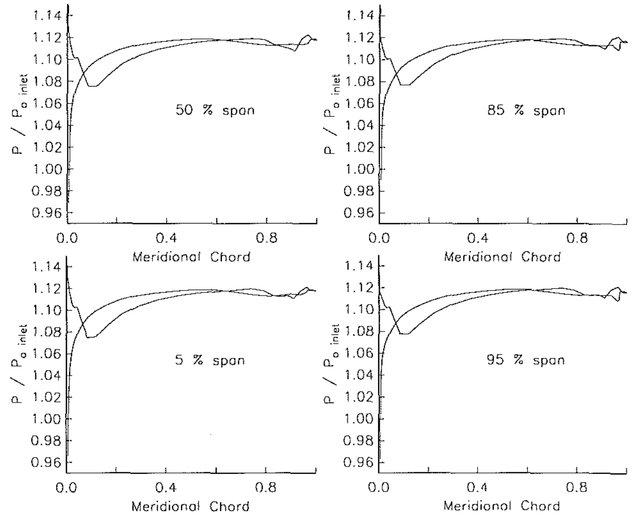

Fig. 8 Vane surface static pressure distribution

Computed isentropic efficiencies are 94 percent for the impeller and 86 percent for the stage versus estimated efficiencies of 93.4 percent and 90 percent for the impeller and stage, respectively. The computed total pressure rise for the impeller is 1.149 compared to the design value of 1.17 at 100 percent speed. The stage total pressure ratio is 1.134. The actual values of all these parameters have not yet been measured.

The origin of some of the additional loss can be seen in Fig. 9. Figure 9(*a*) shows static pressure contours at midspan. The low pressure at the throat, which gives rise to the negative pressure recovery coefficient, is clearly visible. The oscillations in the pressure contours arise from the highly sheared computational mesh near the leading edge, which is unavoidable due to the large 72 deg stagger angle. The high incidence leads to large boundary layer growth on the suction side, which is described using streamlines and a measure of entropy, $s = [1/(\gamma-1)]\ln(p\,\rho^{-\gamma})$ in Figs. 9(*b*) and 9(*c*), respectively. The strongly adverse pressure gradient on the suction side, which gives rise to the strong boundary layer growth, can be seen in Fig. 8. In the vane wake, the flow is of very low momentum and much of it is separated. The rounding of the vane trailing edge is not considered important to the flow development in the wake region.

The role of the impeller-generated secondary flow on the development of the vane flow can be studied using Figs. 10 and 11. Figure 10 shows the location of reporting stations in the vane passage. Figure 11 presents the absolute helicity and total velocity at these reporting stations as in Fig. 4. In the average passage framework, the flow upstream of the vane consists of the axisymmetric average of the impeller flow along with the average passage stress, which ensures that vorticity is conserved from the impeller frame of reference to the vane and introduces the effect of the periodic unsteady jet/wake inhomogeneity on the vane flow.

Upstream of the vane leading edge, Figs. 11(*a*) and 11(*b*), the flow is nearly axisymmetric with slight variations due to vane potential effects. The shed vorticity from the impeller trailing edge averages out, but the hub passage vortex and the tip leakage vortex persist. The impeller-generated leakage vortex, now of positive sense in the absolute frame, is diffused from that in Fig. 5 after passing through the gap between impeller and vane.

In Figs. 11(*c*) and 11(*d*), the pressure (or uncovered) side leg of a horseshoe vortex is visible near the shroud and the impeller leakage vortex is distorted close to the vane surface. In Fig. 11(*e*) and 11(*f*), the impeller leakage flow has turned down the span in response to the wall. In addition, the suction side leg of the shroud horseshoe vortex arises. The hub boundary layer is sufficiently thin and so does not give a visible horseshoe vortex system.

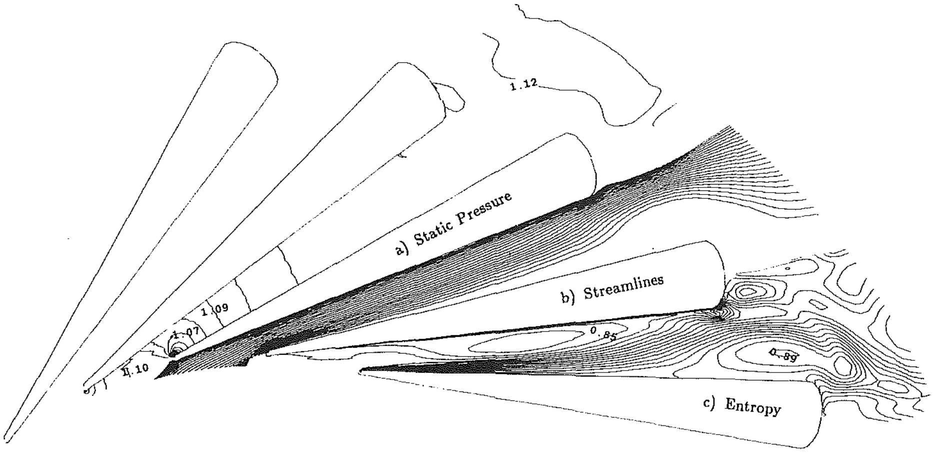

Fig. 9 Vane flow field at midspan

The strong acceleration of the flow near the suction side is present in Fig. 11(*f*). The suction side flow begins to decelerate and the boundary layer grows rapidly. The impeller leakage flow not only reduces the incidence at the tip but generates spanwise inward flow on the suction side, which energizes the near-shroud suction side boundary layer and prevents it from detaching. No such energizing mechanism exists near the hub, and massive hub–suction side boundary layer detachment ensues. This flow detachment is the dominant flow feature in the vane aft of the throat and generates most of the loss in the vane. The impeller-generated secondary flow, which was very strong upstream of the vane leading edge, dissipates quickly past the throat. This quick dissipation is consistent with the authors' interpretation of measurements presented by Stein and Rautenberg (1988). In their narrow diffuser build, the large flow angle distortions across the pitch at the impeller exit seem to have mixed out to a nearly axisymmetric flow near the vane leading edge at a radius ratio of 1.15.

Blade Row Interactions

First-order potential interactions have been identified as weak and confined to the reduction of shroud separated flow in the trailing edge region of the impeller due to the additional downstream blockage provided by the diffuser vane. The deterministically unsteady pressure interactions are equally weak. Figure 12(*a*) shows contours of the normalized fluctuating pressure $p_{\mathrm{rms}} / p_{\mathrm{axi}}$ from pressure variations generated by the impeller and vane, which impact the vane and impeller flows, respectively. The vane experiences fluctuations less than one half percent in the vicinity of its leading edge. Likewise, the vane imposes pressure fluctuations upon the impeller trailing edge of only one half percent of the exit static pressure. Additional blade row interactions can be studied by viewing contours of the divergence of the average passage stress in Fig. 12(*b*). Recall that the average passage stress includes terms that measure the level of deterministic unsteadiness. The particular component chosen for display is the divergence of the deterministic unsteady stress, $\overline{\rho \tilde{u}_i \tilde{u}_\theta}$, which quantifies the mixing across axisymmetric streamwise streamsheets due to deterministic unsteadiness, as indicated by Adamczyk et al. (1989).

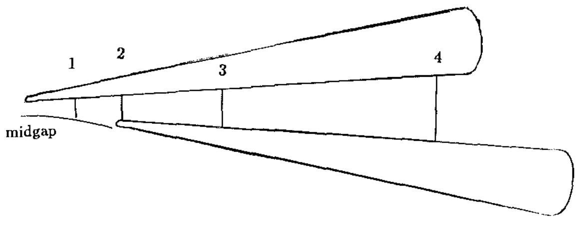

Fig. 10 Vane reporting stations

In the vane frame of reference, Fig. 12(*b*), the considerable three dimensionality of the impeller flow gives rise to the deterministic unsteadiness in the impeller space. The tip clearance region yields the largest degree of unsteadiness; as does the complicated wake structure along the span of the trailing edge. However, the deterministic stress decays quickly in the vaneless space, due to a decaying tip vortex. In the vane space, this stress is no longer large except near the shroud. Aft of the throat region, it is nearly zero and thus does not play an important role in the flow development past the throat.

To measure the relative importance of the deterministic stress in the vane frame of reference, the divergence of $\overline{\rho \tilde{u}_i \tilde{u}_\theta}$ is compared to the divergence of the Reynolds stress, $\overline{\rho u'_i u'_\theta}$, as modeled using renormalization group theory. In Fig. 13(*a*), the comparison is made midway between he impeller and vane, near the leading edge, and near the throat. At midgap, the divergence of the deterministic unsteady stress is larger than the Reynolds stress across the span except very near the shroud where the turbulence is more intense. Near the vane leading edge, the impeller-generated secondary flows that give rise to the deterministic unsteadiness have begun to dissipate, but $\partial \overline{\rho \tilde{u}_i \tilde{u}_\theta}/\partial x_i$ is still greater than $\partial \overline{\rho u'_i u'_\theta}/\partial x_i$ except close to the end walls. Near the throat, the deterministic unsteadiness has all but dissipated and the mixing across axisymmetric streamsheets is dominated by the turbulence.

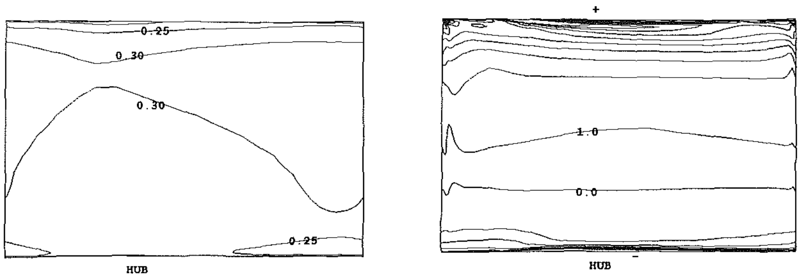

a) Absolute Velocity at Midgap

b) Absolute Helicity at Midgap

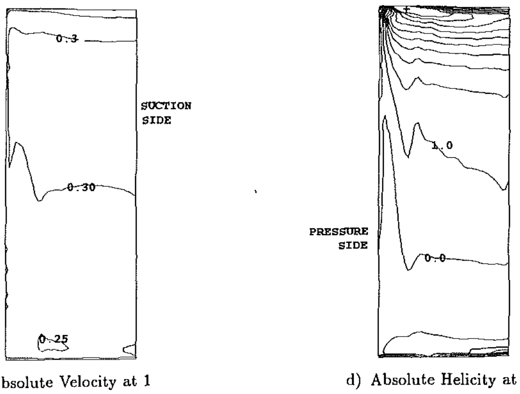

c) Absolute Velocity at 1

d) Absolute Helicity at 1

Fig. 11 Diffuser vane flow

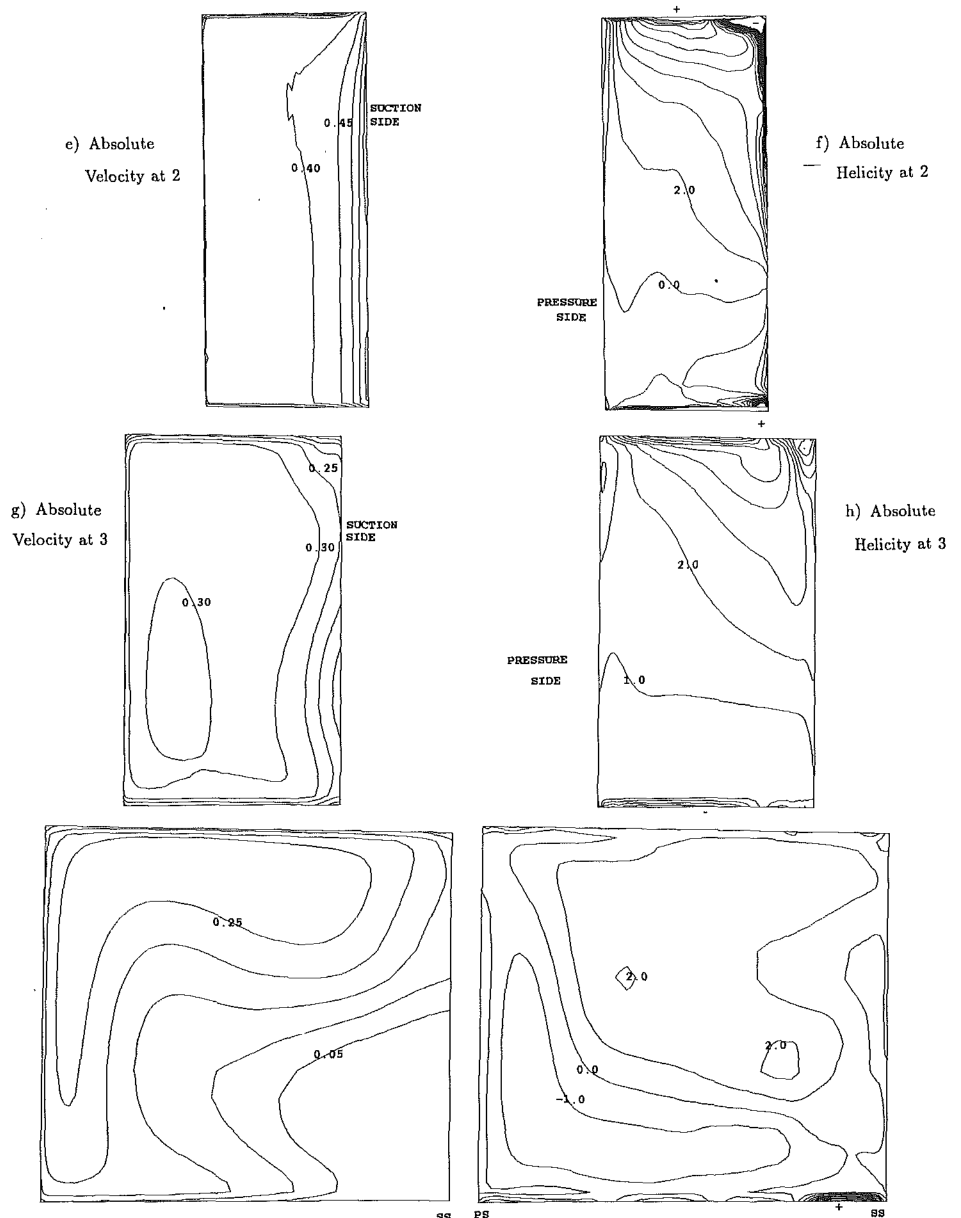

e) Absolute Velocity at 2

f) Absolute Helicity at 2

g) Absolute Velocity at 3

h) Absolute Helicity at 3

i) Absolute Velocity at 4

j) Absolute Helicity at 4

Fig. 11 (continued)

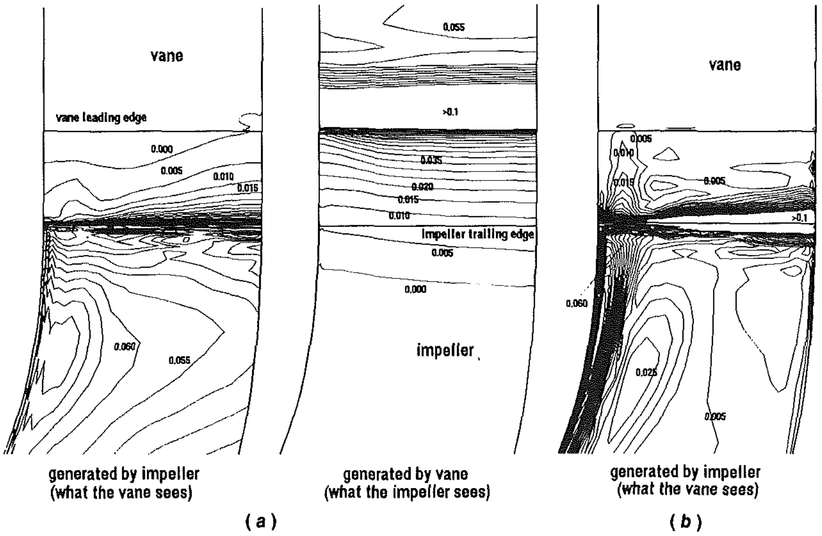

generated by impeller (what the vane sees)

generated by vane (what the impeller sees)

generated by impeller (what the vane sees)

Fig. 12 Levels of deterministic unsteady interactions: (*a*) normalized static pressure fluctuations; (*b*) divergence of average passage stress

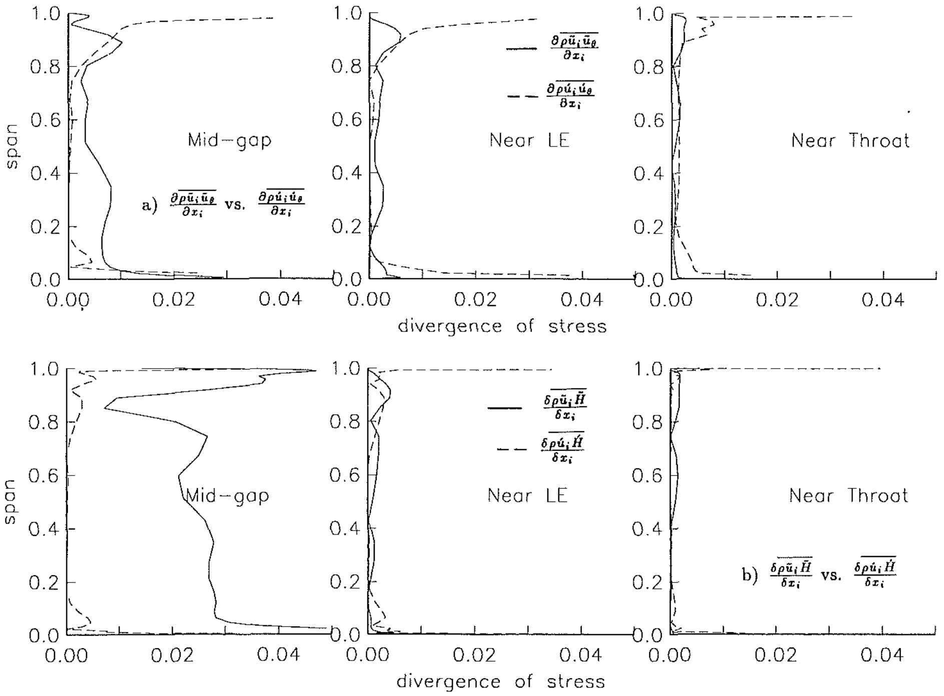

Fig. 13 Comparison of divergence of deterministic unsteady stress and Reynolds stress

To complete the comparison. Fig. 13(*b*) shows the level of energy transfer across axisymmetric streamsheets due to $\delta\rho\overline{\tilde{u}_i H}/\delta x_i$ and $\delta\rho\overline{\acute{u}_i H}/\delta x_i$, where H is the enthalpy. At midgap, the energy transfer due to the deterministic unsteadiness is substantial and much greater than the effect of random unsteadiness; however, the deterministic unsteadiness dissipates quickly. By the leading edge, the picture looks similar to that in Fig. 13(*a*). Thus, in the vane frame of reference, the deterministic unsteadiness is as important as the turbulence upstream of the diffuser throat. Aft of the throat, only the first-order effects namely the high incidence angle to the vanes, are important.

Conclusions

The three-dimensional viscous flow in the NASA Low-Speed Centrifugal Compressor Stage has been computed using the average passage Navier–Stokes equations. The isolated impeller calculation shows a jet/wake discharge flow, with the wake confined to the shroud near the pressure side. The wake flow is coincident with the tip leakage vortex. In the stage calculation, the impeller flow is found to be similar to the isolated impeller flow except for the reduction of shroud separation due to the additional blockage that the vane provides. Thus, it appears that the potential interactions between blade rows in this low speed machine are small.

The large secondary flows generated in the impeller give rise to deviations in the exit flow angle, which cause the vane to operate off design incidence. The result is negative pressure recovery up to the throat of the vane and a large suction side boundary layer which eventually detaches. The impeller tip leakage vortex persists through the vaneless space up to the throat and energizes suction side flow near the shroud where it inhibits flow detachment. Comparisons of the levels of deterministic unsteadiness from the impeller discharge inhomogeneity and the turbulence show that within the gap between the impeller and vane, the divergence of the deterministic stress is larger than the divergence of the Reynolds stress except very close to the end walls. Near the vane leading edge and near the throat, the stresses are comparable, but aft of the throat the deterministic stress decays to near zero.

Acknowledgments

This work was supported by the NASA Lewis Research Center under contract NAS3-25266 with Dr. J. Adamczyk as monitor. Special thanks are given to J. Wood, A. Strazisar and M. Hathaway of NASA Lewis for many helpful discussions, and K. Dugas for editing the manuscript.

References

Adamczyk, J. J., 1985, "Model Equation for Simulating Flows in Multistage Turbomachinery," ASME Paper No. 85-GT-226; NASA TM 86869.

Adamczyk, J. J., Beach, T. A., Celestina, M. L., Mulac, R. A., and To, W.-M., 1989, "The Numerical Simulation of Multistage Turbomachinery Flows," AGARD CP-469, pp. 18-1–18-13.

Bansod, P., and Rhie, C. M., 1990, "Computation of Flow Through a Centrifugal Impeller With Tip Leakage," AIAA Paper No. 90-2021.

Beach, T. A., 1990, "An Interactive Grid Generation Procedure for Axial and Radial Flow Turbomachinery," AIAA Paper No. 90-0344.

Eckardt, D., 1976, "Detailed Flow Investigations Within a High Speed Centrifugal Compressor Impeller," ASME *Journal of Fluids Engineering*, Vol. 98, pp. 390–402.

Fradin, Ch., 1988, "Detailed Measurement of the Flow in the Vaned Diffuser of a Backswept Transonic Centrifugal Impeller," ICAS Report ICAS-88-2.6.2, pp. 848–854.

Hah, C., and Krain, H., 1990, "Secondary Flows and Vortex Motion in a High-Efficiency Backswept Impeller at Design ad Off-Design Conditions," ASME JOURNAL OF TURBOMACHINERY, Vol. 112, pp. 7–13.

Hathaway, M. D., 1990, Private Communication.

Kirtley, K. R., Beach, T. A., and Adamczyk, J. J., 1990, "Numerical Analysis of Secondary Flow in a Two-Stage Turbine," AIAA Paper No. 90-2356.

Kirtley, K. R., 1991, "An Algebraic RNG Based Turbulence Model for Three-Dimensional Turbomachinery Flows," AIAA Paper No. 91-0172.

Krain, H., 1988, "Swirling Impeller Flow," ASME JOURNAL OF TURBOMACHINERY, Vol. 110, pp. 122–128.

Moore, J., and Moore, J. G., 1990, "A Prediction of 3-D Viscous Flow and Performance of the NASA Low-Speed Centrifugal Compressor," ASME Paper No. 90-GT-234.

Stein, W., and Rautenberg, M., 1988, "Analysis of Measurement in Vaned Diffusers of Centrifugal Compressors," ASME JOURNAL OF TURBOMACHINERY, Vol. 110, pp. 115–121.

Wood, J. R., Adam, P. W., and Bugele, A. E., 1983, "NASA Low-Speed Centrifugal Compressor for Fundamental Research," NASA TM 83398.

S. Mizuki
Hosei University,
Tokyo, Japan

Y. Oosawa
Nippon Telegraph & Telephone,
Tokyo, Japan

Unsteady Flow Within Centrifugal Compressor Channels Under Rotating Stall and Surge

Unsteady flow patterns throughout a centrifugal compressor system during the rotating stall and the surge were measured experimentally. Various kinds of unsteady behavior of the flow appeared both continuously and suddenly as the flow rate decreased. The part-span stall, the full-span stall, the mild and deep stalls, and the deep surge appeared clearly. The fluctuations caused by the full-span stall were seen even during surge and affected the flow within the scroll through the vaneless diffuser. The experimental results were compared with those computed by the lumped parameter theory. Good agreements between them were obtained when appropriate values were selected for the lumped parameters.

Introduction

It is well known that the performance characteristics of a compressor exhibit two types of unsteady nature at reduced flow rates: rotating stall and surge. Rotating stall is the unsteady propagation of fluctuations of the flow limited to a few components of a compressor, such as the inlet duct, the impeller, or the diffuser, while surge accompanies the propagation and resonance of fluctuations throughout a compressor system. They occur for both axial and centrifugal compressors, and knowledge for the former has been accumulated more than for the latter. Based on the definite natures of rotating stall and surge, the theoretical relationships between the performance characteristics and the responses to fluctuations of the flow have been clarified well for axial compressors. On the other hand, there still remain many problems for centrifugal compressors, such as the cause of the generation of rotating stall at the vaneless diffuser (Frigne and Van den Braembussche, 1984; Moore, 1989), whether the stall and the surge could be predicted on the same theoretical basis as for axial compressors (McCaughan, 1989a, 1989b), and so on. One reason for the superior clarification of these unsteady natures for axial compressors might be attributed to the simpler configurations of flow passages and the resultant simpler flow mechanisms, even in the cases of multiple stages, compared with those of centrifugal compressors. Moreover, experimental as well as theoretical investigations have been commonly focused on the flow within a few components of a centrifugal compressor due to the complex flow mechanisms (Frigne and Van den Braembussche, 1985; Haupt et al., 1988). However, the essential mechanisms of these unsteady natures of flow have been clarified to be similar for both compressors; for example, the extensions of the lumped parameter theory first applied to axial compressors were applied to centrifugal compressors and proved to be consistent (Pinsley et al., 1991; Gysling et al., 1991). Thus, it will be necessary to know more about the complex unsteady flow patterns in centrifugal compressors in order to establish precise theoretical models for the propagations and resonances to disturbances and fluctuations throughout the system.

On the abovementioned point of view, the unsteady flow throughout a centrifugal compressor was measured experimentally. Various kinds of unsteady behavior of flow appeared both continuously and suddenly as the flow rate decreased. Although there have been many words used attempting to typify the natures of stall and surge, such as mild stall, progressive stall, abrupt stall, classic surge, deep surge, and so on, it was very difficult to apply them completely for the present results. Part-span and full-span stall, mild and deep stalls, and deep surge could be distinguished. The fluctuations caused by the full-span stall were seen even under the surge and affected the flow within the scroll through the vaneless diffuser. Because the present results were obtained from a compressor with a low pressure ratio, a check for universality would be necessary. At the end of the present investigation, one of the lumped parameter theories (Greitzer, 1976) was applied to them by carefully examining the constants for parameters. The computed results were in good agreement with those from the experiments.

Experimental Facility and Instrumentation

The experimental arrangement is shown in Fig. 1. The compressor system was composed of an inlet duct, an impeller, a parallel-walled vaneless diffuser, a scroll, a delivery duct, an orifice, and a throttle valve. The impeller has twelve straight radial blades including splitters. The blade angle of the mean camber line at the mean radius of the inducer inlet was 60 deg from the axial direction. The speed of rotation was 10,000 rpm. Therefore, the frequency of the impeller rotation was

---

Contributed by the International Gas Turbine Institute and presented at the 36th International Gas Turbine and Aeroengine Congress and Exposition, Orlando, Florida, June 3–6, 1991. Manuscript received at ASME Headquarters February 19, 1991. Paper No. 91-GT-85. Associated Editor: L. A. Riekert.

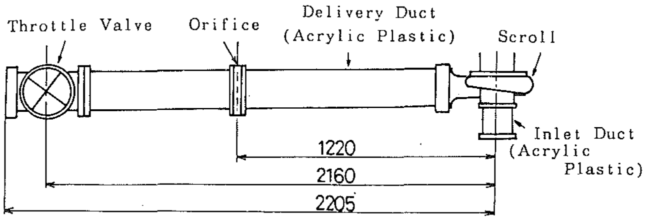

Fig. 1 Experimental arrangement

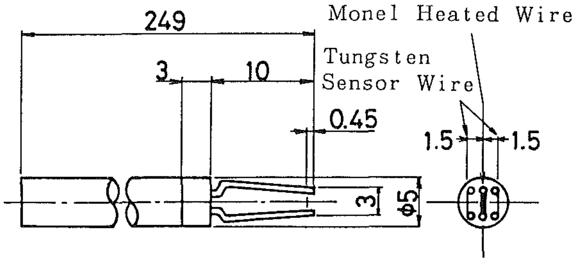

Fig. 2(*a*) Configuration of a thermal-tuft probe

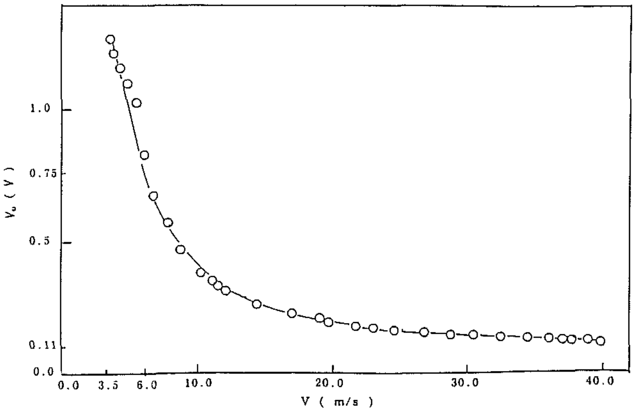

Fig. 2(*b*) Calibration curve of a thermal-tuft probe

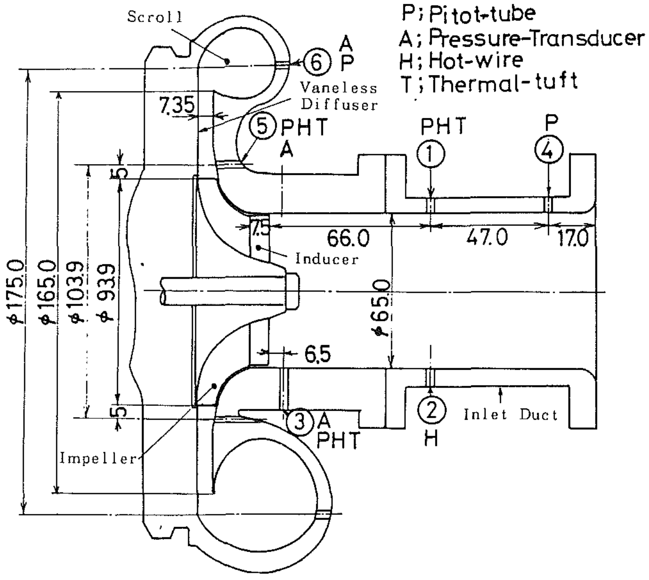

Fig. 3(*a*) Meridional positions

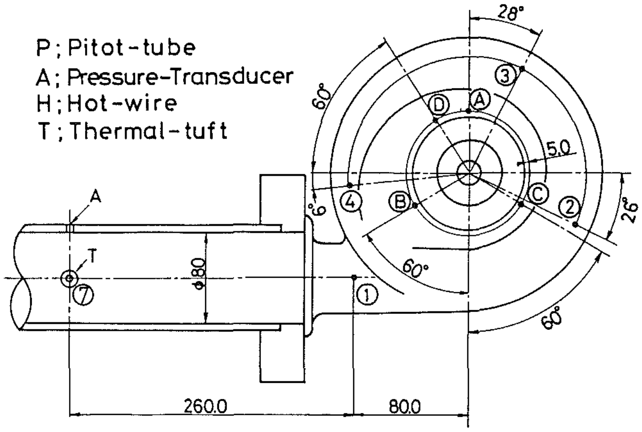

Fig. 3(*b*) Circumferential positions

Fig. 3 Measurement sites

166.78 Hz, the blade passing frequency was 2000 Hz for twelve blades and half that for the splitters. The time-averaged flow was measured by cobra-type three-hole yaw probes with inclined manometers. For the time-dependent flow, I-shaped hot wires, semiconductor pressure transducers, and thermal-tuft probes were used. The configuration and the calibration curve of a thermal-tuft probe are shown in Fig. 2. They were installed to get the maximum responses to the axial flow at the inlet and delivery ducts; i.e., the sensor wires were placed perpendicular to the axial velocities. Within the vaneless diffuser and the scroll, the maximum responses were obtained for the radial velocities by setting the sensor wires parallel to the circumferential direction.

The measurement sites for these probes and transducers are shown in Fig. 3. The positions from ① to ④ in Fig. 3(*a*) are different from those in Fig. 3(*b*). At the impeller inlet, the

Nomenclature

A_C = area at impeller exit, m^2
A_T = area at throttle
f = frequency, Hz
i_C = number of rotating stall cells
L = effective length, m
N = rotational speed, rps
P = pressure, kPa
ΔP = pressure rise, kPa
T = temperature, K
T_i = period of rotating stall cell, s
ΔT_i = time difference of the periods measured by two sensor wires, θ_p apart tangentially, s
t = time, ms
U = peripheral speed, m/s
V = velocity, m/s
V_p = plenum volume, m^3
ΔV = fluctuating velocity, m/s
θ_p = angular distance of two sensor wires, rad
ρ = density, kg/m^3
τ = nondimensional time = $\omega_0 t/(2\pi)$
φ = flow coefficient = V_{2r}/U_2
ω = Helmholtz resonator frequency, Hz
ω_s = ratio of velocity of stall cell to that of impeller rotation
ω_b = angular velocity of blades, rad/s
ω_0 = angular velocity of impeller rotation, rad/s

Subscripts

1 = impeller inlet
2 = impeller exit
a = atmosphere
C = compressor
d = delivery duct
P = plenum
r = radial component
T = throttle
z = axial component

Superscripts

$-$ = time-averaged

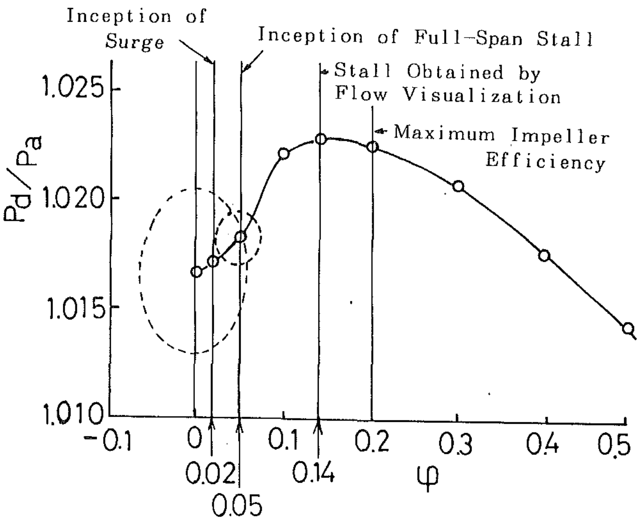

Fig. 4 Performance characteristics of compressor

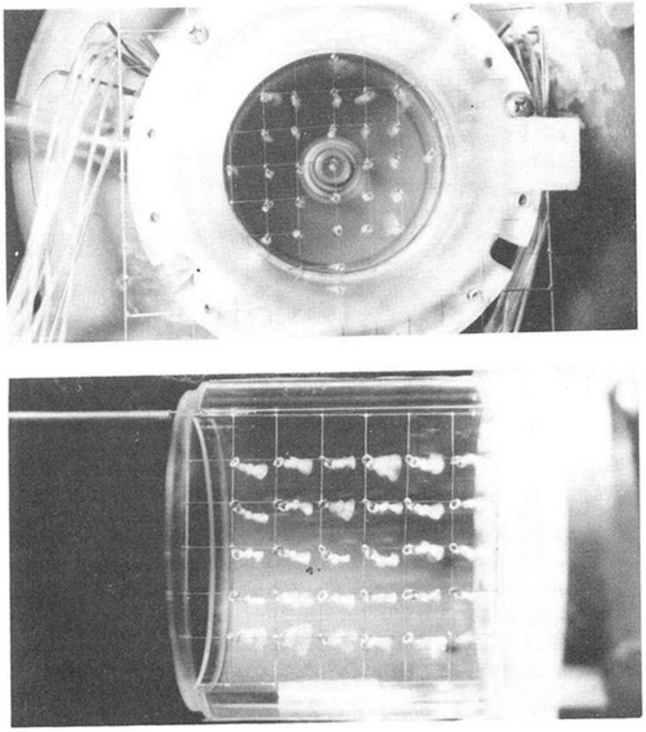

Fig. 5 Flow visualization by tufts at inlet duct

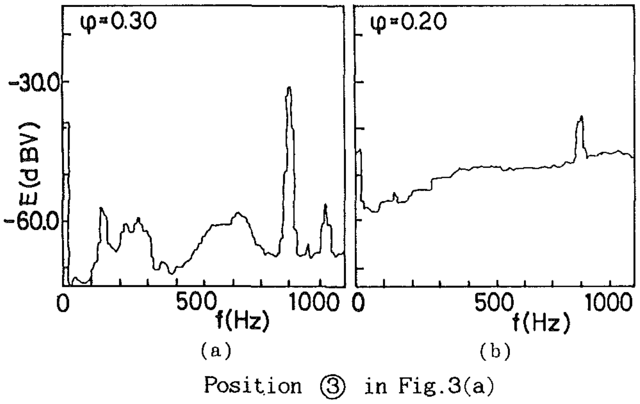

Fig. 6 Spectrum of pressure fluctuation at inlet duct

rotating stall cells were measured by two hot-wire probes 180 deg apart tangentially from each other (③ in Fig. 3(*a*)). At the entrance to the vaneless diffuser, the probes were placed at positions Ⓐ, Ⓑ, Ⓒ, and Ⓓ, in Fig. 3(*b*). The number of rotating stall cells and the rotational speed of the cells were computed from the following equations by using a data acquisition system:

$$i_c = \frac{2\pi}{\theta_p}\frac{\Delta T_i}{T_i}$$

$$\omega_s = \frac{2\pi}{i_c \omega_0 T_i}$$

The frequencies of the rotational speed of rotating stall cells will be employed in the following in order to compare them with those measured at the stationary components of the compressor. The flow visualizations were also made by using tufts at the inlet duct.

Performance Characteristics

The performance characteristics of the present compressor system are shown in Fig. 4. The flow rates of maximum impeller efficiency, full-span stall, surge, and rotating stall known by the flow visualization as will be shown in the following are also indicated. The dotted circles show the fluctuations of pressures and flow rates from the time-averaged values measured at the centers. Because the main objective of the present investigation was the measurement of the unsteady flow patterns and their interferences between the components of this compressor, the experiments were always made by decreasing the flow rates. Although it is well known that the relationship between the hysteresis in the performance characteristics and the disturbances propagating into the components of the compressor plays an important role for the inceptions and the continuations of rotating stall and surge (Greitzer, 1981), the essential flow patterns were estimated to be similar except for the shifts on the flow rates caused by the hysteresis.

Inception of Part-Span Stall

The flow visualization by tufts at the inlet duct is shown in Fig. 5. The apparent rotating stall cell appeared at $\varphi = 0.14$, and the number of the cell was unity with the frequency of 55 Hz. At this condition, no rotating stall cell appeared at the entrance of the vaneless diffuser. Therefore, the rotating stall in the present compressor was induced by the impeller, and the stall at the vaneless diffuser might be suppressed as was mentioned by Frigne and Van den Braembussche (1984). Although the visualization showed the occurrence of rotating stall at $\varphi = 0.14$, the pressure on the wall of the inlet duct showed the unstable fluctuations at much higher flow rates, where the pressure-flow coefficient curve showed the negative slope in Fig. 4. The spectra of the pressure fluctuations at 6.5 mm upstream of the inducer showed the frequency about 800 Hz both at $\varphi = 0.20$ and 0.30 as in Fig. 6. The increase of the pressure fluctuations with lower frequencies at $\varphi = 0.20$, compared with those at $\varphi = 0.30$, could be seen. These fluctuations indicated the increasing unsteady nature of flow as the flow rate decreased and would also indicate the existence of very thin stall cells with a higher frequency than that measured at $\varphi = 0.14$, which could not be clearly recognized by the flow visualization. We were not able to estimate the number of very thin stall cells and the values of the frequency were much higher than those observed by Frigne and Van den Braembussche (1984). Because the reverse flow from the impeller passages could not be seen, these fluctuations with lower frequencies would be attributed to the unsteady disturbances of the flow at the leading edge of the impeller with the higher

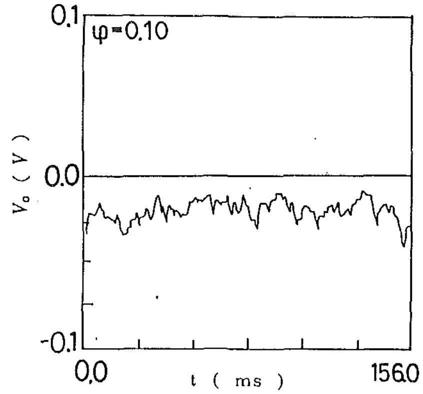

Position ③ in Fig.3(a)

0.5mm from shroud wall

Fig. 7 Output signal from thermal-tuft probe

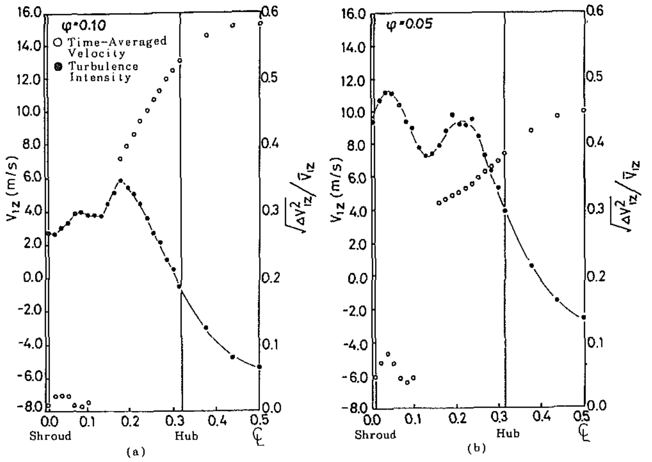

Position ① in Fig.3(a)

Fig. 8 Distribution of time-averaged velocity and turbulence intensity

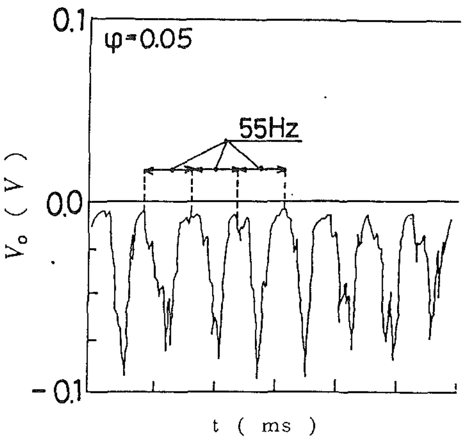

Position ③ in Fig.3(a)

(a) 0.5mm from shroud wall

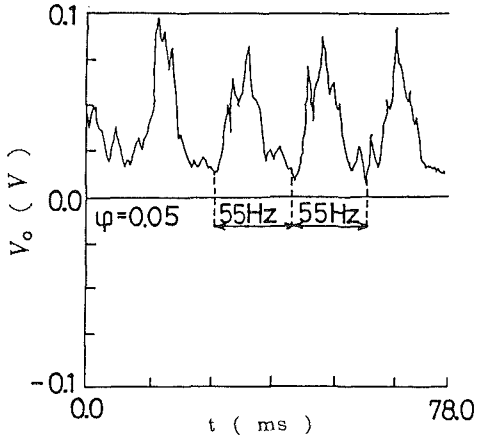

Position ③ in Fig.3(a)

(b) 0.5mm from Hub

Fig. 9 Output signals of thermal tuft during full-span stall

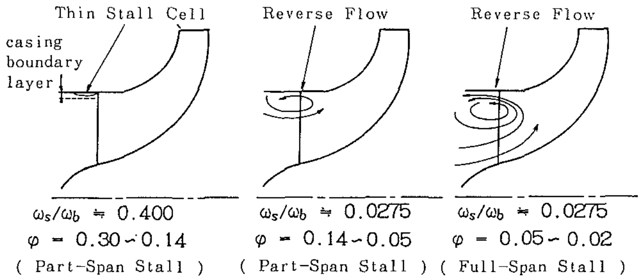

Fig. 10 Schematic drawing of stall cells

incidence angles in the casing boundary layer (Chen et al., 1989).

The fluctuations of the reverse flow near the casing were also measured by the thermal tuft at $\varphi = 0.10$, which is shown in Fig. 7. Although the waves seemed quite random, the major value of the frequency was at 55 Hz as for $\varphi = 0.14$. Therefore, the signal also indicated the existence of the rotating stall cell and the number of the cell was unity. The negative value of the signal also showed the reverse flow near the shroud casing. The higher values of the turbulence intensities and the negative values of the time-averaged axial velocities could be seen in Fig. 8(*a*) at 66 mm upstream of the impeller inlet. The higher value of the intensity at the boundary between the cell and the time-averaged negative axial velocity in the stall cell appeared clearly. This result was also consistent with the existence of very strong reverse flow from the impeller channel obtained by the time-averaged measurements on the rotating impeller (Mizuki et al., 1976). Because this region of the cell appeared only near the shroud casing, it could be called a part-span stall. This stall also could be classified as a mild stall due to the smaller fluctuations compared with that shown in the following.

Full-Span Stall

As the flow rate decreased further, at $\varphi = 0.05$, the part-span stall changed to a full-span stall as in Fig. 8(*b*). It showed two peaks for the turbulence intensities near the shroud and the hub, and the time-dependent fluctuations of the axial velocities were clearly shown (Fig. 9). Although the rotational speed and the corresponding frequency were measured by two hot-wire sensors, the fluctuating velocities measured by a thermal-tuft probe exhibited the same frequency for the rotating stall cell. When the reverse flow in the rotating stall cell increased near the shroud casing, the throughflow near the hub also decreased and vice versa. These results also implied that the strong fluctuation of the throughflow was given to the impeller channels by the full-span stall, although the frequency of the cell was the same as that of the part-span stall at $\varphi = 0.14$ and 0.10. Thus, this full-span stall could be considered a deep stall. The circumferential variation for the region of the stall cell was not clear because measurements were made at only two circumferential positions. The time-averaged behaviors of the stall cells on the rotating impeller are shown schematically in Fig. 10. As the flow rate decreased, the development

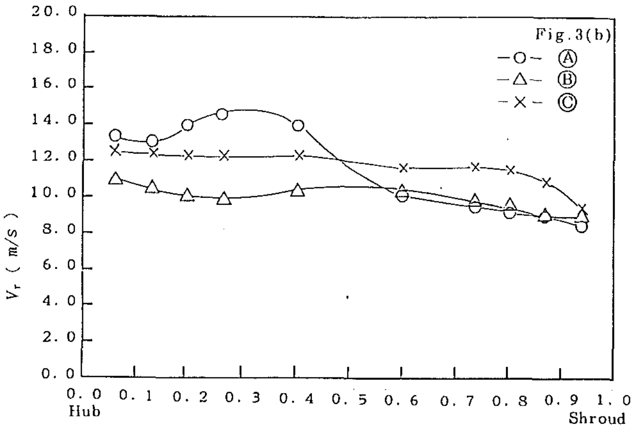

(a) φ = 0.10

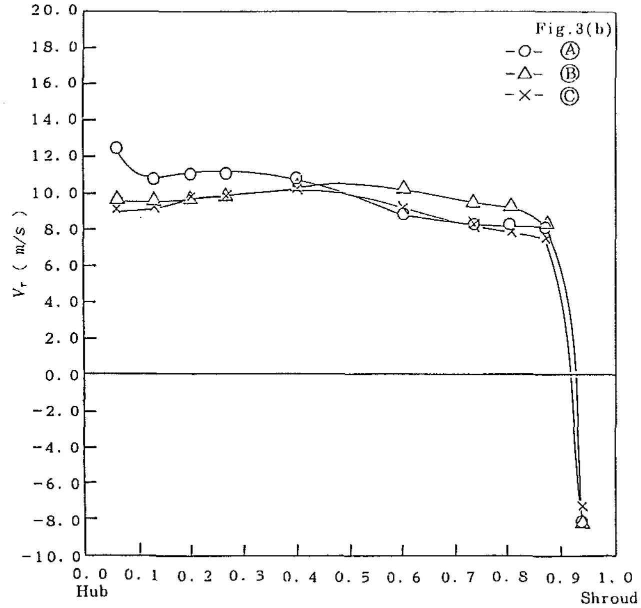

(b) φ = 0.05

Fig. 11 Distribution of radial component of velocity at entrance of vaneless diffuser

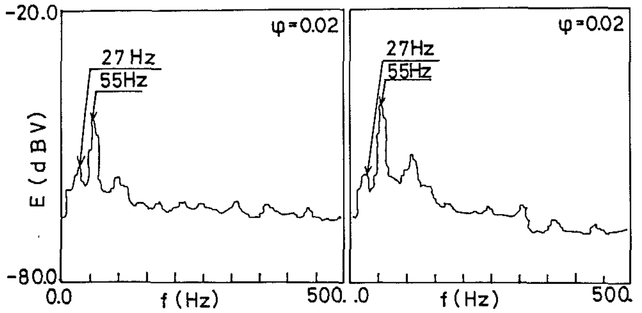

Position ③ in Fig.3(a)

(a) Impeller Inlet

Position Ⓓ in FIg.3(b)

(b) Entrance of Vaneless Diffuser

Fig. 12 Spectrum of pressure fluctuation

of the cell might occur in the circumferential direction at the initial stage and, after that, enlarge the size toward blade height as was shown for axial compressors (Jackson, 1987).

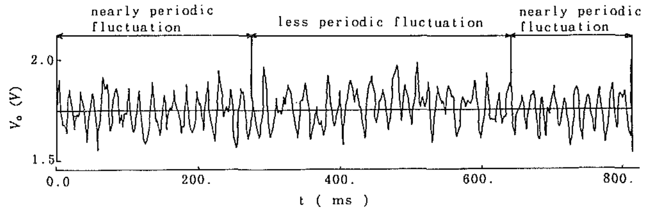

(Position ③ in Fig.3(a))

Fig. 13 Time-dependent variation of pressure fluctuation during surge

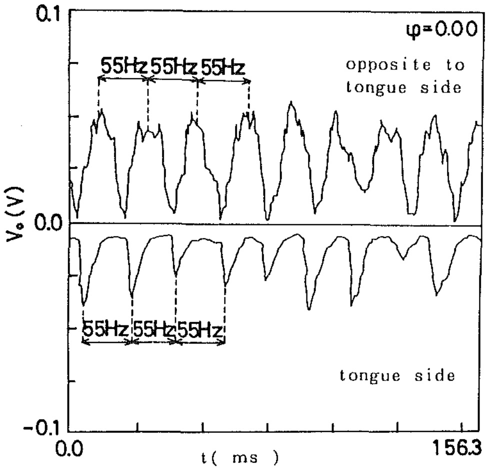

Position Ⓒ in Fig.3(b), 2.95mm from Shroud

Position Ⓑ in Fig.3(b), 1.95mm from Hub

Fig. 14 Output signals of thermal-tuft probes at entrance of vaneless diffuser during surge

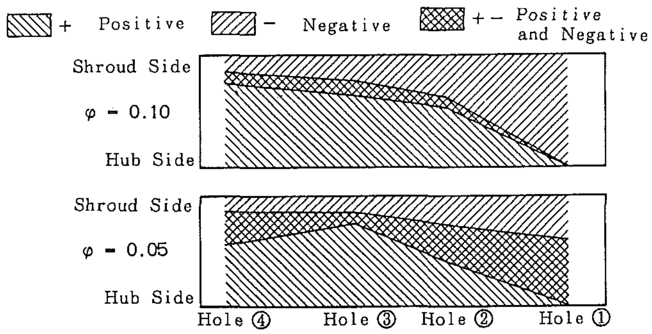

Fig. 15 Distribution of positive and negative components of radial velocity

Although small stall cells might be generated at the entrance of the vaneless diffuser, they were not clearly recognized until the flow rate was less than $\varphi = 0.05$. Then, the apparent time-averaged reversed flow appeared as in Fig. 11. At this condition, the number of the cell was unity and the frequency was 55 Hz, which were the same as those at the impeller inlet. Although the circumferential variation for the region of the stall cell was also not clear at the inlet to the vaneless diffuser, the unsteady blockage effect with the stronger fluctuations given at the impeller inlet by the full-span stall generated this stall cell at the entrance of the vaneless diffuser.

Surge

At $\varphi = 0.02$, the surge occurred in this system. Moreover, the strong influence of the full-span stall at the impeller inlet appeared even during the surge. The spectra of the pressure fluctuations exhibited both the frequencies of 55 Hz of the stall and 27 Hz of the surge at the impeller inlet and the entrance of the vaneless diffuser as in Fig. 12. The variation of the fluctuations at the inlet duct exhibited a strong time-dependent interference between the stall and the surge, and the fluctuations could be divided into nearly periodic and less periodic periods as in Fig. 13.

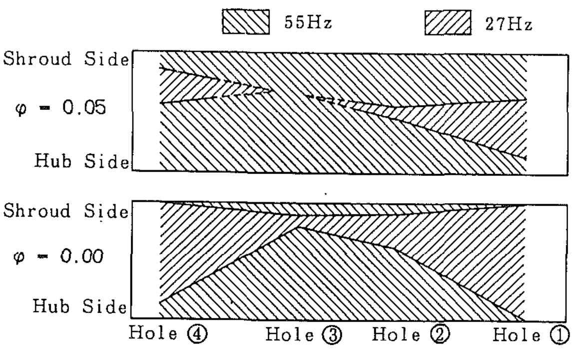

Fig. 16 Distribution of maximum frequency within scroll

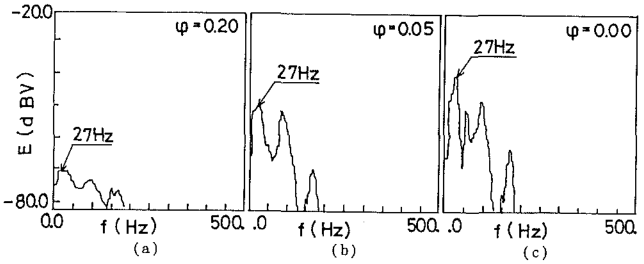

(a) (b) (c)

Fig. 17 Spectrum of pressure fluctuation within delivery duct

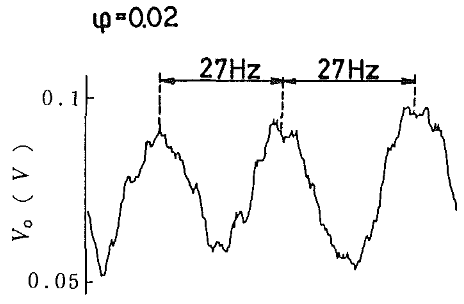

(a) Pressure-Transducer

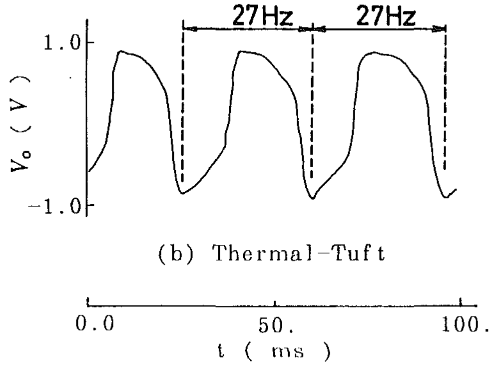

(b) Thermal-Tuft

Fig. 18 Correlation of fluctuating signals within delivery duct

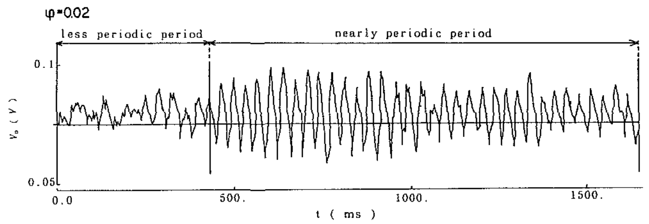

(a) Pressure Transducer

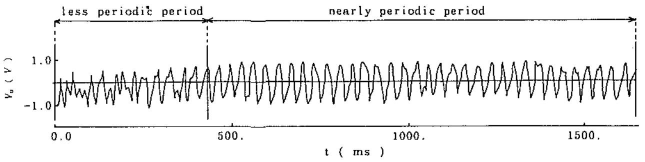

(b) Thermal-Tuft

Fig. 19 Time-dependent variations of velocity and pressure within delivery duct during surge

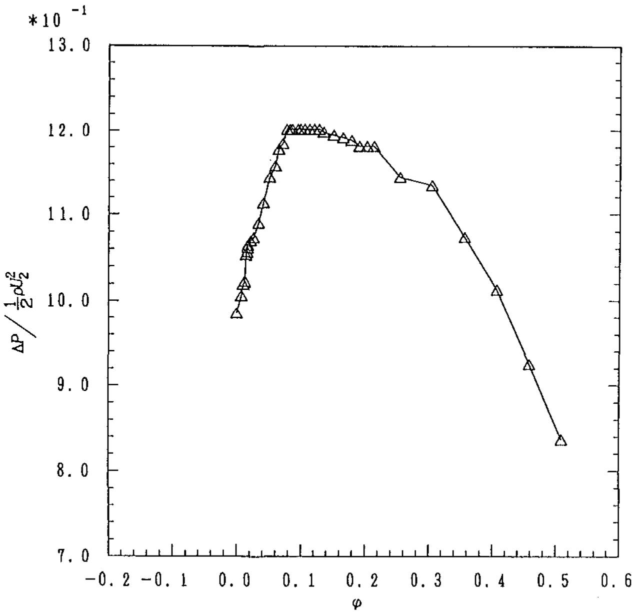

Fig. 20 Performance characteristics of impeller

At the entrance of the vaneless diffuser, the full-span stall at the impeller inlet generated quite strange fluctuations of the flow during the surge as in Fig. 14. The most severe circumferential variations of the flow could be recognized at the flow rate of zero. The positive and negative components of the radial velocities and the appearance of the less periodic fluctuations showed the very complex time-dependent three-dimensional flow within the vaneless diffuser.

The spatial variation of the positive and negative components of the radial velocities and the distributions of the frequencies as the variations of the flow rates within the scroll are shown in Figs. 15 and 16. The flow rate during surge was excluded from Fig. 15, because the whole region was occupied by the flow with positive and negative components. The frequency of the surge appeared at the boundary between the positive and the negative components of the radial velocities. In other words, the variation of the frequency from rotating stall to surge was made through the variation of the flow direction in the radial components. This also showed that the resonance of the system to the fluctuation of the surge mainly occurred there.

The frequencies of the flow at the delivery duct were examined as in Fig. 17. The frequency attributed to surge, 27 Hz, appeared irrespective of the variation of the flow rate, which showed remarkable increases after the occurrence of full-span stall at the impeller inlet. Thus, 27 Hz could be considered as the system resonance frequency. The fluctuations of the pressure and velocity during the surge are shown in Fig. 18. The deep surge appeared clearly. The differences of the wave shapes and the time lag between them also could be seen. The pressure fluctuation was axisymmetric about the peak. However, the velocities showed the sudden increases of the throughflow from the reverse flow, the initially gradual and the following sudden decreases.The periodicity and the am-

Table 1 Values for parameters

A_C (m^2)	0.00208
L_C (m)	0.03943
V_p (m^3)	0.01218
U_2 (m/s)	46.166
N (rps)	2 (φ = 0.02) 5 (φ = 0.05) 5 (φ = 0.07)
A_T ($\times 10^{-5}$ m^2)	4.283 (φ = 0.02) 9.858 (φ = 0.05) 11.359 (φ = 0.07)
B	0.8716
ω (Hz)	113.84
G	12.32 (φ = 0.02) 5.35 (φ = 0.05) 3.88 (φ = 0.07)

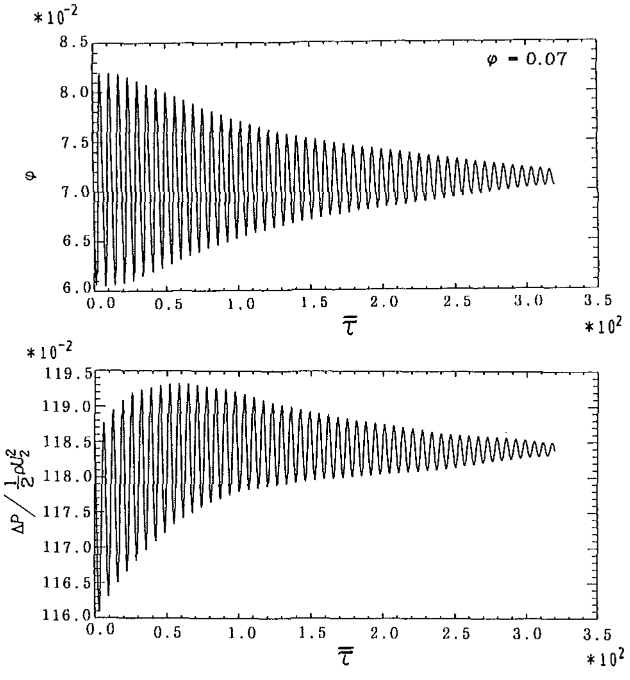

(*a*)

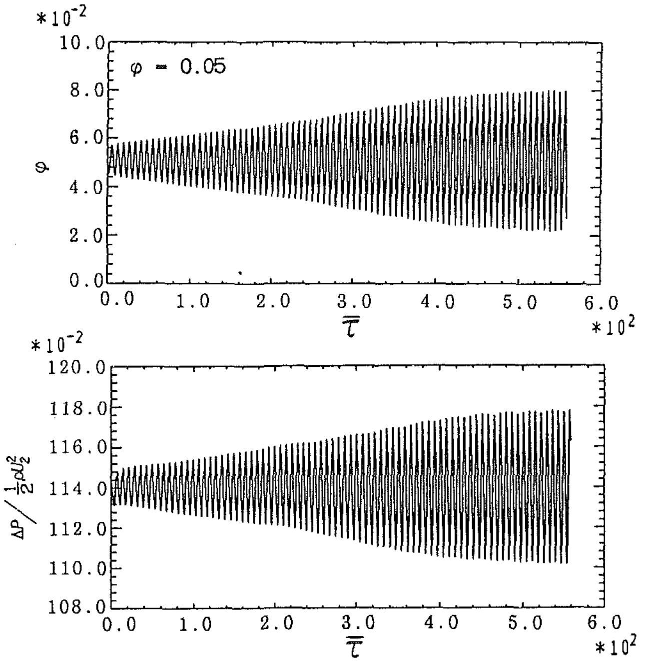

(*b*)

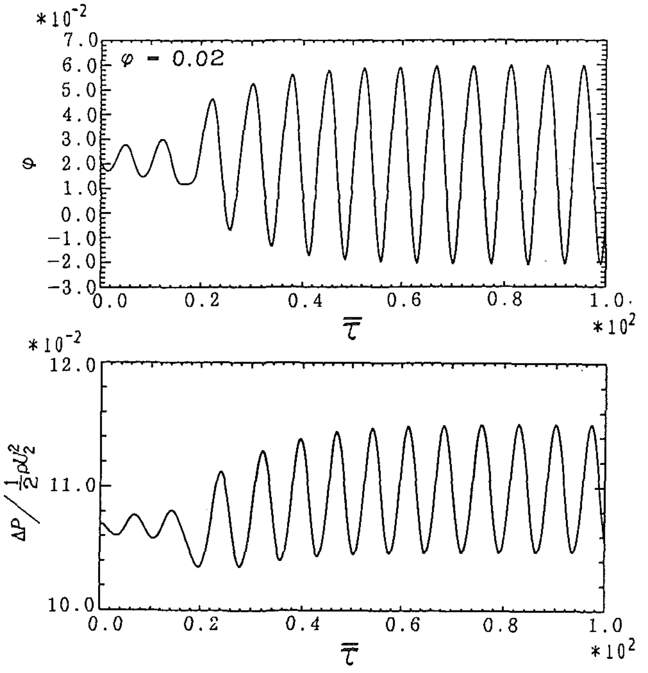

(*c*)

Fig. 21 Computed time-dependent variation of fluctuation

plitude of the fluctuations varied as in Fig. 19. They were also divided into the nearly periodic and the less periodic periods as were those at the impeller inlet in Fig. 13. Because no fluctuation related to the full-span stall was recognized within the delivery duct as in Fig. 18, the cause of these time-dependent variations could not be explained clearly by these results. However, the similar time-dependent variations appeared at the impeller inlet during the surge (Fig. 13) and the fluctuations were continuously supplied by the impeller. The delivery duct was always a kind of resonator, which selectively amplified the fluctuations containing the frequency attributed to the surge. The transient period between the nearly periodic, fully developed surge period to the less periodic, not fully surge period would be obtained by the interferences and the resonances of the flow through the scroll. This result would be related to the post-stall transient behavior of a centrifugal compressor as for axial compressors (Moore, 1984). As the time-dependent variations of the products of the throughflow velocity and the pressure were proportional to the time-dependent variations of the energy flux, very complex three-dimensional and time-dependent variations of the energy flux were taking place within the scroll.

Thus, the behavior of the development of the stall cell at the impeller inlet, the strong blockage effect of the full-span stall, and the variations of the time-dependent interferences and resonances of fluctuations during the surge between the impeller inlet and the delivery duct were clarified. In the present results, the fluctuations classified as progressive stall, abrupt stall, classic surge, and so on could not be obtained clearly. In addition, the frequency of the surge was only half of that

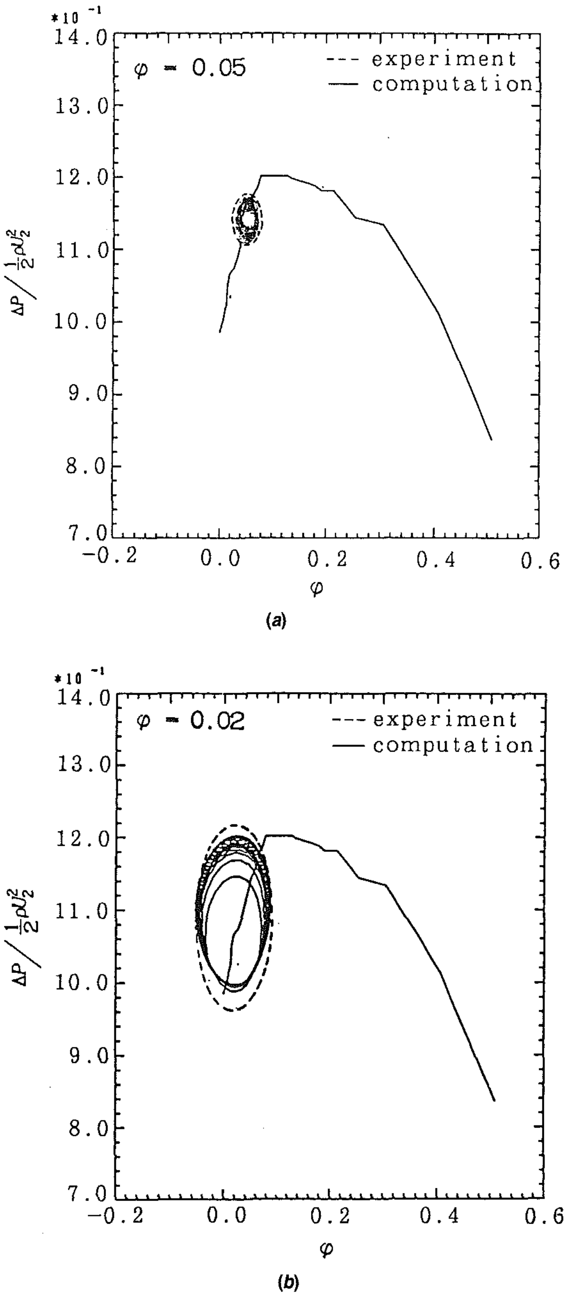

(a)

(b)

Fig. 22 Computed pressure-flow coefficient

of the rotating stall and the abrupt variations of unsteady behaviors as appeared for high-pressure compressors did not occur. Although these behaviors were exactly the problems just mentioned as the interferences and the resonances of the flow between the components and throughout the system of this compressor, many investigations distinctively showed the unsteady behaviors and the performance characteristics somewhat differently from the present results. If the essential factors for the present rotating stall and the surge were the same except for the unknown nonlinear effects, they would be predicted by a lumped parameter theory. By these considerations, one of the lumped-parameter theories (Greitzer, 1976) was applied to the present results by carefully selecting values for the parameters as will be shown below.

Application of Lumped Parameter Theory

The method and the assumptions for the present analysis were the same as reported by Greitzer (1976). The Eqs. (11)-(14) in the reference were used for the time-dependent variations of the compressor mass flow, the throttle mass flow, the pressure rise in the plenum, and the axial velocity with the time constant. The implicit fourth-order predictor-corrector method was employed with the Runge-Kutta-Gill method for the initial conditions. The performance characteristics of the impeller shown in Fig. 20 were used. The values for parameters are shown in Table 1. The volume of the plenum was assumed to be equal to the sum of the volumes from the vaneless diffuser to the delivery duct. Although we tried to obtain the effective length of the duct from the length including the logarithmic spiral at the vaneless diffuser, no computed results showing the instability coincided with the present results. Therefore, the length of the mean streamline of the impeller was used. The length of the throttle was conventionally chosen as 10 mm in order to get the agreements between the calculations and experiments. The flow rates were selected at $\varphi = 0.07$, 0.05, and 0.02. The computed results are shown in Fig. 21. At $\varphi = 0.07$, the given disturbance was converged to the state without the fluctuation (Fig. 21(*a*)). The disturbance converged to fluctuations with a constant amplitude and after that, the constant amplitude continued at $\varphi = 0.05$ (Fig. 21(*b*)). The limit cycle was formed as in Fig. 22(*a*) and the computed cycle shown by the full line coincided well with the experiments by the dotted line. At $\varphi = 0.02$, when the surge occurred in the experiments, the given disturbance increased in amplitude toward constant oscillation (Fig. 21(*c*)). The computed amplitude of the pressure fluctuation was slightly larger than those from the experiments and the mass fluctuation showed the opposite tendency (Fig. 22(*b*)). The frequencies for these results were at 32 Hz, which was close to the experimental value of the surge.

Although there still remains the problem about the selections of the values for parameters, the lumped parameter theory was able to be applied to the present results. Similar methods were successfully applied to the surge control of the centrifugal compressor with the high pressure ratio (Pinsley et al., 1991; Gysling et al., 1991), and the lumped parameter theory was also effective for the present results in the fundamental prediction. If appropriate assumptions could be introduced for the performance characteristics and the fluctuations of pressures and velocities including the lagging effect between them, the prediction for the bifurcation between the rotating stall and the surge for centrifugal compressors would be expected as for axial compressors (McCaughan, 1989a, 1989b). However, the unsteady behaviors shown in the present study were more complicated than those of axial compressors, and further information about the unsteady behaviors throughout various types of centrifugal compressor will be necessary in order to find the high-resolution prediction method.

Conclusion

Part-span stall appeared at the inlet duct. Then, the stall at the entrance of the vaneless diffuser did not occur. When the flow rate decreased further, full-span stall occurred. The stall cell enlarged the size toward the blade height by reverse flow from the impeller. The number of the cell was unity. The periodic blockage effect by the big stall cell from the hub to the shroud at the impeller inlet generated the rotating stall at the entrance of the diffuser with the same rotational speed and the number of the cell. This stall cell caused three-dimensional time-dependent flow patterns toward the scroll through the vaneless diffuser. During surge, the fluctuations of the full-span stall also existed at both the impeller inlet and the entrance of the vaneless diffuser. The surge period was divided into the nearly periodic period and the less periodic period due to the interference between the fluctuations of the full-span stall and the surge. The fluctuations caused by the full-span stall changed to those caused by the surge within the scroll through the variations of the radial component of velocities and only the fluctuations of the surge were seen within the delivery duct.

The measured results were compared with those computed by employing the lumped parameter theory and good agreements were obtained except for the problem about selected values for the parameters.

References

Chen, Y. N., Haupt, U., and Rautenberg, M., 1989, "The Vortex-Filament Nature of Reverse Flow on the Verge of Rotating Stall," ASME JOURNAL OF TURBOMACHINERY, Vol. 111, pp. 450-466.

Frigne, P., and Van den Braembussche, R., 1984, "Distinction Between Different Types of Impeller and Diffuser Rotating Stall in a Centrifugal Compressor With Vaneless Diffuser," ASME *Journal of Engineering for Gas Turbines and Power*, Vol. 106, pp. 468-474.

Frigne, P., and Van den Braembussche, R., 1985, "A Theoretical Model for Rotating Stall in the Vaneless Diffuser of a Centrifugal Compressor," ASME *Journal of Engineering for Gas Turbines and Power*, Vol. 107, pp. 507-513.

Greitzer, E. M., 1976, "Surge and Rotating Stall in Axial Flow Compressors," ASME *Journal of Engineering for Power*, Vol. 98, pp. 190-197.

Greitzer, E. M., 1981, "The Stability of Pumping Systems," ASME *Journal of Fluids Engineering*, Vol. 103, pp. 193-242.

Gysling, D. L., Dugundji, J., Greitzer, E. M., and Epstein, A. H., 1991, "Dynamic Control of Centrifugal Compressor Surge Using Tailored Structures," ASME JOURNAL OF TURBOMACHINERY, Vol. 113, pp. 710-722.

Haupt, U., Seidel, U., Abdel-Hamid, A. N., and Rautenberg, M., 1988, "Unsteady Flow in a Centrifugal Compressor With Different Types of Vaned Diffusers," ASME JOURNAL OF TURBOMACHINERY, Vol. 110, pp. 293-302.

Jackson, A. D., 1987, "Stall Cell Development in an Axial Compressor," ASME JOURNAL OF TURBOMACHINERY, Vol. 109, pp. 492-498.

McCaughan, F. E., 1989a, "Application of Bifurcation Theory to Axial Compressor Instability," ASME *Journal of Engineering for Gas Turbines and Power*, Vol. 111, pp. 426-433.

McCaughan, F. E., 1989b, "Numerical Results for Axial Flow Compressor Instability," ASME *Journal of Engineering for Gas Turbines and Power*, Vol. 111, pp. 434-441.

Mizuki, S., Hattori, T., Ariga, I., and Watanabe, I., 1976, "Reverse Flow Phenomena Within Centrifugal Compressor at Low Flow Rates," ASME Paper No. 76-GT-86.

Moore, F. K., and Greitzer, E. M., 1986, "A Theory of Post-Stall Transients in Axial Compression Systems: Part I—Development of Equations," ASME *Journal of Engineering for Gas Turbines and Power*, Vol. 108, pp. 68-78.

Moore, F. K., 1989, "Weak Rotating Flow Disturbances in a Centrifugal Compressor With a Vaneless Diffuser," ASME *Journal of Engineering for Gas Turbines and Power*, Vol. 111, pp. 442-449.

Pinsley, J. E., Guenette, G. R., Epstein, A. H., and Greitzer, E. M., 1991, "Active Stabilization of Centrifugal Compressor Surge," ASME JOURNAL OF TURBOMACHINERY, Vol. 113, pp. 723-732.

Van den Braembussche, R. A., and Haende, B. M., 1990, "Experimental and Theoretical Study of the Swirling Flow in Centrifugal Compressor Volutes," ASME JOURNAL OF TURBOMACHINERY, Vol. 112, pp. 38-43.

D. A. Fink[1]
Engineer, Fan and Compressor Aerodynamics,
General Electric Aircraft Engine Business Group,
Lynn, MA 01910

N. A. Cumpsty
Director, Whittle Laboratory,
Department of Engineering,
Cambridge University,
Cambridge CB3 0DY, United Kingdom

E. M. Greitzer
Director, Gas Turbine Laboratory,
Massachusetts Institute of Technology,
Cambridge, MA 02139

Surge Dynamics in a Free-Spool Centrifugal Compressor System

Turbocharger surge has been investigated in a radial impeller-vaneless diffuser free-spool system. Several different aspects are addressed. First, two very different compression systems, one with a large downstream volume and one with the smallest possible downstream volume, are employed to examine stall initiation phenomena as well as the behavior of the compressor characteristics when operating in surge. The measurements show impeller stall at the inducer tips to be a key phenomena in initiating surge. The inducer stall is stationary and asymmetric, due to the presence of the volute, and is most severe near the volute tongue angular position. The compressor characteristic in the large volume system (which gave surge) is observed to be flatter and to lag that in the stabilized small volume system. The difference arises because of the slow development time and differing circumferential extent of the inducer stall present at a given mass flow. A nonlinear simulation of the system is also presented. The model deviates from previous treatments of unsteady flow in compressor systems in that the assumption of constant rotor speed is relaxed. Including a time lag on the order of the compressor throughflow time, together with proper treatment of speed variations, is shown to improve agreement with the observed surge behavior dramatically.

Introduction

Most compressors demonstrate marked changes in behavior and flow patterns when operated at flow rates substantially below those for which they were designed. For axial compressors, which are generally much better understood than centrifugal compressors, it is well known that there are two quite different ways in which the machine can adapt to reduced flow. In one of these, the compressor can surge so that an essentially axisymmetric pulsing of the flow occurs. In the other, a rotating stall pattern can be set up so part of the annulus passes little or no flow, with the low flow portion rotating around the circumference. Whether an axial compressor exhibits surge or rotating stall depends not only on the compressor but on the system in which it is installed.

The understanding of stall and surge in centrifugal compressors is considerably poorer than for axial compressors, and it remains an open question whether rotating stall has a role in surge for centrifugal compressors. Rotating stall *can* occur in centrifugal compressors, as was seen in the pioneering work with centrifugal compressors of Emmons et al. (1955). Evidence of rotating stall has also been found in both the impeller and diffuser by Kammer and Rautenberg (1982) and by Abdel-Hamid et al. (1978). However, the time-resolved measurements of the flow in a centrifugal compressor entering surge made by Toyama et al. (1977) and by Dean and Young (1977) did not show rotating stall prior to the reversal of the overall flow that is characteristic of surge. Instead they found that surge was preceded by stall in the inlet region of the vaned diffuser.

One difficulty in arriving at a general description of centrifugal compressor instability is that the speeds, the overall system, and the compressor geometries cover a very wide range. With a centrifugal stage having a vaned diffuser and designed for a pressure ratio of, say, 4:1, the element likely to stall at design speed is the vaned diffuser. The same machine operated at lower speed so that the pressure ratio is only, say, 2:1 is likely to stall in the impeller inducer. The point is that, as described by Cumpsty (1989), there is an overwhelming effect of matching between components. This difficulty is echoed by the variation in available data; Toyama et al. (1977) operated at high speed with a vaned diffuser, whereas Adbel-Hamid et al. (1978) used a compressor at much lower speed with a vaneless diffuser.

The present research is concerned with the type of machine often used in turbocharger systems: a high-speed radial impeller with vaneless diffuser surrounded by a volute or scroll. At a given operating speed, there is only one mass flow rate at which the volute produces an axisymmetric pressure field; at all flow rates for which surge is possible, the pressure field from the volute will generally be highly nonaxisymmetric (Lorett and Gopalakrishnan, 1986), and this circumferential nonuniformity can be detected upstream of the impeller inducer. At the inception of this research project, it was not appreciated how significant this nonuniformity would be; essentially the rotating stall common in machines that are nominally axisymmetric is replaced by a stationary (casing fixed) flow distortion.

The operation of many centrifugal compressors, including

---

[1] Work done prior to GE employment at the MIT Gas Turbine Laboratory under Cummins Engine Company and Air Force Research in Aero Propulsion Technology (AFRAPT) sponsorship.

Contributed by the International Gas Turbine Institute and presented at the 36th International Gas Turbine and Aeroengine Congress and Exposition, Orlando, Florida, June 3-6, 1991. Manuscript received at ASME Headquarters February 6, 1991. Paper No. 91-GT-31. Associate Editor: L. A. Riekert.

those in turbochargers, is normally limited by the occurrence of surge, which is a self-excited system oscillation. Surge can be classified according to the amplitude of the mass flow fluctuation. "Mild surge" refers to the condition where the annulus average mass flow oscillates but remains in forward flow at all times: The frequency is of the order of the Helmholtz resonator frequency.[2] With low frequency response instrumentation, a compressor in mild surge would appear to be operating stably, although a change may be perceived in the noise. The Helmholtz frequency is thus the inverse of the characteristic time of the compression system up to the point at which it enters deep surge, when an entirely different time scale is relevant. In "deep surge," the mass flow variations are large and the overall flow direction generally reverses for part of the cycle. The frequency is set by the plenum emptying and filling times and is normally well below the Helmholtz frequency. The onset of deep surge terminates the useful operating range of the compressor, so that when a compressor operating map has a line denoted as the "surge line," it usually refers to the condition at which the compressor enters deep surge.

An important nondimensional parameter in describing the dynamics of compression systems (both axial and centrifugal) is:

$$B=\frac{U}{2a}\sqrt{\frac{V_p}{A_cL_c}} \qquad (1)$$

where U is the tip speed. B may be rewritten in terms of Helmholtz frequency as

$$B=\frac{1}{2}\frac{U}{\omega_H L_c}$$

For a given compressor, the system will exhibit a surge as the result of an instability if the value of B exceeds a critical value. If B is less than this, the compression system will maintain itself at an overall steady equilibrium point. For axial compressors, this equilibrium point is generally in rotating stall.

Table 1 System parameters

System Parameter	Large B System	Small B System
Plenum Volume (m^3)	0.21	0.0014
Stage Inductance L/A (m^{-1})	350	283.3
Reference Area (m^2)	3.58×10^{-3}	3.58×10^{-3}
Helmholtz Frequency @ 48 KRPM (Hz)	7.4	99
Tip Speed @ 48 KRPM (m/s)	322	322
B Parameter @ 48 KRPM	2.7	0.25

The first part of this paper describes experiments that were carried out with the same turbocharger compressor in two different compression systems. One system had the throttle valve immediately downstream of the compressor outlet and thus a small value of B (0.25, see Table 1). The other system had a large value of B (0.7), obtained by having a large volume between the compressor outlet and the throttle.

Many compressor systems operate with large values of B, but there were additional reasons for choosing this configuration in the present series of experiments. With large B, surge frequency is low, and the cycle of deep surge can be used to take the compressor essentially quasi-steadily through the stalling process. The long time scale that goes with a large plenum also makes it possible to measure the backflow characteristic of the compressor in deep surge during the plenum blowdown part of the cycle. The large plenum also ensures a wide frequency separation between the phenomena of rotating stall (time scale is on the order of a rotor revolution) and surge. Finally, the large value of B allows the effect of plenum size on the position of the surge line to be specified.

The reason for operating the compressor with low B, that is, with the throttle valve just downstream of the compressor, is that the positively sloped flow characteristics at low flow can be measured using steady state instrumentation. These are generally inaccessible on most stands, because of system instability. The stabilizing aspect of small values of B (i.e., small storage volumes between the compressor and throttle) is now

Nomenclature

a = speed of sound
A = flow area
B = dimensionless parameter; defined in Eq. (1)
C_x = axial velocity
C' = slope of compressor pressure rise characteristic = $d(\widetilde{\Delta P}_c)/d\Phi$
F = spool inertia parameter; defined in Eq. (8)
I = polar moment of inertia of turbospool
L = length
$\dot{m}$ = mass flow
$\dot{m}^*$ = choked flow through impeller eye area A_{ref} at ambient P_o and T_o
M_{to} = impeller tip Mach index = U/a_o
N = rotational speed
P = pressure
r, R = radius
T = temperature
T' = slope of throttle characteristic = $d(\widetilde{\Delta P}_p)/d\Phi$
t = time
U = impeller blade tip velocity
V_p = volume of compression system plenum
γ = ratio of specific heats = c_p/c_v
θ = nondimensional temperature = T/T_{ref}
Π = nondimensional pressure = P/P_{ref}
ρ = density
τ = total temperature ratio, characteristic time
ϕ = flow coefficient; defined by $\dot{m}_c/(\rho A_c U) = C_x/U$, where ρ is appropriate density; C_x/U in plots
Φ = flow coefficient; defined by $\dot{m}_c/(\rho_o A_c U) = C_{xo}/U$
ψ = isentropic head coefficient = $(\Pi^{(\gamma-1)/\gamma}-1)/((\gamma-1)\text{M}_{to}^2)$
$\widetilde{\Delta P}$ = nondimensional pressure rise = $(P-P_o)/(0.5\,\rho U^2)$
ω_H = Helmholtz frequency

Subscripts

c = compressor
d = drive
H = Helmholtz
in = inlet
p = plenum conditions
ref = reference condition value
t = throttle
0 = at or relative to ambient condition, equilibrium value
1 = inducer eye position
2 = impeller tip diameter position
3 = volute discharge position

Other

~ = nondimensional quantity

---

[2] The Helmholtz frequency ω_H is given by $a\sqrt{A_c/(V_pL_c)}$, where V_p is the plenum volume, L_c the compressor duct length, A_c the duct area, and a the speed of sound.

sufficiently well known to be in recent textbooks (e.g., Cumpsty, 1989). Linear stability analysis predicts that the system will be unstable when the slope of the compressor characteristic $C' = d\widehat{\Delta P}/d\phi$ reaches a value

$$C' > \frac{1}{B^2 T'} \tag{2}$$

where T' is the slope of the throttle characteristic. In the limit as $B \rightarrow \infty$, instability occurs when $C' > 0$, i.e., at the peak of the total-to-static pressure rise characteristic. As B decreases, the compression system can operate stably at increasingly positive values of compressor slope.

The second part of the paper describes a lumped parameter analysis of the system dynamics. The overall approach is along lines somewhat similar to those used by Emmons et al. (1955), Taylor (1964), Stenning (1980), and others, but a significant difference is that the effect of speed variation during the surge cycle is now included. This will be shown to be important in capturing the system dynamics. Toyama et al. (1977) and Dean and Young (1977) had speculated about the effect of speed variation but were not able to make any quantitative statements. Speed variations during surge also occur in jet engines, but the high energy transfer in relation to spool inertia existing in radial machines makes this effect particularly important for the turbocharger.

Experimental Facility

Figure 1 shows schematically the arrangement for small and large B configurations and Table 1 lists the important parameters of each. Additional details are discussed by Fink (1984, 1988) and Capece (1982). The test turbocharger was driven by the turbine using the laboratory compressed air and vacuum capability.

A cross section of the instrumented turbocharger impeller and diffuser is shown in Fig. 2. There are no inlet guide vanes. The impeller blades are radial at exit; most recent impellers have backsweep, but this difference is unlikely to alter the conclusions of this research because stall is initiated in the inducer. Design parameters and geometry of the compressor are shown in Table 2.

Eight high-response pressure transducers (d-c coupled Kulite model XT-140-50) were installed in the compressor case, with a ninth located downstream of the compressor in the connecting plenum. Unsteady mass flow in the calibrated inlet tube was measured by a single platinum hot wire mounted six impeller inducer diameters upstream of the inducer leading edge, as well as by a continuity balance on the plenum. Instantaneous rotor speed was detected by a reflective scanner fiber optic probe, which senses blade passing frequency. High-response microminiature K-type thermocouples (Beckman model 300, time constant at roughly 1 ms) were positioned at midspan in front of the impeller inducer and downstream of the impeller. These were used to track the temperature ratio across the impeller during surge. During surge, the flow and head coefficient were calculated using the instantaneous speed measured by the photo optic probe.

The results and discussion of three separate data sets are presented. For the large B system, high response instrumentation was used to measure the instantaneous mass flow, the speed, and pressures in the compressor and downstream plenum during surge. The instantaneous compressor characteristic was computed using the unsteady pressures and taking account of the inertia in the compressor duct (Koff, 1985). The duct inertance required for the correction was measured experimentally by finding the Helmholtz frequency with the duct-plenum system containing a well defined plenum.

With the turbocharger operating in the small B system, time-resolved and time-averaged data were obtained. Flow asymmetry, and extent of local reversed flow near the volute tongue, were investigated with the small B system.

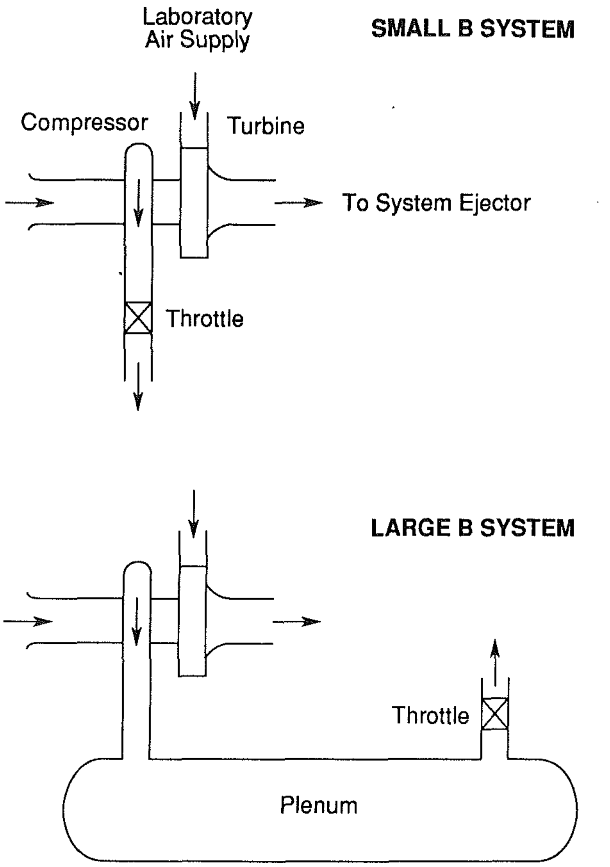

Fig. 1 Schematic of compression systems examined

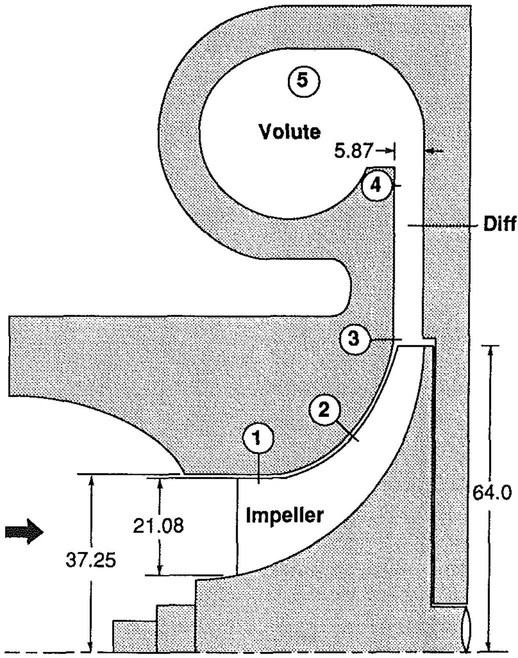

Fig. 2 Instrumentation meridional positions (in millimeters); steady-state and high response probes at locations shown

Performance Maps. The measured performance map of total pressure ratio versus mass flow, including data for both the large and small B system, are shown merged together in

Table 2 Compressor design data

Total-to-total pressure ratio	3.58
Corrected mass flow (Kg/s)	.522
Corrected speed (rev/s)	1150
Impeller Type	Cummins ST50
No. of Blades	20
Inducer Tip Blade Angle (deg)	54.4
Rotor Exit Blade Angle (deg)	0
Rotor Tip Diameter (cm)	12.8
Inducer Hub/Tip Ratio	.428
Inducer Tip/Rotor Tip Ratio	.576
Tip Clearance/Inducer Height Ratio	.020
Diffuser Type	vaneless + volute
Diffuser Exit/Inlet Radius Ratio	1.619
Diffuser Width/Inlet Radius Ratio	.092

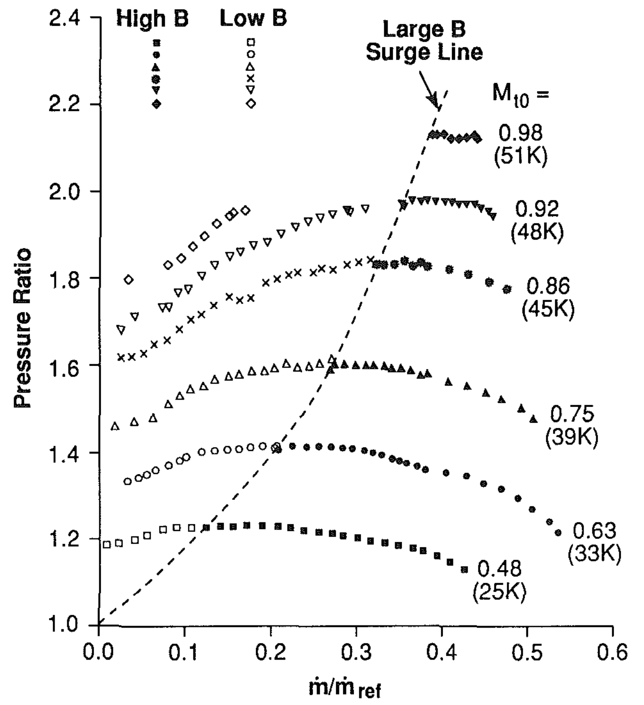

Fig. 3 Compressor map; large and small B data shown, M_{t0} denotes tip Mach number

Fig. 3. The abscissa is compressor corrected flow nondimensionalized by the choked flow through the impeller eye at reference conditions (0.842 kg/s at 303 K, 1.013 bar). Lines of pressure ratio versus flow for constant corrected rpm, from 25 K to 51 K, are shown. These represent tip Mach numbers, M_{t0} (based on tip speed and inlet stagnation temperature), from 0.48 to 0.98. To the right of the large B surge line, the results are identical for the high and low B systems.

In the large B system, mild surge oscillations were encountered when the compressor was throttled to (time-mean) operation just to the right of the surge line. The oscillation amplitude increased as the mean operating point approached the surge line. To the left of the surge line, the compressor in the large B system operated in a deep surge cycle, with period depending on speed and amount of throttling. At 48K corrected speed, the surge cycle (which lasted on the order of 1 s) included an audible plenum blowdown with reverse flow in the inlet and large plenum pressure variation. During the blowdown there was a several thousand rpm drop in compressor speed. The surge line was well defined and repeatable within 1 percent of maximum mass flow at each speed.

Compressor operating points with the small B system are shown to the left of the large B surge line in Fig. 3. With small B, this region of the compressor map is now stable, and the speedlines extend nearly to shutoff. (Near shutoff, the mass flow and pressure ratio exhibit some unsteadiness, but there is no discernible deep surge.)

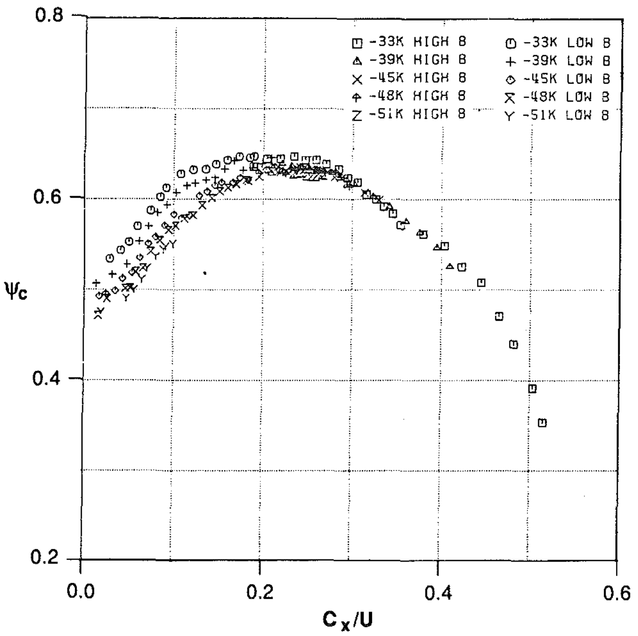

Fig. 4 Compressor isentropic head coefficient versus C_x/U

Compressor performance in terms of isentropic head coefficient, ψ_c, versus flow coefficient, ϕ, is shown in Fig. 4 for the small B system. When plotted in this fashion, the data nearly collapse into a single curve, although compressibility effects preclude complete similarity of the speedlines. In particular, the peak value of ψ_c occurs at a higher flow coefficient at the higher speeds. In the large B system the instabilities were seen to grow in a region around the peak of the ψ_c versus ϕ curve; thus mild (and deep) surge occur at high values of ϕ as corrected speed increases.

Large *B* System Unsteady Behavior During Surge. Instantaneous compressor flow coefficient, tip Mach number, and isentropic head coefficient are shown for mild surge in Fig. 5. The data are taken at a mean flow coefficient of $\phi = 0.23$, and a corrected speed of 48K, but similar behavior was found at other speeds. The system surge frequency is 7.3 Hz and an audible chugging noise accompanies operation in this mode. The amplitude of the roughly sinusoidal mass flow oscillation is 20 percent of the mean flow. This is the type of (relatively) small amplitude limit cycle phenomena that Toyama et al. (1977) and Dean and Young (1977) reported during so-called stable operation. As Dean showed by calculation, mild surge limit cycles can occur in the vicinity of the peak due to the curvature of the compressor characteristic.

A deep surge cycle is shown in Fig. 6. The surge is initiated by a 1-2 percent reduction in throttle area compared to the conditions of Fig. 5. Three different time scales are seen in Fig. 6: a Helmholtz oscillation of approximately 7 Hz, a longer one (roughly 0.65 s) associated with the plenum blowdown and recovery (deep surge), and a still longer time scale associated with the rotor speed fluctuations.

Four regimes exist in the deep surge cycle. The first is a quiescent period, with the tip Mach number increasing, flow coefficient decreasing, and the compressor moving to the left on its unstalled characteristic. In the second phase, fluctuations grow as the compressor operates in mild surge. In the third phase, the mass flow reverses and the plenum pressure decreases during blowdown. (The flow coefficient is measured

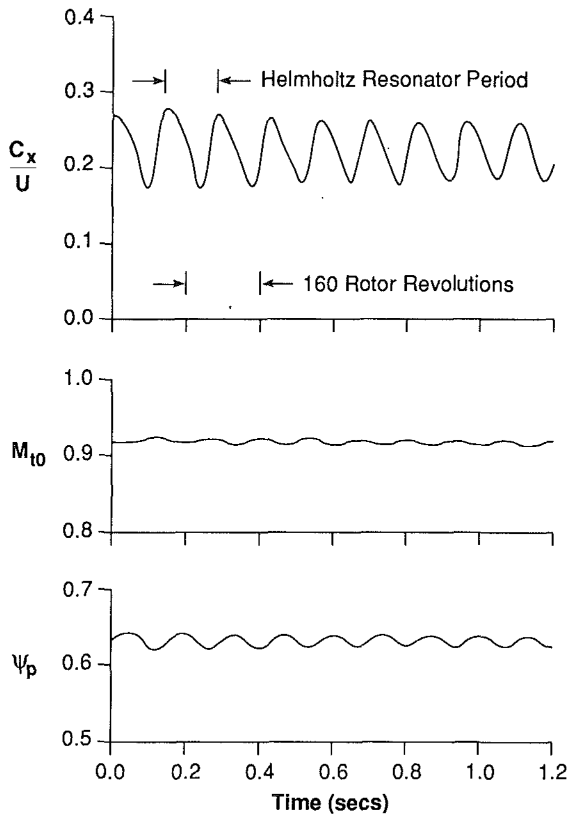

Fig. 5 System parameters during mild surge ($\phi_T \approx 0.23$); large *B* system

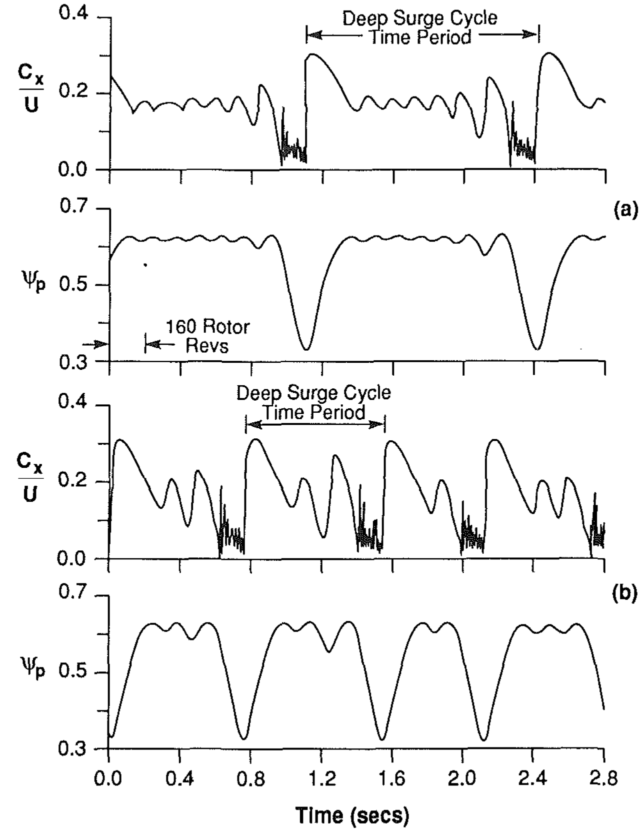

Fig. 7 Effect of operating point on time-resolved behavior during deep surge (large *B* system); (*a*) ($\phi_T \approx 0.19$); (*b*) ($\phi_T \approx 0.16$)

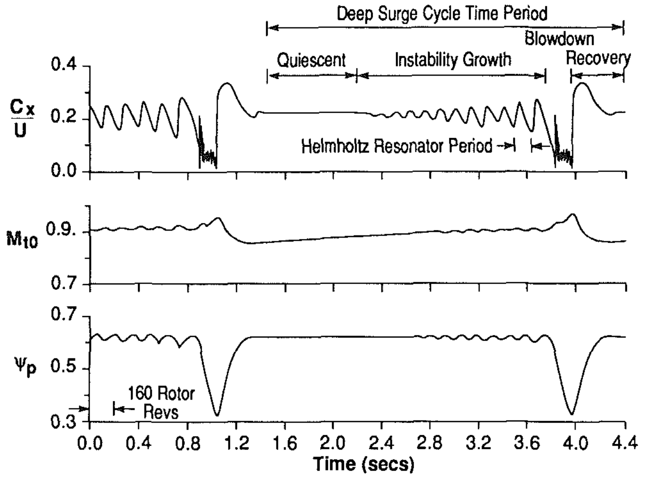

Fig. 6 Large *B* system parameters during deep surge ($\phi_T \approx 0.225$)

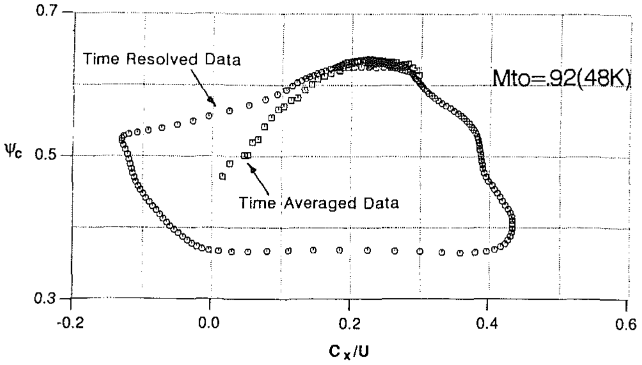

Fig. 8 Time-averaged data versus large *B* time-resolved data; $M_{t0} \cong 0.92$

by the inlet hot wire, which is insensitive to flow direction. A high flow rate is thus registered during the backflow phase. However, measurements made using the plenum continuity balance confirmed that reversed flow was indeed present.) In the fourth phase, the blowdown finishes and the flow recovers rapidly to the forward direction and then decreases gradually to the flow rate for the quiescent flow. The cycle then repeats. In the backflow region in Fig. 6, high response thermocouples showed the temperature in the inlet duct exceeds the rotor exit temperature. At the end of the blowdown phase of the cycle, the compressor reingests the residual hot gas present in the inlet and returns to operation in forward flow.

Figure 6 is for a throttle area just small enough to yield deep surge. As the throttle was closed, the repetition time for the deep surge became shorter. The latter stages of the surge cycle (the maximum amplitude Helmholtz frequency oscillations followed by deep surge) were altered little but the periods in which the Helmholtz oscillations were small became shorter as the throttle was closed. Figures 7(*a*) and 7(*b*) show this behavior for throttle settings corresponding to a time-mean, ϕ, of 0.19 and 0.16. The time history of flow and pressure rise can be compared directly with the corresponding traces in Fig. 6 (The speed variations are not shown but the trend is the same (Fink, 1988).) The latter part of the surge transient in Fig. 6 can be seen to be similar to the wave forms shown at the lower mass flows.

The (inertially corrected) overall compressor head coefficient is shown versus the instantaneous flow coefficient during a deep surge cycle in Fig. 8. Also shown are the time-averaged data for small *B* at flow coefficients below that for surge initiation at large *B*. The points are 3.2 ms apart in time (2.6 rotor revolutions at 48K corrected speed). The instability growth phase is shown by the cloud of data centered roughly on $\phi = 0.225$, with oscillations developing around the peak of the compressor characteristic. Compressor operation to the right of the peak is essentially quasi-steady. In the forward to backflow transition region (the range $0.1 > \phi > -0.1$) the data indicate rapid movement of the operating point along a positive sloped characteristic. In backflow, it appears that the compressor operates quasi-steadily on a steady-state backflow characteristic. Most of the decrease in compressor pressure rise occurs during this period. In the forward flow phase, when the plenum is being filled, the compressor also moves relatively slowly along its characteristic to re-enter the instability growth regime, which is the precurser to another deep surge.

The different pressure rise of the shutoff points defined by $\phi = 0$ for the two curves should be noted. In transition to reverse flow, most of the pressure rise decrease of the compressor in surge occurs well *after* the overall flow in the compressor has reversed. The differences between instantaneous and quasi-steady compressor performance are also seen by an examination of the transition regions. During the forward-reverse transition, the compressor head exceeds the small B steady value for the same flow coefficient (0.57 versus 0.47 at $\phi \sim 0.2$). In the reverse-forward flow transition, the head is less than the steady-state value for more than 30 revolutions of the impeller.

In the reverse-forward transition region, varying inlet gas temperature is a contributor to the lag. Low-density (hot) air in the inlet duct from the plenum blowdown is reingested by the compressor, resulting in a lower compressor pressure rise. The time of reingestion is roughly the time it takes to empty the inlet tube. Taking ambient pressure in the tube with the measured temperature ratio of 1.27, an average mass flow in transition of 0.3 kg/s, and a tube volume of 5.9×10^{-3} m^3, the time to clear the inlet is 19 ms. The data of Fig. 8, however, show this phase to take much longer and hence temperature effects are not solely responsible for the observed lag.

Casing static pressures (in terms of head coefficient) versus time in the compressor during deep surge at 48K are displayed in Fig. 9 with the time interval near flow reversal shown on an expanded scale in Fig. 10. Kulite traces are shown from the two circumferential positions, one near the volute tongue and the other 90 deg from this. The traces are labeled 1 (ahead of inducer) through 4 (near diffuser exit), as shown in Fig. 2, with the plenum Kulite trace marked 5. The bottom two traces of Figs. 9 and 10 show compressor flow coefficient and tip Mach number. The time period of the flow reversal region is approximately 0.15 seconds.

The link between surge and and impeller stalling due to local flow reversal at the inducer tips can be observed in Figs. 9 and 10. At maximum flow during the period of mild surge, the inducer inlet (trace 1) has a value below ambient, indicating forward flow into the inducer. At the flow minima, on the other hand, the inducer inlet static pressure is observed to be *above* ambient for both circumferential locations, implying local reverse flow at the inducer tips. These local flow reversals in the inducer occur well in advance of overall flow reversal of deep surge.

In the time history shown in expanded scale in Fig. 10, evidence of inducer tip flow reversal occurs first at the circumferential position near the tongue approximately 120 ms (96 rotor revolutions) before overall flow reversal. At 90 deg from the tongue, flow reversal at the inducer tip is found approximately 90 ms (72 rotor revolutions) before overall flow reversal. The instantaneous value of overall mass flow coefficient at which the local flow reversals are seen at the inducer tip is approximately $\phi = 0.26$ for the near tongue position and $\phi = 0.225$ for the position away from the tongue; these can be compared with the peak in the compressor characteristic shown in Fig. 4 at $\phi = 0.225$. This suggests that the characteristic peak is in fact the point on the map where the onset of the tip inducer stall begins over all or most of the circumference. In this compressor, the fluid dynamic circumstance that causes the positively sloped compressor characteristic necessary for surge is an inducer tip stall.

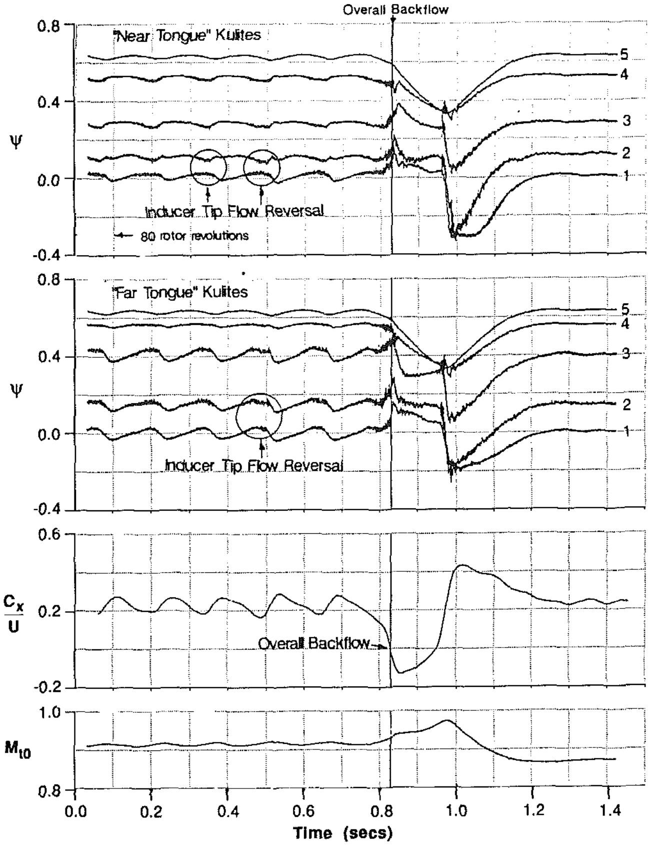

Fig. 9 **Compressor static head coefficients versus time in deep surge; numbers refer to instrumentation locations shown in Fig. 2; $M_{T0} \cong 0.92$**

The inducer tip flow reversal is seen to be most severe at the circumferential position corresponding to the volute tongue. The inducer pressure recovery at the circumferential position of the tongue, shown in Fig. 9 by the difference between traces 1 and 2, diminishes when the overall mass flow is a minimum during the mild surge. Away from the tongue, on the other hand, there is less evidence of loss in pressure rise in the final few cycles of mild surge. In Fig. 10 the pronounced drop in pressure rise in the impeller inducer at the tongue circumference occurs approximately 13 ms (or, more relevantly, 10 rotor revolutions) before overall reverse flow. The overall flow does not reverse until after the decrease in inducer pressure rise occurs at the tongue.

Evidence that the inducer tip flow is locally reversed at the circumferential position of the volute tongue, while the overall average flow is still forward, can also be seen by examining the pressure levels in traces 1, 2, and 3. When the flow is a minimum during mild surge, these are essentially the same as the values when the overall mass flow has reversed during deep surge. For example, the pressure levels are more or less equal at $t = 0.135$ seconds in Fig. 10 (in the precursor period to deep surge) and at a later instant of $t = 0.21$ seconds during plenum blowdown with overall reverse flow. This is not the case for the traces (at these same times) obtained well away from the tongue since, in the precursor period, the inducer is still producing a large pressure rise.

The asymmetric stalling of the impeller at the circumferential location of the volute tongue is linked to the onset of deep surge. This is seen more clearly if the impeller total to static head coefficient of Figs. 9 and 10 is plotted versus overall flow

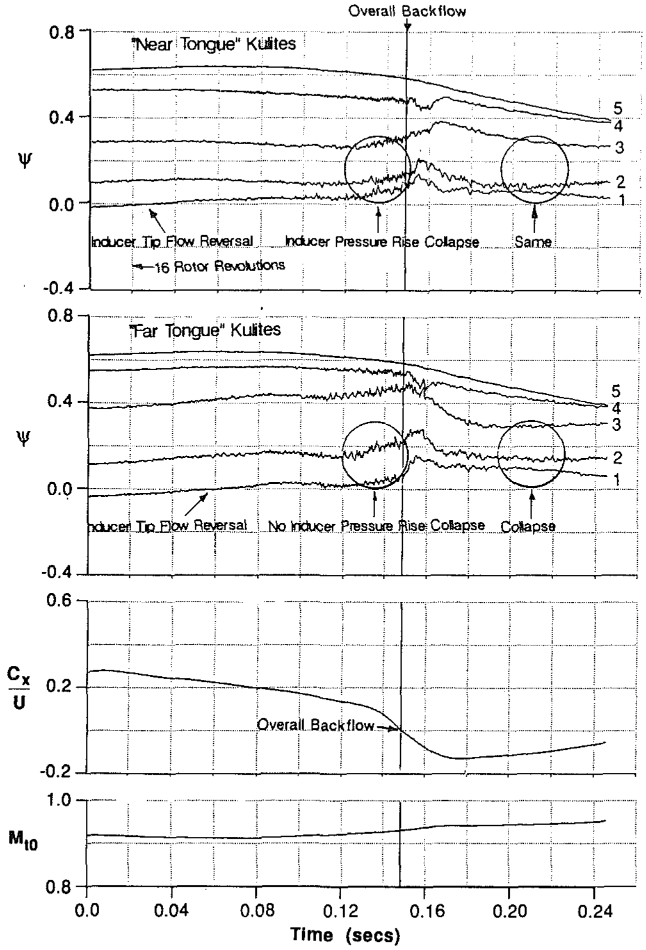

Fig. 10 Detail of deep surge onset; numbers refer to instrumentation locations shown in Fig. 2; $M_{t0} \cong 0.92$

coefficient, rather than versus time. Figure 11 shows such a plot, for a speed of 48K, and includes data from both near and far tongue circumferential positions. Also marked in the plots are the values of overall flow coefficient at which the system enters deep surge. The impeller head at the near tongue circumferential location peaks at $\phi = 0.25$ compared with the deep surge throttle point of $\phi = 0.225$. In contrast to the impeller behavior shown in Fig. 11, the vaneless diffuser pressure rise coefficient versus flow coefficient data, as given by Fink (1988), has a positive slope, indicating that the vaneless diffuser has a destabilizing effect on the overall system at all flow rates.

Rotating Stall. Rotating stall disturbances were observed (with the inducer inlet Kulites) during part of the surge cycle. Static pressure amplitudes associated with this rotating stall were less than 0.01 in terms of head coefficient (Fink, 1988). The signals were strongest in the inducer section, growing weaker as one progressed meridionally back in the machine. Some evidence of this is seen in the pressure (trace 1) of Fig. 10, where the rotating stall disturbances are superimposed on the much lower surge frequencies and occur in bursts at the mass flow minima of surge. The magnitude of the rotating stall pressure fluctuations is seen to be small relative to the fluctuations due to mild surge. The amplitudes associated with rotating stall were largest at a throttle condition where the scroll distortion was minimum, i.e., were less when scroll-induced circumferential pressure nonuniformity was high. The rotating stall disturbances thus appear, for this type of machine, to have little impact on the surge inception process.

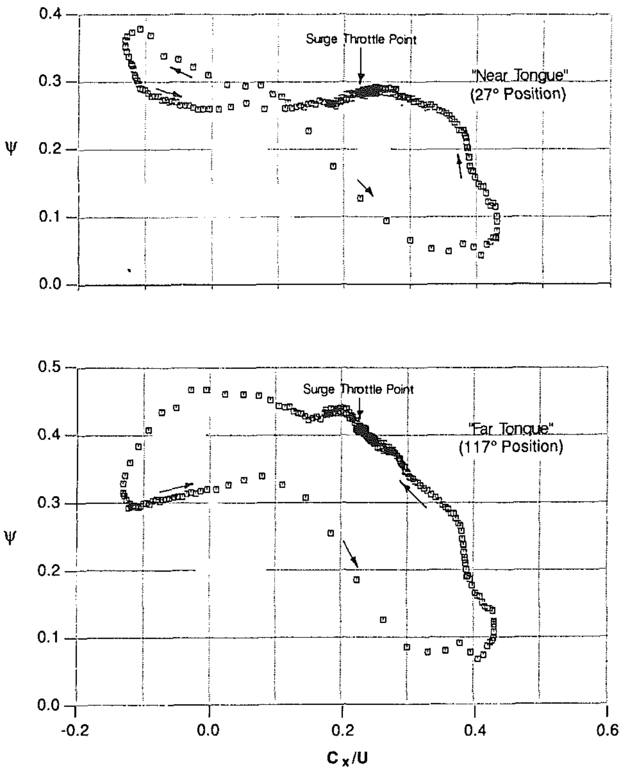

Fig. 11 Impeller head coefficient versus C_x/U; $M_{t0} \cong 0.92$

Small *B* System Stall Results. The circumferentially averaged impeller head coefficient (total to static) and the vaneless diffuser pressure rise coefficient (static to static), measured with the throttle close to the compressor outlet, are shown in Fig. 12. At $\phi = 0.225$ for a rotational speed of 48K, the slope of the vaneless diffuser characteristic is flatter than at higher flows; conversely the impeller characteristic slope is seen to change from negative at high flows to slightly positive at this same flow coefficient. This flow coefficient is approximately that at which surge was initiated for the large *B* system, and this indicates that the surge initiation point is being set by the impeller.

The asymmetry in flow can be assessed by examining the circumferential pressure distribution at the compressor inlet and exit. Total to static head coefficients versus circumferential position around the impeller are shown in Fig. 13 for several flow rates. (The tongue location is at zero degrees with circumferential position positive in direction of rotor rotation.) Near the tongue, the pressure rise is depressed relative to angular positions away from the tongue. This was also seen in the pressure traces in Figs. 9 and 10 for the large *B* system.

The asymmetry is also seen in the inducer leading edge wall static pressures. The measured pressures allowed an estimate of the local variation in tip flow coefficient, and Fig. 14 shows the results of this calculation. As the compressor is throttled, the axial velocity at the tip drops to zero at the tongue at a mean flow coefficient of $\phi = 0.150$.

The rotating stall obtained at low flow coefficient for the small *B* system was also of relatively low amplitude, but at very low flow rates ($\phi < 0.10$), the unsteadiness detected was in phase at both circumferential positions, indicating a mild surge and not a rotating stall.

Overall System Dynamics and Variable Speed Surge Modeling

We have not yet discussed the overall system behavior in any detail. In doing this we also present the results of a lumped

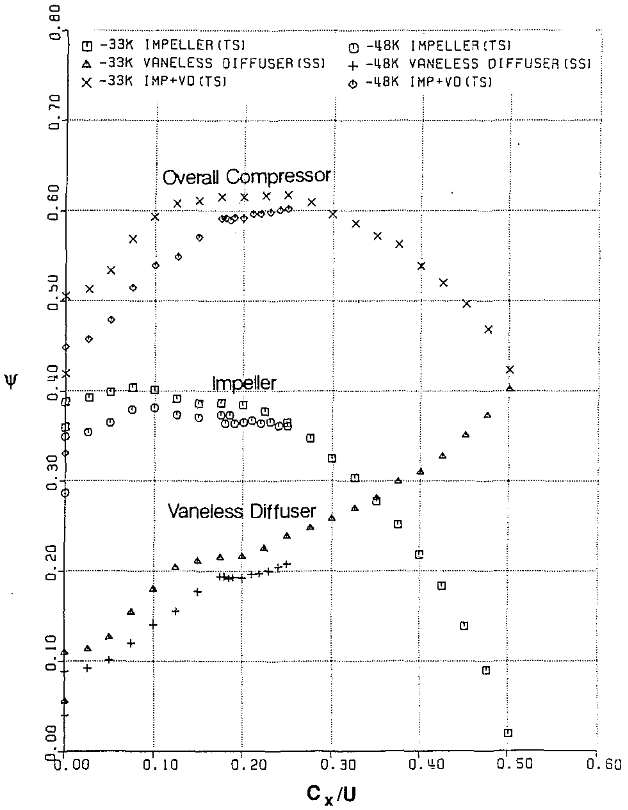

Fig. 12 Component head coefficient versus C_x/U

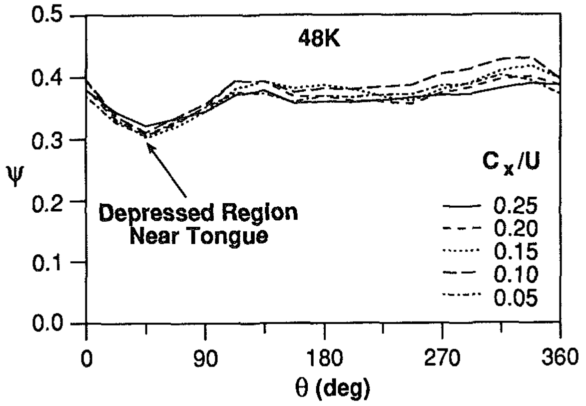

Fig. 13 Impeller head coefficient versus circumferential position (θ) at low mean flows

parameter analysis, which shows that the inclusion of a speed variation is needed for proper simulation. Lumped parameter compression system models have been discussed elsewhere (summarized by Cumpsty, 1989), and we enumerate only the major assumptions made:

1 One-dimensional incompressible flow in the compressor duct.
2 Isentropic plenum expansion or compression.
3 Density and pressure discontinuity across the compressor, which is modeled as an actuator disk. Two types of compressor characteristics are investigated: quasi-steady (a unique actuator characteristic) and unsteady, with the compressor response simulated by a first-order time lag on the order of the throughflow time of the compressor.
4 Choked throttle nozzle.
5 Throttle duct length is short (inductance free).

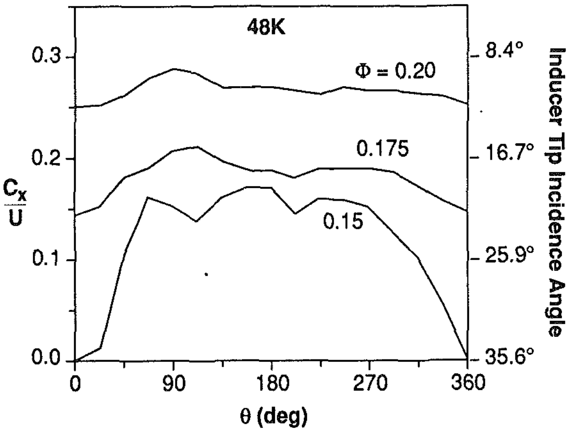

Fig. 14 Estimated circumferential distribution of inducer flow coefficient at low mean flow coefficients

6 Negligible velocity in the plenum.
7 Negligible gas angular momentum in the compressor passages compared to the wheel angular momentum.

This last is an additional equation compared to earlier analyses. The equations to be used describe conservation of momentum in the duct, conservation of mass in the plenum, and angular momentum variations in the turbo-spool.

Conservation of momentum in the duct is written as

$$L_c \frac{d}{dt}(\rho_2 C_x) = P_{\text{inlet}} - P_{\text{plenum}} + \Delta P_c \tag{3}$$

where the subscript 2 refers to conditions downstream of the compressor. Mass conservation in the plenum is given by

$$\frac{d}{dt}(\rho_p V_p) = \dot{m}_c - \dot{m}_t \tag{4}$$

where $\dot{m}_c$ and $\dot{m}_t$ are the mass flow rates through the compressor and the throttle, respectively. Conservation of angular momentum in the turbocharger spool is given by

$$I \frac{d\omega}{dt} = T_d - T_c \tag{5}$$

where T_c and T_d are the compressor torque and drive torque, respectively. T_c includes the torque needed to overcome the shroud wall friction.

Equations (3)–(5) are nondimensionalized as follows: mass flows are nondimensionalized by $\rho_o A_c U$, pressure differences by $1/2\ \rho_o U^2$, time by the inverse Helmholtz frequency $1/\omega_h$, and torques by $\rho_o A_c R_t U^2$. The density ρ_o is at ambient conditions. The Helmholtz resonator frequency at equilibrium conditions is calculated using a_{po}, the speed of sound in the plenum at the steady-state operating point. Recalling that $B = 0.5\ (U/\omega_H L_c)$, it can be seen that, for a given system, B may be used as the nondimensional wheel speed. Employing this nondimensionalization, Eqs. (3) and (4) can be written as

$$\frac{1}{B^2}\frac{d}{dt}(\Phi_c B) = \widetilde{\Delta P}_c - \widetilde{\Delta P}_p \tag{6}$$

$$\frac{1}{B^2}\frac{d}{dt}(\widetilde{\Delta P}_p B^2) = \frac{\tau_p}{\tau_{po}}(\Phi_c - \Phi_t) \tag{7}$$

where τ_p is the instantaneous plenum temperature ratio.

If we define a parameter F, based on the spool inertia I, as

$$F = \frac{2\rho_o L_c A_c r_t^2}{I}, \tag{8}$$

the equation for the rate of change of the spool angular momentum may be expressed in terms of net torque, $\Gamma\ (= \Gamma_d - \Gamma_c)$, as

$$\frac{dB}{d\tilde{t}} = FB^2\Gamma \qquad (9)$$

If we substitute Eq. (9) into Eqs. (6) and (7) we obtain

$$\frac{d\Phi_c}{d\tilde{t}} = B(\widetilde{\Delta P}_c - \widetilde{\Delta P}_p) - FB\Phi_c\Gamma \qquad (10)$$

and

$$\frac{d\widetilde{\Delta P}_p}{d\tilde{t}} = \frac{1}{B}\frac{\tau_p}{\tau_{po}}(\Phi_c - \Phi_t) - 2FB\widetilde{\Delta P}_p\Gamma \qquad (11)$$

Equations (9), (10), and (11) are a coupled set of nonlinear equations to be solved for B, Φ_c, and $\widetilde{\Delta P}_p$, with $\widetilde{\Delta P}_c(\phi_c)$ and Γ (ϕ_c) the specified compressor pressure and torque characteristics respectively. Further details can be found in Fink (1988).

The simultaneous solution of Eqs. (9)-(11) (using the necessary additional relations between plenum density and pressure, throttle characteristics, etc.) requires compressor rise and torque characteristics, $\widetilde{\Delta P}_c(\phi_c)$ and $\Gamma(\phi_c)$. The flow coefficient used here is defined with the appropriate density ρ, the impeller eye area A_c, and tip speed U. The data used for $\widetilde{\Delta P}_c(\phi_c)$ and $\Gamma(\phi_c)$ are shown in Fig. 15. In forward flow, the fluid properties used in the definition of these characteristics are those based on inlet condition, but in reverse flow the properties in the plenum are used. The forward flow characteristics were measured with the small B system, whereas the characteristics in reverse flow were deduced from the deep surge data obtained using the large B system.

Several classes of disturbances can be examined. The first, and simplest, are those of sufficiently small amplitude that the equations describing the system can be linearized about the equilibrium operating point. A thorough discussion of these is given by Fink (1988), as well as Greitzer (1981). Perhaps the most important result of the linearized analysis is that, for values of B from 0.5 up, with the present compressor characteristic, neither the wheel speed variation nor the inclusion of the simple model of compressor unsteady response discussed below had a substantial effect on the instability point. Put another way, changes in the rotor inertia by factors of five had less than a 1 percent effect on the flow coefficient at which the linear system exhibited growing oscillations. Further, for $B = 0.5$, changes in the time constant used in the unsteady response, from zero to twice our best estimate, resulted in less than a 4 percent change in flow coefficient for linear instability. For $B = 1.0$, the change in flow at instability is roughly 2 percent. For smaller values of B or much larger time constants, one can *calculate* larger effects (due to the highly unsteady flow through the compressor), but it is not clear whether the simple model is even appropriate in this regime. In summary, over a wide range of parameters, the point of linear instability can be estimated reasonably well by the simple quasi-steady, constant rotor speed lumped parameter model. This conclusion has also been made by Pinsley et al. (1991) and Gysling et al. (1991), who pointed out the utility of the simple linear models in examining dynamic control schemes to stabilize compression system instability.

Although the linearized analyses give good prediction of the flow at which instability will be encountered, our interest is also in the behavior once the disturbances grow to finite amplitude. In particular, we wish to ascertain whether the different features of the mild and deep surge cycles can be captured by the lumped parameter analyses or, equivalently, what effects must be included to describe the system adequately in the regime where the oscillations are nonlinear. To examine the nonlinear system response, Eqs. (9)-(11) were solved numerically. The equilibrium B value used was 2.7, representative of the experiments at large B when operating at 48 krpm. The inertia parameter F was set to 0.043, the value obtained from measurements supplied by the turbocharger manufacturer. Drive torque from the turbine was assumed to be constant. The throttle was set for a specified flow coefficient and a small decrease (1 percent, say) in compressor mass flow was then introduced.

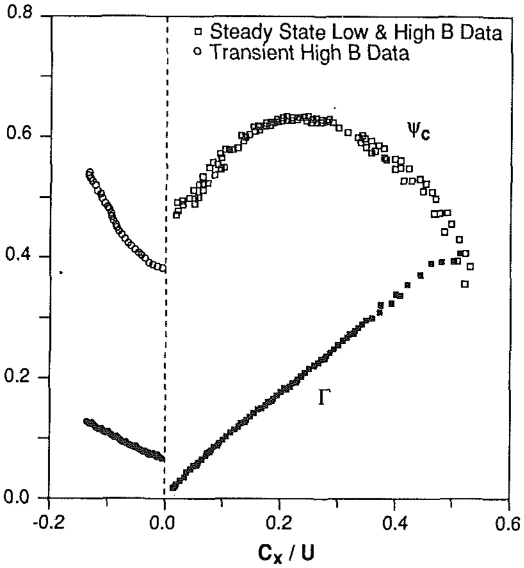

Fig. 15 Head and torque coefficients versus C_x/U; open symbols are head coefficient, filled symbols are torque coefficient

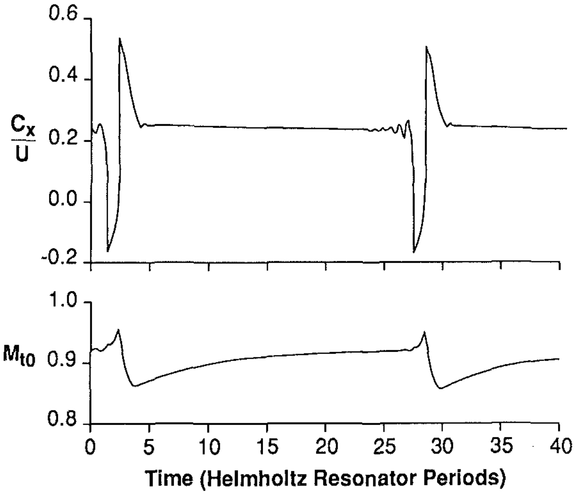

Fig. 16 Computed system response with speed allowed to vary

For an equilibrium flow of $\phi = 0.235$, which corresponds to operation to the right of the compressor peak, the system response is given in Fig. 16, which shows instantaneous flow coefficient and speed for the system undergoing deep surge. Time is given in terms of Helmholtz resonator periods. The main features are growing oscillations in mass flow followed by a rapid transient to reverse flow and then a plenum blowdown. The speed peaks during the blowdown phase and then drops below the equilibrium value; the speed drops rapidly during the forward flow recovery phase because compressor flow and torque are higher than the equilibrium values. After recovery of the mass flow, there is a long period (an order of magnitude longer than the blowdown phase) in which the compressor speed slowly recovers to the equilibrium value.

It is to be stressed that the compressor characteristic used for the calculation in Fig. 16 is *time independent*; both torque and pressure characteristic are assumed quasi-steady and con-

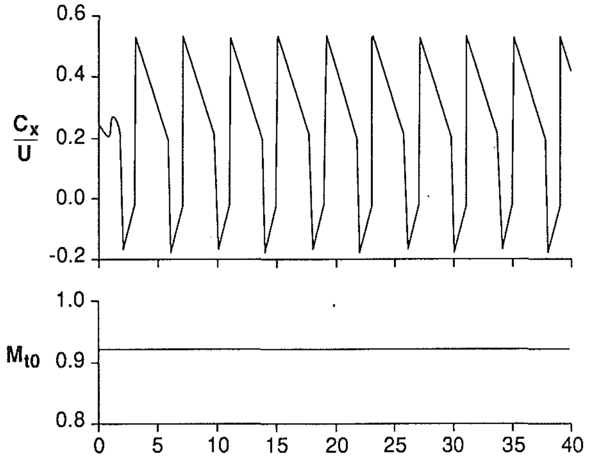

Fig. 17 Computed system response with no speed fluctuation (infinite inertia)

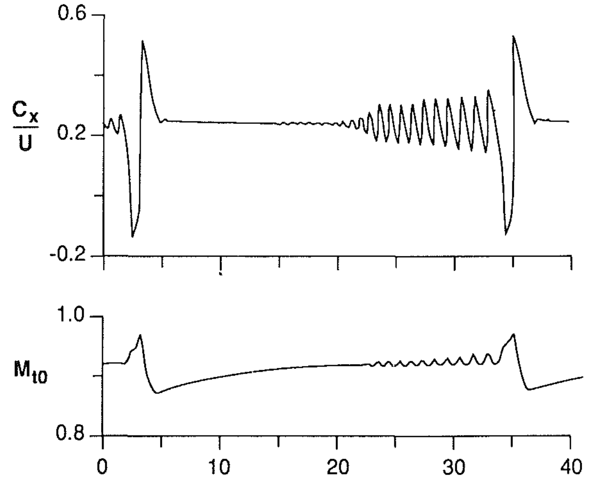

Fig. 18 Computed system response with speed variations and time lag

tinuous in the two flow regimes of positive and negative flow. The deep surge event depends only on a positively sloped compressor characteristic and a B value of sufficient size.

There are three different time scales in Fig. 16: one corresponding to the Helmholtz frequency, the blowdown and fill-up time, and the time associated with the speed variation. The last is due to a new energy storage element in the compression system, which introduces a time scale that is long compared to the first two. Deep surge appears to start when the increasing speed (and B) reaches some critical value.

To show that the long period between blowdowns is a result of speed variations only, the system response was calculated with infinite wheel inertia ($F=0$), so that there was constant rotor speed. The infinite inertia results are shown for a throttle setting of $\phi = 0.235$ in Fig. 17. Compared to Fig. 16, the long quiet period between deep surges is eliminated if the speed is constant. Even when relatively small rotor speed variations are present (5 percent, say), the system response is substantially different from that with constant speed.

In Fig. 8, the instantaneous compressor pressure rise trajectory, measured in the large B system, was shown to be flatter at flow coefficients below $\phi \sim 0.2$ than the measured steady-state values for the low B system. The instantaneous compressor pressure rise seen with the large B system thus lags that for steady-state operation. As discussed earlier, this appears to be due to the differing circumferential extent of impeller stalling seen in the two situations. One might therefore define a time constant that corresponds roughly to a convection time through the impeller and vaneless diffuser. If so, we can model the relation between instantaneous and steady-state compressor pressure rise coefficients as

$$\frac{d\widetilde{\Delta P}_c}{d\tilde{t}} = \frac{1}{\tilde{\tau}_c}\left(\widetilde{\Delta P}_{css} - \widetilde{\Delta P}_c\right) \tag{12}$$

where $\widetilde{\Delta P}_c$ is the instantaneous compressor pressure rise coefficient, $\widetilde{\Delta P}_{css}$ is the steady-state value, and $\tilde{\tau}_c$, the time constant, is throughflow time nondimensionalized by the Helmholtz resonator period. Equations (9), (10), and (11), along with Eq. (12), now form the set of coupled nonlinear equations for the system response.

The compressor throughflow time in Eq. (12) is assumed to be given approximately by

$$\tau_t = \left|\frac{L_t}{C}\right|$$

where $L_t \approx 0.085$ m is the meridional throughflow length of the impeller and vaneless diffuser and C is the meridional average flow velocity. The nondimensional throughflow time constant is thus:

$$\tilde{\tau}_c = \left(\frac{1}{2}\frac{L_t}{L_c}\right)\frac{1}{B|\Phi_c|} \tag{13}$$

For the large B system (at $\phi = 0.1$, $B = 2.7$, $L_c = 1.27$ m), the numerical value of $\tilde{\tau}_c$ is 0.12, approximately 2.2 rotor revolutions.

For the large B system, at an initial equilibrium operating point of $\phi = 0.235$, the results of the numerical integration with time lag are shown in Fig. 18. The main difference introduced by the time lag (compared with the quasi-steady results of Fig. 16) is the long period of mild surge precursor period to deep surge. Physically, the time lag has the effect of flattening the instantaneous compressor characteristic relative to the quasi-steady curve; this leads to a slower growing instability.

The result of the simulation including the time lag is shown in Fig. 19 with the corresponding large B experimental results. For a throttle setting of $\phi = 0.236$, Fig. 19, the compression

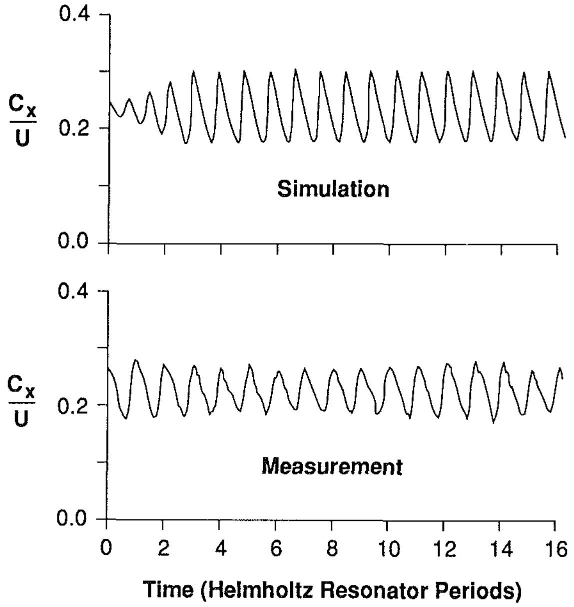

Fig. 19 Time lag model results versus measurements in mild surge ($\phi_T = 0.236$)

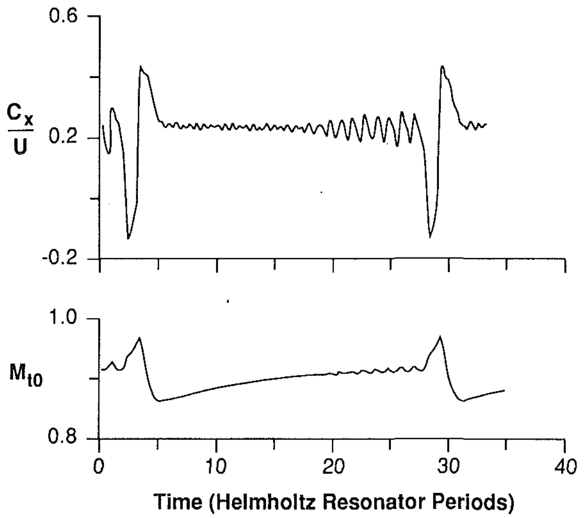

Fig. 20 Experimental measurements in deep surge ($\phi_T = 0.235$)

system is seen in both the simulation and experiment to enter continuous mild surge. The large amplitude sustained mild surge oscillation in Fig. 7 could not be duplicated without the time lag, i.e., the time lag has the effect of stabilizing the mild surge oscillations.

Reducing the throttle to $\phi = 0.235$ causes the compression system to enter deep surge as shown in Fig. 20, which can be compared directly with the simulation in Fig. 18. Good agreement is seen between the theory and experimental data over all four regions of the cycle. A deep surge precursor period of large amplitude mild surge is seen; this was attenuated in the earlier quasi-steady results. The long period between deep surges of the compressor due to speed variations is again visible, as it was in the quasi-steady compressor characteristic computations.

Conclusions

The conclusions can be divided into three parts.

(A) Conclusions From the Experimental Work Specific to This Class of Machine

1 The stalling element most responsible for surge initiation in this turbocharger compressor is the impeller. This agrees with the conclusion reached by Flynn and Weber (1979).

2 During surge initiation, stall of the impeller occurs first in the inducer at the circumferential location nearest the volute tongue. The tongue-induced stall in the impeller increased in severity at higher values of compressor tip Mach number if the compressor is operated away from the volute match point.

3 The instantaneous compressor characteristic is continuous and exhibits no abrupt stalling behavior to initiate surge.

4 When operating in a deep surge cycle, the largest pressure falloff in the compressor occurs well after the overall flow in the compressor has reversed.

5 Rotating stall in the compressor tested was much weaker than the volute induced pressure nonuniformity, suggesting that a stationary redistribution of flow is usual in this geometry rather than the rotating ones formed in more nearly axisymmetric machines.

(B) Conclusions General to Radial Compression Systems

1 The vaneless diffuser is a destabilizing element since its characteristic slope is positive. Its characteristic slope is nearly constant near the surge line, however, and it is thus not the component whose performance change is responsible for initiating instability and surge.

2 The position of the pressure rise peak is speed dependent due to compressibility and its effect on the volute matching condition.

3 For a system with large B, surge occurs at the peak of the whole compressor characteristic. Surge oscillations develop about this point, at the Helmholtz frequency, and grow slowly, culminating in deep surge. The frequency of deep surge, which is much lower than the Helmholtz frequency, is set by the plenum blowdown and refilling time.

4 Time-averaged characteristics in the low flow range are steeper than the instantaneous ones measured during surge.

(C) Conclusions From the Compression System Modeling

1 For a turbocharger in deep surge, the rotational speed fluctuation can be important. Accounting for the effects of variable impeller speed, even with a quasi-steady compressor characteristic, changes the predicted time behavior of the system substantially from that given by a constant-speed model.

2 A precursor period of mild surge before deep surge is shown to be present due to the speed variation. The surge dynamics are affected by the addition of another energy storing element, compressor rotor. A main effect is to increase the time interval between blowdowns compared to the constant speed case.

3 The magnitude of speed fluctuations present and its effect on the overall dynamics is governed by spool inertia; decreases in inertia make speed effects more important.

4 Inclusion of a simple time-lag model of the effect of unsteadiness in the inducer stall process improves the qualitative and quantitative agreement with experiment. In the computations performed here, the unsteady response was simulated by a first-order time lag, with time constant approximately equal to the throughflow time of the compressor.

5 A lumped parameter model with the features discussed in (1)-(4) seems adequate to examine the overall system dynamic behavior.

Acknowledgments

This work was supported by the Cummins Engine Company under the direction of Dr. H. G. Weber. His encouragement and helpful suggestions are gratefully acknowledged. Support for the first author was also provided by the Air Force Research in Aero Propulsion Technology (AFRAPT) Program of the Air Force Office of Scientific Research, and this support is greatly appreciated. It is a pleasure to acknowledge the constructive criticism and very useful advice of Dr. C. S. Tan, Prof. J. L. Kerrebrock, Dr. P. L. Lavrich, Prof. A. H. Epstein, Dr. J. Guenette, Dr. R. N. Gamache, and Dr. V. G. Filipenco; these were instrumental during the course of the project. The authors are also indebted to R. Haimes, W. Cook, and V. Dubrowski for computer, data acquisition, electronics, and machining assistance, and to Ms. D. Park for her extremely able editorial efforts.

References

Abdel-Hamid, A. N., Colwill, W. H., and Barrows, J. F., 1978, "Experimental Investigation of Unsteady Phenomena in Vaneless Radial Diffusers," ASME Paper No. 78-GT-23.

Capece, V. R., 1982, "Investigation of Turbocharger Stall: I—Facility Design and Construction and Initiation Performance Data," MIT Gas Turbine Laboratory Report No. 165.

Cumpsty, N. A, 1989, "Stall and Surge," in: *Compressor Aerodynamics*, Longmans Press, United Kingdom.

Dean, R. C., and Young, L. R., 1977, "The Time Domain of Centrifugal Compressor and Pump Stability and Surge," ASME *Journal of Fluids Engineering*, Vol. 99, pp. 53–63.

Emmons, H. W., Pearson, C. E., and Grant, H. P., 1955, "Compressor Surge and Stall Propagation," *ASME Transactions*, Vol. 77, pp. 455–469.

Fink, D. A., 1984, "An Experimental Investigation of Centrifugal Compressor Surge and Stall Phenomena in Turbochargers," MIT MS Thesis, Department of Aeronautics and Astronautics, Cambridge, MA.

Fink, D. A., 1988, "Surge Dynamics and Unsteady Flow Phenomena in Centrifugal Compressors," MIT Gas Turbine Laboratory Report No. 193, Cambridge, MA.

Flynn, P. F., and Weber, H. G., 1979, "Design and Test of an Extremely Wide Flow Range Compressor," ASME Paper No. 79-GT-80.

Greitzer, E. M., 1981, "The Stability of Pumping Systems," ASME *Journal of Fluids Engineering*, Vol. 103, pp. 193–243.

Gysling, D. L., Dugundji, J. Greitzer, E. M., and Epstein, A. H., 1991, "Dynamic Control of Centrifugal Compressor Surge Using Tailored Structures," ASME JOURNAL OF TURBOMACHINERY, Vol. 113, pp. 710–722.

Kammer, N., and Rautenberg, M., 1982, "An Experimental Investigation of Rotating Stall Flow in a Centrifugal Compressor," ASME Paper No. 82-GT-82.

Koff, S. G., 1983, "Stalled Flow Characteristics for Axial Compressors," MIT MS Thesis, Department of Mechanical Engineering, Cambridge, MA.

Lorett, J. A., and Gopalakrishnan, S., 1986, "Interaction Between Impeller and Volute of Pumps at Off-Design Conditions," ASME *Journal of Fluids Engineering*, Vol. 108, pp. 12–18.

Pinsley, J. P., Guenette, G. R., Epstein, E. H., and Greitzer, E. M., 1991, "Active Control of Centrifugal Compressor Surge," ASME JOURNAL OF TURBOMACHINERY, Vol. 113, pp. 723–732.

Stenning, A. H., 1980, "Rotating Stall and Surge," ASME *Journal of Fluids Engineering*, Vol. 102, pp. 14–20.

Taylor, E. S., 1964, "The Centrifugal Compressor," in: *Aerodynamics of Turbines and Compressors*, Princeton University Press, Princeton, NJ, pp. 553–586.

Toyama, K., Runstadler, P. W., and Dean, R. C., 1977, "An Experimental Study of Surge in Centrifugal Compressors," ASME *Journal of Fluids Engineering*, Vol. 99, pp. 115–131.

Two-Dimensional Flow Analysis of a Laboratory Centrifugal Pump

S. M. Miner
Assistant Professor,
U.S. Naval Academy,
Annapolis, MD 21402

R. D. Flack
Professor.

P. E. Allaire
Professor.

Department of Mechanical
and Aerospace Engineering,
University of Virginia,
Charlottesville, VA 22901

Two-dimensional potential flow was used to determine the velocity field within a laboratory centrifugal pump. In particular, the finite element technique was used to model the impeller and volute simultaneously. The rotation of the impeller within the volute was simulated by using steady-state solutions with the impeller in ten different angular orientations. This allowed the interaction between the impeller and the volute to develop naturally as a result of the solution. The results for the complete pump model showed that there are circumferential asymmetries in the velocity field, even at the design flow rate. Differences in the relative velocity components were as large as 0.12 m/s for the radial component and 0.38 m/s for the tangential component, at the impeller exit. The magnitude of these variations was roughly 25 percent of the magnitude of the average radial and tangential velocities at the impeller exit. These asymmetries were even more pronounced at off-design flow rates. The velocity field was also used to determine the location of the tongue stagnation point and to calculate the slip within the impeller. The stagnation point moved from the discharge side of the tongue to the impeller side of the tongue, as the flow rate increased from below design flow to above design flow. At design flow, values of slip ranged from 0.96 to 0.71, from impeller inlet to impeller exit. For all three types of data (velocity profiles, stagnation point location, and slip factor) comparison was made to laser velocimeter data, taken for the same pump. At the design flow, the computational and experimental results agreed to within 17 percent for the velocity magnitude, and 2 deg for the flow angle. The stagnation point locations coincided for the computational and experimental results, and the values for slip agreed to within 10 percent.

Introduction

For the purpose of better understanding and predicting the hydraulic and dynamic performance of centrifugal pumps, knowledge of the flow fields within the impellers and volutes of these machines is needed. Japikse (1976), Adler (1980), and McNally and Sockol (1985) have all published articles reviewing the status of turbomachinery analysis. Their reviews indicate that turbomachinery analyses usually consider either the rotating or nonrotating components individually.

McDonald and Howard (1973) reviewed Busemann's conformal transformation method of potential flow analysis. The analysis produces an exact solution, but is limited to impellers with zero thickness logarithmic spiral blades. The impeller must be analyzed by itself.

Other incompressible flow analyses have been performed by Keck (1980), Singh and Vasandani (1983), and Daiguji (1983a, 1983b). These authors used the finite element method to solve the two-dimensional and three-dimensional potential flow equation. In all cases either the rotating or nonrotating component was considered, but not both together.

Three-dimensional potential flow was used by Laskaris (1978), Hamed and Baskharone (1980), and Gunes and Menguturk (1984) to study compressible flow in turbomachinery. Laskaris, and Gunes and Menguturk, studied rotor blade rows, while Hamed and Baskharone considered a turbine scroll. Again, rotating and nonrotating components were considered separately.

Researchers who have considered both the impeller and volute together have typically used one of the following techniques:

1 Superposition of source and vortex to simulate an ideal impeller operating in a volute.

2 Analysis of impeller and volute separately with the solutions matched the interface between the two components.

3 Throughflow calculations based on pitch-averaged meridional equations.

Csanady (1962), Worster (1963), and Senoo (1970) used the first technique to evaluate the pressure distribution around an impeller operating in a volute. Csanady and Worster assumed an ideal impeller flow with uniform flow blade to blade, and no slip. Senoo also assumed uniform flow blade to blade, but did allow for slip. In all three cases the interaction between the impeller and volute produced circumferential variations in the pressure distribution. These variations were present even at design flow.

Kensaku (1980), and Adkins and Brennen (1986) used the

Contributed by the International Gas Turbine Institute and presented at the 35th International Gas Turbine and Aeroengine Congress and Exposition, Brussels, Belgium, June 11-14, 1990. Manuscript received by the International Gas Turbine Institute January 10, 1990. Paper No. 90-GT-50. Associate Editor: S. A. Mosier.

method of solving the impeller and volute flows separately and then matching the solutions at the interface between the components. Both of these studies calculated forces acting on the impeller due to the interaction between the impeller and volute. Although the force was a minimum at the design flow, it did not necessarily go to zero.

Throughflow calculations based on pitch-averaged meridional equations were performed by Hirsch and Warzee (1976). They calculated the velocity fields for the rotor and stator rows together, in both a single-stage and a two-stage axial fan. The method can also be applied to radial machines. In both axial and radial machines, only a single blade passage is considered because the technique assumes axisymmetric flow.

When the rotating and nonrotating components were considered together, the solutions showed significant asymmetries in the flow fields. These asymmetries were present even at the design flow rate. Therefore, both the impeller and volute should be considered together to predict the performance of centrifugal pumps.

The present work seeks to bridge the impeller and volute solutions by determining the flow fields in both components simultaneously. Two-dimensional potential flow analysis is used to calculate the velocity field in a laboratory centrifugal pump. The finite element method is used to model the impeller and volute together. This allows the interaction between these components to develop as a natural consequence of the solution. Results presented here include velocity profiles for the impeller, determination of the tongue stagnation point location, calculation of the slip within the impeller, and comparison to measured velocity data for the same pump. This direct comparison provides a measure of the adequacy of potential flow analysis for predicting the centrifugal pump flow.

Governing Equation

The underlying assumptions for the potential flow analysis of a centrifugal pump are that the flow is inviscid and isentropic, and enters the pump with uniform total enthalpy and zero vorticity. Based on these conditions, Kelvin's circulation theorem guarantees that the absolute flow is irrotational throughout the pump. The equation governing the flow throughout the pump is the continuity equation

$$\nabla\cdot(\rho\nabla\phi_A)=\omega\frac{\partial\rho}{\partial\theta}. \tag{1}$$

In the case of an incompressible fluid, Eq. (1) reduces to

$$\nabla^2\phi_A=0, \tag{2}$$

which is the Laplace equation. The relationship between the absolute velocity potential (ϕ_A), the absolute velocity $(\bar{V}_A)$, and the relative velocity $(\bar{W})$ is

$$\nabla\phi_A=\bar{V}_A=\bar{W}+\bar{\omega}\times\bar{R}. \tag{3}$$

An interesting characteristic of the relative flow, which is a result of the assumptions required for the potential flow analysis, is

$$\nabla\times\bar{W}=2\bar{\omega}. \tag{4}$$

The importance of this characteristic will become evident when the computational results are compared to the measured data.

In addition to the governing Eq. (2), appropriate boundary conditions must be specified. At nonrotating solid surfaces (volute surfaces) the boundary condition is

$$\bar{n}\cdot\bar{V}_A=\bar{n}\cdot\nabla\phi_A=0. \tag{5}$$

For rotating surfaces (impeller) the appropriate boundary condition is

$$\bar{n}\cdot\bar{W}=0, \tag{6}$$

which implies

$$\bar{n}\cdot\nabla\phi_A=\bar{n}\cdot\omega R\bar{e}_\theta. \tag{7}$$

In either case, Eq. (5) or Eq. (7), the boundary condition forces the flow to be tangent to the surface. At the inlet to the pump a uniform radial velocity is assumed

$$\bar{n}\cdot\nabla\phi_A=V_I, \tag{8}$$

and at the exit a uniform flow is also assumed

$$\bar{n}\cdot\nabla\phi_A=V_E. \tag{9}$$

The values of V_I and V_E are picked such that mass flow is conserved within the pump. A more detailed discussion of the governing equation and the appropriate boundary conditions is given by Miner (1988).

Pump Geometry and Computational Domain

Both the impeller and volute used in this study have a logarithmic spiral design. Figure 1 shows the geometry of the pump. The impeller has four 16 deg log-spiral blades. At the trailing edges the blades are overfiled on the pressure surface to produce a sharp trailing edge. The eye of the impeller is at a radius of 38.1 mm, and the blade leading edges and trailing edges are at radii of 50.8 mm and 102 mm, respectively. The volute is also a logarithmic spiral with a 7 deg angle. For this analysis the impeller and volute centers are coincident. The clearance between the impeller outer diameter and the tongue of the volute is 6.4 mm. The operating speed and design flow rate for the pump are 620 rpm and 6.3 L/s. The geometry shown in Fig. 1 is identical to the geometry reported by Miner et al. (1989), and the measured data from that study will be compared to the computational results reported here.

The triangular finite element mesh used for the complete pump analysis is shown in Fig. 2. In this mesh the trailing edge of one of the blades is shown aligned with the tongue. In addition to this mesh, meshes were generated for the impeller in nine other angular orientations. These other orientations were:

Mesh	Blade trailing edge offset, deg
2	10
3	20
4	30
5	40
6	45
7	50
8	60
9	70
10	80

Nomenclature

b = passage width
$\bar{c}_\theta$ = unit vector in the tangential direction
h_o = slip factor
n = number of blades
$\bar{n}$ = outward normal vector
Q = pump flow rate
R = radius
$\bar{R}$ = position vector
t = blade thickness
U = impeller peripheral speed
V_A = absolute velocity vector
V_E = absolute velocity volute discharge
V_I = absolute velocity impeller inlet
V_r = absolute radial velocity
$\tilde{V}_\theta$ = mass-averaged absolute tangential velocity
$\bar{W}$ = relative velocity vector
β = blade angle
ϵ = vane blockage factor
θ = circumferential position
ρ = fluid density
ϕ_A = absolute velocity potential
ω = angular velocity
$\bar{\omega}$ = angular velocity vector

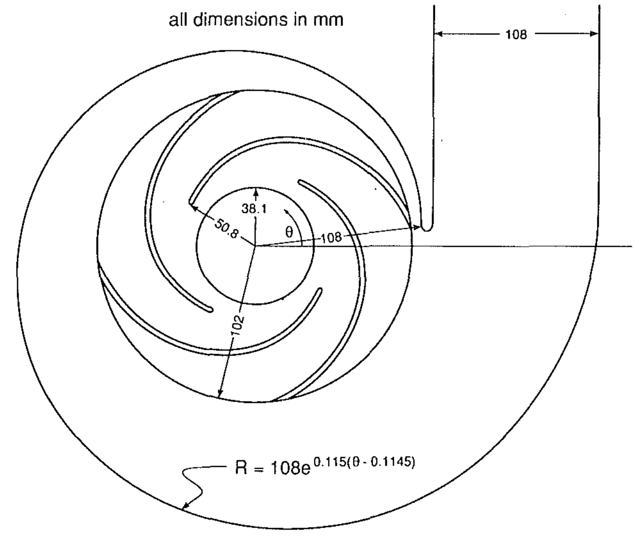

Fig. 1 Pump geometry

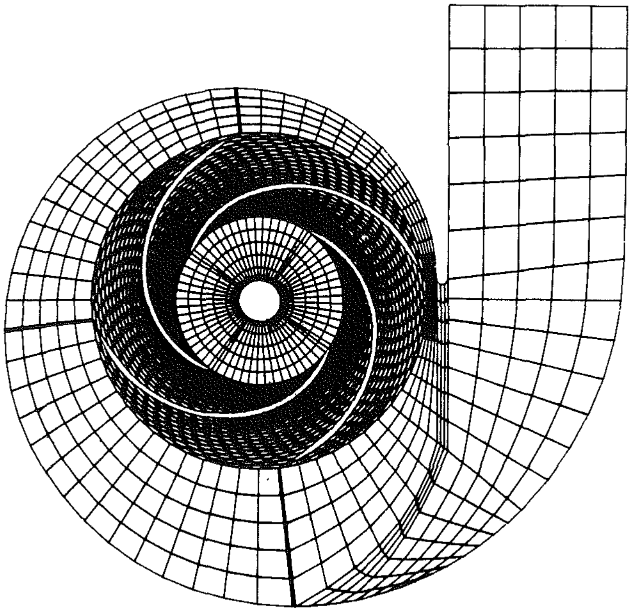

Fig. 2 Potential flow analysis finite element mesh

Due to the fourfold symmetry of the impeller only a rotation through 90 deg is needed. For all ten meshes the number of nodes was roughly 2400, and the number of elements was roughly 2000. These ten meshes were generated to simulate the rotation of the impeller within the volute. This was done so that the computational method would more realistically represent the experimental configuration, where the data collection point is fixed and the impeller rotates past it.

At the inlet to the computational mesh a uniform radial flow is assumed. The design flow boundary condition becomes

$$\nabla \phi_A \cdot \overline{n} = -3.2 \text{ m/s}, \tag{10}$$

at the inlet radius of 12.7 mm. The corresponding condition at the discharge of the volute is a uniform flow in the y direction

$$\nabla \phi_A \cdot \overline{n} = 2.4 \text{ m/s}, \tag{11}$$

along the plane of y equals 71.5 mm. The inlet and exit from the mesh were located far enough upstream and downstream such that the uniform flow conditions could be used without creating an artificial influence on the flow inside the pump.

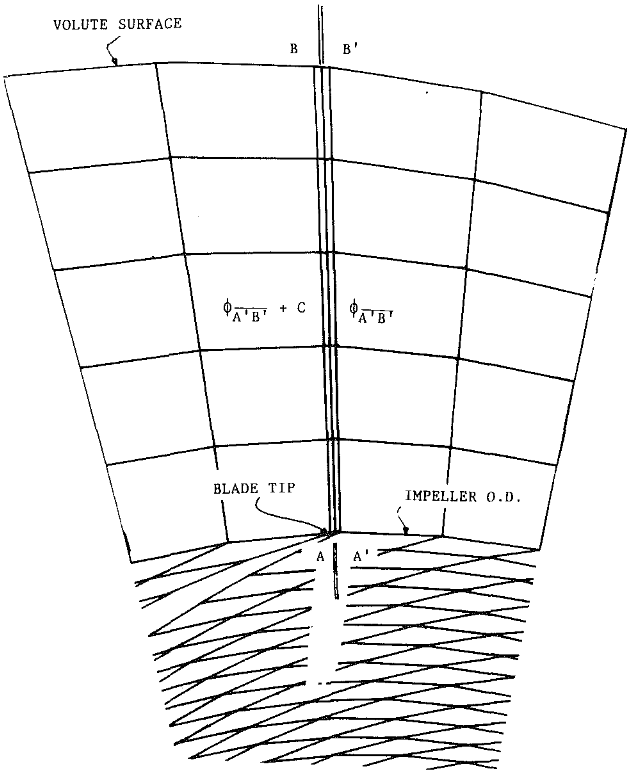

Fig. 3 Potential jump boundary treatment

At any solid surface, blade or volute, the flow must be tangent to the surface. Along the blade surfaces the relative velocity ($\overline{W}$) must be tangent to the blade. This makes the suction surface boundary condition

$$\nabla \phi_A \cdot \overline{n} = \omega R \sin(16 \text{ deg}), \tag{12}$$

and the pressure surface boundary condition

$$\nabla \phi_A \cdot \overline{n} = -\omega R \sin(16 \text{ deg}). \tag{13}$$

At the volute surface the absolute flow ($\overline{V}_A$) must be tangent, making the volute surface boundary condition

$$\nabla \phi_A \cdot \overline{n} = 0. \tag{14}$$

For all the boundary conditions outlined above the outward-facing normal ($\overline{n}$) is used.

In order to do a potential flow analysis the solution domain must be a simply connected region. Therefore, four cuts are made in the mesh at the trailing edges of the blades. Across these cuts the potential field may be discontinuous. However, the velocity field must remain continuous. It is the discontinuity in the potential field that allows the Kutta condition to be satisfied at the trailing edges of the blades.

Along the cuts, boundaries are established be defining two sets of nodes having the same coordinates. This boundary is illustrated in Fig. 3. In order to insure the continuity of the velocity field, the components of velocity parallel and perpendicular to the boundaries $\overline{AB}$ and $\overline{A'B'}$ must be equated. The parallel component is equated by requiring the values of potential along $\overline{AB}$ to equal those along $\overline{A'B'}$ plus a constant

$$\phi_{\overline{AB}} = \phi_{\overline{A'B'}} + C. \tag{15}$$

The components perpendicular to the cut are equated by matching the gradients of the potential across the cut

$$\left.\frac{\partial \phi}{\partial n}\right|_{\overline{AB}} = \left.\frac{\partial \phi}{\partial n}\right|_{\overline{A'B'}} \tag{16}$$

This completes the specification of the geometry and boundary conditions used for the complete pump analysis. A more de-

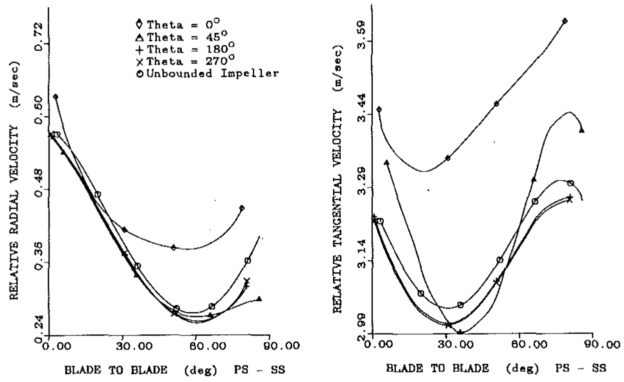

Fig. 4 Potential flow velocity profiles, design flow, R = 100.3 mm

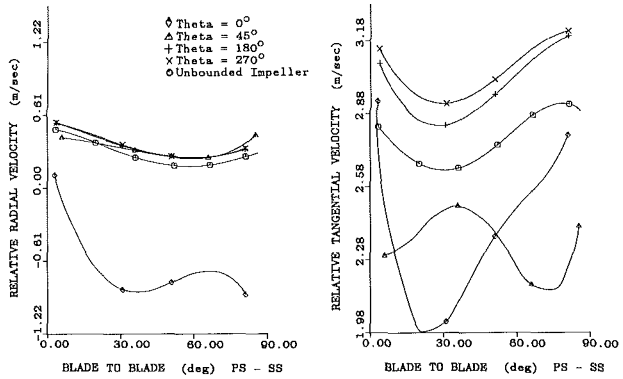

Fig. 5 Potential flow velocity profiles, 75 percent design flow, R = 100.3 mm

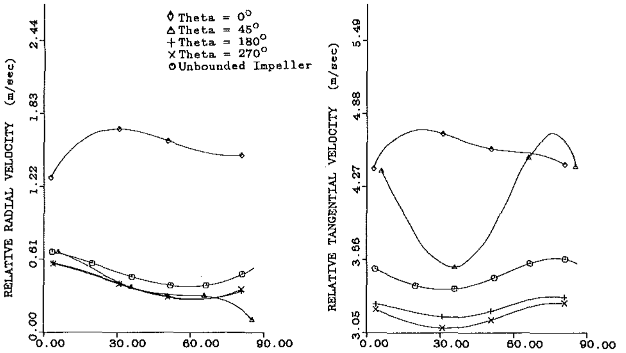

Fig. 6 Potential flow velocity profiles, 125 percent design flow, R = 100.3 mm

tailed presentation of the finite element mesh parameters and the potential jump can be found in Miner (1988).

Computational Results

As a basis for comparison, the velocity profiles for the complete pump (impeller and volute together) will be plotted against the results for a single blade passage of an unbounded impeller. The geometry of the unbounded impeller is identical to the impeller in Fig. 1, and due to the fourfold symmetry a single blade passage can represent the entire impeller. This comparison shows the impact of the interaction between the impeller and volute. Representative results are presented here. A complete presentation and discussion of the computational results are presented by Miner (1988).

Results are presented for four circumferential positions around the impeller: 0, 45, 180, and 270 deg. These positions are used because they correspond to the positions used for the measured data reported by Miner et al. (1989). Figures 4–6 are the relative velocity profiles for 100, 75, and 125 percent of design flow, respectively. For each flow, results at a radius of 100.3 mm are presented. The velocities plotted are computed at the centroids of the elements. Therefore, the velocities shown at the pressure and suction surfaces are not on the blade surfaces themselves. This, along with the fact that at the trailing edges the blades are tapered to a point and the Kutta condition is imposed, causes the relative flow at the pressure and suction surfaces to appear not to follow the blade surface at a radius of 100.3 mm. At the other radii within the impeller, the angle of the relative velocity is typically within ±2 deg of the blade angle.

At the design flow, the variations in profiles around the impeller are up to 0.12 m/s for the radial component and 0.38 m/s for the tangential component. For 75 percent of design flow the circumferential variations are as great as 1.2 m/s for the radial component and 1.4 m/s for the tangential component. At 125 percent of design flow the circumferential variation in the radial component is as large as 1.3 m/s and the tangential variation is as large as 2.0 m/s. In all three cases *the unbounded impeller results most closely match the results* at the 180 and 270 deg positions. This occurs because this quadrant of the impeller is the farthest from the tongue, and the interaction between the impeller and the volute is weakest in this area. Basically, the unbounded impeller analysis gives a circumferentially averaged picture of the velocity field within the impeller.

However, the complete pump analysis predicts significant circumferential variations in the velocity field, even at the design flow. These variations imply that the momentum flux around the impeller is not symmetric. This asymmetry leads to a radial unbalance force acting on the impeller. Therefore, the unbounded impeller analysis is not sufficient for predicting the hydraulic and dynamic performance of the pump. The impeller and volute must be considered together to capture the interaction between the two components.

Comparison of Computational and Experimental Results

In a previous paper by Miner et al. (1989), laser velocimeter data for the centrifugal pump of Fig. 1 were presented. In this section a direct comparison is made between the measured velocity data and the velocities predicted using two-dimensional potential flow. This direct comparison shows the ability of the potential flow solution to predict the velocity field in the pump under consideration. Representative results are shown here; a complete presentation and discussion of the comparison is given by Miner (1988).

Velocity Profiles. At the design flow, comparisons are shown for circumferential positions of 180 and 0 deg. At these positions the correlation between the experimental and the computational results was at its best and worst, respectively. Figures 7–9 show the comparisons for $\theta = 180$ deg. At all three radii the potential flow results correctly predict the shape of the velocity profiles. The magnitude of the radial component of velocity is predicted to within 0.12 m/s for all radii except 63.5 mm. At this inner radius the maximum difference is 0.24 m/s, and is due to the fact that the measured velocity profile is heavily skewed toward the back face of the impeller. The abrupt 90 deg turn the fluid must make to enter the impeller causes this skewing; the two-dimensional analysis does not model this turn. Predicted values for the tangential velocity are within 0.46 m/s for all three radii.

Another aspect of the pump performance that is shown in Figs. 7–9 is the blade loading as a function of radius. Blade loading is the difference in the pressure acting on the pressure and suction surfaces of a blade. This pressure difference is directly related to the difference between the magnitude squared

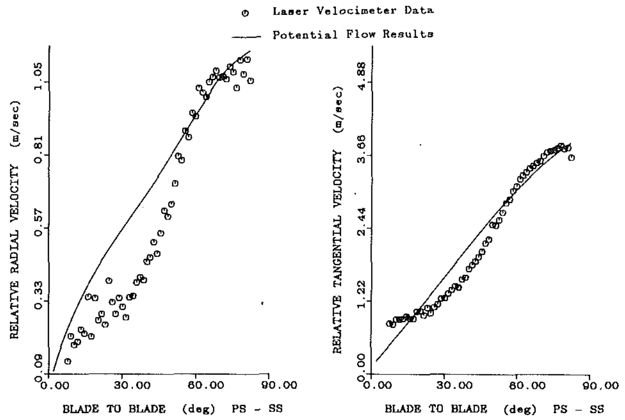

Fig. 7 Computational and experimental velocity profiles, design flow, $R = 63.5$ mm, $\theta = 180$ deg

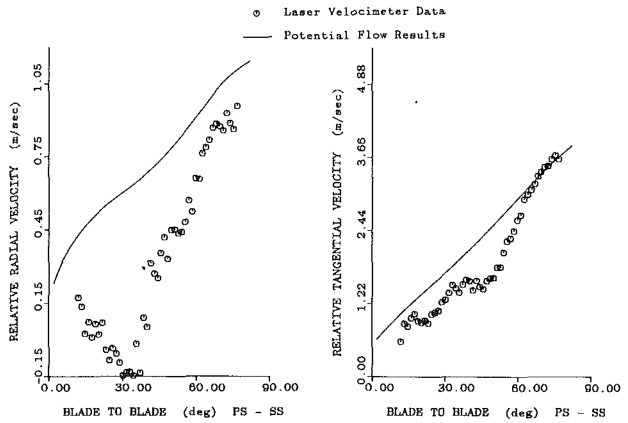

Fig. 10 Computational and experimental velocity profiles, design flow, $R = 63.5$ mm, $\theta = 0$ deg

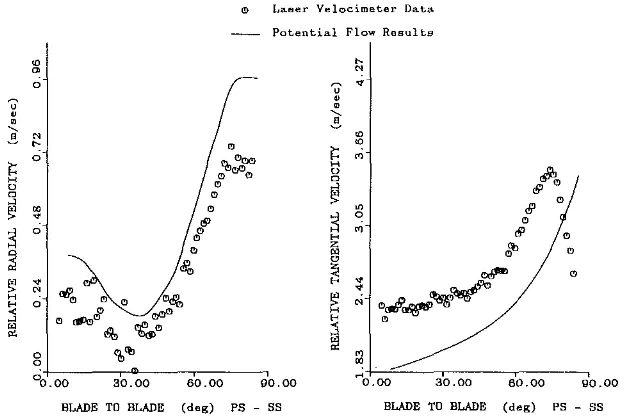

Fig. 8 Computational and experimental velocity profiles, design flow, $R = 88.9$ mm, $\theta = 180$ deg

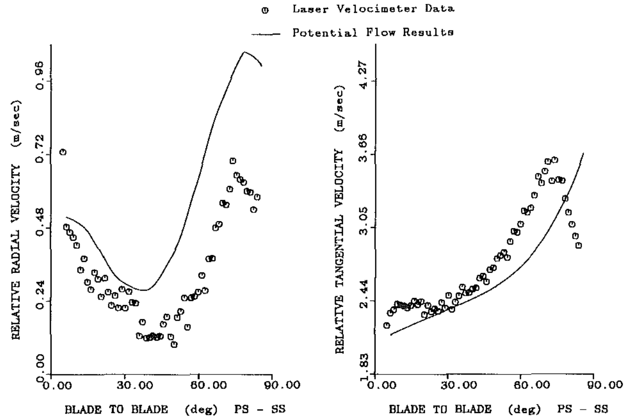

Fig. 11 Computational and experimental velocity profiles, design flow, $R = 88.9$ mm, $\theta = 0$ deg

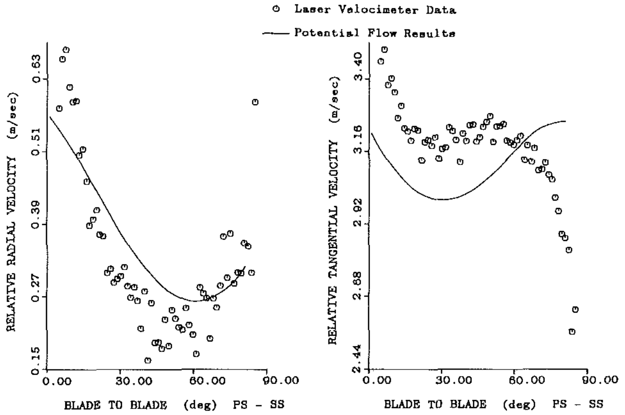

Fig. 9 Computational and experimental velocity profiles, design flow, $R = 100.3$ mm, $\theta = 180$ deg

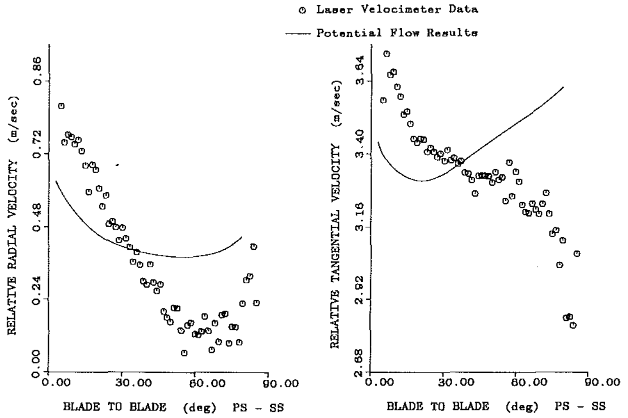

Fig. 12 Computational and experimental velocity profiles, design flow, $R = 100.3$ mm, $\theta = 0$ deg

of the relative velocity at the pressure and suction surfaces of a blade. Positive loading occurs when the relative velocity increases from the pressure surface to the suction surface. Under this condition the blades transmit energy to the fluid, by doing work on the fluid. At radii of 63.5 mm and 88.9 mm, the computational results correctly show the positive blade loading of the measured results. At 100.3 mm the measured data shows a slightly negative loading, while the computational results predict zero loading. Throughout the impeller the trend in loading is correct, with the loading being drastically reduced at the outer radius. Imposition of the Kutta condition at the trailing edges of the blades drives the loading to zero at the outer radius of the impeller.

Figures 10–12 show the comparison for $\theta = 0$ deg. Results at this orientation show the greatest interaction between the impeller and volute, due to the presence of the tongue. For all three radii the trend and level of the radial velocity component is correctly predicted. Again, the discrepancy at the inner radius is due to the skewing of the measured velocity profile. At the outer radius (100.3 mm) the differences are caused by the nonideal interaction that takes place between the impeller and tongue. Except for the data at $R = 100.3$ mm, the predicted

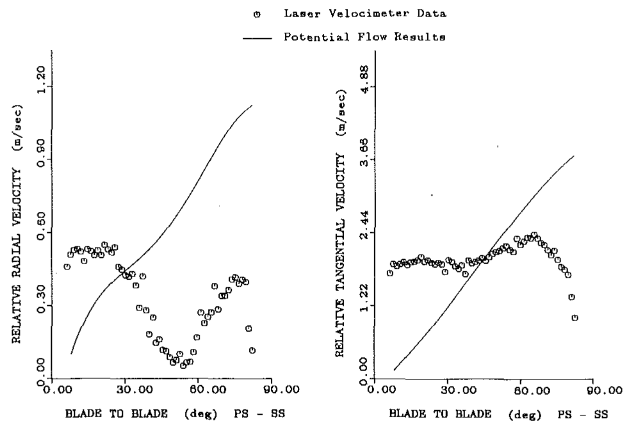

Fig. 13 Computational and experimental velocity profiles, 40 percent of design flow, $R = 63.5$ mm, $\theta = 270$ deg

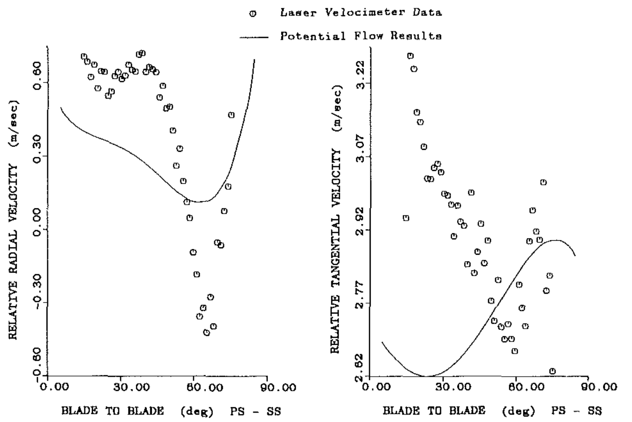

Fig. 14 Computational and experimental velocity profiles, 40 percent of design flow, $R = 98.8$ mm, $\theta = 270$ deg

tangential velocities also show the proper trend and level. At 100.3 mm the computational results predict a positive blade loading, while the measured results show a negative loading. Here again, the differences are due to the nonpotential nature of the flow between the impeller exit and the tongue. However, even for this "worst" comparison the magnitude and direction of the predicted velocities are within 17 percent and 2 deg of the measured velocities, respectively.

In the volute, the magnitude and flow direction of the predicted velocities were within 10 percent and 5 deg of the measured data, respectively. This was the case for all four circumferential positions.

Comparisons were also done for flows other than the design flow. For flow rates above design, the agreement between the potential flow results and the measured data was similar to that seen for the design flow case. When the flow rate is below the design flow the agreement is not as good as that seen for the design flow. Figures 13 and 14, for 40 percent of design flow, illustrate the problem. At the outer radius there is a region of negative radial flow near the suction surface, and at the inner radius the flow at the suction surface is suppressed relative to the pressure surface. These results indicate the presence of a recirculating region within the impeller. This recirculation, with outward flow along the pressure surface and inward flow along the suction surface, would be in the same direction as the rotation of the impeller. This results in a negative blade loading within the impeller, and the more the flow rate is below the design flow, the more pronounced the recirculation. However, in the potential flow formulation the relative flow has a circulation that is in the opposite direction of the impeller rotation. This was shown in Eq. (4). Based on this, the potential flow solution is not suited to flows below design, where there is a chance of recirculating flow in the passages. The potential flow theory does not handle this phenomenon.

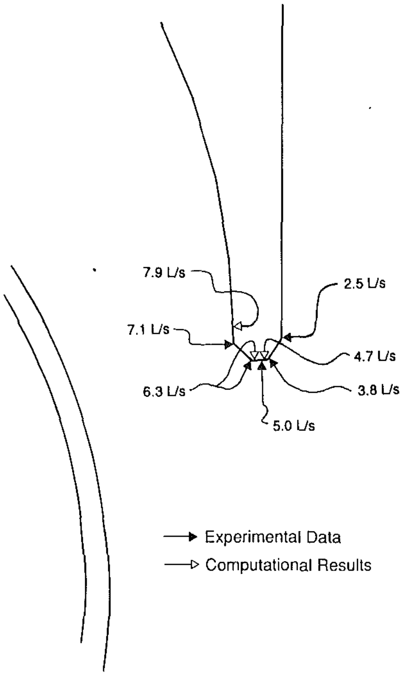

Fig. 15 Tongue stagnation point location: computational and experimental results

Tongue Stagnation Point. By plotting the absolute velocity vectors in the vicinity of the tongue, the change in location of the tongue stagnation point as a function of flow rate can be seen. Figure 15 shows the stagnation point locations for both the computational and experimental results. Both sets of results show the stagnation point moving from the discharge side of the tongue to the impeller side, as the flow rate increases from below design to above design. At the design flow the location of the stagnation point for the potential flow results and the measured data coincide at the tip of the tongue. For both the computational and experimental results, the angle of the flow approaching the tongue varied by roughly ±6 deg. This variation was caused by the change in the orientation of the blades with respect to the tongue as the impeller rotated.

Slip Factor Calculation. The final parameter compared is the slip factor. The equation used to calculate the slip for the potential flow analysis is

$$h_o = \epsilon\left[\frac{Q}{2\pi RbU}\right]\cot\beta + \frac{\tilde{V}_\theta}{U} \tag{17}$$

where ϵ is the vane blockage factor given by

$$\epsilon = \left[1 - \frac{nt}{2\pi R\sin\beta}\right]^{-1}. \tag{18}$$

U, R, and $\tilde{V}_\theta$ are evaluated at the radius of interest. In computing the slip for the experimental data two techniques were used. The first used Eq. (17), where Q was the measured flow from an orifice meter. This technique does not include the effects of leakage flow. The second technique uses measured radial velocity data in place of $Q/2\pi Rb$. By using the measured data an attempt is made to account for all the flow passing through the impeller, flow making it to the pump discharge, and flow leaking back to the impeller inlet. In addition, slip factors based on Busemann's work and Wiesner's work (1967) are included for comparison. Figure 16 shows the comparison of slip factors for five techniques:

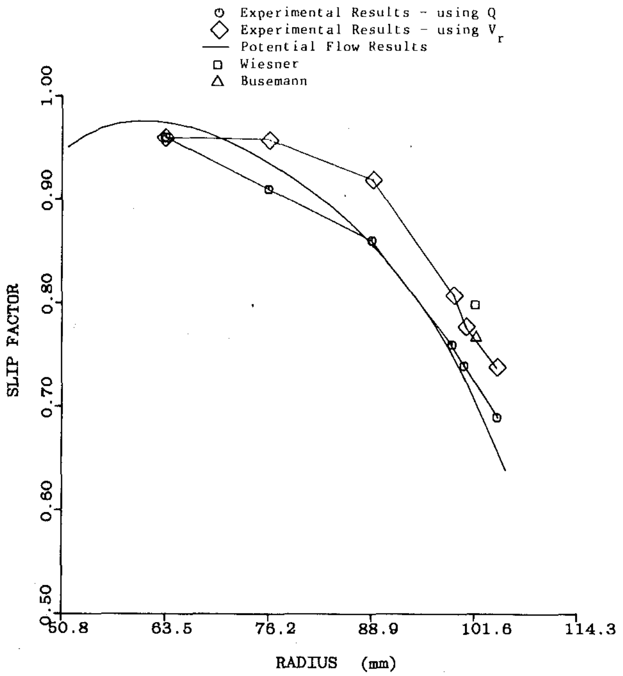

Fig. 16 Slip factor comparison at design flow

1 Potential flow results
2 Measured data using Q
3 Measured data using V_r
4 Busemann
5 Wiesner

For all five techniques the values of slip are within 10 percent of each other. Neither the computational results nor the measured data show the slip reaching a value of unity. A value of 1.0 would imply that the flow in the impeller passages is matching the blade, and values less than 1.0 measure the deviation of the flow angle from the blade angle.

The mechanism that causes slip in the potential flow analysis is the relative circulation within the blade passages. At the blade surfaces the boundary conditions force the flow to follow the blade angle. However, in the interior of the passage no such constraint is imposed and the velocity distribution is driven by the relative circulation. This relative circulation is a result of the inertia of the fluid and the irrotationality of the potential flow. As a result, the fluid within the blade passage lags behind the motion of the blades.

This same effect is present in real impellers, in the inviscid core away from the hub, shroud, and blade surface boundary layers. However, due to the influence of the boundary layers, the effect of the relative circulation is somewhat diminished. The hub and shroud surface friction help to promote rotary motion within the impeller channel, which would cause the slip factor in the real impeller to be higher than the value predicted from the potential flow theory.

Conclusions

Potential flow was used to determine the velocity field within a laboratory centrifugal pump. In this analysis the impeller and volute were modeled together. This allowed the interaction between these components to develop naturally as a result of the solution. The solution showed significant asymmetries in the flow field that are a direct result of the interaction between the impeller and volute. In addition, the computational results were compared to measured data for the same pump. Specific conclusions are as follows:

1 Even at the design flow rate the flow within the impeller is not axisymmetric. Variations as large as 30 percent for the radial component and 13 percent for the tangential component were predicted. These variations cannot be predicted in an unbounded impeller analysis.

2 The potential flow solution correctly predicts that the tongue stagnation point moves from the discharge side to the impeller side as the flow is increased from below design to above design.

3 At design flow the predicted slip factor ranged from 0.96 to 0.71, from impeller inlet to impeller exit; at no point did it reach unity.

4 At design flow, the computational results were within 17 percent for magnitude, and 2 deg for flow angle of the measured velocity profile.

5 At design flow, computational and measured slip factors were within 10 percent.

6 Predicted and measured tongue stagnation points coincided with each other.

Acknowledgments

This work was sponsored by the ROMAC Industrial Research Program at the University of Virginia.

References

Adkins, D. R., and Brennen, C. E., 1986, "Origins of Hydrodynamic Forces on Centrifugal Pump Impellers," *Proc. of the Rotordynamic Instability Problems in High-Performance Turbomachinery Workshop*, Texas A&M University, College Station, TX, June 2–4, pp. 467–491.

Adler, D., 1980, "Status of Centrifugal Impeller Internal Aerodynamics: Part 1," ASME *Journal of Engineering for Power*, Vol. 102, pp.728–737.

Csanady, G. T., 1962, "Radial Forces in a Pump Impeller Caused by a Volute Casing," ASME *Journal of Engineering for Power*, Vol. 84, pp. 337–340.

Daiguji, H., 1983a, "Numerical Analysis of 3-D Potential Flow in Axial Flow Turbomachines," *Bull. of JSME*, Vol. 26, No. 215, May.

Daiguji, H., 1983b, "Numerical Analysis of 3-D Potential Flow in Centrifugal Turbomachines," *Bull of JSME*, Vol. 26, No. 219, Sept.

Gunes, D., and Menguturk, M., 1984, "A Finite Element Computer Code to Calculate Full 3-D Compressible Potential Flow in Turbomachinery," ASME Paper No. 84-GT-238.

Hamed, A., and Baskharone, E., 1980, "Analysis of the Three-Dimensional Flow in a Turbine Scroll," ASME *Journal of Fluid Engineering*, Vol. 102, pp. 297–301.

Hirsch, C. H., and Warzee, G., 1976, "A Finite-Element Method for Through Flow Calculations in Turbomachines," ASME *Journal of Fluids Engineering*, Vol. 98, pp. 403–421.

Japikse, D., 1976, "Review—Progress in Numerical Turbomachinery Analysis," ASME *Journal of Fluids Engineering*, Vol. 88, pp. 592–606.

Keck, H., 1980, "Finite Element Analysis of Flows in Hydraulic Turbomachinery," *Escher Wyss News*, No. 1/2.

Kensaku, I., 1980, "A Two-Dimensional Analysis of the Interaction Effects of Radial Impeller in Volute Casing," *Proceedings of IAHR AIRH Symposium*.

Laskaris, T. E., 1978, "Finite-Element Analysis of Three-Dimensional Potential Flow in Turbomachines," *AIAA Journal*, Vol. 16, No. 7, pp. 717–722.

McDonald, G. B., and Howard, J. H. G., 1973, "The Computation and Utilization of Busemann's Analysis of Potential Flow in an Impeller," ASME Paper No. 73-GT-45.

McNally, W. D., and Sockol, P. N., 1985, "Review—Computational Methods for Internal Flows With Emphasis on Turbomachinery," ASME *Journal of Fluids Engineering*, Vol. 107, pp. 6–22.

Miner, S. M., 1988, "Potential Flow Analysis of a Centrifugal Pump: Comparison of Finite Element Calculation and Laser Velocimeter Measurement," Ph.D. Dissertation, University of Virginia, Department of Mechanical and Aerospace Engineering, Charlottesville, VA.

Miner, S. M., Beaudoin, R. J., and Flack, R. D., 1989, "Laser Velocimeter Measurements in a Centrifugal Flow Pump," ASME JOURNAL OF TURBOMACHINERY, Vol. 111, pp. 205–212.

Senoo, Y., 1970, "Analysis of the Pressure Distribution Around the Impeller of Volute Pumps," *Bull. of JSME*, Vol. 13, No. 60, pp. 802–811.

Singh, A., and Vasandani, V. P., 1983, "Analysis of Flow Through Pump Impellers by Finite Element Method," *Indian Journal of Technology*, Vol. 21, pp. 12–16.

Wiesner, F. J., 1967, "A Review of Slip Factors for Centrifugal Impellers," ASME *Journal of Engineering for Power*, Vol. 89, pp. 558–572.

Worster, R. C., 1963, "The Flow in Volutes and Its Effect on Centrifugal Pump Performance," *Proceedings of the Inst. of Mechanical Engineers*, Vol. 177, No. 31, pp. 843–875.

Laser Velocimeter Measurements in a Centrifugal Pump With a Synchronously Orbiting Impeller

R. J. Beaudoin
Development Engineer,
General Electric Co.,
Schenectady, NY 12345

S. M. Miner
Assistant Professor,
U.S. Naval Academy,
Annapolis, MD 21402

R. D. Flack
Professor,
Department of Mechanical and Aerospace Engineering,
University of Virginia,
Charlottesville, VA 22901

Velocity profiles were measured in the impeller of a centrifugal pump with a two-directional laser velocimeter. Blade-to-blade profiles were measured at four circumferential positions and four radii within and one outside the four-bladed impeller. Data are presented herein at two circumferential and three radial locations. The pump was tested in two configurations; with the impeller running centered within the pump, and with the impeller orbiting with a synchronous motion ($\epsilon/r_2 = 0.016$). Variation in velocity profiles among the individual passages in the orbiting impeller were found. At design flow rate, these variations ranged from 30 to 60 percent for the radial component, and 15 to 25 percent for the tangential component. Tangential velocity profiles near the impeller exit ($r/r_2 = 0.973$) were near uniform across each individual passage. Differences in the magnitude of the exit tangential velocities among the passages however, were detected. Systematic differences in the velocity profile shapes of the centered and orbiting impellers were in general not measured, the only exception being at $r/r_2 = 0.973$ at 40 percent of the design flow rate. At this condition, two distinct radial velocity profiles were measured. Two of the impeller passages of the orbiting impeller contained a recirculation region covering 20–30 percent of the blade passage while the other two passages contained no recirculation region. The centered impeller also contained this region of reverse flow. Finally, velocity data were numerically integrated to find the forces and stiffnesses due to momentum fluxes on the impeller for the orbiting condition.

Introduction

Understanding and predicting the hydraulically induced force fields in any turbomachine requires detailed knowledge of the flow field. These forces can be static or dynamic (subsynchronous, synchronous, or supersynchronous). Even at design conditions,the forces can be significant and result in premature bearing failures and high operating costs, or worse, catastrophic failures with extended down times. Details of the force producing flows, however, especially for the dynamic force generators, are not well known. To provide insight into hydraulic force generation, this paper presents velocity measurements of the flow field in the impeller and volute of a laboratory centrifugal pump with a synchronously orbiting impeller.

A comprehensive review of the available literature on hydraulically induced forces on pump impellers is presented by Flack and Allaire (1984). A number of researchers have predicted static forces using potential flow methods. Also, several researchers have experimentally measured static forces and pressures in pumps. Recently, a few papers on experimental dynamic forces have been published.

For example, Chamieh et al. (1982), developed a test facility that allows an impeller to be orbited at speeds from antisynchronous to synchronous with the shaft speed in a standard volute type pump. They presented preliminary results for a whirl speed of 3 rpm with pump speed varying from 600 to 2000 rpm. The nondimensional force was plotted versus flow coefficient, ranging from shutoff conditions to 150 percent of the design flow rate. The nondimensional force was not a function of pump speed at flow coefficients greater than design, but was slightly affected at lower flow coefficients. Both positive and negative whirl speeds of 3 rpm were tested with no noticeable effect on the generated force.

More recently, Jery et al. (1985, 1984) greatly expanded the database of impeller forces in volute type pumps. Testing was conducted by systematically varying orbit/pump speed ratio, pump speed, and flow coefficient in several impeller volute combinations. The normalized, time-averaged force, both normal and tangential to the impeller orbit, was plotted for a given speed or flow coefficient over a range of orbit/pump speed ratios. The force was demonstrated to be proportional to the square of the pump speed. At the design flow coefficient, the radial force was found to be positive for whirl/shaft speed ratios from antisynchronous to $\Omega/\omega = 0.5$, beyond which the radial force became nominally zero. The tangential force opposed the whirling motion for all negative whirl/shaft speed ratios (a stabilizing force), but was destabilizing in the region

---

Contributed by the International Gas Turbine Institute and presented at the 35th International Gas Turbine and Aeroengine Congress and Exposition, Brussels, Belgium, June 11–14, 1990. Manuscript received by the International Gas Turbine Institute January 15, 1990. Paper No. 90-GT-258.

of positive whirl speed ratios from 0 to 0.4. The nondimensional tangential force varied linearly with Ω/ω over the range tested. The tangential force did not show a great dependence on flow coefficient for flows from 70 to 160 percent of design flow. Forces at shutoff condition followed the same trend over the range of whirl speeds, but were lower than other flow conditions. At the shutoff condition the forces were stabilizing at all orbit/shaft speed ratios, and at the design flow coefficient the range of destabilizing forces was highest and occurred for $0<(\Omega/\omega)<0.5$.

Uchida et al. (1971) measured both static and dynamic radial forces on the shaft of a centrifugal pump with single volute discharge. The dynamic force component was found to be of the same order of magnitude as the static component. The dominant frequencies of the dynamic force were found to be at the shaft speed and the blade pass frequency. The dynamic force was a minimum at 80 percent of design flow. A relative force peak occurred within the range of Q/Q_n between 0.2 and 0.4. The force increased rapidly with flow rate at flow rates above the design value. These results showed that a hydraulically induced dynamic force does exist, and it is not negligible in comparison with the static force.

Kanki et al. (1981) presented dynamic force data for four rigs. Low-frequency data and blade pass frequency data were not nondimensionalized, and no balancing procedure was described. Thus, the reported synchronous component of force could be a combination of mechanical and hydrodynamic forces. The authors do show that the forces increase at low flow rates.

Although all of the papers on hydraulically generated forces are important and necessary, and they represent data that can be scaled to yield approximations to forces in other pumps, they do not indicate how the dynamic forces are generated by the flow field. Thus, the data do not indicate any means by which the dynamic performance can be improved.

A number of researchers have also studied the details of the internal flow fields in pumps. All have only studied nonorbiting impellers. For example, with the advent of laser velocimetry, a nonintrusive means of measuring velocity fields became available. Eckardt (1976, 1979) used the Laser-2-Focus method to obtain data in radially bladed and backward swept bladed centrifugal compressors. In both cases the impellers discharged into diffusers that did not distort the impeller flow. Results showed that the velocity profile in the backward swept impeller was not as prone to separation and was more uniform at the exit.

Adler and Levy (1987) and Howard et al. (1980) used a laser-Doppler velocimeter to measure the flow in shrouded, backswept impellers. In both studies the discharge was designed not to distort the flow within the impeller. The backswept impellers showed no evidence of separation. In addition, as the fluid approached the exit, the high-velocity flow shifted from the suction side to the pressure side of the blade.

Thomas et al. (1986) used laser velocimetry (LV) to measure the velocities within the logarithmic spiral volute of a laboratory centrifugal pump. A swirl generator was used to replace the impeller. Flows of 121 and 160 percent of design were simulated. In both cases the circumferential distribution of radial flow was nonuniform.

Mizuki et al. (1971) and Murakami et al. (1980) measured pressures and velocities within single blade passages of centrifugal impellers operating in volutes. However, no measure of the circumferential variation in flow was presented.

Kannemans (1980) used a laser-Doppler velocimeter to measure the velocity field in a radial impeller operating in a volute. Data were collected in the impeller and just outside the impeller, for one circumferential position. Circumferential variations were not considered.

Howard et al. (1987) tested three laboratory pumps. One was a single volute and the others were double volute/single discharge. They noted the effects of volute geometry on both local flow fields in the impeller and volute as well as the developed head and pressures.

Hamkins and Flack (1987) and Miner et al. (1989) used a two-directional laser velocimeter to measure the velocities within unshrouded and shrouded impellers. Impellers were concentrically operated in a logarithmic spiral volute. Data were also taken outside the impeller exit. Results showed that the flow was asymmetric, even at design flow. The asymmetries worsened as the flow rate differed from the design flow.

As summarized by the work listed here, much of the previous work in this field has focused on the impeller or the volute separately. Also, in all previous flow field studies orbiting impellers were not used. Thus, the only unsteady components of the flow were due to "blade passing" and off-design conditions. Studies that have used impellers operating in volutes have concentrated on the impeller. The previous work has clearly demonstrated that the asymmetries found in impeller flows are due to the interaction between the impeller and volute. When an impeller has been operated without a volute or with a symmetric discharge region, asymmetries in the impeller flow have not been measured. However, in the case of an impeller-volute combination, circumferential variation in the impeller flow field is usually detected. Whether the flow has been above, below, or at design, these asymmetries have been measured. Therefore, in order to understand the flow in centrifugal pumps better both the impeller and volute are considered together.

The present work seeks to bridge the two pump components by providing measurements in both the impeller and volute for the same operating conditions and identifying systematic variations in the flow field due to an impeller orbit. Such variations can lead to dynamic forces at the synchronous and the blade pass frequencies. The data herein lend insight to the complex flow within the impeller and its interaction with the volute. The data can also be used for verification of ongoing computational predictions of internal flows. The data presented herein are intended to complement the force data directly generated by an orbiting impeller (Chamieh et al., 1982; Jery et al., 1984, 1985) and other data (Uchida et al., 1971; Kanki et al., 1981).

The particular objectives of the present work are to make detailed velocity measurements with a two-directional LV in both the volute and impeller of a centrifugal pump with a synchronously orbiting impeller. On-design and off-design conditions are studied. Blade-to-blade velocity profiles were to be measured for both radial and tangential velocities. These were to be obtained at different circumferential positions

Nomenclature

b = passage width
C_r = absolute radial velocity
Q = flow rate
Q_n = design flow rate
r = radius
r_2 = outer impeller radius
R_w = volute radius
U_2 = impeller peripheral speed
$\tilde{V}$ = passage to passage velocity variation
W_θ = relative (to impeller) tangential velocity
x = horizontal direction
y = vertical direction
z = axial position from centerline
ϵ = orbit eccentricity
θ = circumferential position
ω = rotational speed
Ω = orbit speed

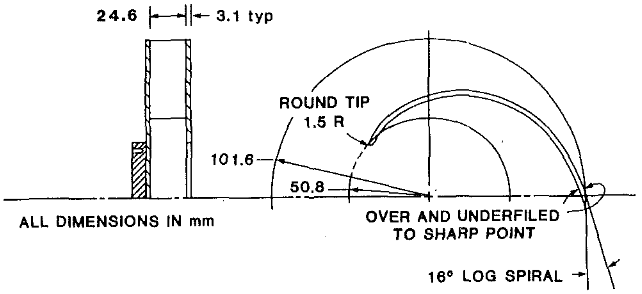

Fig. 1 Impeller geometry

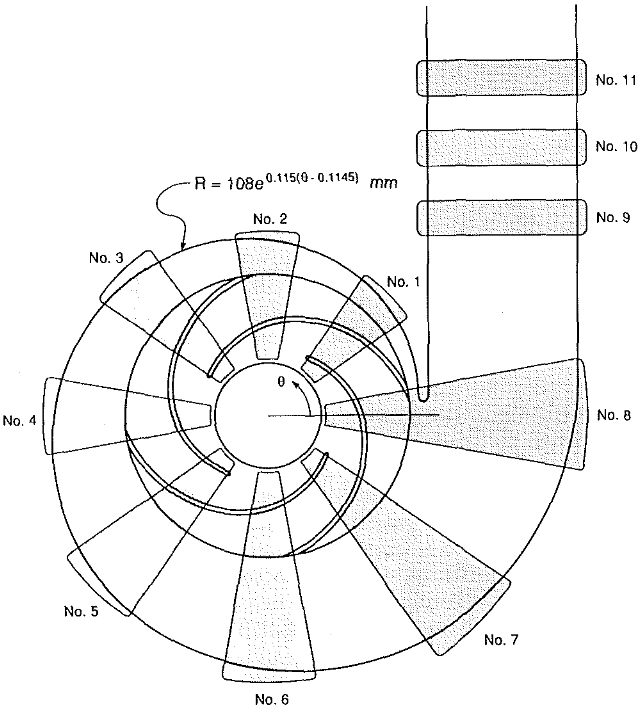

Fig. 2 Volute and window location

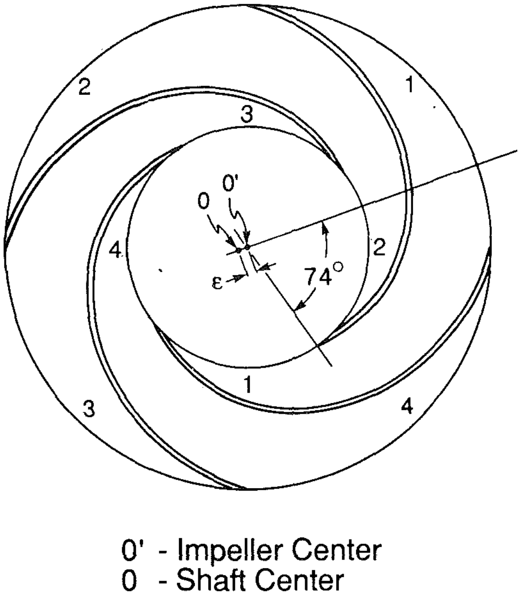

Fig. 3 Impeller eccentricity orientation and passage definition

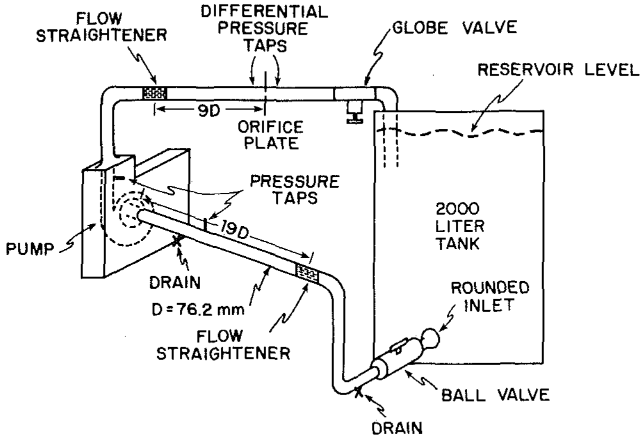

Fig. 4 Flow loop

around the pump. Velocity data were to be used to evaluate the synchronous forces and stiffnesses due to momentum fluxes. Axial traverses were also to be made. The pump is similar to that used by Hamkins and Flack (1987) and Miner et al. (1989) except that the impeller orbited.

Experimental Apparatus

Pump. The pump used for this study is documented by Hamkins and Flack (1987) and Miner et al. (1989). The flow width (*b*) is 24.6 mm. The specific speed of the pump is 1583 US units, which corresponds to a design flow coefficient of 0.063. Figures 1 and 2 depict the impeller and volute geometry. The impeller is a four-bladed geometry with 16 deg logarithmic spiral blades and the volute is also a logarithmic spiral with an 83 deg angle. Window locations for the laser velocimeter measurements are shown in Fig. 2. The pump is constructed of Plexiglas and the casing walls are 50.8 mm thick. However, in the windows the thickness is reduced to 9.5 mm, to facilitate the use of the laser velocimeter.

For the present work, the impeller is allowed to orbit. This was accomplished by offsetting the impeller center from the shaft center. Thus, the impeller orbited with the synchronous frequency ($\Omega/\omega = 1$). The orbit size was $\epsilon/r_2 = 0.016$ and the angular orientation of the impeller center to shaft center relative to a blade leading edge is shown in Fig. 3. In choosing the orbit amplitude, it should be large enough so that the synchronous velocity variations are measurable but small enough so that the tongue clearance does not change appreciably. Similar orbit sizes were used by Jery et al. (1984). The passage definitions (1 to 4) are also shown in Fig. 3.

The flow loop is shown in Fig. 4. This is a closed-loop system fed from a 2000 liter reservoir tank. The flow straighteners in the 76.2-mm-dia pipe upstream of the pump inlet provide a swirl free inlet flow to the pump. Static pressure taps are located five pipe diameters upstream of the impeler inlet and just beyond window 11 in the discharge. Yaw probe traverses in the inlet pipe indicated that the flow was swirl free three diameters upstram of the pump at shutoff conditions for both orbiting and nonorbiting impellers. The second flow straightener, nine pipe diameters upstream of the orifice flow meter, conditions the flow for the orifice plate. The globe valve is used to adjust the flow. The running speed for the pump is 620 rpm. Figure 5 shows the head-capacity curve both for the concentric operation and orbiting impeller. The design point for the present pump design is 6.3 *l*/s at 0.178×10^5 N/m^2. This design point is based on an estimate of the impeller-volute matching point. The matching point is the condition that causes the average angular momentum of the flow at the impeller exit to equal the average angular momentum in the throat of the volute.

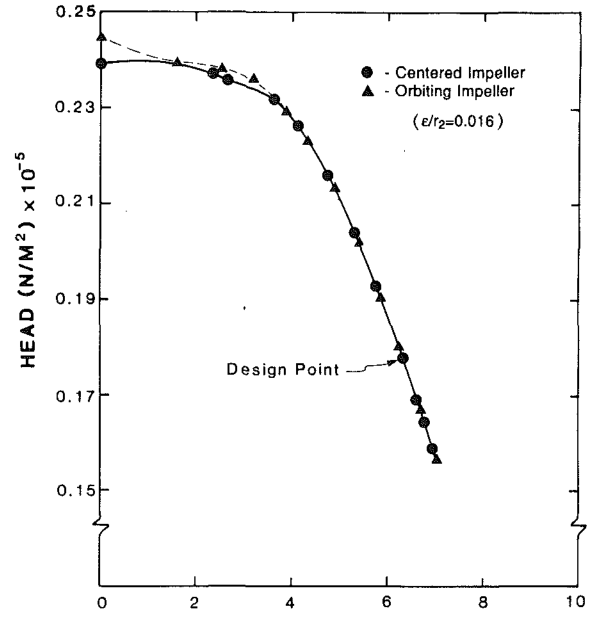

Fig. 5 Pump head-capacity curves

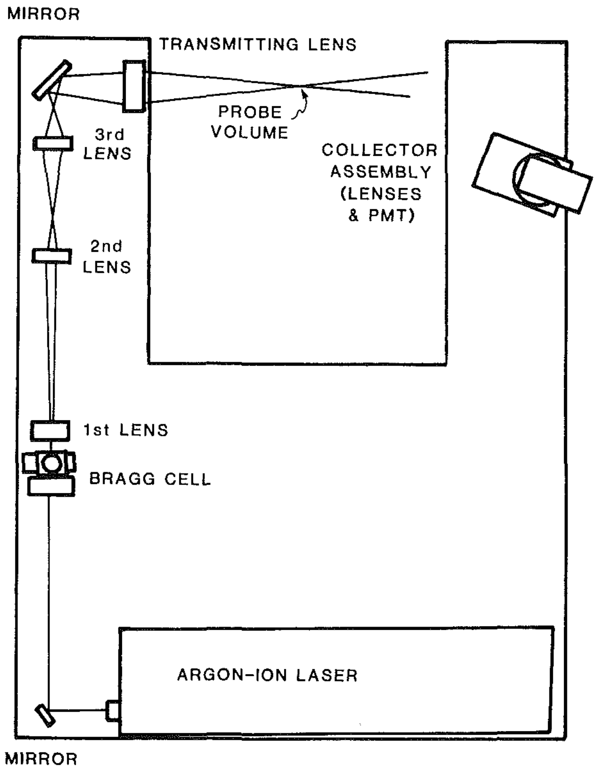

Fig. 6 LV system

Laser Velocimeter. The laser and optics for this system are shown in Fig. 6. The system is three-beam frequency shifted, operated in the forward scatter mode.The Bragg cell performs the dual functions of beam separation and frequency shifting. A single primary beam enters the cell and the primary beam and an orthogonal grid of secondary beams emerges. However, only three of the beams are used, the primary beam and two secondary beams. The secondary beams are shifted by different frequencies. These three beams form a 90 deg angle. Therefore, when the beams are focused and crossed at the probe volume, two sets of perpendicular interference fringes are created.These two sets of fringes allow the simultaneous measurement of two orthogonal components of velocity. The entire optical system was mounted on a three-directional traversing mechanism with digital position readouts. The probe volume was easily and accurately moved in the x, y, and z directions with this mechanism.

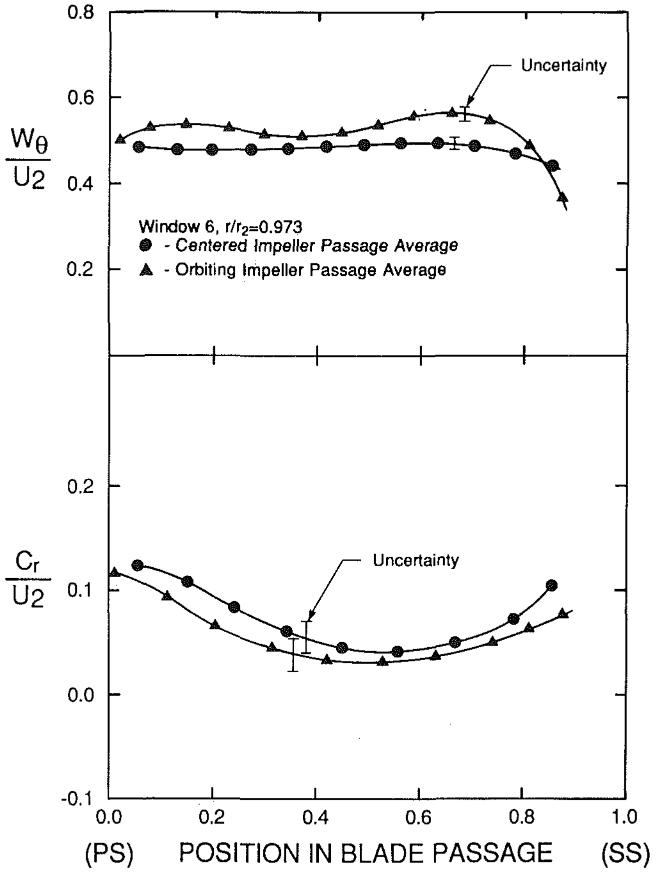

Fig. 7 Passage-averaged velocity profiles: centered and orbiting impellers (window 6, r/r_2 = 0.973, Q/Q_n = 1.00)

The frequency of light scattered from the probe volume determines the velocity. Light was scattered by naturally occurring particles in the water. The water was filtered, using a taste and odor filter. This provided particles of 5 μm and smaller. Two burst-type signal processors with adjustable threshold and five/eight count comparison with adjustable tolerances were used. Signals from both sets of beams are checked for coincidence. If the signals occur at the same time, then they are considered valid.

Once a valid LV signal is generated, the impeller angular position is recorded with a shaft encoder. The encoder divides each revolution into 256 parts. The two velocity signals and the shaft position are simultaneously recorded onto floppy disks by a dedicated microcomputer. A typical test had 5000 data points, approximately 20 per each of the 256 "shaft angle bins." This gave two-dimensional velocity and angular position data for the four blade passages, which were analyzed after the test.

Uncertainty. The uncertainty in probe volume position was 0.5 mm radially and 1 mm axially. The uncertainty in the angular position was 0.30 deg. The uncertainty in the angular orientation of the probe volume fringes with respect to the reference axes was 0.85 deg. This was the dominant factor in flow direction uncertainty. The typical uncertainty in the radial velocity component was 0.04 m/s and the typical uncertainty in the tangential velocity component was also 0.04 m/s. These velocity uncertainties do not include the effect of positional

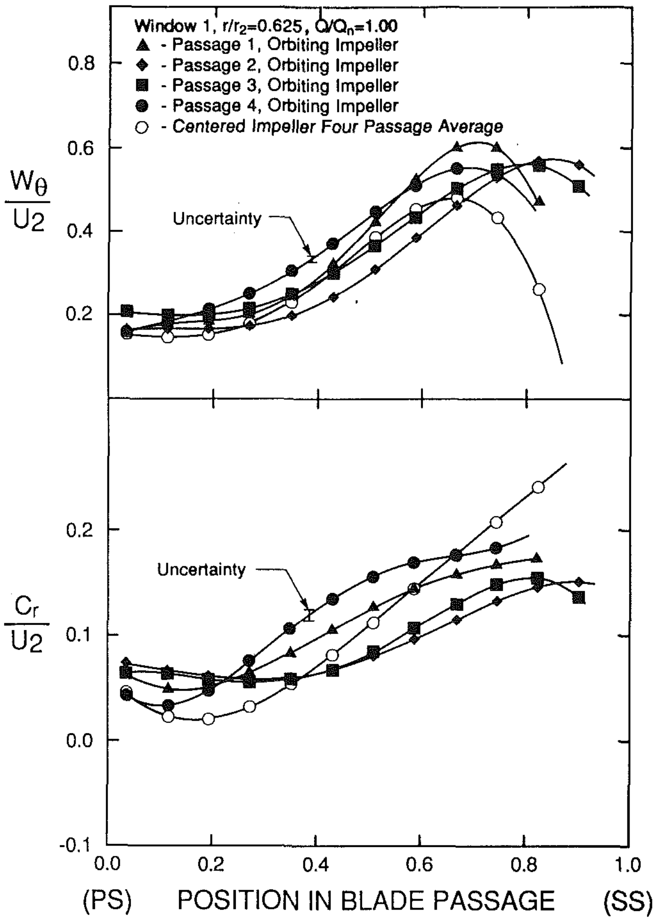

Fig. 8 Velocity profiles (window 1, r/r_2 = 0.625, Q/Q_n = 1.00)

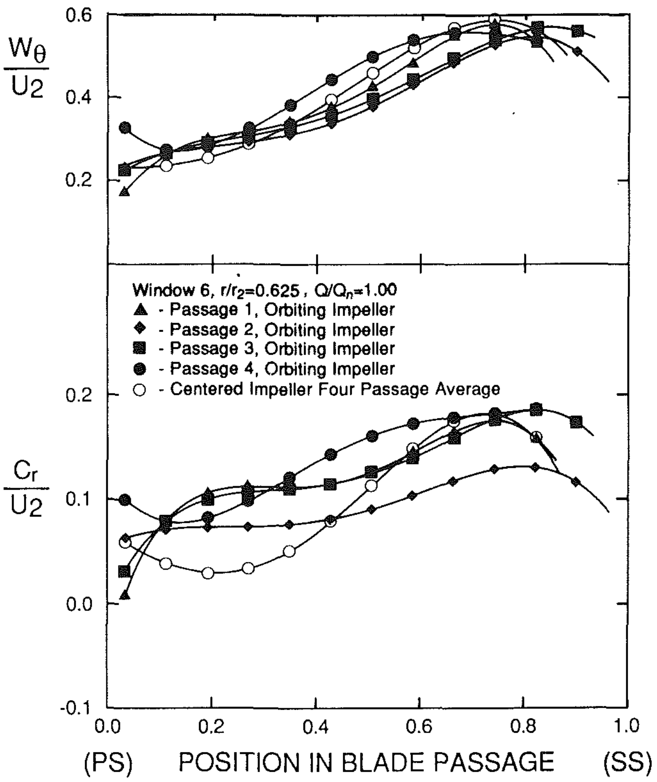

Fig. 9 Velocity profiles (window 6, r/r_2 = 0.625, Q/Q_n = 1.00)

uncertainty in the presence of velocity gradients. The position of the probe volume is uncertain, particularly in the axial direction. Since spatial velocity gradients are present, a misplaced probe volume will measure the incorrect velocity. This spatial uncertainty results in a total uncertainty of 0.10 m/s for the radial velocity and also 0.10 m/s for the tangential velocity.

When examining the differences between the four different blade-to-blade profiles for the orbiting impeller data, one only had to consider the effect of random uncertainty. For these cases the data were recorded without moving the probe volume and thus data were acquired for exactly the same probe volute location. The uncertainty due to the axial gradient, however, must be considered when comparing the profiles for the centered and orbiting impeller passages, since these data were recorded at different times, and the probe volume location was not exactly the same for the two sets of data (due to positional uncertainty).

Results

Experimental data for this study were taken in windows 1, 4, 6, and 8. For each window, data were taken at four radial positions within the impeller. Volute data in window 1 were taken at only one radial position; data at 4 radial volute positions were measured in the other three windows. These data were taken at the axial centerline of the pump at the design flow of 6.3 l/s. In addition, data for five flow rates were taken in window 6 at the axial centerline. Representative results are presented here and are nondimensionalized by the impeller tip velocity. Data at other axial locations were taken but are not presented herein for the sake of brevity. Results are presented in the form of fourth-order polynomial least-squares curve fits to the average velocity data profiles. The symbols are used only as a means of identifying the curves and do not represent actual data. In general, data are presented for the four different passages and compared to the nonorbiting impeller data. Complete presentation and discussion of the results can be found in Beaudoin (1987) and Miner (1988).

Figure 7 contains the passage-averaged profiles of all four passages for both the orbiting and centered impeller cases for a typical test run (window 6, $r/r_2 = 0.973$, $Q/Q_n = 1.00$). The two impeller conditions have similar profile shapes for both the radial and tangential velocites. There are, however, differences in the magnitudes of the profiles. These are due to uncertainty in the probe volume position (as shown) in addition to the differences in the data between the centered and orbiting impellers due to the unsteady nature of the flow.

Next, typical impeller data for variations in radius and circumferential position are presented to demonstrate the passage to passage variations.These are presented in Figs. 8–11 for two radius ratios and two circumferential positions. When comparing velocity data for the passages the uncertainty is much smaller, as indicated in Fig. 8. It is important to note that the different passage data for the nonorbiting impeller fell within the small uncertainty band indicated in Fig. 8. These data are not presented for the sake of brevity.

At a radius of 0.625 (Figs. 8 and 9, windows 1 and 6), passage 4 tended to have the highest radial velocity across the central portion of the passage span. Variations in velocities in midstream and near the blade surfaces, particularly the suction surface, are systematic, i.e., one can see a repetitive pattern. For example, for the midspan portion of C_r/U_2 for window 1 (Fig. 8) one can see the velocity varies from $C_r/U_2 = 0.135$ to 0.085 to 0.090 to 0.155 and back to 0.135 as the impeller varies from passage 1 to 2 to 3 to 4 and back to 1. Such periodicity is seen on most profiles. Passage 1 had the second highest radial velocity values at each of the four circumferential positions tested. All the radial profiles were skewed toward the

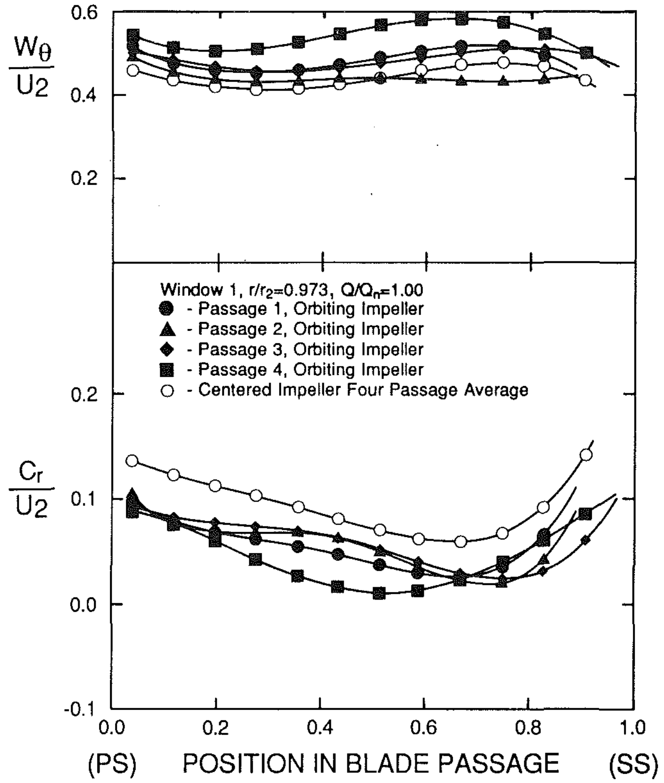

Fig. 10 **Velocity profiles (window 1, r/r_2 = 0.973, Q/Q_n = 1.00)**

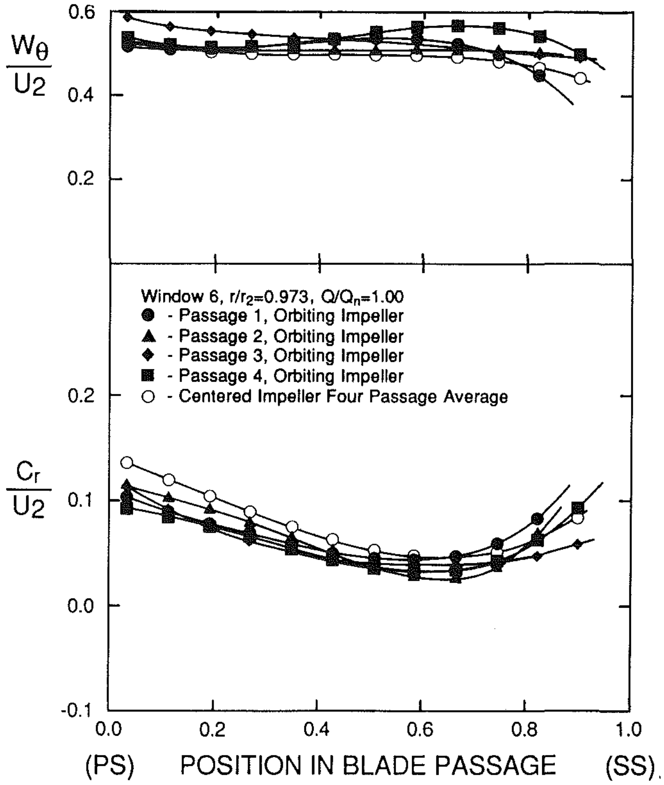

Fig. 11 **Velocity profiles (window 6, r/r_2 = 0.973, Q/Q_n = 1.00)**

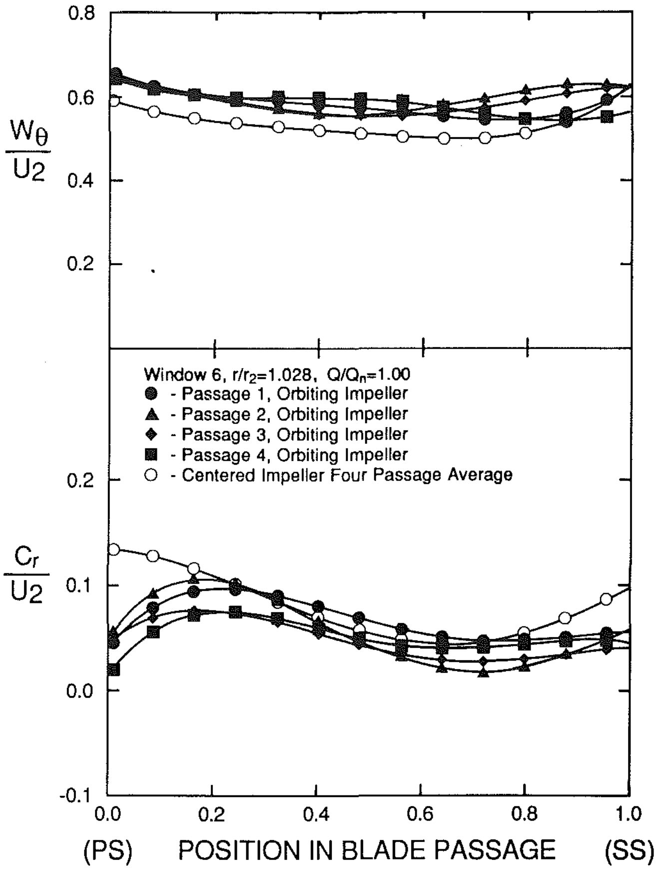

Fig. 12 **Velocity profiles (window 6, r/r_2 = 1.028, Q/Q_n = 1.00)**

suction surface, with the profile peak values occurring in the range of 80 percent of the passage span.

Tangential profiles show passage 4 to have the highest relative tangential velocity, i.e., lowest absolute velocity, in the central portion of the blade span at each circumferential position. Passage 2 had the lowest relative tangential velocity in each of the four cases. One should again note a systematic variation in the blade-to-blade profile on these figures.

In Figs. 10 and 11, data for a radius ratio of 0.973 are presented for windows 1 and 6. Variations in the radial profiles are now more symmetric than profiles measured at the smaller radii, with equal peaks at the suction and pressure surfaces, with the lowest value near the midspan. Near the impeller exit for all conditions the largest passage-to-passage fluctuations occurred in window 1 (Fig. 10). In this region the impeller/volute clearance is smallest, indicating that this varying clearance strongly influences the flow field in the impeller.

For a radius ratio of 0.973 the tangential profiles are nearly uniform across the passage up to 80 percent span, where the relative velocity becomes small. Absolute tangential velocity data for radius ratios 0.875 (data not shown) to 0.973 (Figs. 10 and 11) indicate that very little additional rotational energy is added to the flow between these radius ratios in the region from pressure surface to midspan. Passage 2 consistently demonstrated the highest absolute tangential velocity (lowest relative tangential velocity) across the span and passage 4 showed the lowest absolute velocity as measured at the four circumferential probe volume locations. Thus, the lowest relative tangential velocity was in the passage that lagged (by approximately 90 deg) the minimum impeller/volute clearance.

Typical measurements in the volute near the impeller exit are presented in Fig. 12 (window 6, $r/r_2 = 1.028$). These measurements were made in the volute, from nondimensional distances of 0.012 to 0.043 from the impeller exit, depending on the circumferential location relative to the eccentricity. Passages 1 and 2 tended to have a wider peak to peak variation in the radial profile. All the passage profiles had maximum values at 20 percent of the blade "span." The measurements are made outside the impeller, so the angular locations of the blade tips at the impeller exit are used to bracket the profiles.

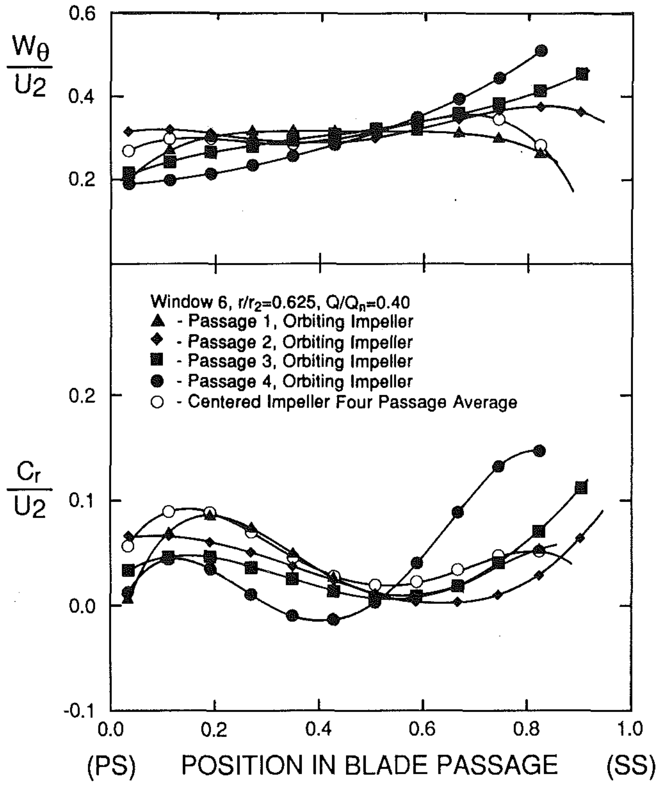

Fig. 13 **Velocity profiles (window 6, r/r_2 = 0.625, Q/Q_n = 0.40)**

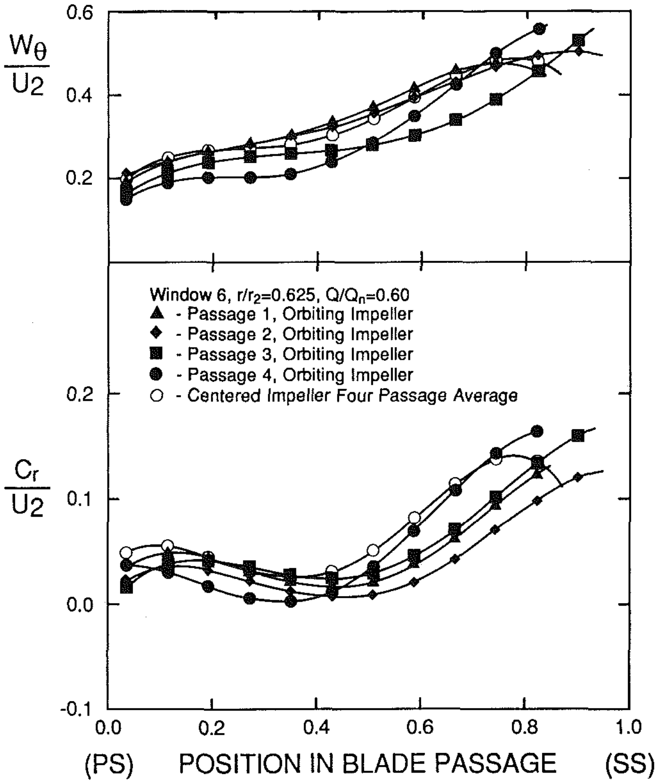

Fig. 14 **Velocity profiles (window 6, r/r_2 = 0.625, Q/Q_n = 0.60)**

By examining Figs. 10, 11, and 12 ($r/r_2 = 0.973$ and 1.028) one can see that differences between the nondimensional velocity profiles for passages 2 and 4 ranged from 0.05 to 0.14 in the central portion of the blade span. Systematic periodic trends among the radial velocity profiles are again observed at these radii. Although the data are similar they are not within the uncertainty indicated in Fig. 8.

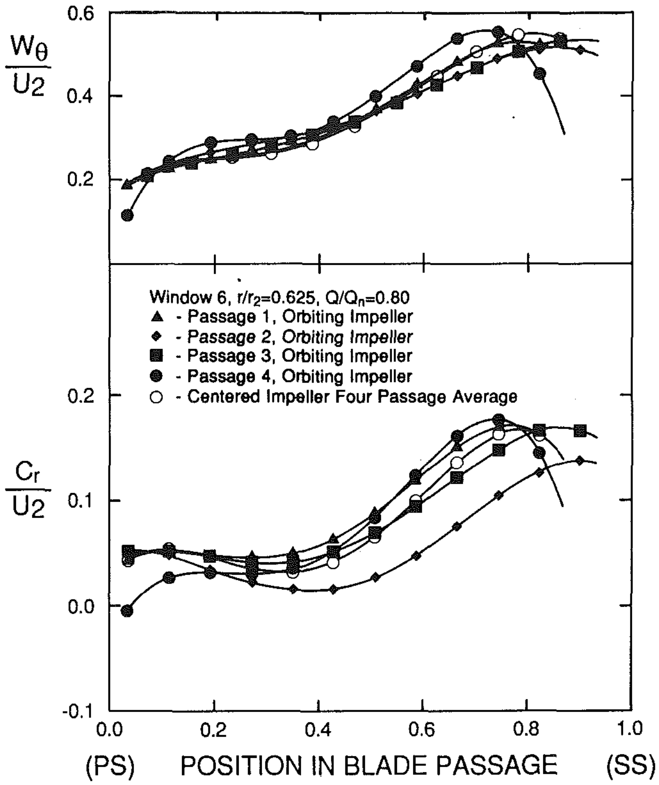

Fig. 15 **Velocity profiles (window 6, r/r_2 = 0.625, Q/Q_n = 0.80)**

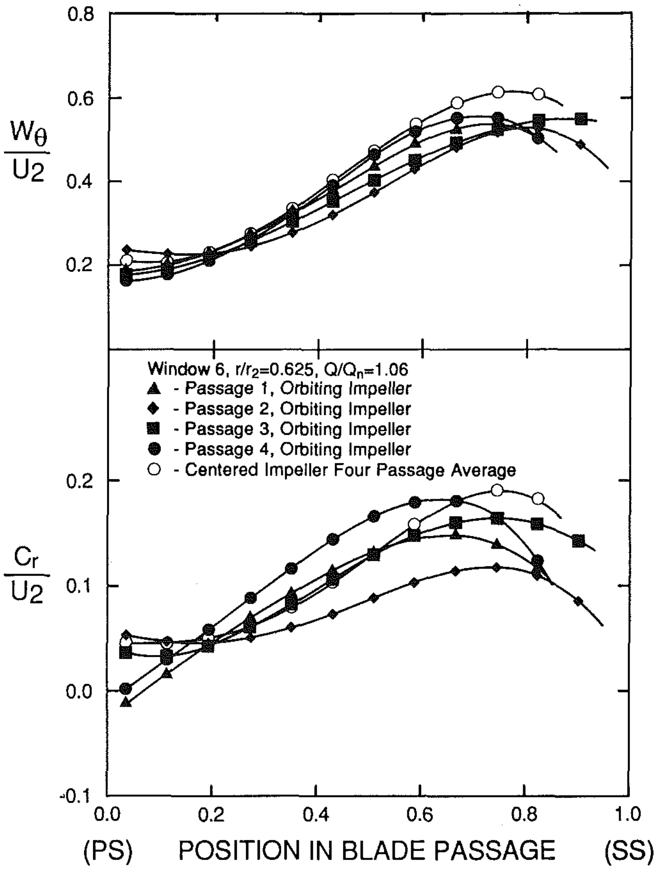

Fig. 16 **Velocity profiles (window 6, r/r_2 = 0.625, Q/Q_n = 1.06)**

Tangential velocity profiles show passage 2 to have the highest absolute velocity of the four orbiting passages for the majority of the span at three of the four circumferential positions

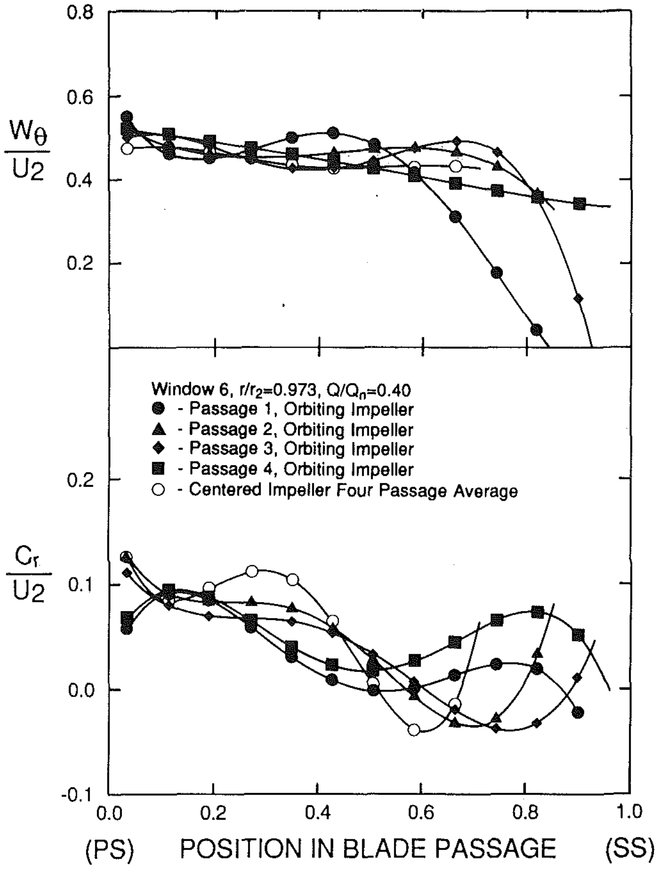

Fig. 17 Velocity profiles (window 6, r/r_2 = 0.973, Q/Q_n = 0.40)

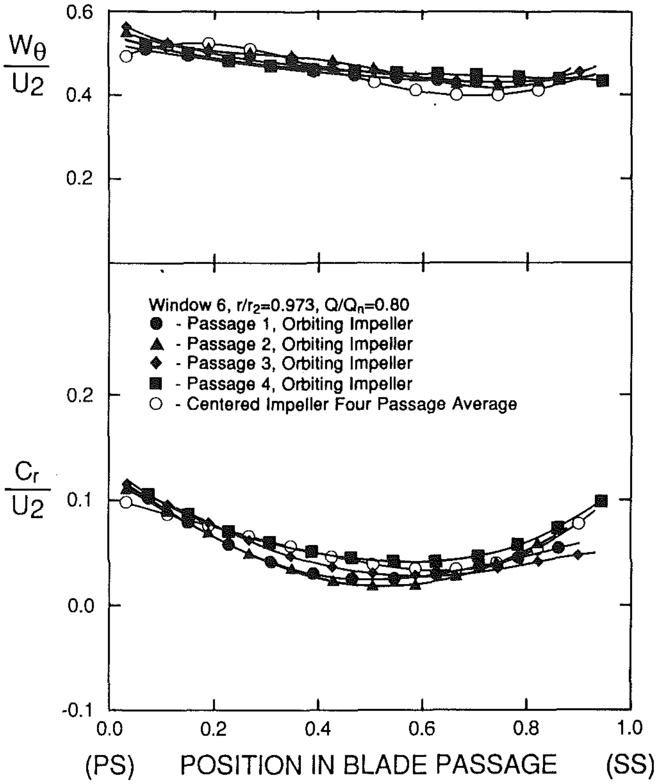

Fig. 19 Velocity profiles (window 6, r/r_2 = 0.973, Q/Q_n = 0.80)

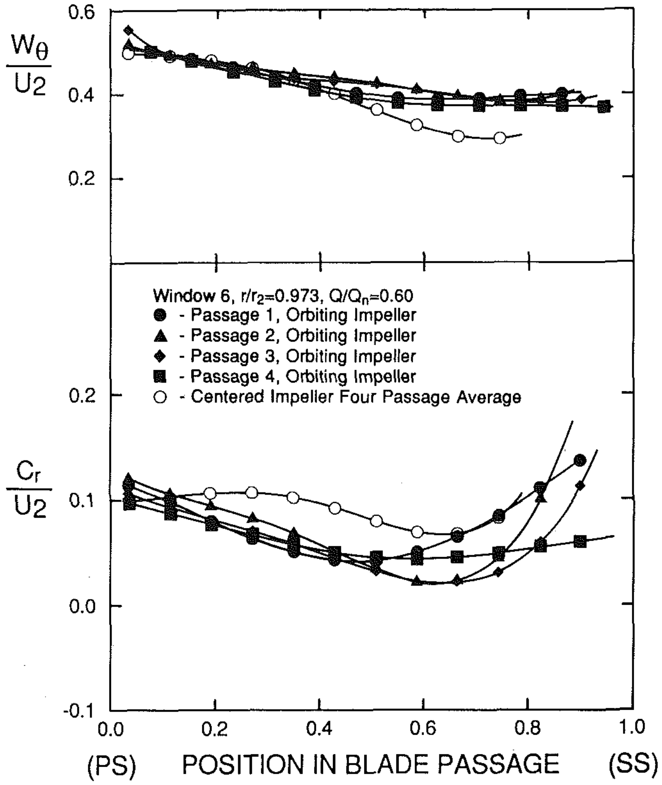

Fig. 18 Velocity profiles (window 6, r/r_2 = 0.973, Q/Q_n = 0.60)

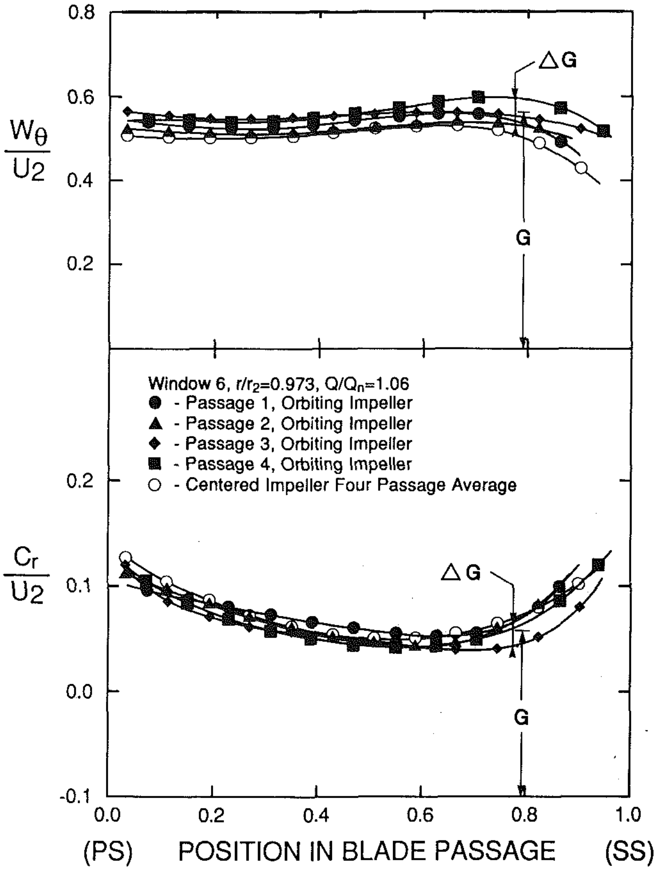

Fig. 20 Velocity profiles (window 6, r/r_2 = 0.973, Q/Q_n = 1.06)

tested, the exception being window 8. Passage 4, on the average, had the lowest absolute tangential velocities.

Flow variation studies were conducted in window 6 at radii ratios of 0.625 and 0.973. Figures 9 and 13 through 16 are for $r/r_2 = 0.625$ and show the passage-to-passage comparison for the orbiting impeller for the range of flows tested. In general passage 4 had the highest radial peak velocity of the four orbiting passages for all tested flow rates, while passage 2 had

Table 1 Variation in blade-to-blade velocity profiles in orbiting impeller ($\epsilon = e/r_2 = 0.016$)

r/r_2	Window	Q/Q_n	$\tilde{V}_r$	$\tilde{W}_\theta$
0.625	1	1.00	0.30	0.20
0.625	4	1.00	0.30	0.25
0.625	6	1.00	0.40	0.20
0.625	8	1.00	0.50	0.20
0.75	1	1.00	0.40	0.15
0.75	4	1.00	0.55	0.20
0.75	6	1.00	0.30	0.15
0.75	8	1.00	0.45	0.15
0.875	1	1.00	0.35	0.20
0.875	4	1.00	0.50	0.15
0.875	6	1.00	0.30	0.20
0.875	8	1.00	0.40	0.15
0.973	1	1.00	0.60	0.20
0.973	4	1.00	0.50	0.10
0.973	6	1.00	0.30	0.10
0.973	8	1.00	0.35	0.15
1.028	1	1.00	0.55	0.05
1.028	4	1.00	0.75	0.05
1.028	6	1.00	0.50	0.05
1.028	8	1.00	0.90	0.05
0.625	6	0.40	1.80	0.25
0.625	6	0.60	0.90	0.30
0.625	6	0.80	0.60	0.30
0.625	6	1.00	0.40	0.20
0.625	6	1.06	0.50	0.15
0.973	6	0.40	2.50	0.40
0.973	6	0.60	0.40	0.10
0.973	6	0.80	0.40	0.05
0.973	6	1.00	0.30	0.10
0.973	6	1.06	0.30	0.10

the lowest peak value. As with the centered impeller profiles (Miner et al., 1989), orbiting passage radial peak values were located at 80 percent of span, the exception being at $Q/Q_n = 0.4$. The absolute tangential velocity along a passage profile varied inversely to radial velocity for all the passages at all flow rates except $Q/Q_n = 0.4$.

The orbiting impeller radial velocity profiles at $r/r_2 = 0.973$ (Figs. 10 and 17 through 20) have the same basic shapes for flow rates from 60 to 106 percent of design flow. Peak values are present on the two blade surfaces with the minimum value near midspan. At $Q/Q_n = 0.4$ (Fig. 17) two distinct profile shapes are seen; passages 1 and 4 have two relative maxima (at 10 and 80 percent of span) and relative minima at 50 percent span and negative velocities near the suction surface. Passages 2 and 3, and the centered impeller profiles, are highest on the pressure surface and have pronounced minima, which vary in location from 60 to 80 percent of span, depending on the passage, and with negative velocities, which vary in span length from 16 to 28 percent.

Tangential velocity profiles show a change from an essentially flat profile across the span at 100 and 106 percent of design flow to a profile, where turning is increased along the span from pressure side to suction side for low flow rates. At $Q/Q_n = 0.4$ the profiles fluctuate along the span. Passages 1 and 3 have profiles where the relative tangential velocity decreases markedly from 60 percent span to the blade suction surface.

To summarize the passage-to-passage variations due to the orbiting operation, Table 1 is presented. This table shows the mean variation among the four individual passage profiles of the orbiting impeller for both velocity components. The variation is defined by:

$$\tilde{V} \equiv \frac{2}{\pi} \int_0^{\pi/2} \frac{\Delta G(\theta)}{G(\theta)} \, d\theta$$

where ΔG and G are illustrated in Fig. 20 and where ΔG = maximum variation among profiles at a given span location; G = mean value of profiles at a given span location; θ = span location.

From this table three trends can be seen. First, the passage-to-passage variation for the radial component increases with increasing radius.

In fact the largest fluctuations occur in the volute at a radius ratio of 1.028. Second, the trend is the opposite for the tangential component, that is, this variation decreases with increasing radius; the smallest variation occurs in the volute. Third, near the impeller periphery the largest fluctuations in a radial velocity occur near the tongue, indicating that the tongue clearance influences the flow rate in the adjacent passage. And fourth, when examining the different flow rates, one sees that the largest variations for both components occur at off-design conditions. At the design flow rate, the radial velocity profiles had passage-to-passage variations from 30 to 60 percent of the mean value. The relative tangential velocity profiles had variations from 15 to 25 percent at design condition. At 40 percent flow the variations are as much as eight times the variations at design conditions. This implies that at low flow rates synchronous forces (and noise) and multiples thereof will be largest. This has in fact been found to be the case as reported by Uchida et al. (1971) and Kanki et al. (1981). Internal flow measurements are now available to help explain why these forces are generated.

To summarize a portion of the velocity data into such forces, one can numerically integrate the momentum fluxes at the exit of the impeller. Allaire et al. (1984) showed that for pumps of this scale with an unbounded volute, the predominant force on the impeller results from the momentum fluxes as opposed to the pressure forces. By numerically integrating the velocities around the impeller exit for one impeller angular orientation (i.e., position in the orbit) one can find the force vector due to momentum fluxes at that impeller position:

$$\mathbf{F} = \int \mathbf{V} \rho \mathbf{V} \cdot d\mathbf{A}$$

$$\cong \sum_{\theta=0}^{360^\circ} \mathbf{V} \rho C_r r_2 \Delta\theta$$

By finding the periodic fluctuating forces due to the orbit, one can find the stiffnesses by:

$$K_{xx} = -\Delta F_x/\Delta_x \qquad K_{yy} = -\Delta F_y/\Delta_y$$

$$K_{yx} = -\Delta F_y/\Delta_y \qquad K_{xy} = -\Delta F_x/\Delta_y$$

For example, one finds K_{xx} when the impeller position is $\Delta x = \pm \epsilon$ and $\Delta y = 0$, and evaluates ΔF_x as the difference between the x-component of force at this position and the average x force. One can nondimensionalize these by

$$\bar{K}_{ij} = K_{ij} r_2 / [1/2 \rho A_2 U_2^2]$$

where $A_2 = 2\pi r_2 b$.

The above numerical integration was carried out for design flow conditions for four impeller positions. The synchronous results are presented in Table 2. As can be seen, the stiffnesses are not symmetric, i.e., $\bar{K}_{xx} \neq \bar{K}_{yy}$ and $\bar{K}_{xy} \neq \bar{K}_{yx}$. This is due to the nonsymmetry of the volute and the fact that the tongue clearance changes as the impeller orbits. One should also note that the magnitudes of the stiffnesses are of the same order as predicted by Allaire et al. (1984) and measured by Jery et al. (1984) for similar but not identical sized pumps. Of particular importance is the negative sign on K_{xx} as also reported in Allaire et al. (1984) and Jery et al. (1984), indicating a destabilizing mechanism.

Table 2 Nondimensional Stiffnesses for Design Flow Due to Momentum Fluxes

$\bar{K}_{xx} = -0.161$

$\bar{K}_{yy} = -0.005$

$\bar{K}_{yx} = -0.029$

$\bar{K}_{xy} = -0.229$

Conclusions

Measurements of fluid velocities in the impeller of a single volute type pump were made in two pump configurations: (*i*) with the impeller running centered and (*ii*) with a whirling motion on the impeller that was induced by offsetting the impeller center from the shaft center. Blade-to-blade velocity profiles were generated as the impeller rotated through an LV probe volume located at various fixed positions in the pump. Comparisons were made both between the individual passage profiles of the orbiting impeller and to the four passage average profile of the centered impeller.

The average variations among the individual passage velocity profiles in the orbiting impeller were calculated for each test conducted. At the design flow rate, the radial velocity profiles had passage-to-passage variations from 30 to 60 percent of the mean value. The relative tangential velocity profiles had variations from 15 to 25 percent at design condition. Passage-to-passage variations were systematic and periodic as the four flow passages swept by the fixed measurement location. At off-design conditions the variation in radial velocity profiles increased by as much as eight times as flow rate decreased. Such increases in velocity variations imply increased momentum variations, which result in increased dynamic forces, as have been previously measured and reported. The current data represent the first internal velocity data to complement the force measurements.

Next, the passage-to-passage variation for the radial component was seen to increase with increasing radius. In fact the largest fluctuations occurred in the volute. This trend was the opposite for the tangential component. That is, this variation decreased with increasing radius and the smallest variation occurred in the volute.

At radius ratios of 0.973 and 1.028, the tangential velocity profiles were relatively flat across the individual blade passages. Systematic variations of the velocity levels of the different passages were measured, however. Passage 2 contained the highest absolute tangential velocities of the four orbiting passages while passage 4 contained the lowest velocities. Differences between the nondimensionalized velocity profiles for passages 2 and 4 ranged from 0.05 to 0.14 in the central portion of the blade span. At the impeller exit the largest fluctuations were seen in Window 1, which is adjacent to the tongue (smallest clearance area).

At a radius ratio of 0.625 at the design flow rate, absolute tangential velocity was found to be inversely related to radial velocity both for a given passage along the span, and among the four passages at a given span location in the central portion of the blade span. Passage 4 had the highest radial values and lowest absolute tangential values. This trend was also true at tests conducted at a radius ratio of 0.750, but not at the larger radii in the impeller.

At the off-design flow rate of $Q/Q_n = 0.4$, two distinct radial velocity profiles were measured at a radius ratio of 0.973. The radial velocity profile of the centered impeller and passages 2 and 3 of the orbiting impeller contained regions of negative velocity covering 16 to 28 percent of the passage span. The recirculation zones were located from 60 to 80 percent of the passage span. Passage 1 and 4 profiles contained negative velocities near the suction surface (100 percent passage span) but had relative maxima at both 10 and 80 percent passage span. Such systematic variations in profile shapes among the passages were not measured at a radius ratio of 0.625 at $Q/Q_n = 0.4$.

To demonstrate use of the data, the velocity momentum profiles were numerically integrated around the impeller periphery at the design flow rate. This resulted in fluctuating forces due to fluctuating momentum fluxes. Using these force variations, stiffnesses were found previously, both theoretically and experimentally, for similar sized pumps.

Acknowledgments

This research was sponsored by the Rotating Machinery and Controls (ROMAC) Industrial Research Program at the University of Virginia.

References

Adler, D., and Levy, Y., 1979, "A Laser-Doppler Investigation of the Flow Inside a Backswept, Closed, Centrifugal Impeller," *Journal of Mechanical Engineering Science*, Vol. 21, No. 1, pp. 1-6.

Allaire, P. E., Sato, C. J., and Branagan, L. A., 1984, "Hydraulic Forces on Centrifugal Impeller Undergoing Synchronous Whirl," *Rotordynamic Instability Problems in High-Performance Turbomachinery*, NASA CP-2338, May, pp. 123-136.

Beaudoin, R. J., 1987, "Laser Velocimetry Measurements in a Centrifugal Pump With an Orbiting Impeller," M.S. Thesis, University of Virginia, Charlottesville, VA.

Chamieh, D. S. Acosta, A. J., Brennen, C. E., Caughy, T. K., and Franf, R., 1982, "Experimental Measurements of Hydrodynamic Stiffness Matrices for a Centrifugal Pump Impeller," Workshop on Rotordynamic Instability Problems in High-Speed Turbomachinery, Texas A&M University, NASA CP 2250, May, pp. 382-398.

Eckardt, D., 1976, "Detailed Flow Investigations Within a High Speed Centrifugal Compressor Impeller," ASME *Journal of Fluids Engineering*, Vol. 98, No. 3, pp. 390-402.

Eckardt, D., 1979, "Flow Field Analysis of Radial and Backswept Centrifugal Compressor Impellers, Part 1: Flow Measurements Using a Laser Velocimeter," *Performance Prediction of Centrifugal Pumps and Compressors*, ASME 100127, pp. 77-86.

Flack, R. D., and Allaire, P. E., 1984, "Lateral Forces on Pump Impellers — A Literature Review," *The Shock and Vibration Digest*, Vol. 16, No. 1, pp. 5-14.

Hamkins, C. P., and Flack, R. D., 1987, "Laser Velocimeter Measurements in Shrouded and Unshrouded Radial Flow Pump Impellers," ASME JOURNAL OF TURBOMACHINERY, Vol. 109, No. 1, pp. 70-76.

Howard, J. H. G., Mukker, O. S., and Naoem, T., 1980, "Laser Doppler Measurements in a Radial Pump Impeller," *Measurement Methods in Rotating Components of Turbomachinery*, ASME 100130, pp. 133-138.

Howard, J. H. G., Abramian, M., and Hermann, P., 1987, "Experimental Investigation of Impeller and Volute Flow Fields for a Low Specific Speed Pump With Single and Double Volutes," *Proceedings of the 1987 ASME/JSME Thermal Engineering Joint Conference*, Vol. 2, pp. 51-61.

Jery, B., Acosta, A. J., Brennen, C. E., and Caughy, T. K., 1984, "Hydrodynamic Impeller Stiffness, Damping, and Inertia in Rotordynamics of Centrifugal Flow Pumps," *Proceedings of the Workshop on Rotordynamic Instability Problems in High Performance Turbomachinery*, Texas A&M University, May, NASA-CP2338, pp. 137-160.

Jery, B., Brennen, C. E., Caughy, T. K., and Acosta, A., 1985, "Forces on Centrifugal Pump Impellers," *Proceedings of the Second International Pump Symposium*, Texas A&M University, College Station, TX, pp. 21-29.

Kanki, H., Kawata, Y., and Kawatani, T., 1981, "Experimental Research on the Hydraulic Excitation Force on the Pump Shaft," ASME Paper No. 81-DET-71.

Kannemans, H., 1980, Radial Pump Impeller Measurements Using a Laser Doppler Velocimeter," ASME Paper No. 80-GT-94.

Miner, S. M., 1988, Potential Flow Analysis of a Centrifugal Pump: Comparison of Finite Element Calculation and Laser Velocimeter Measurement," Ph.D. Dissertation, University of Virginia, Dept. of Mechanical & Aerospace Engr., Jan.

Miner, S. M., Beaudoin, R. J., and Flack, R. D., 1989, "Laser Velocimetry Measurements in a Centrifugal Flow Pump," ASME JOURNAL OF TURBOMACHINERY, Vol. 111, No. 3, pp. 205-212.

Mizuki, S., Sakai, T., and Watanabe, I., 1971, "A Study of the Flow Pattern Within the Centrifugal and Mixed-Flow Impellers," ASME Paper No. 71-GT-41.

Murakami, M., Kikuyama, K., and Asakura, E., 1980, "Velocity and Pressure Distributions in the Impeller Passages of Centrifugal Pumps," ASME *Journal of Fluids Engineering*, Vol. 102, No. 4, pp. 420-426.

Thomas, R. N., Kostrzewsky, G. J., and Flack, R. D., 1986, "Velocity Measurements in a Pump Volute With a Non-rotating Impeller," *Int. J. Heat and Fluid Flow*, Vol. 7, No. 1, pp. 11-20.

Uchida, N., Kenasku, I., and Shirai, I., 1971, "Radial Forces on the Impeller of a Centrifugal Pump," *Bulletin JSME*, Vol. 14, No. 76, pp. 1106-1117.

Turbulence Measurements in a Centrifugal Pump With a Synchronously Orbiting Impeller

R. D. Flack
Professor,
Department of Mechanical and Aerospace Engineering,
University of Virginia,
Charlottesville, VA 22901

S. M. Miner
Assistant Professor,
U.S. Naval Academy,
Annapolis, MD 21402

R. J. Beaudoin
Development Engineer,
General Electric Company,
Schenectady, NY 12345

Turbulence profiles were measured in a centrifugal pump with an impeller with backswept blades using a two-directional laser velocimeter. Data presented include radial, tangential, and cross product Reynolds stresses. Blade-to-blade profiles were measured at four circumferential positions and four radii within and one radius outside the four-bladed impeller. The pump was tested in two configurations: with the impeller running centered within the volute, and with the impeller orbiting with a synchronous motion ($\epsilon/r_2 = 0.016$). Flow rates ranged from 40 to 106 percent of the design flow rate. Variation in profiles among the individual passages in the oribiting impeller were found. For several regions the turbulence was isotropic so that the cross product Reynolds stress was low. At low flow rates the highest cross product Reynolds stress was near the exit. At near-design conditions the lowest cross product stress was near the exit, where uniform flow was also observed. Also, near the exit of the impeller the highest turbulence levels were seen near the tongue. For the design flow rate, inlet turbulence intensities were typically 9 percent and exit turbulence intensities were 6 percent. For 40 percent flow capacity the values increased to 18 and 19 percent, respectively. Large local turbulence intensities correlated with separated regions. The synchronous orbit did not increase the random turbulence, but did affect the turbulence in the individual channels in a systematic pattern.

Introduction

Understanding and predicting the hydraulically induced loss and force fields in any turbomachine requires detailed knowledge of the flow field. Losses are related to turbulence levels in an impeller. Highly turbulent flows will induce large losses, and thus reduce the efficiency. To provide insight into these losses, this paper presents turbulence measurements of the flow field in the impeller and volute of a laboratory centrifugal pump.

A number of researchers have studied the details of the internal flow fields in pumps. Most have only studied nonorbiting impellers and none have fully documented the turbulence field. Early work on the flow in pump impellers was done by Fischer and Thoma (1932). They used die injection as a means of visualizing the flow in an impeller. The impeller discharged into a symmetric collector. For flows above 40 percent of design the flow pattern remained symmetric. Below 40 percent of design flow recirculating flow among the blade passages was seen.

Beveridge and Morelli (1950), Acosta (1954), and Acosta and Bowerman (1957) performed studies on a series of two-dimensional impellers operating in a symmetric collector. These studies measured the pressure distribution along the blades. For flows at and near design no separation was seen. Results indicated that about half of the impeller losses occurred at the inlet, and these losses could be reduced if a more uniform inlet flow could be provided.

Howard and Kittmer (1975) used hot-wire anemometry and hydrogen bubble flow visualization to investigate a shrouded impeller and an unshrouded impeller. Both impellers discharged into axisymmetric collectors. The impellers had backward swept blades and neither impeller showed signs of separation.

Binder and Knapp (1936) took pressure and velocity data in the volutes of two centrifugal pumps. Their results showed that the radial velocities and the static pressures around the volute were nonuniform for all flow rates.

Iverson et al. (1960) measured both the pressure distribution in the volute, and the radial force on the impeller of a centrifugal pump. This study showed a nonuniform static pressure distribution and a force unbalance at design flow.

The effect of the volute on pump performance was studied by Bowerman and Acosta (1957), and Hira and Vasandani (1975). These studies showed that volute geometry has a direct effect on performance. This effect comes primarily from a nonuniform distribution of pressure and radial velocity around the impeller.

Eckardt (1979) used the Laser-2-Focus method to obtain

Contributed by the International Gas Turbine Institute and presented at the 36th International Gas Turbine and Aeroengine Congress and Exposition, Orlando, Florida, June 3-6, 1991. Manuscript received at ASME Headquarters February 12, 1991. Paper No. 91-GT-70. Associate Editor: L. A. Riekert.

data in radially bladed and backward swept bladed centrifugal compressors. In both cases the impellers discharged into diffusers that did not distort the impeller flow. Results showed that the velocity profile in the backward swept impeller was not as prone to separation and was more uniform at the exit.

Adler and Levy (1979) and Howard et al. (1980) used a laser-Doppler velocimeter to measure the flow in shrouded, backswept impellers. In both studies the discharge was designed not to distort the flow within the impeller. The backswept impellers showed no evidence of separation.

Moore and Moore (1981) measured and predicted the losses in total pressure in an impeller (no volute) with radial exit blades. Strong secondary flows were noted and strongly nonuniform exit conditions were found. The loss was found to increase with radius.

Thomas et al. (1986) used laser velocimetry (LV) to measure the velocities within the logarithmic spiral volute of a laboratory centrifugal pump. Flows of 121 and 160 percent of design were simulated. In both cases the circumferential distribution of radial flow was nonuniform.

Mizuki et al. (1971) and Murakami et al. (1980) measured pressures and velocities within passages of centrifugal impellers with radial blades operating in volutes. However, circumferential variations were not measured.

Kannemans (1980) used a laser-Doppler velocimeter to measure the velocity field in a radial impeller operating in a volute. Data were collected in the impeller and just outside the impeller, for only one circumferential position.

Howard et al. (1987) tested three laboratory pumps. One was a single volute and the others were double volute/single discharge. They noted the effects of volute on the developed head, local pressures, and flow fields in the impeller and volute.

Hamkins and Flack (1987) and Miner et al. (1989) used a two-directional laser velocimeter to measure the velocities within unshrouded and shrouded pump impellers with backward swept blades. Impellers were concentrically operated in a logarithmic spiral volute. Data were also taken outside the impeller exit. Results showed that the flow was asymmetric around the volute, even at design flow. The asymmetries worsened as the flow rate differed from the design flow. However, Miner et al. (1992) found excellent agreement between experimental blade-to-blade profiles and an inviscid prediction of velocity profiles near the impeller exit.

More recently, Beaudoin et al. (1992) measured the average velocities in the four passages for an orbiting impeller. Such orbits can result from interactions between the fluid dynamics of the impeller/volute and shaft dynamics, a bowed shaft, an unbalance in the impeller or a pump bearing instability. Large controlled orbits were used so that the effects of impeller orbit were measurable in the impeller and volute flow field. The objective of this effort was to obtain data so that the details of unsteady predictive methods for impeller loads could be verified. They found that the velocities (and thus flow rates) were significantly different in the different passages due to the orbit. They related the momentum flux variations to induced radial forces.

Chamieh et al. (1982) and Jery et al. (1985) developed a facility and expanded the data base of impeller forces in volute pumps. Testing was conducted by systematically varying orbit/pump speed ratio, pump speed, and flow coefficient in several impeller/volute combinations. The time-averaged force on the impeller was determined; however, details of the flow field were not measured.

As summarized by the work listed here, in all but two of the previous flow field studies, orbiting impellers were not used. Thus, the only unsteady components of the flow were due to "blade passing" and off-design conditions. Turbulence measurements have not been published. The previous work has clearly demonstrated that the asymmetries found in impeller flows are due to the interaction between the impeller and volute at all flow rates. Therefore, in order to understand better the flow in centrifugal pumps, the impeller and volute must be considered together.

In general the exit conditions of backward swept blades are better behaved than those for radial exit blades; less separation has been found for backward swept blades. Turbulence data are not available for correlation with pressure loss data for backward swept blades. The present effort is intended to provide turbulence information for both orbiting and nonorbiting impellers and to identify regions of high turbulence intensity and cross product Reynolds stresses, where losses occur. The present work also seeks to bridge the two pump components by providing turbulence measurements in both the impeller and volute for the same operating conditions and identify systematic variations in the turbulence field due to an impeller orbit and due to flow rate changes. The data can be used for verification of ongoing computational predictions of internal flows. The data presented are intended to complement the average velocity data directly generated by a nonorbiting impeller (Miner et al., 1989) and an orbiting impeller (Beaudoin et al., 1992).

The particular objectives of the present work were to make detailed velocity turbulence measurements with a two-directional LV in both the volute and impeller of a centrifugal pump, first with a centered impeller and second with a synchronously orbiting impeller. On-design and off-design flow conditions were studied. Blade-to-blade profiles were measured for radial, tangential, and cross Reynolds stresses. These were obtained at different circumferential positions around the pump.

Experimental Apparatus

Pump. The pump used for this study is documented by Hamkins and Flack (1987) and Miner et al. (1989). The flow width (b) is 24.6 mm and the impeller peripheral radius is 101.6 mm. The dimensionless specific speed ($\omega Q^{0.50}/(gH)^{0.75}$)

Nomenclature

a = general direction
b = passage width
$\overline{C_r}$ = absolute radial velocity
$\overline{C_r'^2}$ = radial Reynolds stress
$\overline{C_r' W_\theta'}$ = radial/tangential cross Reynolds stress
g = gravitational constant
H = developed head
Q = flow rate
Q_n = design flow rate

r = radius
r_2 = outer impeller radius
r_o = particle path curvature
R_w = volute radius
TI = Turbulence Intensity = $\sqrt{(\overline{C_r'^2} + \overline{W_\theta'^2})/2} / \sqrt{W_\theta^2 + C_r^2}$
U_2 = impeller peripheral speed
V = total particle velocity

$\overline{W_\theta}$ = relative (to impeller) tangential velocity
$\overline{W_\theta'^2}$ = tangential Reynolds stress
x = horizontal direction
y = vertical direction
z = axial position from centerline
ϵ = orbit eccentricity
θ = circumferential position
ν = kinematic viscosity
ω = rotational speed
Ω = orbit speed

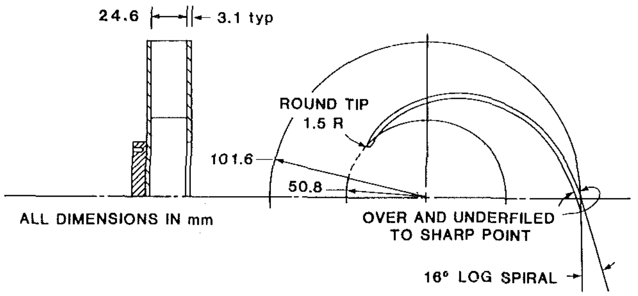

Fig. 1 Impeller geometry

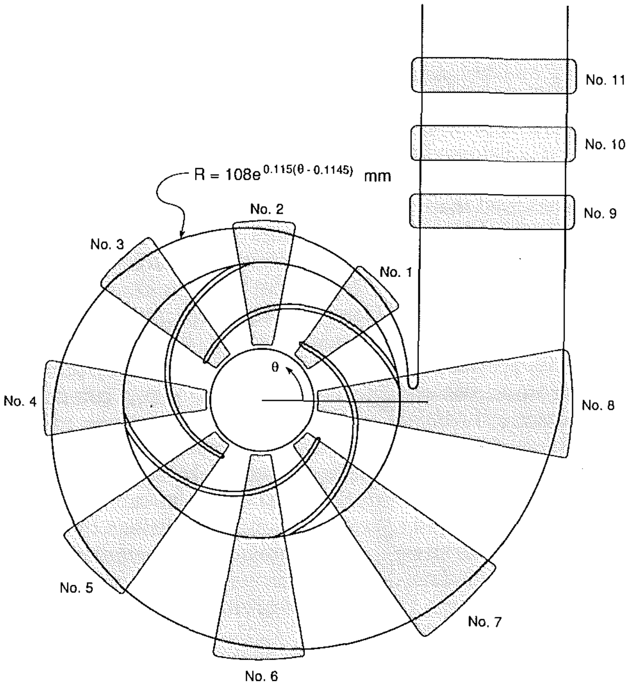

Fig. 2 Volute and window locations

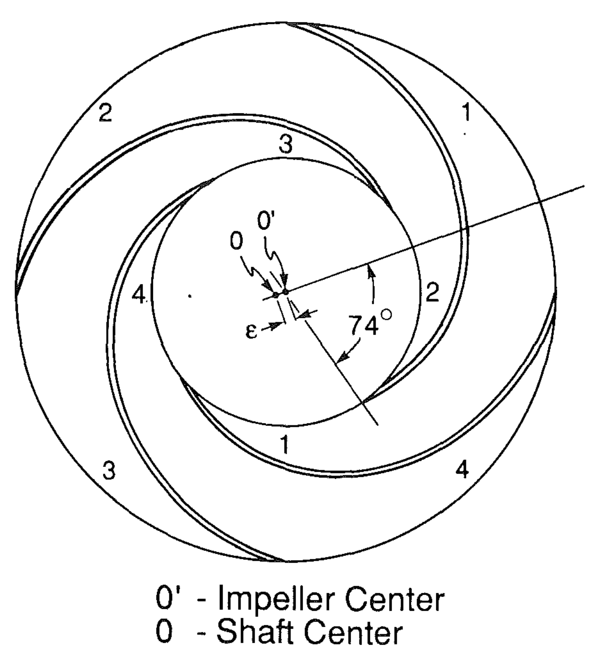

Fig. 3 Impeller eccentricity orientation and passage definition

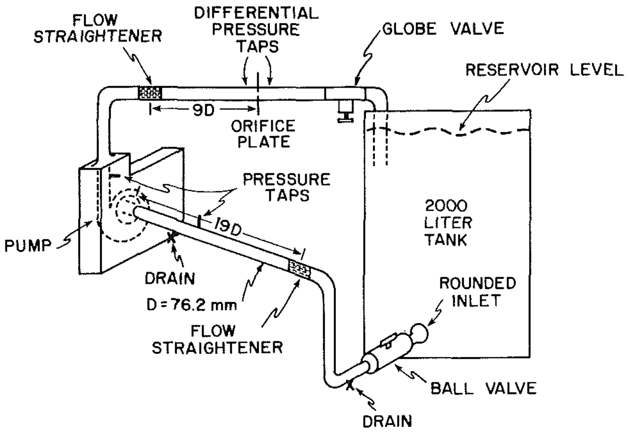

Fig. 4 Flow loop

of the pump is 0.60 (1583 US units), which corresponds to a dimensionless design flow coefficient ($Q/(2\pi r_2 b U_2)$) of 0.063. The Reynolds number ($C_{r2}R_2/\nu$) at design conditions is 4.0×10^4. Figures 1 and 2 depict the impeller and volute geometry. The impeller is a four-bladed geometry with 16 deg logarithmic spiral blades and the volute is also a logarithmic spiral with an 83 deg angle. Window locations for the laser velocimeter measurements are shown in Fig. 2. The pump is constructed of Plexiglas and the casing walls are 50.8 mm thick. However, in the windows the thickness is reduced to 9.5 mm, to facilitate the use of the laser velocimeter.

For the present work the impeller was allowed to orbit. This was accomplished by offsetting the impeller center from the shaft center. Thus, the impeller orbited with the synchronous frequency ($\Omega/\omega = 1$). The orbit size was $\epsilon/r_2 = 0.016$ and the angular orientation of the impeller center to shaft center relative to a blade leading edge is shown in Fig. 3. In choosing the orbit amplitude, it was large enough so that the synchronous velocity variations were measurable but small enough so that the tongue clearance did not change appreciably. Similar orbit sizes were used by Jery et al. (1985). The passage definitions (1–4) are also shown in Fig. 3.

The flow loop is shown in Fig. 4. This is a closed-loop system fed from a 2000 liter reservoir tank. The flow straightener in the 76.2-mm-dia pipe upstream of the pump inlet provides a swirl free inlet flow to the pump. Static pressure taps are located 5 pipe diameters upstream of the impeller inlet and just beyond window 11 in the discharge. Yaw probe traverses in the inlet pipe indicated that the flow was swirl free three diameters upstream of the pump at shut-off conditions for both orbiting and nonorbiting impellers. The second flow straightener, 9 pipe diameters upstream of the orifice flow meter, conditions the flow for the orifice plate. The globe valve is used to adjust the flow. The running speed for the pump is 620 rpm, yielding a tip velocity (U_2) of 6.60 m/s. Figure 5 shows the head-capacity curve both for the concentric operation and orbiting impeller. The design point for the present pump design is 6.3 l/s at 0.178×10^5 N/m^2. This design point is based on an estimate of the impeller-volute matching point. The matching point is the condition that causes the average angular momentum of the flow at the impeller exit to equal the average angular momentum in the throat of the volute.

Laser Velocimeter. The laser and optics for this system are shown in Fig. 6. The system is three-beam frequency shifted, operated in the forward scatter mode. The Bragg cell performs the dual functions of beam separation and frequency shifting. A single primary beam enters the cell and the primary beam and an orthogonal grid of secondary beams emerge. However, only three of the beams are used, the primary beam and two secondary beams. The secondary beams are shifted by different frequencies. These three beams form a 90 deg angle. Therefore, when the beams are focused and crossed at the probe volume, two sets of perpendicular interference fringes are created. These

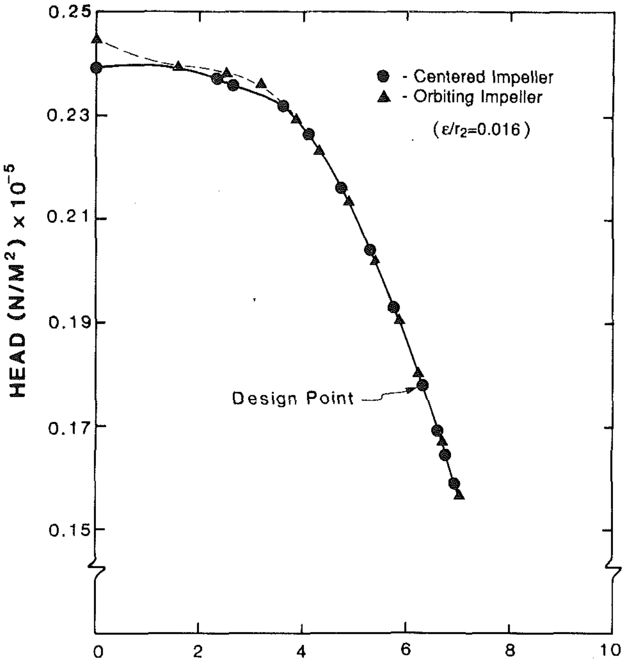

Fig. 5 Pump head: capacity curves

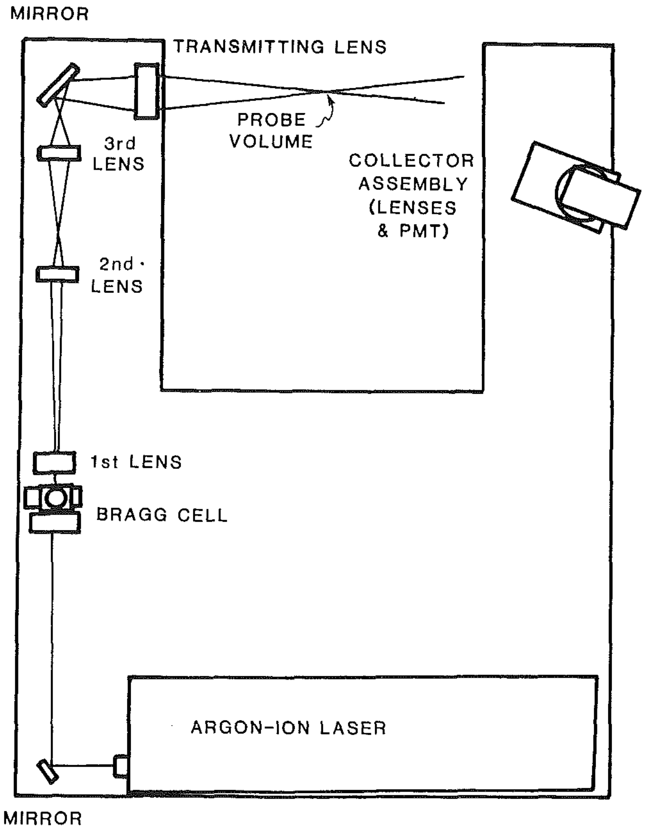

Fig. 6 LV system

two sets of fringes allow the simultaneous measurement of two orthogonal components of velocity. The entire optical system was mounted on a three-directional traversing mechanism with digital position readouts. The probe volume was easily and accurately moved in the *x*, *y*, and *z* directions with this mechanism.

The frequency of light scattered from the probe volume determines the velocity. Light was scattered by naturally occurring particles in the water. The water was filtered, using a taste and odor filter. This provided particles of 5 μm and smaller. Two burst-type signal processors with adjustable threshold and five/eight count comparison with adjustable tolerances were used. Signals from both sets of beams were checked for coincidence. If the two signals occurred within 5 μs, then they were considered valid.

Once a valid LV signal was generated, the impeller angular position was recorded with a shaft encoder. The encoder divided each revolution into 256 parts. The two velocity signals and the shaft position were simultaneously recorded onto floppy disks by a dedicated microcomputer. Thus, for a given position in the rotating impeller, obtaining data was only possible once per revolution. As a result, obtaining temporal data of the fluctuations at a given point in the rotating frame was not possible. However, by obtaining enough samples at each point in the rotating frame, the measurement of $\overline{C_r'^2}$, $\overline{W_\theta'^2}$, and $\overline{C_r' W_\theta'}$ was possible. A typical test had 5000 data points, approximately 20 per each of the 256 "shaft angle bins." This gave detailed two-dimensional velocity and angular position data for the four-blade passages. After the tests were completed, blade-to-blade profiles were assembled by grouping the blade passage data into twelve angular regions. Thus, for the orbiting impeller tests, each region contained approximately 100 individual data points. When passage data were combined for the nonorbiting tests, each region contained approximately 400 points. Also, after this grouping was completed, fourth-order polynomial curves were fit through the data, which are presented in the following section.

Independent studies indicate that if one curve fits coherent smooth data, one obtains an uncertainty at any point on the fitted curve of approximately only 1/3 or less of the uncertainty of any of the individual data points. Briefly, a comprehensive series of computer experiments were run by the authors. For these tests individual points on curves of known shapes (linear, second order, etc.) were randomly perturbed by fixed uncertainties. Least-square curve fits were then performed on these individual points. By comparing points on the approximate curves and the true curves, the uncertainties of the fitted curves were found. Thus, for the uncertainty analysis, curve fitting had the effect of increasing the effective number of individual data points.

Uncertainty. The uncertainty in probe volume position was 0.5 mm radially and 1 mm axially. The uncertainty in the angular position was 0.30 deg. The uncertainty in the angular orientation of the probe volume fringes with respect to the reference axes was 0.85 deg. This was the dominant factor in flow direction uncertainty. The typical uncertainty in the radial velocity component was 0.04 m/s and the typical uncertainty in the tangential velocity component was also 0.04 m/s. In dimensionless form (using U_2) these are 0.0061 and 0.0061, respectively. Typical uncertainties in the radial Reynolds stress, tangential Reynolds stress and cross Reynolds stress were 0.004, 0.004, and 0.006 m^2/s^2, respectively. In dimensionless form (using U_2^2) these are 0.00009, 0.00009, and 0.00014, respectively. These velocity uncertainties did not include the effect of positional uncertainty in the presence of velocity gradients. The position of the probe volume was uncertain, particularly in the axial direction. Since spatial velocity gradients were present, a misplaced probe volume would measure the incorrect velocity. This spatial uncertainty resulted in a total uncertainty of 0.10 m/s for the radial velocity and 0.10 m/s for the tangential velocity. The total uncertainties in the radial Reynolds stress, tangential Reynolds stress, and cross Reynolds stress were 0.006, 0.006, and 0.008 m^2/s^2, respectively. In dimen-

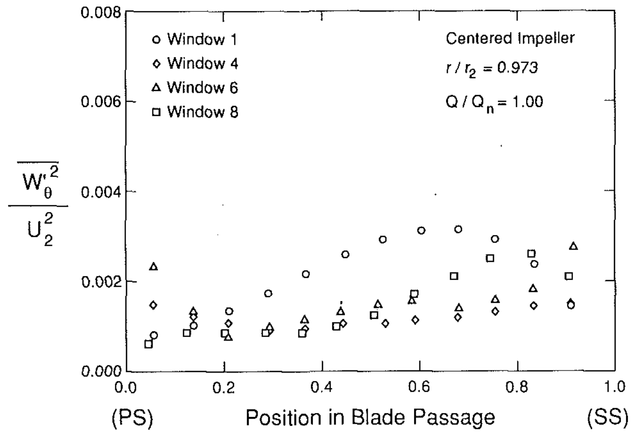

Fig. 7 Tangential Reynolds stress profiles—centered impeller (windows 1, 4, 6, 8; r/r_2 = 0.973; Q/Q_n = 1.00)

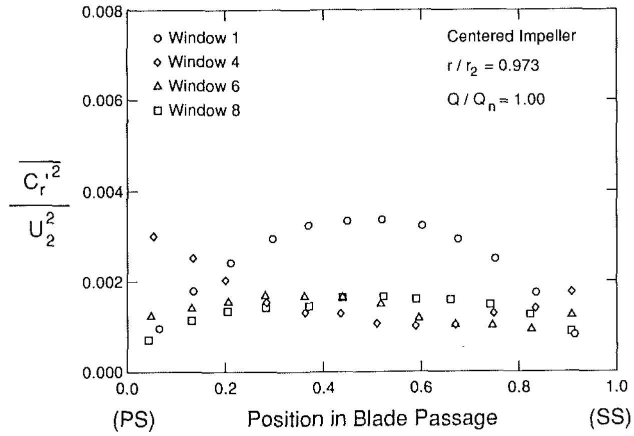

Fig. 8 Radial Reynolds stress profiles—centered impeller (windows 1, 4, 6, 8; r/r_2 = 0.973; Q/Q_n = 1.00)

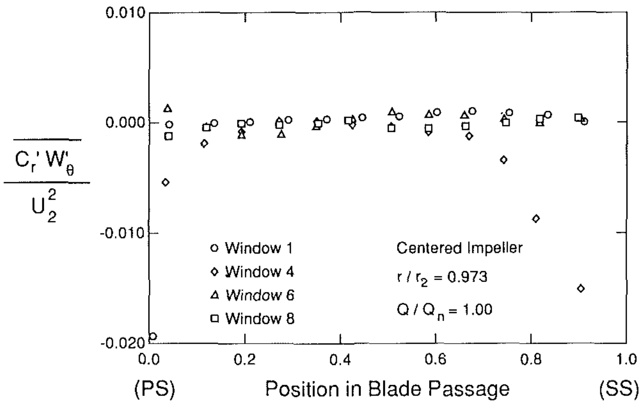

Fig. 9 Coupled Reynolds stress profiles—centered impeller (windows 1, 4, 6, 8; r/r_2 = 0.973; Q/Q_n = 1.00)

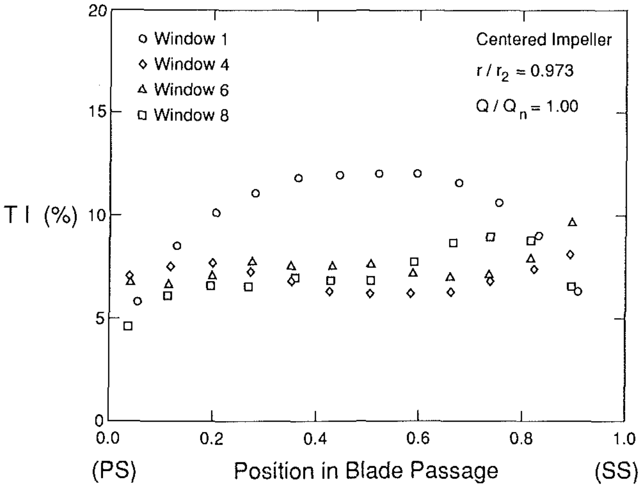

Fig. 10 Turbulence intensity profiles—centered impeller (windows 1, 4, 6, 8; r/r_2 = 0.973; Q/Q_n = 1.00)

sionless form these are 0.00014, 0.00014, and 0.00018, respectively.

When examining the differences between the four different blade-to-blade profiles for the orbiting impeller data, only the effect of random uncertainty has to be considered. For these cases the data were recorded without moving the probe volume and thus data were acquired for exactly the same probe volute location. The uncertainty due to the axial gradient, however, must be considered when comparing the profiles for the centered and orbiting impeller passages, since these data were recorded at different times, and the probe volume location was not exactly the same for the two sets of data (due to positional uncertainty).

Results

Experimental data for this study were taken in windows 1, 4, 6, and 8. For each window, data were taken at four radial positions within the impeller. Volute data in window 1 were taken at only one radial position; data at four radial volute positions were measured in the other three windows. These data were taken at the axial centerline of the pump at the design flow of 6.3 l/s. In addition, data for five flow rates were taken in window 6 at the axial centerline. Representative results for Reynolds stresses are presented here and are nondimensionalized by the square of the impeller tip velocity. Data at other axial locations were taken but are not presented herein for the sake of brevity. As indicated earlier, results are presented in the form of fourth-order polynomial least-squares curve fits to the average turbulence data profiles. The symbols are used as a means of identifying the curves and represent grouped data. In general, data are presented for the case of the centered impeller and for the four different passages and compared to the nonorbiting impeller data. The four passages were averaged for the centered impeller data.

Circumferential Variations—Centered Impeller. In Figs. 7–10 the blade-to-blade variations of tangential Reynolds stress, radial Reynolds stress, coupled Reynolds stress, and local turbulence intensity are presented for r/r_2 = 0.973 (near the impeller o.d.) at the design flow rate and for all four windows. As can be seen in Figs. 7, 8, and 10, the turbulence tends to be highest in window 1, particularly near the center of the blade passage. This is probably due to an interaction of the flow in the impeller with the tongue. Also, Fig. 9 indicates that the turbulence is nearly isotropic, since the coupled Reynolds stress is nearly zero, except near the blades.

Next, in Fig. 11 the blade-to-blade variation of turbulence intensity is presented for r/r_2 = 0.625 (near the impeller eye) at the design flow rate and for all four windows. From this figure it is apparent that for a blade-to-blade profile the highest turbulence intensities occur near the pressure surface. The average velocities at the same locations (Miner et al., 1989) are zero or near zero indicating, a separated area. Thus, one would expect a large turbulence intensity in these regions.

Radial Variations—Centered Impeller. The variation of

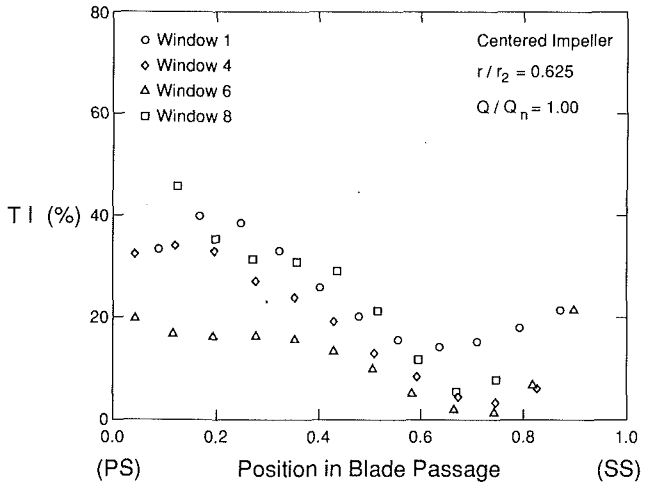

Fig. 11 **Turbulence intensity profiles—centered impeller (windows 1, 4, 6, 8; r/r_2 = 0.625; Q/Q_n = 1.00)**

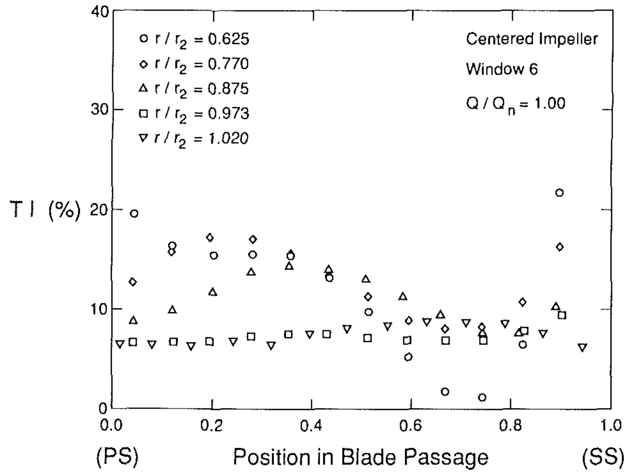

Fig. 12 **Turbulence intensity profiles—centered impeller (window 6; r/r_2 = 0.625, 0.770, 0.875, 0.973, 1.028; Q/Q_n = 1.00)**

turbulence intensity in window 6 at the design flow rate is shown as a function of radius in Fig. 12. The maximum turbulence is seen to move from the pressure surface and diminish as the radius is increased. For example, the turbulence intensity near the pressure surface at the smallest radius (r/r_2 = 0.625) is approximately 20 percent but decreases to 1 percent at 75 percent span before increasing again very near the suction surface. For r/r_2 = 0.875 the peak is close to midchannel and is at 15 percent. Finally, near the impeller exit (both inside and outside of the impeller) the turbulence profile is nearly uniform and at only 8 percent. The abrupt 90 deg turn the flow must make from the inlet pipe to the impeller passages contributes to the higher turbulence levels. Average velocity data at r/r_2 = 0.625 (Miner et al., 1989) shows the radial velocity highly skewed toward the back face of the impeller. In addition, the average velocity data indicated the presence of a separation zone on the front face of the impeller. As the radius increases both the skewing and the separation subside. This is consistent with the higher levels of turbulence at the inner radii. Furthermore, Miner et al. (1989) showed uniform average velocity profiles near the exit and Miner et al. (1992) showed that these profiles matched a potential solution very well. Such well-behaved profiles and absence of the jet-wake profile are indicative of small losses in impellers with backward swept blades.

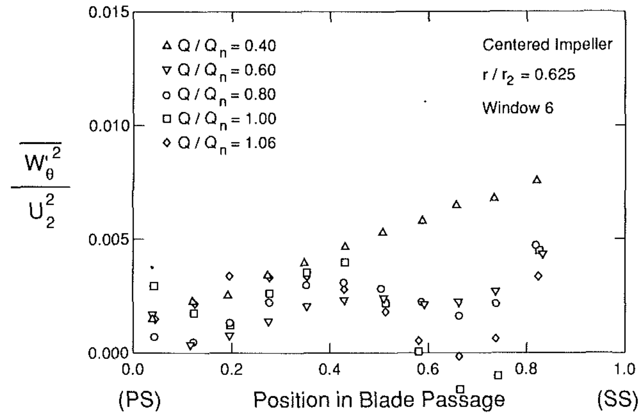

Fig. 13 **Tangential Reynolds stress profiles—centered impeller (window 6; r/r_2 = 0.625; Q/Q_n = 0.40, 0.60, 0.80, 1.00, 1.06)**

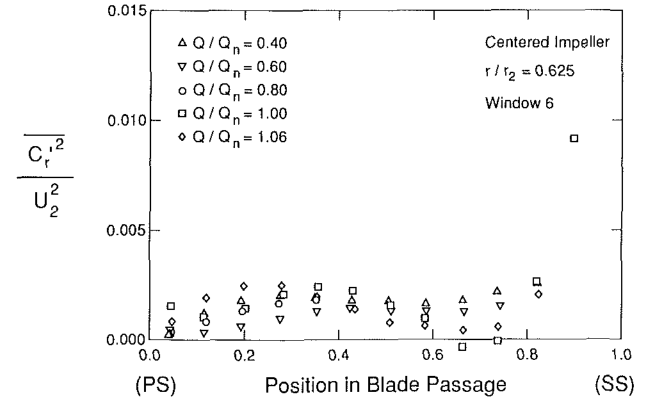

Fig. 14 **Radial Reynolds stress profiles—centered impeller (window 6; r/r_2 = 0.625; Q/Q_n = 0.40, 0.60, 0.80, 1.00, 1.06)**

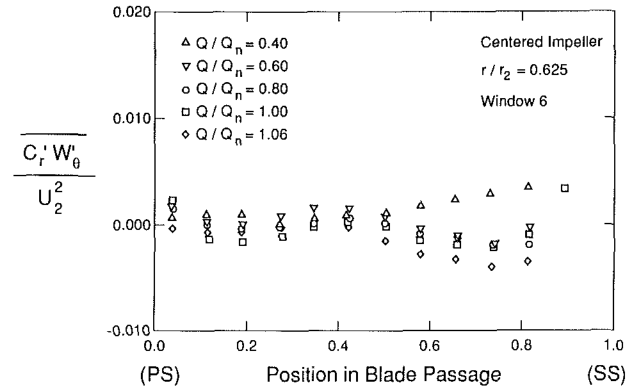

Fig. 15 **Coupled Reynolds stress profiles—centered impeller (window 6; r/r_2 = 0.625; Q/Q_n = 0.40, 0.60, 0.80, 1.00, 1.06)**

Flow Rate Variations—Centered Impeller. In Figs. 13-16 all four profiles are presented for window 6 and r/r_2 = 0.625 for five flow rates. As indicated above, at the design flow rate the turbulence intensity at the pressure surface is 21 percent but decreases to 7 percent at 75 percent span. However, at low flow rates the actual fluctuation levels, as well as intensity levels, are highest near the suction surface. For example, at 40 percent flow the turbulence intensity is 10 percent at the pressure surface and increases to 26 percent at 81 percent span. The average velocity data (Miner et al., 1989) indicate a recirculating flow within the blade passage at 40 percent of design flow, with inward flow along the suction surface of the blade. This recirculating flow contributes to the higher levels of tur-

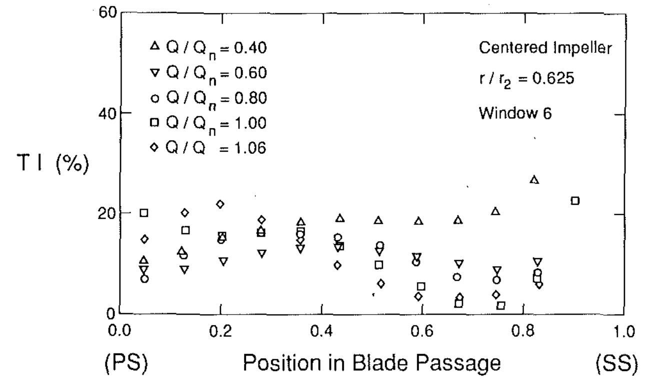

Fig. 16 **Turbulence intensity profiles—centered impeller (window 6; r/r_2 = 0.625; Q/Q_n = 0.40, 0.60, 0.80, 1.00, 1.06)**

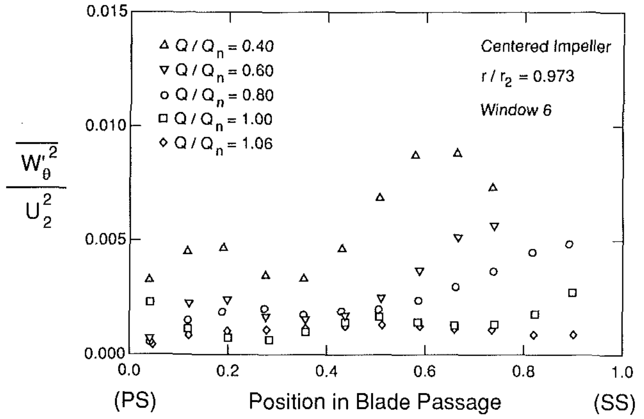

Fig. 17 **Tangential Reynolds stress profiles—centered impeller (window 6; r/r_2 = 0.973; Q/Q_n = 0.40, 0.60, 0.80, 1.00, 1.06)**

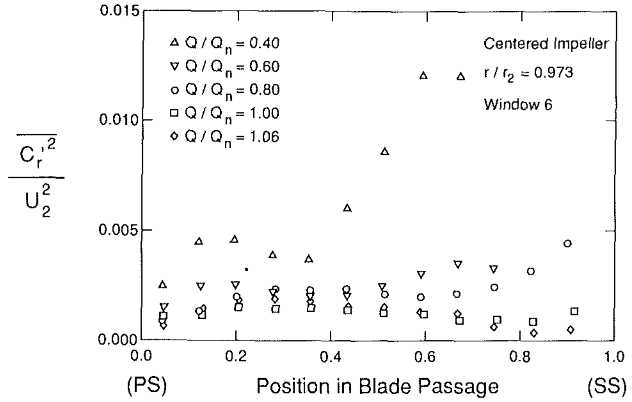

Fig. 18 **Radial Reynolds stress profiles—centered impeller (window 6; r/r_2 = 0.973; Q/Q_n = 0.40, 0.60, 0.80, 1.00, 1.06)**

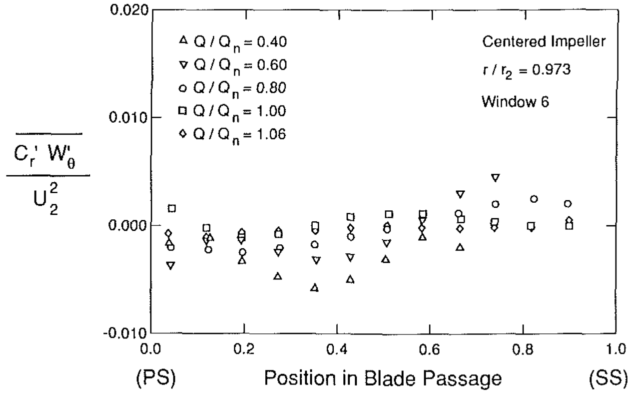

Fig. 19 **Coupled Reynolds stress profiles—centered impeller (window 6; r/r_2 = 0.973; Q/Q_n = 0.40, 0.60, 0.80, 1.00, 1.06)**

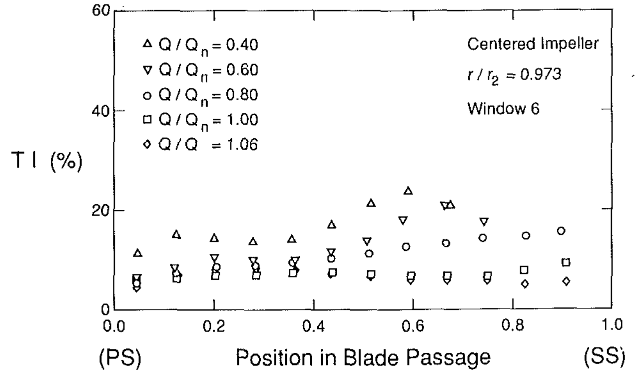

Fig. 20 **Turbulence intensity profiles—centered impeller (window 6; r/r_2 = 0.973; Q/Q_n = 0.40, 0.60, 0.80, 1.00, 1.06)**

bulence. Also, the coupled stresses indicate that the turbulence is not isotropic near the suction surface. Also, $\overline{W_\theta'^2}$ and $\overline{C_r'^2}$ are different near the suction surface indicating nonisotropic turbulence. Furthermore, for low flow rates, the turbulence intensity is higher than for high flow rates. For example, at 40 percent capacity the average turbulence intensity is 18 percent, whereas at 100 percent flow the average turbulence intensity is 9 percent.

All four profiles for window 6 and $r/r_2 = 0.973$ are shown for five flow rates in Figs. 17-20. Once again the highest turbulence intensity is seen for 40 percent flow with an average of 19 percent. For comparison the average intensity for design flow is only 6 percent. For large flow rates the turbulence profiles are uniform. For low flow rates, however, the maximums are seen near the suction surface. Nonisotropic turbulence is once again observed, particularly for low flow rates.

To summarize some of the data Table 1 is presented. In this table the nondimensional mass-averaged blade-to-blade cross product Reynolds stress, which is indicative of the loss, is presented for five flow rates and two radii. As can be seen the absolute value is largest near the impeller exit for low flow rates. However, the trend reverses for high flow rates. At high flow rates the trend is opposite to the loss reported by Moore and Moore (1981). That is, at nominal flow rates they found the largest losses near the exit. However, the data presented by Moore and Moore were for an impeller with radial blades, whereas the current impeller has backswept blades. Moore and Moore also reported a significant variation in average velocities from blade to blade unlike Miner et al. (1989). Thus, although the trends are different, they should be expected because of the impeller design, as discussed previously.

Furthermore, whether or not turbulence levels are decreased (stabilized) or increased (destabilized) is determined by the interaction between the centrifugal forces due to rotation ($r\omega^2$), centrifugal forces due to curvature of the particle path (V^2/r_o), and pressure forces due to pressure gradients ($1/\rho\ dp/da$) acting on a particle of fluid as discussed by Adler (1980). Along the pressure surface for the current impeller, all three of these forces act to destabilize the flow, that is, they are positive away from the blade. This would give rise to the relative increase in turbulence intensity at the pressure surface over the suction surface. Along the suction surface the rotational, curvature, and pressure forces act as restoring forces on the fluid; namely, all are positive toward the blade. This tends to stabilize the flow, which tends to reduce the turbulence intensity. This is clearly demonstrated in Figs. 11 and 12.

The stabilizing or destabilizing effects of the forces due to rotation, curvature, and pressure gradients for the present

Table 1 **Mass-averaged $\overline{C_r' W_\theta'}/U_2^2$ values (window 6)**

Q/Q_n	$r/r_2 = 0.625$	$r/r_2 = 0.973$
0.40	−0.0001	−0.0045
0.60	−0.0009	−0.0028
0.80	−0.0016	−0.0011
1.00	−0.0020	0.0001
1.06	−0.0032	−0.0004

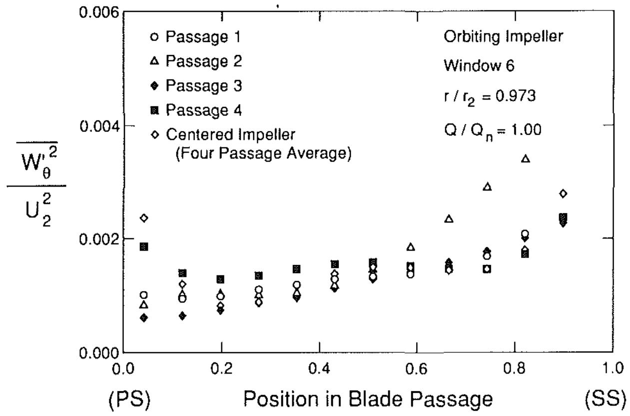

Fig. 21 **Tangential Reynolds stress profiles—orbiting impeller (window 6; $r/r_2 = 0.973$; $Q/Q_n = 1.00$)**

work are consistent with similar effects reported by So and Mellor (1973), and Johnston and Eide (1976). So and Mellor reported on the effects of curvature on turbulent boundary layers. For convex curvature the force due to the pressure gradient points toward the surface, which tends to decrease turbulence levels. The opposite is true to concave surfaces. In the present study the pressure force points away from the convex or pressure surface. Therefore, the pressure force would increase turbulence levels on the pressure surface and decrease them on the suction surface.

Johnston and Eide discussed the effects that rotation has on turbulent boundary layers. Their results showed that turbulence levels were increased when the rotational forces had a component pointing away from the rotating surface. The opposite effect was noted for rotational forces pointing toward the rotating surface. For the present impeller geometry the rotational forces have components that point away from the pressure surface, and point toward the suction surface. As a result, the rotational forces increase turbulence on the pressure surface and decrease turbulence on the suction surface.

Passage Variations—Orbiting Impeller. Typical results for an orbiting impeller are presented in Figs. 21–24. These results are for window 6, $r/r_2 = 0.973$, and design flow. In these figures the blade-to-blade profiles for the four individual passages are shown and compared to the four-passage average for the centered impeller. Significant variations are shown between the four passages. Similar magnitudes of variations were shown in the average velocity profiles (Beaudoin et al., 1992). These four figures indicate that the forced orbit did not increase the random turbulence fluctuations, i.e., fluctuations at frequencies other than the synchronous or blade pass frequency. Namely, the four-blade average turbulence intensity at a given passage span is the same for centered and orbiting impellers. This conclusion is true regardless of measurement location or flow rate.

Second, the highest turbulence was seen near the suction surface of passage 2 and the lowest turbulence was seen near the pressure side of passage 3. This observation was made for

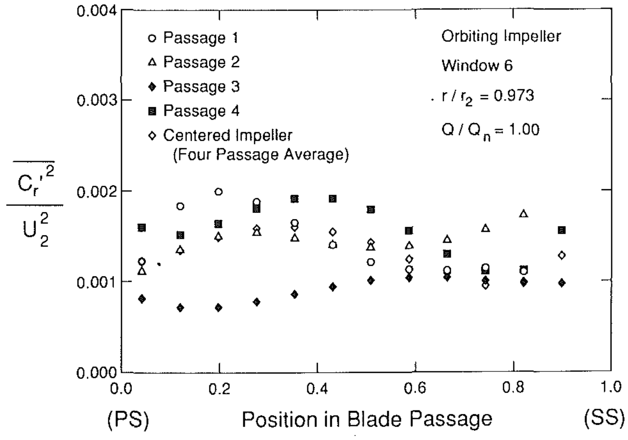

Fig. 22 **Radial Reynolds stress profiles—orbiting impeller (window 6; $r/r_2 = 0.973$; $Q/Q_n = 1.00$)**

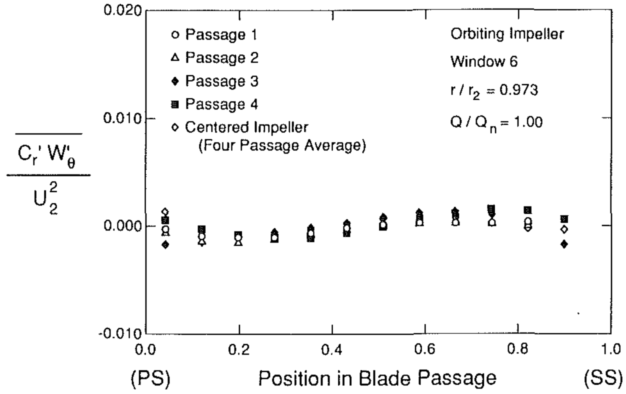

Fig. 23 **Coupled Reynolds stress profiles—orbiting impeller (window 6; $r/r_2 = 0.973$; $Q/Q_n = 1.00$)**

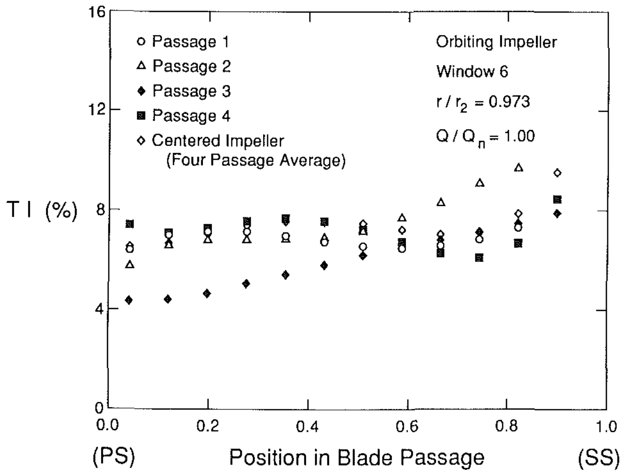

Fig. 24 **Turbulence intensity profiles—orbiting impeller (window 6; $r/r_2 = 0.973$; $Q/Q_n = 1.00$)**

all windows at $r/r_2 = 0.973$. It is important to note that these two areas are 180 deg apart. It is also important to note that the highest turbulence area is in the portion of the blade with the highest negative radial velocity (due to the orbit). Thus, the highest turbulence area coincides with where the impeller is moving away from the volute with the highest velocity. Conversely, the smallest turbulence intensity coincides with where the impeller is moving towards the volute with the highest velocity. At smaller radii in all windows the lowest turbulence occurred near the pressure surface in passage 4 and the highest turbulence occurred near the suction surface in passage 3.

Conclusions

Measurement of turbulence profiles in the backswept impeller of a single volute type pump was made in two pump configurations: (*i*) with the impeller running centered, and (*ii*) with a whirling motion on the impeller, which was induced by offsetting the impeller center from the shaft center. Blade-to-blade turbulence intensity and Reynolds stress profiles were generated as the impeller rotated through an LV probe volume located at various fixed positions in the pump. Comparisons were made both between the individual passage profiles of the orbiting impeller and to the four-passage average profile of the centered impeller. Specific conclusions include:

1 Although the impeller offset affected the turbulence in the different passages, the whirling did not increase the random turbulence. Thus, overall trends for the whirling impeller are the same for the centered impeller, so far as effects of radial position, window location, and flow rate are concerned. Therefore, a synchronous orbit on an impeller should not significantly increase the losses in an impeller as compared to centered operation.

2 For the orbiting impeller at large radii, the highest turbulence was seen for the impeller portion that was moving away from the volute with the highest velocity. On the other hand the lowest turbulence was seen for the impeller area that was moving toward the volute with the greatest velocity.

3 Near the impeller periphery the highest turbulence was seen in the tongue region.

4 For small radii at the design flow rate, the largest turbulence levels were seen near the pressure surface due to separation, and the destabilizing interaction of pressure and centrifugal forces.

5 The largest turbulence intensities were seen for small radii.

6 The turbulence intensity profiles were more uniform at large radii than for small radii, as were the average velocity profiles.

7 The turbulence intensity level increased as the flow rate decreased from the design condition.

8 The largest mass-averaged cross product Reynolds stress at low flow rates was near the exit; however, at high flow rates the lowest value was observed at the impeller exit. This observation was consistent with uniformity of average velocity profiles.

Acknowledgments

This research was sponsored by the Rotating Machinery and Controls (ROMAC) Industrial Research Program at the University of Virginia.

References

Acosta, A. J., 1954, "An Experimental and Theoretical Investigation of Two-Dimensional Centrifugal Pump Impellers," *Trans. ASME*, Vol. 76, No. 3, pp. 749-763.

Acosta, A. J., and Bowerman, R. D., 1957, "An Experimental Study of Centrifugal Pump Impellers," *Trans. ASME*, Vol. 79, pp. 1821-1839.

Adler, D., and Levy, Y., 1979, "A Laser-Doppler Investigation of the Flow Inside a Backswept, Closed, Centrifugal Impeller," *Journal of Mechanical Engineering Science*, Vol. 21, No. 1, pp. 1-6.

Adler, D., 1980, "Status of Centrifugal Impeller Internal Aerodynamics, Part II, Experiments and Influence of Viscosity," ASME *Journal of Engineering for Power*, Vol. 102, No. 3, pp. 738-746.

Beaudoin, R. J., Miner, S. M., and Flack, R. D., 1992, "Laser Velocimeter Measurements in a Centrifugal Pump With a Synchronously Orbiting Impeller," ASME JOURNAL OF TURBOMACHINERY, Vol. 114, this issue.

Beveridge, J. H., and Morelli, D. A., 1950, "Evaluation of a Two Dimensional Centrifugal Pump Impeller," ASME Paper No. 50-A-147.

Binder, R. C., and Knapp, R. T., 1936, "Experimental Determination of the Flow Characteristics in the Volutes of Centrifugal Pumps," *Trans. ASME*, Vol. 58, pp. 649-661.

Bowerman, R. D., and Acosta, A. J., 1957, "Effect of the Volute on Performance of a Centrifugal Pump Impeller," *Trans. ASME*, Vol. 79, No. 5, pp. 1057-1069.

Chamieh, D. S., Acosta, A. J., Brennen, C. E., Caughy, T. K., and Franf, R., 1982, "Experimental Measurements of Hydrodynamic Stiffness Matrices for a Centrifugal Pump Impeller," Workshop on Rotordynamic Instability Problems in High-Speed Turbomachinery, Texas A&M University, NASA CP 2250, May, pp. 382-398.

Eckardt, D., 1979, "Flow Field Analysis of Radial and Backswept Centrifugal Compressor Impellers, Part 1: Flow Measurements Using a Laser Velocimeter," *Performance Prediction of Centrifugal Pumps and Compressors*, ASME, New York, pp. 77-86.

Fischer, K., and Thoma, D., 1932, "Investigation of the Flow Conditions in a Centrifugal Pump," *Trans. ASME*, Vol. 54, HYD-54-8.

Hamkins, C. P., and Flack, R. D., 1987, "Laser Velocimeter Measurements in Shrouded and Unshrouded Radial Flow Pump Impellers," ASME JOURNAL OF TURBOMACHINERY, Vol. 109, No. 1, pp. 70-76.

Hira, D. S., and Vasandani, V. P., 1975, "Influence of Volute Tongue Length and Angle on the Pump Performance," *Journal of the Institute of Engineers India*, Part M.E., No. 56, pp. 55-59.

Howard, J. H. G., and Kittmer, C. W., 1975, "Measured Passage Velocities in a Radial Impeller With Shrouded and Unshrouded Configurations," ASME *Journal of Engineering for Power*, Vol. 97, No. 2, pp. 207-213.

Howard, J. H. G., Mukker, O. S., and Naoem, T., 1980, "Laser Doppler Measurements in a Radial Pump Impeller," *Measurement Methods in Rotating Components of Turbomachinery*, ASME, New York, pp. 133-138.

Howard, J. H. G., Abramian, M., and Hermann, P., 1987, "Experimental Investigation of Impeller and Volute Flow Fields for a Low Specific Speed Pump With Single and Double Volutes," *Proceedings of the 1987 ASME/JSME Thermal Engineering Joint Conference*, Vol. 2, pp. 51-61.

Iversen, H. W., Rolling, R. E., and Carlson, J. J., 1960, "Volute Pressure Distribution, Radial Force on the Impeller and Volute Mixing Losses of a Radial Flow Centrifugal Pump," ASME *Journal of Engineering for Power*, Vol. 82, No. 2, pp. 136-144.

Jery, B., Brennen, C. E., Caughy, T. K., and Acosta, A., 1985, "Forces on Centrifugal Pump Impellers," *Proceedings of the Second International Pump Symposium*, Texas A&M University, College Station, TX, pp. 21-29.

Johnston, J. P., and Eide, S. A., 1976, "Turbulent Boundary Layers on Centrifugal Compressor Blades: Prediction of the Effects of Surface Curvature and Rotation," ASME *Journal of Fluids Engineering*, Vol. 98, pp. 374-381.

Kannemans, H., 1980, "Radial Pump Impeller Measurements Using a Laser Doppler Velocimeter," ASME Paper No. 80-GT-94.

Miner, S. M., Beaudoin, R. J., and Flack, R. D., 1989, "Laser Velocimetry Measurements in a Centrifugal Flow Pump," ASME JOURNAL OF TURBOMACHINERY, Vol. 111, No. 3, pp. 205-212.

Miner, S. M., Flack, R. D., and Allaire, P. E., 1992, "Two-Dimensional Flow Analysis of a Laboratory Centrifugal Pump," ASME JOURNAL OF TURBOMACHINERY, Vol. 114, this issue, pp. 333-339.

Mizuki, S., Sakai, T., and Watanabe, I., 1971, "A Study of the Flow Pattern Within the Centrifugal and Mixed-Flow Impellers," ASME Paper No. 71-GT-41.

Moore, J., and Moore, J. G., 1981, "Calculations of Three-Dimensional Viscous Flow and Wake Development in a Centrifugal Impeller," ASME *Journal of Engineering for Power*, Vol. 103, No. 2, pp. 367-372.

Murakami, M., Kikuyama, K., and Asakura, E., 1980, "Velocity and Pressure Distributions in the Impeller Passages of Centrifugal Pumps," ASME *Journal of Fluids Engineering*, Vol. 102, No. 4, pp. 420-426.

So, R. D., and Mellor, G. L., 1973, "Experiment on Convex Curvature Effects in Turbulent Boundary Layers," *Journal of Fluid Mechanics*, Vol. 60, pp. 43-62.

Thomas, R. N., Kostrzewsky, G. J., and Flack, R. D., 1986, "Velocity Measurements in a Pump Volute With a Non-Rotating Impeller," *Int. J. Heat and Fluid Flow*, Vol. 7, No. 1, pp. 11-20.

Conclusions

Measurement of turbulence profiles in the backswept impeller of a single volute type pump was made in two pump configurations: (*i*) with the impeller running centered, and (*ii*) with a whirling motion on the impeller, which was induced by offsetting the impeller center from the shaft center. Blade-to-blade turbulence intensity and Reynolds stress profiles were generated as the impeller rotated through an LV probe volume located at various fixed positions in the pump. Comparisons were made both between the individual passage profiles of the orbiting impeller and to the four-passage average profile of the centered impeller. Specific conclusions include:

1 Although the impeller offset affected the turbulence in the different passages, the whirling did not increase the random turbulence. Thus, overall trends for the whirling impeller are the same for the centered impeller, so far as effects of radial position, window location, and flow rate are concerned. Therefore, a synchronous orbit on an impeller should not significantly increase the losses in an impeller as compared to centered operation.

2 For the orbiting impeller at large radii, the highest turbulence was seen for the impeller portion that was moving away from the volute with the highest velocity. On the other hand the lowest turbulence was seen for the impeller area that was moving toward the volute with the greatest velocity.

3 Near the impeller periphery the highest turbulence was seen in the tongue region.

4 For small radii at the design flow rate, the largest turbulence levels were seen near the pressure surface due to separation, and the destabilizing interaction of pressure and centrifugal forces.

5 The largest turbulence intensities were seen for small radii.

6 The turbulence intensity profiles were more uniform at large radii than for small radii, as were the average velocity profiles.

7 The turbulence intensity level increased as the flow rate decreased from the design condition.

8 The largest mass-averaged cross product Reynolds stress at low flow rates was near the exit; however, at high flow rates the lowest value was observed at the impeller exit. This observation was consistent with uniformity of average velocity profiles.

Acknowledgments

This research was sponsored by the Rotating Machinery and Controls (ROMAC) Industrial Research Program at the University of Virginia.

References

Acosta, A. J., 1954, "An Experimental and Theoretical Investigation of Two-Dimensional Centrifugal Pump Impellers," *Trans. ASME*, Vol. 76, No. 3, pp. 749–763.

Acosta, A. J., and Bowerman, R. D., 1957, "An Experimental Study of Centrifugal Pump Impellers," *Trans. ASME*, Vol. 79, pp. 1821–1839.

Adler, D., and Levy, Y., 1979, "A Laser-Doppler Investigation of the Flow Inside a Backswept, Closed, Centrifugal Impeller," *Journal of Mechanical Engineering Science*, Vol. 21, No. 1, pp. 1–6.

Adler, D., 1980, "Status of Centrifugal Impeller Internal Aerodynamics, Part II, Experiments and Influence of Viscosity," ASME *Journal of Engineering for Power*, Vol. 102, No. 3, pp. 738–746.

Beaudoin, R. J., Miner, S. M., and Flack, R. D., 1992, "Laser Velocimeter Measurements in a Centrifugal Pump With a Synchronously Orbiting Impeller," ASME JOURNAL OF TURBOMACHINERY, Vol. 114, this issue.

Beveridge, J. H., and Morelli, D. A., 1950, "Evaluation of a Two Dimensional Centrifugal Pump Impeller," ASME Paper No. 50-A-147.

Binder, R. C., and Knapp, R. T., 1936, "Experimental Determination of the Flow Characteristics in the Volutes of Centrifugal Pumps," *Trans. ASME*, Vol. 58, pp. 649–661.

Bowerman, R. D., and Acosta, A. J., 1957, "Effect of the Volute on Performance of a Centrifugal Pump Impeller," *Trans. ASME*, Vol. 79, No. 5, pp. 1057–1069.

Chamieh, D. S., Acosta, A. J., Brennen, C. E., Caughy, T. K., and Franf, R., 1982, "Experimental Measurements of Hydrodynamic Stiffness Matrices for a Centrifugal Pump Impeller," Workshop on Rotordynamic Instability Problems in High-Speed Turbomachinery, Texas A&M University, NASA CP 2250, May, pp. 382–398.

Eckardt, D., 1979, "Flow Field Analysis of Radial and Backswept Centrifugal Compressor Impellers, Part 1: Flow Measurements Using a Laser Velocimeter," *Performance Prediction of Centrifugal Pumps and Compressors*, ASME, New York, pp. 77–86.

Fischer, K., and Thoma, D., 1932, "Investigation of the Flow Conditions in a Centrifugal Pump," *Trans. ASME*, Vol. 54, HYD-54-8.

Hamkins, C. P., and Flack, R. D., 1987, "Laser Velocimeter Measurements in Shrouded and Unshrouded Radial Flow Pump Impellers," ASME JOURNAL OF TURBOMACHINERY, Vol. 109, No. 1, pp. 70–76.

Hira, D. S., and Vasandani, V. P., 1975, "Influence of Volute Tongue Length and Angle on the Pump Performance," *Journal of the Institute of Engineers India*, Part M.E., No. 56, pp. 55–59.

Howard, J. H. G., and Kittmer, C. W., 1975, "Measured Passage Velocities in a Radial Impeller With Shrouded and Unshrouded Configurations," ASME *Journal of Engineering for Power*, Vol. 97, No. 2, pp. 207–213.

Howard, J. H. G., Mukker, O. S., and Naoem, T., 1980, "Laser Doppler Measurements in a Radial Pump Impeller," *Measurement Methods in Rotating Components of Turbomachinery*, ASME, New York, pp. 133–138.

Howard, J. H. G., Abramian, M., and Hermann, P., 1987, "Experimental Investigation of Impeller and Volute Flow Fields for a Low Specific Speed Pump With Single and Double Volutes," *Proceedings of the 1987 ASME/JSME Thermal Engineering Joint Conference*, Vol. 2, pp. 51–61.

Iversen, H. W., Rolling, R. E., and Carlson, J. J., 1960, "Volute Pressure Distribution, Radial Force on the Impeller and Volute Mixing Losses of a Radial Flow Centrifugal Pump," ASME *Journal of Engineering for Power*, Vol. 82, No. 2, pp. 136–144.

Jery, B., Brennen, C. E., Caughy, T. K., and Acosta, A., 1985, "Forces on Centrifugal Pump Impellers," *Proceedings of the Second International Pump Symposium*, Texas A&M University, College Station, TX, pp. 21–29.

Johnston, J. P., and Eide, S. A., 1976, "Turbulent Boundary Layers on Centrifugal Compressor Blades: Prediction of the Effects of Surface Curvature and Rotation," ASME *Journal of Fluids Engineering*, Vol. 98, pp. 374–381.

Kannemans, H., 1980, "Radial Pump Impeller Measurements Using a Laser Doppler Velocimeter," ASME Paper No. 80-GT-94.

Miner, S. M., Beaudoin, R. J., and Flack, R. D., 1989, "Laser Velocimetry Measurements in a Centrifugal Flow Pump," ASME JOURNAL OF TURBOMACHINERY, Vol. 111, No. 3, pp. 205–212.

Miner, S. M., Flack, R. D., and Allaire, P. E., 1992, "Two-Dimensional Flow Analysis of a Laboratory Centrifugal Pump," ASME JOURNAL OF TURBOMACHINERY, Vol. 114, this issue, pp. 333–339.

Mizuki, S., Sakai, T., and Watanabe, I., 1971, "A Study of the Flow Pattern Within the Centrifugal and Mixed-Flow Impellers," ASME Paper No. 71-GT-41.

Moore, J., and Moore, J. G., 1981, "Calculations of Three-Dimensional Viscous Flow and Wake Development in a Centrifugal Impeller," ASME *Journal of Engineering for Power*, Vol. 103, No. 2, pp. 367–372.

Murakami, M., Kikuyama, K., and Asakura, E., 1980, "Velocity and Pressure Distributions in the Impeller Passages of Centrifugal Pumps," ASME *Journal of Fluids Engineering*, Vol. 102, No. 4, pp. 420–426.

So, R. D., and Mellor, G. L., 1973, "Experiment on Convex Curvature Effects in Turbulent Boundary Layers," *Journal of Fluid Mechanics*, Vol. 60, pp. 43–62.

Thomas, R. N., Kostrzewsky, G. J., and Flack, R. D., 1986, "Velocity Measurements in a Pump Volute With a Non-Rotating Impeller," *Int. J. Heat and Fluid Flow*, Vol. 7, No. 1, pp. 11–20.

DISCUSSION

N. A. Cumpsty[1]

The authors are to be complimented on attacking an important and difficult topic. There are, however, two points that it is proper to question. The authors assert in the introduction that losses are related to turbulence levels in an impeller and that highly turbulent flows will induce large losses and thus reduce efficiency. I am afraid that I do not agree with either of these statements. Common experience is that when

---

[1] Whittle Laboratory, Cambridge University, Cambridge, United Kingdom.

the Reynolds number is increased, and turbulent flow is more prevalent, the efficiency of most turbomachines also rises. Furthermore I do not believe that the authors are measuring turbulence in the conventional sense. They have clearly made measurements in a machine in which there are very high levels of unsteadiness, but this is not the same as high levels of turbulence for which conclusions relating to the flow physics can be made.

Turbulence is normally understood to mean the random motion of a fluid and is contrasted with the steady flow. This description begins to fail when the amplitude of the fluctuating motion is comparable to the mean motion, or when the basic flow is unsteady. Such a flow is that in an impeller running in a volute; whichever frame of reference one adopts, the flow is unsteady. One can retain some of the usual meaning of the term turbulence by removing the unsteadiness characteristic of the impeller motion, and this is normally done by a process of ensemble averaging. Ensemble averaging has been carried out in the present paper, whereby a laser anemometer sample is taken for each rotation of the impeller to give measurements at particular positions inside the impeller. These samples can then be averaged to give a mean at each position inside the impeller where measurements were taken; an estimate for the variance in velocity can be obtained by averaging the square of the difference between each sample and the mean. This variance is the square of what I believe that the authors have called turbulence.

Unfortunately the variance obtained is not really turbulence in anything like the normal meaning of the word. What has really been obtained is simply a measure of the variation in the passage flow from one realization to another. A clear indication that the unsteadiness is not turbulence by any conventional definition is the very high level: Fig. 11, for example, shows levels of so-called turbulent intensity in excess of 30 percent extending over about half the passage. Experimenters will know that it is quite difficult to generate turbulence levels in ordinary flows above about 10 percent.

One can give a concrete example of what is meant by considering the flow in a simple diffuser with a relatively large included angle. Suppose that the inlet velocity to the diffuser is 10 m/s and that the diffuser is 1 m long. There will undoubtedly be fluctuations in the flow, but one is unlikely to term those unsteady motions with frequencies below 10 Hz as turbulence; turbulence will be mainly that associated with the boundary layers and shear layers and this will be typically one or two orders of magnitude higher in frequency. One can distinguish between overall unsteadiness and what might be called real turbulence only if there is some frequency information: with the method of measurement used for these tests this is unfortunately impossible. In flows of a more complicated type one would expect this unsteadiness to be of largest magnitude where the flow is most likely to separate, near the suction surface of a blade.

It can be argued that a word only means what the user chooses it to mean, and that the authors may therefore call their unsteadiness turbulence if they wish. Unfortunately others should not follow this by attributing to this quantity the conventional meaning or significance of turbulence. The Reynolds stresses based on this unsteadiness will not, for example, have the same significance that they have with true turbulence in a boundary layer or wake. Nevertheless the authors do associate their unsteadiness with turbulence in its usual meaning in the latter paragraphs of the section "Flow Rate Variations—Centered Impeller."

Authors' Closure

The comments by Professor Cumpsty are welcomed. He indicates some viable points that need both further explanation and further investigations. The authors will respond to each of the points separately.

First, the authors made a general statement that as the turbulence is increased the losses increase and reduce efficiency. The reviewer responds that as the Reynolds number increases so does the turbulence but usually the efficiency increases. The authors certainly agree with this. The only point that the authors were trying to make was that for a given operating condition (i.e., Reynolds number, specific speed, general flow patterns, etc.), if the turbulence increases, so do the losses. The energy equation bears this out in that if energy is used to heat the fluid by turbulent action, the energy that can be used to generate head is decreased.

All of the other comments relate to the relevance of the reported fluctuation levels. The authors will discuss different ramifications. For example, earlier data taken in the discharge region (i.e., window 11) indicated fluctuations of 4–5 percent at all flow rates. These fluctuations would have certainly had some blade pass frequency variations (4X synchronous components) and probably some 1X buried in the measurements. Unfortunately, these velocity data were not correlated with any frequencies in these early measurements. Regardless, the point here is that the overall flow rate was not varying to the extent of some of the fluctuations reported in the recent paper. The throughflow was not unsteady to the extent of the reported turbulence levels.

Furthermore, measurements were also made in the inlet duct at the centerline two diameters from the inlet. Here fluctuations were measured to be only 2–3 percent. Again, the mass flow rate for the system is obviously not grossly fluctuating and is very steady and, thus, would not contribute to the measured fluctuations in the impeller.

Commenting on the high levels of turbulence, the authors should point out that these were in general in regions of low velocity (very near or in separation regions). Also, the largest values were often for small radii, where a poor inlet condition produced a skewed axial profile and a separation region on the front shroud (in the radial direction) as was reported earlier (Miner et al., 1989). At larger radii the values were more in line with the reviewers' comments (< 10 percent) and what the authors would expect. The authors also should point out that both 4X and 1X correlations of the data with running speed were performed and these yielded the same values of fluctuations for the nonorbiting case.

The authors agree with the reviewers' comments that all frequencies cannot be extracted from the data system used for this paper. He does imply, however, that the authors made no attempts to correlate at any frequencies. As noted above, the system was used to correlate data at both 1X and 4X synchronous frequencies. The reported fluctuations are at frequencies other than these. The variations reported here are the same as those that would be sensed by an instrument mounted on the rotating impeller, if that were possible. The authors do agree that "local unsteadiness" at other frequencies cannot be separated from the fluctuations, namely, unsteadiness that does not show up in the mass flow rate for the overall system. For example, if a rotating local unsteadiness was present in the flow at some frequency at a factor other than 1 or 4 of the running frequency, this would be "buried" in the so-called turbulence.

the Reynolds number is increased, and turbulent flow is more prevalent, the efficiency of most turbomachines also rises. Furthermore I do not believe that the authors are measuring turbulence in the conventional sense. They have clearly made measurements in a machine in which there are very high levels of unsteadiness, but this is not the same as high levels of turbulence for which conclusions relating to the flow physics can be made.

Turbulence is normally understood to mean the random motion of a fluid and is contrasted with the steady flow. This description begins to fail when the amplitude of the fluctuating motion is comparable to the mean motion, or when the basic flow is unsteady. Such a flow is that in an impeller running in a volute; whichever frame of reference one adopts, the flow is unsteady. One can retain some of the usual meaning of the term turbulence by removing the unsteadiness characteristic of the impeller motion, and this is normally done by a process of ensemble averaging. Ensemble averaging has been carried out in the present paper, whereby a laser anemometer sample is taken for each rotation of the impeller to give measurements at particular positions inside the impeller. These samples can then be averaged to give a mean at each position inside the impeller where measurements were taken; an estimate for the variance in velocity can be obtained by averaging the square of the difference between each sample and the mean. This variance is the square of what I believe that the authors have called turbulence.

Unfortunately the variance obtained is not really turbulence in anything like the normal meaning of the word. What has really been obtained is simply a measure of the variation in the passage flow from one realization to another. A clear indication that the unsteadiness is not turbulence by any conventional definition is the very high level: Fig. 11, for example, shows levels of so-called turbulent intensity in excess of 30 percent extending over about half the passage. Experimenters will know that it is quite difficult to generate turbulence levels in ordinary flows above about 10 percent.

One can give a concrete example of what is meant by considering the flow in a simple diffuser with a relatively large included angle. Suppose that the inlet velocity to the diffuser is 10 m/s and that the diffuser is 1 m long. There will undoubtedly be fluctuations in the flow, but one is unlikely to term those unsteady motions with frequencies below 10 Hz as turbulence; turbulence will be mainly that associated with the boundary layers and shear layers and this will be typically one or two orders of magnitude higher in frequency. One can distinguish between overall unsteadiness and what might be called real turbulence only if there is some frequency information: with the method of measurement used for these tests this is unfortunately impossible. In flows of a more complicated type one would expect this unsteadiness to be of largest magnitude where the flow is most likely to separate, near the suction surface of a blade.

It can be argued that a word only means what the user chooses it to mean, and that the authors may therefore call their unsteadiness turbulence if they wish. Unfortunately others should not follow this by attributing to this quantity the conventional meaning or significance of turbulence. The Reynolds stresses based on this unsteadiness will not, for example, have the same significance that they have with true turbulence in a boundary layer or wake. Nevertheless the authors do associate their unsteadiness with turbulence in its usual meaning in the latter paragraphs of the section "Flow Rate Variations—Centered Impeller."

Authors' Closure

The comments by Professor Cumpsty are welcomed. He indicates some viable points that need both further explanation and further investigations. The authors will respond to each of the points separately.

First, the authors made a general statement that as the turbulence is increased the losses increase and reduce efficiency. The reviewer responds that as the Reynolds number increases so does the turbulence but usually the efficiency increases. The authors certainly agree with this. The only point that the authors were trying to make was that for a given operating condition (i.e., Reynolds number, specific speed, general flow patterns, etc.), if the turbulence increases, so do the losses. The energy equation bears this out in that if energy is used to heat the fluid by turbulent action, the energy that can be used to generate head is decreased.

All of the other comments relate to the relevance of the reported fluctuation levels. The authors will discuss different ramifications. For example, earlier data taken in the discharge region (i.e., window 11) indicated fluctuations of 4–5 percent at all flow rates. These fluctuations would have certainly had some blade pass frequency variations (4X synchronous components) and probably some 1X buried in the measurements. Unfortunately, these velocity data were not correlated with any frequencies in these early measurements. Regardless, the point here is that the overall flow rate was not varying to the extent of some of the fluctuations reported in the recent paper. The throughflow was not unsteady to the extent of the reported turbulence levels.

Furthermore, measurements were also made in the inlet duct at the centerline two diameters from the inlet. Here fluctuations were measured to be only 2–3 percent. Again, the mass flow rate for the system is obviously not grossly fluctuating and is very steady and, thus, would not contribute to the measured fluctuations in the impeller.

Commenting on the high levels of turbulence, the authors should point out that these were in general in regions of low velocity (very near or in separation regions). Also, the largest values were often for small radii, where a poor inlet condition produced a skewed axial profile and a separation region on the front shroud (in the radial direction) as was reported earlier (Miner et al., 1989). At larger radii the values were more in line with the reviewers' comments (< 10 percent) and what the authors would expect. The authors also should point out that both 4X and 1X correlations of the data with running speed were performed and these yielded the same values of fluctuations for the nonorbiting case.

The authors agree with the reviewers' comments that all frequencies cannot be extracted from the data system used for this paper. He does imply, however, that the authors made no attempts to correlate at any frequencies. As noted above, the system was used to correlate data at both 1X and 4X synchronous frequencies. The reported fluctuations are at frequencies other than these. The variations reported here are the same as those that would be sensed by an instrument mounted on the rotating impeller, if that were possible. The authors do agree that "local unsteadiness" at other frequencies cannot be separated from the fluctuations, namely, unsteadiness that does not show up in the mass flow rate for the overall system. For example, if a rotating local unsteadiness was present in the flow at some frequency at a factor other than 1 or 4 of the running frequency, this would be "buried" in the so-called turbulence.

The Effects of Inlet Flow Modification on Cavitating Inducer Performance

J. Del Valle

D. M. Braisted

C. E. Brennen

California Institute of Technology,
Pasadena, CA 91125

This paper explores the effect of inlet flow modification on the cavitating and noncavitating performance of two cavitating inducers, one of simple helical design and the other a model of the low-pressure LOX pump in the Space Shuttle Main Engine. The modifications were generated by sections of honeycomb, both uniform and nonuniform. Significant improvement in the performance over a wide range of flow coefficients resulted from the use of either honeycomb section. Measurements of the axial and swirl velocity profiles of the flows entering the inducers were made in order to try to understand the nature of the inlet flow and the manner in which it is modified by the honeycomb sections.

1 Introduction

The purpose of this report is to document one effort to determine the effect of inlet flow modification on the performance of pumps, in particular axial flow inducers under cavitating and noncavitating conditions. Many test facilities, including that used for the present tests, take care to ensure a quite uniform velocity profile in the flow at inlet to the pump being tested. Yet frequently the prototype must function with inlet flows that are quite distorted and nonuniform. For example, aircraft fuel pumps frequently have a 90 deg bend just upstream of the leading edge of the impeller (Grennan, 1978). Moreover, manufacturers of axial flow pumps are often not free to provide a sufficient length of inlet ducting to ensure that the performance is unaffected by whatever inlet piping the customer chooses to attach to the pump.

The focus of the present paper will be on those inlet flow distortions produced by asymmetries in the structure. However, it should also be recognized that, particularly at flow rates below design, nonuniform axial velocities and swirl velocities may be generated by backflow from the impeller itself and the associated prerotation (Acosta, 1958; Toyokura, 1961; Badowski, 1970; Janigro and Ferrini, 1973). We delay further discussion of this until section 5.

Inlet flow distortion will have a number of consequences. Even in the absence of cavitation, nonuniform axial velocities or swirl velocities could lead to deviations from the design angles of attack and therefore to alteration in performance. If the pump is cavitating, the circumferential variation in the effective cavitation number could lead to cavities that, on a particular blade, grow and collapse during one rotation of the impeller in much the same way as cavities grow and collapse on the blade of a ship's propellor due to changes in hydrostatic pressure during a revolution. This would lead to deterioration in the cavitation performance and increase in the levels of noise and cavitation damage. Although the results that emerged were somewhat different, one of the initial objectives of this study was to examine some of these effects on the steady-state hydraulic performance of typical axial flow inducers.

There are, however, other potential effects of inlet flow distortion that, though not addressed in this report, nevertheless deserve mention. In modern high-speed pumps one is concerned with the radial loads and rotordynamic forces imposed on the impeller by the flow. Large radial loads on the impeller can cause excessive bearing wear or failure and large rotordynamic forces can lead to large or unstable whirl motions (Brennen et al., 1986; Jery et al., 1985). It is probable that inlet flow distortion could produce substantial lateral loading. In addition to overall impeller loads, one must also be concerned with the dynamic loading on individual impeller blades. Recently, Arndt et al. (1989) have shown that the unsteady loads on diffuser blades due to the passage of an upstream impeller blade can be much larger than the time-averaged load. While this is a function of the gap between the rotor and stator blades, Arndt et al. measured unsteady loads with amplitudes as large as three times the time-averaged load. In the present context this leads one to be concerned about the loads on individual inducer blades caused by wakes or other flow distortion in the inlet flow. A current project in our laboratory is directed toward measuring some of these loads and these concerns will therefore be addressed at a later date.

Another concern might be the extent to which inlet flow distortion might affect the dynamic rather than static hydraulic performance of the pump. This would result in changes in the limits of stable operation of the pump. Braisted (1979) showed that installation of flow-straightening devices in the inlet could cause changes in both the onset and frequency of auto-oscillation of cavitating inducers. However, some measurements of the dynamic transfer functions for those same inducers (in the manner described by Brennen et al., 1982) with and without

---

Contributed by the International Gas Turbine Institute for publication in the Journal of Turbomachinery. Manuscript received by the International Gas Turbine Institute September 1991. Associate Editor: L. S. Langston.

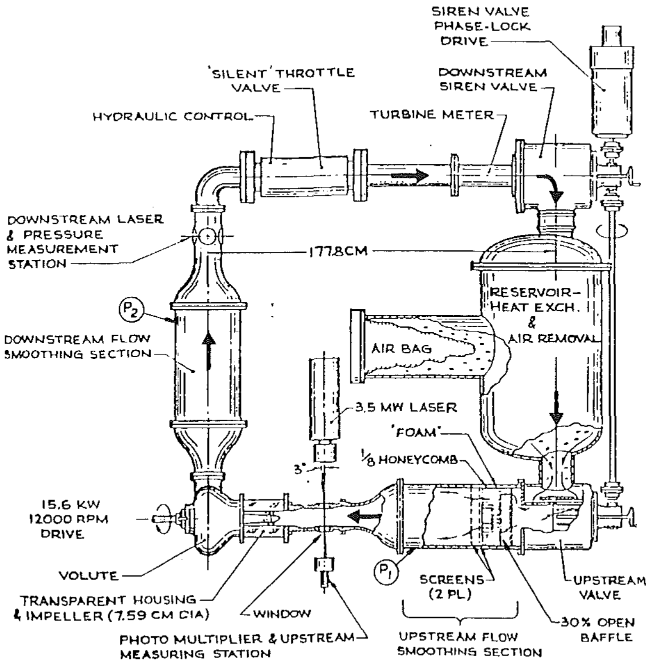

Fig. 1 Schematic of the Dynamic Pump Test Facility (DPTF)

the flow straighteners indicated very little measurable effect of the flow straighteners on those transfer functions.

2 Dynamic Pump Test Facility and Test Impellers

The facility used for the measurement of the effects of both the uniform and nonuniform inlet flow straighteners on the steady-state performance of axial flow pumps and inducers is known as the Dynamic Pump Test Facility (DPTF) and is shown diagramatically in Fig. 1. This system was originally designed to measure not only the steady-state characteristics of cavitating inducers but also transfer functions and other dynamic characteristics under cavitating and noncavitating conditions; further details can be found from Ng (1976) and Ng and Brennen (1978). It will be suffice here to discuss only those aspects pertinent to the measurement of the steady-state performance of the impellers.

The mean flow rate at a particular rotational pump speed was adjusted by means of a hydraulically operated throttle valve, labeled the "silent" throttle valve in Fig. 1. Just downstream of this is a turbine flow meter, which was used for both measurement of the mean flow rate and also as a signal input to a hydraulic servo system, which operated the "silent" valve and thereby maintained a preset value of the mean flow in the pump loop.

The pressure level in the circuit was controlled by means of air pressure regulation of the interior of a large plastic bag that communicates with the large tank, as shown in Fig. 1. This reservoir was also used to maintain constant temperature by means of a heat exchanger and for the collection and removal of air from the circuit.

The primary mean pressure measurements were made using pressure transducers placed near the downstream end of the two smoothing chambers as shown by P_1 and P_2 in Fig. 1. These were calibrated prior to each experiment against an accurate Heise gage. The calibrations were both linear and repeatable. The steady or mean pressure rise across the pump was determined from the difference in the two pressure transducer measurements. The total pressure drop across the elements of the downstream smoothing section was measured and found to be negligible in comparison.

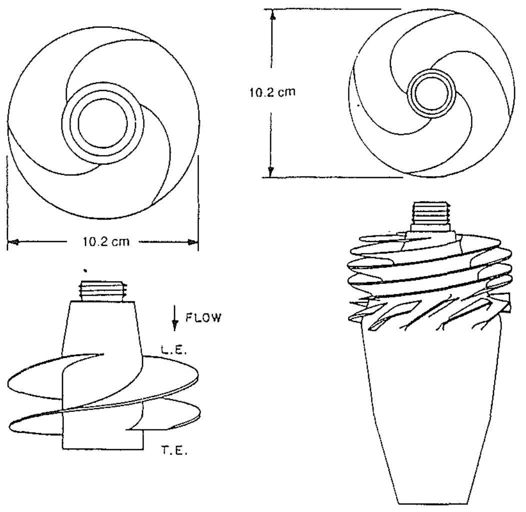

Fig. 2 Inducers used in present experiments: Impeller VII (left) is a 9 deg helical inducer; Impeller VI (right) is a model of the low-pressure LOX impeller in the Space Shuttle Main Engine

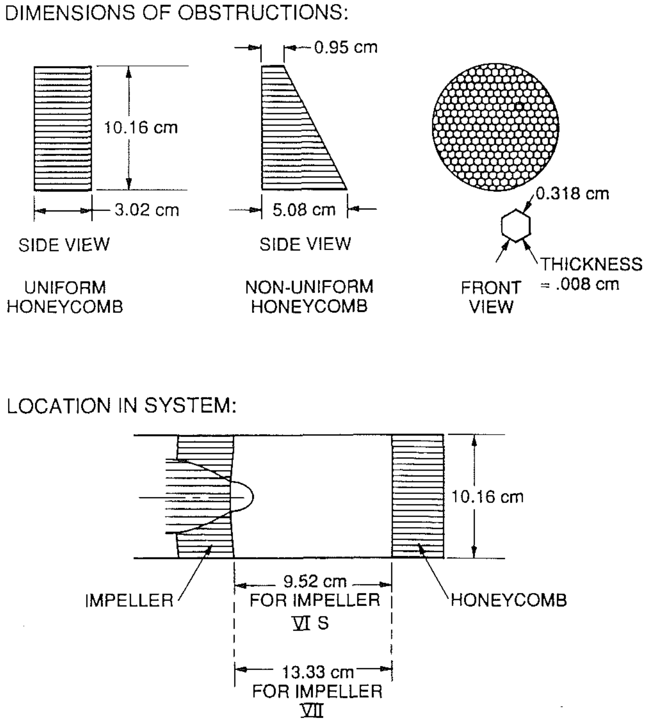

Fig. 3 Schematic showing the shape and positioning of both the uniform and nonuniform honeycomb devices installed in the impeller inlet flow

Two different impellers were used in the present experiments and these are sketched in Fig. 2. One, designated Impeller VII, was a simple 9 deg helical inducer (10.2 cm in diameter) with swept leading edges and made from stainless steel. The other, Impeller VI, was an accurate aluminum model (about 1/3 scale) of the low-pressure oxidizer turbopump in the Space Shuttle main engine. More detailed information on these impellers is contained in the works by Ng (1976) and Ng and Brennen (1978).

3 Modifications of the Inlet Flow

The purpose of the present tests was to investigate the dependence of the pump performance on inlet flow distortion. It was therefore, necessary to design devices that would impose simple and calibrated distortions on the inlet flow. Develop-

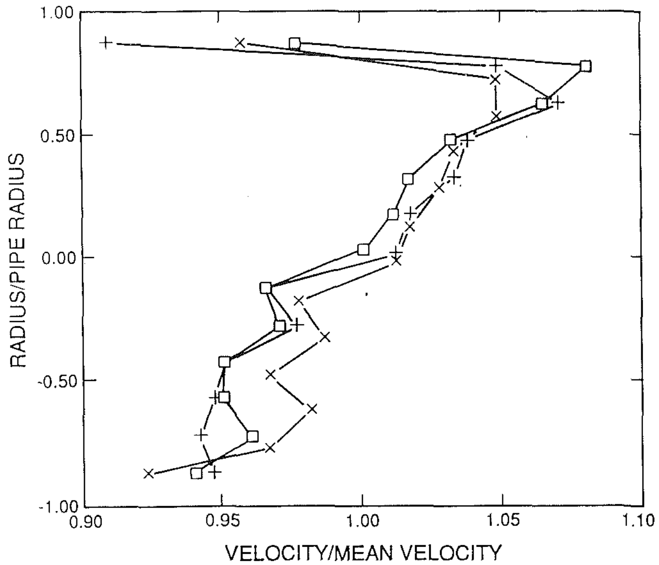

Fig. 4 Velocity profiles (measured in air tunnel) 9.52 cm downstream of the nonuniform honeycomb as a function of radial position within the 10.2-cm-dia pipe. Data for mean velocity of 9.4 m/s: × ; for 8.78 m/s: ☐ , for honeycomb rotated one half-turn and velocity of 9.4 m/s: +.

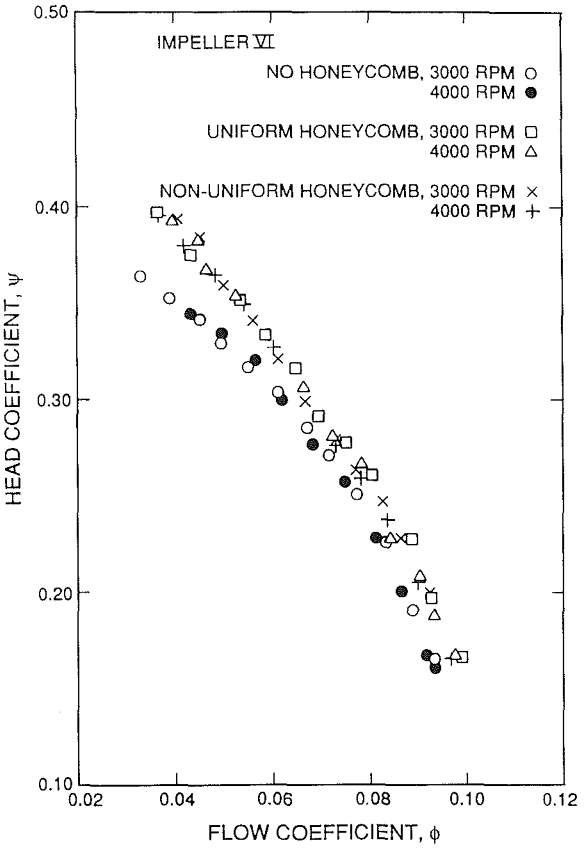

Fig. 5 Dimensionless, noncavitating performance of Impeller VI at various speeds and with and without the honeycomb devices installed in the inlet flow

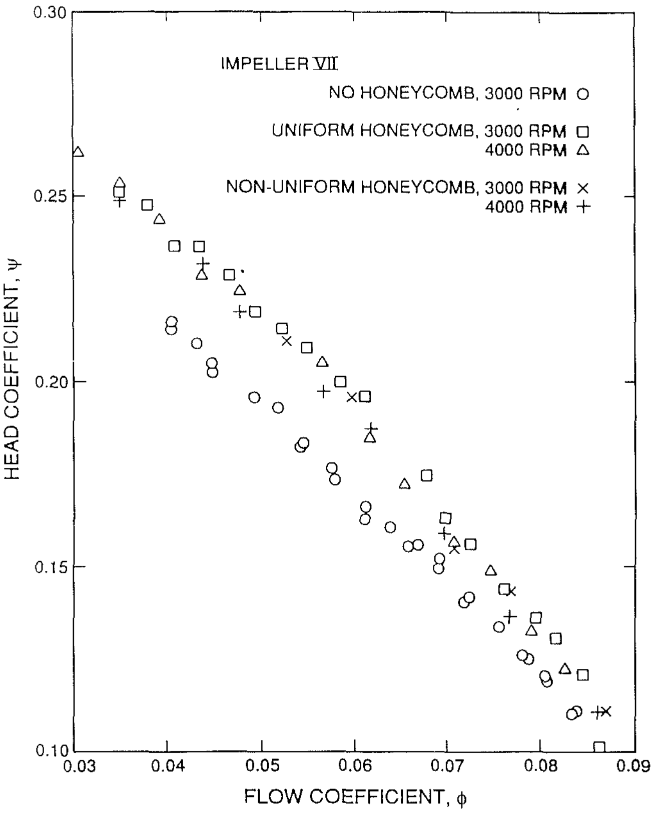

Fig. 6 Dimensionless, noncavitating performance of Impeller VII at various speeds and with and without the honeycomb devices installed in the inlet flow

ment of such devices was most readily done in a small air tunnel using velocities that corresponded to the appropriate Reynolds scaling. Since the typical inlet axial velocity of water in the DPTF was about 1.8m/s, the air tunnel (whose working section was a piece of 10.2-cm-dia pipe) was operated at a mean velocity of about 10m/s.

Many different obstructions made from metal honeycomb with very thin walls (0.008 cm thick) were tested in this air tunnel. Measurements of the velocity profiles resulting from these obstructions were made with a hot-wire anemometer at a distance 9.52 cm downstream of the trailing edge of the obstruction. It was concluded that the tapered or nonuniform honeycomb insert shown in Fig. 3 produced an appropriate nonuniformity consisting of a relatively simple shear flow.

Three different velocity distributions resulting from this nonuniform honeycomb measured in the air tunnel are shown in Fig. 4. Two of these are at mean velocities that differ by about 10 percent. The other was taken with the obstruction rotated by 180 deg in order to distinguish between nonuniformities produced by the honeycomb and any that might have been inadvertently introduced by the facility. The profiles are all essentially the same and represent a flow with a shear of about 10 percent between the extremes of a diameter. The fact that the profile is unchanged by rotation of the orientation of the honeycomb provides assurance that the nonuniformity is due to the honeycomb.

Because initial results from the steady-state performance tests using the obstruction differed significantly from those without one, it was decided that a second "uniform" obstruction should be included in the testing so as to deduce how much of the effect was attributable to factors other than the nonuniformity of the profile such as, for example, the flow straightening effect of the honeycomb. Both obstructions and their location relative to the impeller are shown in Fig. 3.

4 Steady-State, Noncavitating Performance

In order to determine the effects of the inlet flow obstructions on the steady-state performances of both impellers, a variety of experiments were conducted. The first series of tests involved measurements of the steady-state, noncavitating hydraulic performance of the two impellers at speeds of both 3000 and 4000 rpm. The flow rate was measured using cali-

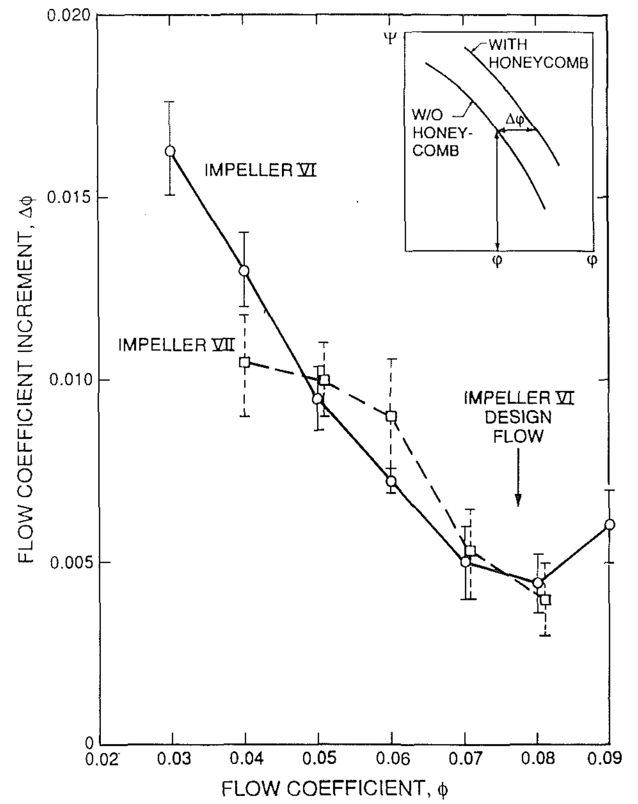

Fig. 7 The flow coefficient increment, $\Delta\varphi$, caused by the honeycomb inserts as a function of the flow coefficient, φ, in the absence of the inserts

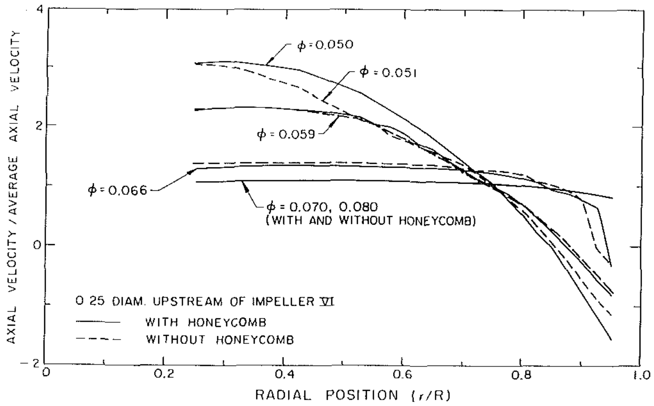

Fig. 8 Axial velocity profiles 0.25 diameters upstream of Impeller VI at various flow coefficients, φ, and with (———) and without (– – –) honeycomb inserts. Data points taken each $\Delta(r/R) = 0.025$ have been omitted for clarity; uncertainty is ±0.05 on the ordinate.

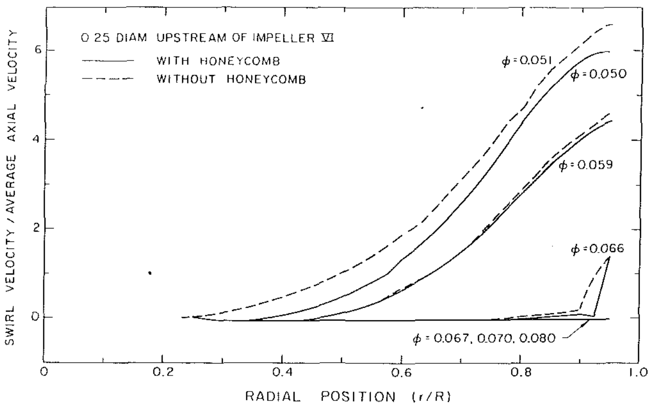

Fig. 9 Swirl velocities corresponding to the axial velocities of Fig. 8

brated turbine flow meter (Fig. 1) and the total head was measured in the upstream and downstream smoothing sections shown in Fig. 1. Note that the inlet total head is therefore measured upstream of the honeycomb inserts. Data were taken at two speeds in order to check for any significant Reynolds number effects. As will be seen in Figs. 5 and 6, no such effect was discernible and hence the data for the two speeds will be treated as one larger set. The hydraulic performance under noncavitating conditions is presented as follows. The total head rise, ΔH, is converted to a head coefficient, ψ, by dividing by ρu_T^2 (where ρ is fluid density and u_T is the inducer tip speed) and plotted against the flow coefficient, φ, obtained by nondimensionalizing the flow rate by Au_T where A is the inlet area, πr_T^2, where r_T is the inducer tip radius. Data for both impellers with no honeycomb, with the uniform honeycomb and with the nonuniform honeycomb, are presented in Figs. 5 and 6.

Several conclusions can be drawn from these data. First the installation of either of the honeycombs has caused a substantial increase in the pump performance. Later we examine the possibility that this effect may be the result of the attenuation of the induced prerotation or inlet swirl caused by any honeycomb. By fitting curves to the data with and without a honeycomb insert, we plot in Fig. 7 the incremental increase in flow caused by the insertion of the honeycomb as a function of the flow coefficient without the honeycomb. Both impellers yield very similar results, the improvement being larger at flow coefficients below the design values. The incremental flow coefficients imply changes in the angle of attack at the inducer tip of less than a degree (0.29 deg at $\Delta\varphi = 0.005$ to 0.86 deg at $\Delta\varphi = 0.015$).

The second major conclusion to be drawn from Figs. 5 and 6 is that one cannot discern any effect of the nonuniform honeycomb relative to the uniform honeycomb. The effect that either honeycomb has in inhibiting prerotation is much larger than the effect of the nonuniformity introduced by the nonuniform honeycomb. Indeed, any artifact that could introduce nonuniformity would also affect prerotation and one conclusion that can be drawn from these tests is that the change in prerotation may dominate any effect of nonuniformity, at least insofar as hydraulic performance is concerned.

5 Swirl and Axial Velocity Profiles

To investigate these effects in more detail, inlet axial and swirl velocity profiles were obtained by means of a wedge probe and total head traverses (Braisted, 1979). The wedge probe was used to determine the direction of the flow and subsequent total head probe measurements were made using these angles. Profiles for the swirl and axial velocities were calculated from these measurements by assuming radial equilibrium, which previous investigations have established as valid for these inlet flows (Janigro and Ferrini, 1973). Data taken 0.25 diameters upstream of the leading edge of Impeller VI are shown in Figs. 8 and 9; similar data 0.5 diameters upstream are included in Figs. 10 and 11. Data were taken at both 4000 and 6000 rpm but yielded essentially the same profiles at the two speeds.

These velocity profiles are consistent with those measured previously (Badowski, 1970). They clearly show that the annular jet produced by the tip clearance flow occurs below a certain critical flow coefficient (φ_c) and penetrates farther upstream the lower the flow coefficient (see also Acosta, 1958). The variation of the critical flow coefficient with Reynolds number and hub-to-tip ratio has recently been explored by Alpan and Peng (1989). In Figs. 8, 9, 10, and 11 the backflow

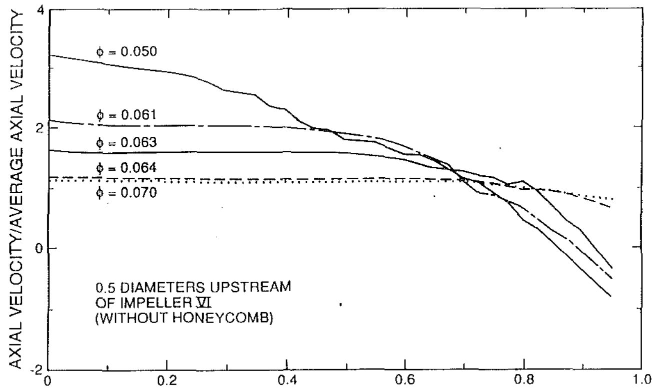

Fig. 10 As Fig. 9 but 0.5 diameters upstream of Impeller VI

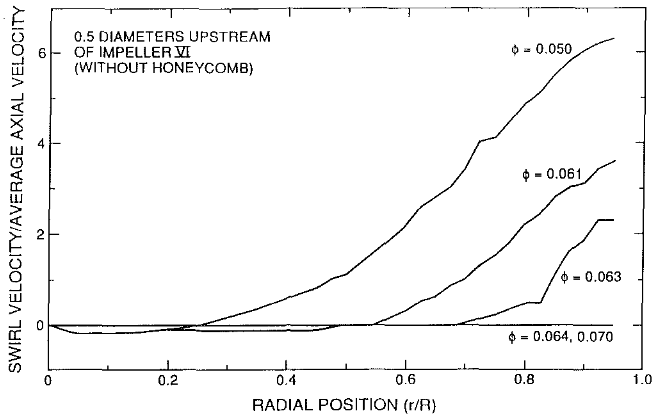

Fig. 11 Swirl velocities corresponding to the axial velocities of Fig. 10

can be clearly identified as the region of negative axial velocity. Note from Figs. 8 and 10 that the backflow has penetrated 0.25 diameters upstream at $\phi \approx 0.067$ and 0.5 diameters upstream at $\varphi \approx 0.064$. As discussed by Badowski (1970) and Murakami and Heya (1966), the backflow is the source of the vorticity or swirl velocity. At higher flow coefficients above the critical the backflow vanishes and the swirl is essentially zero as it must be from Kelvin's theorem. However, we can also see that, in the presence of backflow, the nonzero swirl velocities are not confined to the backflow region. Braisted (1979) has observed that this inward diffusion of vorticity occurs much too rapidly to be caused by molecular viscosity. Thus it would appear that the high degree of turbulence and unsteadiness in this flow must cause the diffusion of swirl over almost the entire cross section of the inlet flow.

The data of Fig. 9 indicate that, as earlier surmised, the honeycomb insert reduces the prerotation or swirl, at least at low flow coefficients. However this does not explain the favorable effect of the honeycomb over the entire range of flow coefficients; even at the lower flow coefficients the changes in prerotation exhibited in Fig. 9 seem too small to explain the change in performance. We conclude that, as yet, there is no satisfactory explanation for the performance enhancement caused by the honeycomb. These inlet flows are very unsteady and one might speculate that this unsteadiness may well affect performance adversely. If the honeycomb dampens this unsteadiness, then that might provide a possible explanation for the observed effects.

One tenuous previously mentioned piece of evidence that might support such an explanation emerges from the work of Braisted (1979) on the auto-oscillation of the same cavitating inducers. Braisted observed that both the onset and frequency of auto-oscillation were affected by the presence of the honeycomb in the inlet flow. For example, the frequency of auto-oscillation of Impeller VII was increased by about 20 percent by the insertion of the honeycomb. This suggests a significant change in dynamics of the flow.

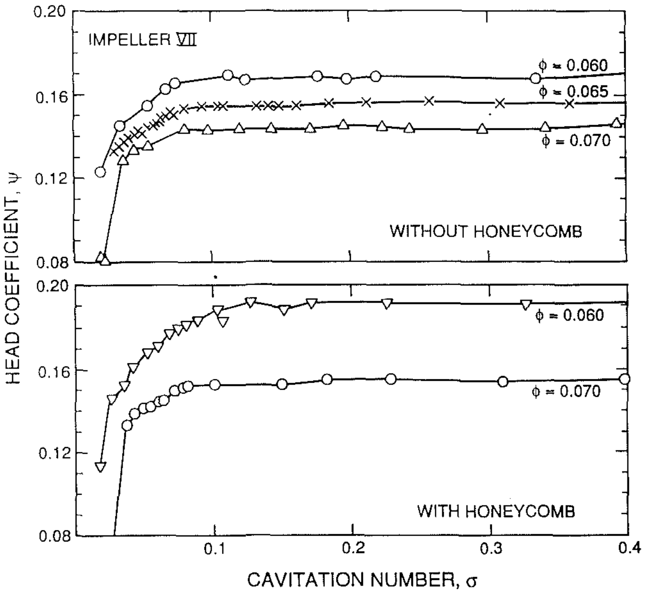

Fig. 12 Cavitation performance for Impeller VII at 7000 rpm and various flow coefficients, φ, as indicated and with and without honeycomb insert

6 Cavitation Performance

Cavitation performance measurements were made with both impellers at several speeds and flow coefficients and with and without honeycomb inserts. More details on the procedures used for these tests may be found in Ng (1976) and Braisted (1979). For example, the tests were all performed after substantial de-aeration of the water in the facility. Typical nondimensional results are presented in Fig. 12 and 13 where the head coefficient, ψ, for a given flow coefficient, ϕ, is plotted against the cavitation number defined as $\sigma = (p_1 - p_v)/1/2\rho u_T^2$ where p_1 and p_v are respectively the inlet static pressure and the vapor pressure at the operational water temperature. The data exhibit the conventional breakdown characteristics, which were more readily documented for the helical Impeller VII than for the more advanced and better-performing Impeller VI because the former begins to break down at higher cavitation numbers.

The first conclusion to be drawn from these tests represents an extension of the earlier conclusion on the effect in noncavitating flow, namely that the results for the uniform and nonuniform honeycomb were essentially identical but differed from the performance without any honeycomb. Consequently we compare in Figs. 12 and 13 the cavitation performance with and without a honeycomb. When the data of Fig. 12 are compared one can see that the cavitation performance at $\varphi = 0.070$ with the honeycomb is essentially the same as the data at $\varphi = 0.065$ without the honeycomb and that the rest of the data are also consistent with a similar shift in the effective flow coefficient of the order of 0.005. Hence we may expand the other principal conclusion that emerged from the noncavitating performance data, namely, that the cavitation performance change caused by the honeycomb inserts can be described simply as an effective change in the flow coefficient as given in Fig. 7.

Parenthetically we note that Braisted (1979) found that some inlet velocity profile measurements under cavitating conditions ($\sigma = 0.1$) indicated that the profiles are not greatly effected by

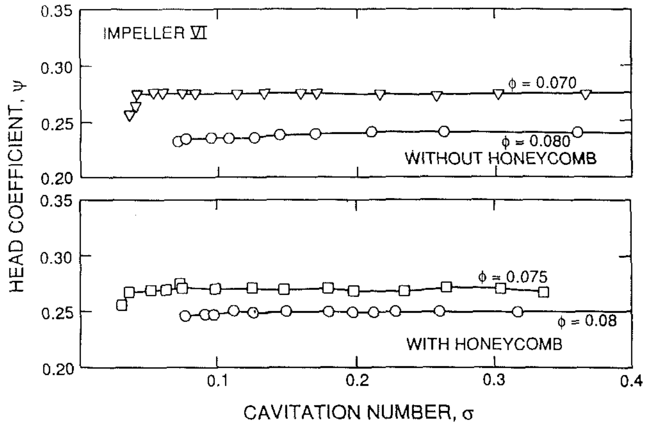

Fig. 13 Cavitation performance for Impeller VI at 6000 rpm and various coefficients, φ, as indicated and with and without honeycomb insert

the presence of cavitation as long as one is above the value of σ at which the head is significantly affected.

7 Conclusions

Sections of honeycomb installed in the inlet flow to two cavitating inducers caused a substantial improvement in the hydraulic performance of those inducers. This performance enhancement, which could be characterized by an increase in the flow coefficient, $\Delta\varphi$, at the same head rise, occurred over a wide range of flows, though it was greater below the design flow coefficient. The changes in both the noncavitating and cavitating performance could be represented by a change in the effective flow coefficient designated the flow coefficient increment, $\Delta\varphi$. The increment and its dependence on the flow coefficient were similar for the two inducers tested. Parenthetically we should note that the improvement referred to above applies to an increase in the head rise for a given flow. The effect on efficiency was not measured and would be interesting to investigate.

Honeycomb sections that were both uniform and nonuniform were tested, the latter in an attempt to evaluate the effect of nonuniform axial velocity profiles on inducer performance. However, if such an effect exists, it was much smaller than the change occurring with and without honeycomb inserts.

Measurement of axial and swirl velocity profiles were made in order to provide further documentation of the actual inlet flow at two locations, 1/4 and 1/2 diameter upstream of the inlet plane of one of the inducers. These measurements are consistent with the previous measurements of Badowski (1970) and confirm that, as the loading is increased (φ decreased), the backflow jet generated by the tip clearance flow is initiated at a certain critical flow coefficient, φ_c, and penetrates farther upstream with further decrease in φ. Nonzero swirl velocities (prerotation) only occur for $\varphi < \varphi_c$. However, the swirl is not confined to the backflow jet; the vorticity from this jet is diffused inward so that swirl velocities are measured over virtually all of the inflow. The mechanism for such rapid diffusion of vorticity must be turbulent convection resulting from the high degree of unsteadiness associated with the backflow.

Velocity profiles were obtained with and without the honeycomb flow straightener installed. While this device caused some decrease in the swirl velocity at inlet to the inducer, it appears insufficient to explain the performance enhancement which the device caused over the full range of flow coefficient.

Acknowledgments

The authors would like to thank NASA George Marshall Space Flight Center for support of this research under Contracts NAS8-29313, NAS8-29046, and Grant No. NAG8-118.

References

Acosta, A. J., 1958, "An Experimental Study of Cavitating Inducers," *Proc. Second Symp. on Naval Hydrodynamics*, ONR/ACR-38, pp. 533–557.

Alpan, K., and Peng, W. W., 1989, "Suction Reverse Flow in an Axial-Flow Pump," *ASME Symp. on Pumping Machinery—1989*, ASME FED-Vol. 81, pp. 141–148.

Arndt, N., Acosta, A. J., Brennen, C. E., and Caughey, T. K., 1989, "Rotor-Stator Interaction in a Diffuser Pump," ASME JOURNAL OF TURBOMACHINERY, Vol. 111, pp. 213–221.

Badowski, H. R., 1970, "Inducers for Centrifugal Pumps," Internal report, Worthington Canada, Ltd.

Braisted, D. M., 1979, "Cavitation Induced Instabilities Associated With Turbomachines," Ph.D. thesis and Eng. and Appl. Sci. Report No. E184.2, California Institute of Technology, Pasadena, CA.

Brennen, C. E., and Braisted, D. M., 1980, "Stability of Hydraulic Systems With Focus on Cavitating Pumps," *Proc. 10th Symposium of IAHR*, Tokyo, Japan.

Brennen, C. E., Meissner, C., Lo, E. Y., and Hoffman, G. S., 1982, "Scale Effects in the Dynamic Transfer Functions for Cavitating Inducers," ASME *Journal of Fluids Engineering*, Vol. 104, pp. 428–433.

Brennen, C. E., Acosta, A. J., and Caughey, T. K., 1986, "Impeller Fluid Forces," *NASA Prod. Advanced Earth-to-Orbit Propulsion Technology Conference*, Huntsville, AL, NASA Conf. Publ. 2436, pp. 270–295.

Grennan, C. W., 1978, "Polyphase Flow in Gas Turbine Fuel Pumps," in: *Polyphase Flow in Turbomachinery*, C. Brennen, P. Cooper, and P. W. Runstadler, eds., ASME, New York.

Janigro, A., and Ferrini, F., 1973, "Inducer Pumps," in: *Recent Progress in Pump Research*, von Karman Inst. for Fluid Dynamics, Lecture Series 61.

Jery, B., Acosta, A. J., Brennen, C. E., and Caughey, T. K., 1985, "Forces on Centrifugal Pump Impellers," presented at the Second International Pump Symposium, Houston, TX, Apr. 29–May 2, 1985.

Murakami, M., and Heya, M., 1966, "Swirling Flow in Suction Pipe of Centrifugal Pumps," *Bull. Japanese Soc. Mech. Eng.*, Vol. 9, No. 34.

Ng, S. L., 1976, "Dynamic Response of Cavitating Turbomachines," Ph.D. Thesis and Eng. and Appl. Sci. Report No. E183.1, California Institute of Technology, Pasadena, CA.

Ng, S. L., and Brennen, C., 1978, "Experiments on the Dynamic Behavior of Cavitating Pumps," ASME *Journal of Fluids Engineering*, Vol. 100, No. 2, pp. 166–176.

Toyokura, T., 1961, "Studies on the Characteristics of Axial-Flow Pumps," Parts 1–6, *Bull. Japan. Soc. Mech. Eng.*, Vol. 4, pp. 287–340.

Experimental Study of the Swirling Flow in the Volute of a Centrifugal Pump

T. Elholm[1]

E. Ayder

R. Van den Braembussche

von Karman Institute for Fluid Dynamics,
B-1640 Rhode Saint Genèse, Belgium

Detailed three-dimensional velocity distributions, corresponding to design and off-design operation, were measured in two different circumferential cross sections of a volute by means of LDV. It is shown that the swirl has a forced vortex type velocity distribution and that the location of the swirl center changes with mass flow. The throughflow velocity distribution is primarily defined by the conservation of angular momentum. A strong interaction between the throughflow and swirl velocity is observed. Flow visualization in the tongue region reveals a reversal of the velocity at the volute inlet with increasing mass flow. The pressure drop between volute outlet and inlet at low mass flow pushes extra fluid through the tongue gap and increases the mass flow in the volute. The abrupt pressure rise at high mass flow results in local return flow perturbing the flow in the outlet pipe.

Introduction

The objectives of research on flow in volutes are the prediction of overall performance and of radial forces on the impeller due to circumferential pressure distortion at off-design operation.

Overall performance is defined by the volute cross-sectional shape (Mishima and Gyobu, 1978), circumferential variation of cross-sectional area (Stiefel, 1972; Sideris, 1988), tongue geometry (Lipski, 1979; Brownell and Flack, 1984) and the shape of the exit diffuser (Flörkemeier, 1977). The radial forces resulting from the circumferential pressure variation at off-design operation have been studied by Iversen et al. (1960).

Most volute prediction methods assume a uniform flow over the cross section (Iversen et al., 1960; Japikse, 1982; Lorett and Gopalakrishnan, 1986). However, detailed flow measurements by Van den Braembussche and Hände (1990) reveal large changes in the velocity and pressure distribution over a cross section that are dependent on the operating conditions. They have shown that the increase or decrease of the throughflow velocity in the center of the volute is related to swirl velocity and total pressure distribution. The negative or positive blockage factor, corresponding to variations in throughflow velocity, has a major influence on the circumferential pressure variation and is an important input for prediction methods.

The purpose of the research described in this paper is to extend previous observations from data taken on a straight volute, to reveal the basic mechanisms defining the flow structure in a curved volute, and to provide detailed experimental data, which can be used to help verify more refined theoretical and numerical studies.

Experimental Facility

Measurements and flow visualization studies in water have been performed on the closed-loop P1 centrifugal pump test stand of the von Karman Institute. On the system sketch in Fig. 1, the mass flow is measured by a venturi between the settling chamber and the pump inlet, and is controlled by a throttling valve downstream of the pump. A variable speed d-c motor drives the impeller and the speed in rpm is measured by means of a photo-cell and a perforated disk mounted on the shaft.

The impeller and casing are manufactured of plexiglass and have been specially designed for optical flow measurements (Fig. 2). The shrouded radial flow impeller has an outlet radius of 100 mm, an outlet width of 20 mm, and eight blades with

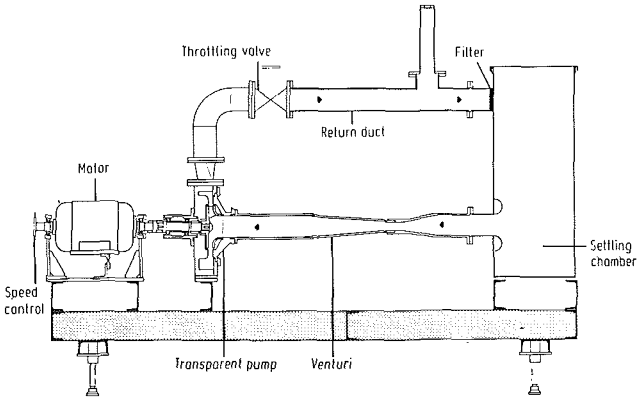

Fig. 1 Pump test facility P1

---

[1] Present address: Norwegian Institute of Technology, Department of Hydro- and Gas Dynamics, Trondheim, Norway.

Contributed by the International Gas Turbine Institute and presented at the 35th International Gas Turbine and Aeroengine Congress and Exposition, Brussels, Belgium, June 11-14, 1990. Manuscript received by the International Gas Turbine Institute January 10, 1990. Paper No. 90-GT-49.

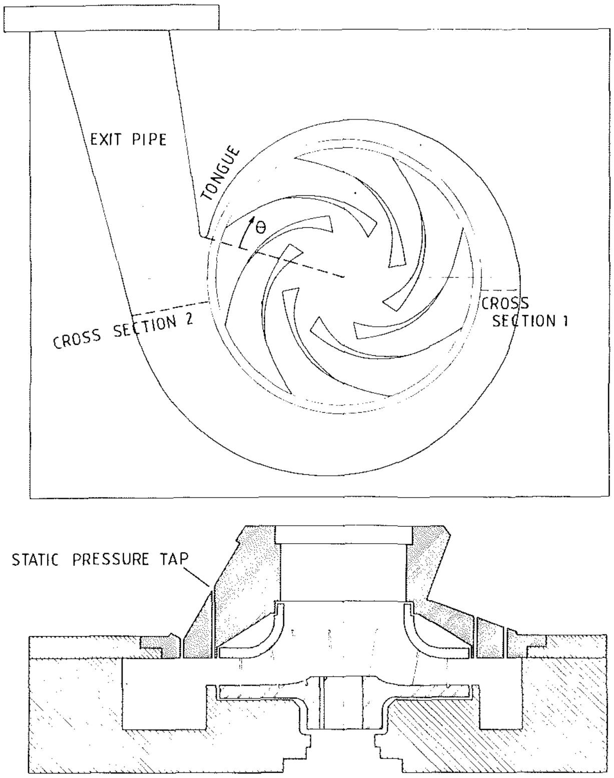

Fig. 2 Pump geometry and measuring locations

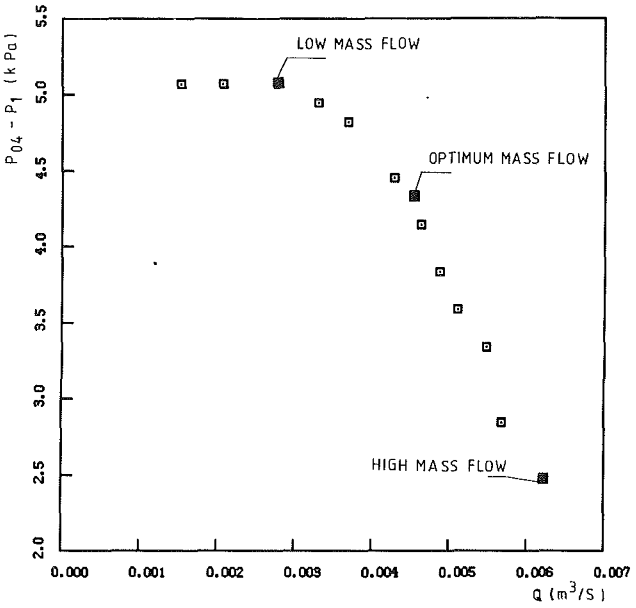

Fig. 3 Pump performances at 300 rpm

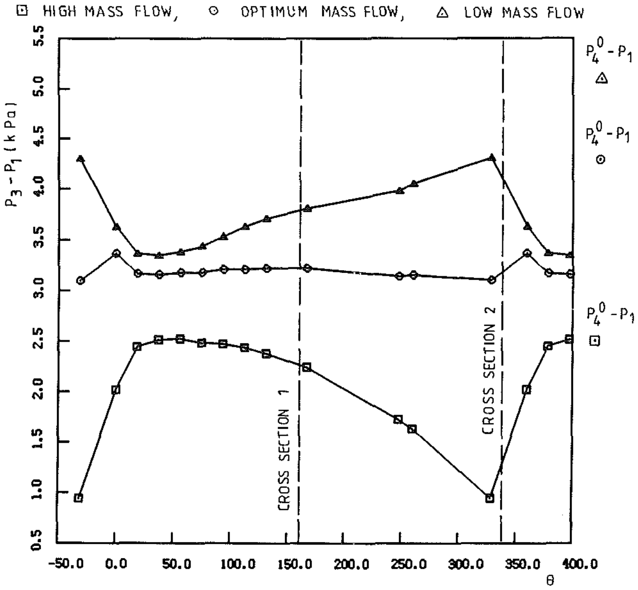

Fig. 4 Circumferential static pressure variation on the volute wall

a 63.5 deg outlet lean angle, measured from the radial direction.

An 8-mm-long vaneless diffuser connects the impeller to a nonsymmetric volute. The rectangular cross-sectional volute has a constant width, with the cross-sectional area variation resulting from the logarithmic spiral shape of the volute outer wall (Fig. 2). The gap between the tongue and the volute inner wall is 6 mm and extends over the whole volute width.

The head/flow rate performance of the pump at 300 rpm is shown in Fig. 3. The filled symbols indicate the three operating points of high, optimum, and low mass flow rates for which detailed measurements inside the volute have been made. The volute locations selected for detailed measurements are indicated as cross sections 1 and 2 in Fig. 2.

The circumferential static pressure variation was measured by means of 12 static pressure tappings at the impeller outlet (R = 102 mm) and inside the volute (R = 127 mm). The results shown in Fig. 4 are typical for the three operating conditions. At low mass flow, the pressure increases from the tongue to the volute outlet resulting in an abrupt pressure drop at the tongue. It is nearly constant at optimum mass flow and decreases throughout the volute at high mass flow with an abrupt pressure rise at the tongue.

LDV Measurements

A one-dimensional LDV measurement system was used to measure the three components of the velocity over the two volute cross sections located at angles of 165 and 335 deg from the volute tongue (Fig. 2). The LDV system utilizes a 5-W argon-ion laser and a TSI backward scatter optical system that provides fringes with a 1.917 μm spacing. This system was used because it facilitates access to all measuring positions.

The V_R and V_T velocity components for the coordinate system shown in Fig. 5 were measured with the laser beams en-

Nomenclature

d = particle diameter
P = pressure
Q = volume flow
R = radius
R_c = curvature radius
V = velocity
θ = circumferential position (Fig. 2)
ρ = density
σ = standard deviation

Subscripts

R = radial component
S = swirl component
T = throughflow component
Z = axial component
1 = pump inlet
2 = impeller outlet (R = 102 mm)
3 = inside the volute (R = 127 mm)
4 = volute outlet

Superscripts

o = total conditions
— = average value

tering the volute in the axial direction, by rotating the beam splitter over 90 deg. The V_Z velocity component was measured with the beams entering the volute radially. A Bragg cell, included in the system allowed distinction between positive and negative V_R and V_Z components, and improved the quality of the signal when measuring small values of V_Z and V_R at locations with large V_T components.

Natural seeding of the water was used but all particles larger than 10 μm were taken out by a filter located in the return duct. Velocity components were taken at points equally distributed at 5-mm intervals in the axial and radial directions. An aggregate of 1024 samples was used to calculate a time-averaged value of each of the velocity components.

A simple averaging of each component results in a first estimation of the mean value

$$\overline{v}_i{}' = \frac{1}{1024} \sum_{1}^{1024} V_{in} \tag{1}$$

with a standard deviation

$$\sigma = \sqrt{\frac{1}{1024} \sum_{1}^{1024} (V_{in} - \overline{V}_i{}')^2} \tag{2}$$

where V_{in} indicates the nth sample of the ith velocity component. σ is about 10 percent of the mean throughflow velocity with a peak of 20 percent near the impeller outlet. Data that fall more than 2σ away from the mean value are removed and the remaining N measurements are used for further data reduction.

The corrected average value is then calculated using a modified version of the equation proposed by McLaughlin and Tiederman (1973) to correct for biasing errors in turbulent flow measurements.

$$\overline{V}_i = \frac{\sum_{n=1}^{N} V_{in}/\sqrt{\overline{V}_j'^2 + V_{in}^2}}{\sum_{n=1}^{N} 1/\sqrt{\overline{V}_j'^2 + V_{in}^2}} \tag{3}$$

where $\overline{V}_j'$ indicates the first estimation of the mean value of the velocity component perpendicular to V_i.

The difference between the simple averaging in Eq. (1) and corrected averaging in Eq. (3) amounts to about 6 percent in the region of fluctuating flow near the impeller outlet.

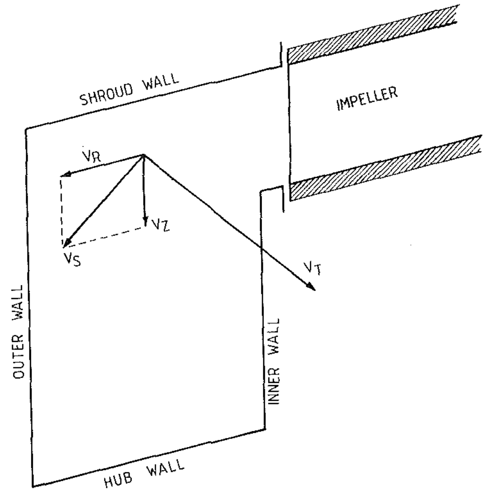

Fig. 5 Definition of velocity components

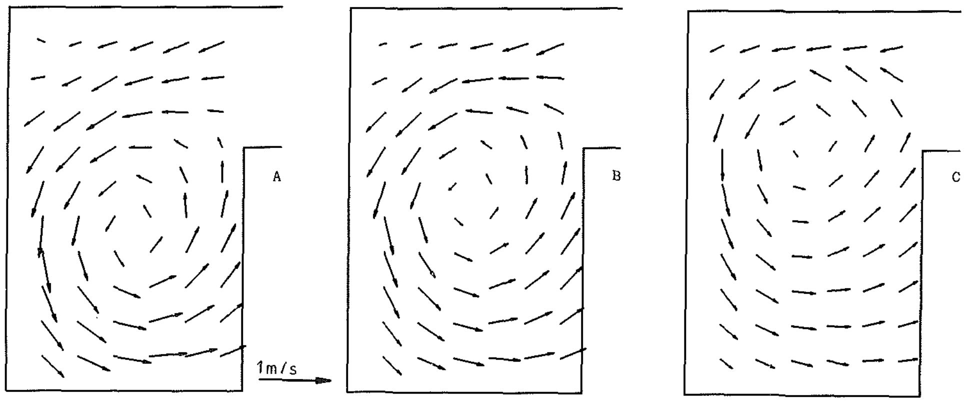

Fig. 6 Swirl velocity distribution at cross section 1 corresponding to high (A), optimum (B), and low (C), mass flow

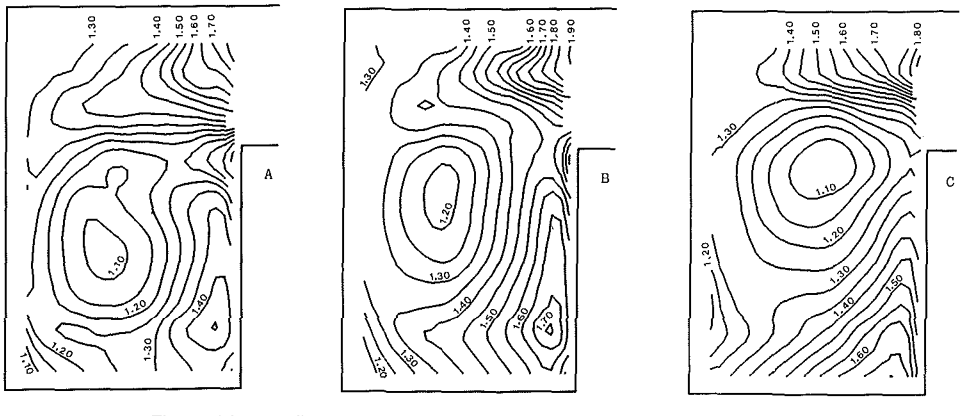

Fig. 7 Throughflow velocity distribution at cross section 1 corresponding to high (A), optimum (B), and low (C) mass flow (velocity in m/s)

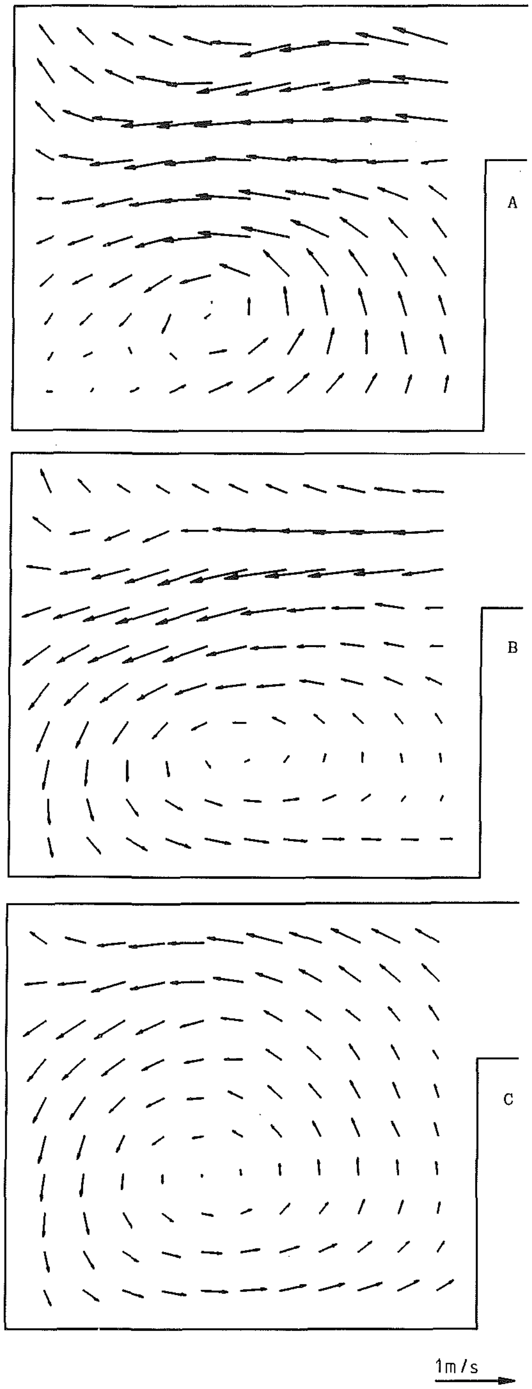

Fig. 8 Swirl velocity distribution at cross section 2 corresponding to high (A), optimum (B), and low (C) mass flow

Results of LDV Measurements

The axial and radial velocity components (V_Z and V_R) allow the calculation of the swirl velocity component V_S indicated in Fig. 5 at each measuring location of the cross sectional plane.

The time mean values of the swirl velocity V_S and throughflow velocity V_T, measured at cross section 1 for high, optimum, and low mass flow are shown in Figs. 6 and 7. These results are very similar to those measured by Van den Braembussche and Hände (1990) in a straight volute. The radial velocity at the impeller exit is transformed into a swirling motion, with a forced vortex type of velocity distribution in the center and a nearly constant swirl velocity away from it. Minimum throughflow velocity is again observed at the center of the vortex.

The main differences from previous measurements are a change in location of the swirl center with mass flow and a nonuniformity of the throughflow velocity outside the swirl center.

The variation in the location of the swirl center with mass flow is due to the change in circumferential pressure distribution. Figure 4 indicates a sudden pressure drop over the tongue at low mass flow. This results, as will later be confirmed by flow visualizations, in an extra amount of fluid entering the volute through the gap at the volute tongue. This fluid fills the lower part of the volute cross section and prevents the swirl center from moving to the center of the volute. Furthermore, the increase of impeller outlet pressure with θ results in a decrease of the radial velocity at the impeller outlet and helps to maintain the asymmetry of the swirl (Fig. 6C).

The opposite occurs at high mass flow. The flow visualizations will show how the sudden pressure rise at the volute tongue pushes the fluid back from the volute inlet to the exit pipe. The swirl center is therefore moved further inside the volute (Fig. 6A).

The circumferentially uniform pressure distribution at impeller outlet for optimum flow condition results in a nearly constant velocity at the impeller outlet, and a symmetric swirl inside the volute as shown in Fig. 6(B).

The variation of the throughflow velocity outside the swirl center is due to the curvature of the volute centerline. The conservation of momentum

$$R \cdot V_T = \text{const} \tag{4}$$

results in a decrease of the throughflow velocity from the inner to the outer radius of the volute as observed in Fig. 7 for all three mass flows.

The change of average throughflow velocity in this cross section is much smaller than the changes in the pump overall mass flow shown in Fig. 3. This is explained by the relatively small difference in pressure level in the region between the tongue and cross section 1 at all three mass flows, and by the positive and negative leakage flows under the tongue at low and high mass flow.

A completely different velocity distribution is observed at cross section 2. The swirl center is always eccentric to the volute cross section, as shown in Fig. 8, and the gradients of the throughflow velocity are no longer in the radial direction as shown in Fig. 9.

The flow in a curved channel is governed by the equilibrium between centrifugal forces and the pressure gradient given by

$$\frac{1}{\rho}\frac{dP}{dR} = \frac{V_T^2}{R_c} \tag{5}$$

where R is the radius measured from the axis and R_c is the curvature radius of the fluid element streamline.

This relation explains the reverse flow in the boundary layer along the shroud wall, which is only suggested by the swirl velocity distribution on Fig. 8(A) but is confirmed by flow visualization.

The throughflow velocity distributions at cross section 2 are shown in Figs 9(A, B, C) for high, medium, and low mass flow. The large hub-to-shroud velocity gradient observed at high mass flow gradually changes into a smaller radial velocity gradient at low mass flow. Minimum throughflow velocity no longer coincides with the center of the swirl, as was observed at cross section 1.

The large gradient of the throughflow velocity at large mass flow is a consequence of the circumferential pressure gradient at impeller outlet. The fluid in the hub-inner wall corner has entered the volute near the inlet (low values of θ) at a higher back pressure. This results in a smaller radial and larger tan-

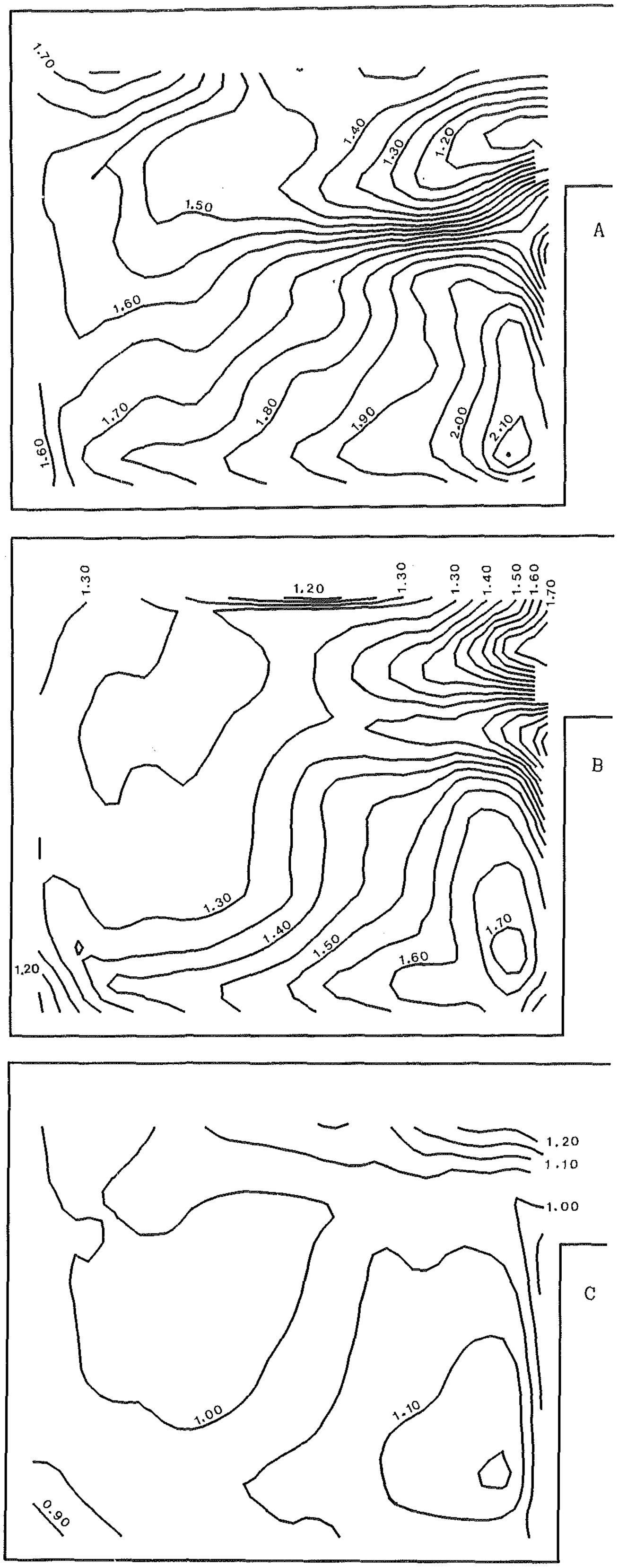

Fig. 9 Throughflow velocity distribution at cross section 2 corresponding to high (A), optimum (B), and low (C) mass flow (velocity in m/s)

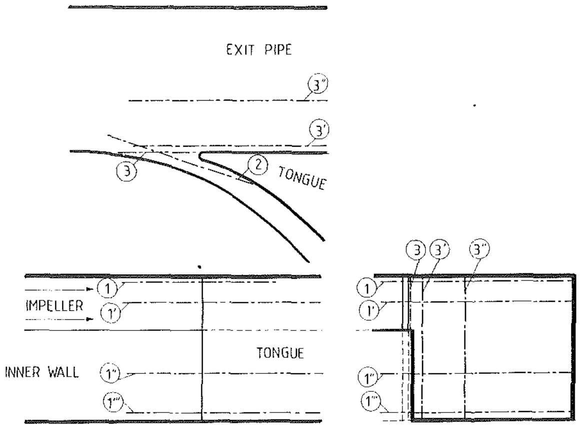

Fig. 10 Position of flow visualization planes

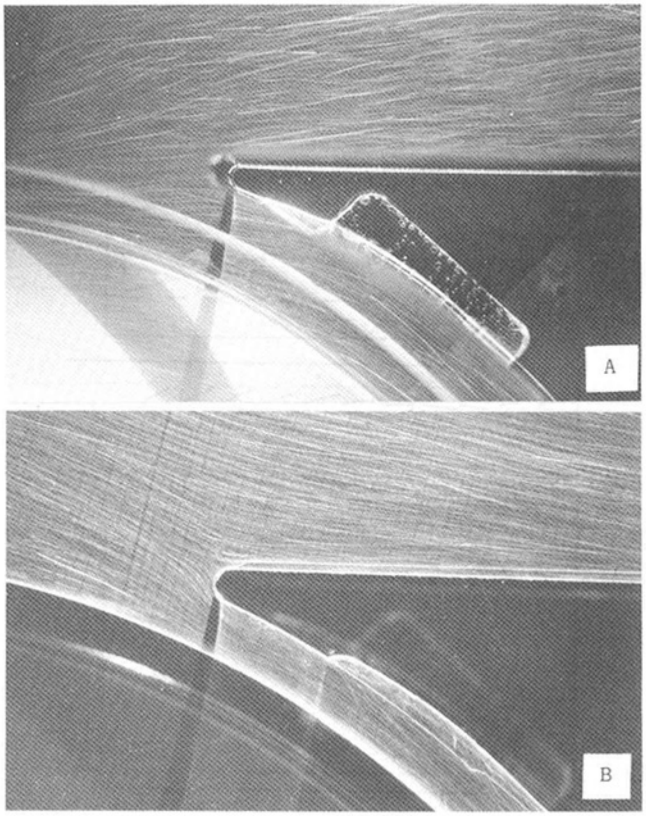

Fig. 11 Flow visualization at optimum mass flow in plane 1′ (A) and in plane 1‴ (B)

gential velocity of the fluid. The fluid near the shroud side has left the impeller in a region of low pressure, which explains the large radial and small throughflow velocities.

The resulting hub-to shroud velocity gradient also has an influence on the intensity and location of the swirl, as shown in Fig. 8(A). If it is assumed that there is no pressure variation in the axial direction, the same pressure gradient exists along the hub and shroud walls. Equation (5) indicates that the high throughflow velocity fluid near the hub wall will migrate outward with a larger curvature radius than the low velocity fluid near the shroud wall. This results in a clockwise rotation of the fluid, which counteracts the initial swirl distribution. It explains the low vorticity at high mass flow, where one would expect a high swirl intensity because of the large radial velocity at the volute inlet.

The swirl distribution is more symmetric at lower mass flows and the throughflow velocity shows only a radial variation as dictated by the conservation of angular momentum.

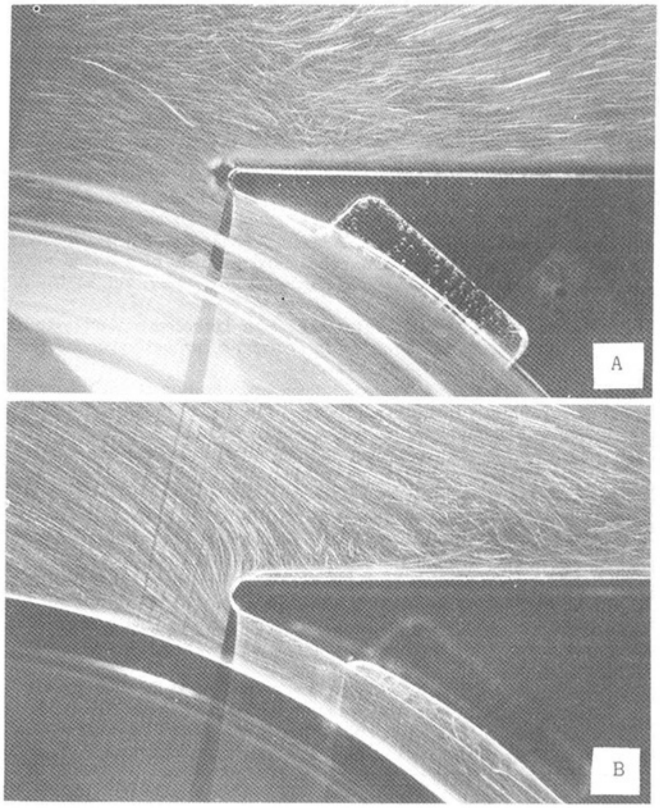

Fig. 12 Flow visualization at low mass flow in plane $1'$ (A) and in plane $1'''$ (B)

Flow Visualizations

The LDV measurements in the area of the tongue were supplemented by flow visualization.

Tongue region flow visualization was produced by expanding a 5-W argon-ion laser beam into a thin light sheet to illuminate metallic coated microspheres (TSI 10087) with which the fluid was seeded. The density of these particles is higher than water (2.6 g/cm^3) but their dimensions are sufficiently small (d = 4 μm) to allow the particles to follow the flow.

Visualizations were made in four planes perpendicular to the axis (1 to $1'''$) and four planes orthogonal to them as shown in Fig. 10 to enhance the understanding of the flow structure observed from the LDV measurements.

The flow visualization photos in Figs. 11(A, B), taken at optimum mass flow, show a minimum flow distortion by the tongue. The zero incidence observed in plane $1'$ in Fig. 11(A) changes into a small negative incidence at plane $1'''$ in Fig. 11(B) because of the swirl inside the volute as measured at cross section 2. This is in contrast to the large flow distortions observed at both low and high mass flow.

The small radial and large tangential velocities at low mass flow result in a negative incidence on the volute tongue at all axial positions (Figs. 12A, B). A large amount of fluid enters the volute through the tongue gap and increases the mass flow inside the volute. This has a favorable effect on the circumferential pressure distortion and as already discussed, influences the swirl distributions and location of the swirl center in cross section 1.

The large radial velocity at impeller outlet at high mass flow results in a high positive incidence on the tongue and a subsequent flow separation in the exit pipe as illustrated in Fig. 13(A) by the flow visualizations in plane $1'$. The large circumferential pressure rise in the tongue region at high mass flow (Fig. 4) pushes the fluid backward through the tongue gap. This also results in a flow separation in the exit pipe as shown in Fig. 13(B) by the visualization in plane $1'''$.

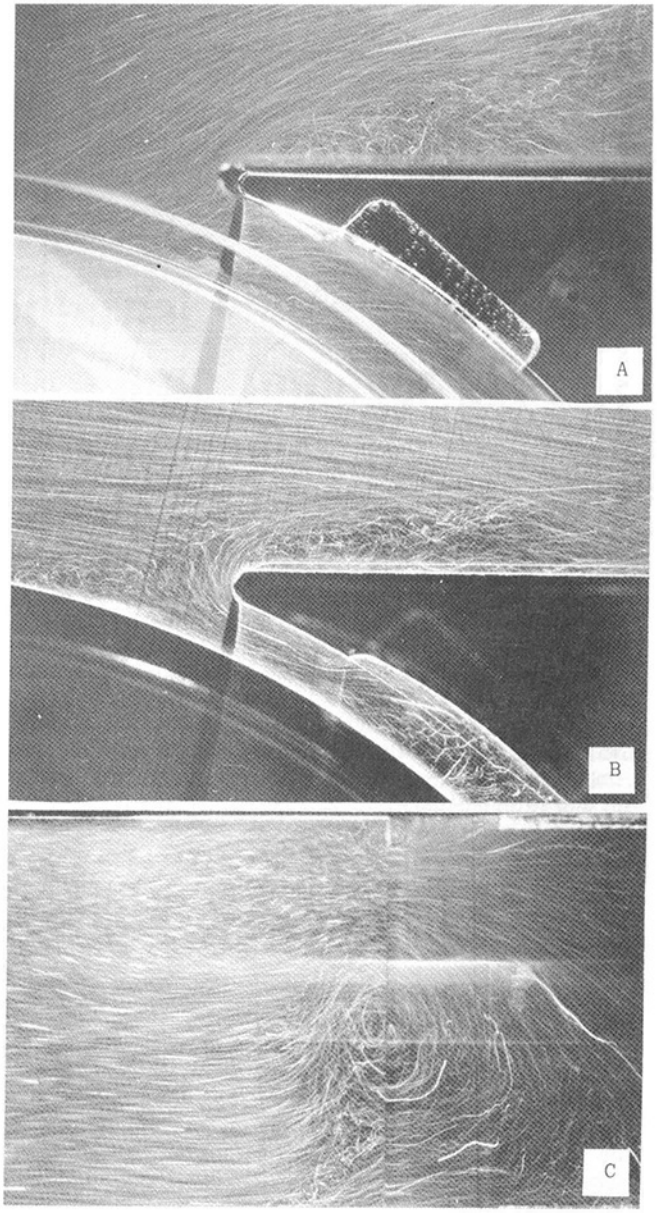

Fig. 13 Flow visualization at high mass flow in plane $1'$ (A), plane $1'''$ (B), and plane 2 (C)

It results in a swirling motion at the volute inlet as illustrated by the flow visualization in plane 2 (Fig. 13C). LDV measurements in the tongue gap (Fig. 14) confirm the large throughflow velocity at low mass flow and indicate that the zone of return flow, at high mass flow, extends over more than 60 percent of the volute width.

Conclusions

LDV measurements inside a logarithmic spiral volute show a flow structure that is similar to one observed previously in a straight simplified volute. The differences, due to the circumferential curvature of the volute and leakage flows in the tongue region, can be summarized as follows:

- The circumferential curvature of the volute is responsible for a radial gradient of the throughflow velocity. It also allows the throughflow velocity to influence the strength of the cross-sectional swirl.

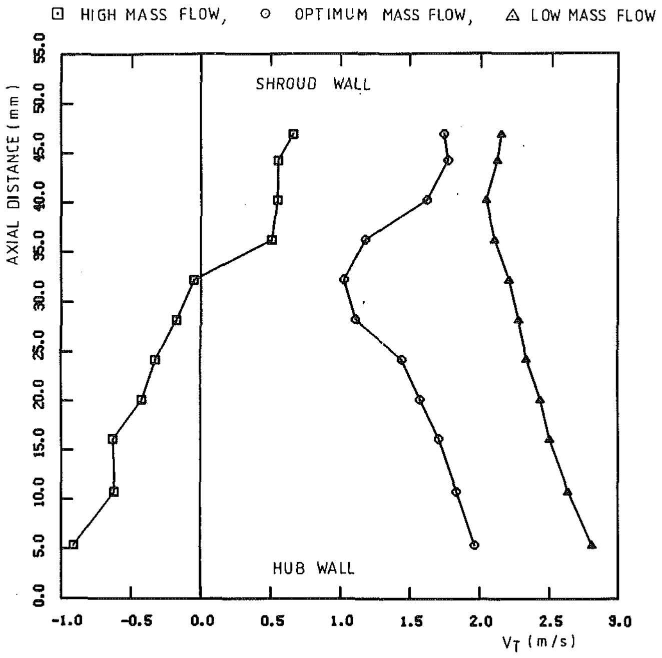

Fig. 14 Velocity distribution at the tongue gap for three different mass flows

- Leakage flows in the tongue region have an important impact on the location of the swirl center. They increase or decrease the flow in the volute and therefore influence the circumferential pressure distribution.

References

Brownell, R. B., and Flack, R. D., 1985, "Flow Characteristics in the Volute and Tongue Region of a Centrifugal Pump," ASME Paper No. 85-GT-82.

Flörkemeier, K. H., 1977, "Experimentelle Untersuchungen zur Optimierung von Spiral-gehause fur Kreiselpumpen mit tangentialen und radialen Druckstutzen," Diss. TU, Braunschweig, Federal Republic of Germany.

Iversen, N., Rolling, R., Carlson, J., 1960, "Volute Pressure Distribution, Radial Force on the Impeller, and Volute Mixing Losses of a Radial Flow Centrifugal Pump," ASME *Journal of Engineering for Power*, Vol. 82, No. 2, pp. 120–126.

Japikse, D., 1982, "Advanced Diffusion Levels in Turbocharger Compressors and Component Matching," *Proc. 1st Int. Conf. on Turbocharging and Turbochargers*, IMechE, London, pp. 143–155.

Lipski, W., 1979, "The Influence of Shape and Location of the Tongue of Spiral Casing on the Performance of Single Stage Radial Pumps," *Proc. 6th Conference on Fluid Machinery*, Budapest, pp. 673–682.

Lorett, J. A., and Gopalakrishnan, S., 1986, "Interaction Between Impeller and Volute of Pumps at Off-Design Conditions," ASME *Journal of Fluids Engineering*, Vol. 108, No. 1, pp. 12–18.

McLaughlin, D. K., and Tiederman, W. G., 1973, "Biasing Correction for Individual Realization of Laser Anemometer Measurements in Turbulent Flows," *The Physics of Fluids*, Vol. 16, No. 12, pp. 2082–2088.

Mishima, H., and Gyobu, I., 1978, "Performance Investigation of Large Capacity Centrifugal Compressors," ASME Paper No. 78-GT-3.

Sideris, M. Th., 1988, "Circumferential Distortion of the Flow in Centrifugal Compressors Due to Outlet Volutes," Ph.D. Thesis, VKI-University, Gent, Belgium.

Stiefel, W., 1972, "Experiences in the Development of Radial Compressors," in: *Advanced Radial Compressors*, von Karman Institute Lecture Series 50.

Van den Braembussche, R. A., and Hände, B. M., 1990, "Experimental and Theoretical Study of the Swirling Flow in Centrifugal Compressor Volutes," ASME JOURNAL OF TURBOMACHINERY, Vol. 112, pp. 38–43.

A. Goto[1]
Ebara Research Co., Ltd.,
4-2-1 Honfujisawa, Fujisawa-shi, Japan

Study of Internal Flows in a Mixed-Flow Pump Impeller at Various Tip Clearances Using Three-Dimensional Viscous Flow Computations

The complex three-dimensional flow fields in a mixed-flow pump impeller are investigated by applying the incompressible version of Dawes' Three-Dimensional Navier–Stokes code. The applicability of the code is confirmed by comparison of computations with a variety of experimentally measured jet-wake flow patterns and overall performances at four different tip clearances, including the shrouded case. Based on the computations, the interaction mechanism of secondary flows and the formation of jet-wake flow are discussed. In the case of large tip clearances, the reverse flow caused by tip leakage flow is considered to be the reason for the thickening of the casing boundary layer followed by the deterioration of the whole flow field.

Introduction

To improve mixed-flow pumps further, including performance at part-load conditions, appropriate understanding of the internal flow of impellers is essential. The flow pattern inside the impeller not only affects the performance of the impeller itself, but also dominates the performance of the diffuser, which accepts the impeller discharge flow. However, the complex flow fields in mixed-flow impellers are not fully understood because of the strong secondary flows caused by the flow passage curvature, Coriolis force, centrifugal force, the tip leakage flow, the inlet casing boundary layer, and so on.

The performance difference between shrouded and unshrouded impellers is a matter of great interest, because both kinds of impeller are widely used in centrifugal and mixed-flow turbomachinery. They often show quite different characteristics, especially at partial flow rates.

The effect of increasing tip clearance in unshrouded impellers is another point of interest, because the tip leakage flow affects not only peak efficiency but also performance at part-load conditions. There has been much discussion about optimum clearance, and Engeda and Rautenberg (1987) reported that some impellers are highly sensitive to tip clearance.

Eckardt (1976) measured the internal flow of an unshrouded high-speed centrifugal impeller, and Johnson and Moore (1983) discussed the development of jet-wake flow in a shrouded centrifugal impeller. Lenneman and Howard (1970), Howard and Kittmer (1975), Harada (1985), and Hamkins and Flack (1987) carried out comparisons between shrouded and unshrouded centrifugal impellers. However, the interaction mechanism between tip leakage flow and passage vortex is still unclear and only a few studies have been done to investigate the internal flow of mixed-flow impellers. Fraser et al. (1985) and Carey et al. (1986) measured the internal flows of mixed-flow impellers under various operating conditions using a laser-Doppler anemometry system.

The value of detailed measurements of internal flow fields is obvious. However, we have to admit that research programs based purely on experiments are time consuming, costly, and will give restricted information. The highly three-dimensional geometry of the flow passage often restricts the measurement of the internal flow, especially in endwalls and blade surface boundary layers.

Recently remarkable progress in three-dimensional Navier–Stokes solvers for turbomachinery flows by Moore et al. (1984), Hah et al. (1988), Dawes (1988), etc., is very encouraging, because they have been able to deal with the two basic features of the viscous flow in impellers: the development of secondary flows and the tip leakage flow. Although the computational methods are still not completely satisfactory, the application of a reliable computational code is very helpful in understanding internal flow and developing a new design concept. Because it is easy to process the computed results from many different points of view, we can obtain a great deal of useful information that is almost impossible to obtain through experiments.

---

[1] The computational work presented in this paper was carried out at the Whittle Laboratory while the author was a visitor at Cambridge University.

Contributed by the International Gas Turbine and presented at the 35th International Gas Turbine and Aeroengine Congress and Exposition, Brussels, Belgium, June 11–14, 1990. Manuscript received by the International Gas Turbine Institute January 31, 1990. Paper No. 90-GT-36. Associate Editor: S. A. Mosier.

Table 1 Design of impeller

	hub / midspan / shroud	
β_{1b} (deg)	27.8 / 18.3 / 14.8	Nmber of blades : 5
β_{2b} (deg)	31.8 / 25.3 / 20.7	Design flow rate : 8.7 m^3 / min
r_1 (mm)	58.0 / 102.3 / 132.5	Design pump head : 7.0 mH_2O
r_2 (mm)	142.5 / 157.8 / 171.7	Rotational speed : 800 rev. / min

Table 2 Computational mesh

Case	Clearance (mm)	Grid	Number of mesh in clearance
S	0.0	$29 \times 53 \times 29$	0
U05	0.5	$29 \times 53 \times 29$	2
U10	1.0	$29 \times 53 \times 31$	4
U15	1.5	$29 \times 53 \times 33$	6

(Grid : blade-to-blade × streamwise × spanwise)

In the present paper, the incompressible version of the Navier–Stokes solver developed by Dawes (1988) has been applied to a mixed-flow pump impeller at four different tip clearances, including the shrouded case. The predicted results are compared with the experimental results measured at the exit of the impeller using the two-hole pitot probe with high-frequency response developed by Goto (1988). Based on the predicted internal flow, the interaction mechanism between passage vortices and tip leakage flow and the effects of increasing tip clearance are discussed.

Computational Method

Numerical Scheme. The unsteady Reynolds-averaged Navier–Stokes equations in a rotational frame are discretized in integral finite volume form using cylindrical coordinates. The flow field is divided into nonorthogonal hexahedral cells and the flow variables are stored at cell centers. The discretized equations are time-marched using an implicit "pre-processed" algorithm (Dawes, 1988). Turbulence is modeled by a two-layer mixing length model patterned after Baldwin and Lomax (1978). The multigrid acceleration technique was not used in the present computations because of an as yet unexplained numerical instability.

Computational Grid. The computations were performed for one mixed-flow impeller design (Table 1) at four different tip clearances, including the shrouded case as shown in Table 2. Figure 1 shows the computational grid in case U05 (un-

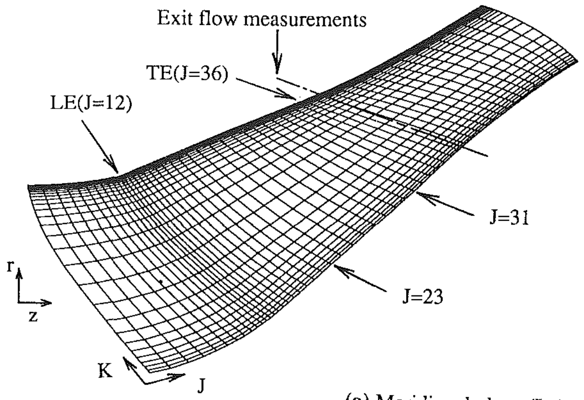

(a) Meridional plane (I=15)

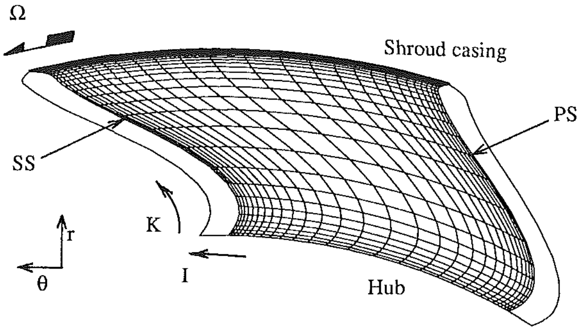

(b) Quasi-orthogonal plane (J=31)

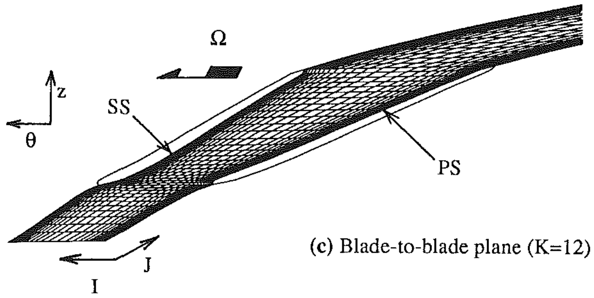

(c) Blade-to-blade plane (K=12)

Fig. 1 Computational grid (unshrouded case U05)

Nomenclature

C = absolute velocity
H = pump head, m H_2O
(I, J, K) = grid coordinates (blade-to-blade, streamwise, spanwise)
$\overline{K}$ = mass-averaged kinetic energy flux
Q = volumetric flow rate, m^3/s
Q^* = flow rate ratio = $Q/(Q$ at design point)
(r, θ, z) = cylindrical coordinates
U = peripheral blade speed
W = relative velocity
β = flow yaw angle = $\sin^{-1}(\sqrt{W_z^2+W_r^2}/W)$
β_b = blade angle
γ = flow pitch angle = $\tan^{-1}(W_r/W_z)$
ξ = vorticity
Ψ^* = head coefficient = (head) / (U_{2m}^2/g)
Ψ_e^* = mass-averaged Euler's head coefficient = U_2C_{u2}/U_{2m}^2 (C_{u1} = 0 is assumed)
Ψ_t^* = mass-averaged total head at impeller exit
Ψ_p^* = pump head coefficient
$\Delta\Psi^*$ = loss head coefficient
Ω = angular rotation frequency, rad/s

Subscripts

1 = inlet
2 = exit
$2m$ = exit midspan
i = inviscid
n = component normal to stream surface
r = radial component
s = streamwise component
z = axial component
θ = circumferential component
τ = component perpendicular to streamline on stream surface

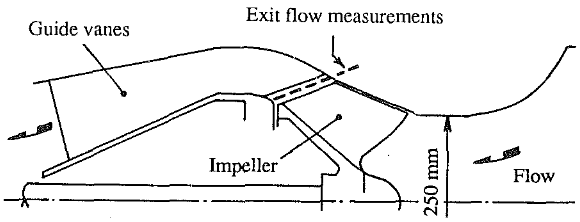

Fig. 2 Mixed-flow pump geometry (unshrouded case)

shrouded impeller with a tip clearance of 0.5 mm). The grid points are clustered near the endwalls and blade surfaces, and the nodes inside the tip clearance are equally spaced. The blade tip is rounded off in the simulation.

Initially, relatively coarse grids of $19 \times 53 \times 29$ and $29 \times 53 \times 19$ (pitchwise × streamwise × spanwise) were applied for cases S and U05. It was confirmed by comparison with measurements that a fine grid in the blade-to-blade direction should be used for the shrouded impeller because the contribution of the blade boundary layers to the thickening of the endwall boundary layer is relatively large in this case. On the other hand, in the case of the unshrouded impeller, the tip leakage flow dominates the whole flow field and a fine grid in the spanwise direction is required. However, for the final computations, fine grids in both directions are used to keep the spatial resolution almost the same for every case.

The inlet boundary is placed at a minimum distance, 50 percent of the meridional chord length, from the leading edge in order to avoid mesh distortion caused by the high stagger angle of the present impeller. The $29 \times 53 \times 29$ grid requires about 13 Mbytes storage and 7 hours of CPU time on an Alliant FX/4 computer (four vector processors driven concurrently). The code processes at about 0.8 ms per point per time step on a single processor, and about 2500 time steps were required to achieve convergence.

Boundary Conditions. At the inlet, the total pressure, the yaw angle, and pitch angle of the flow were specified and fixed. In every case, the inlet endwall boundary layer thickness was assumed to be 13 mm (5 percent of the inlet diameter) on the basis of preliminary experiments. The prerotation was assumed to be zero. At the exit boundary, the hub static pressure was specified and fixed, and its radial variation was derived from a simple radial equilibrium equation.

Periodic conditions were enforced along the boundaries upstream, downstream, and inside the tip clearance. For cell faces aligned with solid boundaries, zero fluxes of mass and momentum were imposed. The wall function was used to prescribe the shear stress on solid surfaces in regions where the mesh was too coarse to resolve down to laminar sublayer scale. While the shroud casing was stationary, the hub surface rotated at the blade speed.

Experimental Procedures and Pump Characteristics

Apparatus. Performance tests and exit flow measurements were carried out on a mixed-flow pump (Fig. 2) at four different tip clearances of the impeller including the shrouded case (Table 2). The geometry of the impeller and design conditions are given in Table 1. The specific speed of the pump at the best efficiency point is $\Omega \cdot \sqrt{Q}/\ (gH)^{3/4} = 1.34$. The pump was placed in a closed flow loop consisting of a 440-mm-dia suction pipe, a 350-mm-dia delivery pipe, and a reservoir tank. Water was used as the test fluid and the flow rate was measured with venturi tubes and mercury manometers. The performance tests were conducted according to ISO standards.

The unshrouded impeller was in fact a shrouded impeller with the front shroud removed. The tip clearance of the unshrouded impeller was adjusted by sliding the casing in the axial direction. Since the meridional shape of the blade tip is linear, the tip clearance was changed uniformly along the casing. All of the tests were carried out at a rotational speed of 800 rpm.

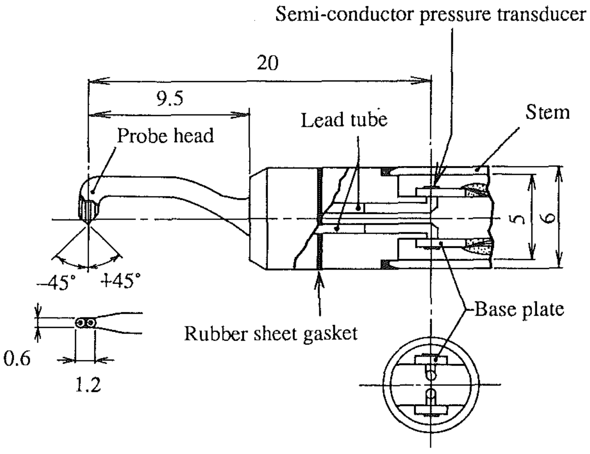

Fig. 3 Construction of two-hole pitot probe

Exit Flow Measurements. The three-dimensional exit flow fields of the impeller were measured using the two-hole pitot probe developed by Goto (1988). Figure 3 shows the probe construction schematically. Two diffusive semiconductor pressure transducers with a maximum pressure of 0.1 MPa and a frequency response of 100 kHz were placed in the stem tube. Two pressure holes on the probe head were connected to the transducers by lead tubes of 0.4-mm inside diameter filled with silicon oil. The resonance frequency of the pressure sensing system was about 5.6 kHz and was high enough compared with the blade passing frequency of 67 Hz.

The pitot probe was mounted on a traverse unit with two stepping motors controlled by a microcomputer. The exit flow field was measured at 13 spanwise locations between the hub and the shroud casing. The pitot probe was placed parallel to the trailing edge of the blade (Fig. 1*a*). The distance between the probe and the trailing edge was 6.3 percent of the meridional blade chord length at the midspan. The pressure fluctuation sensed by the pressure transducers was measured by a phase-locked multisampling and averaging technique using the on-line computer. A set of 11 pressure data for each pressure hole, obtained at different probe setting angles, was used to calculate the velocity vector and the static pressure from the calibration curves.

Accuracy of Measurements. The probable uncertainty in the data reduction process and the measuring system of the pitot probe has been evaluated by Goto (1988) using a calibration test rig. The accuracy is ±2.5 percent in the static pressure, ± 1.3 percent in the velocity, ±0.3 deg in the yaw angle, and ±1 deg in the pitch angle.

It has also been confirmed that the steady-state calibration curves are correctly applicable to the present unsteady flow (Goto, 1988). Since the velocity vector and the static pressure at each sampling point are calculated using 4950 sampled data (=11 probe angle positions × 450 samples), the flow field phase-locked to the impeller is considered to be properly averaged in the statistical sense.

The flow rates measured by the two-hole pitot probe deviated -5.5 ± 2.5 percent from those obtained by the venturi tubes. If we assume that the bias of -5.5 percent was caused by the error in the initial setting of the probe yaw angle, it corresponds to 0.5 deg error.

Head-Flow Characteristics. Figure 4 shows the head-flow characteristics at four different clearances. Euler's head coef-

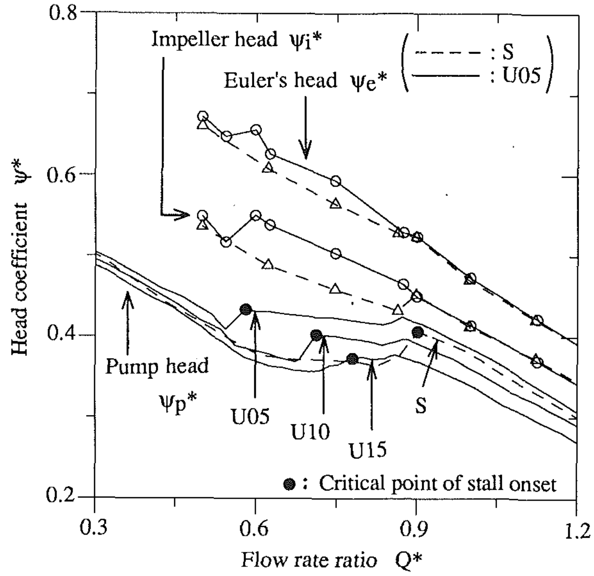

Fig. 4 Head-flow characteristic curves

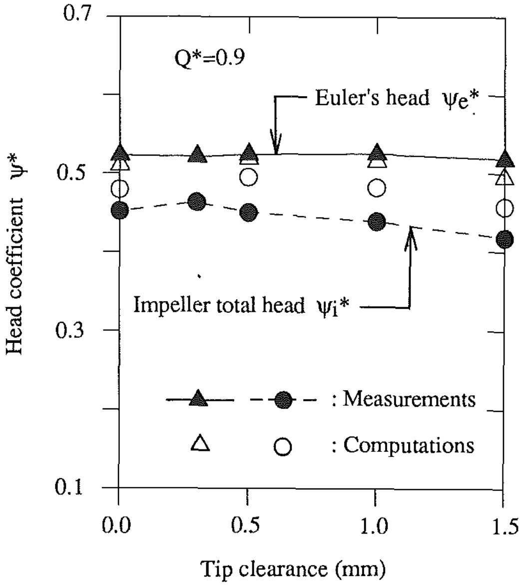

Fig. 5 Comparison of overall performance

ficient Ψ_e^* and the total head coefficient Ψ_i^* are also presented in cases S and U05. All the cases exhibit positively sloped head-flow characteristics when the flow rate is decreased below critical values. However, the critical flow rate in case S (shrouded impeller) is fairly high compared with that in case U05 (unshrouded impeller).

Euler's head Ψ_e^* in case S is nearly equal to that in case U05 between $Q^*=0.9$ and $Q^*=1.2$. However, in case S, the total head Ψ_i^* at the exit of the impeller drops suddenly at $Q^*=0.87$ and the fall almost corresponds to that of the pump head Ψ_p^*. The measured loss distribution behind the impeller (the data are not presented in this report) shows an abrupt expansion of the high loss region near the shroud at this flow rate. From this, it is concluded that the positive head-flow characteristic in case S was caused by a stall onset in the impeller. The stall in case U05 occurred at the lower flow rate of $Q^*=0.54$ and both cases show similar head-flow characteristics below this flow rate. This fact suggests that some amount of tip leakage flow might improve the flow fields near the casing and delay the onset of a stall.

Despite both shrouded and unshrouded cases revealing similar characteristic curves above $Q^*=0.9$, there should be large differences in the internal flow fields of the impeller. Because of this, all computations presented in this report have been carried out at the critical flow rate of $Q^*=0.9$ and the difference of the flow fields will be discussed in the following sections.

The tip clearance has a great influence on pump performance. Although the impeller efficiency at design point is almost the same between cases S and U05, it was observed that the overall pump efficiency in case S was lower than that in case U05 by 3.7 percent. In case U10, the pump and impeller peak efficiency were lower than those of impeller U05 by 5 percent and 3.5 percent, respectively (the data are not presented in this report). Widening the clearance by only 0.5 mm, i.e., 0.8 percent of the exit blade span or 0.15 percent of the blade chord length, caused the internal flow to deteriorate completely. Figure 4 also shows that the critical flow rate at the stall point increases with tip clearance.

Comparison Between Computations and Measurements

Overall Performance. The mass-averaged Euler's head and impeller head coefficients are shown in Fig. 5 for various tip clearances including the shrouded case.

It is said that Euler's head decreases with tip clearance because of the increased blockage in the tip region. However, the experimental data show that Euler's head Ψ_e^* is independent of tip clearances in the present clearance range. Also note that the shrouded impeller has achieved the same Euler's head as the unshrouded impellers. These phenomena were well predicted by the computations almost within the accuracy of the measurements.

The impeller head decreases with tip clearance because of the increase in tip leakage loss and associated secondary losses. The predicted results show a similar rate of decrease with increased tip clearance. However, the flow losses were underestimated in all cases. This discrepancy is considered to be caused by the slower mixing of the predicted jet-wake flow as discussed in the following section.

Exit Flow-Field. Figures 6 and 7 compare the predicted flow fields with the measurements on quasi-orthogonal planes behind the impeller for various tip clearances. Figure 6 shows contour maps of the relative velocity, and Fig. 7 the loss distribution for 1.5 pitches. The left column shows measurements and the right computations. The top figures show the shrouded cases and the bottom figures the unshrouded cases with the largest tip clearance. The locations of the trailing edges (TE) are shown by broken lines. The contour lines are drawn with the same contour interval. The velocity and the loss head are normalized by U_{2m} and U_{2m}^2/g, respectively.

The computations have succeeded in predicting many of the important features of the exit flow of mixed-flow impellers. The jet-wake flow pattern, for example, is clearly predicted and shows good agreements with patterns measured experimentally. In shrouded case S, the wake flow region is observed at the casing-suction surface corner region. In unshrouded case U05, this region disappears because of the blowing effect of the tip leakage flow. The wake flow, in this case, is formed at the midpitch region near the casing.

The great effects of differences in tip clearance are apparent if we compare the measured flow fields for impellers U05 and U10. The experimental results show that only the 0.8 percent widening (based on the blade height) of the clearance changes the flow fields drastically; expansion of high loss wake flow region. In cases U10 and U15, the prediction also shows remarkable expansion of the wake flow. The low-momentum fluid migrates closer to the blade suction surface (Figs. 6*c* and *d*) compared to case U05 (Fig. 6*b*). This phenomenon seems to be very unusual. According to some research on axial com-

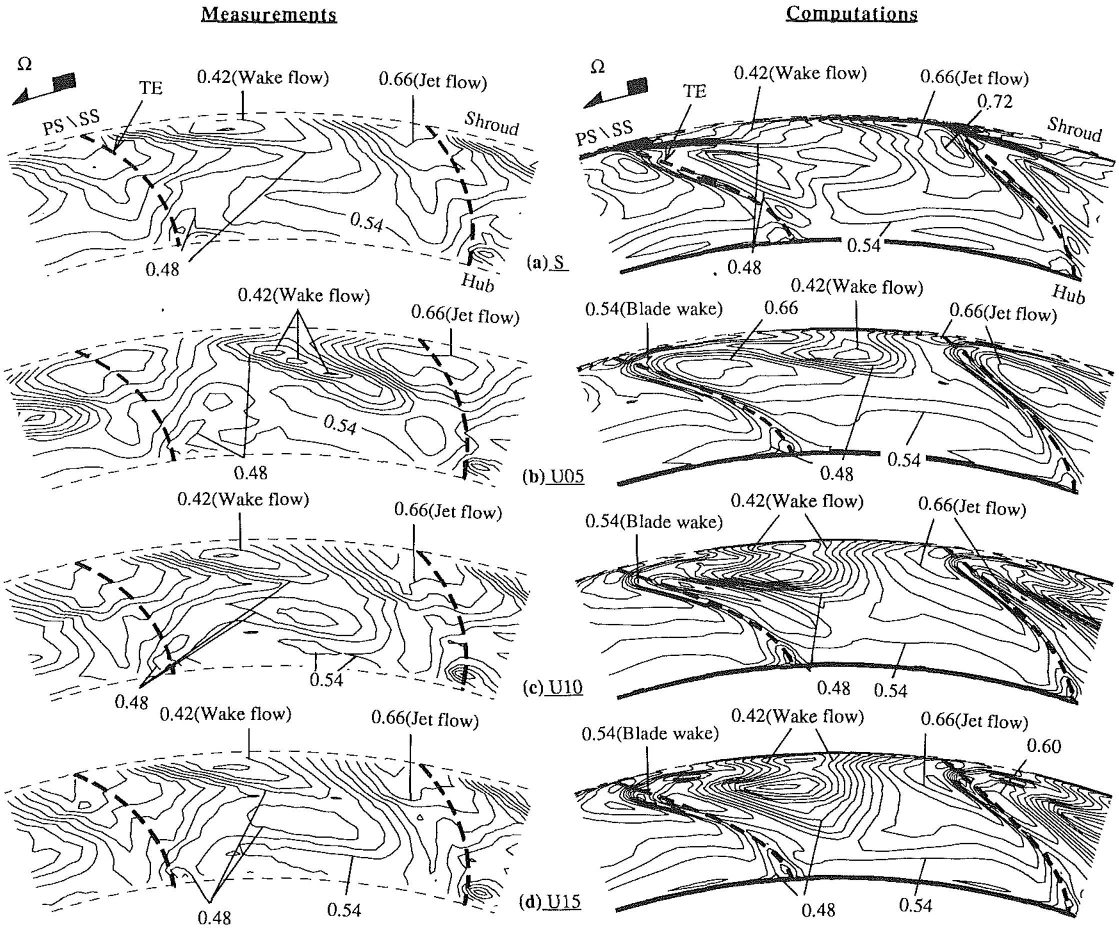

Fig. 6 Comparison of exit velocity distribution (contour interval = 0.03)

pressor rotors, tip leakage flow becomes stronger with increasing clearance and the wake flow region moves toward the pressure side of the adjacent blade wake. However, the wake regions in cases U10 and U15 move in the opposite direction toward the suction side of the blade. This phenomenon is also well predicted by computations. Its mechanisms is investigated in the next section.

Some discrepancy is also observed between computations and measurements. The computational results for the unshrouded cases show a clear region of blade wake between the hub and the shroud casing, each with a region of jet flow on either side (Figs. 6*b*, *c*, *d*, right column). This flow pattern is not observed in the measurements, and it is considered that quicker mixing between the blade wake and the two adjacent jet flows takes place in reality. This might be one reason for the underestimation of the flow loss by computations (Fig. 5). The peak values of the jet flows are well predicted. Computations give $W(\text{Jet})/W(\text{Mean}) = 1.26 \sim 1.37$ compared with measurements of $1.26 \sim 1.31$. On the other hand, the predicted depth of the wake flows tends to be deeper than that of measurements. Computations show $W(\text{Wake})/W(\text{Mean}) = 0.57 \sim 0.80$ compared with measurements of about 0.74. In addition, the measurements in unshrouded cases, especially in case U05, show that the high loss region penetrates in the spanwise direction towards the hub. This phenomenon was not observed clearly in the predictions.

Discussion of Computational Results

The above-described agreement between computations and measurements of jet-wake flow patterns is quite encouraging in view of the complex and strong interaction between tip leakage flow and passage vortices that dominates the flow fields in mixed-flow impellers. In this section, the predicted internal flow is discussed more fully from the secure standpoint that the basic features of the internal flow fields have been satisfactorily simulated by present computations.

Presentation of Results. Besides velocity contour and vector maps, three kinds of presentation of computed results are introduced to help the understanding of flow fields: vorticity contour maps, secondary velocity vector maps, and particle path lines.

The vorticity vector components (ξ_z, ξ_θ, ξ_r) are calculated through numerical differentiation by applying the P-spline function to the predicted absolute velocity distribution (C_z, C_θ, C_r). That is,

$$\xi_z = (1/r)\cdot\partial(r\cdot C_\theta)/\partial r - (1/r)\cdot\partial C_r/\partial\theta$$

$$\xi_\theta = \partial C_r/\partial z - \partial C_z/\partial r$$

$$\xi_r = (1/r)\cdot\partial C_z/\partial\theta - \partial C_\theta/\theta_z$$

The vorticity vector is normalized by twice the angular velocity of the impeller $2\cdot\Omega$ and then transformed into the streamwise, perpendicular, and normal components (ξ_s, ξ_τ, ξ_n) as follows:

$$\xi_s = (\sin\beta\cdot\cos\gamma\cdot\xi_z - \cos\beta\cdot\xi_\theta + \sin\beta\cdot\sin\gamma\cdot\xi_r)/(2\cdot\Omega)$$

$$\xi_\tau = (\cos\beta\cdot\cos\gamma\cdot\xi_z + \sin\beta\cdot\xi_\theta + \cos\beta\cdot\sin\gamma\cdot\xi_r)/(2\cdot\Omega)$$

$$\xi_n = (-\sin\gamma\cdot\xi_z + \cos\gamma\cdot\xi_r)/(2\cdot\Omega)$$

The streamwise vorticity ξ_s is very useful for understanding the secondary flow motion on quasi-orthogonal planes, the perpendicular vorticity ξ_τ for the endwall boundary layer development on meridional planes, and the normal vorticity ξ_n

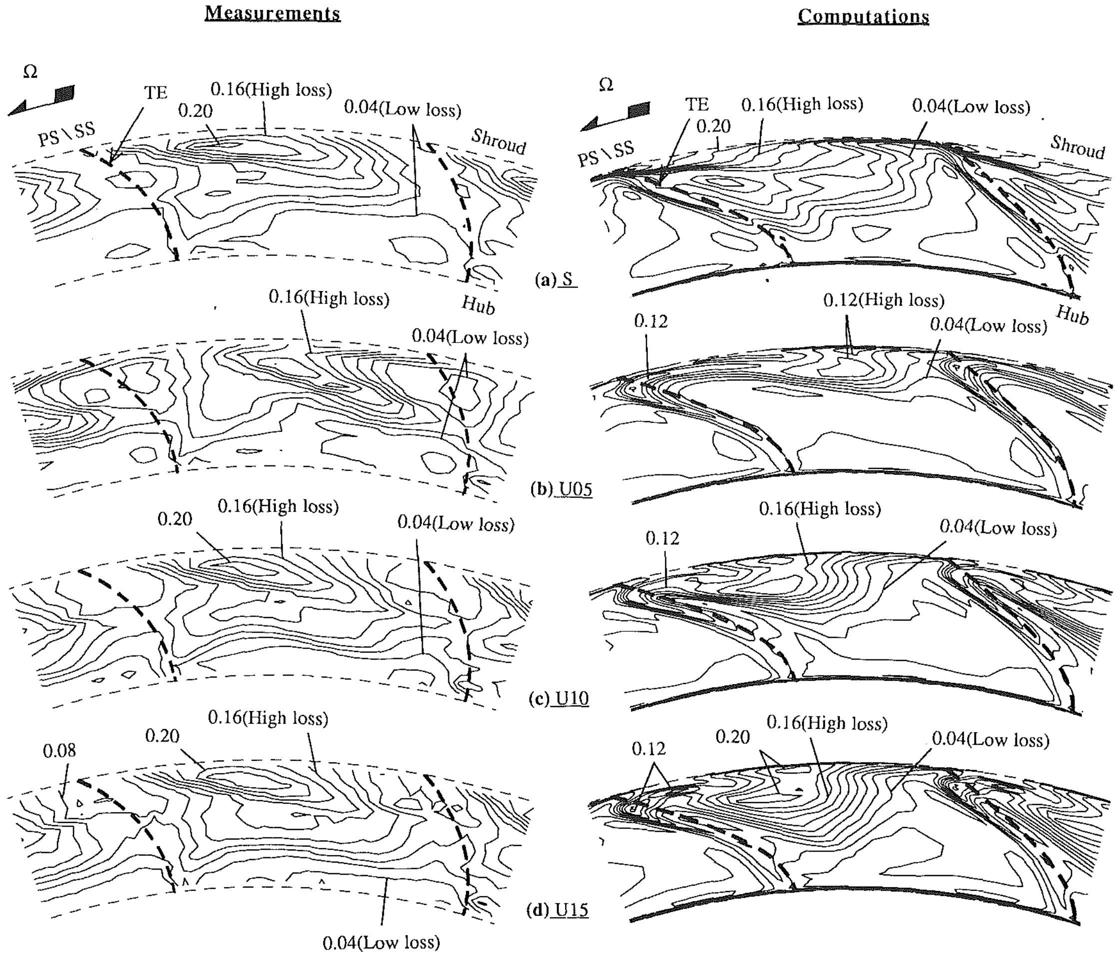

Fig. 7 Comparison of exit loss distribution (contour interval = 0.02)

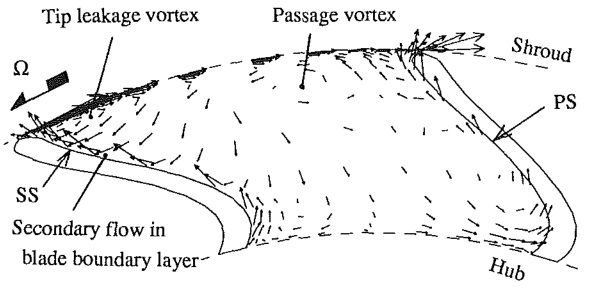

Fig. 8 Secondary flow vectors on quasi-orthogonal planes (unshrouded case U10, $J = 31$)

for the blade surface boundary layer development on blade-to-blade planes.

The secondary flow vector (W_τ, W_n) on a quasi-orthogonal plane is calculated as the velocity vector that represents departures from the inviscid flow direction.

$$W_\tau = \cos\beta_i \cdot \cos\gamma_i \cdot W_z + \sin\beta_i \cdot W_\theta + \cos\beta_i \cdot \sin\gamma_i \cdot W_r$$

$$W_n = -\sin\gamma_i \cdot W_z + \cos\gamma_i \cdot W_r$$

For simplicity, the inviscid flow yaw angle β_i at each span position is calculated from the area-averaged flow direction at the midspan assuming a free vortex flow pattern between the hub and the casing. The pitch angle γ_i is calculated from the streamwise meridional mesh direction. An example of secondary flow vectors obtained this way on a quasi-orthogonal plane is shown in Fig. 8 for the unshrouded case (at $J = 31$, case U10). We can observe the tip leakage vortex, the passage vortex, and the secondary flow on the blade surfaces.

The particle path lines on quasi-orthogonal planes are generated by following markers introduced every two grid node points. Each marker is moved at the locally interpolated secondary flow velocity with a constant time step. The time step is sufficiently small not to influence the path lines thus obtained.

Comparison of Shrouded and Unshrouded Cases. Figure 9 shows the relative velocity vectors on meridional planes close to the blade surfaces in the shrouded case S and the unshrouded case U05. In the latter case, only the tip region is presented, because the flow pattern in other regions is almost the same. Strong secondary flows from the hub to the tip induced by the centrifugal force acting on the fluid in the blade boundary layer are clearly observed, especially on the suction surface of the blade (Fig. 9*b*). The almost stagnant flow near the hub on the pressure surface (Fig. 9*d*) increases its relative velocity quickly toward the trailing edge. This acceleration is caused by an inflow of the main flow into the hub-pressure surface corner because of the blockage at the opposite corner, i.e., the casing-suction surface corner. In the unshrouded case U05, the tip leakage flows crossing over the blade tip are observed as reverse flows on the meridional planes (Figs. 9*a* and *c*), because the stagger angle of the blade is large and the leakage flows tend to be normal to the blade camber.

Figure 10 shows the relative velocity vectors on the endwall blade-to-blade planes. The secondary flows on the hub surface are almost the same for the shrouded and unshrouded cases. The secondary crossflows from the pressure side to the suction side are clearly observed. On the shroud surface in case S, the crossflows interact with the throughflows around the midpitch region. On the other hand, in case U05 (Fig. 10*c*), strong tip leakage flows cause negative axial velocity near the suction surface, and this tendency becomes significant with increasing tip clearance. The tip leakage flow is strongest near the leading edge where the blade loading is highest.

Figures 11–13 show the flow fields on quasi-orthogonal planes at three meridional stations: 46 percent ($J=23$), 79 percent ($J=31$), and 100 percent ($J=36$, trailing edge) of me-

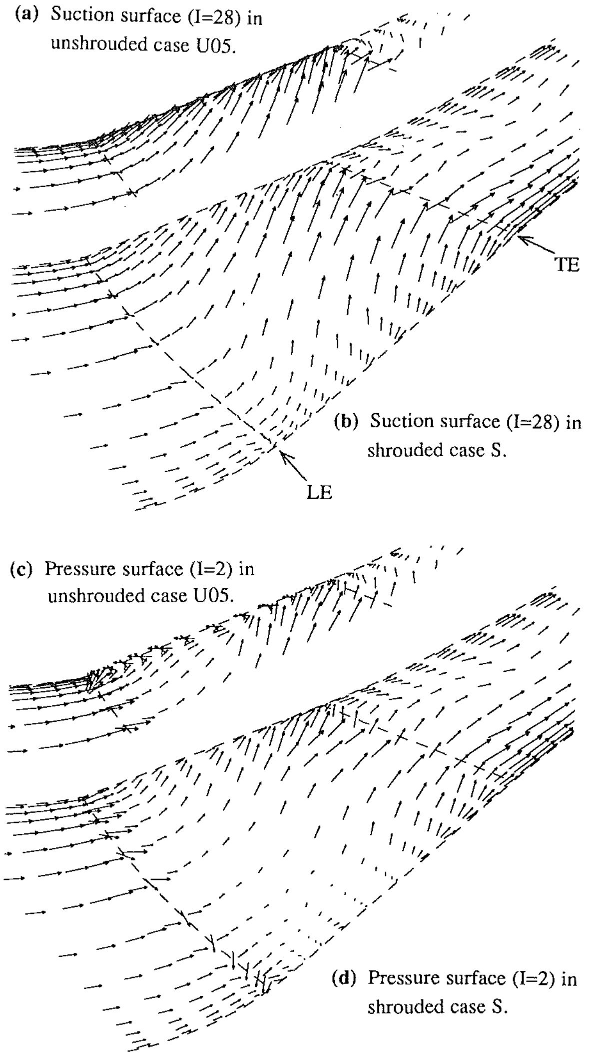
(a) Suction surface (I=28) in unshrouded case U05.

(b) Suction surface (I=28) in shrouded case S.

(c) Pressure surface (I=2) in unshrouded case U05.

(d) Pressure surface (I=2) in shrouded case S.

Fig. 10 Relative velocity vectors on blade-to-blade planes

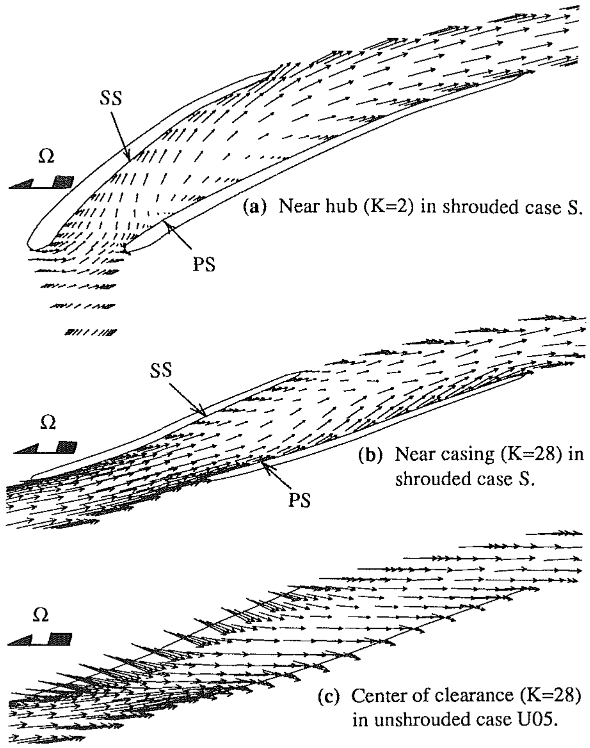
(a) Near hub (K=2) in shrouded case S.

(b) Near casing (K=28) in shrouded case S.

(c) Center of clearance (K=28) in unshrouded case U05.

Fig. 9 Relative velocity vectors on meridional planes

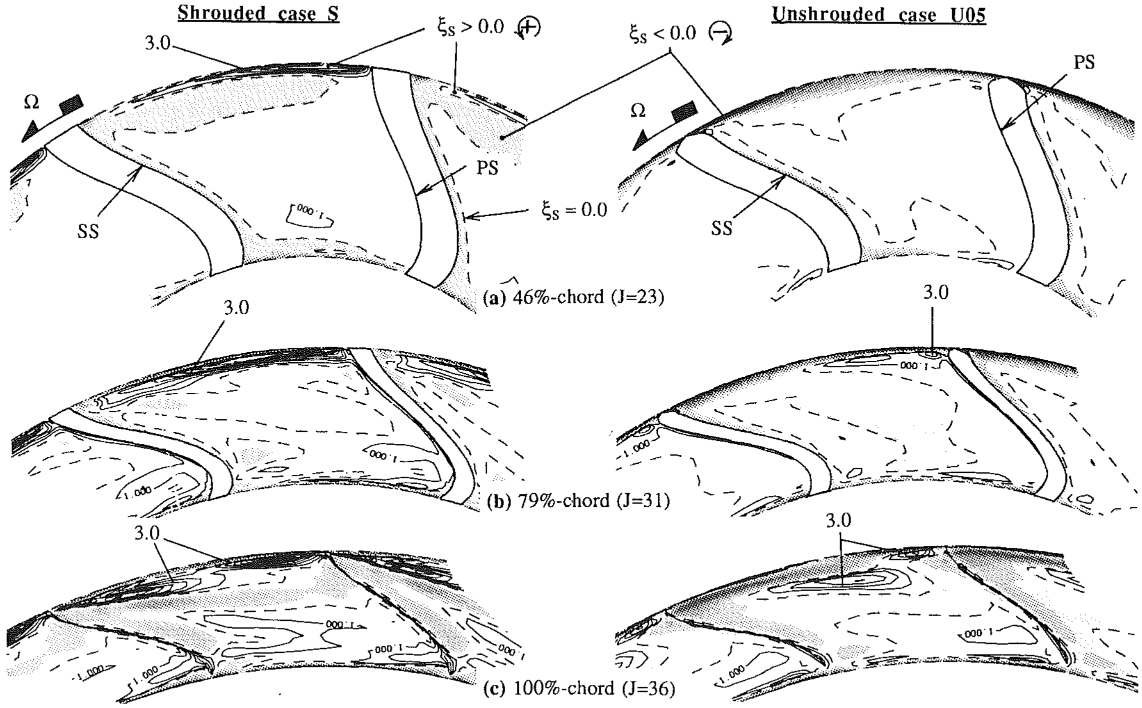

Fig. 11 Comparison of streamwise vorticity development (contour interval = 1.0)

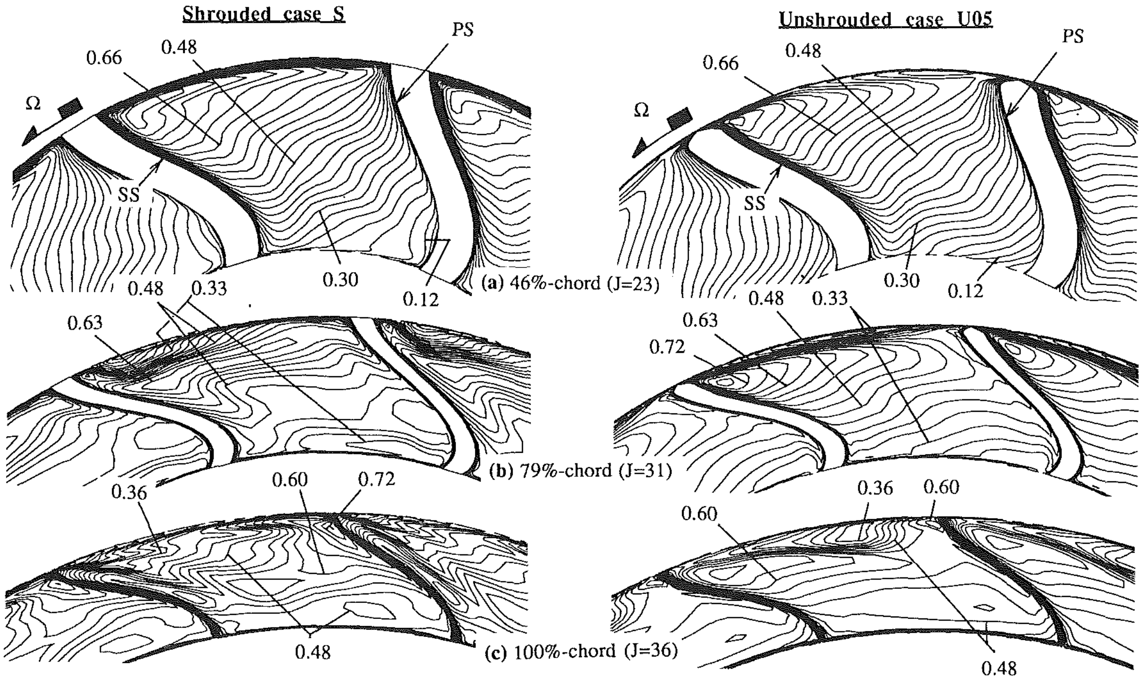

Fig. 12 Comparison of relative velocity development (contour interval = 0.03)

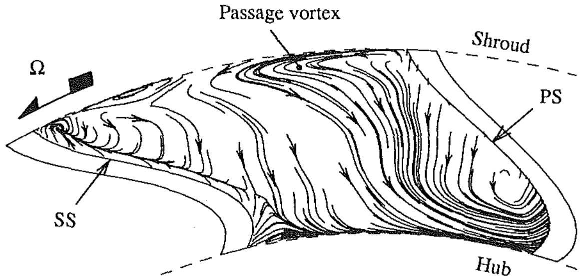

(a) Shrouded case S

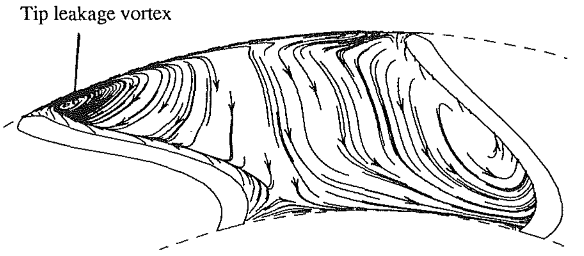

(b) Unshrouded case U05

Fig. 13 Comparison of particle path lines (79 percent chord, $J = 31$)

ridional blade chord; see Fig. 1(*a*). In each figure, the left column shows the shrouded case (S) and the right column the unshrouded case (U05). Figures 11 and 12 show contour maps of the streamwise vorticity and the relative velocity, respectively, and Fig. 13 shows the particle path lines at 79 percent chord location. The impeller is rotating in the counterclockwise direction. In Fig. 11, the positive counterclockwise vorticity is presented by ordinary contour lines, and the negative clockwise vorticity by shaded contours. The broken lines show the zero vorticity contours.

In shrouded case S (see left column), a strong passage vortex with positive vorticity has already developed at 46 percent chord station near the shroud-pressure surface corner (Figs. 11*a* and 13*a*). The low-momentum fluid in the casing and pressure surface boundary layer is displaced by this passage vortex toward the shroud-suction surface corner. The low-momentum fluid in the suction surface boundary layer is also conveyed to this region by the strong secondary flows on the blade (Fig. 9*b*). The potential core, originally situated at the shroud-suction surface corner (Fig. 12*a*), is displaced toward the midspan position (Fig. 12*b*) and then toward the pressure surface (Fig. 12*c*), and finally the well-known jet-wake flow pattern is established. In this case, the wake flow at the exit is settled close to the suction surface, and the jet flow close to the pressure surface of the blade.

In the unshrouded case U05 (see right column), the tip leakage flow with strong negative vorticity is observed at the casing-suction surface corner (Fig. 11*a*). Because of the leakage flow from the pressure to the suction surface of the blade, the relative velocity around the casing-pressure surface corner is relatively high. The casing boundary layer at the 46 percent chord position becomes fairly thin (Fig. 12*a*). The development of the passage vortex is obstructed by the tip leakage flow, and the positive vorticity is not observed at the 46 percent chord position (Fig. 11*a*). As is observed in the downstream positions (79 and 100 percent chord), the passage vortex interacts with the tip leakage vortex around the middle of the flow passage near the casing (Figs. 11*b* and 13*b*). Although the center of the tip leakage vortex is situated close to the casing-suction surface corner, the high loss fluid migrates around the interaction region and the wake flow is established in this region (Fig. 12*c*).

For both cases, counterclockwise vortex motion is observed near the hub-pressure surface corner (Figs. 8 and 13). Since no strong streamwise positive vorticity is observed in this region (Fig. 11*b*), this flow pattern is considered to be caused not by secondary flow but by the deflection of the main flow due to the blockage in the casing region.

Effects of Tip Clearance. Measured loss distribution (Fig 7, left column) shows a drastic change in flow pattern between tip clearances of 0.5 mm (U05) and 1.0 mm (U10). Moore and Adhye (1985) worked on the loss generation mechanism in turbine cascades and reported the dissipation of the secondary kinetic energy at the downstream of the trailing edge generating

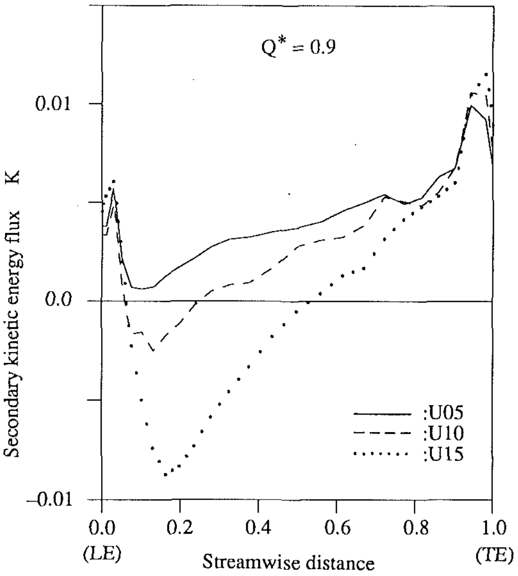

Fig. 14 Mass-averaged secondary kinetic energy flux of unshrouded impellers

a substantial amount of flow loss. The computational results of Pouagare and Delaney (1986) showed a high rate of dissipation of secondary kinetic energy from the midchord location when the compressor cascade had a tip clearance. They concluded that this was caused by the interaction between tip leakage flow and the passage vortex.

In this report, the mass-averaged kinetic energy flux of the secondary flow is defined as follows:

$$\overline{K}=\int_A W_q\cdot(W_\tau^2+W_n^2)/2/U_{2m}^2\cdot dA/\int_A W_q\cdot dA$$

where dA represents the area of a cell face and W_q the throughflow velocity normal to the cell face. Figure 14 shows the streamwise development of the mass-averaged secondary kinetic energy flux $\overline{K}$ for three different tip clearances.

The flux of the kinetic secondary energy peaks near the trailing edge and reaches nearly the same values for every tip clearance. This suggests that the amounts of loss generated by the dissipation of the secondary kinetic energy downstream of trailing edge are almost the same for these three cases. However, negative fluxes of kinetic energy are observed at the fore part of the blade for clearances greater than 1.0 mm. This is simply due to the strong reverse flow near the tip caused by tip leakage flow as shown in Figs. 9(*a*) and 10(*c*). Figure 15 compares the perpendicular vorticity on the meridional plane at the midpitch in cases U05 and U10. The quick development of the casing boundary layer is clearly observed in the negative flux region of the large clearance case. Lakshminarayana et al. (1982) reported the "energizing" of the casing boundary layer by the tip leakage flow. However, the present computations suggest that the casing boundary layer is de-energized near the leading edge by the negative flux of the mass-averaged kinetic energy of the tip leakage flow. This causes a rapid increase in the boundary layer thickness (Fig. 15*b*) and deterioration in the flow fields (Fig. 7*c*). Probably, the energizing and/or de-energizing effects will depend on the stagger angle of the blade, the blade loading, and the geometry of the clearance.

As has already been pointed out in the previous section, the wake flow of the unshrouded impeller with large tip clearance settles closer to the casing-suction surface corner than that of the unshrouded impeller with small clearance (compare Fig. 6*c* with Fig. 6*b*). The mechanism of this particular phenomenon is explained as follows. The tip leakage vortex becomes strong as the clearance increases. However, the passage vortex also becomes strong and develops quickly (compare Figs. 16*a* and

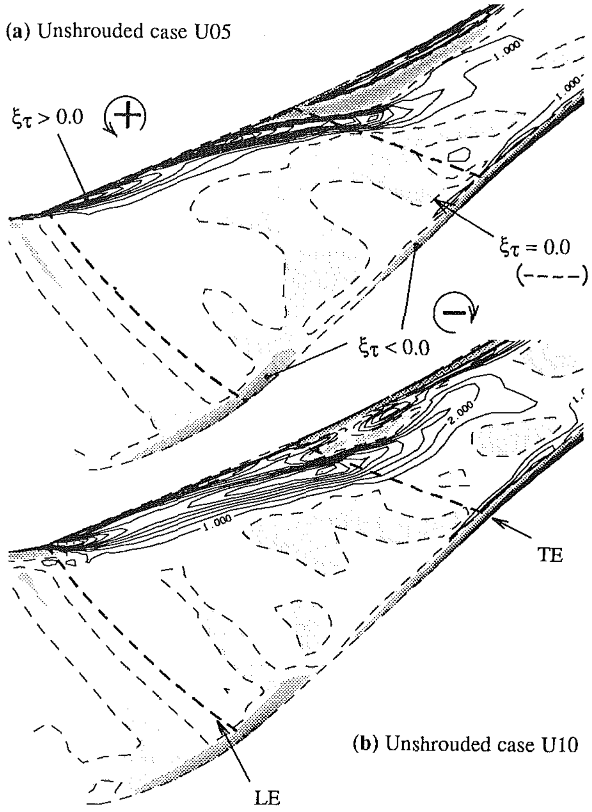

Fig. 15 Contour maps of perpendicular vorticity on meridional planes (I = 15, contour interval = 1.0)

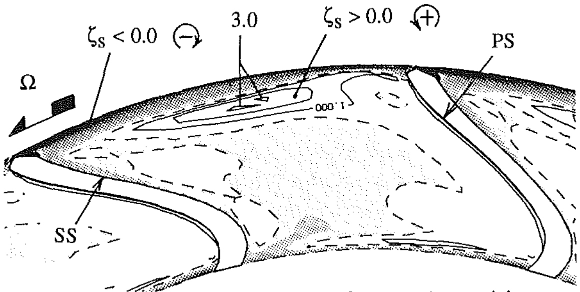

(a) Contour map of streamwise vorticity
(Contour interval = 1.0)

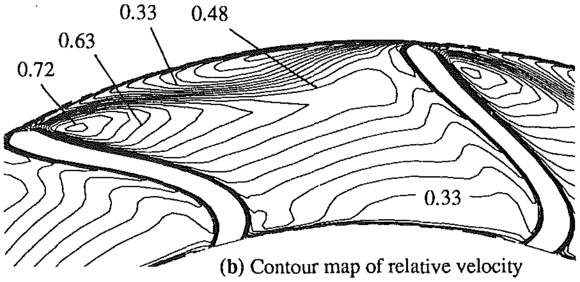

(b) Contour map of relative velocity
(Contour interval = 0.03)

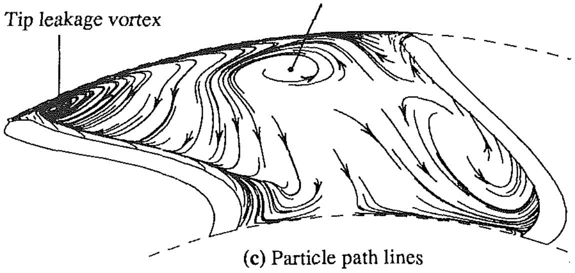

(c) Particle path lines

Fig. 16 Internal flow of unshrouded case U10 (79 percent chord, J = 31)

c with Figs. 11b and 13b) because of the thick casing boundary layer (Fig. 15b) caused by the tip leakage induced reverse flows. Consequently, the location of the wake flow, formed in the interaction region between the tip leakage flow and the passage vortex, settles closer to the suction surface.

Concluding Remarks

The application of a reliable computational code enables us to improve our understanding of the internal flow fields of turbomachines. The applicability of the incompressible version of the three-dimensional Navier-Stokes code developed by Dawes (1988) has been confirmed by comparison of computations with experimental measurements for a mixed-flow pump impeller at four different tip clearances including the shrouded case. Although in all cases, the overall loss tends to be underestimated, a variety of jet-wake flow patterns at the exit of the impeller have been well predicted.

Based on the computations, the interaction mechanism of secondary flows and the process of jet-wake flow formation have been discussed. The tip leakage flow displaces the wake flow from the casing-suction surface corner to the middle passage location. In the case of a large tip clearance, the reverse flow due to the tip leakage flow causes the thickening of the casing boundary layer. The wake flow, in this case, settles closer to the casing-suction surface corner because of the strong passage vortex developed by the thickened casing boundary layer.

The experimental results (Figs. 4 and 6a-d) show that positively sloped head-flow characteristics (stall points) appear at higher flow rates as the wake regions located closer to the casing-suction surface corner. The link between the location of the wake region inside the flow passage and the stall onset is now under investigation.

Acknowledgments

The author would like to thank Dr. W. N. Dawes for allowing him to use his three dimensional flow code while the author was a visitor at the Whittle Laboratory, Cambridge University. This research work was carried out at the suggestion of Prof. N. A. Cumpsty of the Whittle Laboratory, who also offered helpful and encouraging discussion.

The author would also like to thank Ebara Research Co., Ltd., for permission to publish this paper, and Mr. T. Katsumata for his assistance in conducting the measurements.

References

Baldwin, B., and Lomax, H., 1978, "Thin Layer Approximation and Algebraic Model for Separated Turbulent Flows," AIAA Paper No. 78-257.

Carey, C., Shamsolahi, S., Fraser, S. M., and Wilson, G., 1986, "Comparison of the Three-Dimensional Relative Flow in Two Mixed-Flow Impellers," *Proceedings of the IAHR-AIRH Symposium*, Montreal, Canada, No. 48.

Dawes, W. N., 1988, "Development of a 3D Navier-Stokes Solver for Application to All Types of Turbomachinery," ASME Paper No. 88-GT-70.

Eckardt, D., 1976, "Detailed Flow Investigations Within a High-Speed Centrifugal Compressor Impeller," ASME *Journal of Fluids Engineering*, Vol. 98, pp. 390-402.

Engeda, A., and Rautenberg, M., 1987, "Comparisons of the Relative Effect of Tip Clearance on Centrifugal Impellers," ASME JOURNAL OF TURBOMACHINERY, Vol. 109, pp. 545-549.

Fraser, S. M., Carey, C., and Wilson, G., 1985, "Behavior of Air in the Rotor of a Model Mixed-Flow Pump Operating at Peak Efficiency," ASME *Journal of Fluids Engineering*, Vol. 107, pp. 183-190.

Goto, A., 1988, "Phase-Locked Measurements of Three-Dimensional Periodic Flow From an Impeller Using a Two-Hole Pitot Probe," *Proceedings of the 2nd International Symposium on Fluid Control and Measurement (FLUCOME '88)*, Sheffield, United Kingdom.

Hah, C., Bryans, A. C., Moussa, Z., and Tomsho, M. E., 1988, "Application of Viscous Flow Computations for the Aerodynamic Performance of a Backswept Impeller at Various Operating Conditions," ASME JOURNAL OF TURBOMACHINERY, Vol. 110, pp. 303-311.

Hamkins, C. P., and Flack, R. D., 1987, "Laser Velocimeter Measurements in Shrouded and Unshrouded Radial Flow Pump Impellers," ASME JOURNAL OF TURBOMACHINERY, Vol. 109, pp. 70-76.

Harada, H., 1985, "Performance Characteristics of Shrouded and Unshrouded Impellers of a Centrifugal Compressor," ASME *Journal of Engineering for Gas Turbines and Power*, Vol. 107, pp. 528-533.

Howard, J. H. G., and Kittmer, C. W., 1975, "Measured Passage Velocities in a Radial Impeller With Shrouded and Unshrouded Configurations," ASME *Journal of Engineering for Power*, Vol. 97, pp. 207-213.

Johnson, M. W., and Moore, J., 1983, "Secondary Flow Mixing Losses in a Centrifugal Impeller," ASME *Journal of Engineering for Power*, Vol. 105, pp. 24-32.

Lakshminarayana, B., Pouagare, M., and Davino, R., 1982, "Three-Dimensional Flow Field in the Tip Region of a Compressor Rotor Passage: Part 1—Mean Velocity Profiles and Annulus Wall Boundary Layer," ASME *Journal of Engineering for Power*, Vol. 104, pp 760-771.

Lenneman, E., and Howard, J. H. G., 1970, "Unsteady Flow Phenomena in Rotating Centrifugal Impeller Passages," ASME *Journal of Engineering for Power*, Vol. 92, pp. 65-72.

Moore, J., Moore, J. G., and Timmis, P. H., 1984, "Performance Evaluation of Centrifugal Compressor Impellers Using Three-Dimensional Viscous Flow Calculations," ASME *Journal of Engineering for Gas Turbines and Power*, Vol. 106, pp. 475-481.

Moore, J., and Adhye, R. Y., 1985, "Secondary Flows and Losses Downstream of a Turbine Cascade," ASME *Journal of Engineering for Gas Turbines and Power*, Vol. 107, pp. 961-968.

Pouagare, M., and Delaney, R. A., 1986, "Study of Three-Dimensional Viscous Flows in an Axial Compressor Cascade Including Tip Leakage Effects Using a SIMPLE-Based Algorithm," ASME JOURNAL OF TURBOMACHINERY, Vol. 108, pp. 51-58.

The Effect of Tip Leakage Flow on Part-Load Performance of a Mixed-Flow Pump Impeller

A. Goto
Ebara Research Co., Ltd.,
Fujisawa-shi 251, Japan

The flow phenomena around the positive slope region of the head-flow characteristic were investigated experimentally on a mixed-flow pump impeller at various tip clearances for both shrouded and unshrouded cases. A positively sloped head-flow characteristic (abrupt decrease in pressure head) was caused by the onset of extensive flow separation in the impeller at the casing-suction surface corner. The corner separation in unshrouded cases appeared at a much lower flow rate than the shrouded case due to the favorable effect of the tip leakage flow, which displaced the wake region away from the corner. The interaction between the tip leakage flows and secondary flows and the formation of the wake regions in shrouded and unshrouded cases were explained based on experimental observation and computations by the Dawes three-dimensional Navier–Stokes code. In the shrouded case, the flow rate at which an abrupt decrease in pressure head appeared was lowered substantially by introducing a leakage flow through a slit made between the shroud and the blade tip. Inlet recirculation was triggered by the corner separation and developed more gradually for larger tip clearances. Both the increased loss, due to the extensive flow separation, and the decreased Euler's head, due to the abrupt change in flow pattern caused by the inlet recirculation, were responsible for the generation of positively sloped head-flow characteristic in the unshrouded case when the tip clearance was small, while the increased loss was the primary factor in the shrouded case.

Introduction

Mixed-flow pumps often show an abrupt decrease in pressure head and positively sloped head-flow characteristic when the flow rate is reduced below a critical value. In the present paper, this condition when the slope becomes positive will be referred to as "stall onset." Since the occurrence of a positively sloped characteristic is more likely to cause instabilities in a pumping system, it is usually a contractual requirement to guarantee a substantial margin between operating and stall points or to achieve a head-flow curve with a monotonously negative slope. Despite a lot of experimental investigations (see review by Engeda and Rautenberg, 1988), the flow phenomena under part-load operating condition and the generation mechanism of positively sloped head-flow characteristic are not well understood.

The performance difference between shrouded impellers (most commonly used for multistage configurations) and unshrouded impellers at various tip clearances is a matter of great interest, because they often show quite different characteristics, especially at partial flow rates. With regard to centrifugal impellers, Lenneman and Howard (1970), Howard and Kittmer (1975), Harada (1985), and Hamkins and Flack (1987) carried out a comparison of internal flows between shrouded and unshrouded cases. Engeda and Rautenberg (1987) discussed the effect of tip clearance and reported that some impellers are highly sensitive to tip clearance. On the other hand, mixed-flow turbomachines are the least well understood machines, even around the design points, because of the complex three-dimensional flow fields caused by the strong interaction of secondary flows, and only a few studies have been done so far. Fraser et al. (1985) and Carey et al. (1986) measured the internal flows of mixed-flow fan impellers under various operating conditions using a laser-Doppler anemometry system. Based on these measurements, Carey et al. (1988) discussed the generation mechanism of positively sloped head-flow characteristic curves. More recently, the author (Goto, 1992) investigated the formation of jet-wake flow patterns in a mixed-flow pump impeller at various tip clearances, including those in the shrouded case, by applying Dawes three-dimensional Navier–Stokes code (Dawes, 1988) at 90 percent flow rate of the design point. The complex flow fields under part-load operation, including extensive flow separation and inlet/exit recirculation, seem to be practically still out of reach of numerical computations. However, a great deal of information, useful in understanding flow mechanics under part-load operation, were drawn from computations at higher flow rates. Goto (1992) also reported that the shrouded impeller showed a positively sloped head-flow characteristic at a much higher

---

Contributed by the International Gas Turbine Institute and presented at the 36th International Gas Turbine and Aeroengine Congress and Exposition, Orlando, Florida, June 3–6, 1991. Manuscript received at ASME Headquarters February 19, 1991. Paper No. 91-GT-84. Associate Editor: L. A. Riekert.

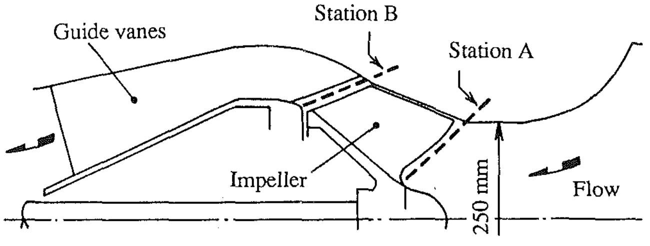

Fig. 1 Mixed-flow pump geometry

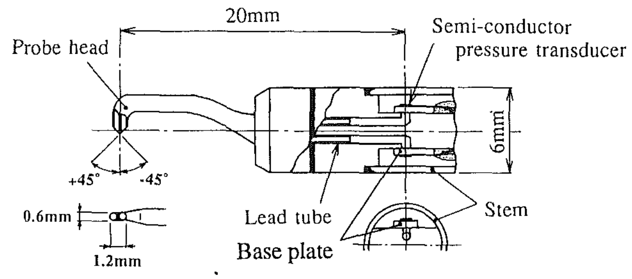

Fig. 2 Construction of two-hole pitot probe

Table 1 Design of impeller

	hub	midspan	shroud	
				Number of blades : 5
β_{1b} (deg)	27.8	18.3	14.8	Design flow rate : 8.7 m^3 / min
β_{2b} (deg)	31.8	25.3	20.7	Design pump head : 7.0 mH_2O
r_1 (mm)	58.0	102.3	132.5	Rotational speed : 800 rev / min
r_2 (mm)	142.5	157.8	171.7	

flow rate than that in unshrouded cases having the same blading.

In the present paper, the onset of a positively sloped head-flow characteristic in a mixed-flow pump impeller at various tip clearances, including that in the shrouded case, is investigated experimentally. The different mechanism of the onset of extensive flow separation and the production of positively sloped characteristic is discussed based on Navier-Stokes computations by Goto (1992) at a higher flow rate and experimentally measured inlet/exit flow fields at lower flow rates. For the purpose of stability enhancement in shrouded impellers, the effect of a leakage flow through a slit along the shroud is also discussed in conjunction with the effect of inlet casing boundary layer.

Experimental Apparatus and Method

Mixed Flow Pump. Figure 1 schematically shows the test section of a mixed-flow pump used for performance tests and flow field measurements. The geometry of the impeller and design conditions are given in Table 1. The specific speed of the pump at its best efficiency point is $\omega \cdot \sqrt{Q}/(gH)^{3/4} = 1.34$, i.e., $N \cdot \sqrt{Q}/H^{3/4} = 548$ (rpm, m^3/min, mH_2O). The pump was placed in a closed flow loop consisting of a 440-mm-dia suction pipe, a 350-mm-dia delivery pipe, and a reservoir tank. Water was used as the test fluid, and the flow rate was measured with venturi tubes and mercury manometers. The performance tests were conducted according to ISO standards. The impeller speed was 800 rpm giving a Reynolds number of $\mathrm{Re} = 1.33 \times 10^6$ at the design point.

The measurements were carried out on one impeller at five different tip clearances including the shrouded case (S, U03, U05, U10, and U15): S represents the shrouded case, U03 the unshrouded case with a tip clearance of 0.3 mm, and so on. The unshrouded impeller was in fact a shrouded impeller with the front shroud removed. The tip clearance of the unshrouded impeller was adjusted by sliding the casing in the axial direction. Since the meridional shape of the blade tip was linear, the tip clearance was changed uniformly along the casing.

Flow Field Measurements. Besides the performance tests, inlet and exit flow measurements of the impeller were carried out using two types of pressure probe. The inlet flow was measured by an ordinary three-hole cobra probe at Station A (Fig. 1), 10 mm upstream of the leading edge at midspan. On the other hand, the exit flow was measured by a two-hole pitot probe with high frequency response developed by Goto (1988) at Station B, 8 mm downstream of the trailing edge. Figure 2 shows the construction of the two-hole pitot probe. Two diffusion type semiconductor pressure transducers with a range of $-0.1 \sim 0.1$ MPa and a frequency response of 100 kHz were placed in the stem tube. Two pressure holes on the probe head were connected to the transducers by lead tubes of 0.4-mm i.d. filled with silicon oil. The resonance frequency of the pressure sensing system was about 5.6 kHz and was high enough compared with the blade passing frequency of 67 Hz.

The pitot probe was mounted on a traverse unit with two

Nomenclature

C = absolute velocity
D^*_{eq} = equivalent diffusion factor at blade tip
H = head
i = incidence angle, deg
l_m = meridional chord length at midspan
n = number of blades
N = rotational speed, rpm
PS = pressure surface
Q = flow rate
Q^* = flow rate ratio = $Q/(Q$ at design point)
(r, θ, z) = cylindrical coordinates
R^* = radius ratio = $(r - r_{\text{hub}})/(r_{\text{shroud}} - r_{\text{hub}})$
Re = Reynolds number = $W_1 l_m/\nu$
SS = suction surface
U = peripheral blade speed
U_{TE} = peripheral blade speed at midspan trailing edge
W = relative velocity
β = flow angle measured from circumferential direction
β_b = blade angle measured from circumferential direction
γ = stagger angle on mapped plane
ξ_r = vorticity component perpendicular to streamline on stream surface
σ = solidity on mapped plane
ψ^* = head coefficient = $H/(U^2_{TE}/g)$
ψ^*_e = Euler's head coefficient
ψ^*_t = total head coefficient at impeller exit
ψ^*_p = pump head coefficient
ω = angular rotation frequency, rad/s

Subscripts

1 = inlet
2 = exit
m = meridional component
TE = impeller trailing edge
t = blade tip
u = circumferential component

Superscripts

* = nondimensional value (velocity and pressure head are normalized by U_{TE} and U^2_{TE}/g, respectively)

stepping motors controlled by a microcomputer and placed parallel to the blade trailing edge. The pressure fluctuation sensed by the pressure transducers was measured by a phase-locked multisampling and averaging technique. A set of 11 pressure data for each pressure hole, obtained at 11 probe setting angles over 450 sampling revolutions, was used to calculate the velocity vector and the static pressure from the calibration curves. Since the velocity vector and the static pressure were calculated using 4950 samples (= 11 probe angle positions × 450 revolutions), the flow field was considered to be properly averaged in the statistical sense. Details on the measuring system and the data reduction method have been described in a previous paper by Goto (1988).

Accuracy of Measurements. The probable uncertainty in the data reduction process and the measuring system of the two-hole pitot probe has been evaluated by Goto (1988) using a calibration test rig. The accuracy is ±2.5 percent in static pressure, ±1.3 percent in velocity, ±0.3 deg in the yaw angle, and ±1 deg in the pitch angle. It has also been confirmed that the steady-state calibration curves, obtained for uniform steady nozzle flows in the calibration rig, are correctly applicable to the present unsteady flow.

The drift of the pressure transducers between calibrations largely depends on the mounting condition of the gauges onto the base plates. The drift observed was less than 1 percent of the mean output voltage for 67 cases in 88 measured cases, while 5 cases revealed a drift of over 3 percent. The estimated maximum errors due to the drift are ±0.3 percent in static pressure, ±0.2 percent in velocity, ±0.01 deg in the yaw angle, and ±1 deg in the pitch angle.

The flow rates measured by the pitot probe deviated −5.5 ± 2.5 percent from those obtained by the venturi tubes. The error tends to increase as the flow rate is reduced. If we simply assume that the error in the initial setting of the probe yaw angle caused the bias of −5.5 percent, it corresponds to a 0.5 deg error.

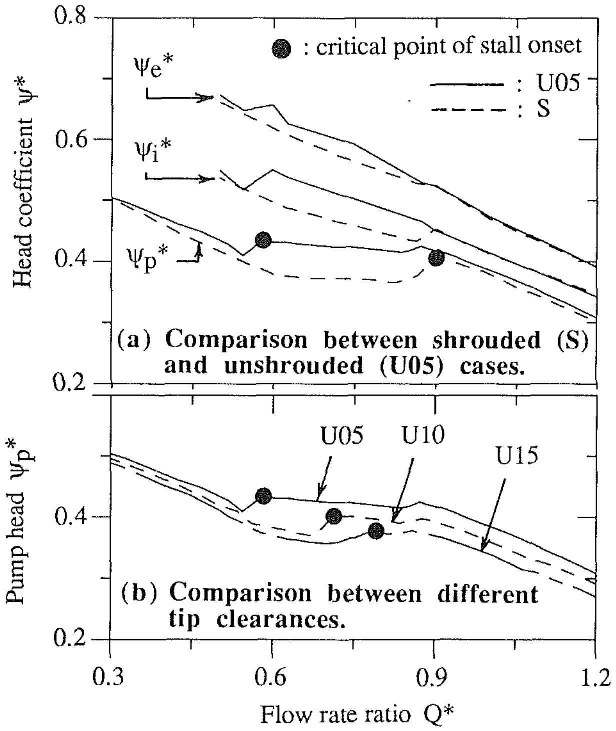

Fig. 3 Head-flow characteristic curves

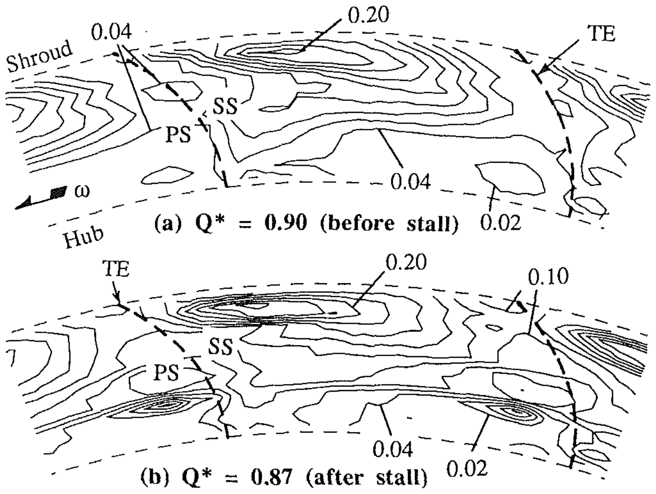

Fig. 4 Exit loss distribution in shrouded case S (contour interval = 0.02)

Flow Phenomena Toward Stall

Head-Flow Characteristic Curve. Figure 3(*a*) compares the head-flow characteristic curves between the shrouded case S and the unshrouded case U05 (with a tip clearance of 0.5 mm), and Fig. 3(*b*) between cases with different tip clearances. Mass-averaged Euler's head ψ_e^* and the total head ψ_i^*, obtained by exit flow measurements at Station B, are also presented in Fig. 3(*a*). All the cases exhibit positively sloped head-flow characteristics (stall onset) when the flow rates are reduced below critical values (indicated by solid circles in Fig. 3). At this critical point, similar flow pattern of an abrupt expansion of high loss region due to corner separation was observed at the exit of the impeller in every case. However, the dominant frequency of the flow field, after stall onset, was still the blade passing frequency and no evidence of rotating stall was found.

Although the unshrouded impeller was in fact a shrouded impeller with the front shroud removed, the stall occurs at a much lower flow rate than in shrouded case S (Fig. 3*a*). Head coefficients in case S are nearly equal to those in case U05 between $Q^* = 0.9$ and $Q^* = 1.2$. However, the total head ψ_i^* at the exit of the impeller S drops suddenly at $Q^* = 0.87$, while the Euler's head ψ_e^* is nearly the same as that in case U05. Figure 4 shows the contour maps of the loss on the quasi-orthogonal plane behind the impeller measured by the two-hole pitot probe. The loss is defined as the rothalpy difference between the measuring plane and the upstream of the impeller, where the flow is considered to be uniform. There is an abrupt expansion of the high loss region near the shroud-suction surface corner at $Q^* = 0.87$. From this, it is concluded that the positively sloped characteristic in case S is mainly caused by a sudden increase in flow loss due to the onset of the extensive flow separation within the impeller. On the other hand, in the unshrouded case U05, the positively sloped curve appears at a much lower flow rate of $Q^* = 0.54$ (Fig. 3*a*) and a similar expansion of the high loss region is observed in the same region at this flow rate (Fig. 5*b*). So, despite both shrouded and unshrouded cases revealing similar overall characteristics above $Q^* = 0.9$, there are large differences in the internal flow fields of the impeller, and some amount of tip leakage flow improves the flow fields near the casing and delays the onset of a corner separation.

The tip clearance has great influence on pump performance. Figure 3(*b*) compares the head-flow characteristic curves of an unshrouded impeller between 0.5-mm, 1.0-mm, and 1.5-mm tip clearances. The critical flow rate at stall onset increases substantially with the tip clearance. Since a 0.5-mm clearance corresponds to 0.8 percent of the exit passage height or 0.15 percent of the blade chord length, the performance of the tested

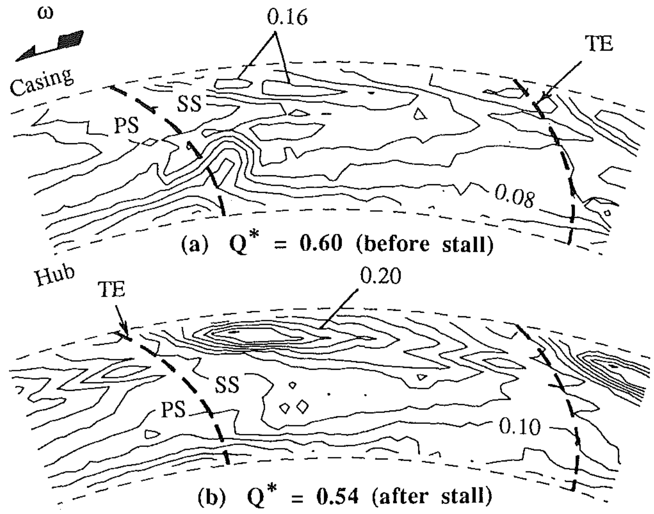

Fig. 5 Exit loss distribution in unshrouded case U05 (contour interval = 0.02)

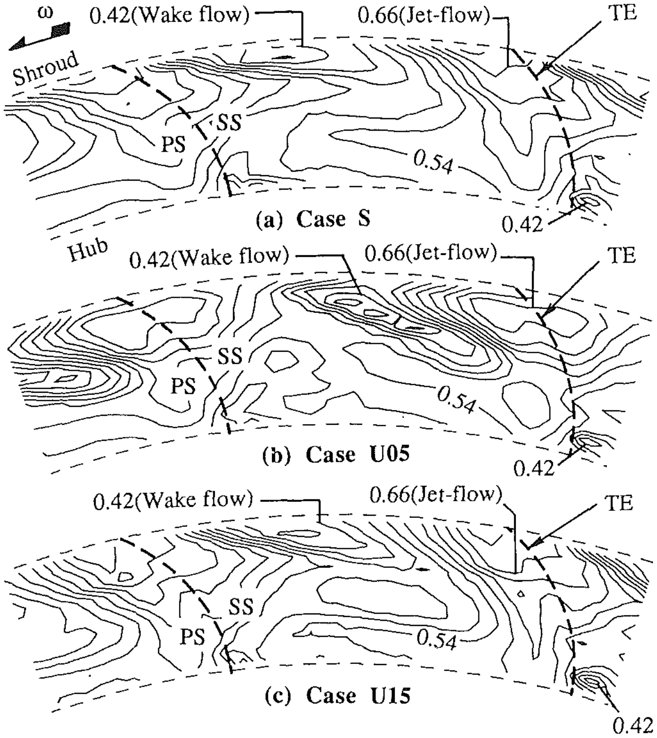

Fig. 6 Exit velocity W_2^* at $Q^* = 0.90$ (contour internal = 0.03)

mixed-flow impeller is quite sensitive to tip clearance. However, all head-flow curves below $Q^* = 0.54$ are basically independent of the tip clearance, including those in shrouded case S. While the stall is progressive in the largest clearance case U15, the impeller at a small tip clearance stalls abruptly. The pump head at higher flow rates decreases as the tip clearance is enlarged due to an increase in tip leakage loss and corresponding secondary losses, and lower energy transfer associated with smaller effective blade area.

Formation of Jet-Wake Flow. The author (Goto, 1992) had investigated the interaction mechanism of secondary flows and the process of jet-wake flow formation in the present impeller by applying the incompressible version of the Dawes three-dimensional Navier-Stokes code (Dawes, 1988). The major conclusions relating with the present study are included in

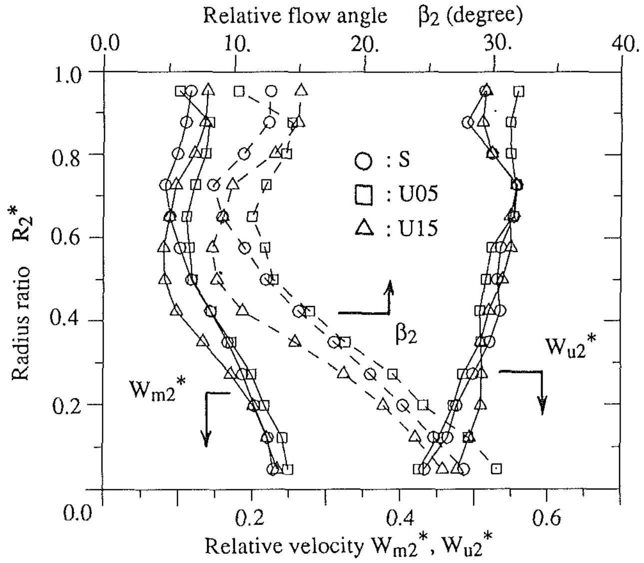

Fig. 7 Exit flow fields at $Q^* = 0.90$

the appendix. Although the numerical computations were carried out at the flow rate of $Q^* = 0.9$, they also provide a great deal of useful information to support the discussions on flow phenomena at partial flow rates.

Figure 6 compares experimentally measured exit velocity contours at $Q^* = 0.9$. In the shrouded case S, the wake flow settles close to the shroud-suction surface corner (Fig. 6*a*) because of the passage vortex, which induces strong secondary flows along the shroud toward the corner. As we can see in Fig. 7 (curves with circles), the passage vortex tends to overturn the flow and increases the loading near the shroud. The low-momentum fluid accumulated in the corner region is very likely to cause early onset of the corner separation. On the other hand, in the unshrouded case U05, the tip leakage flow displaces the wake flow from the casing-suction surface corner toward the middle passage location (Fig. 6*b*) and underturns the flow in the tip region (curves with squares in Fig. 7). These alterations in flow patterns are considered to be responsible for the increased margin for the onset of the corner separation.

As the tip clearance is increased, the tip leakage flow becomes stronger. However, the wake flow tends to settle closer to the casing-suction surface corner opposing against the tip leakage flow (compare the location of wake region between Figs. 6*c* and 6*b*), overturning the flow in the casing region (curves with triangles in Fig. 7). As described in the appendix, three-dimensional Navier-Stokes computations by Goto (1992) have shown that: (1) The reverse flow due to the strong tip leakage flow through large clearance promotes the thickening of the casing boundary layer, and (2) the wake flow, in this case, settles closer to the casing-suction surface corner because of the strong passage vortex (the secondary flow toward the blade suction side along the casing) developed by the thickened casing boundary layer. Because of this, as the tip clearance is increased, the wake flow settles closer to the corner region and the corner separation is more likely to occur at higher flow rates.

The comparison of exit flow fields between the cases S and U05 at $Q^* = 0.9$ (Figs. 6*a* and 6*b*) shows that the flow fields are substantially improved by the introduction of a small tip clearance. However, if the flow rate is reduced further, the unshrouded case U05 also reveals the stall onset at $Q^* = 0.54$ (Fig. 5*b*). Since the critical flow rate of stall onset ($Q^* = 0.54$) is much lower than that of the shrouded case S ($Q^* = 0.87$) and the jet-wake flow pattern at $Q^* = 0.9$ is so different between these two cases, the mechanism of the stall onset in

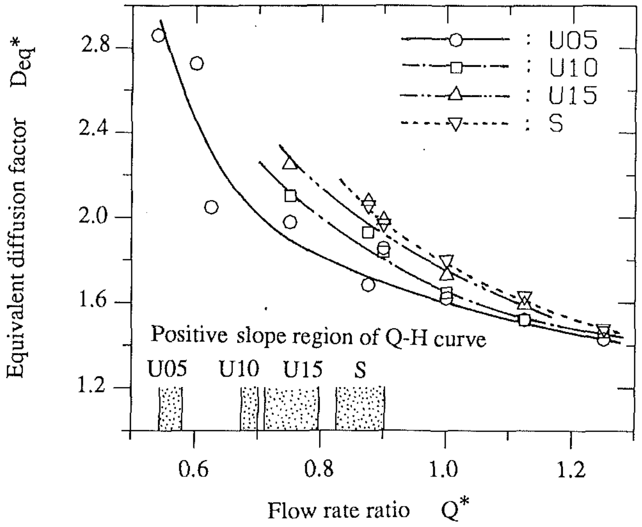

Fig. 8 Equivalent diffusion factor

case U05 looks different from the shrouded case. However, the stall onset was in reality caused by the same mechanism, i.e., by the extensive flow separation at the casing-suction surface corner. The reduction of the flow rate has the same effect on flow fields as the enlargement of the tip clearance, since increased blade loading generates a strong tip leakage flow. The casing boundary layer becomes thick, because of the strong tip leakage reverse flow, and the wake settles closer to the casing-suction surface corner as the flow rate is reduced, because of the strong passage vortex developed by the thickened casing boundary layer. The location of the wake flow observed just before the stall onset (Fig. 5*a*, $Q^* = 0.6$) is identical to that in the shrouded case (Fig. 4*a*, $Q^* = 0.9$).

Equivalent Diffusion Factor. Since it has been clarified that the positively sloped head-flow curves are caused by the extensive flow separation at the casing-suction surface corner in the impeller, for all cases including the shrouded case, it is interesting to look into the loading limits for the present impeller.

The mixed-flow cascade is mapped into a linear cascade having a stagger angle γ and solidity σ through the following equations:

$$\gamma = \tan^{-1}\{\sin \phi \cdot (\theta_1 - \theta_2)/(\ln r_2 - \ln r_1)\}$$

$$\sigma = n(\ln r_2 - \ln r_1)/(2\pi \cdot \sin \phi \cdot \cos \gamma)$$

$$\phi = \tan^{-1}\{(r_2 - r_1)/(z_2 - z_1)\}$$

The values of γ_t and σ_t for the tip section are 70.8 deg and 1.75, respectively, for the present impeller. Then the equivalent diffusion factor D^*_{eq} (Lieblein, 1959) is defined as follows:

$$D^*_{eq} = (C_{m1t} \cdot \sin \beta_{2t})/(C_{m2t} \cdot \sin \beta_{1t}) \cdot (1.12 + 0.01 \cdot i_t^{1.43} + 0.305 \cdot F)$$

$$F = (2 \cdot \sin^2 \beta_{1t}/\sigma_t) \cdot \{1/\tan \beta_1 - (r_2 \cdot C_{m2})/(r_1 \cdot C_{m1})/\tan \beta_2 - (r_1 \cdot \omega)/C_{m1} \cdot (1 - r_2^2/r_1^2)\}_t$$

where velocity components and flow angles are circumferentially averaged experimental values. Figure 8 shows reasonable correlation between corner stall onset and the equivalent diffusion factor at the tip section, and all cases exhibit positively sloped head-flow curves between $D^*_{eq} = 2.4$ and $D^*_{eq} = 2.0$. The value of D^*_{eq} as the loading limit may vary with a given cascade because the actual deceleration on the blade suction surface depends on the detail of the blade geometry. However, the loading limit obtained here is quite reasonable comparing with the diffusion ratio limit of 2.0 obtained by Lieblein (1959).

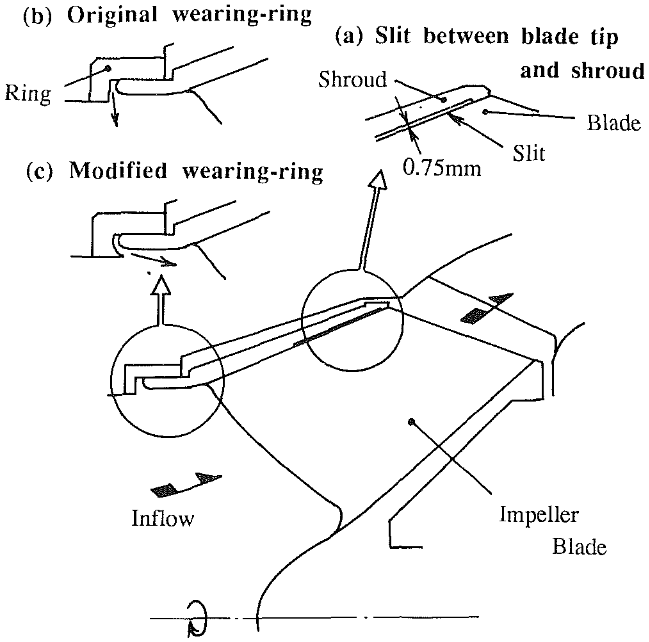

Fig. 9 Geometry of modified shrouded impeller

Stability Enhancement in Shrouded Case. Shrouded impellers are more widely used than unshrouded impellers for multistage configurations and small machines, since there are difficulties in controlling the latter's tip clearances accurately. As was pointed out in the previous discussion, the flow pattern within a shrouded impeller tends to cause earlier onset of the corner separation than in unshrouded cases, provided the same blading is adopted for both cases. A passive way to enhance stability under part-load operation was tried for the shrouded case.

In the previous discussions, it has been clarified that the absence of the tip leakage flow is an unfavorable factor of the flow fields within the shrouded impeller, since the low kinetic energy fluid tends to migrate in the shroud-suction surface corner and causes earlier onset of the corner separation. Taking this into account, a slit of 0.75-mm width (1.2 percent of the exit blade span) was made between the shroud and the blade tip (Fig. 9*a*) to generate a leakage flow through a slitted shroud. Since the tip leakage flow also has unfavorable effects on flow fields, by causing reverse flows around the leading edge region and thickening the inlet casing boundary layer, the slits were made in the latter half of the impeller between the 50 percent and 95 percent chord locations along the shroud. Another unfavorable factor in flow fields of the shrouded case is the thick inlet boundary layer on the shroud casing due to a leakage flow entering radially inward through a wearing ring (Fig. 9*b*). Since the extensive corner separation originates in the shroud region, this thickened inlet casing boundary layer is very disadvantageous to corner stall onset. The ring geometry was modified as shown in Fig. 9(*c*) so that the leakage flow through the wearing ring would have lower velocity normal to the main inlet flow.

Figure 10 compares the exit flow losses between the shrouded impeller with these two modifications and the unshrouded case U05 at the flow rate of $Q^* = 0.87$, whereby case S revealed a stall onset. Substantial reduction in the flow loss is observed by the introduction of the tip leakage flow (Fig. 10*a*). The onset of extensive flow separation has been avoided at this flow rate and the high loss region is quite narrow compared with the case without a slit (Fig. 4*b*). Adoption of the improved wearing ring in addition to the slit further improves the flow fields. The amount of loss within the wake is reduced even more and the wake flow (high loss region) settles around the

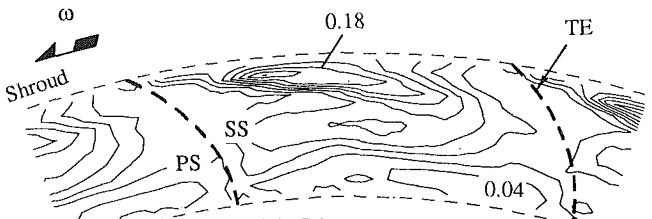

(a) Slitted shroud.

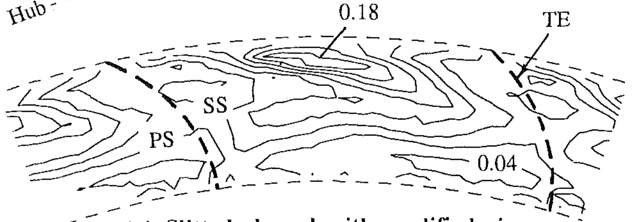

(b) Slitted shroud with modified ring.

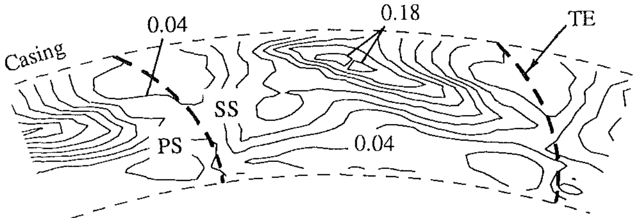

(c) Unshrouded case U05.

Fig. 10 Comparison of exit loss distribution between unshrouded and modified shrouded cases (Q^* = 0.87, contour interval = 0.02)

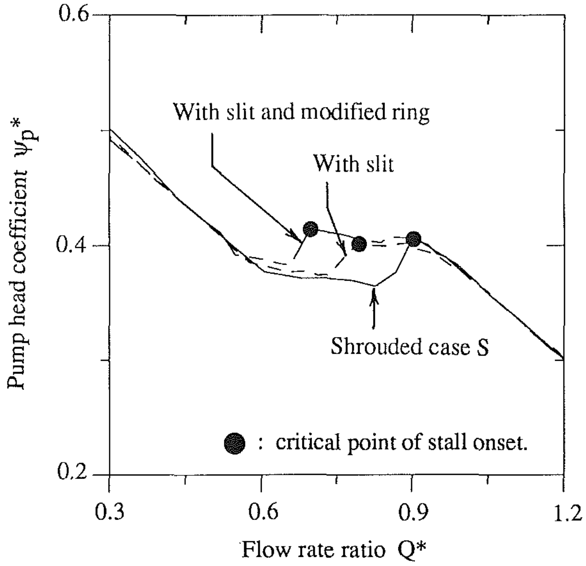

Fig. 11 Head-flow characteristics of modified shrouded impeller

midpitch location (Fig. 10*b*) as in the unshrouded case (Fig. 10*c*). The wake flow in Fig. 10(*b*) settles closer to the pressure side than the case of Fig. 10(*a*) because of the thin inlet boundary layer and the resulting relatively weak passage vortex near the shroud (weak secondary flow towards the suction side along the casing).

The comparison of head-flow characteristic curves under these configurations (Fig. 11) confirms that a substantial improvement on the stall onset is possible for shrouded impellers by the introduction of a tip leakage flow and a thin inlet casing boundary layer, almost without affecting the characteristics in the higher flow rate region. Thus obtained improvement in the stall margin defined by (1 − Q^*_{stall}) is shown in Table 2.

Table 2 Stall margin

Type of impeller	$1 - Q^*_{\mathrm{stall}}$
Shrouded case S	0.125
Case S with slit	0.207
Case S with modified ring	0.175
Case S with slit & modified ring	0.302
(Unshrouded case U05	0.46)

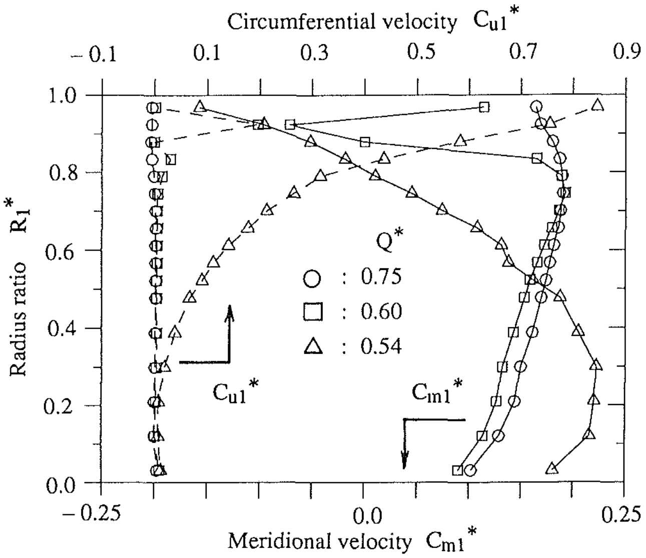

Fig. 12 Inlet flow fields in case U05

Onset of Inlet Recirculation

Inlet Recirculation. The inlet flow fields in case U05 were measured using a three-hole cobra probe at three different flow rates (Fig. 12). Although a weak reverse flow is observed near the casing at $Q^* = 0.6$ (just before the stall onset), the overall inlet flow pattern remains unchanged above this flow rate. However, following a stall at $Q^* = 0.54$, a drastic change in the flow field is observed. The meridional velocity distribution shows an extensive recirculating flow region occupying the outer half of the flow passage. The flow in the hub region is accelerated because of blockage due to the flow recirculation near the casing. The recirculating flows convey the angular momentum given by the impeller to the incoming flow, and the flow starts prerotating between a 30 percent span and the casing.

Figure 13 shows the development of the inlet recirculation at four different tip clearances. The flow rates where the flow velocity at $R_1^* = 0.97$ reveals prerotations of $Cu_1^* = 0.0$ (no recirculation), 0.5 (intermediate one), and 0.8 (fully developed one) are plotted in Fig. 13 for each tip clearance. The flow regions where positively sloped head-flow characteristics appeared are also presented in Fig. 13. This figure suggests that the onset of extensive corner separation is the triggering mechanism for inlet recirculation in the present impeller. Although the development of recirculation is more progressive for larger tip clearance, fully developed recirculation is observed around $Q^* = 0.54$ in every case. It was found by the inlet flow traversing that the flow pattern of fully developed recirculation is independent of tip clearance.

Head Generation Mechanism. A comparison of head-flow characteristic curves in Fig. 3(*a*) shows the difference in the generation mechanism of positively sloped head-flow characteristics between shrouded case S and unshrouded case U05. Namely, the increase in flow loss is mainly responsible for the positively sloped curve at $Q^* = 0.87$ in shrouded case S, because Euler's head is nearly equal to that of the unstalled unshrouded case around this flow rate. In contrast, abrupt decrease of Euler's head is observed at $Q^* = 0.54$ in unshrouded case U05 (also see ψ_e^* curve in Fig. 14), suggesting a relatively important role of Euler's head in the production of a positively sloped curve.

The generation mechanism of positively sloped head-flow characteristics of the present impeller is investigated based on Euler's equation by a similar method used by Carey et al. (1988). The head generation of Euler's head in an impeller can be attributed to three factors: centrifugal head, dynamic head, and diffusion head, as follows:

$$\psi_e^* = (U_2\cdot C_{u2} - U_1\cdot C_{u1})/U_{TE}^2$$

$$= \{(U_2^2 - U_1^2) + (C_2^2 - C_1^2) + (W_1^2 - W_2^2)\}/(2\cdot U_{TE}^2)$$

Centrifugal Dynamic Diffusion

Figure 14 shows the mass-averaged Euler's head-flow curve and its three components in case U05. Euler's equation holds on each streamsurface entering at radius r_1 and leaving at r_2, and the spanwise distribution of Euler's head components around the stall point is plotted in Fig. 15 against the exit radius ratio R_2^*. Since the onset of inlet recirculation causes drastic change in the radial location of the stream surfaces at the inlet, the peripheral blade speed U_1^* on the stream surface, plotted against the exit radius R_2^*, varies with the flow rate. After the onset of inlet recirculation at $Q^* = 0.54$, there is an abrupt change in the flow field, and the throughflow steamlines are shifted remarkably toward the hub at the inlet, due to the large blockage caused by the inlet recirculation. This reduces the peripheral speed U_1 (Fig. 15*a*) and increases the centrifugal effect (Fig. 14). However, the overall Euler's head drops at $Q^* = 0.54$ because of decrease in dynamic and diffusion effects. The large decrease in diffusion head (at $Q^* = 0.54$, Fig. 14) is not caused by the blade stall but by the reduced inlet relative velocity W_1 (Fig. 15*c*) due to the prerotation and decreased peripheral speed U_1. Once the inlet recirculation is fully developed, the pump shows negatively sloped head-flow characteristics in all cases because of the increasingly dominating centrifugal effect.

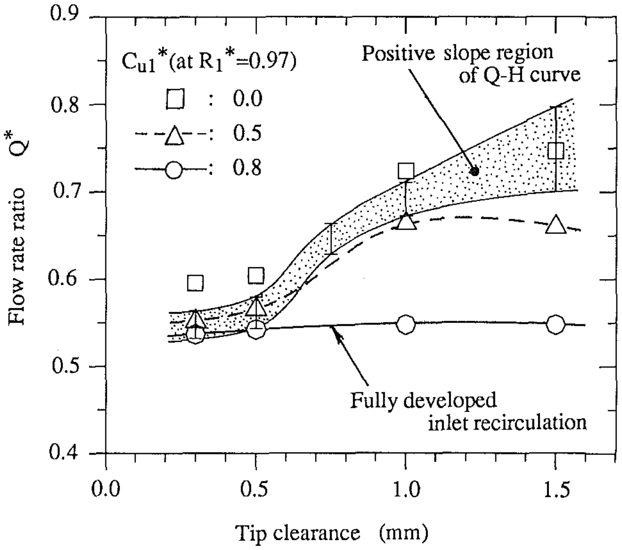

Fig. 13 Effect of tip clearance on corner stall onset and inlet recirculation (unshrouded impeller)

In shrouded case S, the inlet recirculation develops progressively after the stall onset and there is no abrupt change in the flow field at $Q^* = 0.9$. Because of this, Euler's head plays a less important role in the shrouded case and the increase in flow losses is the main factor that generates the positively sloped head-flow characteristic.

Conclusions

The following conclusions are drawn from the experimental investigation on stall onset and inlet recirculation in a mixed-flow pump impeller for both shrouded and unshrouded cases at various tip clearances:

1 Positively sloped head-flow characteristics appeared at $Q^* = 0.87$ in the shrouded case, and at the much lower flow rate of $Q^* = 0.54$ in the unshrouded case U05. However, this

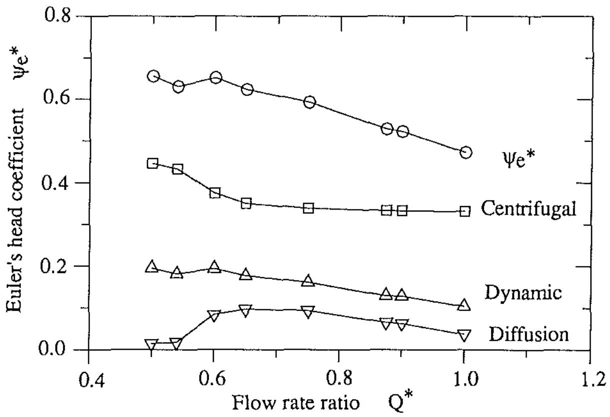

Fig. 14 Euler's head in case U05

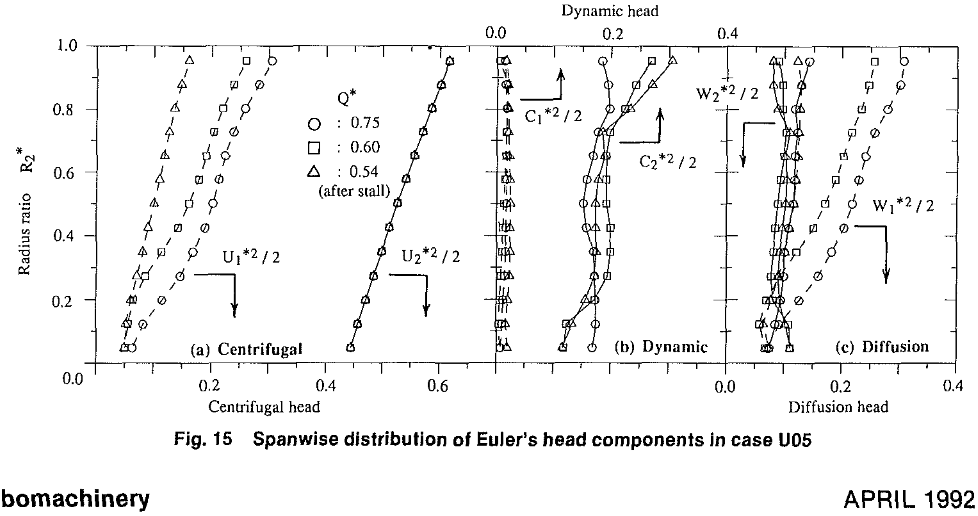

Fig. 15 Spanwise distribution of Euler's head components in case U05

critical flow rate increased as the tip clearance was enlarged. In all cases, the positively sloped curves occurred following the onset of extensive flow separation at the shroud-suction surface corner. After the impeller stalled, no evidence of rotating stall was found, but there was instead a region of recirculating flow in the upstream direction at the impeller inlet.

2 In the shrouded case S, the low kinetic energy fluid, accumulated in the shroud-suction surface corner due to the strong secondary flows, was responsible for the early onset of the corner separation.

3 In unshrouded cases, the tip leakage flow displaced the wake flow from the corner region toward the midpitch location and increased the stall margin. However, when the tip clearance was large, the strong tip leakage reverse flow thickened the casing boundary layer and developed the passage vortex. In this case, the wake region was located closer to the corner region, because of the strong passage vortex opposing the tip leakage flow, and the stall margin was decreased.

4 The onset of stall in the shrouded case was substantially delayed by introducing a leakage flow through a slit made between the shroud and the blade tip.

5 The equivalent diffusion factor was found to provide a reasonable basis for determining the loading limit for corner separation onset in the present impeller at different tip clearances.

6 The corner separation was the triggering mechanism for the inlet recirculation. Although the development of recirculation was more progressive for cases with larger tip clearances, the flow pattern of fully developed inlet recirculation was independent of tip clearance.

7 The positively sloped head-flow curve in the unshrouded case with small tip clearance was caused by two factors: the increase in flow loss, due to the extensive flow separation, and the decrease in Euler's head (reduced diffusion effect), due to the abrupt change of the flow field (extensive inlet recirculation). In the shrouded case, it was mainly caused by the loss increase due to the corner separation, since the development of the inlet recirculation was progressive and there was no abrupt change in the flow pattern that may cause reduction in Euler's head.

Acknowledgments

The author would like to express his appreciation to Mr. T. Katsumata for his assistance in setting up the experimental apparatus and conducting the measurements. The author also would like to thank Dr. M. Aoki who offered him useful discussions, and Ebara Research Co., Ltd., for permission to publish this paper.

References

Carey, C., Shamsolahi, S., Fraser, S. M., and Wilson, G., 1986, "Comparison of the Three-Dimensional Relative Flow in Two Mixed-Flow Impellers," *Proceedings of the IAHR-AIRH Symposium*, Vol. 2, No. 48, Montreal, Canada, Sept. 2-5.

Carey, C., Fraser, S. M., and McEwen, D., 1988, "Flow Analysis and Part-Load Performance of Model Mixed-Flow Pumps," *Proceedings of the International Conference on Part-Load Pumping Operation, Control and Behaviour* (IMechE 1988-5), Herriot-Watt University, Edinburgh, United Kingdom, Sept. 1-2.

Dawes, W. N., 1988, "Development of a 3D Navier-Stokes Solver for Application to All Types of Turbomachinery," ASME Paper No. 88-GT-70.

Engeda, A., and Rautenberg, M., 1987, "Comparisons of the Relative Effect of Tip Clearance on Centrifugal Impellers," ASME JOURNAL OF TURBOMACHINERY, Vol. 109, pp. 545-549.

Engeda, A., and Rautenberg, M., 1988, "Pump Instabilities at Partial Flow—A Review," *Proceedings of the International Conference on Part-load Pumping Operation, Control and Behaviour* (IMechE 1988-5), Herriot-Watt University, Edinburgh, United Kingdom, Sept. 1-2.

Fraser, S. M., Carey, C., and Wilson, G., 1985, "Behavior of Air in the Rotor of a Model Mixed-Flow Pump Operating at Peak Efficiency," ASME *Journal of Fluids Engineering*, Vol. 107, pp. 183-190.

Goto, A., 1988, "Phase-Locked Measurements of Three-Dimensional Periodic Flow From an Impeller Using a Two-Hole Pitot Probe," *Proceedings of the 2nd International Symposium on Fluid Control and Measurements* (FLUCOME '88), Sheffield, United Kingdom, Sept. 5-9.

Goto, A., 1992, "Study of Internal Flows in Mixed-Flow Pump Impellers With Various Tip Clearances Using 3D Viscous Flow Computations," ASME JOURNAL OF TURBOMACHINERY, Vol. 114, this issue.

Hamkins, C. P., and Flack, R. D., 1987, "Laser Velocimeter Measurements in Shrouded and Unshrouded Radial Flow Pump Impellers," ASME JOURNAL OF TURBOMACHINERY, Vol. 109, pp. 70-76.

Harada, H., 1985, "Performance Characteristics of Shrouded and Unshrouded Impellers of a Centrifugal Compressor," ASME *Journal of Engineering for Gas Turbines and Power*, Vol. 107, pp. 528-533.

Howard, J. H. G., and Kittmer, C. W., 1975, "Measured Passage Velocities in a Radial Impeller With Shrouded and Unshrouded Configurations," ASME *Journal of Engineering and Power*, Vol. 97, pp. 207-213.

IMechE, 1988, "The International Conference on Part-load Pumping Operation, Control and Behaviour," held at Herriot-Watt University, Edinburgh, United Kingdom, Sept. 1-2.

Lenneman, E., and Howard, J. H. G., 1970, "Unsteady Flow Phenomena in Rotating Centrifugal Impeller Passages," ASME *Journal of Engineering for Power*, Vol. 92, pp. 65-72.

Lieblein, S., 1959, "Loss and Stall Analysis of Compressor Cascades," ASME *Journal of Basic Engineering*, Vol. 81, pp. 387-400.

APPENDIX

The complex three-dimensional flow fields in the present impeller have been investigated numerically by Goto (1992) by applying the incompressible version of the Dawes three-dimensional Navier-Stokes code. The computational grid on the meridional plane is shown in Fig. A1, and all computations have been carried out at the flow rate of $Q^* = 0.9$. The applicability of the code has been confirmed by comparison with a variety of experimentally measured jet-wake flow patterns for both shrouded and unshrouded cases at various tip clearances.

The difference in the formation of jet-wake flow pattern between the two cases has been explained by the different way of interaction between secondary flows. Namely, in the shrouded case, the wake flow settles at the shroud-suction surface corner because of strong secondary flows along the shroud and the blade suction surface towards the corner region. The introduction of a small tip clearance (unshrouded case) displaces the wake flow from the corner to the middle passage location because of the tip leakage flow and establishes a different jet-wake flow pattern.

The tip leakage flow, crossing the blade tip from the pressure side to the suction side of the blade, causes a reverse flow near the casing (Fig. A1). When the tip clearance is enlarged, the

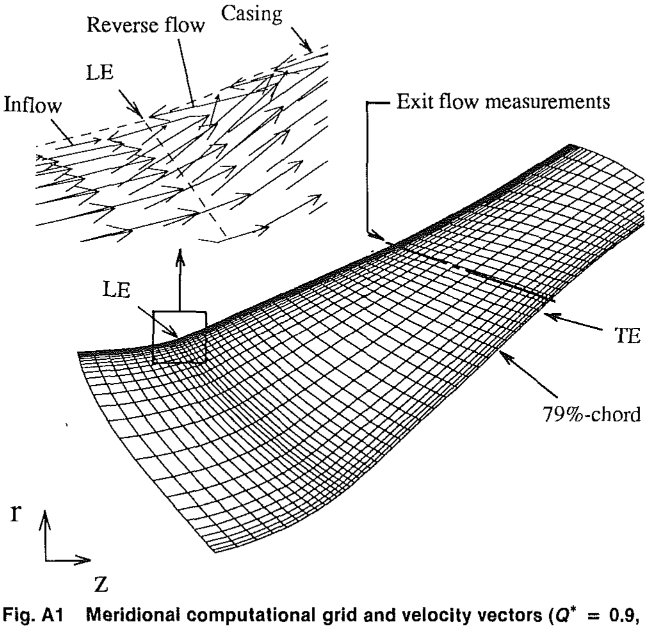

Fig. A1 Meridional computational grid and velocity vectors ($Q^* = 0.9$, suction side, unshrouded case U05)

(a) Small clearance case U05.

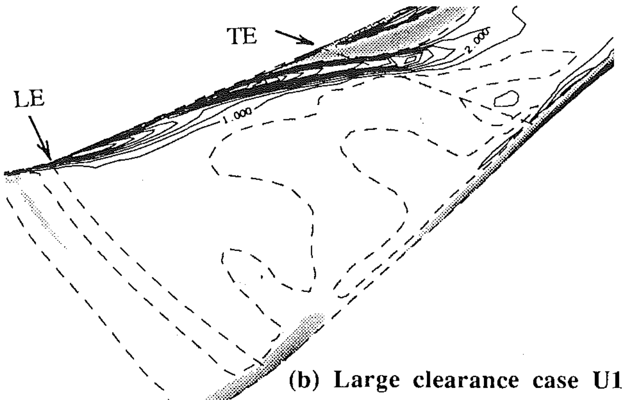

(b) Large clearance case U10.

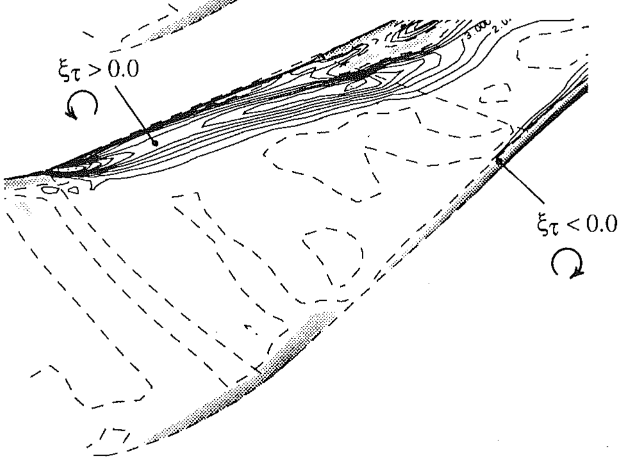

Fig. A2 Casing boundary layer development ($Q^* = 0.9$, perpendicular vorticity contours, contour interval = 1.0, midpitch location)

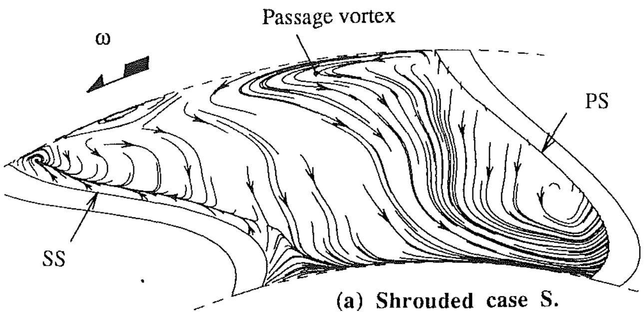

(a) Shrouded case S.

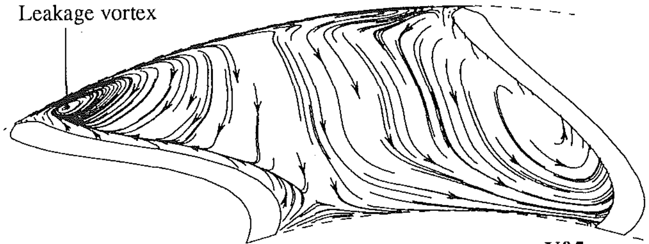

(b) Unshrouded case U05.

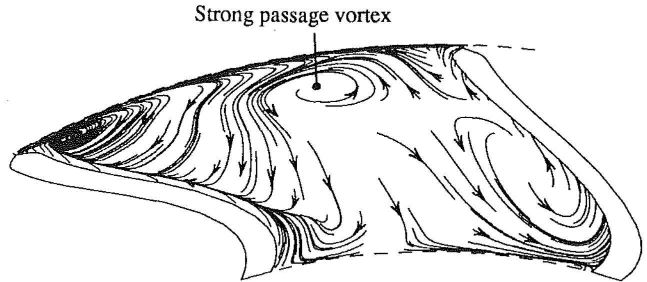

(c) Unshrouded case U10.

Fig. A3 Particle path lines on quasi-orthogonal plane ($Q^* = 0.9$, at 79 percent chord location)

strong tip leakage reverse flow interacts with the incoming flow and makes the casing boundary layer thicker. Figure A2 compares the development of the boundary layer on the casing between two different tip clearances in the form of perpendicular vorticity contours. The tip leakage flow becomes strong as the clearance increases. However, the passage vortex (secondary flow along the casing toward the suction side) also develops quickly and becomes strong as shown in Fig. A3, which compares the different pattern of the secondary flows on a quasi-orthogonal plane at a 79 percent chord in the form of particle path lines of secondary flows. The quick development of the passage vortex in the large clearance case is caused by the thick casing boundary layer due to tip-leakage-induced reverse flows. Consequently, the location of the wake flow, formed in the interaction region between the tip leakage flow and the passage vortex, settles closer to the suction surface as the tip clearance is enlarged.

Inlet Reverse Flow Mechanism in Axial Flow Turbomachines With Neither Stall Nor Significant Radial Flow

M. Aoki

K. Yamamoto

Ebara Research Company,
Fujisawa, Japan

The cause of inlet reverse flow was studied in axial flow turbomachinery. A helical inducer, in which neither stall nor significant radial flow was observed, was selected as the experimental model. The flow between the blades was measured by a laser-Doppler velocimeter and investigated using the end-wall boundary-layer theory. Results showed that the inlet reverse flow occurs adjacent to the pressure surface between the blades in the vicinity of the casing wall. Inlet reverse flow, caused by a momentum defect in the axial direction in the boundary layer on the casing wall and a significant pressure gradient in the axial direction adjacent to the inlet blade pressure surface at partial flow rate, was found even though there was no significant radial flow or stall. In this paper, radial flow is defined as flow that causes a nonnegligible increase in the pressure on the casing wall.

Introduction

Clarification of the characteristics at partial flow rate in axial flow turbomachinery is an important problem in practice, and many studies have been made on this problem. Reverse flow at the impeller inlet causes an increase in shaft power and sometimes causes flow pulsation when cavitation occurs. Therefore the cause of inlet reverse flow is a matter of great concern for many turbomachinery engineers.

When reducing the flow of an axial pump or axial fan, inlet reverse flow often occurs after stall. In the case of axial pumps, inlet reverse flow often occurs after the onset of outlet reverse flow, usually due to an increase of radial flow. Accordingly in past studies, inlet reverse flow was considered to be caused by stall or significant radial flow [1, 2].

However, in some cases, the inlet reverse flow occurs without significant radial flow or stall. We have used a laser-Doppler velocimeter to take three-dimensional measurements of the interblade flow of an axial impeller, which generates inlet reverse flow without displaying significant radial flow or stall. We investigated the balance of axial forces adjacent to the casing wall at impeller inlet, using end-wall boundary-layer theory, and found that inlet reverse flow does not arise from significant radial flow or stall. The effect of inlet reverse flow on the internal flow of impeller is also studied.

Measurement and Instrumentation

The shape and major data of the present impeller are shown in Fig. 1 and Table 1. Table 1 also indicates the major data for the reference impeller [3], in which stall and significant radial flow were observed. The present impeller is a flat-plate helical inducer with two blades 4 mm thick, having a tip diameter D_t = 158 mm and a hub diameter D_h = 50 mm. The blade angle at the tip (β_t) is 14 deg, and the solidity (l/t) is 2.0. The incidence angle at inlet tip at the best efficiency point is about 4 deg. The casing, which has an internal diameter of 159.5 mm, is made of acrylic resin, permitting measurement of the internal flow by laser-Doppler velocimeter (LDV). A pressure-measuring hole 2 mm in diameter is provided on the casing wall for installing a small pressure transducer. A volute-type diffuser was installed downstream of the impeller in an effort to eliminate rotating components in the flow. The rotational speed of the impeller is 2000 min^{-1}.

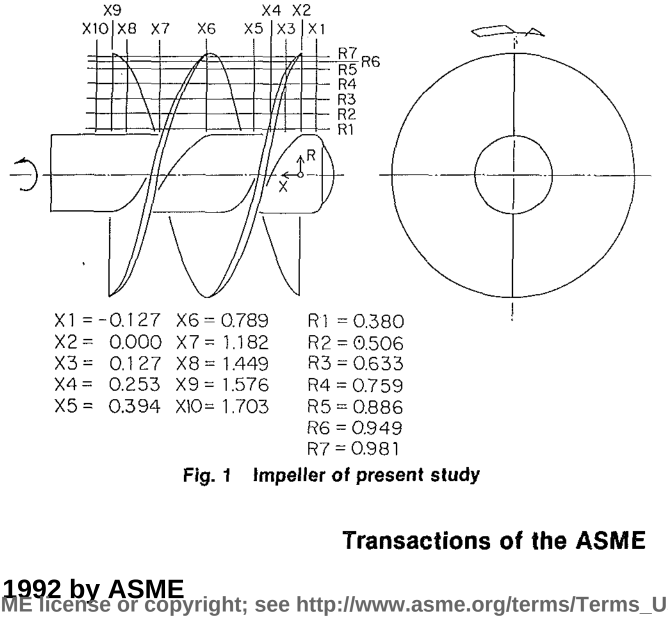

Fig. 1 Impeller of present study

Contributed by the International Gas Turbine Institute for publication in the Journal of Turbomachinery. Manuscript received at ASME Headquarters May 1991. Associate Editor: L. A. Riekert.

Table 1 Major data of impellers

		Present impeller	Reference impeller(3)
Tip diameter	mm	158.0	228.0
Hub diameter	mm	50.0	113.0
Number of blades		2	3
Solidity		2.00	0.62
Tip inlet angle	deg	14.0	13.0
Tip outlet angle	deg	14.0	15.8
Hub inlet angle	deg	38.4	24.7
Hub outlet angle	deg	38.4	67.5
Tip clearance	mm	0.7	1.0
Speed of rotation	min^{-1}	2000.0	1000.0

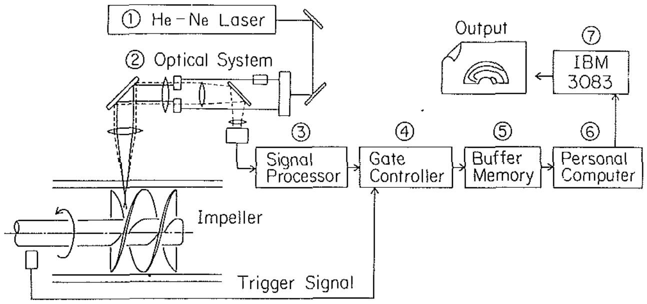

Fig. 2 LDV measuring system

The LDV measurement system consists of the following components, as shown in Fig. 2:

1 A 15 mW He-Ne laser energy source.

2 An optical device to detect scattered light from particles by focusing it on the measuring point, a frequency shifting device to measure negative speed, a laser spectroscope rotating device and polarized plane rotator, and a traverse device for moving measuring points are installed.

3 A counter-type signal processor to measure the frequency of scattered light being detected.

4 A gate controller to transfer processing signals in each address to buffer memory by generating 256 addresses per rotation of impeller with reference to the trigger signal, which indicates the rotational position of the impeller.

5 Buffer memory (capacity 128 K-bytes) to read a significant number of processing signals quickly and transfer them to personal computers.

6 A 16-bit personal computer to calculate flow velocity through processing signals.

7 A large-scale computer to process and plot the measured data.

LDV flow measurements were taken at ten axial planes (X1 to X10) at seven radial positions (R1 to R7) on each plane. A series of 256 points in the circumferential direction was taken per revolution of the impeller. Aluminum oxide powder mixed with surfactant and water was used as seed particles for reflecting scattered light. Pump head was measured by inserting a Pitot tube with three holes at the X1 and X10 positions in Fig. 1.

Accuracy in Measurement

About 140 data points were sampled per address in the LDV measurement, and the data were processed to obtain mean velocity values. The mean values were examined by varying the number of data sampling per address from 5 to 10,000, and checking the mean value for each case. As a result, error due to shortage in number of samples was found negligible if the number of data exceeded 80. The cross angle of the laser beam varies when it penetrates through a curved casing of acrylic resin. Flow velocity was calculated using the correction factor of the individual velocity components obtained from the refractive index and the curvature of the casing. The positions of the measuring points were confirmed by focusing the laser beam on a predetermined mark on the impeller. The integral of axial velocity component at each sectional plane of measurement is compared with the flow rate measured by a venturi flow meter to find the accuracy of flow velocity measured by LDV, and the difference between the two methods was less than 5 percent.

Initiation of Inlet Reverse Flow

The pump characteristic of the present impeller is shown in solid line in Fig. 3. The broken line indicates the characteristic

Nomenclature

c = tip clearance
C_r = nondimensional absolute velocity component in radial direction
C_u = nondimensional absolute velocity component in peripheral direction = u/u_t
C_Z = nondimensional absolute velocity component in axial direction = v/u_t
DF = diffusion factor = $(1 - w_2/w_1) + (w_{u1} - w_{u2})/(2w_1 l/t)$
D_t = tip diameter of impeller
E = entrainment factor
F = force defect
H = shape factor = δ_1/δ_2
l = blade chord
r = radius position
R = nondimensional radius = $2r/D_t$
t = blade pitch at tip
u = tangential velocity
u_t = peripheral tip velocity
v = axial velocity
W = nondimensional relative velocity = w/u_t
x = axial distance measured from front edge
X = nondimensional distance in axial direction = $2x/D_t$
y = radial distance measured from casing wall
α = coefficient of contraction [7]
β_t = angle between blade tip and tangential direction
Δp = pressure difference on blade surface in tangential direction
δ = boundary layer thickness
δ_1 = boundary layer displacement thickness
δ_2 = boundary layer momentum thickness
μ = nondimensional shaft power coefficient = torque/$\{\pi \rho g u_t^2 D_t (D_t^2 - D_h^2)/4\}$
ν = liquid kinematic viscosity
ρ = liquid density
τ_w = wall shear stress
ϕ = nondimensional flow coefficient = $Q/\{\pi(D_t^2 - D_h^2)u_t/4\}$
ψ = nondimensional pressure coefficient = head/(u_t^2/g)
$^-$ = average value in peripheral direction

Subscripts

0 = main flow
1 = inlet
2 = outlet
st = static
t = total
w = wall surface

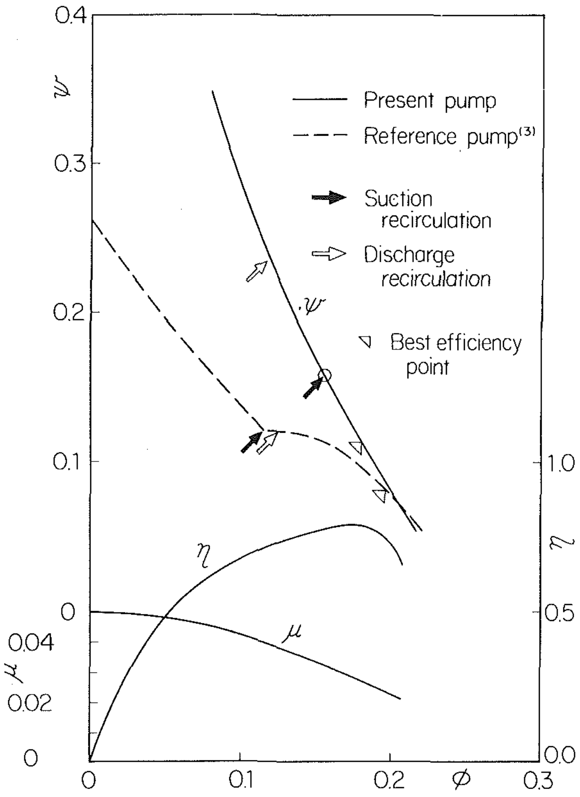

Fig. 3 Pump characteristics

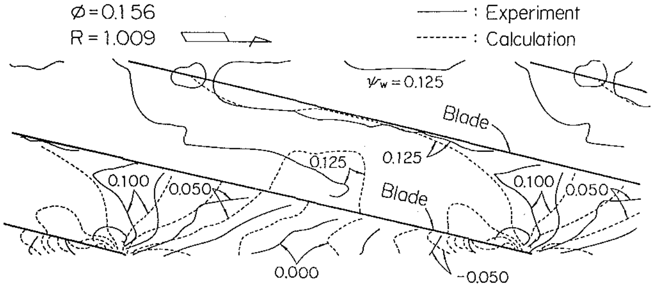

Fig. 4 Interblade pressure distribution on casing wall (at inlet reverse flow onset)

of the reference impeller (Table 1), in which stall and significant radial flow are observed. The head curve of the present impeller is linear, and stall is not observed. The solid and open arrows indicate the onset point of inlet and outlet reverse flow, respectively. The inlet reverse flow for the present impeller occurs at the point where flow coefficient ϕ is 0.156 (87 percent of the flow at the maximum efficiency). Our discussion will center mainly on the flow conditions at $\phi = 0.156$ where there is no cavitation.

Figure 4 shows the interblade pressure distribution on the casing wall. The solid line in the figure indicates the measured values by use of pressure transducer while the broken line indicates the values calculated by three-dimensional potential flow theory using the finite element method [4]. A significant pressure gradient in the axial direction occurs adjacent to the blade pressure surface at the impeller inlet because of an angle of attack. It is observed that the pressure rise is produced in the first half of the impeller and that the blade loading is very small in the latter half.

The absolute velocity vector between blades measured at the position of mean radius of impeller, where $R = 0.759$, is shown in Fig. 5. The axial velocity component C_Z at the inlet ($X = 0.0$) is large on the suction side of blade and small on the pressure side, corresponding to the axial pressure gradient.

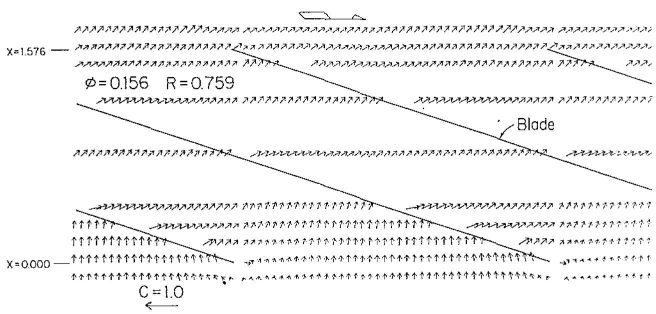

Fig. 5 Absolute velocity at the mean radius (at inlet reverse flow onset)

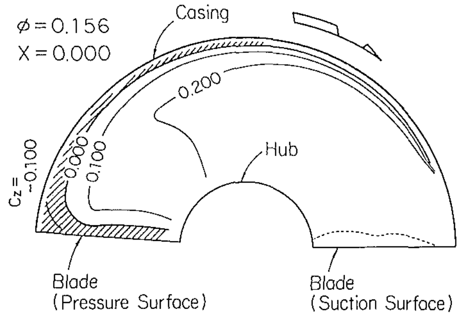

Fig. 6 Distribution of C_Z at the leading edge section (at inlet reverse flow onset)

Almost no peripheral velocity component is indicated in the flow at the inlet of impeller. The absolute velocity vector in the upstream direction is observed in the close vicinity of the leading edge of the blade pressure surface because the pressure side flow passes around the blade into the suction surface ($C_Z \leq 0$).

The distribution of C_Z between blades at the blade leading edge ($X = 0.0$) is shown in Fig. 6. The shaded area in this figure where $C_Z \leq 0$ can be divided into two regions: the region along the blade pressure surface, and the region along the casing wall. The region of $C_Z \leq 0$ along pressure surface at the leading edge of blade is caused by the abovementioned flow passing around the leading edge (Fig. 5), and differs from so-called inlet reverse flow. The region of $C_Z \leq 0$ along the casing wall is widely spread in the peripheral direction and can be recognized as a reverse flow.

The distribution of the relative velocity vector between blades at $R = 0.981$ adjacent to the impeller tip is shown in Fig. 7. The interblade distribution of the radial velocity component C_r at the blade leading edge ($X = 0.0$) is shown in Fig. 8. The region enclosed with a dotted line on the blade pressure surface adjacent to the hub in Fig. 8 indicates locations where measurements could not be taken because of the blade blocking the laser beam.

The flow adjacent to the blade suction surface at the impeller inlet is directed parallel to the blade, and significant separation is not observed. In the latter half of the blades flow follows the blades and indicates no stall. As indicated in Fig. 8, the impeller inlet flow has little radial velocity component. But C_r along the outer peripheral zone between blades close to the suction surface is considerably larger. Accordingly, notwithstanding the fact the impeller is operating at partial flow rate, significant separation is not observed on the suction surface at the blade leading edge (Fig. 7). Flow along the blade suction surface enters the blade passage at the point where the radius is smaller. The flow close to the tip does not enter the blade passages near the pressure side at the impeller inlet, thus producing the value of $C_Z \leq 0$ in the whole region upstream (at the bottom of the Fig. 7) of the dotted line in Fig. 7. The region where $C_Z \leq 0$ penetrates deeply into the blades near

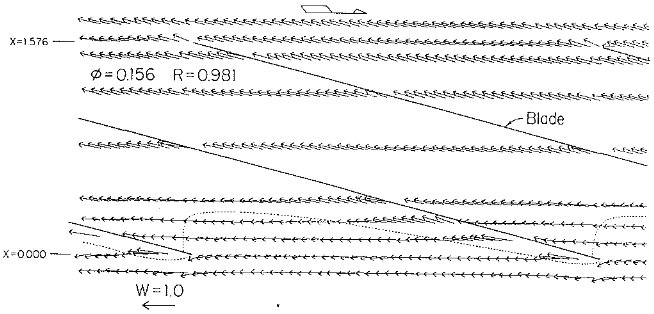

Fig. 7 Relative velocity vector adjacent to the tip (at inlet reverse flow onset)

the pressure surface, where inlet reverse flow can be observed. The stagnation point on the blade pressure surface seems to be located close to the leading edge, and the measurement of flow along the pressure surface where $C_Z < 0$ could not be obtained.

At a lower flow rate, the flow close to the tip ($\phi = 0.104$, $R = 0.981$) is seen to have developed farther from the initial inlet reverse flow, as shown in Fig. 9. The flow seems to separate right after the leading edge on the blade suction side, but it reattaches again immediately, without any accompanying stall. The region of forward flow ($c_z > 0$) on the blade suction side is larger than the one corresponding to the initial state of the inlet reverse flow (Fig. 7), and an increase in the radial flow is noted. Reverse flow on the blade pressure side is also increased so much that the fluid around the leading edge is not allowed to enter fully between the blades and flows back toward the upstream of the impeller. The above reverse flow condition qualitatively coincides with the results observed in the past [5].

Inlet Reverse Flow Mechanism

As shown by the head curve (Fig. 3), no significant stall seems to have occurred before inlet reverse flow starts in the present impeller. Therefore it is hardly reasonable to consider that inlet reverse flow is caused by the pressure rise near the casing outlet due to tip stall, as has been observed by Nakajima and Shiramoto [1] in a fan. Outlet reverse flow is not observed when inlet reverse flow started in the present impeller (Fig. 3), and the radial velocity component is small, $C_r \doteqdot 0.03$ (Fig. 11). The increased pressure on the casing wall caused by this C_r is less than 0.001 in a pressure coefficient. Accordingly, in the case of the present impeller, it is difficult to argue that the inlet reverse flow is caused by the pressure rise on the casing wall due to significant radial flow as was reported by Toyokura [2] for a pump in which outlet reverse flow occurs first.

The balance of the axial forces was examined to study the inlet reverse flow mechanism in the present impeller by a limited use of end-wall boundary-layer theory in the vicinity of casing wall at the impeller inlet. The flow was examined by taking the average value in the peripheral direction at the impeller inlet ($X_1 < X < X_3$ in Fig. 1), where the effect of radial and tangential velocity component of flow is considered to be small in absence of inlet reverse flow.

According to Mellor [6], the equation for axial momentum on the wall surface in the end-wall boundary-layer can be expressed as follows:

$$\frac{d}{dx}\,(\bar{v}_0^2\delta_2)+H\delta_2\bar{v}_0\,\frac{d\bar{v}_0}{dx}=\frac{\tau_w}{\rho}+\frac{d}{dx}\left(\frac{\bar{v}_0^2+\bar{u}_0^2}{2}\,F\right) \tag{1}$$

The flow, immediately after entering the blade passage, does not have an appreciable tangential velocity component, due to the fact that the influence of angular momentum given by the blades is limited to the flow very close to the blade pressure surface (Fig. 5). Thus, we place $\bar{v}_0^2 + \bar{u}_0^2 = \bar{v}_0^2$ for the second term on the right-hand side of Eq. (1) for simplification. Assuming the difference in the shearing stress on the blade surfaces is small between main flow and boundary layer, force defect F can be expressed by tangential pressure difference Δp on the blade surface.

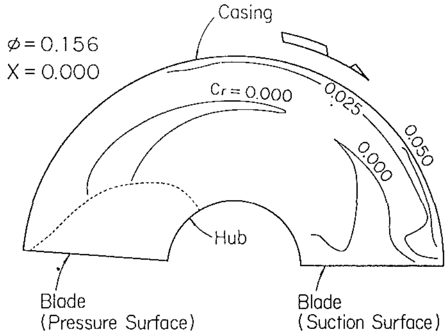

Fig. 8 Distribution of C_r at the leading edge section (at inlet reverse flow onset)

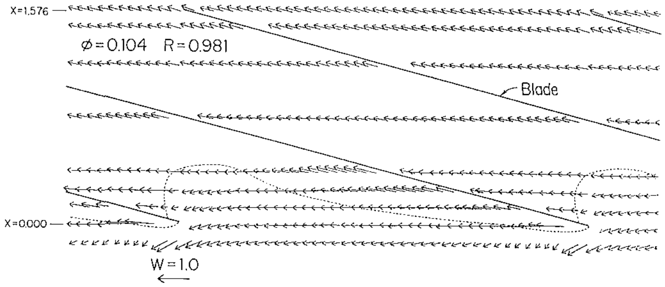

Fig. 9 Relative velocity vector adjacent to the tip (with fully developed inlet reverse flow)

$$\frac{d}{dx}\left(\frac{\rho\bar{v}_0^2}{2}\,F\right)=\frac{1}{\rho t\,\tan\beta_t}\int_0^\delta(\Delta p_0-\Delta p)dy \tag{2}$$

According to Seno'o and Ishida [7], assuming α is a coefficient of contraction, the blade loading is negligible on the distance of $(2\alpha - 1)c$ from the blade tip. Let:

$$\int_0^\delta(\Delta p_0-\Delta p)dy=2\alpha c\Delta p_0 \tag{3}$$

Then the following equation can be derived from the equation of axial flow momentum in the main flow, assuming that the pressure gradient in the main flow dp_0/dx is equal to the pressure gradient on the wall dp_w/dx:

$$\Delta p_0=\left(\frac{dp_w}{dx}+\rho\bar{v}_0\,\frac{d\bar{v}_0}{dx}\right)t\,\tan\,\beta_t \tag{4}$$

Then Eq. (1) can be transformed as follows:

$$\frac{d\delta_2}{dx}=\frac{\tau_w}{p\bar{v}_0^2}-(2+H)\,\frac{\delta_2 d\bar{v}_0}{\bar{v}_0^2 dx}+\frac{2\alpha c}{\rho\bar{v}_0^2}\left(\frac{dp_w}{dx}+\rho\bar{v}_0\,\frac{d\bar{v}_0}{dx}\right) \tag{5}$$

We used Head's Entrainment equation [8] to obtain the following:

$$\frac{dH^*}{dx}=\frac{E}{\delta_2}-\frac{\tau_w}{\rho\bar{v}_0^2}\,\frac{H^*}{\delta_2}+(H+1)\,\frac{H^*}{\bar{v}_0^2}\,\frac{d\bar{v}_0}{dx} -\frac{2\alpha cH^*}{\rho\bar{v}_0^2\delta_2}\left(\frac{dp_w}{dx}+\rho\bar{v}_0\,\frac{d\bar{v}_0}{dx}\right) \tag{6}$$

where

$$H^*=(\delta-\delta_1)/\delta_2$$

Next, we solve Eqs. (5) and (6) for the shape factor H using Nicall–Ramaprian's equation [9]:

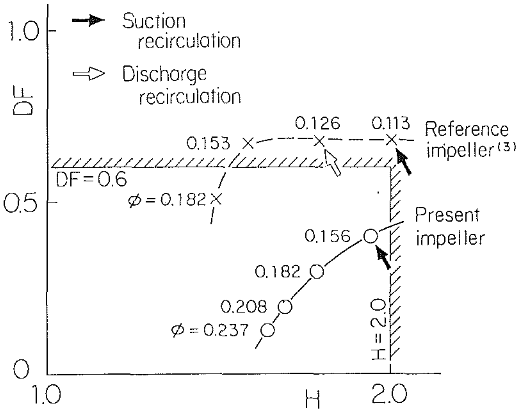

Fig. 10 Shape factor and diffusion factor

$$E=0.035(H-1.25)^{0.5} \tag{7}$$

and Ludwieg–Tillmann's friction law [10] on the wall surface:

$$\frac{\tau_w}{\rho\bar{v}_0^2}=0.123\times 10^{-0.678H}\left(\frac{\bar{v}_0\delta_2}{\nu}\right)^{-0.268} \tag{8}$$

Next, we enter the measured values for the momentum thickness δ_2, the initial value of H, and dp_w/dx. The coefficient α is assumed as 0.8 [7].

To set up a basis for relative comparison, the reverse flow is assumed to occur when the shape factor H of the boundary layer on the casing wall, which is 10 mm downstream ($X = X_3$ in Fig. 1) from the impeller inlet, increases excessively to break the balance of axial forces of the peripherally average flow.

The diffusion factor DF, which was obtained from the measured velocity triangle, was used as a criterion for the possibility of stall of the blade. However in the case of the present impeller, DF at the blade tip is derived by using that partial length of the blade chord (90 percent) at which the average wall pressure in the peripheral direction reached 90 percent of the same at the impeller outlet (the maximum value).

Figure 10 shows, in solid and broken lines, the relationship between H and DF for various flow coefficients for both the present impeller and the reference impeller characterized by occurrence of stall (Table 1). The solid and the open arrows indicate the starting points of inlet reverse flow and outlet reverse flow, respectively. Axial velocity decreases as the axial pressure gradient in the impeller increases, caused by the decrease in flow coefficient ϕ, and the subsequent increase of the discharge head ψ. Consequently H increases gradually. Also DF gradually increases with decreasing flow coefficient ϕ. In the case of the reference impeller as shown by the broken line in the figure, the blade loading per unit area is large due to the small solidity, and the DF value exceeds its critical value of 0.6 before H reaches an excessive value. As for the reference impeller, the slope in the head discharge curve is lowered (broken line in Fig. 3) after $\phi = 0.153$ where $DF > 0.6$, and stall is considered to have occurred. Radial flow in the impeller also increases following the occurrence of outlet reverse flow. In the case of the reference impeller, further increase in axial pressure gradient due to the pressure rise by the radial flow causes an inlet reverse flow to occur at $\phi = 0.113$, where H value exceeds the critical value of 2.0.

As the blade loading per unit area is small in the case of the test impeller due to the higher solidity, the H value exceeds its critical value (2.0) before the DF value reaches 0.6, the threshold value of stall. Consequently, in the present impeller the condition for reverse flow resulting from an unbalance in axial forces in the peripherally averaged flow is reached before the occurrence of stall at the impeller inlet. Value of dp_w/dx used for calculating H for the present impeller is hardly affected by the stagnation of the radial flow. From the above, inlet reverse flow is known to occur following the unbalance of axial forces in the peripherally averaged flow in the vicinity of the casing wall at the impeller inlet, even without stall or large radial flow.

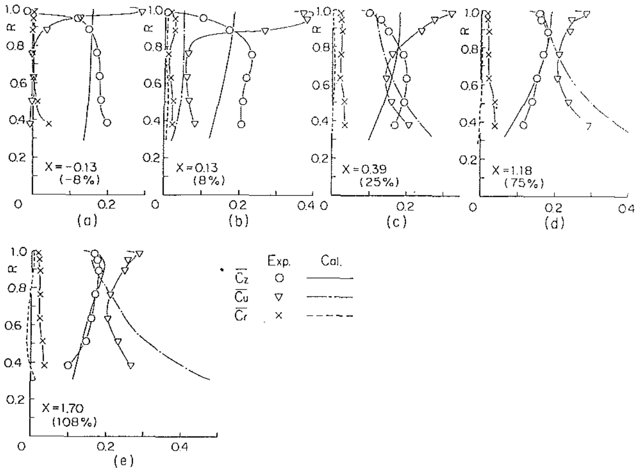

Fig. 11 Interblade flow condition (at inlet reverse flow onset)

Summarizing the above, the inlet reverse flow mechanism can be explained as follows. Generally inlet reverse flow is made ready to start in the impeller by the increase in the axial pressure gradient, following the decrease in axial momentum of flow entering the impeller, and the subsequent increase in pump head and the decrease of the flow rate. The balance of the axial force can easily be disturbed, especially in the vicinity of the casing wall, due to the defect of axial momentum caused by the boundary-layer, and the increase in axial pressure gradient by blade action. At partial flow rate, the balance of force begins to be disturbed near the pressure side. This causes upstream flow because of the extra-large axial pressure gradient (Fig. 4) adjacent to the inlet blade pressure surface, which is affected by the angle of attack. This partial reverse flow, thus initiated, will develop gradually in the peripheral direction to become noticeable as a reverse flow, even if it is considered as a peripherally averaged flow. Stall or significant radial flow is not a requirement for the occurrence of inlet reverse flow, but has a great effect on the occurrence of inlet reverse flow since it produces a significant change in the axial pressure gradient in the impeller (Fig. 10).

Effect of Inlet Reverse Flow

The abovementioned effect of inlet reverse flow on the internal flow of the impeller is now discussed.

Each velocity component averaged in the peripheral direction was measured at each axial position, and its distribution is shown in Fig. 11(*a*)–(*e*). The solid line, chain line, and broken line in the figure indicate the calculated values of C_Z, C_u, and C_r, respectively, by three-dimensional potential flow theory [4]. The figures in parentheses indicate the ratio of the distance between the inlet leading edge and the measured point to the total length of the impeller.

The flow in the vicinity of impeller tip at inlet (Fig. 11(*a*), (*b*)) is given significant angular momentum from the impeller because of the inlet reverse flow. Although reverse flow is not indicated at $X = 0.39$ (Fig. 11(*c*)), C_Z in the vicinity of the tip is considerably smaller than the calculated value. Accordingly, the peripheral velocity component C_u becomes smaller than the calculated value in the main flow, since C_Z exceeds the calculated values. The radial velocity component C_r is not large in the impeller as a whole. But in going downstream, the gradual increase of C_Z in the vicinity of the tip, and the gradual decrease in the vicinity of the hub caused by this radial flow,

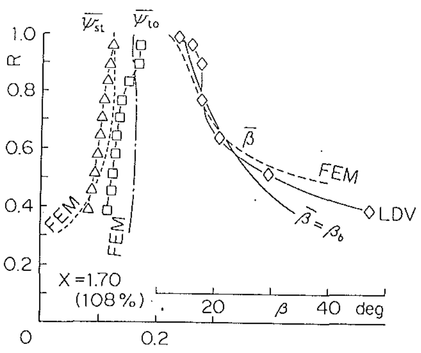

Fig. 12 Exit flow condition (at inlet reverse flow onset)

brings the measured value close to the calculated value. The distribution of the calculated C_Z does not vary much in axial direction and the calculated C_r is also small. The calculated value of C_u comes close to a free-vortex velocity distribution as it goes downstream. But the measured C_u in the vicinity of tip is larger than the calculated value because of the angular momentum supplied to the inlet (Fig. 11(*c*), (*d*)). Therefore, immediately downstream of the impeller outlet (Fig. 11(*e*)), the distribution of the measured C_Z conforms fairly well with the calculated value, while C_u does not.

Figure 12 indicates the total pressure ψ_{to}, static pressure ψ_{st}, and flow angle β immediately after the impeller outlet ($x = 1.70$). The flow angle β is larger than the blade angle β_b in the vicinity of the hub and the tip. The large value of β in the vicinity of the hub is attributed to the secondary flow between the blades. The fact that the value of β measured in the vicinity of impeller tip is larger than β_t is caused by the significant angular momentum imparted to the flow by the inlet reverse flow. When inlet reverse flow occurs along the casing wall, the angle of attack decreases due to the increase in C_Z and also in C_u in the main flow. Consequently, even with the further decrease in flow rate, it is hard to cause stall, and the pump head increases linearly with decrease in the flow rate.

Conclusion

Three-dimensional measurements of the interblade flow in a flat plate type helical inducer were taken by means of a laser-Doppler velocimeter, and investigated to determine the inlet reverse flow mechanism in axial flow turbomachines.

In general, inlet reverse flow in axial turbomachines is often caused by special phenomena attributable to the partial flow rate such as stall or significant radial flow. We have shown that inlet reverse flow can occur at the blade pressure surface near the casing wall due to the significant axial pressure gradient at partial flow rate adjacent to the inlet pressure surface between the blades, and due to the axial momentum defect near the casing wall at the impeller inlet. This occurrence can be independent of the significant radial flow that causes the pressure rise on the casing wall and of stall. By using the measurements of the interblade flow and the results of three-dimensional analysis, we have also shown the effect of inlet reverse flow, indicating how it propagates from the impeller inlet to the outlet.

Acknowledgments

The authors wish to express their thanks to Dr. Tomitaro Toyokura and Dr. Jun'ichi Kurokawa of Yokohama National University, and Dr. Masahiro Inoue of Kyushu University for their guidance in the study.

References

1 Nakajima, Y., and Siramoto, K., 1972, "Design Method of Axial-Flow Blades and Fan Characteristics" [in Japanese], *Trans. JSME*, Vol. 38, No. 314, pp. 2583–2592.

2 Toyokura, T., 1961, "Studies on the Characteristics of Axial-Flow Pumps, Part 2," *Bull. JSME*, Vol. 4, No. 14, pp. 294–301.

3 Toyokura, T., 1961, "Studies on the Characteristics of Axial-Flow Pumps, Part 1," *Bull. JSME*, Vol. 4, No. 14, pp. 287–293.

4 Daiguji, H., 1983, "Finite Element Analysis for 3-D Compressible Potential Flow in Turbomachinery," *Proc. Tokyo Int. Gas Turbine Congr.*, Vol. 2, pp. 445–462.

5 Carey, C., Shamsolahi, S., and Fraser, S. M., 1989, "Comparison of the Three-Dimensional Relative Flow in Two Mixed-Flow Impellers," *IAHR/AIRH Symposium* (*Montréal*), p. 48.

6 Mellor, G. L., and Wood, G. M., 1971, "An Axial Compressor End-Wall Boundary Layer Theory," ASME *Journal of Basic Engineering*, Vol. 93, No. 2, pp. 300–316.

7 Seno'o, Y., and Ishida, M., 1986, "Deterioration of Compressor Performance Due to Tip Clearance of Centrifugal Impellers" [in Japanese], *Trans. JSME*, Vol. 52, No. 473.

8 Head, M. R., and Patel, V. C., 1968, "Improved Entrainment Method for Calculating Turbulent Boundary Layer Development," ARC, R&M, No. 3643.

9 Nicoll, W. B., and Ramaprian, B. R., 1969, "A Modified Entrainment Theory for Prediction of Turbulent Boundary Layer Growth in Adverse Pressure Gradients," ASME *Journal of Basic Engineering*, Vol. 91, No. 4.

10 Ludwieg, H., and Tillmann, W., 1949, "Untersuchungen über die Wandschub-spannung in turbulenten Reibungsschichten," *Ing. Arch.*, Vol. 17.

A Comparison of Two Methods for Utilizing Steam Turbine Exhaust Hood Flow Field Data

R. H. Tindell

T. M. Alston

Grumman Aircraft Systems Division,
Bethpage, NY 11714

This article describes the effects of two methods for representing the nonuniform distribution of flow properties across a steam turbine discharge annulus, on the hood loss coefficient. One method uses a mass-weighted integration of the property across the station, while the other is based on a mass-derived representative value of the property. The former has the potential for very high accuracy provided a sufficient number of points are integrated. The latter, while less accurate, is easier to apply and therefore more commonly used. The analytical modeling includes a simplistic step profile of pressure across the annulus, as well as a three-dimensional exhaust hood, flow-field simulation calculated using a Navier–Stokes code. Results show that significant errors can occur in the hood loss coefficient with the mass-derived approach. Although the analysis centers on hood loss coefficient as the performance parameter whose sensitivity is being monitored, the results highlight the pitfalls of improper application of measured data for any internal flow system.

Background

During the development of internal flow systems, it is often required to identify the effects of flow-field properties, such as pressures, temperatures, and velocities, on the system's performance. The flow field properties may be obtained from numerical calculations, such as with Navier–Stokes solvers, or from test measurements of physical models. When properties at any flow station are nonuniform, which is frequently the case, the calculation of performance parameters can impose some difficult problems. The basic idea is to represent the nonuniform distribution of pressure, velocity, etc., so that a meaningful performance parameter results.

Problem Definition

Good examples of the problem are represented in the calculation of hood loss coefficient and/or static pressure recovery coefficient from a nonuniform flow field in a low-pressure steam or gas turbine exhaust hood. A typical exhaust hood arrangement is seen in Fig. 1. Hood loss is defined as the isentropic static enthalpy drop from the annulus plane to the condenser flange plane and is shown in the enthalpy-entropy diagram in Fig. 2. The hood loss coefficient represents the ratio of the hood loss to the energy equivalent of the annulus dynamic head or turbine exit leaving loss (*LL*). In terms of pressure ratios, the hood loss coefficient for an adiabatic ideal gas can be expressed as:

$$\frac{HL}{LL}=\frac{\left(\dfrac{P_{S_{\mathrm{ANN}}}}{P_{T_{\mathrm{ANN}}}}\right)^{\frac{\gamma-1}{\gamma}}-\left(\dfrac{P_{S_F}}{P_{T_{\mathrm{ANN}}}}\right)^{\frac{\gamma-1}{\gamma}}}{1-\left(\dfrac{P_{S_{\mathrm{ANN}}}}{P_{T_{\mathrm{ANN}}}}\right)^{\frac{\gamma-1}{\gamma}}} \tag{1}$$

where $P_{S_{\mathrm{ANN}}}$ and $P_{T_{\mathrm{ANN}}}$ are the inlet annulus static and total pressures and P_{S_F} is the exit static pressure at the condenser flange plane. The static pressure recovery coefficient is defined as:

$$C_{PR}=\frac{\left(\dfrac{P_{S_F}}{P_{T_{\mathrm{ANN}}}}\right)-\left(\dfrac{P_{S_{\mathrm{ANN}}}}{P_{T_{\mathrm{ANN}}}}\right)}{1-\left(\dfrac{P_{S_{\mathrm{ANN}}}}{P_{T_{\mathrm{ANN}}}}\right)} \tag{2}$$

Both the hood loss and static pressure recovery coefficients are useful for describing the static pressure change across the exhaust hood. Positive values of hood loss coefficient indicate a static pressure reduction across the system while negative values indicate a pressure rise. The static pressure recovery coefficient has opposite trends. The problem is to determine how to describe the most meaningful representation of each of the pressure terms in the equations, from the nonuniform pressure distributions across each of the relevant flow stations, i.e., at the annulus and condenser flange plane stations in the exhaust hood.

These equations are applicable to both gas and steam turbines. In a large steam turbine exhaust, the fluid medium is usually wet steam, i.e., two-phased fluid. Typical operation is

---

Contributed by the Power Division for publication in the JOURNAL OF TURBOMACHINERY. Manuscript received by the Power Division December 4, 1990. Associate Editor: R. W. Porter.

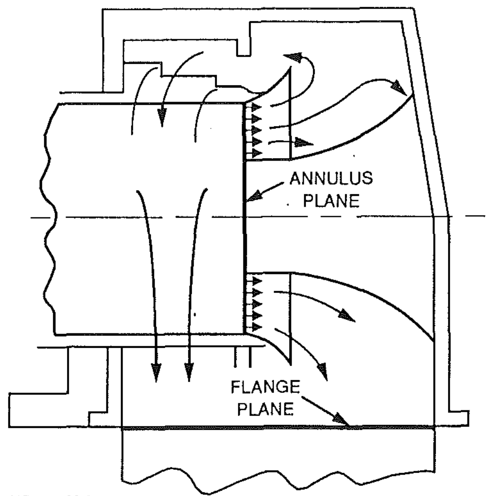

- ENTRY = ANNULUS PLANE
- EXIT = FLANGE PLANE

Fig. 1 Low-pressure turbine exhaust hood

in a pressure temperature region where the ratio of specific heats γ does not vary significantly from exhaust hood inlet to exit. A constant value of $\gamma = 1.10$ provides a good representation for the flow of wet steam in this region.

Mass-Averaged Method

The method recommended as sufficiently accurate for internal flow calculations is to define static and total pressure averages that reflect mass-weighted integration across stations. Similar integrations of local momentum and energy terms define a thermodynamically consistent representation of the nonuniform flow throughout the system. The mass-weighted integrated pressures, when used to determine the hood-loss coefficient, will assure that the result is consistent with the mass flow, energy, and momentum inherent in the nonuniform flow. Under practical circumstances, use of this method frequently requires determining the mass flow by numerical integration, or in the case of model tests, using calibrated orifices. The mass-averaged method for determining the hood loss coefficient consists of the following:

- Determine the mass-averaged exhaust hood inlet annulus total and static pressures from:

$$P_{T_{\mathrm{ANN}}} = \frac{\int P_{T}\rho V dA}{\int \rho V dA} \tag{3}$$

and

$$P_{S_{\mathrm{ANN}}} = \frac{\int P_{s}\rho V dA}{\int \rho V dA} \tag{4}$$

- Determine the exhaust hood exit mass-averaged static pressure by applying Eq. (4) to the condenser flange plane.
- Calculate the hood loss coefficient from Eq. (1).
- The associated mass flow and Mach number at a given station can be determined from:

$$m = \int \rho V dA \tag{5}$$

and

$$M_{MA} = \frac{\int M\rho V dA}{\int \rho V dA} \tag{6}$$

Use of the mass-averaged method is limited to situations where detailed flow field information is available (e.g., from a computational fluid dynamics (CFD) analysis).

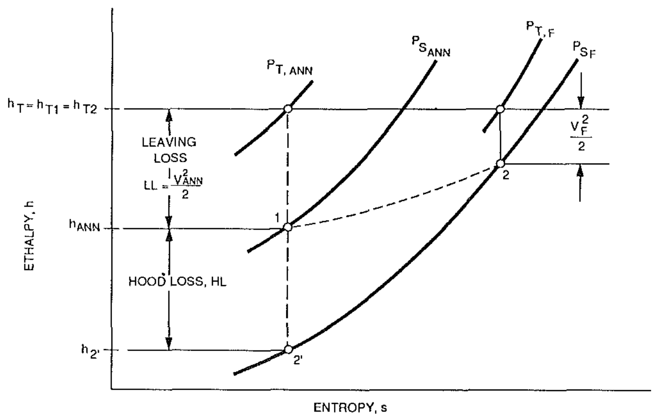

Fig. 2 Definition of losses on the enthalpy-entropy diagram

Mass-Derived or Continuity Method

Since a detailed representation of the flow field is not always available, other methods of averaging are generally used. One of these is the mass-derived or continuity method. This method is usually employed in experimental investigations when there is no capability to measure large pressure gradients, due to inadequate instrumentation and/or physical access. In this approach, the measured or otherwise known mass flow, total temperature, and mass-averaged total pressure (for example) are combined to define a nondimensional mass flow rate at a given station. This leads to a mass-derived Mach number and a mass-derived static pressure.

The procedure for determining hood loss coefficient using the mass-derived method is as follows:

- Measure or calculate the mass flow through the exhaust hood using Eq. (5).
- Measure or calculate the annulus inlet total pressure $P_{T_{\mathrm{ANN}}}$ using Eq. (3).
- The total temperature T_T is measured or calculated using a flow-weighted procedure and assumed to be constant.
- Calculate the nondimensional mass flow rate, for an ideal gas, from:

$$\frac{m\sqrt{RT_T}}{P_{T_{\mathrm{ANN}}}A_{\mathrm{ANN}}}$$

where A_{ANN} is the inlet annulus area and R is the gas constant.

- Using the nondimensional mass flow rate, determine the inlet annulus static to total pressure ratio ($P_{S_{\mathrm{ANN}}}/P_{T_{\mathrm{ANN}}}$).
- Measure or calculate the exhaust hood exit static pressure, P_{SF}, by applying Eq. (4) to the condenser flange plane.
- Calculate the hood loss coefficient from Eq. (1).
- The associated inlet annulus static pressure and Mach number can be determined from the appropriate compressible flow equations.

Basically, the hood loss coefficient is calculated using the mass flow, the mass-averaged total pressure and mass-derived static pressure at the annulus, and the measured or calculated condenser flange plane static pressure. Unfortunately, the mass-derived Mach number and static pressure do not reflect any consideration of the momentum and kinetic energy in the actual nonuniform flow. These values are not conserved in the one-dimensional representation of the mass-derived method. Momentum, kinetic energy, and Mach number are lower and static pressure is higher in the annulus station for the mass-derived case than for the mass-weighted average case. Rigorous treatments of this classical problem are given by McLafferty (1954), Wyatt (1955), and Benedict (1980).

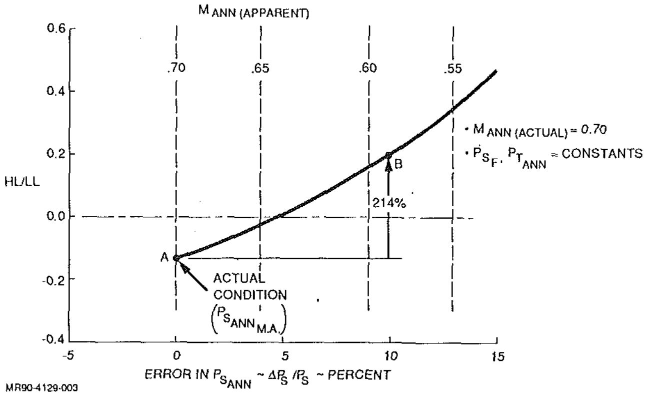

Fig. 3 **Sensitivity of hood loss coefficient to errors in Ps_{ANN}**

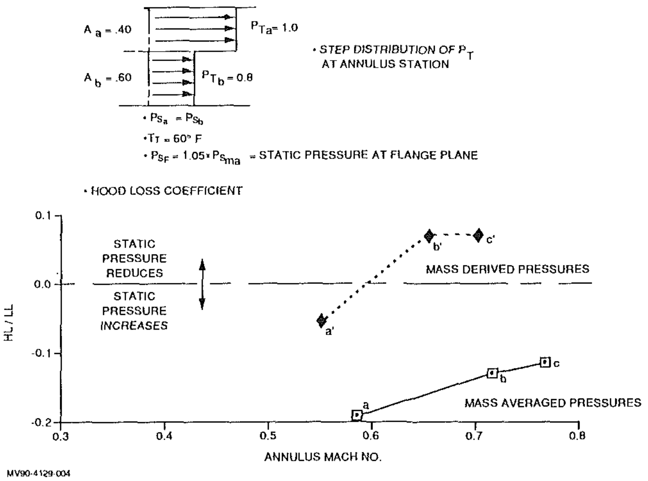

Fig. 4 **Comparison of two methods for calculating hood loss coefficient, using a simplistic flow model**

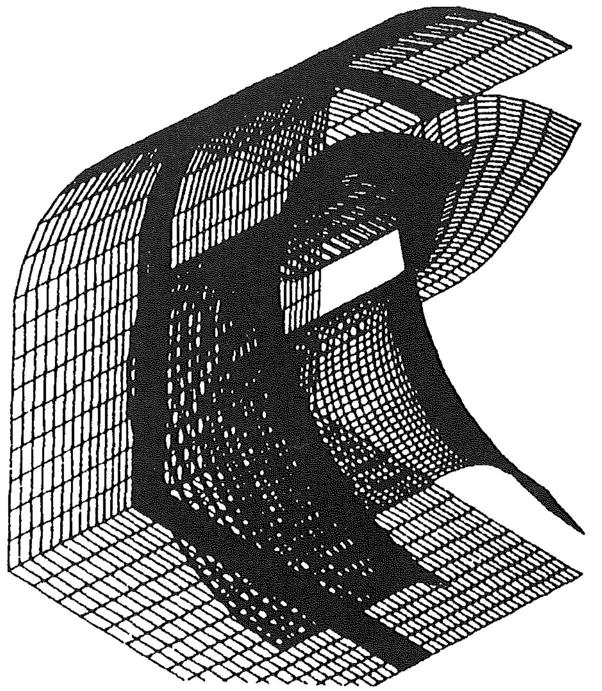

Fig. 5 **Surface grid for Parc Navier-Stokes model for exhaust hood**

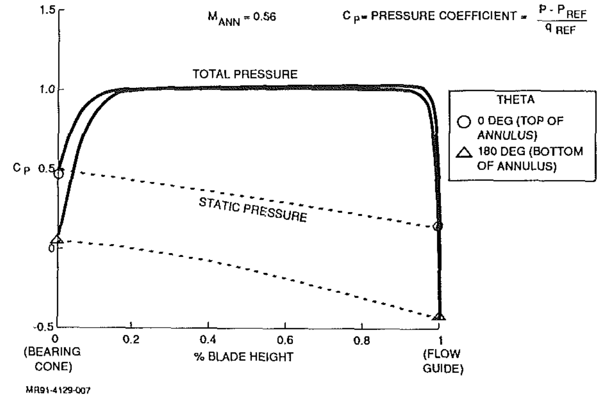

Fig. 6 **Pressure distributions across turbine discharge annulus for uniform flow Navier-stokes code model**

Performance Parameter Sensitivity

The effects of errors in exhaust hood annulus static pressure on hood loss coefficient are shown in Fig. 3, for an annulus station Mach number of M_{ANN} = 0.70. The annulus total pressure and flange plane static pressure are constant, at the "correctly" measured or calculated values, i.e., the zero error values. Notice that the apparent annulus Mach number is reduced as the static pressure is (erroneously) increased. A 10 percent error in static pressure, shown by point B, incurs a 214 percent error in hood loss coefficient. Since the hood loss coefficient has gone from a negative to a positive value, points A to B, we see that the error falsely describes the system as having static pressure reduction rather than a pressure rise, between the annulus and flange plane stations.

Comparison of Calculation Methods

A comparison of the two methods for calculating hood loss coefficient that incorporates the sensitivities to static pressure errors exemplified by the plot in Fig. 3, is shown in Fig. 4, for an annulus total pressure variation described by a step profile. The static pressure is assumed to be constant across the annulus station, and the flange plane static pressure is 5 percent greater than the (correct) annulus static pressure. Calculations of hood loss coefficient were derived by using the mass-averaged and mass-derived methods for three mass-averaged annulus Mach numbers, points a, b, and c in Fig. 4. The total pressures were held constant and the static pressure was varied to achieve the range of annulus Mach numbers. Then, using the integrated mass flows, the mass-averaged total pressures and total temperature, the mass-derived Mach numbers, static pressures and hood loss coefficients were calculated, points a', b', and c'.

The mass-derived method yields a higher loss coefficient, implying poorer performance at all Mach numbers. The relatively large error, 150 percent at M_{ANN} = 0.70 for example, is the penalty for the simplification of not having to measure (or calculate) an accurate representation of the annulus static pressure. Notice that the mass-derived results indicate that the loss coefficient is positive at the higher Mach numbers, thus erroneously indicating that the hood system is reducing the pressure.

The above example can be readily substantiated by the reader. It is a simple two-dimensional flow, not representative of actual exhaust hood characteristics. A better example, representing the three-dimensional flow field in a typical low-pressure turbine exhaust hood, was modeled for a Navier-Stokes CFD calculation (Tindell et al., 1991). Although this modeling included simulation of turbine-induced swirl and total pressure variation, the simulation taken for the work in this paper represents a uniform flow approaching the annulus station, as in an air model. Surface grids for the flow guide and bearing cone housings are shown in Fig. 5. A total of 129,150 grid

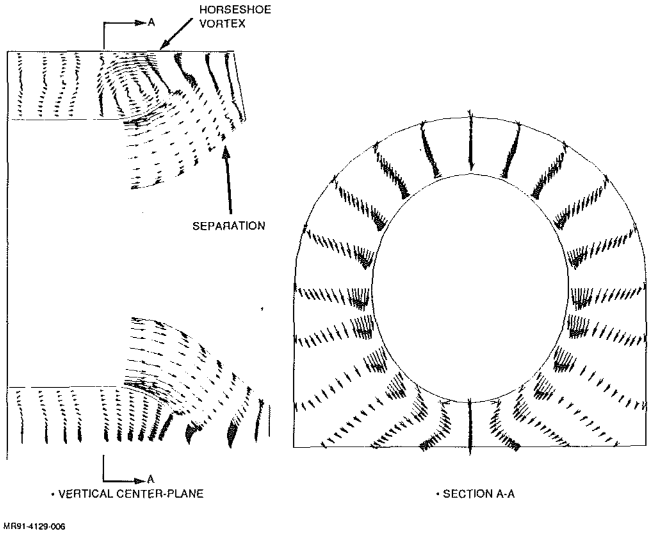

Fig. 7 Velocity patterns calculated for typical computer exhaust hood

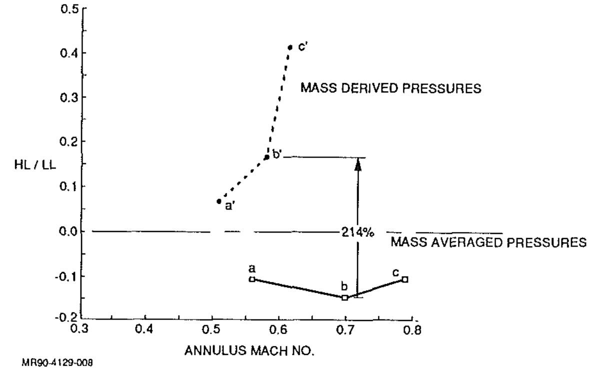

Fig. 8 Comparison of methods for calculating hood loss coefficient with realistic flow model

points were used to define the complete flow field. Figure 6 depicts the pressure distributions across the inlet annulus station. Due to the hood geometry and the boundary layer, nonuniform pressures developed in the approach duct. Results of the flow field calculation describing the velocities in two planes are illustrated in Fig. 7. A complete description of the exhaust hood flow fields is given in the references. The following is a brief description of the significant features of Fig. 7.

First, we notice that the flow on the upper bearing cone, in the vertical center plane, is separated. Furthermore, it is apparent that some of the flow from the upper half of the annulus flows forward and downward, around the bearing cone. Much of the upper half flow, however, turns upward and backward around the flow guide and develops into a large horseshoe vortex. There is a large amount of energy lost in the development of this vortex. It is subsequently turned downward by the hood walls. Finally, both branches of the upper annulus flow are recombined along with the flow from the lower half, at the flange plane. Analysis of the flange plane, not shown here, indicates that the low-energy vortex dominates the flow pattern.

These data were used to calculate the mass flow and the mass-averaged annulus pressures, the mass-averaged flange plane static pressure, and the hood loss coefficient. Then, as with the simpler step profile case, a mass-derived hood loss coefficient was calculated. The results of both cases are shown in Fig. 8. The three calculations for the mass-averaged and mass-derived cases are shown as the unprimed and primed letters, respectively. As previously shown, the mass-derived results indicate poorer performance than the mass-averaged results. At an annulus Mach number of 0.70, an error of 214 percent is seen. By comparison with Fig. 3, we see that the static pressure error induced by the mass-derived calculation at this Mach number is 10 percent.

Concluding Remarks

It is understood that the mass-averaged method of representing a nonuniform flow is not easily applied in most practical situations. However, when using simpler methods, such as the mass-derived approach, the investigator should be aware of the problems associated with their use. The problems associated with the use of the mass-derived method for calculating hood loss coefficient, for a low-pressure turbine exhaust hood, were identified. Similar problems should be expected with other performance parameters such as static and total pressure coefficients, thrust coefficients, etc., that reflect the change of static pressure across the system.

Results of this study indicate that the penalty for using the mass-derived method, relative to the mass-averaged method for calculating performance, can be significant. Not only can overly pessimistic evaluations of performance result, but also a false description of the flow process can be implied, i.e., a pressure reduction rather than a pressure rise. This is particularly important when using sparse pressure data to assess performance of relatively inaccessible elements of flow systems. For example, the inaccessibility of a low-pressure turbine exhaust hood annulus for pressure measurements could lead to an incomplete survey that does not reflect the three-dimensional annulus flow. Conclusions about system performance based upon such data could result in wasteful expenditures of resources. This suggests the requirement for developing pressure instrumentation that can accurately measure the nonuniform distributions across the inlet annulus and condenser flange plane stations of an exhaust hood.

These results also highlight the usefulness of CFD for accurately assessing the performance of low-pressure turbine exhaust hoods. Although the CFD results used in this paper were for a uniform axial flow approaching the annulus station, the velocity swirl and total pressure distributions that characterize turbine exhaust flows can be readily calculated (Tindell et al., 1991). This suggests the possibility of using CFD in conjunction with sparse pressure measurements of relatively inaccessible flows to establish an empirical-analytical approach for improving the ability to assess performance.

Acknowledgments

Some of the results in this paper were obtained from Navier-Stokes calculations performed under a contract sponsored by the Consolidated Edison Company of New York.

References

Benedict, R. P., 1980, *Fundamentals of Pipe Flow*, Wiley, New York, pp. 217-223.

McLafferty, G. H., 1954, "A Generalized Approach to the Definition of Average Flow Quantities in Nonuniform Streams," Report No. R-13534-9, Research Dept., United Aircraft Corp, Hartford, CT.

Tindell, R. H., Alston, T. M., Sarro, C. A., Stegmann, G. C., Gray, L., and Davids, J., 1991, "Computational Fluid Dynamics Analysis of a Steam Power Plant Low Pressure Turbine Downward Exhaust Hood," in: *Design, Repair, and Refurbishment of Steam Turbines*, A. S. Warnock, ed., ASME PWR-Vol. 13, pp. 43-55.

Wyatt, D. D., 1955, "Analysis of Errors Introduced by Several Methods of Weighting Nonuniform Duct Flows," NACA TN 3400, Hampton, VA.

A Two-Dimensional Flow Analysis Model for Designing a Nozzle-less Volute Casing for Radial Flow Gas Turbines

H. O. Owarish
RAM Research and Engineering, Ltd.,
The Lord Rank Research Centre.

M. Ilyas
Senior Lecturer.

F. S. Bhinder
Professor,
School of Engineering.

Hatfield Polytechnic,
Hatfield, Hertsfordshire, United Kingdom

This paper describes a two-dimensional model for flow analysis and design of a single entry nozzle-less volute casing for inward flow radial turbines. The model takes into account the cross-sectional shape of the casing by dividing it into a number of segments, which are further subdivided into control volumes. Changes in flow properties are calculated by considering the changes in momenta of fluid in the tangential and radial directions across each control volume. The model has been computerized using Fortran 77 for the IBM AT or 100 percent compatible micro-computers.

Introduction

The isentropic efficiency of an inward flow radial (IFR) gas turbine fitted with a nozzle-less volute casing tends to be a few percentage points lower than one fitted with a casing incorporating nozzles. However, because of its lower cost and wider operating range, the nozzle-less volute casing is widely used in small turbochargers for automotive class diesel engines. However, it has been seen that the performance handicap of the nozzle-less casing can be overcome by using better design techniques. The aim of this paper is to describe the details of a two-dimensional flow analysis model, which may be used to improve the quality of design of such casings.

Radial flow turbines are suitable for a variety of applications including auxiliary power units for spacecraft. Hence considerable research effort has gone into improving their performance and a large number of papers have been written on the aerothermodynamics, design, and performance of these machines. However, much of the published work deals with the rotor. In contrast, the casing does not appear to have excited the imagination of researchers and design engineers to the same extent. This is in spite of the fact that flow in the casing is very complex, being three dimensional, compressible, viscous, and, in the case of turbochargers, also unsteady.

The available design methods for the casing invariably assume the flow to be steady and one dimensional [1-6]. Hamed and Bashkarone [4] developed a three-dimensional flow analysis method, which made a valuable contribution, but perhaps it was too advanced for the design office use. A detailed review of the published literature is omitted from here for the sake of brevity, but the reader's attention is drawn to the work by Hussain [3] for further study.

Design Requirements

The constructional features of a typical single entry nozzle-less volute casing are shown in Fig. 1(*a*). In addition to housing the rotor, the casing must be designed to perform the following aerothermodynamic functions:

(*a*) to convert some of the static enthalpy of the working fluid into kinetic energy and hence accelerate the fluid to the desired rotor entry Mach number;

(*b*) to direct the high-velocity fluid streams into the rotor at the prescribed absolute flow angle and to achieve the congruence of the velocity triangles around the periphery of the rotor;

(*c*) to achieve (*a*) and (*b*) with minimum loss of stagnation pressure in the casing.

The expansion process that takes place in the casing is shown on the temperature-entropy diagram in Fig. 1(*b*). The flow in the casing is influenced by the detailed design of the following sections:

(*i*) the entry region, in particular the volute tongue;

(*ii*) the cross-sectional area versus the azimuth angle distribution;

(*iii*) the cross-sectional shape of the volute.

The important performance parameters that must be optimized are: the stagnation pressure loss factor ζ, total-to-static isentropic efficiency η, and the variation of the absolute flow angle α at rotor entry with the azimuth angle ϕ. The loss factor and efficiency are defined as follows:

Stagnation pressure loss factor

$$\zeta=\frac{P_{01}-P_{02}}{P_{01}}$$

$$=\frac{\sum_{1}^{2}\delta P_0}{P_{01}} \tag{1}$$

Contributed by the International Gas Turbine Institute and presented at the 36th International Gas Turbine and Aeroengine Congress and Exposition, Orlando, Florida, June 3-6, 1991. Manuscript received at ASME Headquarters March 4, 1991. Paper No. 91-GT-263. Associate Editor: L. A. Riekert.

Pressure taps, 1.5 mm dia.
15 deg. spacing, at centroid
along the volute length.

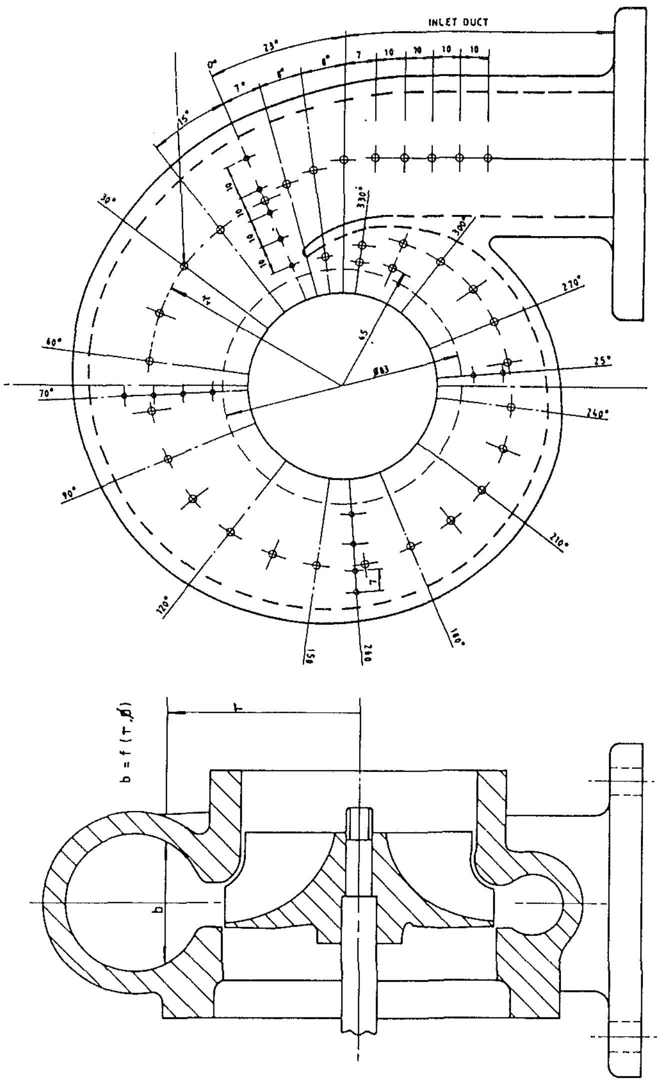

Fig. 1(*a*) Constructional features of a nozzle-less volute casing

Total-to-static isentropic efficiency

$$\eta_{t-s}=\frac{T_{01}-T_2}{T_{01}-T_2}, \tag{2a}$$

Since the stagnation temperature is assumed to remain constant, i.e., $T_{02}=T_{01}$, Eq. (2*a*) can be written as follows:

$$\eta_{t-s}=\frac{1-T_2/T_{02}}{1-T_2'/T_{02}}$$

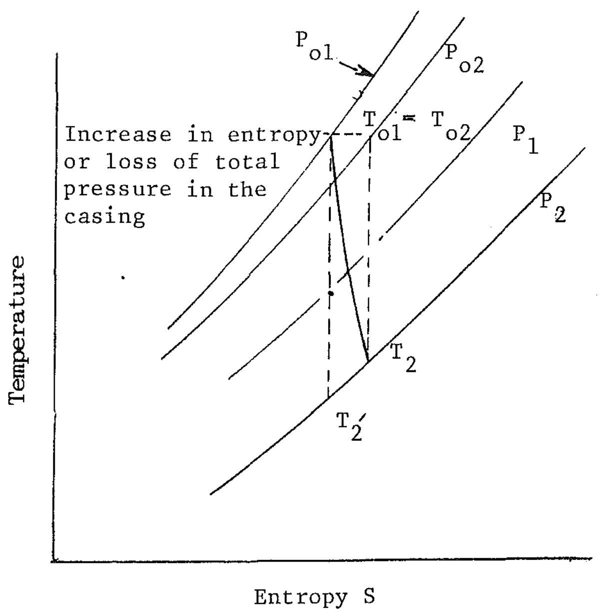

Fig. 1(*b*) The expansion process in the casing on the temperature-entropy plane

From Fig. 1(*b*)

$$\eta_{t-s}=\frac{1-(P_2/P_{02})^{\frac{\gamma-1}{\gamma}}}{1-(P_2/P_{01})^{\frac{\gamma-1}{\gamma}}} \tag{2b}$$

This equation can be written also in terms of ζ.

Two-Dimensional Flow Model

By considering the forces acting on the fluid element shown in Fig. 2(*a*), a set of equations can be derived to calculate the step changes in the following fluid properties across the element:

(*a*) absolute static pressure
(*b*) absolute flow angle
(*c*) radial velocity
(*d*) absolute static temperature
(*e*) fluid density

The derivations of the basic equations are given in the following:

(*a*) **Change in Static Pressure.** The relationship between the mean static pressure and radius can be obtained by considering the forces acting on the control volumes in the radial direction; Figs. 2(*a*) and 2(*b*).

Nomenclature

A = area, m^2
a = acceleration, m/s^2
b = width, m
C = absolute velocity, m/s
C_p = specific heat at constant pressure, kJ/kg K
C_f = friction coefficient
m = mass flow rate, kg/s
P = absolute pressure, N/m^2
R = gas constant, kJ/kg K
Re = Reynolds number
T = temperature, K
V = volume, m^3
α = absolute flow angle, rad
γ = ratio of specific heats = C_p/C_v
δ = small difference or incremental value
ζ = pressure loss factor
η = isentropic process efficiency
ρ = density, kg/m^3
ϕ = azimuth angle, rad

Subscripts

0 = stagnation conditions
1 = inlet condition, also as defined in Fig. 2
2 = exit condition, also as defined in Fig. 2
3 = as defined in Fig. 2
r = in the radial direction
t = in the tangential direction

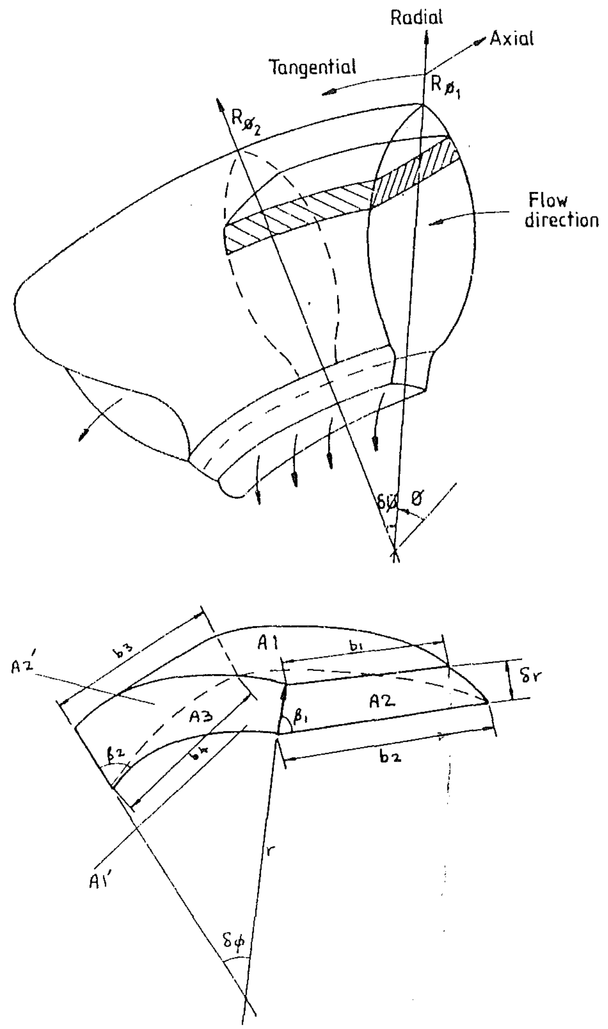

Fig. 2(*a*) **Definition of the control volume and other geometric parameters**

$$-PA_1-\left(P+\frac{\delta P}{2}\right)\cdot(A_{1'}-A_1)+(P+\delta P)A_1$$
$$+C_f\rho C^2A_3\sin(\alpha)=\rho Va_r \qquad (3)$$

where a_r is the acceleration in the radial direction given by:

$$a_r=\frac{C_w^2}{r}-C_r\left(\frac{\delta C_r}{\delta r}\right) \qquad (4)$$

and f_r is the friction factor. A number of expressions are available in the published literature to calculate the effect of friction, but here one from Mager [5], as given below, has been used.

$$C_f=0.0148\,\mathrm{Re}^{-0.0148}\left(\frac{T_0}{T}\right)^{-0.45} \qquad (5)$$

Equation (3) can be simplified and written in terms of δP as follows:

$$\delta P=\frac{\rho Va_r-C_fA_3C^2\rho\sin(\alpha)}{(A_{1'}+A_1)/2} \qquad (6)$$

(*b*) **Change in Absolute Flow Angle.** The relationship between the absolute flow angle and the radius can be obtained by differentiating the equations for radial and tangential velocities with respect to radius and substituting the result into the equation for momentum in the tangential direction. The derivation is given below:

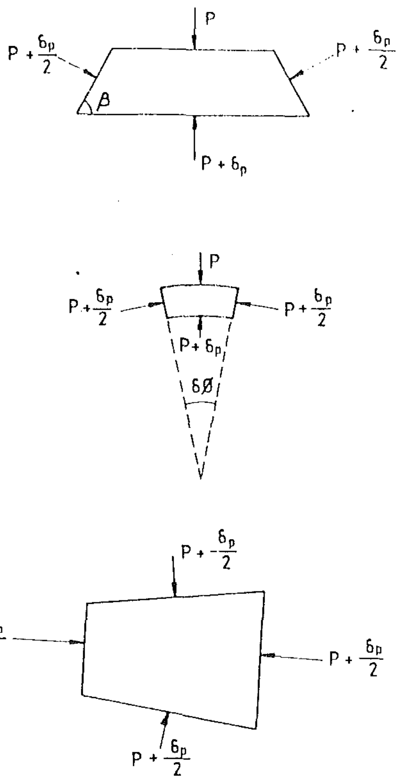

Fig. 2(*b*) **Pressure forces acting on the fluid element**

$$\rho Va_t=\left(P+\frac{\delta P}{2}\right)A_2-\left(P+\frac{\delta P}{2}\right)A_{2'}$$
$$+\left(P+\frac{\delta P}{2}\right)(A_{2'}-A_2)-F_t$$
$$=-F_t \qquad (7)$$

where a_t is the acceleration and F_t the force due to friction, both in the tangential direction, given by the following expressions:

$$a_t=\frac{C_wC_r}{r}+C_r\frac{\delta C_w}{\delta r} \qquad (8)$$

$$F_t=C_f\rho C^2A_3\cos(\alpha) \qquad (9)$$

The relationship between the tangential and the radial components of the absolute velocity C is given by:

$$\tan\alpha=\frac{C_r}{C_w} \qquad (10a)$$

Differentiating this equation with respect to the radius r:

$$\frac{1}{\tan\alpha}\frac{\delta(\tan\alpha)}{\delta r}=\frac{1}{C_r}\frac{\delta C_r}{\delta r}-\frac{1}{C_w}\frac{\delta C_w}{\delta r} \qquad (10b)$$

Combining Eqs. (7), (8), and (10*b*) and simplifying the expression for change in the absolute flow, the angle with respect to radius can be obtained.

$$\delta(\tan\alpha)=\tan\alpha\left\{\frac{\delta C_r}{C_r}+\left(\frac{F_t}{C_wC_r\rho V}+\frac{1}{r}\right)\delta r\right\} \qquad (11)$$

(*c*) **Change in Radial Velocity.** The change in the radial velocity as a function of the radius can be found by differentiating the equation for mass flux in the radial direction. Assuming mass flux in the radial direction is a function of the radius:

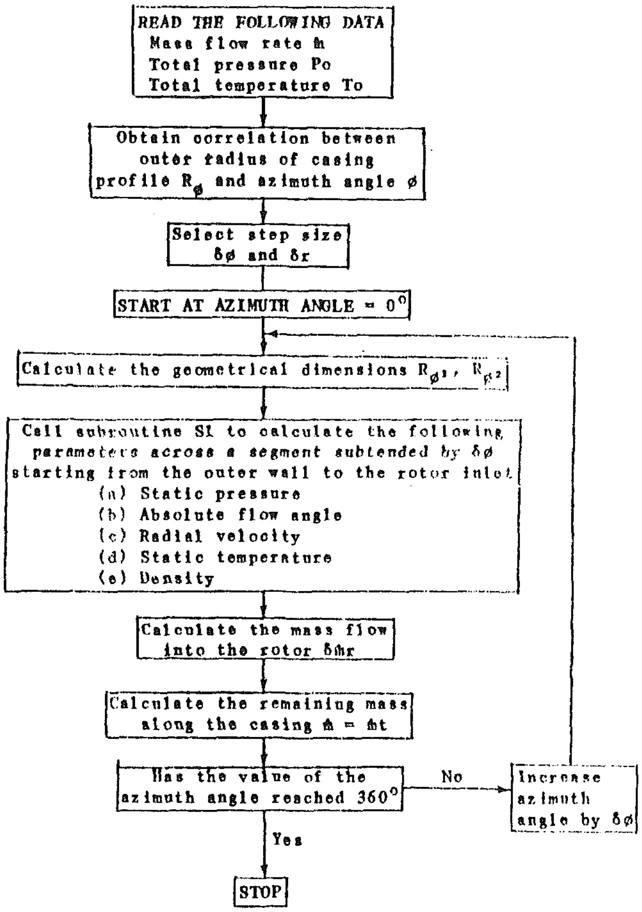

Fig. 3(*a*) Calculation procedure for flow analysis: main program

$$\frac{1}{\rho}\frac{\delta\rho}{\delta r}+\frac{1}{A}\frac{\delta A}{\delta r}+\frac{1}{C_r}\frac{\delta C_r}{\delta r}=\frac{\delta[f(C_r)]}{f(r)\delta r} \tag{12}$$

If mass flux in the radial direction is assumed to be constant, the above equation simplifies to:

$$\delta C_r=-\left(\frac{\delta\rho}{\rho}+\frac{\delta A}{A}\right)C_r \tag{13}$$

(*d*) **Change in Static Temperature.** The change in static temperature with respect to radius can be found by differentiating the energy equation with respect to radius as follows:

$$T_0=T+\frac{1}{2C_p}\left(C_w^2+C_r^2\right) \tag{14}$$

Differentiating with respect to r

$$\frac{\delta T_0}{\delta r}=\frac{\delta T}{\delta r}+\frac{1}{C_p}\left\{C_w\frac{\delta C_w}{\delta r}+C_r\frac{\delta C_r}{\delta r}\right\} \tag{15a}$$

Assuming adiabatic flow and substituting for C_w, this equation can be written as:

$$\frac{\delta T}{\delta r}=-\frac{1}{C_p}\left(\frac{\delta C_r}{\delta r}\{1+\tan\alpha\}+\frac{C_r\delta(\tan\alpha)}{\delta r}\right) \tag{15b}$$

(*e*) **Change in Density.** *Since static pressure and temperature are known, the density of the working fluid can be calculated directly from its equation of state as follows:*

$$\frac{\delta\rho}{\delta r}=\rho\left(\frac{1}{r}\frac{\delta P}{\delta r}-\frac{1}{T}\frac{\delta T}{\delta r}\right) \tag{16}$$

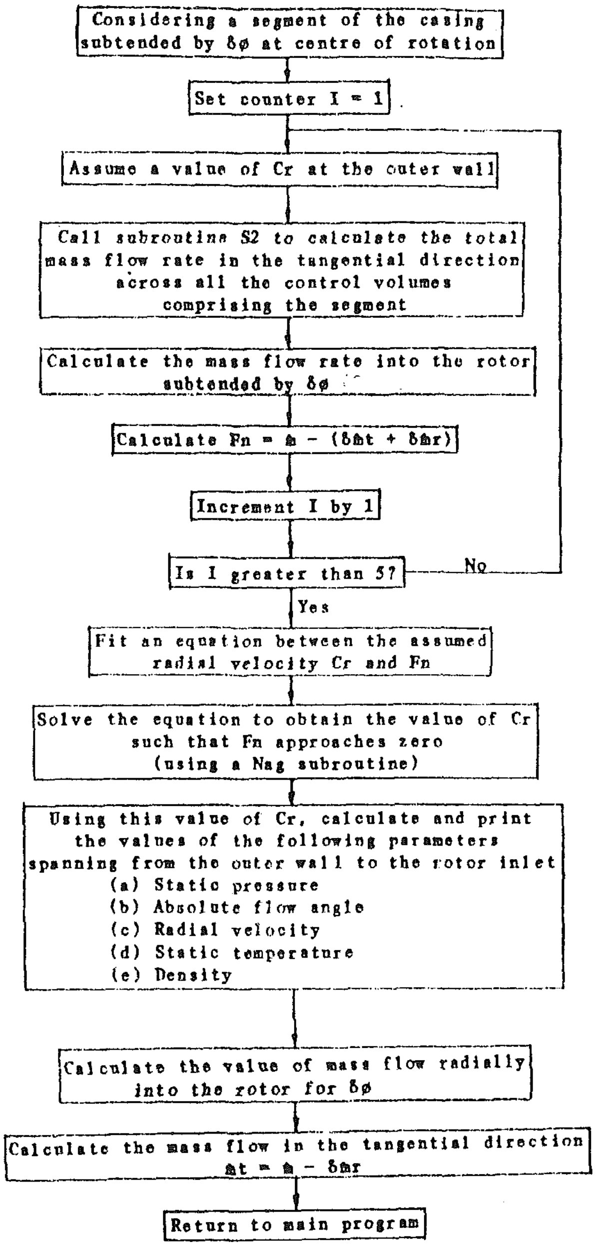

Fig. 3(*b*) Calculation of the total mass flow in the radial direction: subroutine S1

Computer Programs

A suite of programs has been written that included flow analysis as well as design. The calculation procedure is shown in flow diagrams of the programs in Figs. 3(*a*), 3(*b*), and 3(*c*). The program requires the following input data:

(*a*) total pressure at inlet
(*b*) total temperature at inlet
(*c*) mass flow rate at inlet
(*d*) geometric parameter to be used to calculate the casing dimensions

Execution of the program starts with the fitting of a polynomial equation to a given set of data relating the outer radius of the volute to the azimuth angle. Using a least-square fit method, an equation of the following type is obtained:

$$R_\phi=K_1\phi+K_2\phi^2+K_3\Phi^3+\ldots \tag{17}$$

The main program shown in Fig. 3(*a*) uses the subroutine S1 to calculate the flow properties across the segments spanning each incremental azimuth angle $\delta\phi$. A relationship between

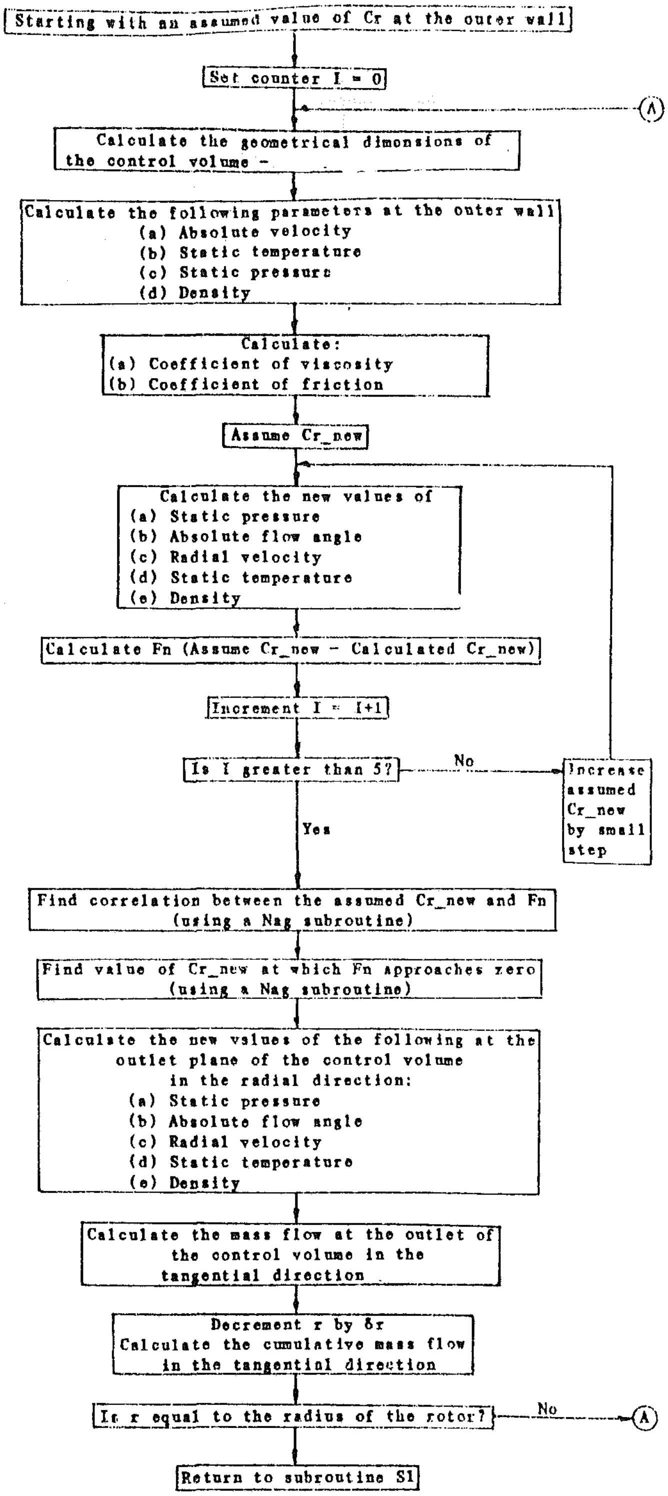

Fig. 3(*c*) Calculation of the total mass flow in the tangential direction: subroutine S2

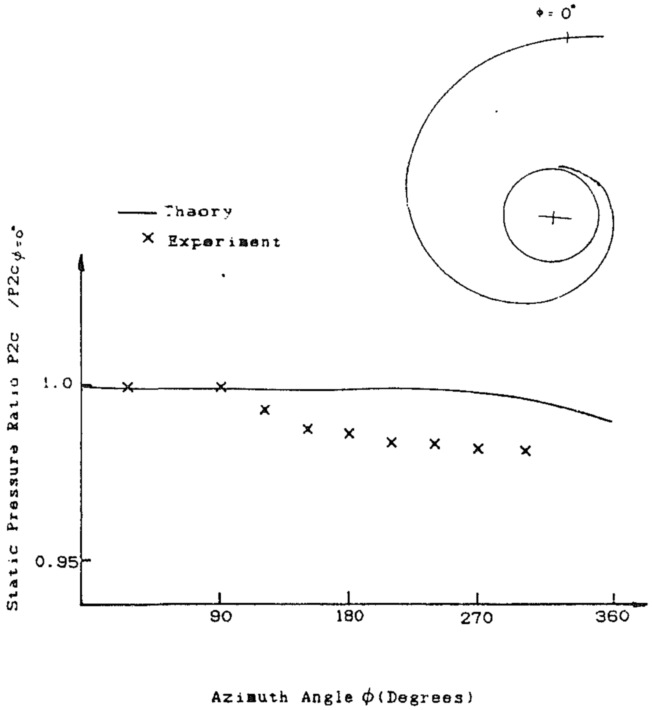

Fig. 4(*a*) Comparison between the graphs of calculated and measured static pressure ratio versus the azimuth angle at the centroid

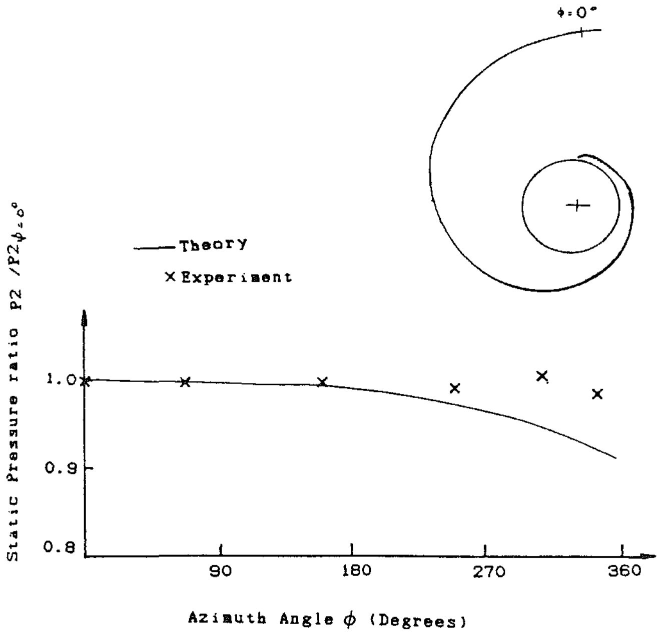

Fig. 4(*b*) Comparison between the graphs of calculated and measured static pressure ratio versus the azimuth angle close to the rotor entry

the radial velocity at the outer wall and the mass balance across the segment is satisfied. The subroutine S2 is used to establish the mass balance.

In subroutine S2, starting with an assumed value of radial velocity at the outer wall, which has been passed across from S1, a function is defined relating the difference between the assumed and the new calculated values of the radial velocity at the control volume exit. In order to find the step change across the control volume, the resulting transcendental equation is solved by using a NAG routine. Other flow properties at the exit of the control volume and the mass flow rate in the tangential direction are also calculated. The process is repeated until the flow properties from the outer wall to the rotor inlet and the total mass flow in the tangential direction have been determined.

The details of the program dealing with the calculation of the geometric dimensions are omitted from here for the sake of brevity, but the reader's attention is drawn to [6].

Validation of the Programs

The programs were validated on an existing single entry

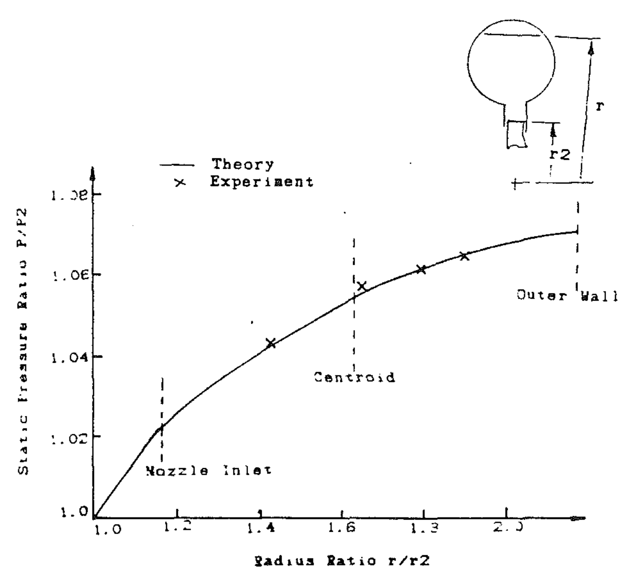

Fig. 4(*c*) Comparison between the graphs of calculated and measured static pressure ratio versus the radius ratio at the zero azimuth angle

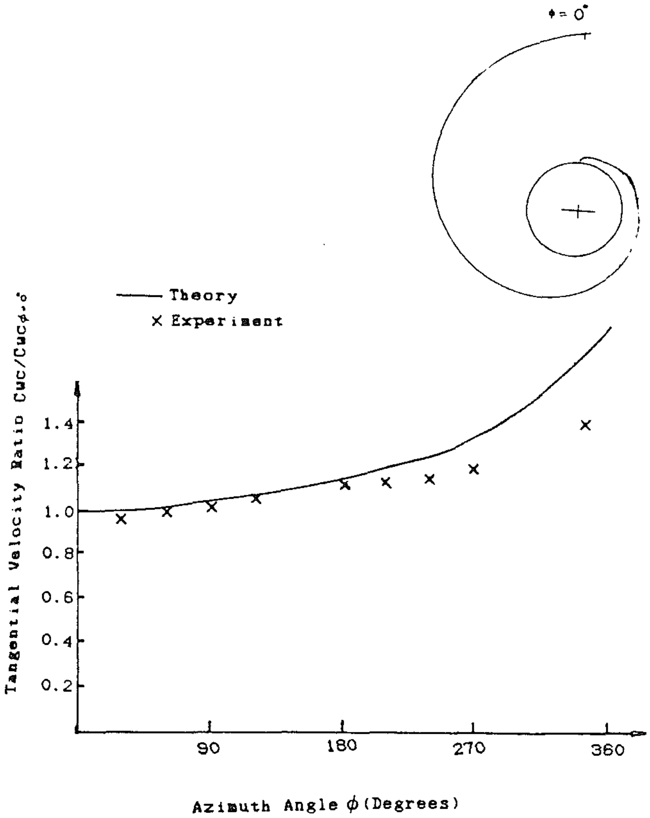

Fig. 5(*a*) Comparison between the graphs of calculated and measured values of tangential velocity versus the azimuth angle at the centroid

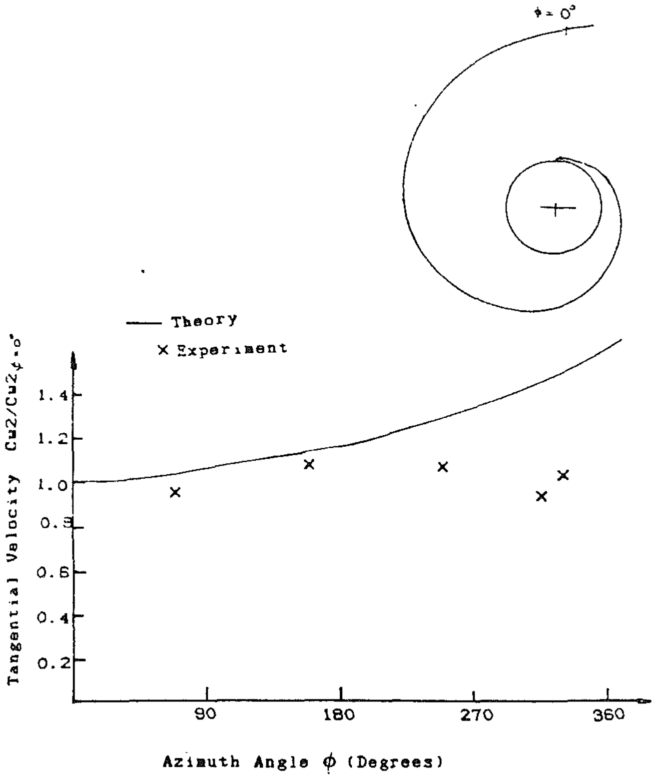

Fig. 5(*b*) Comparison between the graphs of calculated and measured values of tangential velocity versus the azimuth angle close to the rotor entry

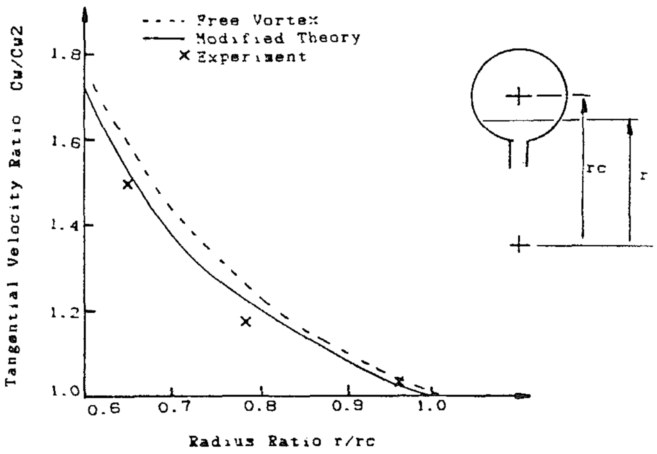

Fig. 5(*c*) Comparison between the graphs of calculated and measured values of tangential velocity versus the radius ratio at zero azimuth angle

nozzle-less volute casing for which comprehensive experimental data were available. Space restrictions do not allow full design details of casing and of the test procedure to be given here, but they may be found in [3]. Here it should suffice to mention that the cross-sectional shape of the casing was circular and the geometric dimensions were measured from the drawings. Results of the validation are discussed in the following.

Static Pressure Calculations. Comparison between the calculated and measured values of static pressure ratio along the centroid of the volute, close to the rotor entry for ϕ ranging from 0 to 360 deg, and at different radius ratios at $\phi = 0$ are shown in Figs. 4(*a*), 4(*b*), and 4(*c*), respectively. The agreement along the centroid is not very good, but it must be remembered that the position of the actual centroid may differ widely from that obtained from the drawing because of the casting inaccuracies.

Tangential Velocity Calculations. Figures 5(*a*), 5(*b*), and 5(*c*) show the comparison between the calculated and measured values of the tangential velocity ratio along the centroid, close to the rotor entry, and at different radius ratios at $\phi = 0$, respectively. In this case the difference between the calculated and measured values at the rotor entry increases as ϕ approaches 360 deg. This may be due to the influence of the

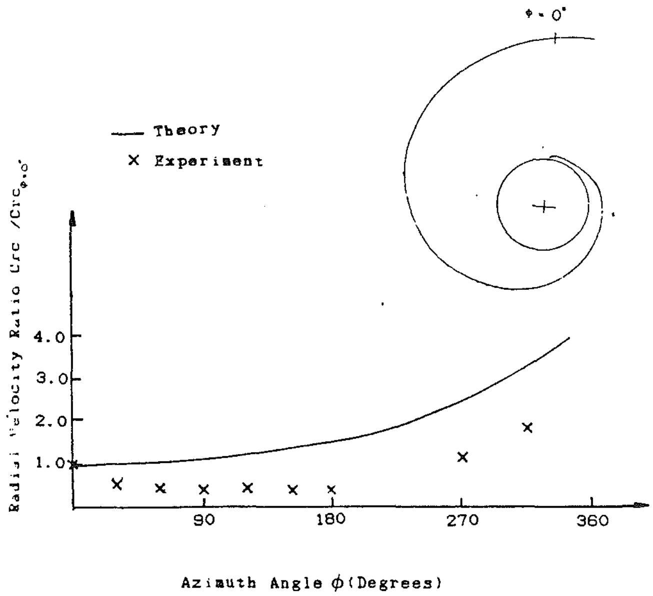

Fig. 6(*a*) Comparison between the graphs of calculated and measured values of radial velocity versus the azimuth angle at the centroid

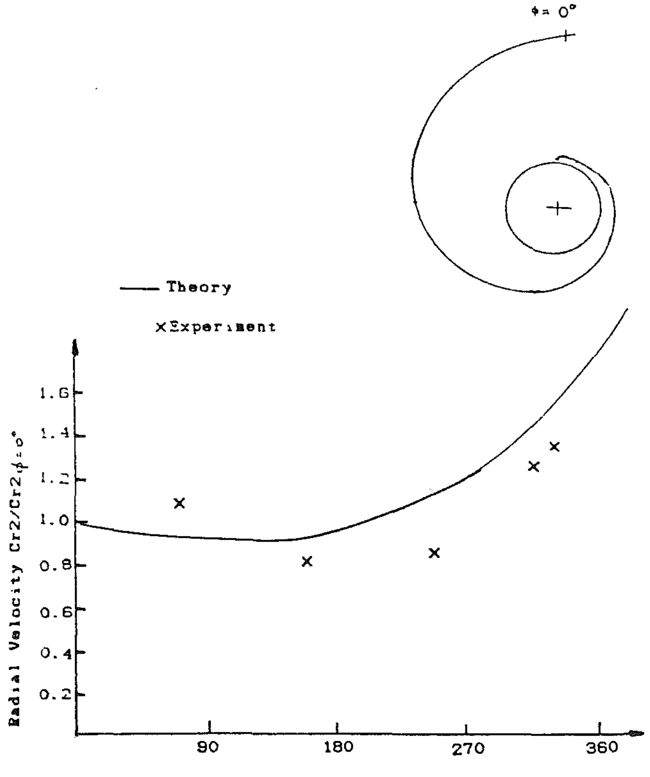

Fig. 6(*b*) Comparison between the graphs of calculated and measured values of radial velocity versus the azimuth angle close to the rotor entry

tongue because toward the tail end of the volute the center of the volute moves close to the rotor.

Radial Velocity Calculations. The calculated and measured values of the radial velocity at the centroid and close to the rotor entry for ϕ ranging from 0 to 360 deg and at different radii for $\phi = 70$ deg are shown in Figs. 6(*a*), 6(*b*), and 6(*c*), respectively. The model appears to overestimate the radial velocity along the centroid, but the trends shown in Figs. 6(*a*) and 6(*b*) are very similar to those observed experimentally.

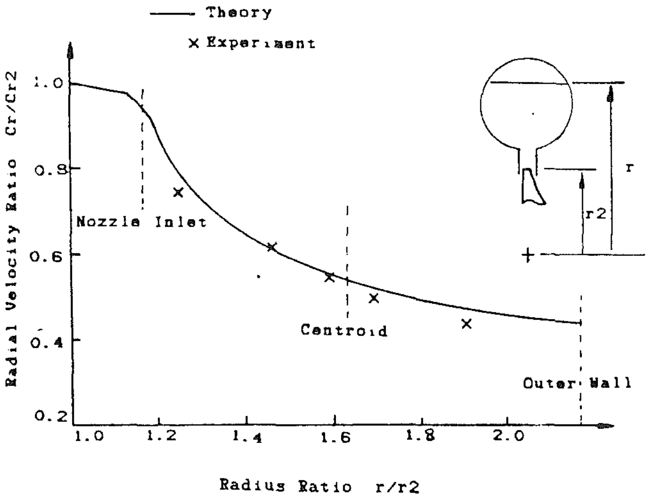

Fig. 6(*c*) Comparison between the graphs of calculated and measured values of radial velocity versus radius ratio at zero azimuth angle

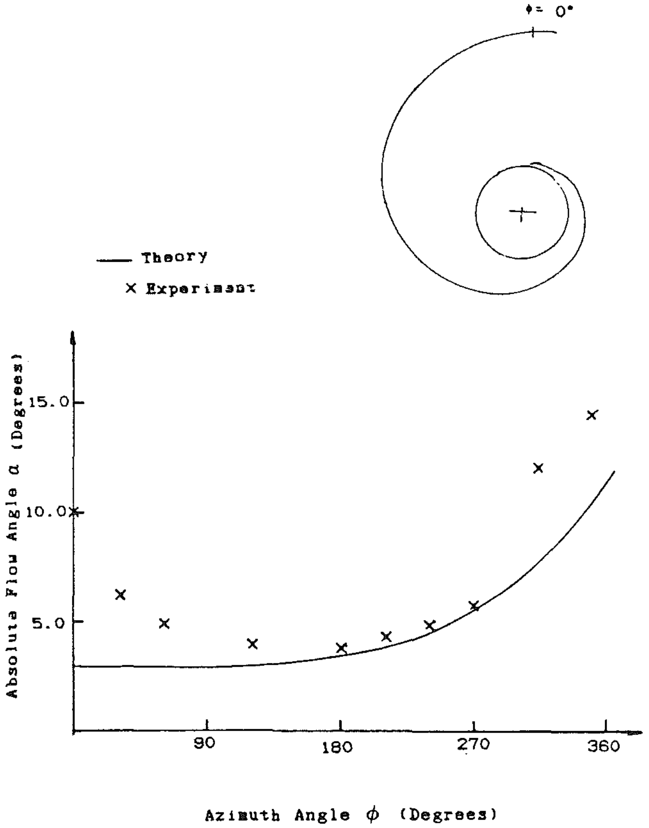

Fig. 7(*a*) Comparison between the graphs of calculated and measured values of absolute flow angle versus the azimuth angle at the centroid

The agreement between the measured and the calculated values at $\phi = 0$ is quite good.

Absolute Flow Angle Calculations. Figures 7(*a*), 7(*b*), and 7(*c*) show the comparison between the measured and calculated values of the absolute flow angle at the centroid, close to the rotor entry for values of ϕ ranging from 0 to 360 deg, and at different radius ratios for $\phi = 70$ deg. Here again the trends shown by the analysis are similar to those given by the experimental data, but the agreement between the theoretical and experimental results is rather poor. However, both the theory and the experiment show quite clearly that a volute casing of circular shape fails to meet the design criteria.

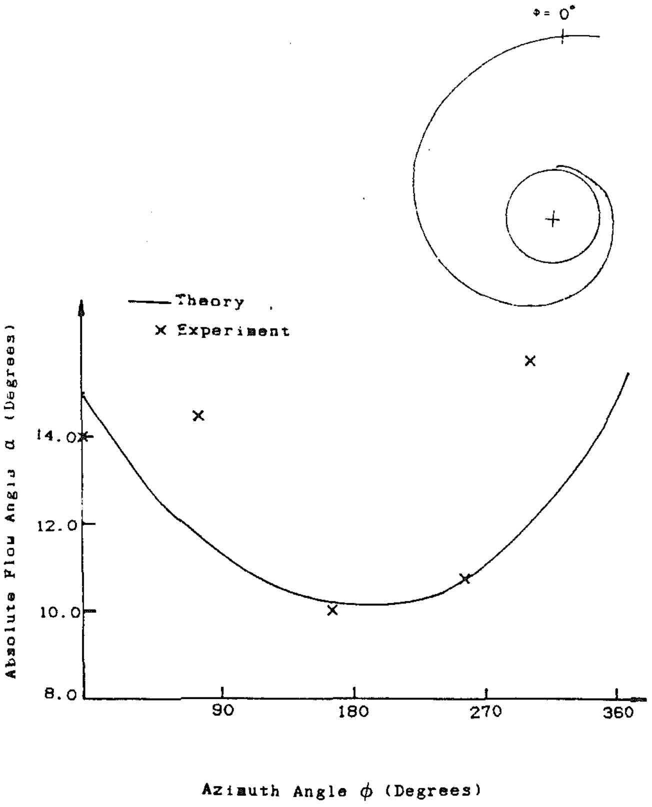

Fig. 7(*b*) **Comparison between the graphs of calculated and measured values of absolute flow angle versus the azimuth angle close to rotor entry**

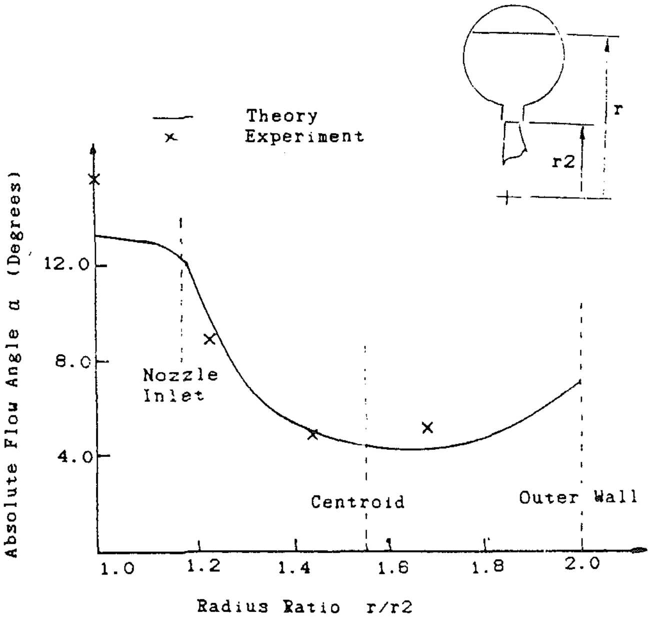

Fig. 7(*c*) **Comparison between the graphs of calculated and measured values of absolute flow angle versus the radius ratio at 70 deg azimuth angle**

The Design Method

In spite of the fact that the flow in the volute casing is very complex, the two-dimensional model described in the paper appears to represent the flow reasonably well. Hence it may be used to study the effect of cross-sectional shape of performance and thus optimize the design. The procedure for design is shown in the form of a flow diagram in Fig. 8.

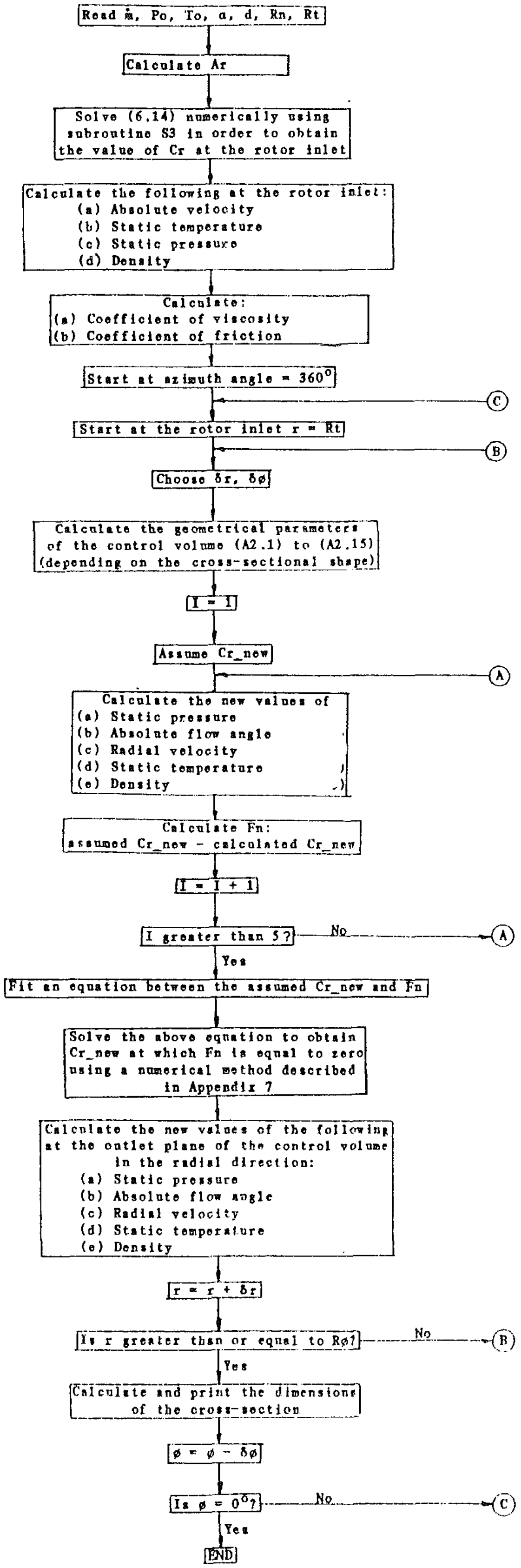

Fig. 8 **Flow diagram for the design of a single entry nozzle-less volute casing**

Conclusions

1 The details of a two-dimensional flow model that takes account of friction, area change, and the cross-sectional shape

of the volute have been described. The agreement between the theoretical results and measurements is not very good but the trends shown by theory are similar to those observed by experiment.

2 The conformity of a manufactured casing with the design is very difficult to ascertain. The differences between the calculated and measured results could well be due to the fact that there were differences between the actual casing and its manufacturing drawing.

3 The results show quite clearly that a casing of circular cross section does not satisfy the design criteria identified in the paper. There is a significant variation of the absolute flow close to the rotor periphery. This would have quite a serious effect on the performance, particularly its efficiency. For best efficiency the absolute flow angle measured from the tangential direction should be constant and close to 17 deg.

Acknowledgments

The authors wish to thank British Aerospace for sponsoring this work and the Directorate of Hatfield Polytechnic for providing the facilities.

References

1 Gubarev, A. V., "Bladeless Guide Vane for Centripetal Turbines," translation from Russian, Foreign Technology Division, Air Force Systems Command, Ohio, FTD-TT/141/124, May 1961.

2 Bhinder, F. S., "Investigation of Flow in the Nozzle-less Spiral Casing of a Radial Inward Flow Gas Turbine," *Proc. IMechE*, Vol. 184, Pt. 3G(II), 1969–70.

3 Hussain, M. A., "Investigation of the Flow in Nozzle-less Volute Casing for Centripetal Turbines," PhD Thesis, Hatfield Polytechnic, United Kingdom, 1983.

4 Hamed, A., and Baskharone, E., "Analysis of the Three-Dimensional Flow in a Turbine Scroll," ASME *Journal of Fluids Engineering*, Vol. 102, 1980, pp. 297–301.

5 Mager, A., "Transformation of the Compressible Turbulent Boundary Layer," Marquardt Aircraft Co., Van Nuys, CA.

6 Owarish, H. O., "Design and Performance of Nozzle-less Volute Casings for Inward Flow Radial Turbines," PhD Thesis, Hatfield Polytechnic, United Kingdom, 1989.

I. Huntsman

H. P. Hodson

Whittle Laboratory,
Cambridge University,
Cambridge, United Kingdom

S. H. Hill

Rolls-Royce plc,
Leavesden, United Kingdom

The Design and Testing of a Radial Flow Turbine for Aerodynamic Research

This paper describes the design of a high-speed radial inflow turbine for use as part of a gas generator, and the design of a large-scale (1.2 m tip diameter) low-speed model of the high-speed turbine. Streamline curvature throughflow, two-dimensional blade-to-blade, and fully three-dimensional inviscid and viscous calculation methods have been used extensively in the analysis of the designs. The use of appropriate scaling parameters and their impact on turbine performance is discussed. A simple model shows, for example, how to model the blade lean in the inducer, which serves to balance the effect of meridional curvature at inlet to the rotor and can be used to unload the rotor tip. A brief description of the low-speed experimental facility is followed by a presentation and discussion of experimental results. These include surface flow visualization patterns on both the rotor and stator blades and blade row exit traverses.

Introduction

Radial inflow turbines offer several advantages for use in small turboshaft applications when compared with axial turbines for the same duty. This is because the radial inflow turbine offers greater work extraction per stage at comparable or higher efficiencies, increased ruggedness, lower cost of manufacture, and improved packaging when used in conjunction with a reversed flow combustor.

Studies at Rolls-Royce have shown that a cooled, high-efficiency radial turbine could offer significant improvement in performance as the gas-generator turbine of a high technology turboshaft engine, if small improvements in current levels of technology could be achieved. An uncooled radial turbine of a similar aerodynamic duty would also present an attractive proposition in smaller power plants. However, the problems facing the designers of today's radial turbines are considerable, particularly in the areas of rotor cooling and rotor aerodynamics.

Many of the published design methods are largely based on the design rules developed by NASA and others (e.g., Hiett and Johnston, 1963; Rohlik, 1975; Glassman, 1976). These methods or their adaptations for specific applications are essentially based on observations of the overall performance of radial turbines. Very few are based on observed physical processes even though many of the flow and loss models purport to model the details of the flow. In such circumstances, the possession of one-dimensional information and models places potentially unnecessary restrictions on the design process. Today, commercial organizations are replacing costly experimental development programs by the use of modern CFD codes such as the viscous analysis code of Dawes (1987), but until the reasons behind such phenomena as "incidence shock loss" or tip clearance losses are understood, trial and error will play a large part in any design process.

This paper describes the initial stages of a research and development program in radial turbines that addresses the identification and understanding of the major sources of loss and the assessment of aerodynamic design and analysis methods. A large-scale, low-speed radial inflow turbine model has been constructed at the Whittle Laboratory, Cambridge University, as part of the research program. The model is based on a low-cost, high-pressure-ratio, uncooled turbine, which is designed to be scaled for turboshaft applications in the range of 50 to 300 kW. This paper describes the design of the base turbine and the scaling of this turbine to produce the aerodynamic model, and presents the results of an initial investigation using the model turbine.

The Design of a High-Speed Radial Inflow Turbine

The baseline turbine duty was selected for a low-cost single-shaft gas turbine in the 200 kW class. This results in modest gas temperature levels. However, the aerodynamic duty would also be appropriate for the gas generator turbine of a higher pressure ratio two-shaft engine. The leading parameters are:

Mass flow	1.58 kg/s
Stator inlet temperature	1161 K
Total–total pressure ratio	4.7
Target total–total efficiency	87 percent

Preliminary Design. The preliminary design process used

Contributed by the International Gas Turbine Institute and presented at the 36th International Gas Turbine and Aeroengine Congress and Exposition, Orlando, Florida, June 3–6, 1991. Manuscript received at ASME Headquarters March 4, 1991. Paper No. 91-GT-220. Associate Editor: L. A. Riekert.

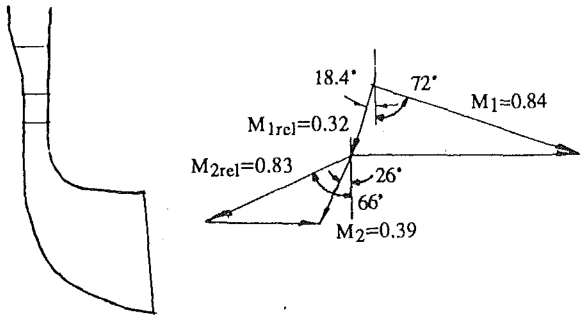

Fig. 1 Meridional geometry and rotor inlet and exit rms velocity triangles for the full size turbine

many of the rules developed by NASA (e.g., Rohlik, 1975, or Glassman, 1976). Several mechanical constraints were placed on the design to enable it to achieve an acceptable life with relatively low manufacturing costs, and to enable it to be scaled for other applications to approximately half size without significant modifications. The aerodynamic design method used was based on that of Glassman (1976). This method was linked to a preliminary geometry definition program and stress calculating routines.

Rohlik (1975) gives the optimum incidence for this turbine as being −26 deg. For zero exit swirl, this would require a tip speed of about 650 m/s. This in turn defines the necessary blade taper ratio to achieve the required stress levels and hence the hub blockage. Figure 1 shows that there is −26 deg of swirl at the turbine rms exit radius in order to extract more work from the turbine exducer and hence minimize the tip speed. The inlet angle has also been compromised a little for the same reason, resulting in high reaction, which should provide favorable flow conditions in the rotor. The rotor blade number was set to 14 with a maximum blockage at the hub of about 60 percent.

The stator blade number and chord were set using a lift coefficient defined as

$$C_L = \frac{\dot{m} r_1 V_{\theta 1} - \dot{m} r_2 V_{\theta 2}}{Z \int_{r_1}^{r_2} (P_{01} - p_2) r b dr} \qquad (1)$$

with a value of 0.6 being initially chosen. This is a modest value by axial turbine standards, and was chosen so that the secondary flows could be minimized. This was important as the aspect ratio of this vane is low compared to those of many axial turbines.

The Glassman model predicted a total–total efficiency of 84 percent for this preliminary turbine configuration, 3 points below the design target.

Detail Design—Nozzle. The detail design of the nozzle utilized standard Rolls-Royce axial turbine blade design programs. A streamline curvature throughflow model of the turbine defined the stator and rotor inlet and exit conditions. The velocity distributions were calculated using a blade-to-blade program, and the final design was chosen by assessing the velocity distributions and the predicted boundary layer behavior.

Detail Design—Rotor. At the outset it was realized that the flow in the rotor passages would be highly three dimensional and that it would be beneficial to design using three-dimensional flow analysis programs.

Having estimated a meridional shape and blade thickness distribution, computed velocity distributions were obtained using the inviscid code of Denton (1983) and were assessed with the aim of minimizing diffusion on the blade surfaces and avoiding flow reversal within the passages. The main region of difficulty appeared in the inducer region, where the high loading led to very high velocity on the suction surface at the shroud, and a large level of diffusion at the hub. This was not surprising, given that the number of blades employed was less than ideal.

Several alternative blade angle and annulus distributions were then assessed, along with the use of more blades, although the high levels of blockage necessitated by the blade taper made this an unattractive option. Finally the use of rake at blade inlet was explored, with the objective of applying blade lean to unload the shroud section. The final design employed 20 deg of rake at the inlet and Fig. 2 compares the final design Mach number distributions to an earlier attempt with no rake. It can be seen that the shroud velocity distribution has been markedly improved by applying the rake, although the hub diffusion has worsened. There is significant hub diffusion even in the earlier design, and it was therefore decided that little could be done to alleviate this, and that as the majority of the work is done in the outer half of the rotor, it would be best to optimize the shroud Mach number distribution.

Aerodynamic Design of Large-Scale Low-Speed Model

To obtain access to the flow within the passages of a radial inflow turbine and to permit high-quality data acquisition, a machine larger than standard has to be built. It was decided at an early stage to construct a model turbine of a similar scale to that of the low-speed axial turbine research facilities at the Whittle Laboratory, thus permitting the best possible resolution of the mainstream, boundary layer, and secondary flows. This new rig would offer, for the first time, the opportunity to acquire data of a detail and quality similar to that so far obtained only in axial flow research programs.

A large number of factors led to the selection of a rotor tip diameter of 1.219 m operating at 450 rpm. This gives approximately the correct Reynolds numbers for the stator and rotor but the peak Mach numbers are of the order of 0.1. It follows that true dynamic similarity cannot be attained because the effects of compressibility cannot be simulated. The use of a low-speed rig therefore adds further complexity to the modeling process. Wisler (1985) and Joslyn et al. (1991) both de-

Nomenclature

b = rotor span
c_{radial} = radial chord
Re = Reynolds number
U = blade speed
V = absolute velocity
W = relative velocity
Y_p = pressure loss coefficient =

$$\left(\frac{\left(p_{03\text{rel}} - \frac{1}{2}\rho U_3^2\right) - \left(p_{0\text{rel}} - \frac{1}{2}\rho U^2\right)}{p_{03} - p_3} \right)$$

Z = number of blades
θ = boundary layer momentum thickness
μ = dynamic viscosity
ν = kinematic viscosity
ρ = density
Ω = rotational speed

Subscripts

m = meridional
θ = tangential (pitchwise)
0 = stagnation conditions
1 = stator inlet
2 = stator exit
3 = rotor inlet
4shroud = rotor exit shroud
4hub = rotor exit hub

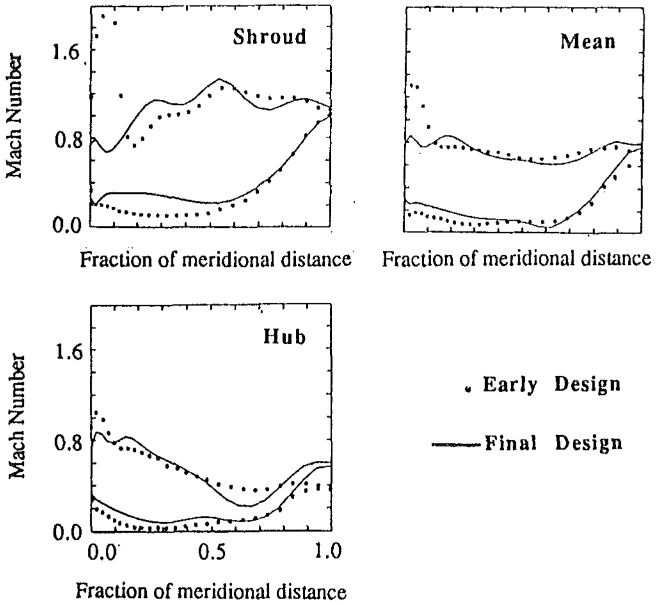

Fig. 2 Mach number distributions for the full size turbine showing the effects of rotor blade inlet rake

scribe approaches to low-speed similarity modeling similar to those adopted here.

Meridional Geometry

Velocity Triangles. The work-mass flow characteristics of any turbine are effectively prescribed by the velocity triangles at inlet to and at exit from the rotor blade. This means that it is essential that any model of the full-size turbine must have equivalent if not identical velocity triangles.

The rotor inlet radius (r_3) is constant across the span so that the angular momentum entering the rotor is also constant. This is not generally true at rotor exit. If the flow conditions and work-mass flow characteristics of the model are to be matched to those of the full-size turbine at *all* flow coefficients along *all* streamlines, then the shroud exit to shroud inlet radius ratio ($r_{4\text{shroud}}/r_3$), the hub-shroud radius ratio at rotor exit ($r_{4\text{hub}}/r_{4\text{shroud}}$), and the radial variation of the swirl velocity $V_\theta(r)$ must be scaled exactly.

Matching the exit flow field of the model rotor in all its details to the flow field behind the full-size rotor means that true matching can only occur at this location. Both the full-size and the model turbine operate at the same nominal specific speed, N_s, of 0.6, which corresponds to the optimum value given by the NASA correlations and design rules (see Rohlik, 1975).

Variation of Streamtube Height. The variation of density is negligible at low speed. Thus, in order to produce meridional velocity variations and, therefore, velocity triangles that are correctly scaled, the heights of the streamtubes would need to vary much less in the low-speed model than in the high-speed turbine. This meant that true geometric similarity could not be maintained. Given that the exit hub-to-shroud radius ratio ($r_{4\text{hub}}/r_{4\text{shroud}}$) was already prescribed, the desired variation in streamtube thickness could only be achieved by increasing the width (b_3) of the inducer.

The width of the inducer in the model turbine was increased by a factor of about two relative to the scaled dimension. Although this is a large increase, the design is not significantly compromised. At rotor inlet, for example, the effects of secondary flow (see Zangeneh et al., 1988) and of tip clearance (see Futral and Holeski, 1970) are not as significant as in the exducer, given that a large-scale incidence-induced separation will not occur at the design point.

Rotor Hub and Shroud Profiles. The importance of streamline (meridional) curvature in the generation of secondary flows may be characterized by reference to the Rossby number

$$\text{Ro} = \frac{W}{\Omega r_c} \tag{2}$$

where r_c is the local radius of curvature and W is the local relative velocity of the flow. Since the radius of curvature is significantly smaller and the loading significantly greater at the shroud than at the hub, it is not unreasonable to find that the secondary flows are more significant near the rotor shroud (see, for example, Zangeneh et al., 1988). Given the desire to obtain similar secondary flow patterns in both the model and the full-size turbine and with the above observations in mind, the less critical hub profile was altered to compensate for the increased width of the inducer. The same shroud contour was employed in the model as in the high-speed turbine.

Reynolds Numbers. Hiett and Johnston (1963) have reported the effect of changes in Reynolds number on the performance of radial inflow turbine rotors. The investigations showed that at Reynolds numbers, defined as

$$\text{Re} = \frac{U_3 b_3}{\nu_1} \tag{3}$$

above 1.25×10^5, there is very little change in efficiency with Reynolds number.

Even though the flow accelerates over much of the rotor blade surfaces, consideration of the high magnitude of the surface length based Reynolds number shows that turbulent flow is already well established over much of the blade when operating above the limits established by Hiett and Johnston. The full-size turbine has a Reynolds number of 2.4×10^5, which indicates that its operation is within the turbulent boundary layer regime.

The absence of a variation in density (and viscosity) through the model turbine and maintaining the nozzle radius ratio (r_1/r_2) would mean that the Reynolds number of the stator blades would be lower in the model by a factor of 0.6. In addition, the aspect ratio of the stator blades would also be greater by about the same factor due to the increased streamtube thickness at the rotor inlet. In an attempt to offset some of the effects of these potential changes, the chord and therefore the radius ratio (r_1/r_2) of the stator blades was increased while maintaining the same radius ratio (r_2/r_3) for the vaneless space and lift coefficient for the stator blades (Eq. (1)). Increasing the radius ratio of the stator blades also reduces the impact of using parallel as opposed to converging endwalls in the model since the velocity ratio V_2/V_1 is increased.

The Reynolds number of the stator blades, when defined as

$$\text{Re}_{\text{stator}} = \frac{\rho_2 V_2 c_{\text{radial}}}{\mu_2} \tag{4}$$

has a value of 2.8×10^5 in the full-size turbine. When based on true chord, the value is 4.5×10^5. This means that these stator blades are operating at conditions where the laminar-turbulent transition may well occur. In order, therefore, to model the flow accurately, the Reynolds number of the stator blades for the model turbine has been chosen to be the same as that for the full-size turbine. This condition increases the Reynolds number of the model rotor 2.6×10^5. In was mentioned earlier that the full-size turbine is expected to have fully turbulent boundary layers on the rotor blades, so this compromise will not significantly affect the flow through the rotor.

Nozzle Guide Vanes. There are 23 NGVs in the model turbine, which represents a reduction of six from the original 29 in the full-size. The majority of this decrease is simply due to the change in radial chord. The rotor inlet flow angle is the same in both cases. The effect of contouring the endwall in

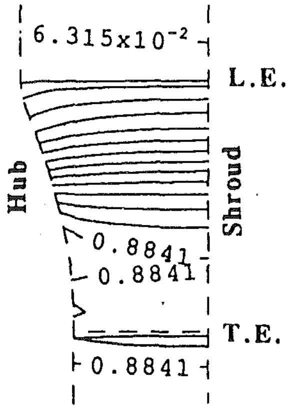

Fig. 3 Meridional view of stator suction surface Mach number contours (Denton) showing the effect of wall curvature

the full-size turbine can be seen by examining Fig. 3. This shows the meridional projection of the predicted suction surface Mach number contours obtained using the method of Denton (1983). The extent of the effects of the wall curvature is limited to less than one half of the span and that rather than being advantageous, the convex curvature of the curved endwall results in a greater amount of diffusion beginning near 75 percent c_{radial}. The parallel endwall has, by contrast, very little back-surface diffusion. These observations further support the original decision to employ parallel endwalls in the model turbine. The blade surface velocity distributions were matched to the Mach number distributions of the straight endwall of the full-size turbine. It may, of course, be argued that altering the endwall contours will lead to substantially different secondary flow fields in the model turbine. Figure 4 shows the predicted secondary flow patterns obtained using the flow prediction method of Dawes (1987). The figure shows that there is very little secondary flow in the model turbine so any changes that might occur will be very small.

Integral boundary layer calculations were carried out using the method of Herbert and Calvert (1982) for the Mach number distributions of the straight endwall of the full-size turbine and for the model turbine. These calculations showed that the momentum thickness based Reynolds number ($\text{Re}_\theta = \theta V/\nu$) was everywhere less than the critical value of 163 (see Herbert and Calvert, 1982), so that transition to turbulent flow would not occur. Because there was little or no diffusion, the boundary layers would also remain attached.

Rotor

Blade Numbers. Stressing considerations dictate that the camberlines of the rotor blades are formed from radial elements. Near the leading edge, the rotor blades are radial. A simple analysis shows that for incompressible flow between radial blades of a many-bladed impeller, the velocity jump across the blades ΔW is given by

$$\frac{\Delta W}{U} \approx \frac{4\pi}{Z} \tag{5}$$

so that the loading is simply determined by the number of blades. Slip factors and therefore optimum inlet loading are also thought to be independent of Mach number below 0.8 (see Stanitz, 1952), further suggesting that the number of blades in the rotor of the model should be the same as in the full size machine.

The Effects of Blade Lean at Rotor Inlet. In the high-speed turbine, the rotor leading edge is leaned so that the pressure side is toward the shroud. Because the density of the flow in the model turbine is effectively constant, the width of the inducer has been increased by a factor of about 2. This presented a difficulty as to the choice of the scaling parameters, which should be used to specify the angle of lean in the low-speed rotor. The need for a simple analysis therefore existed. The analysis described in the appendix is applicable to the general case where shroud curvature exists at the leading edge plane but where there is no blade curvature. Figure A1 shows a plan and meridional view of the rotor blades in the region of the leading edge together with the leading dimensions of the problem. The result of the analysis shows that the important modeling relationship is:

$$\frac{\bar{V}(V_{\text{hub}}-V_{\text{shroud}})}{W_m^2}=\frac{b}{r}\left(2\tan\theta\,\frac{U}{W_m}-\frac{r}{r_c}\right) \tag{A7}$$

where all terms are defined in the appendix.

For the present study, the rotors under consideration have no meridional curvature at the leading edge. The method described by Casey and Roth (1984) for analyzing sweep gives an effective blade curvature of 1.6 deg. This will not, therefore, account for the change in loading distribution observed in Fig. 2. The blade lean has been applied solely to reduce the loading. The blade force is therefore unopposed by streamline curvature forces and the flow is deflected toward the hub. For similarity of flow conditions between the full-size and the model it follows that the value of $(b/r)\tan\theta$ should be preserved. Applying the above equation to the adopted blade geometry for the model results in a 5 percent variation of absolute velocity across the span, corresponding to an incidence variation of ±9 deg. Such a large variation in incidence onto a radial leading edge geometry is expected to increase losses but will be representative of existing radial inflow turbines and interesting to analyze.

Analysis of the Rotor Design Using Viscous Flow Predictions. For comparison between the predicted flow fields for the two machines, midpassage meridional and blade-blade relative Mach number contours are presented in Figs. 5 and

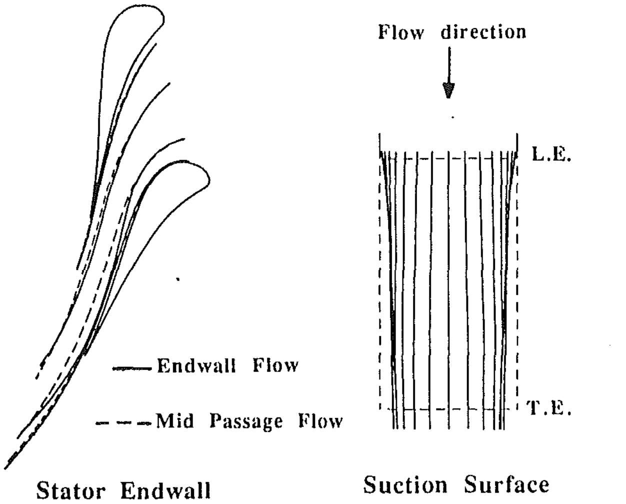

Fig. 4 Predicted flow visualization for the stator endwall and suction surface using the Dawes code

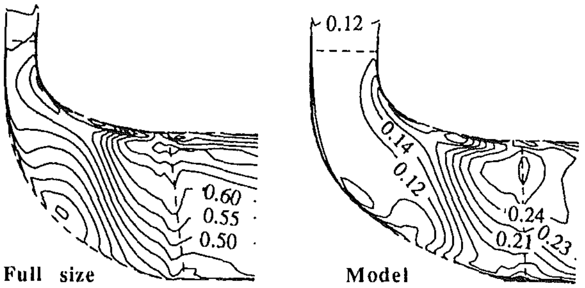

Fig. 5 Meridional midpassage relative Mach number contours

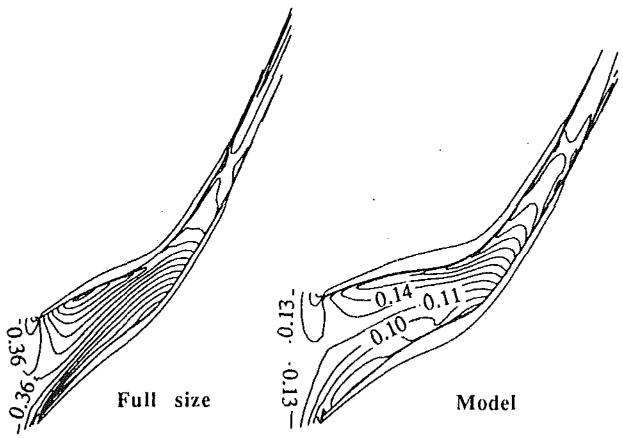

Fig. 6 Midpassage blade-blade relative Mach number contours

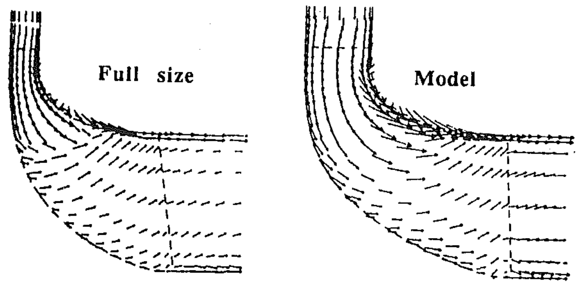

Suction surface

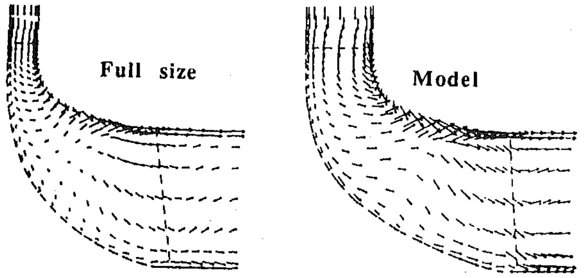

Pressure surface

Fig. 7 Meridional velocity vectors close to the blade surfaces for both turbines

6. Although the two turbines are not identical, the comparison appears to be reasonable.

Velocity vectors, in the meridional view, show the movement of the secondary flows for the different sections of the turbine (see Fig. 7). Comparison between the two turbines is good. As with the predictions of Zangeneh et al. (1988), the secondary flow moves toward the hub on the pressure surface in the exducer and toward the shroud on the suction surface in the exducer under the influence of the reduced static pressure gradient. The effect of tip clearance flow may also be observed on both surfaces and in particular movement of low-momentum flow up the exducer pressure surface toward the clearance region is apparent.

The comparison between the full-size turbine and the model is thought to be adequate to provide a representative turbine on which to undertake aerodynamic research.

Test Facility

The rig operates as an open loop wind tunnel, drawing air from the atmosphere into the model turbine. The turbine exhausts into a circular duct, which connects to a sliding throttle and the centrifugal fan. The open loop configuration with the suction fan after the working section ensures that axisymmetric, low-turbulence flow can be obtained at entry to the blade row under investigation.

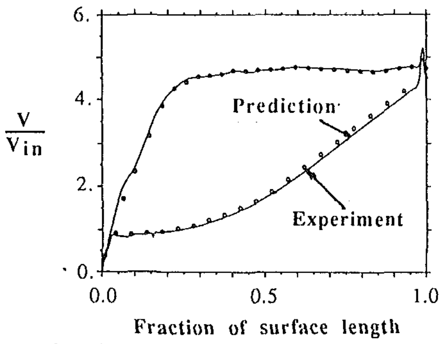

Fig. 8 Comparison between Martensen method prediction and experimental results for the radial stator blade

The stator blades were made from a glass-reinforced epoxy resin cast from a machined mold. Each stator blade is mounted on two pins so that the stagger angle is correctly fixed. The measured variation of throat area corresponds to a variation of less than 0.2 deg in stator exit angle and 4 deg in rotor inlet angle. The rotor blades were manufactured by a slightly different process. A mold was again produced, then a gel-coat of epoxy resin was placed in the mold and allowed to harden before a resin foam was injected into the mold. In this way light, rigid blades were obtained. Static pressure tappings were cast into both the stator and rotor blade surfaces.

Area traversing using a variety of probes can be carried out behind each blade row. The probes may be traversed over two or three pitches in the circumferential direction. A circumferential-radial traverse system is also fitted to the rotor at exit. This enables the investigation of the relative frame and in particular, of the internal passage flow. An on-rotor Scanivalve and pressure transfer system complements the rotor traverse system with slip-rings being used to carry information to the stationary frame.

Discussion of Test Results

Stator. Figure 8 shows the good comparison of experimental results from the stator blade surface static pressure tappings with the predicted values from a Martensen method calculation at the design flow coefficient. The data show that there is no diffusion on the suction surface, which satisfies the design objective, while the continuous acceleration on the pressure surface is a consequence of the relatively low loading coefficient chosen for this blade row.

The state of the blade surface boundary layers has been determined by fitting surface-mounted hot-film anemometers to both blade surfaces. Their operation and usage follows that described by Hodson and Addison (1989). The output signals from the gages contained information characteristic of laminar boundary layers. This is in agreement with the results obtained from the Herbert and Calvert (1982) prediction method and satisfies the design objective of obtaining a stator with attached laminar boundary layers throughout.

The blade and endwall flow fields of the stator blade have been investigated using an oil and dye flow visualization mixture. Figure 9 presents the resulting flow patterns. The upper figure shows the suction surface viewed looking upstream and may be compared to the predictions of Fig. 4. The lift-off line, generated by entrainment of blade surface fluid into the passage vortex, is apparent and shows the edge of the passage vortices to be at about 30 and 70 percent of the span. The lower photograph of the suction surface endwall corner region also shows a lift-off line, which is due to the entrainment of

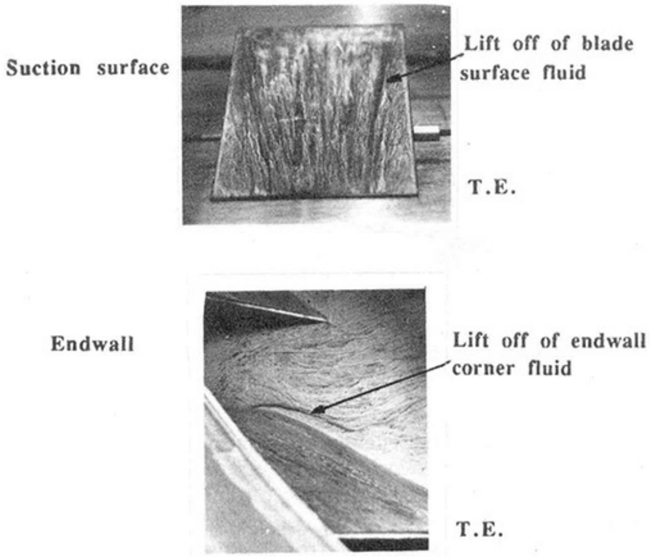

Fig. 9 Flow visualization using oil and dye on the stator blade suction surface

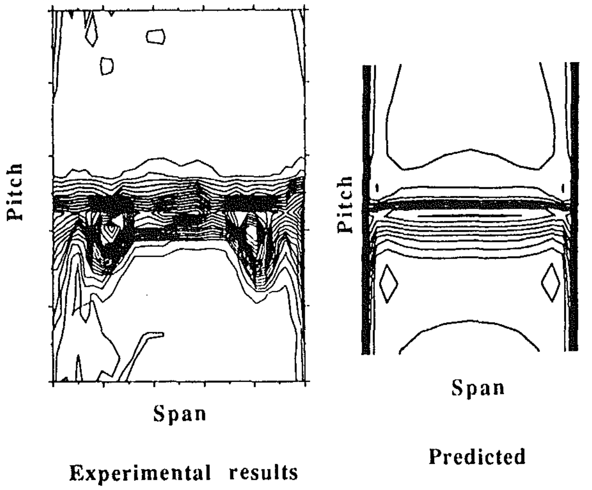

Fig. 10 Comparison of experimental and predicted (Dawes, 1986) stator exit total pressure contours

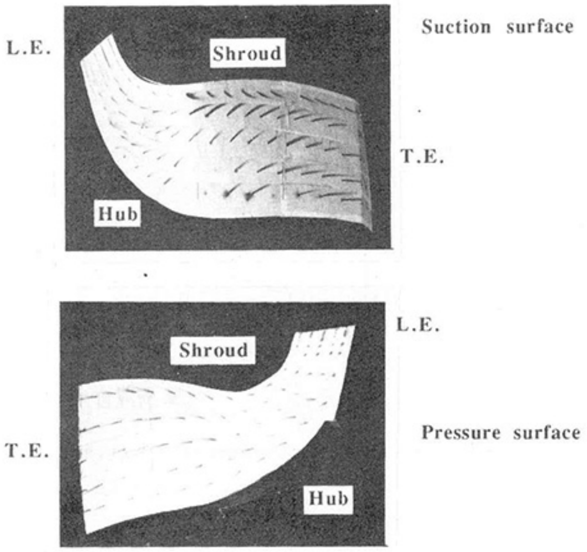

Fig. 11 Flow visualization on the rotor blade using ammonia and Ozalid paper

endwall corner fluid within the passage vortex. There is no evidence of separation at any point on the suction surface. The flow visualization is consistent with the predictions of Fig. 4.

Area traversing has been undertaken in the absolute frame using fixed-direction five-hole pyramidal pressure probes that have been calibrated for the measurement of yaw and pitch angles, total pressure, and dynamic head. The results of traversing the stator exit flow field within the vaneless space are shown along with predicted total pressure contours in Fig. 10. In the measurements, the high loss regions associated with the passage vortices can be seen to be centered on approximately 20 and 80 percent span. Much of the flow remains unaffected by the secondary flow, which is consistent with the flow visualization patterns. The overall pressure loss coefficient (Y_p) for the stator blade is 0.033 with a midspan value of 0.012. Compared to axial turbines, the nozzle blade has a lower loss coefficient and appears to be performing well for an aspect ratio of 0.821 (based on radial chord). The reason for this level of performance is that both surfaces have attached laminar boundary layers over the whole length. For the prediction, the vortices near the two suction surface endwalls observed during flow visualization are apparent, but are much smaller in extent than those measured. This is consistent with the differences between the predicted and measured surface flow patterns and is a consequence of the grid being too coarse to resolve the details of the flow accurately within the vortex.

Rotor. The flow on the rotor blade surfaces has been investigated using a visualization technique described by Joslyn and Dring (1983). At the design point, ammonia gas was passed out of the static pressure tappings in an instrumented blade, and allowed to flow over Ozalid paper. The results obtained using this method are shown in Fig. 11 and may be compared with the predictions of Fig. 7.

On the suction surface, the secondary flow patterns are in good agreement with the predictions. For example, Fig. 11 shows that on most of the suction surface in the exducer, there are relatively strong secondary flows toward the shroud where the reduced static pressure is at a minimum. Very near the shroud, the surface flow is directed toward the hub. The resulting herringbone pattern indicates the presence of a lift-off line. This feature is probably associated with the scraping vortex and suggests that the tip clearance vortex is relatively small in this machine.

The pressure surface flow visualization of Fig. 11 shows that on the rotor, there is a large low-momentum region close to the leading edge. Indeed, at the leading edge, some reversal of the flow direction may be observed. The reversed flow and pressure surface stagnation will be largely an inviscid effect and are to be anticipated since the turbine rotor is operating at an inlet angle that is greater than the "optimum" value. There is no evidence that this reversed flow region has a significant effect on the overall flow, which is consistent with the observations of many researchers that reducing the blade numbers below the limit of pressure surface reversed flow does not necessarily inhibit the performance (e.g., Futral and Wasserbauer, 1970). Downstream of this low-momentum region, the flow responds to the meridional curvature and secondary movements occur toward the shroud. In the exducer, the influence of the reduced static pressure gradient means that the secondary flow is toward the hub as predicted by the Dawes code and by Choo and Civinskas (1985).

The results of traversing a five-hole pyramidal probe at rotor exit are presented in Fig. 12. These plots show the mass flow weighted pitchwise-average of the stagnation pressure loss and flow angle when the turbine is operating at the design flow coefficient. The overall total pressure loss coefficient for the turbine is 0.10. Using the mass-averaged values of total pressure, the total-total efficiency derived using the Euler work equation is of the order of 93 percent. This value is 9 percent higher than expected, although some of this discrepancy may be attributed to the difficulty of measuring the stator and rotor exit flow angle and mass flow distributions with sufficient accuracy.

The spanwise variations in total pressure loss (Y_p) and yaw angle shown in Fig. 12 follow the trends observed in other radial turbines (e.g., Futral and Holeski, 1970), except at the shroud where the loss is reduced and the yaw angle indicates the overturning that is consistent with the existence of a scraping vortex. These differences are probably due to the relatively small tip clearance of the model turbine. If this is indeed the case, then the region of high loss near the shroud is probably due to the accumulation of suction surface low-momentum fluid and is not a direct result of shroud clearance flows. This observation, which is consistent with the rotor flow visualization (Fig. 11), is in agreement with the suggestions of Zangeneh et al. (1988). Future investigations will reveal the true origins of this region of loss.

Conclusions

A gas generator radial inflow turbine has been designed to operate at a total-total pressure ratio of 4.7. This turbine has then been modeled and placed in a large-scale, low-speed test rig at the Whittle Laboratory.

The model stator blades show only weak secondary flow movements and have laminar blade surface boundary layers over the whole blade surface. The overall loss coefficient based on rotor inlet dynamic head is 0.033.

The rotor blades show strong secondary flow movements on both surfaces and a low-momentum region on the pressure surface at inlet when at the design flow coefficient. Exit traverses display similar results to those obtained by other organizations but lower loss and yaw angle are to be observed toward the casing of the machine, suggesting that high shroud losses are due to an accumulation of low-momentum fluid and not due to strong tip clearance flows.

A simple model has been developed to determine the effects of rotor blade inlet lean.

Acknowledgments

The authors would like to acknowledge Rolls-Royce plc for support of the research work and also Rolls-Royce Business Ventures Ltd. for initiating and funding the original high-speed turbine design work.

References

Casey, M. V., and Roth, P., 1984, "A Streamline Curvature Throughflow Method for Radial Turbocompressors," *Computational Methods in Turbomachinery*, IMechE Publications, London, United Kingdom.

Choo, Y. K., and Civinskas, K. C., 1985, "Three Dimensional Inviscid Analysis of Radial Turbine Flow and a Limited Comparison With Experimental Data," NASA TM-8709.

Dawes, W. N., 1987, "A Numerical Analysis of the Three Dimensional Viscous Flow in a Transonic Compressor Rotor and Comparison With Experiment," ASME JOURNAL OF TURBOMACHINERY, Vol. 109, pp. 83-90.

Denton, J. D., 1983, "An Improved Time Marching Method for Turbomachinery Flow Calculation," ASME *Journal of Engineering for Power*, Vol. 105, p. 514.

Futral, S. M., and Holeski, D. E., 1970, "Experimental Results of Varying the Blade Shroud Clearance in a 6.02 inch Radial Inflow Turbine," NASA TN D-5513.

Futral, S. M., and Wasserbauer, C. A., 1970, "Experimental Performance Valuation of a 4.59 inch Radial Inflow Turbine With and Without Splitter Blades," NASA TN-D7015.

Glassman, A. J., 1976, "Computer Program for Design Analysis of Radial Inflow Turbines," NASA TN D-8164.

Herbert, M. V., and Calvert, W. J., 1982, "Description of an Integral Method for Boundary Layer Calculation in Use at NGTE, With Special Reference to Compressor Blades," NGTE memorandum M82019.

Hiett, G. F., and Johnston, I. H., 1963, "Experiments Concerning the Aerodynamic Performance of Inward Flow Radial Turbines," *Proc. IMechE*, Vol. 178, Pt. 31 (*ii*), p. 28-42.

Hodson, H. P., and Addison, J. S., 1989, "Wake-Boundary Layer Interactions in an Axial Turbine Rotor at Off Design Conditions," ASME JOURNAL OF TURBOMACHINERY, Vol. 111, pp. 181-192.

Joslyn, H. D., Brasz, J. J., and Dring, R. P., 1991, "Centrifugal Impeller Aerodynamics: an Experimental Investigation," ASME JOURNAL OF TURBOMACHINERY, Vol. 113, pp. 660-669.

Joslyn, H. D., and Dring, R. P., 1983, "Turbine Rotor Negative Incidence Stall," ASME Paper No. 83-GT-23.

Rohlik, H. E., 1975, "Radial Inflow Turbines," NASA SP 290, Vol. 3, Chap. 10.

Stanitz, J. D., 1952, "Some Theoretical Aerodynamic Investigations of Impellers in Radial and Mixed Flow Centrifugal Compressors," *Trans. ASME*, Vol. 74, No. 4, pp. 473-497.

Wisler, D. C., 1985, "Loss Reduction in Axial Flow Compressors Through Low-Speed Model Testing," ASME *Journal of Engineering for Gas Turbines and Power*, Vol. 107, pp. 354-363.

Zangeneh-Kazemi, M., Dawes, W. N., and Hawthorne, W. R., 1988, "Three-Dimensional Flow in Radial Inflow Turbines," ASME Paper No. 88-GT-103.

Zangeneh-Kazemi, M., 1988, "Three Dimensional Design of Radial Inflow Turbines," PhD thesis, Cambridge University Engineering Department, United Kingdom.

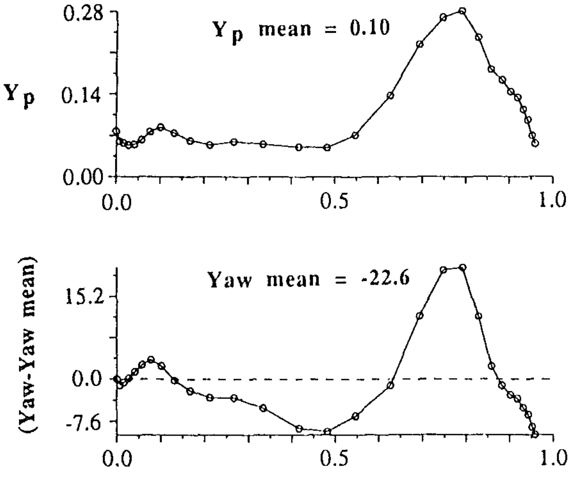

Fig. 12 Measured rotor exit pitchwise-averaged results

APPENDIX

A Simple Analysis of the Effects of Inlet Blade Lean

Figure A1 shows a plan and meridional view of the rotor blades in the region of the leading edge together with the leading dimensions of the problem. The pressure gradient normal to curved streamlines is given by the general expression

$$\frac{\partial p}{\partial n}=\frac{\rho W_m^2}{r_c} \tag{A1}$$

where r_c is the radius of curvature and W_m is the meridional (i.e., mean) velocity. For large r_c this expression can be approximated to

$$\Delta p_c=\frac{\rho W_m^2}{r_c}b \tag{A2}$$

where Δp_c is the pressure difference between the hub and the

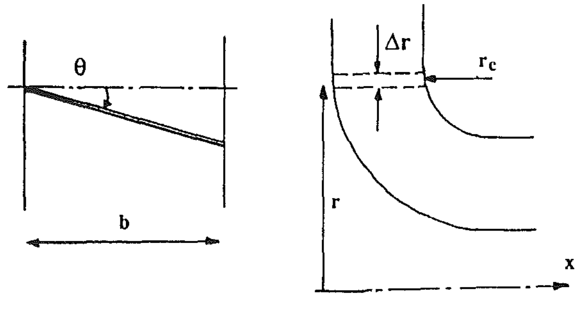

View onto the rotor leading edge   Meridional view

Fig. A1 Determination of the effects of blade inlet rake shroud due to streamline curvature. The axial force developed by the pressure difference is:

$$F_c = 2\pi r \Delta r \Delta p_c = 2\pi r \Delta r \frac{\rho W_m^2}{r_c} b \qquad \text{(A3)}$$

Leaning the blade results in a component of the blade force that acts toward the shroud. This component of force, which is exerted by the fluid on the blades, is given by

$$F_b = b \tan \theta \Delta r \Delta p_b Z \qquad \text{(A4)}$$

where Z is the number of blades and the blade pressure difference is given by the approximate expression

$$\Delta p_b = \rho W_m \Delta W_b = \frac{4\pi}{Z} \rho U W_m \qquad \text{(A5)}$$

from Eq. (5).

It is interesting to note here that if the two forces are equal, then the two effects cancel and so in the inducer, the flow is uniform regardless of the presence of the streamline curvature and blade lean. This probably explains why turbochargers, which often have both lean and shroud curvature, perform better than might be expected even though the shroud radius ratio is greater than the value of 0.7 recommended by the NASA design rules.

When the two forces do not balance, there will be a spanwise variation in the flow properties. Where there is very little curvature, there may be significant variations in the flow properties. The difference between the forces F_c and F_b will result in a reaction force F_x, which will be related to the overall hub-to-shroud pressure difference Δp_x and velocity difference $(V_{\text{hub}} - V_{\text{shroud}})$ by the expression

$$F_x = 2\pi r \Delta r \Delta p_x = 2\pi r \Delta r \, \rho \overline{V}(V_{\text{hub}} - V_{\text{shroud}}) = F_b - F_c \qquad \text{(A6)}$$

so that upon substitution from Eqs. (A3), (A4), and (A5)

$$\frac{\overline{V}(V_{\text{hub}} - V_{\text{shroud}})}{W_m^2} = \frac{b}{r}\left(2 \tan \theta \frac{U}{W_m} - \frac{r}{r_c}\right) \qquad \text{(A7)}$$

the effects of blade lean and shroud curvature can be estimated.

M. I. Goodisman

M. L. G. Oldfield

Department of Engineering Science,
Oxford University,
Oxford, United Kingdom

R. C. Kingcombe

Royal Aerospace Establishment,
Pyestock, Farnborough, United Kingdom

T. V. Jones

R. W. Ainsworth

Department of Engineering Science,
Oxford University,
Oxford, United Kingdom

A. J. Brooks

Royal Aerospace Establishment,
Pyestock, Farnborough, United Kingdom

An Axial Turbobrake

The "Axial Turbobrake" (patent applied for) is a novel turbomachine that can be used to absorb power generated by test turbines. Unlike a compressor, there is no pressure recovery through the turbobrake. This simplifies the aerodynamic design and enables high-stage loadings to be achieved. The blades used have high-turning two-dimensional profiles. This paper describes a single-stage axial turbobrake, which is driven by the exhaust gas of the test turbine and is isolated from the turbine by a choked throat. In this configuration no fast-acting controls are necessary as the turbobrake operates automatically with the turbine flow. Tests on a 0.17 scale model show that the performance is close to that predicted by a simple two-dimensional theory, and demonstrate that the turbobrake power absorption can be controlled and hence matched to that typically produced by the first stage of a modern highly loaded transonic turbine. A full-size axial turbobrake will be used in a short-duration rotating turbine experiment in an Isentropic Light Piston Tunnel at RAE Pyestock.

Introduction

Research into heat transfer in modern gas turbines has led to the construction of rotating turbine facilities that closely model the real engine environment. Short-duration facilities that model the gas/wall/coolant temperature ratios rather than the actual high turbine temperatures are cost effective and are easy to instrument due to their low temperature.

The designer of a short-duration rotating turbine facility has the choice of either allowing the turbine to accelerate during a run or of absorbing the rotor power to hold its speed constant. Tunnels such as the Isentropic Light Piston Tunnel at Oxford University (Ainsworth et al., 1988) and the shock tube rotor at Calspan (Dunn et al., 1984) have been designed without a turbine brake, greatly simplifying their design. At MIT an eddy current brake was used (Epstein et al., 1984).

Brake design is a challenging problem for short-duration facilities, but results in a tunnel potentially capable of more productive and accurate testing. The desired blade speed is maintained during a run, enabling instrumentation traversing. Also, multiple measurements can be taken during a run and averaged without errors due to changing blade speed.

There are also safety issues. The maximum rotor overspeed permitted will limit the run time if there is no brake.

This paper describes a new type of turbomachine, the axial turbobrake. It was designed to absorb the power of the first stage of a modern transonic gas turbine to be tested in the Isentropic Light Piston Cascade (ILPC), a short-duration facility at RAE Pyestock in England (Brooks et al., 1985). This single-stage device is driven by the exhaust gas of the test turbine and is isolated from it by a choked throat. Tests on a 0.17 scale model axial turbobrake are described. These agree surprisingly well with a simple two-dimensional theory. The turbobrake is seen to have applications to both continuous and short-duration facilities.

Braking Requirement

The ILPC rotating section will include a turbine rotor and brake connected to the same shaft (Fig. 1).

The brake must fulfill the following requirements:

(*i*) It must absorb the turbine power for all turbine test conditions.

(*ii*) It must be fail safe.

(*iii*) Its power must be adjustable in order to match the turbine power over the test speed range.

(*iv*) It must not restrict or disturb the turbine flow.

The turbine test conditions are shown in Table 1 and the corresponding ILPC operating conditions are shown in Table 2.

Contributed by the International Gas Turbine Institute and presented at the 36th International Gas Turbine and Aeroengine Congress and Exposition, Orlando, Florida, June 3-6, 1991. Manuscript received at ASME Headquarters January 18, 1991. Paper No. 91-GT-1. Associate Editor: L. A. Riekert.

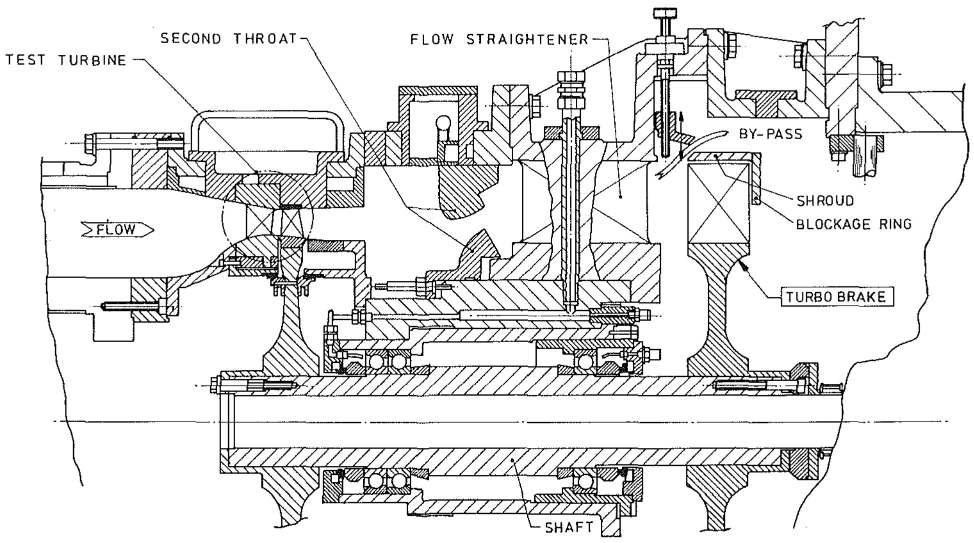

Fig. 1 Proposed axial turbobrake mounted on test turbine in ILPC tunnel at RAE Pyestock

Table 1 Turbine test conditions (total conditions at NGV inlet)

	At design	Off design
Stage loading, $\Delta h_{ot}/U_t^2$	1.53	90–110 percent
Blade Mach number, U_t/a_{01t}	0.60	90–110 percent
Reynolds number, $\dot{m}/\mu_{01t}D_t$	1.38×10^6	50–200 percent
Flow coefficient, $\dot{m}\sqrt{(RT_{01t})}/p_{01t}D_t^2$	0.0483	
NGV gas/wall temperature ratio	1.76	

Table 2 ILPC tunnel design operating conditions

Test time	400 ms
Fluid	Air
Power, P	2.30 MW
Rotational speed	9500 rpm
Mass flow rate, $\dot{m}$	20.7 kg/s
Rotor hub/tip radii	0.252/0.296 m
Total pressure inlet/exit, p_o	5.44/2.10 bar
Total temperature inlet/exit, T_o	508/394 K
Total viscosity inlet/exit, μ_o	$27.0\times10^{-6}/22.6\times10^{-6}$ Pas
Exit absolute swirl angle	22 deg
Mach No. at exit	0.46

Possible Braking Systems

There exist today many braking devices, or dynamometers, capable of absorbing the power produced by a test turbine stage. The cold flow turbine test rig of Westinghouse Canada Inc. (Gosling, 1984) tests turbines up to 7000 rpm. It used a Froude hydraulic dynamometer rated at 600 kW to absorb the power produced by a turbine of tip diameter 686 mm. Hydraulic dynamometers are widely used, heat generated being easily removed by ensuring a steady flow of working fluid through the device. The electric eddy current brake of the DFVLR-AVA rotating cascade rig at Gottingen (Heinemann, 1979) is rated at 500 kW, absorbing the power produced by a 520-mm test wheel rotating up to 15,000 rpm. A full range of dynamometer types is given by Judge (1955).

These brakes, however, have not been developed for use on short-duration facilities. In these facilities, the turbine rotor is spun up to its test speed before the test gas is released. The brake must turn on at the instant the test gas reaches the turbine. Failure to do so at the correct time would result in the wrong test speed or even the turbine accelerating to its burst speed with potentially catastrophic consequences.

The MIT blowdown turbine facility (Epstein et al., 1984, 1985) is a short-duration facility that uses a specially designed eddy current brake to absorb the turbine stage power (1.078 MW) at its design speed of 6190 rpm. At present, this is the only short-duration facility with a brake. The facility has a run time of 400 ms, testing a 500-mm-dia. turbine stage using an Argon/Freon test gas. This test gas permits a much slower rotor angular velocity than for air. Consequently, even if the brake fails, the rotor cannot accelerate to its burst speed.

A number of braking systems were considered for the ILPC (Schultz, 1983). A sufficiently large flywheel was found to be too massive. A disk brake was found to be feasible. However, both it and an eddy current brake require fast-acting controls to activate and deactivate them. Failure of the control system would lead to catastrophic overspeed. For this reason, attention turned to use of an air brake.

An air brake driven by the turbine exhaust gas would be fail safe. No fast-acting controls would be needed, the brake being activated and deactivated by the turbine flow. Pressure

Nomenclature

a = speed of sound
I = moment of inertia
C_P, C_v = specific heat at const. pressure, volume
D = mean rotor blade diameter
Δh_o = change in total enthalpy per unit mass
M = Mach number
NGV = nozzle guide vane
$\dot{m}$ = mass flow rate

N = rpm
P = power
p = pressure
R = gas constant
r = radius
T = temperature
U = mean blade velocity
v = fluid velocity
α = swirl angle
γ = ratio of specific heats
μ_o = total viscosity

ϕ = flow coefficient = $[\dot{m}\sqrt{(RT_{01})}]/[p_{01}D^2]$
ψ = stage loading = $\Delta h_o/U^2$

Subscripts

b = brake
r = relative to rotor
t = turbine
0 = total
1 = at rotor inlet
2 = at rotor exit
* = at throat

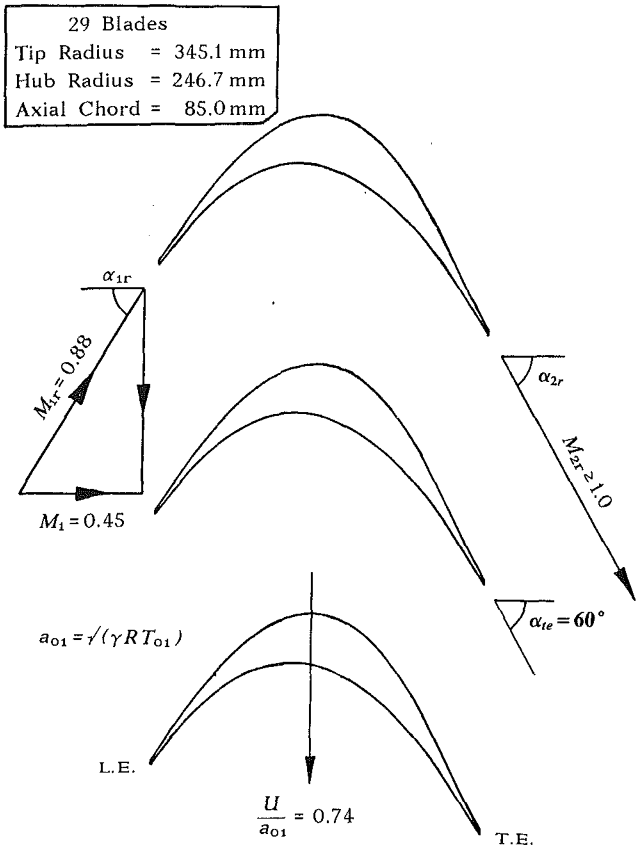

Fig. 2 Midheight section of axial turbobrake blades

fluctuations from the brake could be isolated from the turbine test section by a choked throat (the second throat in Fig. 1) between the turbine and air brake. This throat would also be used to set the turbine back pressure. An additional advantage of an air brake is that the heat generated during braking is carried away by the flow, and so the brake needs no cooling.

Existing compressor technology was considered. For simplicity, a single-stage device was preferred. A centrifugal compressor stage absorbs more power than an axial compressor stage but is still less powerful than a transonic turbine stage of similar diameter and mass flow. Power scales with the square of the compressor diameter, but the brake power required leads to an excessively large centrifugal compressor. Epstein et al. (1985) came to a similar conclusion.

A successful air dynamometer, using a double-sided radial outflow turbine, has been developed by Foor and Jansen (1984). For the power absorption required by the present study, a radial outflow turbine would require a large-diameter exit flow collector, and the cantilevered blading presents stress problems. For these reasons an axial flow geometry is preferred.

Theory of Axial Turbobrake

The axial turbobrake concept comes directly from Euler's pump equation:

$$P/\dot{m}=\Delta h_o=U_2c_2-U_1c_1$$

This shows that the power P transferred by a rotor to a fluid of mass flow rate $\dot{m}$ can be maximized by achieving the maximum change in fluid tangential velocity (or swirl) c coupled with the maximum blade speed, U. This criterion is different from that of a compressor, whose purpose is the efficient compression of gas. With the requirement of compression removed, a new turbomachine, optimized for power adsorption, was designed and termed the axial turbobrake (referred to also as just turbobrake).

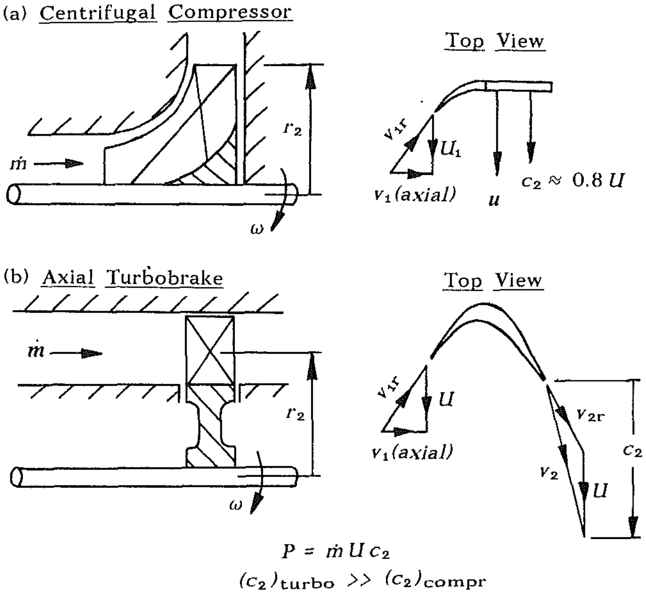

Fig. 3 Comparison of exit whirl velocity c_2 produced by (a) centrifugal compressor and (b) axial turbobrake of similar diameter. The power absorbed, $P=\dot{m}Uc_2$, is far greater for the turbobrake.

The design philosophy adopted was to choose an axial flow device and use a blade profile (Fig. 2) that added as much whirl velocity as possible to the incoming axial flow. The lack of an NGV, together with the high blade speeds planned, gives a high blade relative inlet Mach number (typically $M_{1r}=0.88$) and this in turn dictates the use of a steeply inclined, sharp leading edge. The flow is then turned sharply and leaves the passage supersonically in the direction of blade rotation with about 60 deg swirl, exhausting into a low-pressure downstream region.

Figure 3 compares the turbobrake velocity triangles to those of the centrifugal compressor. It shows the larger tangential velocity changes in the turbobrake for a given blade speed.

In the axial turbobrake, unlike an axial compressor, there exists a net negative pressure difference across the rotor. No pressure recovery is required, so there is no overall diffusion through the rotor and no need for diffusing nozzle guide vanes downstream of the rotor. This negative axial pressure gradient greatly simplifies the design, allowing high blade curvature without catastrophic stall. This should also reduce the possibility of surge.

As high efficiency is not required, flow separations within the blade passage can be tolerated, provided that the acceleration at exit re-attaches the flow and that the effective throat area is not reduced to an extent whereby the turbobrake upstream pressure is raised enough to unchoke the upstream isolating throat.

The profile shown in Fig. 2 was designed by Gareth Horton at RAE Pyestock. For ease of manufacture, a two-dimensional blade profile, with constant tip and hub radii, was chosen.

Although an axial turbobrake can have inlet guide vanes to add inlet swirl, these are not necessary. This study concentrates on the simpler design with axial inlet flow.

With axial flow at the turbobrake inlet and constant blade tip and hub radii, Euler's turbine equation becomes

$$\Delta h_o=Uc_2=U(U+v_{2r}\sin\alpha_{2r}).$$

Assuming perfect gas, adiabatic flow, the brake performance can be nondimensionalized by expressing the stage loading ψ in terms of the blade rotational Mach number U/a_o (equivalent to $N/\sqrt{T}$), relative exit Mach number M_{2r}, and relative exit angle α_{2r}:

$$v_{2r}=\mathrm{M}_{2r}a_{2r}=\mathrm{M}_{2r}a_{01}\sqrt{\left(\frac{T_{or}}{T_{01}}\frac{T_{2r}}{T_{or}}\right)}.$$

The energy equation for adiabatic flow gives

$$\frac{T_{or}}{T_{2r}}=1+\frac{\gamma-1}{2}\mathrm{M}_{2r}^2$$

Equating static enthalpies at the blade entry,

$$h_{01}-\frac{1}{2}v_1^2=h_{or}-\frac{1}{2}v_{1r}^2,$$

or

$$C_pT_{01}-\frac{1}{2}v_1^2=C_pT_{0r}-\frac{1}{2}(v_1^2+U^2).$$

Noting that $C_p=\gamma R/(\gamma-1)$ and that $a_{01}=\sqrt{(\gamma RT_{01})}$, we get

$$\frac{T_{or}}{T_{01}}=1+\frac{\gamma-1}{2}\left(\frac{U}{a_{01}}\right)^2.$$

Combining the above four equations gives

$$\psi=\frac{\Delta h_o}{U^2}=1+\frac{\mathrm{M}_{2r}\sin\alpha_{2r}}{\left(\frac{U}{a_{01}}\right)}\left(\frac{1+\frac{\gamma-1}{2}\left(\frac{U}{a_{01}}\right)^2}{1+\frac{\gamma-1}{2}\mathrm{M}_{2r}^2}\right)^{1/2} \tag{1}$$

Equation (1) clearly shows that ψ can be maximized by using large values of α_{2r} and M_{2r}. In practice, since sin(60 deg) = 0.866, relative exit angles of 60–70 deg are sufficient. A large vacuum vessel is used to maintain the downstream pressure near to vacuum during the run up and this ensures that, during test time, $\mathrm{M}_{2r}>1.0$.

For design purposes, the conservative assumption was that $\mathrm{M}_{2r}=1.0$. Then, for air with $\gamma=1.4$, and at a typical $U/a_{01}=0.74$, Eq. (1) gives $\psi=2.13$ for $\alpha_{2r}=60$ deg, increasing at 2.22 at 70 deg. This is more than double that of a centrifugal compressor of the same diameter, where $\sin\alpha_{2r}\approx 0$, giving $\psi\approx 1.0$.

Since the power absorbed, $P=\dot{m}\Delta h_o=\dot{m}\psi U^2$, it follows that P can be increased, for a given $\dot{m}$, by increasing the turbobrake diameter, and hence U, and still keep within mechanical and structural limits.

Matching Turbobrake to Turbine

The turbine stage loading $\psi_t=\Delta h_{ot}/U_t^2$ is based on the midheight turbine blade speed U_t. Although the turbobrake is mounted on the same shaft (Fig. 1), and rotates at the same angular velocity, it has a different midheight diameter D_b and hence a different midheight blade speed, $U_b=U_t(D_b/D_t)$. The turbobrake has to absorb the turbine Δh_o, and so has a required turbobrake stage loading,

$$\psi_b=\Delta h_{ot}/U_b^2 \tag{2}$$

The turbine cools the flow through it and hence reduces the sound speed a_{01b} upstream of the turbobrake. This changes the rotational Mach number U_b/a_{01b}:

$$\left(\frac{U_b}{a_{01b}}\right)=\left(\frac{U_t}{a_{01t}}\right)\left(\frac{U_b}{U_t}\right)\left(\frac{a_{01t}}{a_{01b}}\right)$$

As $\Delta h_{ot}=C_p(T_{01t}-T_{01b})$, (a_{01t}/a_{01b}) can be found. (U_b/U_t) depends only on the geometry of the turbine and brake, and so the required nondimensional turbobrake speed is given by

$$\left(\frac{U_b}{a_{01b}}\right)=\left(\frac{U_b}{U_t}\right)\left(\frac{U_t}{a_{01t}}\right)\left[1-(\gamma-1)\psi_t\left(\frac{U_t}{a_{01t}}\right)^2\right]^{-1/2} \tag{3}$$

Table 3 Turbobrake at design conditions

Required stage loading (Eq. (2)), $\Delta h_{0t}/U_b^2$	1.32
Theoretical stage loading (Eq. (1)), $\Delta h_{0b}/U_b^2$	2.13
Blade Mach number, U_b/a_{01b} (Eq. (3))	0.74
Number of blades	29
Fluid	Air
Required power, P	2.3 MW
Maximum power	3.8 MW
Rotational speed	9500 rpm
Mass flow rate, $\dot{m}$	20.7 kg/s
Blade axial chord	85 mm
Rotor hub/tip radii	246.7/345.1 mm
Total temperature inlet, T_{01b}	394 K
Total viscosity inlet, μ_{01}	22.6×10^{-6} Pas
Relative exit swirl angle, α_{2r}	60 deg
Relative exit Mach number, M_{2r}	>1.0

Turbobrake Design

Initially a 70 deg exit flow turbobrake was designed and model tested. It worked, but proved to have insufficient throat area. The resulting pressure upstream of the brake permitted the isolating second throat between the turbine and the brake (Fig. 1) to unchoke.

This design was replaced by the larger throat area, 60 deg relative exit angle, brake presented in this paper. This brake was designed to work with the test turbine facility specified in Tables 1 and 2. The blade shape is shown in Fig. 2 and brake details are given in Table 3.

Before manufacturing a full size turbobrake, it was felt wise to validate the design by testing a scale model at representative nondimensional operating conditions.

Model Scaling

In both a full size and a model turbobrake, the mass flow rate, $\dot{m}$, total temperature, T_{01}, turbobrake mean blade speed, U, and downstream pressure, p_2, are set. The test gas used determines viscosity, μ_{01}, gas constant, R, and ratio of specific heats, γ. These independent variables determine the power, P, and upstream total pressure, p_{01}, the dependent variables, for a given run. So,

$$P,\ p_{01}=f(\dot{m},\ T_{01},\ U,\ p_2,\ \mu_{01},\ R,\ \gamma,\ D).$$

There are thus nine interrelated variables in each case and four primary physical quantities (i.e., mass, length, time, and temperature). Buckingham's pi theorem states that these may be reduced to relationships between $9-4=5$ nondimensional groups. These may be chosen as shown below:

$$\frac{P/\dot{m}}{U^2},\ \frac{\dot{m}\sqrt{(RT_{01})}}{p_{01}D^2}=f\left(\frac{U}{\sqrt{(\gamma RT_{01})}},\ \frac{p_{01}}{p_2},\ \frac{\dot{m}}{\mu_{01}D},\ \gamma\right)$$

or

$$\psi,\ \phi=f\left(\frac{U}{a_{01}},\ \frac{p_{01}}{p_2},\ \mathrm{Re},\ \gamma\right)$$

where ϕ is the flow coefficient.

In the model tests described below, all the above parameters were correctly modeled apart from p_{01}/p_2, which was kept sufficiently high to choke the blade passages.

Model Test Facility

Commercial air motors (Tech Developments Inc. Model 51H) were found to provide a quick and inexpensive basis for a 0.17 scale model turbobrake transient test facility. As shown in Fig. 4, the turbine on the first motor is replaced by a model flow straightener and turbobrake rotor. The model turbobrake rotor, shown in Fig. 5, was machined from aluminum alloy as a blisk with integral blades. A coupled second air motor is used to drive the turbobrake up to test speed. A flow of test gas through the turbobrake is then very rapidly turned on, and the angular deceleration measured.

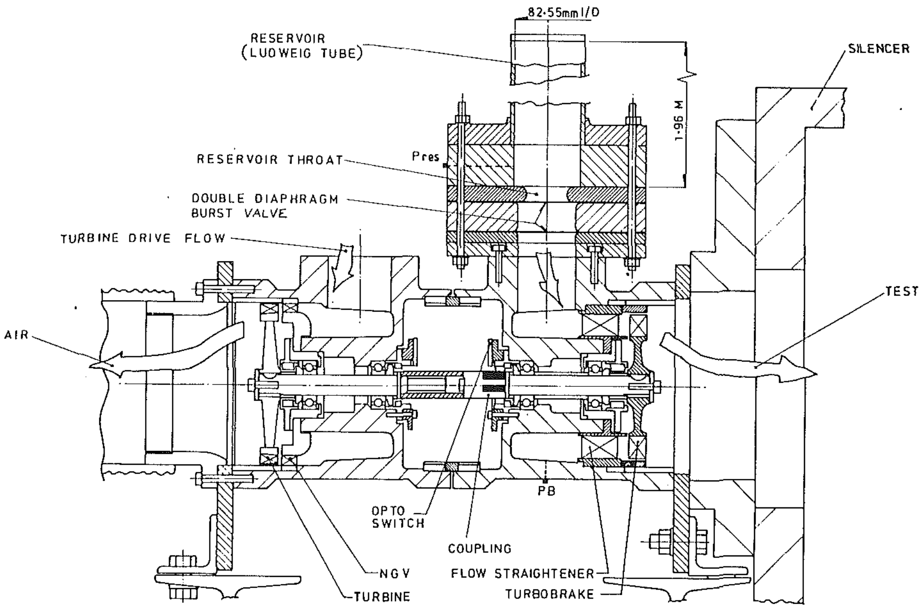

Fig. 4 Model (0.17 scale) axial turbobrake test facility, constructed from two modified air motors mounted back to back

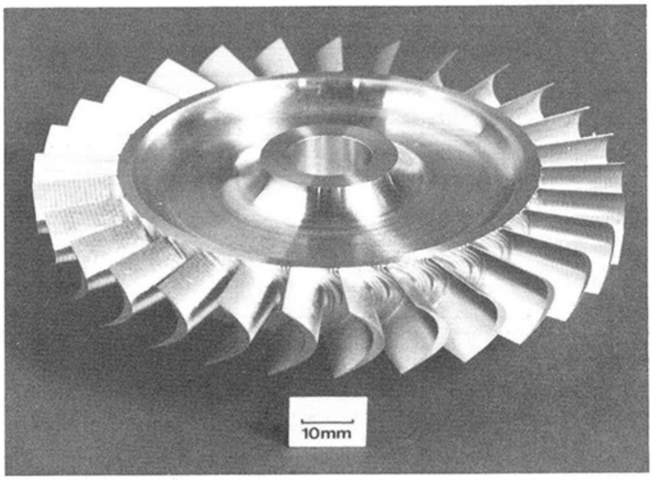

Fig. 5 Photograph of 0.17 scale test axial turbobrake rotor

Immediately before the run all the power of the driving air motor is used to overcome friction in the bearings and carbon-faced seals as well as the turbobrake windage. So, on releasing the test gas, vitually all the power developed *initially* by the turbobrake is used to decelerate the rotating components (provided the turbobrake windage, existing only before test gas release, is small). Therefore, $P = I\,\dot{\omega}\,\omega$, giving stage loading

$$\psi = \frac{I\,\dot{\omega}\,\omega}{\dot{m}\,U^2}.$$

Thus, the angular deceleration $\dot{\omega}$ is a direct measure of stage loading. The total moment of inertia of the rotating components, I, was measured using the tri-filar suspension technique and found to be only 1.6 percent less than that calculated from the design.

To model the higher speeds, it is necessary to use a 54.5 percent carbon-dioxide and 45.5 percent argon mixture (mole fractions) as the test gas. This has the same γ as air, with a lower speed of sound, allowing the design blade Mach number to be reached at 39,000 rpm rather than at 47,000 rpm for air, which is beyond safe operation of the air motor rotor.

A Ludweig Tube (Ludweig, 1957) is used as the test gas reservoir. This simple device supplies the turbobrake with gas at a constant mass flow rate and total temperature during the run. A double diaphragm was burst to start the run, and the mass flow was metered by a choked throat. The 1.96-m-long, 82.55-mm-i.d. Ludweig tube used gave a run time of 14 ms for the CO_2/Ar test gas and 11 ms for air.

For correct scaling, the model turbobrake pressures are higher than those in the ILPC. Consequently, it was possible for the model turbobrake to remain choked while exhausting it to atmospheric (room) pressure instead of a vacuum. This simplified the rig design.

Pressures were measured with SensorTechnic pressure transducers, which have a response time of 1 ms and are temperature compensated to ± 1.5 percent full scale (between 0 and 70°C). Type K thermocouples ($40\ \mu V/{}^\circ C$) measured temperature with a 5 ms response time. A reflective opto-switch detecting the passing of black bands painted on the coupling between the air motors gave angular displacement from which angular velocity and deceleration were found. A Datalab DL1200 transient recorder sampled at 200 kHz for 20.5 ms during a run, and the data was processed with a Matlab software package.

Test Results

Figure 6 shows typical plots of reservoir pressure, turbobrake upstream static pressure, and turbobrake speed for the 0.17 scale model at design conditions. The torque could be measured from the angular velocity curve with good repeatability.

Figure 7 shows that, as expected, the theoretical performance (Eq. (1)) of the turbobrake exceeds that required to absorb the turbine power by a considerable margin over most of the speed range. The highest experimental curve (marked full power) shows that the turbobrake *is* more powerful than the turbine over the turbine test speed range (1.40 times at design speed).

Figure 7 also shows the experimental turbobrake stage loading is in surprisingly close agreement with the simple two-dimensional theory in Eq. (1). Some of the 12 percent shortfall will be due to separations and three-dimensional effects and to the 7 percent tip leakage area between the blade and the shroud. Turbobrake windage, which exits only before test gas release, will also reduce the measured values at high speeds.

Control System

The turbobrake power has to be reduced to match the turbine

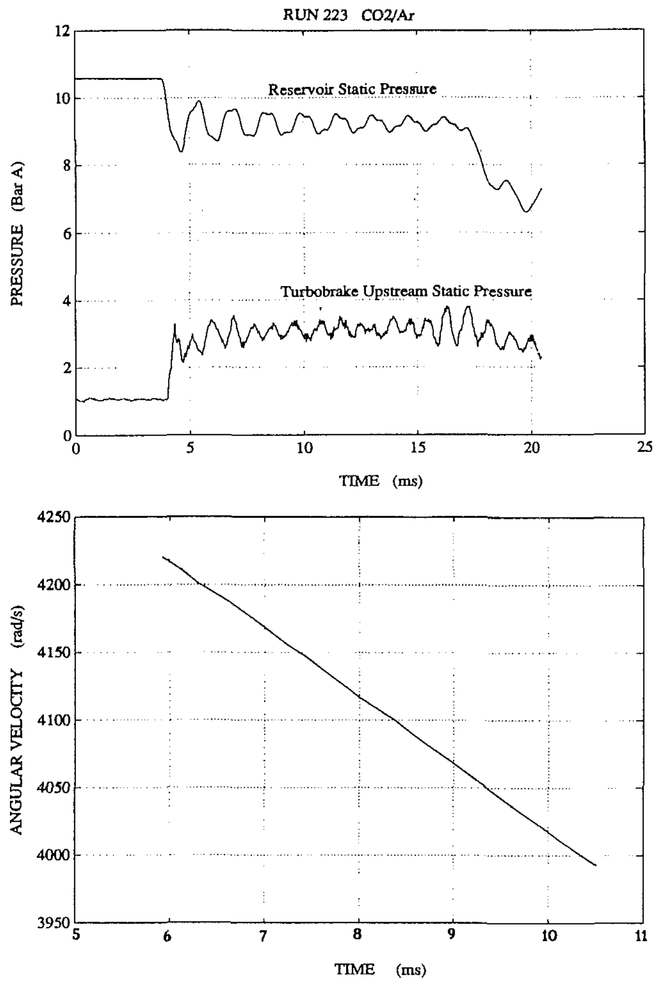

Fig. 6 Typical traces of reservoir static pressure, turbobrake upstream static pressure, and turbobrake shaft angular velocity from a 0.17 scale model test at design conditions. The Ludweig tube gives a steady flow from about 4 ms to 17 ms.

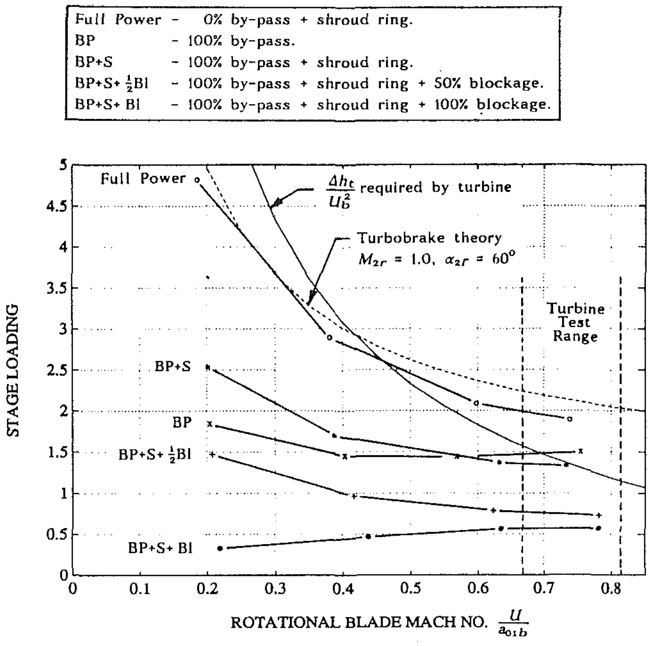

Fig. 7 Predicted and measured stage loadings for 0.17 scale model axial turbobrake. The effects of a range of control settings are shown.

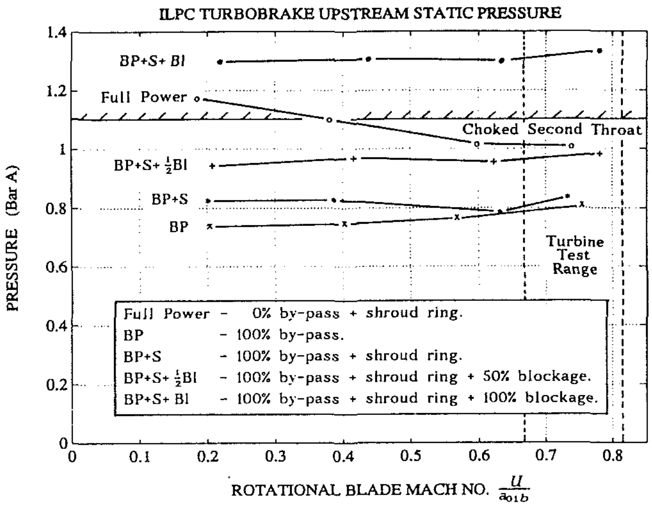

Fig. 8 Full-scale axial turbobrake upstream static pressures obtained by rescaling values measured on 0.17 scale model. The effects of a range of control settings are shown.

power to give a constant speed run. Variable inlet guide vanes were rejected as the possible control range is inadequate and the mechanical complexity high.

The simplest method of control is to bypass mass flow around the turbobrake: Since $P = \dot{m}\,\psi\,U^2$, reducing $\dot{m}$ reduces P. Initial schemes used annular plates forming a shroud around the turbobrake blades, which could be moved radially outward to allow a percentage of the mass flow to leak over the blade tips. In Fig. 7, the curve marked *BP* shows this system to work well at low speeds, but inadequately at higher speeds. The large radial pressure gradient in the swirling exit flow together with flow centrifuged from the blade tips are thought to be responsible.

A second control system (Fig. 1) was tested with a shroud ring to separate the blade tips from the bypass flow. To reduce the turbobrake mass flow further, blockage rings of different internal diameter can be bolted to it to partially block the blade exit flow. Shortened annular plates set the bypass flow over the shroud to allow fine power adjustment.

The results from the model tests in Fig. 7 show this approach to be successful, giving a wide range of controllable turbobrake power. Note that the turbobrake still absorbs power with 100 percent downstream blockage because of leakage around the rings and possible reverse flow at the leading edge tips.

On the basis of these successful model tests, it is intended to use this control system on the full size turbobrake.

The turbobrake power increases, relative to the turbine power, with speed. Once matched, the turbine-turbobrake assembly will maintain itself at a stable, constant speed without the need for a fast-acting control system.

The Second Throat

For the second throat (Fig. 1) to remain choked, and thus aerodynamically isolate the test turbine from turbobrake, its downstream static pressure must be below 1.11 bar at design. The throat downstream static pressure is the same as that upstream of the turbobrake, which is set by the turbobrake throat area.

The static pressure upstream of the model turbobrake was measured and scaled down to that of the full-size ILPC turbobrake, using the fact that the flow coefficient, $\phi = \dot{m}\sqrt{(RT_{01})}]/[p_{01}\,D]$ is the same. The results shown in Fig. 8 show that the pressures are below 1.11 bar except in the extreme, and not relevant, cases of 100 percent downstream blockage or very low speed.

Thus the turbobrake can operate over the turbine test speed range without unchoking the isolating throat.

Future Developments

Following the success of these tests, a full-size turbobrake is now under manufacture and will be installed as part of the new rotating turbine section in the Isentropic Light Piston Cascade at the Royal Aerospace Establishment at Pyestock, England.

Providing the exit pressure can be kept sufficiently low, the model tests have shown that the axial turbobrake could also be used as a brake for a continuously running turbine facility. The only additions required would be simple, lossy, downstream vanes in the exit duct to absorb the high degree of swirl generated. This swirl is not a problem in short duration facilities, as it is dissipated slowly in the dump tank after the run.

Conclusions

A new single-stage turbomachine, the axial turbobrake, has been developed. It can more than absorb the power of the first stage of a large modern transonic gas turbine. A simple two-dimensional theory can be used to predict its performance with surprising accuracy. Model tests have demonstrated that it operates as predicted and that the power absorbed can be controlled over a large range by a combination of flow bypass and downstream blockage. Although initially developed for use on short-duration facilities, the turbobrake is also applicable to continuously running facilities.

Acknowledgments

Thanks are due to the Royal Aerospace Establishment, Pyestock, for their support of this work. Thanks are also due to the late Professor Don Schultz for his work on the design of the ILPC, to Gareth Horton at RAE for his design work on both blade profiles, to the Osney Lab. technicians, including Bob Taylor who machined the blade profiles, and to Richard Harris and his team at Foxley Design Associates Ltd.

References

Ainsworth, R. W., Schultz, D. L., Davies, M. R. D., Forth, C. J. P., Hilditch, M. A., Oldfield, M. L. G., and Sheard, A. G., 1988, "A Transient Flow Facility for the Study of Thermofluid-Dynamics of a Full Stage Turbine Under Engine Representative Conditions," ASME Paper No. 88-GT-144.

Brooks, A. J., Colbourne, D. E., Wedlake, E. T., Jones, T. V., Oldfield, M. L. G., Schultz, D. L., and Loftus, P. J., 1985, "The Isentropic Light Piston Annular Cascade Facility at RAE Pyestock," AGARD CP-390, pp. 31.1–31.23.

Dunn, M. G., Rae, W. J., and Holt, J. L., 1984, "Measurement and Analysis of Heat Flux Data in a Turbine Stage: Part I—Description of Experimental Apparatus and Data Analysis," ASME *Journal of Engineering for Gas Turbines and Power*, Vol. 106, pp. 229–233.

Epstein, A. H., Guenette, G. R., and Norton, R. J. G., 1984, "The MIT Blowdown Turbine Facility," ASME Paper No. 84-GT-116.

Epstein, A. H., Guenette, G. R., and Norton, R. J. G., 1985, "The Design of the MIT Blowdown Turbine Facility," MIT Gas Turbine Lab. Report No. 183, Apr.

Foor, W. B., and Jansen, W., 1984, "The Application of Air Dynamometers for Testing Turbo-shaft Gas Turbine Engines," ASME Paper No. 84-GT-216.

Gosling, M. C., 1984, "The Design, Manufacture and Operation of a Model Turbine Test Rig," ASME Paper No. 84-GT-130.

Heinemann, H., 1979, "The Test Facility for Rotating Annular Cascades of the DFVLR and Its Measurement and Evaluation Method," ICIASF 79 Record, IEEE publication, New York.

Judge, A. W., 1955, *The Testing of High Speed Internal Combustion Engines*, Chapman and Hall, pp. 154–226.

Ludweig, H., 1957, "Tube Wind Tunnel, a Special Type of Blowdown Tunnel," AGARD Report 143, July.

Schultz, D. L., 1983, "A Study of the Feasibility of Installing a Rotor in the R.A.E. Pyestock Free Piston Cascade," Internal Report.

Rim Seal Experiments and Analysis for Turbine Applications

W. A. Daniels

B. V. Johnson

United Technologies Research Center,
East Hartford, CT 06108

D. J. Graber

Pratt and Whitney,
Government Products Division,
West Palm Beach, FL 33410

R. J. Martin

Wright Research and Development Center,
Wright-Patterson Air Force Base,
OH 45433

An experimental investigation was conducted to determine the sealing effectiveness and the aerodynamic characteristics of four rim seal models for a number of flow conditions. The experiments were conducted to obtain an extended data base for advanced turbine rim seal design. The class of rim seals investigated are those found on the downstream side of the rotor where the boundary layer on the disk is pumped directly into the seal gap. The experiments were conducted at disk tangential Reynolds numbers up to 5.1×10^6 *with a simulated gas path flow across the top of the seal. The simulated gas path flow was injected with various amounts of swirl to determine the effect of swirl on the seal effectiveness. The radial gap and the axial overlap of the seal were varied and results compared with a baseline configuration. A rim seal configuration intended to prevent disk pumping directly into the seal gap was also investigated. A mass transfer analogy was used to characterize the rim seal ingestion characteristics and the trace gas chosen for this technique was* CO_2. *The results of this investigation indicate that decreasing the radial gap of the seal produces a better improvement in seal effectiveness than increasing the axial overlap of the seal, that seal effectiveness increases only modestly as the swirl across the top of the seal decreases, and that the trace gas technique employed to determine seal effectiveness is an accurate alternative to pressure measurement or flow visualization techniques used by other investigators. The results of this investigation were compared with results from a boundary layer model for rim seals with axial gap geometries.*

Introduction

In advanced aircraft gas turbine engines, the air that is supplied to the turbine to cool the disks is also used to seal the turbine disk cavities and other internal components from the hot primary gas path. This function of maintaining an acceptable thermal environment in the turbine is becoming more critical as the trend in gas turbine development has been toward higher turbine pressures, temperatures, and rotation rates in an effort to increase engine thrust-to-weight ratio. This same cooling air may also be called upon to perform other functions such as those required in active blade cooling designs in addition to its usual role. Since the amount of cooling air required to perform these functions greatly influences the efficiency of the engine, it is imperative for the gas turbine designer to have an accurate means of predicting sealing requirements for structural integrity at a minimum specific fuel consumption. This critical step in the design process is hampered by the fact that to date no general turbulent transport model has been developed that accurately describes the mixing process for the many types of seals that are used today in the gas turbine industry. The turbine designer must then rely on the limited amount of rim seal data that is in the literature to predict the performance of a candidate seal. In keeping with the goals of the high-performance turbine engine technology initiative of doubling the thrust-to-weight ratio, internal cooling and leakage air will be substantially reduced. It is imperative then, that adequate analytical design tools and experimental data be developed to assess the impact and performance of newly designed internal flow configurations. That was the intent of this sponsored research program.

The purpose of this paper is to present the results of rim seal ingestion experiments for one type of seal, which is typical of those found on the downstream side of a turbine rotor. This type of seal is generally of the radially overlapped type where the rotor shroud overlaps the stator. In this situation, the boundary layer that is developed on the rotor is pumped directly into the seal gap. Three seals of this type were considered. The radial gap and the axial gap was altered and the ingestion and aerodynamic characteristics were measured.

Experimental Apparatus

The experiments were conducted in the Internal Air Systems and Heat Transfer Facility at the United Technologies Research Center. The facility is capable of providing test conditions with nondimensional parameters (Reynolds number, flow parameter, etc.) typical of current and advanced design aircraft gas turbine engines. This is accomplished at moderate rotation rates (up to 3500 rpm) by conducting the experiments with large-scale models in a pressure vessel at pressures up to 10 atm. The facility is described in greater detail by Graber et al. (1987).

Contributed by the International Gas Turbine Institute and presented at the 35th International Gas Turbine and Aeroengine Congress and Exposition, Brussels, Belgium, June 11–14, 1990. Manuscript received by the International Gas Turbine Institute January 16, 1990. Paper No. 90-GT-131. Associate Editor: S. A. Mosier.

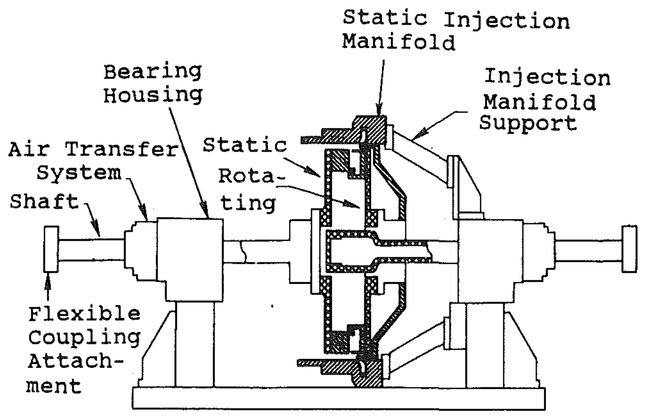

Fig. 1 Sketch of the rim cavity test assembly

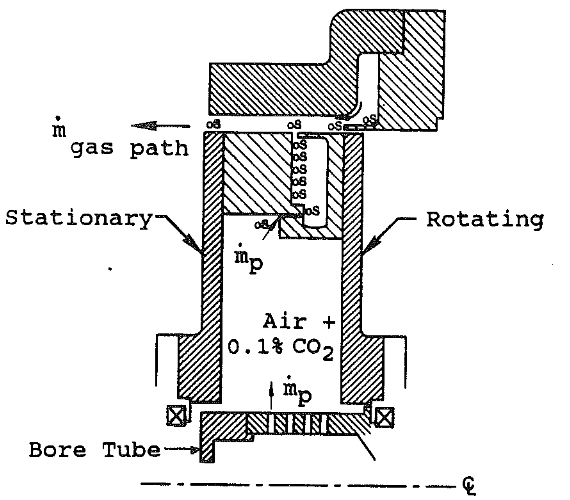

Fig. 2 Cross-sectional sketch of rim cavity model showing location of gas sampling ports

A sketch of the cross section of the rim seal test assembly used in this investigation is shown in Fig. 1. The principal components of the test assembly consist of a rotor model, a stator model, a stationary to rotating frame air transfer system for injecting the sealing flow into the rim cavity model, and a stationary injection manifold. The stationary injection manifold was used to inject a simulated gas path flow across the top of the seal model. The simulated gas path flow was injected with various amounts of swirl. This was accomplished by injecting air through one of three sets of nozzles oriented to discharge in a direction tangent to the rotor. The nozzle sets were sized to produce a swirl velocity equal to $R_o\Omega$, $2R_o\Omega$, or $0.6R_o\Omega$ where $R_o\Omega$ is the rotor tip velocity. The swirl angle of the simulated gas path flow was not measured but, because of the low axial velocity of the flow (≤ 33 cm/s) can be considered to be quite high. The simulated sealing flow was injected through 24 equally spaced holes in the rotating bore tube. This flow then entered the rim seal cavity and was ejected through the seal model into the simulated gas path flow.

The technique used in this investigation to determine the rim seal ingestion characteristics for the class of seals investigated was that of a mass transfer analogy. The main assumption in the mass transfer analogy is that the turbulent Prandtl number, Pr, governing the heat transfer process and the turbulent Schmidt number, Sc, governing the mass transfer process vary in such a way that the ratio Pr/Sc is approximately unity everywhere in the flow field. This is a good approximation if the molecular weight of the trace element used is close to that of the main flow and if the flow is turbulent. The application of the mass transfer analogy is well documented (Eckert and Goldstein, 1976; Pederson et al., 1977; Denton and Usui, 1981; McGreehan et al., 1987). For investigating rim seal ingestion characteristics, this technique is ideal because the boundary conditions can be measured with much greater accuracy than those in the corresponding thermal process.

The trace gas used in this investigation was CO_2. Although there are other gases with molecular weights closer to air, CO_2 was chosen primarily for reasons of safety. The procedure for determining rim seal effectiveness with this technique is shown schematically in Fig. 2. The simulated sealing flow is "seeded" with CO_2 until the concentration of CO_2 in the mixture is approximately 1300 ppm (parts per million). This is approximately 1000 ppm greater than the normal concentration of CO_2 present in a standard sample of air. As the seeded flow enters the rim seal model, the CO_2 concentration within the rim cavity decreases due to the amount of flow ingested from the simulated gas path through the seal model. By withdrawing samples of the air at various locations within the cavity (sample locations are designated as "S" in Fig. 2) and measuring the CO_2 concentration of the sample, the amount of flow that has been ingested may be determined.

For this investigation, CO_2 concentration was measured at 11 locations in and around the rim seal model. These locations are shown in Fig. 2. A total of six radial locations were used inside the rim seal cavity. The sample locations shown in Fig. 2 in the simulated gas path flow were used to assure that the air used for the gas path flow was not "contaminated" by the air/CO_2 mixture in the pressure vessel prior to crossing the top of the seal model. These sampling ports were located at different radial and circumferential locations in the annulus above the seal model. The CO_2 concentrations were measured with a Beckman Model 8085 CO_2 Analyzer.

A sketch of the rim seal cavity model is presented in Fig. 3. The cavity overall height was 2.76 in. (7.0 cm) and the outer diameter was 20.82 in. (52.8 cm). The sealing flow entered the rim seal cavity model at a radius of 8.22 in. (20.9 cm) through

Nomenclature

C = CO_2 concentration, ppm
C_o = CO_2 concentration of gas path flow, ppm
C_p = CO_2 concentration of purge flow, ppm
D = mass diffusivity, ft^2/sec
Pr = Prandtl number = $\mu c/k$
Re_r = radial Reynolds number $= \dot{m}_p/(2\pi\mu R_o)$
Re_t = tangential Reynolds number $= \rho\Omega R_o^2/\mu$
R_o = rotor outer radius, ft
S = seal gap, ft
Sc = Schmidt number = $\mu/\rho D$
S/R_o = seal gap ratio
V = core flow tangential velocity, ft/sec
V_o = rotor tip velocity = $R_o\Omega$, ft/sec
V/V_o = tangential velocity ratio
V_p = purge flow velocity in seal gap, ft/sec
$V_{\phi gas}$ = gas path swirl velocity, ft/sec
c = specific heat, Btu/lb/R
k = thermal conductivity, Btu/ft/hr/R
$\dot{m}_p$ = purge flow rate, lb/sec
r = radius, ft
α = cavity core rotation factor $= \alpha r\Omega$
η_p = dimensionless sealing flow $= Re_r/Re_t^{0.8}$
η_{pmin} = dimensionless sealing flow to prevent ingestion
μ = viscosity, lb/(ft sec)
ρ = density, lb/ft^3
ϕ = sealing effectiveness parameter $= (C-C_o)/(C_p-C_o)$
Ω = rotor angular rotation rate, sec^{-1}

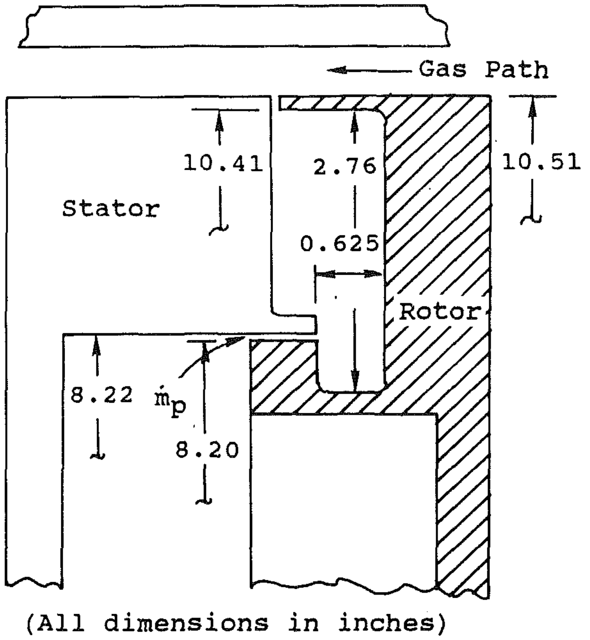

Fig. 3 Rim cavity model geometry

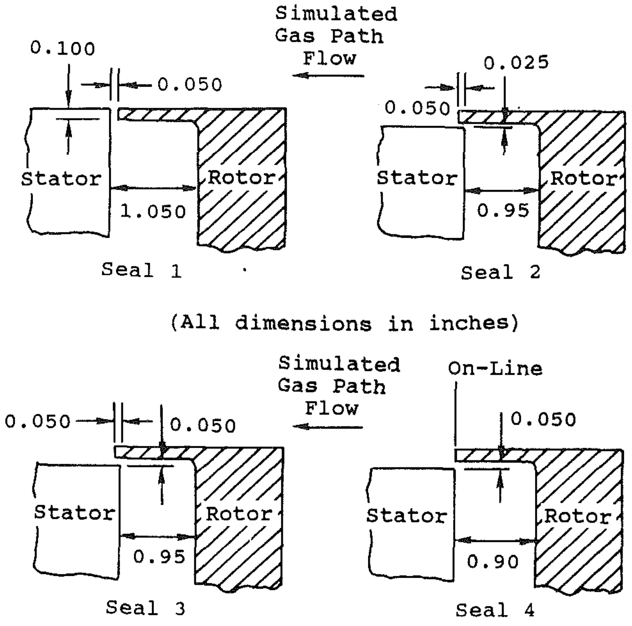

Fig. 4 Schematic of rim seal models investigated

a 0.020 in. (0.05 cm) radial gap between the rotor and the stator. The rotor geometry remained unchanged throughout the experiments. The cavity aspect ratio and the seal model gap to rotor radius ratio, S/R_o, were altered in the experiment by a combination of machining and shimming the stator.

Four seal model configurations were investigated. These are shown in Fig. 4. Seal 1 had an axial gap while seals 2, 3, and 4 had a radial overlap configuration. Seals 2 and 4 are variations of the seal 3 configuration. For seal 2, the radial gap was varied, whereas in seal 4 the axial overlap was varied. For seals 2, 3, and 4, the ingestion experiments were conducted at a tangential Reynolds number of 2.6×10^6 with a simulated gas path swirl velocity equal to the disk tip velocity and at a tangential Reynolds number of 5.1×10^6 with simulated gas path swirl velocities of 1.0, 2.0, and 0.6 times the disk tip speed. For seal 1, only swirl levels of 1.0 and 2.0 times the disk tip velocity were investigated at a tangential Reynolds number of 5.1×10^6. The stator-to-rotor gap clearances quoted in Fig. 4 were measured at assembly and found to be within a tolerance of 0.002 in. (0.8 mm). The rotor growth due to centrifugal forces was estimated to be 0.003 in. (1.2 mm) at 3500 rpm.

Experimental Results and Discussion

Rim seal ingestion characteristics and cavity aerodynamic characteristics were determined for the four seal model configurations investigated. For each seal model, the sealing flow rate was varied and the CO_2 concentration within the cavity and the cavity radial pressure distribution was measured. The flow conditions for the experiment were formulated in nondimensional form with the sealing flow rate written as $\eta_p = \mathrm{Re}_r/\mathrm{Re}_t^{0.8}$ where Re_r is denoted as the radial Reynolds number. The nondimensional parameter used to formulate the ingestion characteristics of a given seal is written as $\phi = (C - C_o)/(C_p - C_o)$ where ϕ is denoted as the sealing effectiveness parameter. Here, C, C_p, and C_o are the measured CO_2 concentrations of the gas within the cavity, the purge gas, and the simulated gas path flow, respectively. The CO_2 concentration level of the gas within the cavity, C, was determined by averaging the measured CO_2 concentrations at the four outermost sampling locations within the cavity (see Fig. 2). This form of the cooling effectiveness parameter can be determined from conservation of mass and conservation of CO_2 within the cavity.

The form of the sealing effectiveness parameter indicates the expected variation of the sealing characteristics of a given seal with coolant flow rate. As the coolant flow is increased, the average concentration of CO_2 within the rim cavity approaches that of the coolant, indicating that less gas path flow is ingested into the cavity. Thus, the seal becomes "effectively sealed" and ϕ approaches the value of unity. Conversely, as the coolant flow rate is decreased, the cavity CO_2 concentration approaches that of the gas path, indicating that a large amount of the gas path fluid has been ingested into the seal cavity. The sealing effectiveness parameter approaches zero for this condition. Therefore, ϕ is expected to vary from zero for no coolant flow to a value of unity when the cavity is effectively sealed for some value of purge flow rate. Each rim seal model will have a different variation of cooling effectiveness parameter with coolant flow rate for a given disk speed, cavity, and seal gap geometry and gas path flow conditions.

Ingestion Experiments. The results of the rim seal ingestion experiments for Seals 1–4 are presented in Figs. 5(*a*–*d*). The results are presented as a plot of the sealing effectiveness parameter ϕ versus the nondimensional purge flow parameter η_p. The data were obtained at disk tangential Reynolds numbers of 2.6×10^6 and 5.1×10^6 and various levels of the simulated gas path swirl velocity, $V_{\phi\mathrm{gas}}$. The dimensionless gap width for seals 1, 3, and 4 was $S/R_o = 0.0048$ and for seal 2, $S/R_o = 0.0024$.

For seal 1, the results shown in Fig. 5(*a*) were obtained at $\mathrm{Re}_t = 5.1 \times 10^6$ and dimensionless gas path swirl levels of $V_{\phi\mathrm{gas}}/V_o = 1.0$ and 2.0. The results shown in Fig. 5(*a*) indicate that gas path swirl had little effect on the sealing characteristics of this seal model. Only a modest improvement in sealing effectiveness was observed when the swirl level was decreased from 2.0 to 1.0 $R_o\Omega$. Examination of the results for seals 2, 3, and 4 shown in Figs. 5(*b*), 5(*c*), and 5(*d*), respectively, also indicates that variations in the simulated gas path flow swirl velocity had little effect on the ingestion characteristics of these seal models.

The sealing effectiveness parameter for the four seals obtained at a given flow condition is presented in Figs. 6(*a*), 6(*b*), and 6(*c*). In Fig. 6(*a*), the sealing effectiveness of seals 1 and 3 is compared. The flow conditions for the data shown in Fig. 6(*a*) are $\mathrm{Re}_t = 5.1 \times 10^6$ and $V_{\phi\mathrm{Gas}} = 1.0\ R_o\Omega$. The results shown in Fig. 6(*a*) indicate that seal 1 and seal 3 have

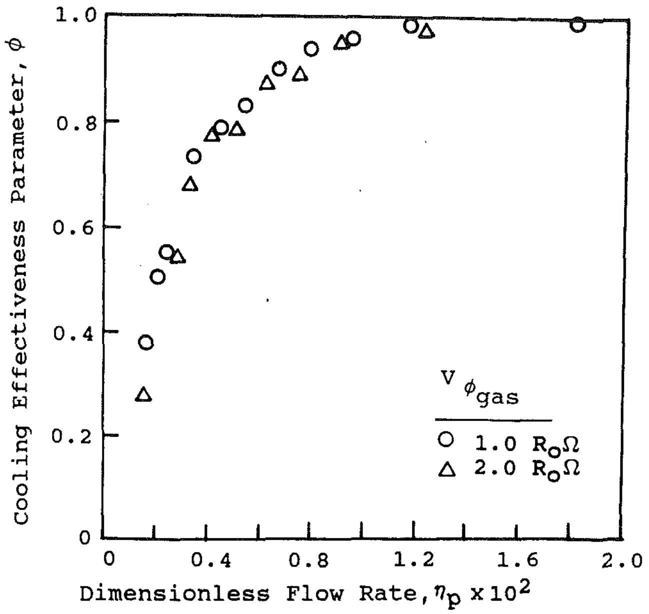

Fig. 5(*a*) Sealing effectiveness parameter for seal 1; Re_t = 5.1 × 10^6, S/R_o = 0.0048

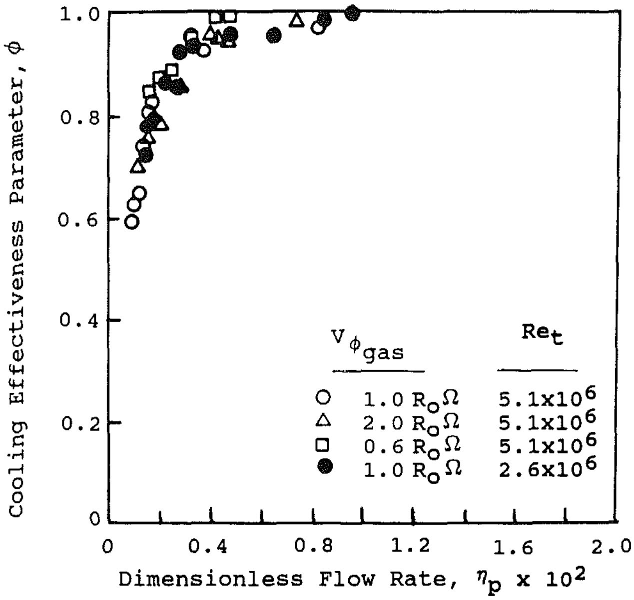

Fig. 5(*b*) Sealing effectiveness parameter for seal 2; S/R_o = 0.0024

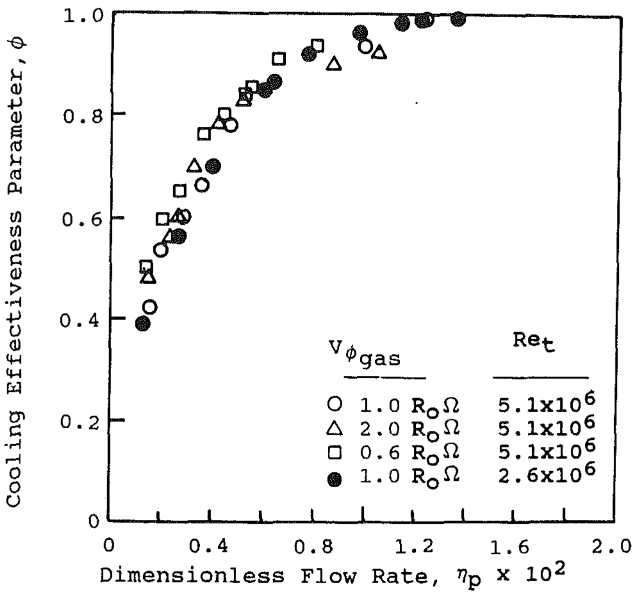

Fig. 5(*c*) Sealing effectiveness parameter for seal 3; S/R_o = 0.0048

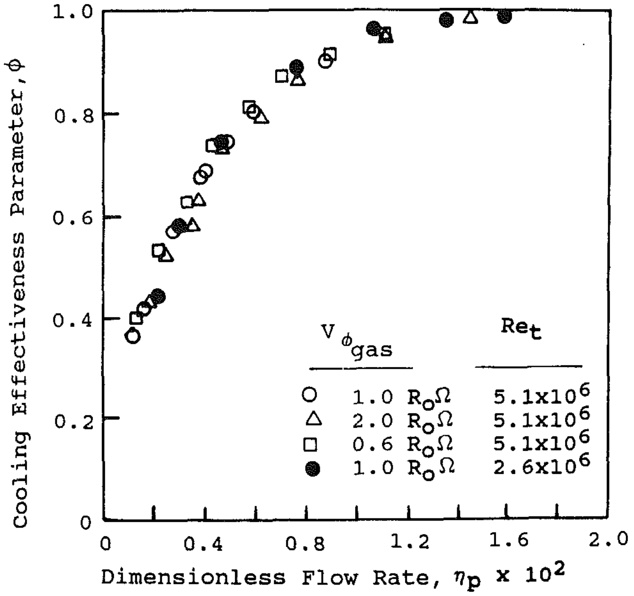

Fig. 5(*d*) Sealing effectiveness parameter for seal 4; S/R_o = 0.0048

similar sealing characteristics. This is somewhat surprising since seal 3 is of the radial overlap type where the boundary layer on the rotor is turned 90 deg by the rotating shroud and is pumped directly into the seal gap, whereas for seal 1, the seal gap is perpendicular to the pumped flow (see Fig. 4). It would be expected that the ingestion process and the turbulent mixing process of the boundary layer with the cavity core flow and the ingested flow for these two seals would be quite different, therefore leading to a difference in sealing characteristics. The similarity in sealing characteristics shown in Fig. 6(*a*) for seal 1 and seal 3 may be due to the influence of the rotating shroud, which is the same for both seals.

The results shown in Figs. 6(*b*) and 6(*c*) show the variations in sealing effectiveness of seal 3 with changes in the radial gap width (Fig. 6*b*) and with changes in the axial overlap (Fig. 6*c*). Comparison of results shown in Fig. 6(*b*) and 6(*c*) indicates that changes in the radial seal gap width have more influence on the sealing effectiveness of seals of type 3 than changes in the axial overlap. Decreasing the radial gap substantially increases the seal performance, as shown in Fig. 6(*b*). For a sealing effectiveness of $\phi = 0.9$, for example, Fig. 6(*b*) indicates that decreasing the radial seal gap by a factor of two reduces the flow required to seal the cavity to the same level by a factor of two also.

Aerodynamic Experiments. In addition to concentration measurements, pressure measurements were made at eight radial locations within the cavity. From the pressure measurements, the nondimensional tangential velocity distribution of the flow within the cavity was estimated. This was accomplished by integrating an approximate form of the radial momentum equation over small radial intervals in which the core rotation factor was assumed constant. Assuming small axial and radial velocities within the cavity, the radial momentum equation (in cylindrical coordinates) is reduced to $dp/dr = \rho\alpha^2\Omega^2 r$ where $\alpha(r)$ is the core rotation factor. The integration intervals over which α was assumed constant contained three pressure taps (one at each end point) and was approximately 0.75 in. (0.3 mm) in length. With dp/dr known, the core flow tangential velocity, $V = \alpha r\Omega$, was calculated.

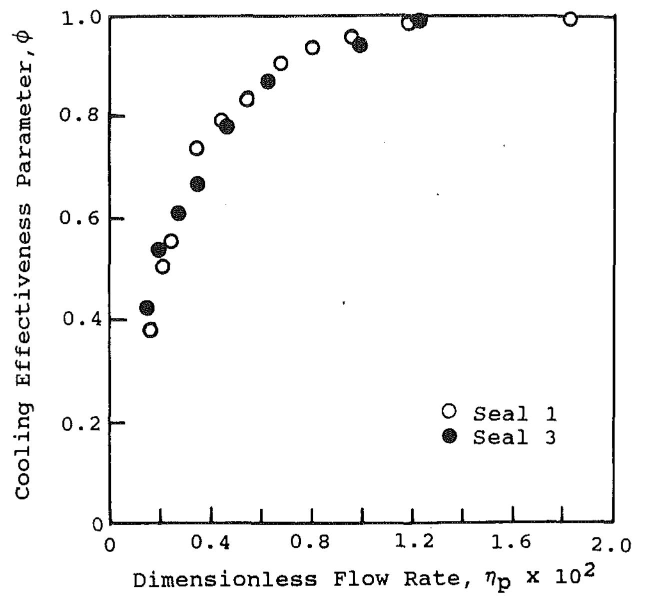

Fig. 6(*a*) Comparison of sealing effectiveness parameter for seal 1 and seal 3; $Re_t = 5.1 \times 10^6$, $S/R_o = 0.0048$, $V_{\phi gas} \approx 1.0\ R_o\Omega$

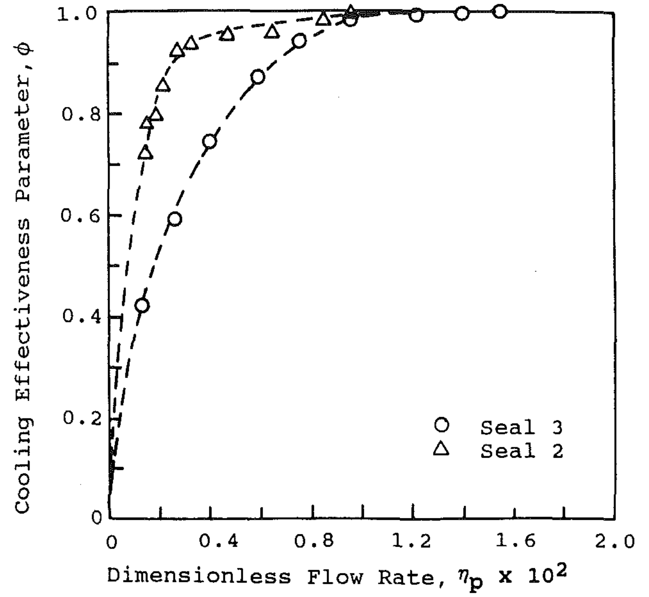

Fig. 6(*b*) Comparison of sealing effectiveness parameter for seal 3 and seal 2; $Re_t = 2.6 \times 10^6$, $V_{\phi gas} \approx 1.0\ R_o\Omega$.

Figure 7 presents results obtained for seal 1 and seal 3. The results are presented as the dimensionless tangential velocity ratio versus the dimensionless radius ratio. The data shown in Fig. 7 were obtained at a tangential Reynolds number of 5.1×10^6, $V_{\phi gas} = 1.0 R_o\Omega$, and various values of purge flow rate. The results shown in Fig. 7 indicate that the core rotation in the upper part of the cavity is greater for seal 1 than for seal 3. This is to be expected since the boundary layer for seal 3 is pumped into the seal gap, resulting in less cavity recirculation than that which would be expected for seal 1. For both seals, Fig. 7 indicates that decreasing the purge flow rate increases the cavity core tangential velocity. Note also that the similarity in sealing characteristics shown by the comparison of ingestion data in Fig. 6(*a*) for these two seals is not due to a similar cavity flow field as indicated in Fig. 7.

The variation in cavity core tangential velocity with variations in gas path swirl is shown in Fig. 8. The results presented in Fig. 8 are for seal 3 with $Re_t = 5.1 \times 10^6$ and the dimensionless purge flow parameter held constant at $\eta_p = 0.0062$. The results shown in Fig. 8 indicate that changes in the gas path swirl velocity had no significant effect on the cavity aerodynamic characteristics. This result is compatible with the finding that the gas path swirl had little effect on the observed cooling effectiveness for each of the seals investigated.

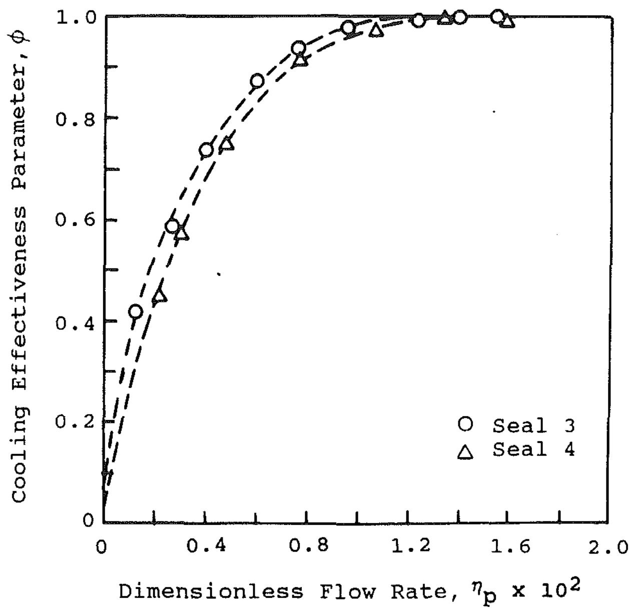

Fig. 6(*c*) Comparison of sealing effectiveness parameter for seal 3 and seal 4; $Re_t = 2.6 \times 10^6$, $V_{\phi gas} \approx 1.0\ R_o\Omega$

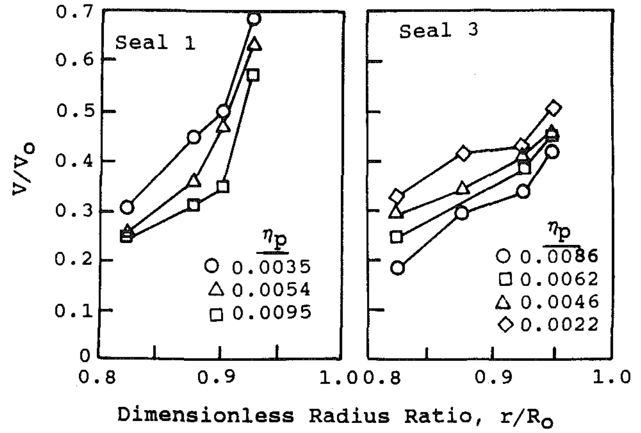

Fig. 7 Comparison of rim cavity tangential velocity profiles with coolant flow for seal 1 and seal 3; $Re_t = 5.1 \times 10^6$, $S/R_o = 0.0048$, $V_{\phi gas} \approx 1.0\ R_o\Omega$

Comparison of Results With Other Investigators

The subject of rim seal ingestion and rim seal design has received increasing attention over the last two decades. Bayley the top of the seal model. For this study, ingress data were experimentally investigate the fundamental fluid mechanics of rotor-stator systems with regard to the problem of ingress. In subsequent studies, Owen and Phadke (1980), Phadke (1982), Phadke and Owen (1983), Chew (1991), and Graber et al. (1987) have experimentally and analytically investigated rim seal ingestion characteristics for a number of seal geometries and flow conditions. Among the seals investigated by Phadke and Owen (1983) was one seal configuration ("E") with a radial overlap geometry similar to seal 3 in this investigation. The data obtained by Phadke and Owen (1983) for this seal configuration were obtained with no crossflow present across the top of the seal model. For this study, ingress data were

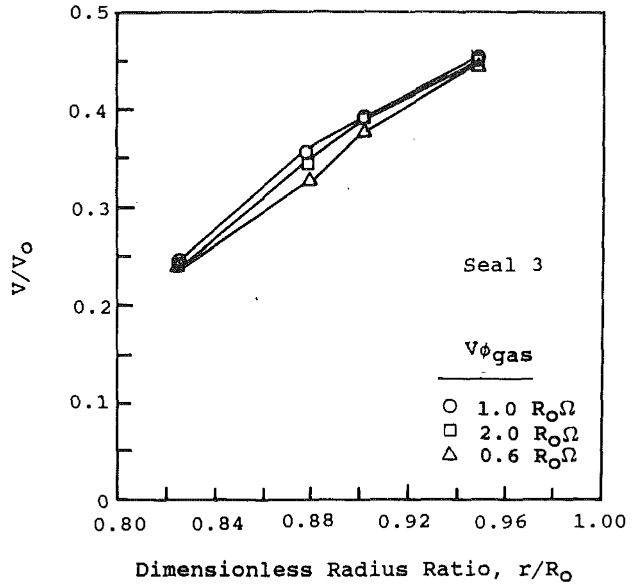

Fig. 8 Comparison of rim cavity tangential velocity ratio at different simulated gas path swirl levels; $\text{Re}_t = 5.1 \times 10^6$, $S/R_o = 0.0048$, $\eta_p = 0.0062$

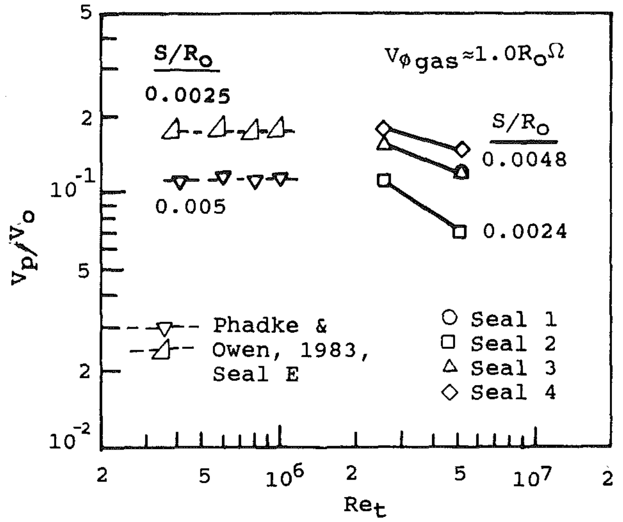

Fig. 9 Comparison of purge flow velocity ratio with results obtained by Phadke and Owen (1983)

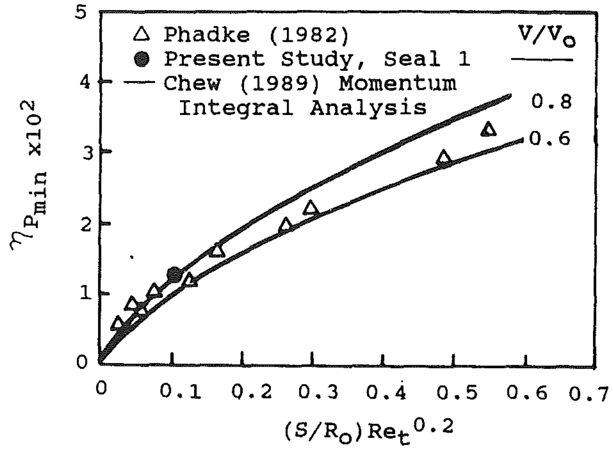

Fig. 10 Comparison of results for seal 1 from present study with those of Phadke (1982) and Chew (1991)

obtained from pressure measurements across the seal and by a flow visualization technique (smoke generator with laser illumination). For the present study, the purge flow velocity was estimated for $\phi = 0.99$, using data for lower values of ϕ and the analytical model delineated by Graber et al. (1987).

For a basis of comparison, a dimensionless purge velocity ratio is defined as V_p/V_o, where V_p is the area-averaged fluid velocity through a minimum gap area, $V_p = \dot{m}_p/(2\pi R_o S)$. Here, $\dot{m}_p$ is the purge flow rate required to just prevent ingestion. The results obtained by Phadke and Owen (1983) for this seal and those obtained in this investigation for all seals are presented in Fig. 9. The dimensionless gap ratios, S/R_o, for the seal similar to seal 3 that was investigated by Phadke and Owen (1983) were $S/R_o = 0.005$ and $S/R_o = 0.0025$. As Fig. 9 indicates, the results obtained in this investigation for seal 3 at $S/R_o = 0.0048$ are compatible with those obtained by Phadke and Owen (1983) for the $S/R_o = 0.005$ configuration. For the $S/R_o = 0.0025$ configuration, however, the results are not compatible with the $S/R_o = 0.0024$ results of this investigation. Chew (1991) has recently compared rim seal ingestion data obtained by several investigators and has speculated that Phadke (1982) may have erred in measuring S/R_o for this gap width. The apparent Reynolds number effect shown in Fig. 10 for the results of this investigation and the apparent lack of Reynolds number effect in the data of Phadke and Owen (1983) may be due to the crossflow across the seal that was present in this investigation and absent in the Phadke and Owen study. Dewey and Vick (1955) were able to show that the presence of a cross-stream affected the discharge coefficients of outlets discharging into the cross-stream. It is therefore reasonable to assume that since the cross-stream affects the exit loss of the seal, the sealing characteristics of the seal are also affected by the presence of a cross-stream.

Recently, Chew (1991) has developed a mathematical model of the flow within the cavity and seal for a rim seal configuration similar to seal 1 in this investigation. In this study, a momentum integral analysis was used to treat the flow within the rim seal cavity and the results were coupled to a simple model of the flow within the seal gap. The predicted results from this mathematical model were compared with experimental results obtained by a number of investigators for a variety of seal configurations. In most of the cases studied, agreement between predicted results and experimental results was achieved. One seal configuration from this study is comparable to seal 1 in this investigation. The experimental data that Chew (1991) used to compare with the analytical model developed were obtained by Phadke (1982).

The results obtained by Phadke (1982) and Chew (1991) for seals similar to seal 1 are presented in Fig. 10. Data obtained in this investigation are shown in Fig. 10 for comparison. The results are presented as η_{pmin} versus the parameter $(S/R_o)\text{Re}_t^{0.2}$. The parameter $(S/R_o)\text{Re}_t$ was employed by Bayley and Owen (1970) to scale the results of their ingestion studies with the dimensionless flow rate and was arrived at by a simple analysis of the core flow. The quantity η_{pmin} is the dimensionless purge flow rate required to just prevent ingestion. The results shown in Fig. 10 indicate that the analysis of Chew (1991), the data obtained by Phadke (1982), and the data obtained in this investigation for seal 1 are compatible. Note also in Fig. 10 that the experimental results obtained in this investigation are predicted by Chew (1991) for a dimensionless cavity core tangential velocity ratio of $V/V_o = 0.8$. The core tangential velocity profiles shown in Fig. 7 for seal 1 appear to approach this value at the higher radii.

Conclusions

An experimental investigation was conducted to determine the aerodynamic and sealing characteristics of several classes of seals typical of those found on the downstream side of a rotor in a gas turbine engine. A mass transfer analogy (use of a trace gas) was used to determine the sealing effectiveness of the seals investigated. This technique was shown to be an accurate means of determining rim seal ingestion characteristics.

The most significant results of this investigation have shown that:

(*a*) The purge flow rates required to prevent ingestion in the seals investigated and compatible with those obtained by other investigators.

(*b*) Seal ingestion characteristics are not significantly affected by changes in the swirl level of a cross-stream flow above the seal.

(*c*) For seals of the radial overlap type, decreasing the radial gap width produces significant improvement in seal effectiveness compared with the modest amount of improvement obtained by increasing the axial overlap of the seal.

Acknowledgments

This work was supported by the Aero Propulsion and Power Laboratory, Wright Research and Development Center and by United Technologies under their independent research program. The experiments were conducted under Contract F33615-83-C-2331 with the Government Products Division of Pratt & Whitney, United Technologies Corporation at the United Technologies Research Center.

References

Bayley, F. J., and Owen, J. M., 1970, "The Fluid Dynamics of a Shrouded Disk System With a Radial Outflow of Coolant," ASME *Journal of Engineering for Power*, Vol. 92, pp. 335–341.

Chew, J. W., 1991, "A Theoretical Study of Ingress for Shrouded Rotating Disk Systems With Radial Outflow," ASME JOURNAL OF TURBOMACHINERY, Vol. 113, pp. 91–97.

Denton, J. D., and Usui, S., 1981, "Use of a Tracer Gas Technique to Study Mixing in a Low Speed Turbine," ASME Paper No. 81-GT-86.

Dewey, P. E., and Vick, A. R., 1955, "An Investigation of the Discharge and Drag Characteristics of Auxiliary Air Outlets Discharging Into a Transonic Stream," NACA TN3466.

Eckert, E. R. G., and Goldstein, R. J., 1976, *Measurement Methods in Heat Transfer*, 2nd ed., Hemisphere Publishing Corp., Washington, DC.

Graber, D. J., Daniels, W. A., and Johnson, B. V., 1987, "Disk Pumping Test," Air Force Wright Aeronautical Laboratories Report AFWAL-TR-87-2050, pp. 2-12.

McGreehan, W. F., Haaser, F. G., and Sherwood, L. T., 1987, "Labyrinth Seal Flow Measurement by Tracer Gas Injection," ASME Paper No. 87-GT-187.

Owen, J. M., and Phadke, U. P., 1980, " An Investigation of Ingress for a Simple Shrouded Rotating Disk System With a Radial Outflow of Coolant," ASME Paper No. 80-GT-49.

Pederson, D. R., Eckert, E. R. G., and Goldstein, R. J., 1977, "Film Cooling With Large Density Differences Between the Mainstream and the Secondary Fluid Measured by the Heat-Mass Transfer Analogy," ASME *Journal of Heat Transfer*, Vol. 99.

Phadke, U. P., 1982, "Aerodynamic Aspects of the Sealing of Rotor-Stator Systems in Gas Turbines," D. Phil. Thesis, University of Sussex, United Kingdom.

Phadke, U. P., and Owen, J. M., 1983, "An Investigation of Ingress for an Air-Cooled Shrouded Rotating Disk System With Radial-Clearance Seals," ASME *Journal of Engineering for Power*, Vol. 105, pp. 178–183.

J. W. Chew
Rolls Royce plc,
Derby, United Kingdom

S. Dadkhah[1]

A. B. Turner

Thermo-Fluid Mechanics Research Centre,
School of Engineering and Applied Sciences,
University of Sussex,
Falmer, Brighton, BN1 9QT,
United Kingdom

Rim Sealing of Rotor-Stator Wheelspaces in the Absence of External Flow

Sealing of the cavity formed between a rotating disk and a stator in the absence of a forced external flow is considered. In these circumstances the pumping action of the rotating disk may draw fluid into the cavity through the rim seal. Minimum cavity throughflow rates required to prevent such ingress are estimated experimentally and from a mathematical model. The results are compared with other workers' measurements. Measurements for three different types of rim seal are reported for a range of seal clearances and for rotational Reynolds numbers up to 3×10^6. The mathematical model is found to correlate the experimental data reasonably well.

1 Introduction

In an earlier paper (Chew, 1991), a mathematical model was proposed for ingestion of external flow into the cavity formed between a rotating disk and a stationary shroud. Some encouraging agreement with the available experimental data was found, but several uncertainties remained owing to apparent inaccuracies in the available data. In the present contribution some new experimental data are presented and the mathematical model is re-examined.

Rim sealing has been investigated by several groups of workers in recent years and it is now generally accepted that the presence of an external flow, simulating the main gas path in an engine, can severely modify or dominate the sealing behavior. In particular, circumferential pressure asymmetries in the external flow are thought to be important. Nevertheless attention here is confined to "rotationally dominated" conditions in which ingress is driven by the pumping action of the rotating disk rather than pressure asymmetries in the external flow. This is a useful test case for modeling and, despite being a simplification of engine conditions, is a severe test of our understanding of the problem. It is also worth noting that there are engine configurations, such as the inner seal in a double-sealed arrangement, where a rotationally dominated model might be expected to apply.

Measurements were obtained from the experimental rig described in a companion paper (Dadkhah et al., 1992) and in more detail by Dadkhah (1989). The outer radius of the rotor in this rig is 200 mm. Apart from the region of the seal the rotor has a plane surface and faces a plane stator, spaced 20 mm axially from the rotor. Sealing flow entered the cavity through a central hole in the stator. The rig has the facility for external flow, with and without swirl, and the measurement techniques applied include static pressure tappings, gas concentrations, and total pressure probes. However, attention here is confined to the static pressure measurements for the case when there is no external flow. Three different seals were tested; a simple axial clearance seal and two radial seals. Details of these seals are given in Fig. 1.

For completeness a brief description of the mathematical model will be given in the next section. Experimental and theoretical results are then presented and compared in the following two sections. A further comparison of the model with the data of Daniels et al. (1992) is then given in section 5, before the conclusions from this study are summarized in section 6.

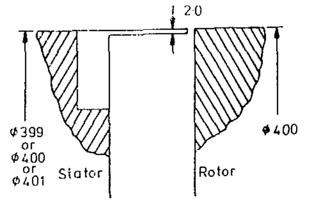

Simple axial clearance seal.

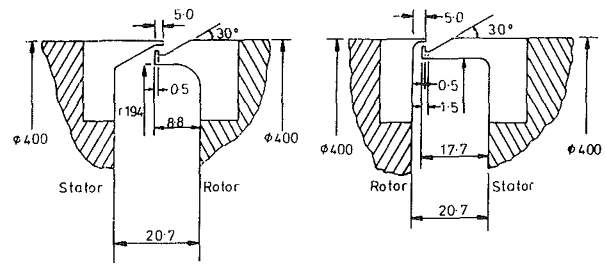

Radial clearance seal A

Radial clearance seal B

Fig. 1 Geometric details of the aerodynamic seals tested

---

[1] Present address: Edwards High Vacuum International, Shoreham, Sussex, United Kingdom.

Contributed by the International Gas Turbine Institute and presented at the 36th International Gas Turbine and Aeroengine Congress and Exposition, Orlando, Florida, June 3-6, 1991. Manuscript received at ASME Headquarters February 6, 1991. Paper No. 91-GT-33. Associate Editor: L. A. Riekert.

2 The Mathematical Model

The approach adopted is to couple a solution for the flow in the wheelspace to a model for the seal flow. A momentum-integral method was chosen to calculate the cavity flow because of its computational efficiency compared to numerical solutions of the governing partial differential equations. For further discussion of this model the reader is referred to Chew (1990, 1991). The main features of the model are described below.

2.1 The Cavity Flow. Separate turbulent boundary layers are assumed to form on the rotating and stationary disks and on the cylindrical outer shroud surface. In the inviscid region between the boundary layers a rotating core, in which the radial velocity component vanishes, forms in the outer part of the wheelspace. Inlet conditions affect the flow toward the center of the cavity, particularly in the inviscid region, but in the rotationally dominated case, the flow in the outer part of the cavity is insensitive to the inlet configuration.

The momentum-integral solution for the boundary layer on the rotating disk involves a direct extension of von Karman's (1921) method for the free disk, allowing for fluid rotation outside the boundary layer. A modified von Karman type treatment is applied on the stationary disk, with the radial momentum equation being dropped and a limiting flow angle at the wall being assumed. On the cylindrical surface a constant mass flow boundary layer and a constant friction factor governing the circumferential shear stress are assumed. The ordinary differential equations for the boundary layer flows are coupled through solutions for the inviscid flow regions. These are the free vortex relations in the source region, and the rotating core solution in which there is no radial motion and axial gradients are zero. The boundary between the source and the rotating core regions is taken as the radius at which all the supplied flow is entrained into the boundary layer on the rotor. Although the model does allow for the inclusion of a specified ingestion flow, this option is not used in the results given here.

Numerical methods are used to obtain solutions to the system of equations described above. For the essentially incompressible conditions considered here, the solution, written in a suitable nondimensional form, is a function of the nondimensional radius $x(=r/R_o)$, the aspect ratio of the cavity $G(=s/R_o)$, and a nondimensional throughflow coefficient λ. In terms of the rotational Reynolds number $\mathrm{Re}_\phi(=\rho\omega R_o^2/\mu)$ and the mass flow coefficient $C_W(=\dot{m}/\mu R_o)$, λ is defined as $\lambda = C_W/\mathrm{Re}_\phi^{0.8}$.

As described in earlier references, this model has been validated against moment coefficient data for rotor-stator systems. A comparison with core velocity measurements (Dadkhah et al., 1992) indicates that the model predicts core velocities somewhat lower than measurements. However, at low values of λ, the model agrees reasonably well with measurements.

2.2 The Seal Model. Consider first the case when the supplied throughflow is greater than the minimum rate required to prevent ingress to the cavity ($C_W > C_{W,\,\min}$). It may be argued from order of magnitude considerations that the effect of rotation on the pressure drop across the seal will be principally through changes induced in the radial and axial velocity distributions, rather than the pressure field directly associated with the centripetal force term. The fluid flowing out of the seal first picks up a radial velocity component as it is entrained into the boundary layer on the rotor. To quantify this effect a mixed-out radial velocity (u_{dm}) is calculated from the integral solution at the rotor outer radius. Assuming that the seal flow is supplied from the near wall region of this layer, u_{dm} is the velocity of a uniform stream that would have the same radial momentum as the flow approaching the seal. It is then postulated (by analogy with pipe orifice flow) that the pressure drop across the seal may be represented by the equation

$$\Delta p = \frac{1}{C_d^2}\frac{\rho}{2}\,(u_m^2 - k^2 u_{dm}^2) \tag{1}$$

where C_d is a discharge coefficient, u_m is the mean velocity in the r-z plane through the seal, and k is a constant, the value of which depends on the seal type and is determined by matching to experimental results.

Assuming that the cavity is just sealed when $\Delta p = 0$, it follows from Eq. (1) that this occurs when $u_m = k u_{dm}$. Calculating u_m from the seal clearances $s_c(=G_c R_o)$ and the throughflow rate $\dot{m}$, and rearranging gives

$$C_{w,\,min} = 2\pi k\left(\frac{u_{dm}}{\omega R_o}\right) G_c \mathrm{Re}_\phi \tag{2}$$

For a given cavity geometry $(u_{dm}/\omega R_o)$ will be a function of λ only. It is interesting to note that, for the axial seal in Fig. 1, k would be expected to be of order unity (from analogy with pipe orifice flow) and $(u_{dm}/\omega R_o)$ is expected to be of order 0.1 (from von Karman's free disk solution). Putting these figures in Eq. (2) gives $C_{w,\,\min} = 0.628\, G_c\mathrm{Re}_\phi$. This is close to Bayley and Owen's (1970) empirical correlation for the minimum sealing flow for this configuration, which gives $C_{w,\,min} = 0.61\, G_c\mathrm{Re}_\phi$.

In terms of the throughflow parameter λ, Eq. (2) gives

$$\lambda_{\min} = 2\pi k\left(\frac{u_{dm}}{\omega R_o}\right)(G_c\mathrm{Re}_\phi^{0.2}) \tag{3}$$

Since $(u_{dm}/\omega R_o)$ depends only on λ, it follows that for a given cavity geometry and seal type $\lambda_{\min}$ will be a function of $(G_c\mathrm{Re}_\phi^{0.2})$ only.

In the experimental work it was impractical to measure the cavity pressure at the outer radial position $x = 1$ for all seals. For consistency across all seal types the estimates of the pressure differences across the seal were based on the cavity pressure at $x = 0.95$. It will be of interest to compare the minimum

Nomenclature

C_d = discharge coefficient
C_w = $\dot{m}/\mu R_o$ = mass flow parameter
G = s/R_o = cavity aspect ratio
G_C = s_c/R_o = seal clearance ratio
k = empirical constant in seal model
$\dot{m}$ = coolant mass flow rate
$\dot{m}_{in}$ = ingress mass flow rate
r = radial coordinate
R_o = outer radius of disk
Re_ϕ = $\rho\omega R_o^2/\mu$ = rotational Reynolds number
s = axial gap between rotor and stator
s_c = seal clearance
u_{dm} = mixed out radial velocity for near-wall flow on the rotating disk at $x = 1$
u_m = mean velocity through the seal in r-z plane
x = r/R_o = nondimensional radius
z = axial coordinate
Δp = pressure difference across seal
Δp_c = pressure difference in cavity from $x = 0.95$ to $x = 1$
λ = $C_W/\mathrm{Re}_\phi^{0.8}$ = throughflow parameter
μ = fluid viscosity
ρ = fluid density
ϕ = $\dot{m}/(\dot{m}+\dot{m}_{in})$ = cooling effectiveness
ω = angular speed of rotor

Subscripts

min = minimum value to seal cavity

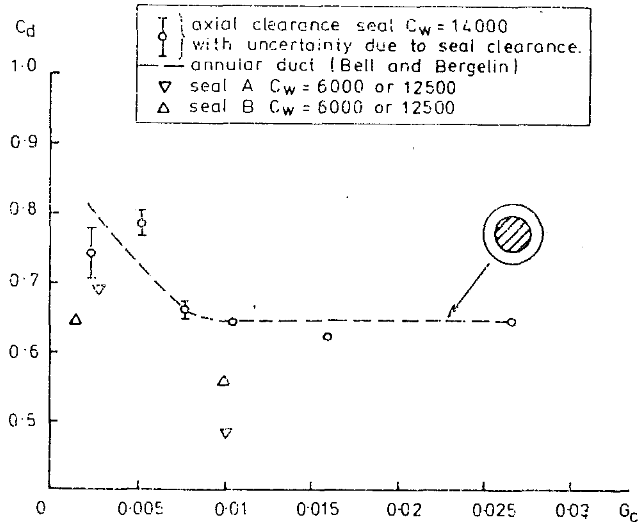

Fig. 2 Discharge coefficients for the three seals: $\mathrm{Re}_\phi = 0$

sealing flows given by the model using the pressure at $x = 0.95$ with those obtained from Eq. (3), and with those estimated from the measurements. Denoting the pressure rise in the cavity between $x = 0.95$ and $x = 1$ as Δp_c, it follows from Eq. (1) that estimating the minimum sealing flow from the pressure at $x = 0.95$ gives

$$\lambda_{\min} = 2\pi G_c \mathrm{Re}_\phi^{0.2}\left[k^2\frac{u_{dm}^2}{\omega^2 R_o^2} + C_d^2\,\frac{2\Delta p_c}{\rho\omega^2 R_o^2}\right]^{0.5} \qquad (4)$$

As expected, for small Δp_c this equation approximates to Eq. (3). Equation (4) again indicates that for a particular configuration $\lambda_{\min}$ will be a function of $G_c\mathrm{Re}_\phi^{0.2}$ only.

When λ is less than $\lambda_{\min}$, ingress occurs. A useful measure of the ingress level is the sealing effectiveness Φ defined as $\dot{m}/(\dot{m}+\dot{m}_{im})$ where $\dot{m}_{in}$ is the ingress mass flow rate. Based on estimates of Φ from concentration measurements, Graber et al. (1987) suggested the exponential formula $\Phi = 1 - e^{-\alpha\lambda}$, where α is a constant for a particular seal clearance. Experimental data from the present rig support this relationship (see Dadkhah et al., 1992). An alternative curve fit to the measured values of Φ is obtained by assuming that the ingress flow rate is 20 percent of $(\lambda_{\min} - \lambda)$. This gives

$$\Phi = \frac{\lambda}{(0.8\lambda + 0.2\lambda_{\min})} \qquad (5)$$

It may be shown that if $\lambda_{\min}$ is taken as the value of λ for which the exponential relationship gives $\Phi = 0.98$, then the maximum difference in Φ given by the two formulae is 0.035 and this is within the scatter of the data used for the curve fit. In the present model of ingress Eq. (5) is used with $\lambda_{\min}$ estimated from Eq. (3) above.

3 The Axial Clearance Seal

This seal has previously been studied experimentally by Bayley and Owen (1970), Owen and Phadke (1980), and Phadke and Owen (1983a, 1983b). As in the present study the minimum sealing flow has been estimated from pressure measurements. Bayley and Owen, and Owen and Phadke used pressure tappings on the cylindrical shroud (at $x=1$) in estimating Δp. Phadke and Owen used tappings on the stator at $x = 0.975$. In the present study a pressure tapping at $x = 0.95$ was used. All workers have assumed that the cavity is just sealed when $\Delta p = 0$. Use of this criterion is supported by comparison with flow visualization in the papers by Owen and Phadke and by comparison with concentration measurements by Phadke and Owen (1983b).

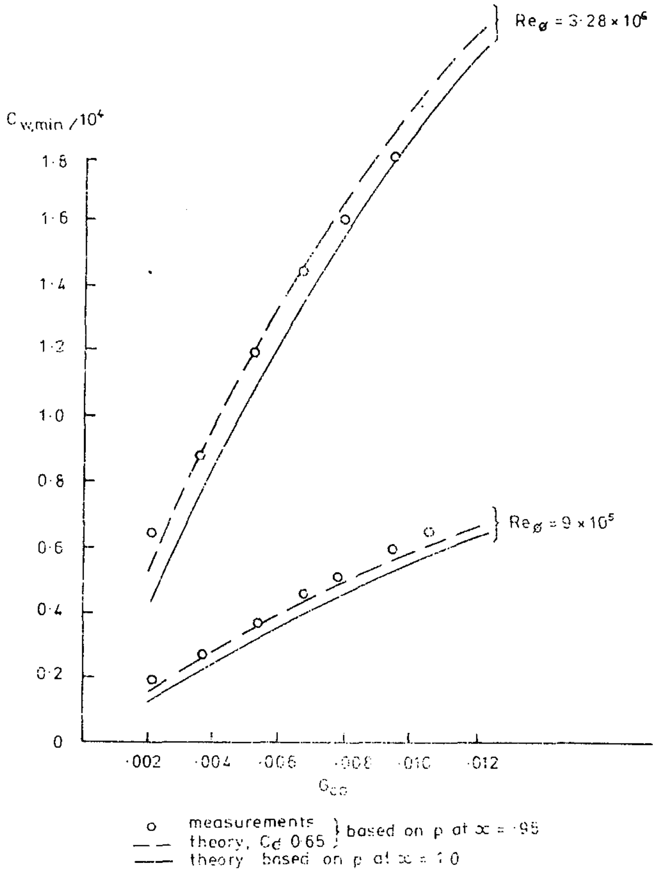

Fig. 3 Minimum sealing flows for the simple axial seal

Before considering the effects of rotation, it is useful to examine the seal behavior for $\mathrm{Re}_\phi = 0$. Figure 2 shows discharge coefficients calculated from the measured pressure drop across the seal at different seal clearances. The error bands on these data show the sensitivity to an error of 0.0254 mm (0.001 in.) in the seal clearance; this was considered to be representative of the uncertainty in these experiments (Dadkhah, 1989). As might be expected, the discharge coefficients for this seal agree fairly well with those for the annular orifice between a circular disk and cylindrical tube. Annular orifice results were obtained from Bell and Bergelin's (1957) correlation and are shown as a line on the figure. The present results confirm difficulties with the Phadke and Owen data, which differ widely from Bell and Bergelin's results at smaller clearances (see Chew, 1991).

A comparison of predicted and measured minimum sealing flows is shown in Fig. 3. Results are shown for two values of Re_ϕ, 9×10^5 and 3.28×10^6, representing the extremes of the experimental range. The constant k in the model was set to 0.8 for this seal. This value was found in earlier studies to give reasonable agreement with Phadke and Owen's data at higher values of G_c and good agreement with Bayley and Owen's data at lower values of G_c. Apart from the lowest seal clearance considered ($G_c = 0.002$), the measurements and the theory based on the cavity pressure at $x = 0.95$ agree to within a few percent. At $G_c = 0.002$ the discrepancy is of order 20 percent. This may partly be explained by the fact that $C_d = 0.65$ in this calculation, which somewhat underestimates the discharge coefficient at the smaller clearance ratios. It may be seen from Eq. (4) that increasing C_d will lead to a higher prediction of $C_{w,\min}$. The difference between the predictions based on pressure at $x = 0.95$ and that at $x = 1$ is proportionally higher at lower values of G_c. This is to be expected as $\lambda_{\min}$ is reduced at low clearances and the nondimensional pressure differential

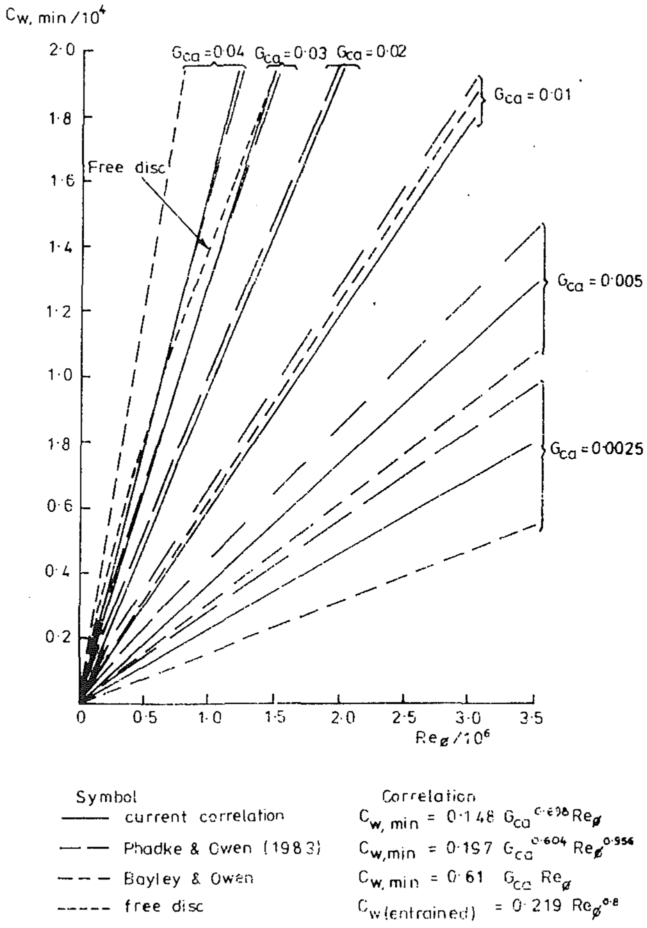

Fig. 4 A comparison of various correlations of $C_{w,\min}$ with Re_ϕ and G_{ca} for the simple axial clearance seal

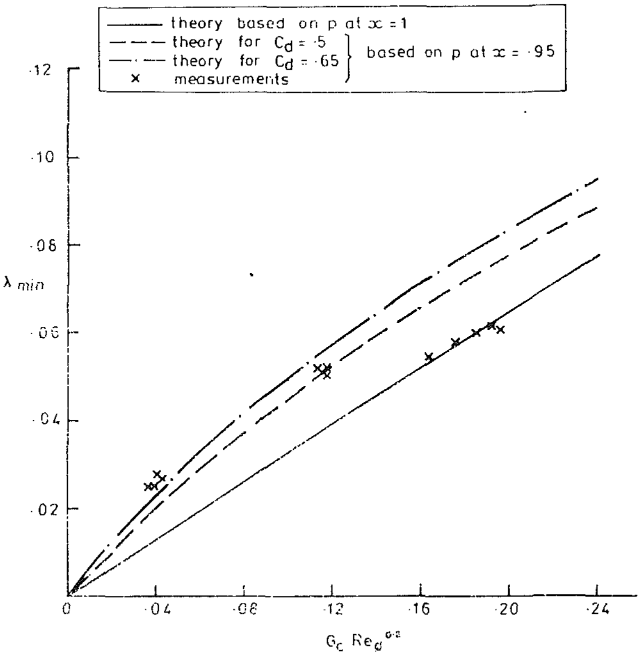

Fig. 5 Minimum sealing flow for seal A

in the cavity $(2\Delta p_c/\rho\omega^2R_o^2)$ will be higher due to increased fluid rotation.

Figure 4 gives a comparison of various correlations for $C_{w,\,\min}$, all of which are based on measurements using the differential pressure criterion for incipient ingestion. Von Karman's (1921) solution for free disk entrainment is also included, as this gives a guide to the expected level of $C_{w,\,\min}$ at high values of G_c. The correlation of the present data was obtained assuming a relation of the form $C_{w,\,\min} \alpha\; G_c^a\mathrm{Re}_\phi$; a good fit to experimental data was found. Bayley and Owen's correlation was based on data for G_c = 0.0033 and 0.0067; the discrepancies of this correlation with the present results and those of Phadke and Owen at G_c = 0.04 is not surprising. For $G_c \geq 0.01$ the present results agree well with those of Phadke and Owen and for G_c = 0.01 these also agree with Bayley and Owen's correlation. There are significant discrepancies between the three correlations at lower values of G_c. At G_c = 0.0025 Phadke and Owen's result is 80 percent higher than that of Bayley and Owen, with the present correlation falling between the two. Considering that the present results are expected to give high values of $C_{w,\min}$ owing to the use of the pressure measurement at x = 0.95, and that the accuracy of the clearance setting in Phadke and Owen's experiments is questionable, Bayley and Owen's correlation should perhaps be preferred at this gap ratio. Overall this comparison supports the use of the present model, which agrees with Bayley and Owen's result at small clearances and with Phadke and Owen's results at larger clearances.

4 Two Radial Clearance Seals

The two radial clearance seals considered are shown in Fig. 1. Seal A has a lip (width 0.5 mm) on the rotor that is overlapped by the stator. With this arrangement the flow pumped outward in the rotor boundary layer will impinge on the stator and be turned before passing through the seal. Seal B has a similar lip on the stator, which is overlapped by the rotor. In this case the shape of the rotor will tend to direct the pumped flow into the seal. As for the axial clearance seal, estimates of the minimum sealing flow were obtained from the differential pressure criterion, using the pressure measurement from an internal tapping at x = 0.95 in the stator and external tappings in the stator shroud some distance away from the seal.

Discharge coefficients for these seals for nonrotating conditions are shown in Fig. 2. These are somewhat lower than the values for the axial clearance seal. This may be due to the small length-to-clearance ratio and the slightly more tortuous path afforded to the air with these seals. Note also that for seal A with G_c = 0.01 the clearance between the tapered surface of the shroud and the corner of the lip is approaching the radial seal clearance. This may account for the surprisingly low discharge coefficient (0.48) in this case.

Experimental and theoretical results for the minimum sealing flow with seal A are shown in Fig. 5. In the model k has been set to 0.4. This value approximately correlates Phadke and Owen's (1983a, 1983b) large clearance results for a simple radial seal in which the stator shroud overlaps the rotor (see Fig. 7(v)). For the predictions based on pressure at x = 0.95 values of C_d of 0.5 and 0.65 have been used. It is apparent that for this seal, which performs somewhat better than the axial clearance seal, the predicted minimum sealing flows are more sensitive to the choice of pressure used in estimating Δp. At the lower value of G_c considered ($\approx$ 0.002) this effect gives almost a 100 percent increase in $\lambda_{\min}$ when the pressure at x = 0.95 is used as opposed to the pressure at x = 1.0. As for the axial clearance seal, the model appears to underpredict the minimum sealing flow at the small clearance ratio, but the measurements for $G_c \simeq 0.006$ (grouped around $G_c\mathrm{Re}_\phi^{0.2} \simeq 0.11$) are in good agreement with the theory. For $G_c \simeq 0.01$, the theory overestimates the minimum sealing flow by about 20 percent. This departure may be related to the rather low discharge coefficient observed in Fig. 2 and discussed above. Obviously some caution is advisable in interpreting these results as the assumptions underlying the model are subject to some

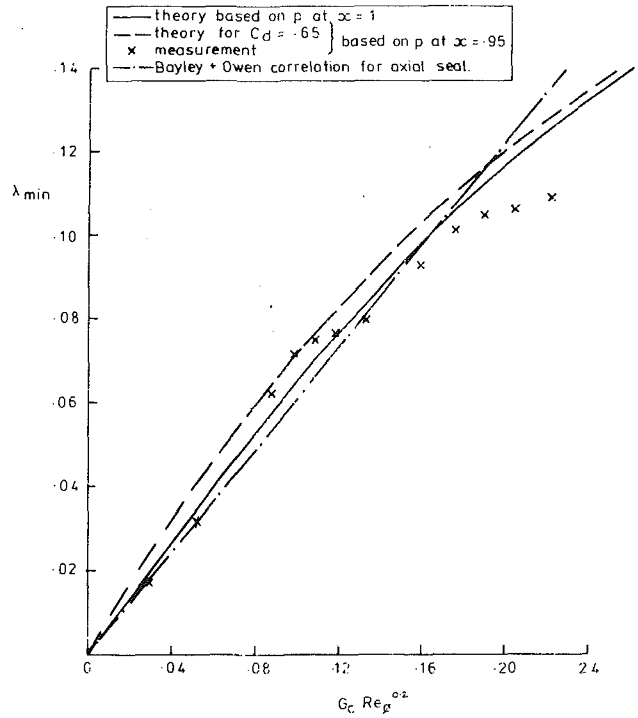

Fig. 6 Minimum sealing flow for seal B

uncertainty. However, this comparison does give further support for the validity of the present analysis in situations where the seal geometry is relatively simple.

Minimum sealing flows for Seal B are shown in Fig. 6. The performance of this seal is similar to that of the axial clearance seal and so a value of $k = 0.8$ has been used in the model. The experimental results in this figure are for nominal values of G_c of 0.002, 0.006, and 0.01. Bayley and Owen's (1970) correlation for the axial clearance seal is also shown on this graph. Agreement between theory and experiment is considered satisfactory, although there is some notable scatter. Note that in the model, the value for C_d of 0.65 is possibly rather high, thus overestimating λ_m based on the pressure at $x = 0.95$.

5 Other Seal Geometries and Rates of Ingestion

The various seal geometries that have been considered with the present mathematical model are illustrated in Fig. 7. Values of the model constant k, associated with each seal, are also given in the figure. Cases (*i*), (*ii*), and (*vi*) are the seals considered above. Seals (*iii*) and (*v*) were discussed by Chew (1991) and seal (*iv*) has been shown by Daniels et al. (1992) to perform similarly to seal (*iii*). Owing to uncertainties and incompleteness in the experimental data available, the model cannot be said to have been completely validated for all these seals, but it does offer a reasonable method of estimating the performance of the seals.

The model constant k provides a measure of the seal performance. Poor seal types have high values of k and good seal types have low values. Examining the seal geometries in Fig. 7 and considering the likely flow paths some explanations for the behavior of the various seals is possible. It should be remembered that fluid will be pumped radially outward in the boundary layer on the rotor, and that this fluid has a relatively high angular velocity and so will tend to centrifuge outwards. For seal (*i*) the pumped flow feeds directly into the seal, resulting in relatively poor seal performance; this is also the case for seal (*ii*). With seals (*iii*) and (*iv*) the disk pumping flow must turn and cross the cavity before reaching the seal; this introduces some extra resistance to the pumped flow and results in an improvement in seal performance. It might be thought

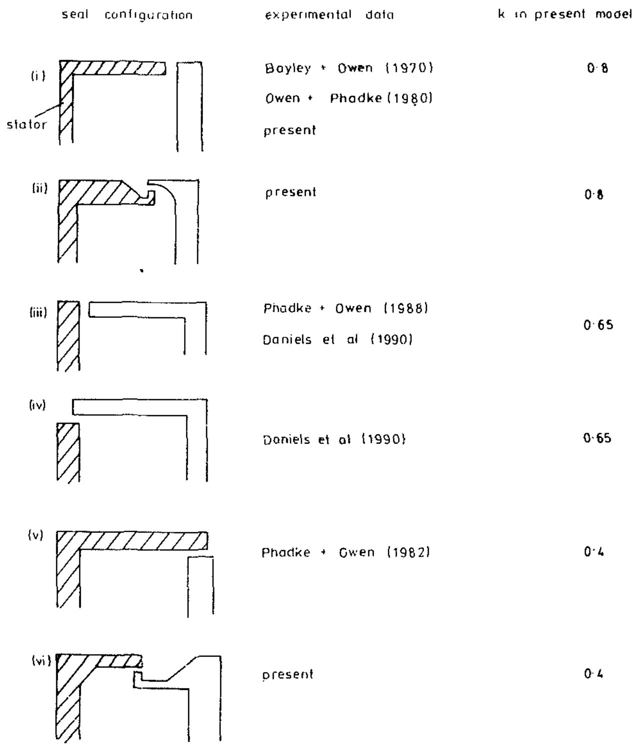

Fig. 7 Model coefficient *k* for various seals

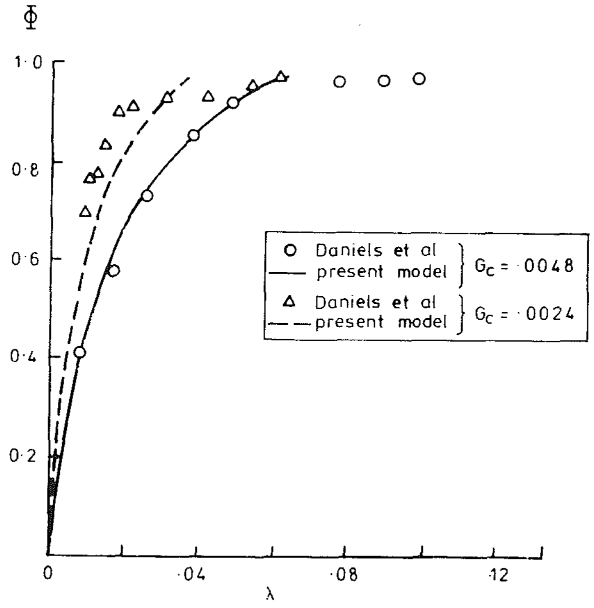

Fig. 8 Sealing effectiveness for seal (*iv*) in Fig. 7

that for seal (*iii*) the pumped flow must impinge on the stator and be turned again before reaching the seal. However, owing to the centrifuging effect, there will be little resistance to this additional turn. In the two best seals, (*v*) and (*vi*), the pumped flow will impinge on the stator and must turn sharply before entering the seal.

Equation (5) for the sealing effectiveness can only be regarded as a guide to the rate of ingestion when the supplied flow is less than the minimum sealing flow. Because mixing of the ingested and supplied flow within the cavity will not be complete, experimental estimates of Φ from concentration measurements will depend somewhat on the choice of sampling positions. Prediction of the distribution of the ingested gas within the cavity is beyond the capabilities of the current model. Nevertheless this model may be useful in supplying quick estimates of the sealing effectiveness for engineering calculations. Application of the method to seal type (*iv*) in Fig. 7 and comparison with the Daniels et al. measurements of sealing effectiveness is shown in Fig. 8. (It is reasonable to apply the rotationally dominated theory to this case as the axial velocity of the external flow in those experiments was small.) Estimates of $\lambda_{\min}$ were obtained from the above model (with $k = 0.65$) and Eq. (5) was then used to calculate Φ. For $G_c = 0.0048$ the agreement of the model with experiment is very good. For $G_c = 0.0024$ the agreement is not so good but, in view of the uncertainty level due to sampling position and other factors, the model may be considered to give a reasonable estimate of Φ.

6 Conclusions

Experimental measurements of the minimum throughflow rate required to prevent ingestion into a shrouded disk system have been presented for three different types of seal. These results were compared with predictions from a mathematical model and with other workers' measurements. A differential pressure criterion has been used to detect incipient ingress; this assumes that the cavity is just sealed when the pressure differences across the seal is zero. Analysis showed that for small seal clearances this criterion is sensitive to the position of the cavity pressure measurement owing to the centripetal pressure gradient in the cavity. When this effect was taken into account reasonable agreement between the mathematical model and the measurements was found.

Axial clearance seal results were compared with earlier correlations of measurements by Bayley and Owen (1970) and Phadke and Owen (1983b). All three correlations agree at a gap ratio (G_c) of 0.01. At higher values of G_c, which are outside Bayley and Owen's experimental range, the present results agree with those of Phadke and Owen. At lower values of G_c the three correlations diverge. Differences between the present correlation and that of Bayley and Owen can largely be explained by the effect of pressure measurement position mentioned above. Differences with Phadke and Owen's results seem to confirm inaccuracies in their experiments at small seal clearances.

Two radial clearance seals were tested. Seal A, with a lip on the rotor and an overlapping stator, was the most effective. For this seal the effect of pressure measurement position was relatively larger and so the results were less conclusive. Nevertheless some encouraging agreement with the mathematical model was found. The performance of Seal B, with a lip on the stator and overlapping rotor, was similar to the axial clearance seal and, again, reasonable agreement with the mathematical model was found.

While the rather elementary nature and limitations of the present model must be acknowledged, it does apparently correlate the available data for a number of different seals and it is to be preferred to earlier empirical correlations. Together with the assumption that for $C_W < C_{w,\min}$ the ingress rate is 20 percent of $(C_{w,\min} - C_w)$, the model can be used to obtain a first estimate of the sealing effectiveness. This relation has been shown to give a reasonable fit to Daniels et al.'s (1992) estimates of sealing effectiveness based on concentration measurements. Clearly much uncertainty remains and further development of the model is needed to account for the influence of external flow.

In this continuing research program, further experimental, modeling, and computational fluid dynamics studies are planned.

Acknowledgments

The authors gratefully acknowledge that the research work reported in this paper was funded jointly by Rolls-Royce plc, Ruston Gas Turbines Ltd., and the SERC.

References

Bayley, F. J., and Owen, J. M., 1970, "The Fluid Dynamics of a Shrouded Disk System With a Radial Outflow of Coolant," ASME *Journal of Engineering for Power*, Vol. 92, pp. 335-341.

Bell, K. J., and Bergelin, O. P., 1957, "Flow Through Annular Orifices," *Trans. ASME*, Vol. 79, pp. 593-601.

Chew, J. W., 1990, "Prediction of Rotating Disc Flow and Heat Transfer in Gas Turbine Engines," *Proc. 3rd Int. Symp. on Transport Phenomena and Dynamics of Rotating Machinery*.

Chew, J. W., 1991, "A Theoretical Study of Ingress for Shrouded Rotating Disk Systems With Radial Outflow," ASME JOURNAL OF TURBOMACHINERY, Vol. 113, pp. 91-97.

Dadkhah, S., 1989, "Ingestion and Sealing Performance of Rim Seals in Rotor-Stator Wheelspaces," D.Phil. thesis, University of Sussex, United Kingdom.

Dadkhah, S., Turner, A. B., and Chew, J. W., 1992, "Performance of Radial Clearance Rim Seals in Upstream and Downstream Rotor-Stator Wheelspaces," ASME JOURNAL OF TURBOMACHINERY, Vol. 114, this issue, pp. 439-445.

Daniels, W. A., Graber, D. J., Martin, R. J., and Johnson, B. V., 1992, "Rim Seal Experiments and Analysis for Turbine Applications," ASME JOURNAL OF TURBOMACHINERY, Vol. 114, this issue, pp. 426-432.

Graber, D. J., Daniels, W. A., and Johnson, B. V., 1987, "Disc Pumping Test," Report AFWAL-TR-87-2050, Wright-Patterson Air Force Base, OH.

Karman, T. von, 1921, "Uber Laminare und Turbulent Reibung," *Z. Angew. Math. Mech.*, Vol. 1, pp. 204-209.

Owen, J. M., and Phadke, U. P., 1980, "An Investigation of Ingress for a Simple Shrouded Rotating Disc System With a Radial Outflow of Coolant," ASME Paper No. 80-GT-49.

Phadke, U. P., and Owen, J. M., 1983a, "An Investigation of Ingress for an 'Air-Cooled' Shrouded Rotating Disk System With Radial-Clearance Seals," ASME *Journal of Engineering for Power*, Vol. 105, pp. 178-183.

Phadke, U. P., and Owen, J. M., 1983b, "The Effect of Geometry on the Performance of "Air-Cooled" Rotor Stator Seals," presented at the 15th CIMAC Congress, Paris.

Phadke, U. P., and Owen, J. M., 1988, "Aerodynamic Aspects of the Sealing of Gas-Turbine Rotor-Stator Systems, Parts 1-3," *Int. J. Heat and Fluid Flow*, Vol. 9, pp. 98-117.

Performance of Radial Clearance Rim Seals in Upstream and Downstream Rotor-Stator Wheelspaces

S. Dadkhah[1]

A. B. Turner

Thermo-Fluid Mechanics Research Centre,
School of Engineering and Applied Sciences,
University of Sussex, Brighton, BN1 9QT,
United Kingdom

J. W. Chew

Rolls Royce plc,
Derby, United Kingdom

A new experimental facility for the investigation of rim sealing is described and measurements are presented for two representative radial clearance seals with a nominally axisymmetric external flow. One radial seal has an upward rotor lip and is upstream of the rotor, while the other has an upward stator lip and is downstream of the rotor. Measurements include surface pressures, tangential velocities in the core region of the disk cavity flow, and traverses of gas concentration in the cavity showing the distribution of mainstream ingestion. Tests were conducted at rotational Reynolds numbers up to 3×10^6 with nominal seal clearance to radius ratios in the range 0.002 to 0.01. For the radial seals a differential pressure criterion is found to overestimate the minimum sealing flow. Tangential velocity measurements in the wheelspace are in excellent agreement with other workers' measurements and with theoretical predictions.

1 Introduction

In modern gas turbines the turbine rotor–stator wheelspaces are fed with a dual purpose supply of air bled from the compressor. This supply cools the disks and, by flowing through a tight clearance rim seal, suppresses the ingestion of hot mainstream gas. Turbine entry temperatures are such that increasingly large quantities of air have to be extracted from the compressor inflicting a substantial penalty on thrust and s.f.c.

The use of the economical minimum of sealing flow is necessary if the thermodynamic advantages of increasing the T.E.T. are not to be lost. This has been recognized for many years; see, for example, Moore (1975), Campbell (1978), and Suo (1978). Current interest is centered not only on developing high-efficiency rim seals but also on determining the effect of supplying less than the minimum flow necessary to seal the wheelspace completely. It has been found that particularly for the cooler downstream stages some mainstream ingestion can be tolerated and that quite small coolant flows can keep the rotor and stator temperatures within acceptable limits. For design purposes, for each type of rim seal under consideration, information is required not only on the actual mass flow rate of ingress over a wide range of coolant supply rates, but also on its subsequent distribution throughout the wheelspace, which influences the heat transfer to the rotor, a critically stressed component.

Recent work agrees that a small reduction of the coolant flow below the minimum sealing flow rate does not suddenly produce massive ingestion and a consequent sharp increase in the temperature level in the wheelspace; see, e.g., Dadkhah and Turner (1986), Graber et al. (1987), and Haaser et al. (1988). The process is a gradual one with the ingested mass flow rate slowly increasing as the coolant flow is progressively reduced.

Initially, work on this topic concentrated on plane rotors and stators, often with simple axial clearance seals, operating in a quiescent environment. Bayley and Owen (1970) studied such a system with coolant admitted centrally through the stator and suggested that the minimum dimensionless coolant flow rate $C_{w,\min}$ ($= \dot{m}/\mu R_o$) was directly proportional to the product of rotational Reynolds number Re_ϕ and the dimensionless axial rim seal clearance G_{ca}:

$$C_{w,\min} \propto G_{ca} \mathrm{Re}_\phi$$

Phadke and Owen (1983) compared a variety of radial clearance rim seals; a linear relationship was again found to exist between the minimum sealing flow, $C_{w,\min}$, and the rotational Reynolds number.

Abe et al. (1979) reported experimental measurements of pressure, temperature, velocity, and propane concentration within model gas turbine wheelspaces, both upstream and downstream. They tested seven types of seal, six of which were of the radial clearance type, with a variable swirl external flow of air induced over the rims. Rotor blades were not used. Estimates were made of the mass flow rate of mainstream air ingested and they found that ingestion was affected principally by the ratio of the coolant velocity through the seal to the mainstream velocity over it, the rim seal clearance, and the shape of the shroud and disk at the seal. These workers also

---

[1] Present address: Ruston Gas Turbines Ltd., Lincoln, United Kingdom.

Contributed by the International Gas Turbine Institute and presented at the 36th International Gas Turbine and Aeroengine Congress and Exposition, Orlando, Florida, June 3–6, 1991. Manuscript received at ASME Headquarters February 6, 1991. Paper No. 91-GT-32. Associate Editor: L. A. Riekert.

showed that the disk rotational Reynolds number had no effect on the ingested flow rate up to $\mathrm{Re}_\phi = 1 \times 10^6$ and that the ingested mass flow/coolant flow ratio decreased approximately exponentially with increasing coolant flow rate. The best seal, a radial clearance one with a rotor lip with a secondary chamber under the stator shroud, showed approximately a twentyfold reduction in ingestion over the simple axial clearance type.

Kobayashi et al. (1984), testing a similar system to that of Abe et al., again without turbine rotor blades but with a hot external flow and radial clearance rim seals, obtained conflicting results in that by using a zero pressure difference across the stator shroud as a sealing criterion, a linear relationship between $C_{w,\min}$ and Re_ϕ resulted, but by using wheelspace temperature fluctuations as a criterion $C_{w,\min}$ was independent of rotational speed, and generally much larger.

Phadke and Owen (1988a, 1988b, 1988c), in a comprehensive series of experiments, showed that increasing circumferential pressure asymmetry in the external flow over the rim seal considerably increased the minimum sealing flows required and that $C_{w,\min}$ eventually became independent of rotational Reynolds number. These results explained, at least up to a Reynolds number of $\mathrm{Re}_\phi = 1 \times 10^6$, the differences between "psuedo-turbine" tests with substantial pressure asymmetry and those rotor-stator experiments conducted in a quiescent environment. These experiments are also discussed in general terms in a very comprehensive text on rotor-stator flows by Owen and Rogers (1989).

Ingestion experiments at the highest Reynolds number so far reported were performed by Graber et al. (1987) on a pressurized model rotor-stator downstream wheelspace. Gas concentration and pressure measurements were made on one simple axial and several radial clearance seals in a weak mainstream flow at rotational Reynolds numbers up to 6×10^6. A sealing effectiveness (ingestion versus coolant flow) for each seal was evaluated based on CO_2 gas concentration measurements made on the stator face only. The sealing effectiveness was found to vary exponentially with the throughflow parameter $\lambda_t = C_w/\mathrm{Re}_\phi^{0.8}$. For the radial seals these workers concluded that the sealing effectiveness was mostly affected by the seal clearance ratio.

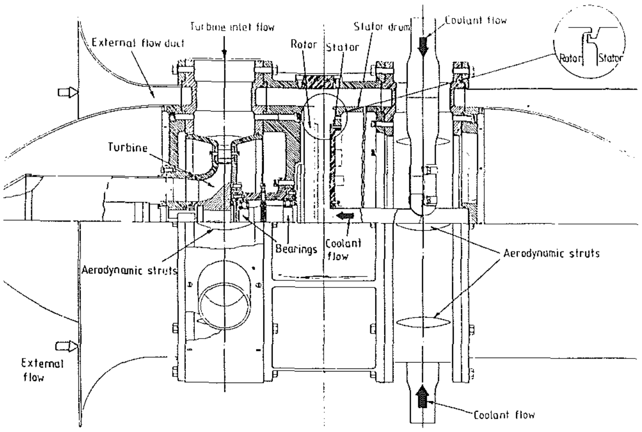

Fig. 1 General assembly of rig

The main objective of this paper is to present the results of rim sealing experiments on two engine representative radial clearance seals, one for a wheelspace upstream of the rotor and one for a downstream wheelspace. The variation of sealing effectiveness for each seal was determined from axial traverses of nitrous oxide gas concentration at four radial positions in one r–z plane of the wheelspace. The concentration measurements were undertaken to determine, for coolant flows less than the minimum to prevent ingress: (*a*) how much mainstream gas is ingested, and (*b*) its eventual distribution throughout the wheelspace.

In addition to the concentration measurements, pressure distributions and estimates of $C_{w,\min}$ from a differential pressure criterion are given and measurements of the core velocity are reported.

2 Experimental Apparatus

The general outline of the rig is shown in Fig. 1 with the seal details shown in Fig. 2. The apparatus consisted of a plane shrouded stator adjacent to a plane disk rotor of 400 mm diameter driven by a radial inflow turbine at speeds up to 12,000 rpm ($\mathrm{Re}_\phi = 3 \times 10^6$). The central rotor-stator and turbine assembly was supported inside the external mainstream flow annulus by eight aerodynamically shaped struts. This assembly was located using substantial aluminum alloy castings

Nomenclature

$C_w \equiv \dot{m}_c/\mu R_o$ = dimensionless coolant mass flow rate
$C_{w,\min}$ = minimum dimensionless coolant mass flow rate
$G \equiv s/R_o$ = rotor-stator gap ratio
$G_{ca} = S_{ca}/R_o$ = axial seal clearance ratio
$G_{cr} \equiv S_{cr}/R_o$ = radial seal clearance ratio
$\dot{m}_c$ = coolant mass flow rate
$\dot{m}_i$ = ingress mass flow rate
p = static pressure
P_{amb} = ambient pressure
P_e = external flow static pressure
$p^* \equiv (P - P_e) \times 1000/P_{\mathrm{amb}}$ = dimensionless static pressure difference
r = radial coordinate
$\mathrm{Re}_\phi \equiv \rho\omega R_o^2/\mu$ = rotational Reynolds number
$\mathrm{Re}_w \equiv \rho \bar{U}_e R_o/\mu$ = external flow Reynolds number
R_o = outer radius of disk
s = axial gap between rotor and stator
S_{ca} = axial seal clearance
S_{cr} = radial seal clearance
$\bar{U}_e$ = mean external flow velocity
V_ϕ = tangential velocity of core flow in wheelspace
z = axial coordinate
$\beta \equiv V_\phi/\omega r$ = core tangential velocity ratio
$\beta^* \equiv [V_\phi/\omega r]_{C_w=0}$ = core tangential velocity ratio at $C_w = 0$
η = nitrous oxide gas concentration ratio
$\bar{\eta}$ = mean gas concentration ratio
η_c = gas concentration in coolant
$\eta^* \equiv (\eta - \eta_c)/\eta_c$ = nondimensional gas concentration ratio
$\lambda_t \equiv C_w/Re_\phi^{0.8}$ = throughflow parameter
μ = fluid viscosity
ρ = fluid density
$\phi \equiv \dfrac{\dot{m}_c}{\dot{m}_c + \dot{m}_i}$ = cooling effectiveness based on gas concentration
ω = angular speed of rotor

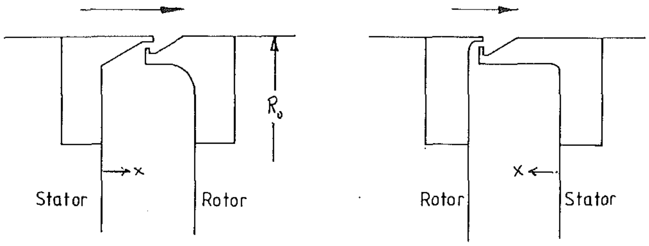

Seal A. UPSTREAM WHEELSPACE
Rotor lip

Seal B. DOWNSTREAM WHEELSPACE
Stator lip

Fig. 2 Schematic arrangement of rim seals

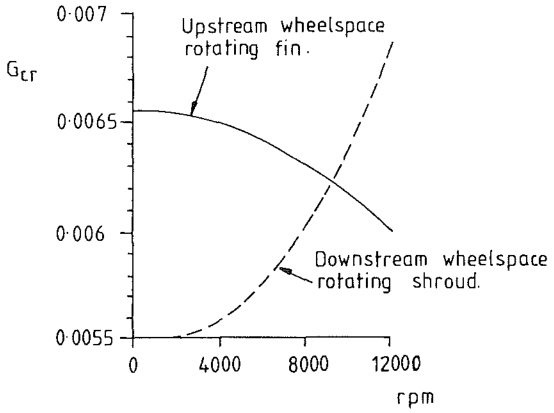

Fig. 3 The measured variation of radial clearance ratio, G_{cr}, with rotational speed

with spigotted flanges, which made accurate setting of the rim seal clearances possible. The whole assembly was easily reversible to enable both upstream and downstream wheelspaces to be tested.

The rotor–stator spacing was maintained constant at $G = 0.1$ ($s = 20$ mm) with the rotor lip rim seal clearance being varied between $G_{cr} = 0.002$ and 0.01 with an overlap of 2 mm. It should be noted that an eccentricity error of 0.025 mm at the smallest seal clearance would produce a circumferential clearance variation of ± 6 percent at a G_{cr} of 0.002.

The clearance ratios listed on the figures, measured using a 3-mm-dia inductive proximity sensor, in a separate series of tests are nominal values since these varied with rotational speed as shown in Fig. 3. For the upstream wheelspace, rotation reduced the clearance and increased it for the downstream wheelspace. The actual change in radial clearance was very similar for nominal clearance ratios of $G_{cr} = 0.002$ and $G_{cr} = 0.01$ over the same speed range of 0 to 12,000 rpm, reducing G_{cr} by 0.00055 upstream and increasing it by 0.0013 downstream. The nominal values apply at maximum speed. As clearances were not monitored continuously, the possibility of small variations due to thermal effects must be acknowledged.

The experiments were run essentially at atmospheric pressure with coolant supplied to the wheelspace centrally through the stator at 50°C and the external mainstream flow drawn through the annulus at atmospheric temperature and pressure at speeds up to 100 m/s ($\mathrm{Re}_w = 1.4 \times 10^6$). Although great care was taken with the manufacture of the external flow annulus, a small circumferential pressure asymmetry still existed, which increased with increasing suction amounting to a maximum-minimum circumferential difference of 0.27 percent of the absolute pressure at the maximum speed. No influence of the wake from the aerodynamic struts was measured; full details of the experimental rig are given by Dadkhah (1989).

2.1 Pressure Measurements. Static pressure taps were made on the stator on three radial lines and on the outside of the stator shroud in the external flow annulus at four circumferential positions 33.5 mm away from the edge of the seal gap. A zero average circumferential static pressure difference across the rim seal (to the $r/R_o = 0.95$ position, owing to the shroud thickness) was taken as the criterion for the determination of the minimum sealing flow rate $C_{w,\mathrm{min}}$. The accuracy of the pressure difference criterion is discussed below and by Chew et al. (1991).

The pressures were read by a microcomputer controlled solenoid switching unit, which allowed an average to be taken of some 200 readings at each point, thus reducing the pressure fluctuation errors.

2.2 Gas Concentration Measurements. A nitrous oxide method of seeding into the coolant supply was used for the detection and quantification of external flow ingestion into the wheelspace.

Gas concentration sampling was made through 1-mm-bore sampling tubes at four radial positions in the wheelspace, $r/R_o = 0.163$, 0.411, 0.658, and 0.905, and at seven axial positions across it. The gas concentration level, maximum 450 ppm, measured in the wheelspace was found to be independent of the sample suction rate. Any uncertainties, estimated at ±2 percent, in the gas concentration measurements were due principally to the averaging of the rapid fluctuations in the wheel space.

2.3 Wheelspace Core Velocity. In this type of wheelspace with this rotor–stator space, it is expected that a rotating core will develop between the boundary layers on the disk. The tangential velocity in this core of fluid, V_ϕ, will depend on radial position, but is to a good approximation independent of axial position. The effects of coolant flow rate and rotational Reynolds number on V_ϕ were examined by converting the mechanically operated gas concentration probes into small total head probes and using the stator wall static pressure taps at the four corresponding radial locations.

3 Radial Pressure Distribution

With no coolant flow admitted to the wheelspace, the pumping action of the rotating disk produces a radial pressure gradient, which increases with increasing rotational speed. The static pressure under the shroud also decreases below the external mainstream pressure and this allows ingress to occur. Introducing a coolant flow into the wheelspace reduces the tangential velocity of the core and thus the radial pressure gradient; the overall pressure level in the cavity is also increased, thus reducing the ingress.

The radial pressure distributions for seal A, upstream wheelspace, are shown in Figs. 4(a, b, c, and d), for nominal gap ratios 0.002 and 0.01.

In general when the value of p^*, $= \left(\dfrac{P-P_e}{P_{\mathrm{amb}}}\right) \times 1000$, is negative throughout the cavity, ingestion is assumed to be present. At the smallest gap ratio with seal A, Figs. 4(a, b), it can be seen that at a coolant flow of $C_w = 2000$ the wheelspace is just about sealed for all speeds and completely sealed for $C_w = 6000$. Figure 4(c) shows that this level of coolant flow is not quite sufficient to seal the cavity when the seal clearance ratio is increased to 0.01. It can also be seen that rotational Reynolds number has less influence on the cavity pressure level at this larger clearance; the main effect comes from the mass flow.

Figures 4(e, f, g, and h) present similar pressure distributions for seal B in the downstream wheelspace. Except for the smaller nominal clearance ratios of 0.002 and 0.0028 with a C_w of 6000, Figs. 4(b, f), both sets of pressure distribution are similar. Note that, as shown in Fig. 3, the variation of clearance ratio with speed is particularly important at the smaller clearance ratios.

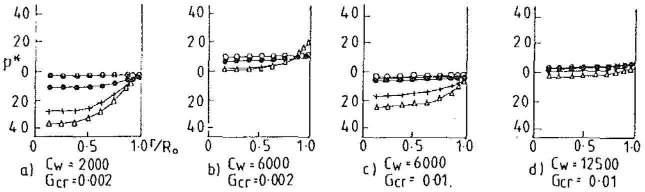

Upstream Wheelspace, Seal A.

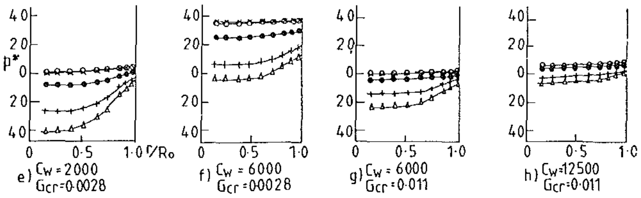

Downstream Wheelspace, Seal B

Fig. 4 Radial distribution of static pressure, p^*, Re_w = 1.38 × 10^6

Symbol	○	x	●	+	△
$Re_\phi/10^6$	0	0.47	1.35	2.25	2.68

4 Minimum Sealing Flow Rate

The minimum coolant flow rates necessary to seal the wheelspace, based on the pressure difference criterion, are given in Figs. 5 for seal A, upstream, and seal B, downstream, for two different nominal seal clearance ratios. For the upstream wheelspace in Figs. 5(*a*, *b*), the external flow appears to have little effect, whereas for the downstream seal this only appears to be true for the smallest clearance ratio, Fig. 5(*c*). At the larger clearance ratio of 0.0112, Fig. 5(*d*), increasing external flow progressively reduces $C_{w,\min}$ although the overall levels are greater than those for the upstream seal. It should be noted that the external, mainstream flow contained only a low circumferential pressure asymmetry in all the experiments reported in this paper.

5 Ingestion Mass Flow Rate and Its Distribution in the Wheelspace

The most important contribution of the present work is illustrated in Figs. 6. These plots of gas concentration for one r-z cross section through the wheelspace, all for conditions for which ingestion was present, show that coolant dilution due to ingress is more evident near the stator than near the rotor. These plots were integrated over the r-z plane to estimate the amount of ingestion present in the form of a ratio $\dot{m}_i/\dot{m}_c$ so that a value of $\dot{m}_i/\dot{m}_c$ of 0.1 represents an ingress of 10 percent of the mass flow of coolant actually supplied.

For the upstream wheelspace, seal A, the gas concentration distributions given in Fig. 6, all for very nearly the same coolant flow rate, rotational speed, and external flow conditions, show that increasing the radial seal clearance initially increases the ingestion from 4.8 percent to 11.5 percent, but that it stays more or less constant ($\approx$ 10 percent) as the clearance is further increased. At the smallest seal clearance, G_{cr} = 0.0024, the gas concentration was radially fairly uniform throughout but for the clearance ratios 0.0064 and 0.0104 the outer radii clearly suffer more dilution due to ingestion than the inner radii. For the downstream wheelspace, seal B, the rate of ingress progressively increased with increasing seal clearance. The general form of the concentration distribution was similar to seal A with ingestion causing most dilution of the coolant at the outer radii.

In all the plots shown in Fig. 6, it can be seen that, except for the stator face values, the concentration profiles for both the outer radii are very similar, r/R_o = 0.658, 0.905. These two probes are probably the only ones in the genuine core region between the rotor and stator boundary layers in which no radial component of velocity exists. At lower radii the supplied flow is greater than the disk pumping flow and there is a radial flow in this "source" region.

The effect of coolant flow rate and rotational speed on the ingested mass flow rate ratio, $\dot{m}_i/\dot{m}_c$, is shown in Fig. 7 for both seals with the same nominal clearance ratio. It should be noted that the ingested flow rate $\dot{m}_i$ does not fall as rapidly as the ratio $\dot{m}_i/\dot{m}_c$ with increasing coolant flow. Increasing coolant flow initially rapidly reduces ingestion for both seals and increasing rotational speed increases it, although the increase is less pronounced for the downstream wheelspace. This could be due to the "curtaining" effect, where the coolant leaving the rotor effectively blankets the wheelspace clearance, improving with increasing rotational speed and offsetting the reducing wheelspace pressure reduction. The amount of ingress present at zero rotational speed represents the effect of the mainstream circumferential pressure asymmetry inherent in the rig.

The effect of radial seal clearance ratio G_{cr} on the mass flow rate of ingress is shown in Fig. 8 for both seal A and seal B.

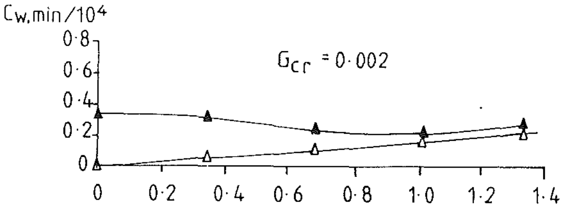

a) Seal A, upstream

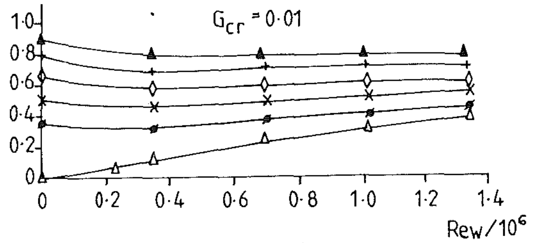

b) Seal A, upstream

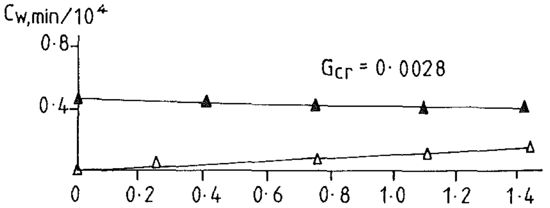

c) Seal B, downstream

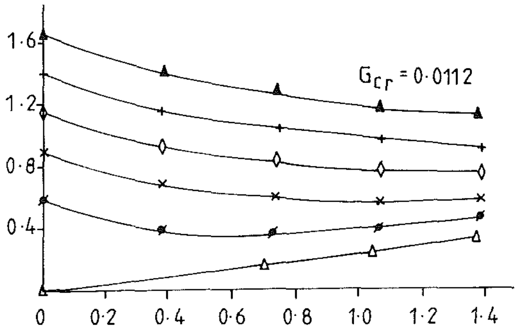

d) Seal B, downstream Rew/10^6

Fig. 5 Minimum sealing flow rate variation with external flow (pressure criterion)

Symbol	○	●	×	◇	+	▲
$Re_\phi/10^6$	0	0.89	1.35	1.81	2.25	2.68

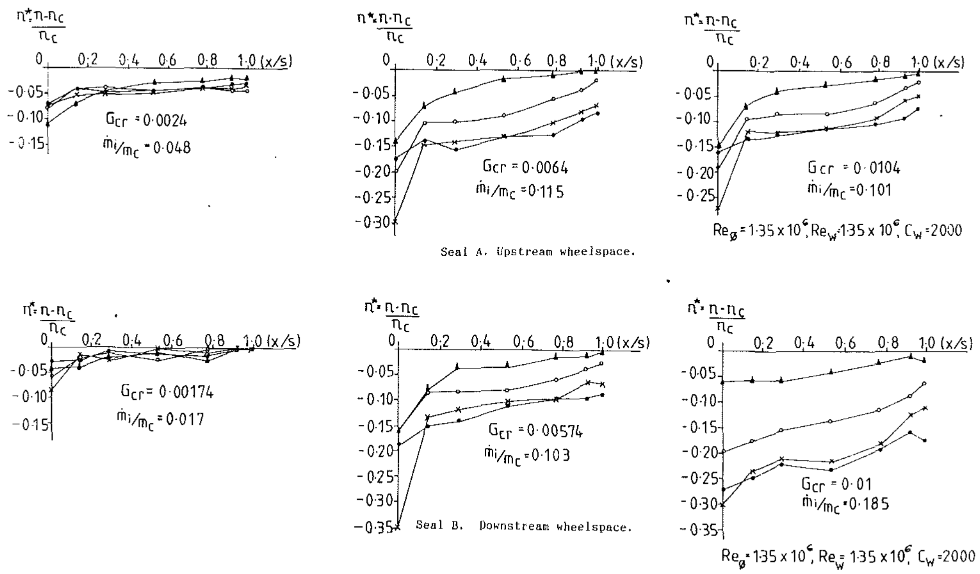

Seal A. Upstream wheelspace.

Seal B. Downstream wheelspace.

Fig. 6 Axial distribution of gas concentration ratio for four radial positions

Symbol	▲	○	x	●
R/r_o	**0.163**	**0.411**	**0.658**	**0.905**

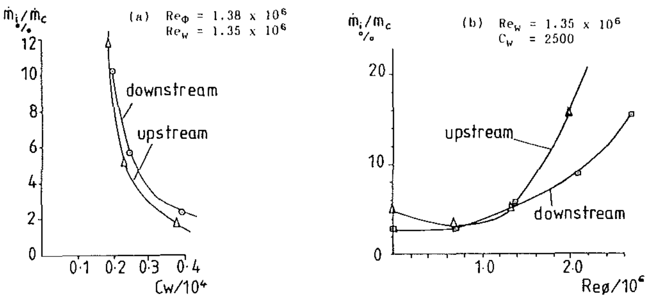

Fig. 7 Variation of ingestion/coolant flow ratio, $\dot{m}_i/\dot{m}_c$, with coolant flow rate and with rotational Reynolds number for G_{cr} = 0.006

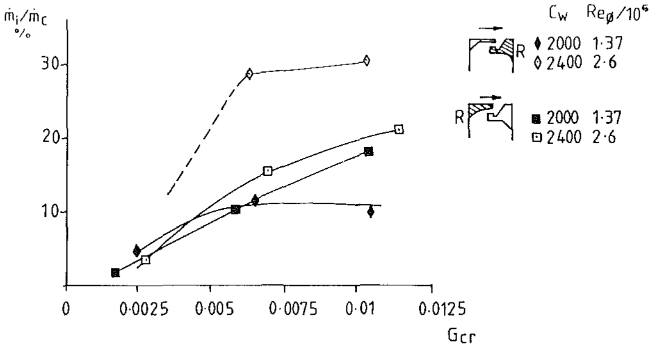

Fig. 8 The effect of seal clearance ratio, G_{cr}, on ingestion mass flow ratio, $\dot{m}_i/\dot{m}_c$ for $Re_w = 1.36 \times 10^6$

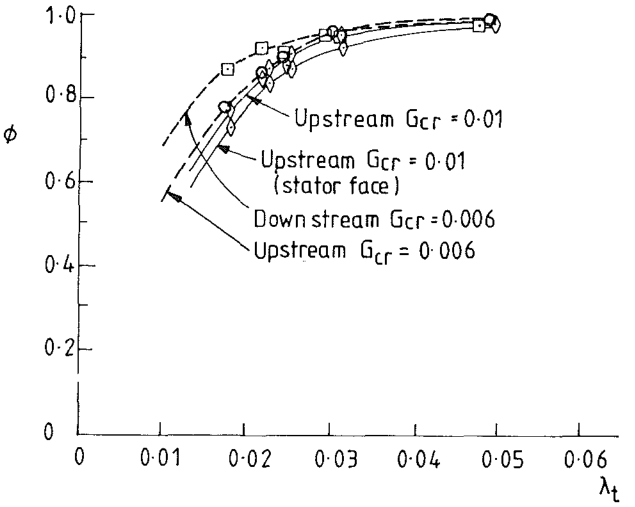

Fig. 9 Seal effectiveness for both upstream and downstream seals versus turbulent flow parameter, $\lambda_t = C_w/Re_\phi^{0.8}$

These plots, for combinations of coolant flow and rotational Reynolds number, show that for small clearance ratios, $G_{cr} \approx 0.002$ (0.4 mm clearance), the mass flow rate of ingestion is similar for both seals for the conditions tested. Although both upstream and downstream seals show an insensitivity to increasing seal clearance, the downstream seal clearly performs better at higher Reynolds numbers.

6 Sealing Effectiveness

A sealing effectiveness $\phi = \dot{m}_c/(\dot{m}_c+\dot{m}_i)$ is defined such that for zero coolant flow, $\phi = 0$, and for zero ingress, $\phi = 1$. Assuming complete mixing in the cavity minus ϕ would be equal to the wheelspace gas concentration ratio. Here ϕ is taken as equal to the wheelspace gas concentration averaged over all the sampling positions.

Recently Graber et al. (1987) found that an exponential curve of the form $\phi = 1 - e^{-\alpha\lambda}$, where $\lambda = C_w/\mathrm{Re}_\phi^{0.8}$ gave a reasonable fit to their sealing effectiveness measurements. The present results give some confirmation of this, as is illustrated in Fig. 9 for both upstream and downstream radial clearance seals. It can be seen that the downstream seal has a slightly better efficiency. Fig. 9 also shows the sensitivity of ϕ to the choice of sampling points used in averaging the concentration measurements. For the case $G_{cr} \simeq 0.01$, using the sample points on the stator face only gives values differing by up to 8 percent from the results averaged over all points. Note that this corresponds to a considerably higher percentage change in $\dot{m}_i/\dot{m}_c$.

Owing to the small gradient of the curves in Fig. 9, as the effectiveness approaches unity, it is difficult to derive a minimum sealing flow from the concentration measurements to compare with the values of $C_{w,\min}$ deduced from the pressure measurements. However, it does appear that the pressure cri-

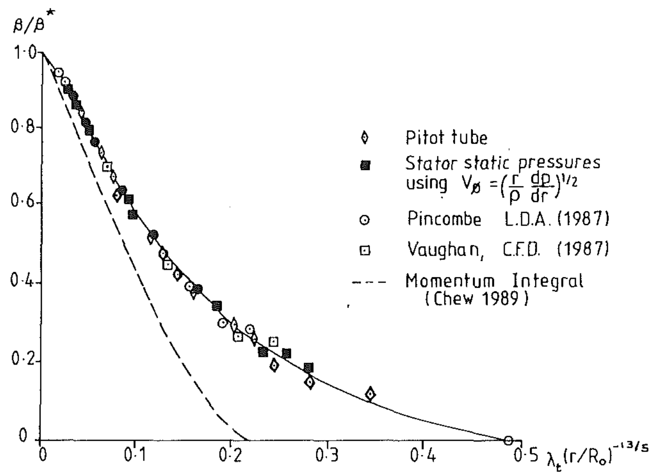

Fig. 10 Variation in the relative tangential velocity of the wheelspace core flow at r/R_o = 0.658 and x/s = 0.5

($\beta = V_\phi/\omega r$, $\lambda_t = C_w/\mathrm{Re}_\phi^{0.8}$)

terion tends to give rather high estimates of $C_{w,\min}$. This is discussed further by Chew et al. (1991).

7 Wheelspace Core Tangential Velocity

The core of fluid between the rotor and stator boundary layers rotates at a velocity that depends upon the disk speed and the coolant flow rate. The tangential velocity of this core has a direct influence on the disk moment coefficient and on the radial static pressure distribution in the wheelspace, which governs the axial thrust calculations.

Measurements are given here for a cavity, with a radial clearance seal, with a gap ratio, G_{cr}, of 0.01. The relative rotational speed of the core is expressed here as the ratio β/β^* where β, = $V_\phi \omega r$, represents the proportion of disk tangential velocity at that radius, and where $\beta = \beta^*$ for $C_w = 0$. For the radial position r/R_o = 0.661 the average β^* value, which showed little variation with Re_ϕ, was found to be 0.433. The variation of β/β^* with the parameter $\lambda_t(r/R_o)^{-13/5}$ is shown in Fig. 10. This parameter was used by Daily et al. (1964) to correlate their core rotation measurements and may be deduced from momentum-integral theory to be a correlating parameter. Figure 10 shows values of β/β^* obtained by several methods: small pitot probes, wall static pressure gradients, the L.D.A. measurements of Pincombe (1987), the momentum-integral solution of Chew (1989), and the finite difference, mixing length turbulence model predictions of Vaughan (1987). The empirical correlation shown (Dadkhah, 1989), is

$$\beta/\beta^* = 0.087[e^{5.2(0.486-\lambda_t(r/R_o)^{-13/5})} - 1]$$

It can be seen that the core rotation is completely suppressed at a value of $\lambda_t(rR_o)^{-13/5}$ = 0.486, which is over double the free disk entrainment value. Good agreement between the various results is apparent, apart from the momentum-integral solution, which underestimates V_ϕ and can only be said to be in fair agreement for low throughflow rates.

8 Conclusions

This paper has described an experimental study of two model gas turbine rotor–stator rim seals with a superimposed external flow. The upstream wheelspace seal had an upward rotor lip while the downstream wheelspace seal had an upward stator lip. Measurements of radial pressure distribution and gas concentration have been presented for situations in which ingestion of mainstream gas is present at rotational Reynolds numbers up to approximately 3 × 10^6. The principal conclusions to be drawn are:

1 Interaction of the coolant flow ejected through the rim seal with the mainstream flow appears to have an important influence on ingestion. Estimates of $C_{w,\min}$ from pressure measurements indicate that seal A is superior to seal B. However, concentration measurements show that, for $C_w < C_{w,\min}$ with an imposed external flow, the level of ingestion for seal A is greater than that for seal B. This behavior may well be due to the different mainstream flow directions in the two cases (i.e., from the stator to the rotor for seal A and from the rotor to the stator for seal B).

2 The gas concentration measurements made throughout the upstream and downstream wheelspaces have answered, in part, two important questions concerning the ingestion of mainstream gas into a wheelspace: (*a*) how is the ingestion distributed throughout the wheelspace, and (*b*) for any coolant flow rate, less than the minimum sealing requirement, how much ingestion occurs?

The present results indicate that any ingress entering through the rim seal proceeds across to and then down the stator to be entrained across the core of fluid in the center of the wheelspace into the rotor boundary layer. Most dilution of the coolant is shown to occur at the outer radii with the rotor surface showing least contamination.

The actual mass flow of ingress was estimated from integrated overall mean gas concentration levels and it is shown that substantially less than the minimum coolant flow rate to seal the cavity may be supplied without significant ingestion occurring. For example, if an ingestion level of $\dot{m}_i/\dot{m}_c$ = 5 percent can be tolerated, then the coolant flow rate could be reduced by as much as 35 percent.

3 The criterion of a zero pressure difference across the external flow/wheelspace stator shroud was found to produce a conservatively high estimate for the minimum sealing flow rate.

4 An experimental correlation is given for the tangential velocity of the rotating core of fluid between the stator and rotor boundary layers, which is shown to be in excellent agreement with other workers.

Acknowledgments

The authors would like to thank Rolls Royce for their continuing support of this research program.

References

Abe, T., Kikuchi, J., and Takeuchi, H., 1979, "An Investigation of Turbine Disc Cooling (Experimental Investigation and Observation of Hot Gas Flow Into a Wheelspace)," presented at the 3rd CIMAC Conf., Vienna, Paper No. GT-30.

Bayley, F. J., and Owen, J. M., 1970, "The Fluid Dynamics of a Shrouded Disc System With a Radial Outflow of Coolant," ASME *Journal of Engineering for Power*, Vol. 92, pp. 335–341.

Campbell, D. A., 1978, "Gas Turbine Disc Sealing System Design," in: *Proc. AGARD Conference on Seal Technology in Gas Turbine Engines*, AGARD-CP-237, London.

Chew, J. W., 1991, "A Theoretical Study of Ingress for Shrouded Rotating Disk Systems With Radial Outflow," ASME JOURNAL OF TURBOMACHINERY, Vol. 113, pp. 91–97.

Chew, J. W., Dadkhah, S, and Turner, A. B., 1992, "Rim Sealing of Rotor-Stator Wheelspaces in the Absence of External Flow,"' ASME JOURNAL OF TURBOMACHINERY, Vol. 114, this issue, pp. 433–438.

Dadkhah, S., and Turner, A. B. 1986, "Rotor-Stator Cavity With External Flow: Pressure and Temperature Measurements With Ingress," Report 86/TFMRC/TN7, EAPS, University of Sussex, United Kingdom.

Dadkhah, S., 1989, "Ingestion and Sealing Performance of Rim Seals in Rotor-Stator Wheelspaces," D. Phil. thesis, University of Sussex, United Kingdom.

Daily, J. W., Ernst, W. D., and Asbedian, V. V., 1964, "Enclosed Rotating Disks With Superposed Throughflow: Mean Steady and Periodic Unsteady Characteristics of the Induced Flow," Report No. 64, M. I. T. Hydrodynamic Lab, Cambridge, MA.

Graber, D. J., Daniels, W. A., and Johnson, B. V., 1987, "Disk Pumping Test," Air Force Wright Aeronaut. Lab., OH, Report No. AFWAL-TR-87-2050.

Haaser, F., Jack, J., and McGreehan, W., 1988, "Windage Rise and Flowpath Gas Ingestion in Turbine Rim Cavities," ASME *Journal of Engineering for Gas Turbines and Power*, Vol. 110, pp. 78–85.

Kobayashi, N., Matsumato, M., and Shizuya, M., 1984, "An Experimental Investigation of a Gas Turbine Disk Cooling System," ASME *Journal of Engineering for Gas Turbines and Power*, Vol. 106, pp. 136-141.

Moore, A., 1975, "Gas Turbine Internal Air Systems: A Review of the Requirements and Problems," ASME Paper No. 75-WA/GT-1.

Owen, J. M., and Rogers, R. H., 1989, *Fluid Flow and Heat Transfer in Rotating-Disc Systems, Volume I: Rotor-Stator Systems*, Research Studies Press, Taunton, United Kingdom.

Phadke, U. P., and Owen, J. M., 1983, "An Investigation of Ingress for an Air-Cooled Shrouded Rotating Disc System With Radial Clearance Seals," ASME *Journal of Engineering for Power*, Vol. 105, pp. 178-183.

Phadke, U. P., and Owen, J. M., 1988a, "Aerodynamic Aspects of the Sealing of Gas Turbine Rotor-Stator Systems, Part 1: The Behaviour of Simple Shrouded Rotating Disk Systems in a Quiescent Environment," *Int. J. Heat Fluid Flow*, Vol. 9, pp. 98-105.

Phadke, U. P., and Owen, J. M., 1988b, "Aerodynamic Aspects of the Sealing of Gas Turbine Rotor-Stator Systems, Part 2: The Performance of Simple Seals in a Quasi-axisymmetric External Flow," *Int. J. Heat Fluid Flow*, Vol. 9, pp. 106-112.

Phadke, U. P., and Owen, J. M., 1988c, "Aerodynamic Aspects of the Sealing of Gas Turbine Rotor-Stator Systems, Part 3: The Effect of Non-axisymmetric External Flow on Seal Performance," *Int. J. Heat Fluid Flow*, Vol. 9, pp. 113-117.

Pincombe, J., 1987, Unpublished Work, TFMRC, University of Sussex, United Kingdom.

Suo, M., 1978, "Turbine Cooling," in: *The Aero-thermodynamics of Aircraft Gas Turbine Engines*," G. C. Oates, ed., AFOSR-75-2783.

Vaughan, C. M., 1987, "A Numerical Investigation Into the Effect of an External Flow Field on the Sealing of a Rotor-Stator Cavity," D. Phil. Thesis, University of Sussex, United Kingdom.

Thermal Details in a Rotor-Stator Cavity at Engine Conditions With a Mainstream

S. H. Ko

D. L. Rhode

Turbomachinery Laboratories,
Mechanical Engineering Department,
Texas A&M University,
College Station, TX 77843

This investigation involves a numerical study of enclosed rotor-stator cavities of gas turbine engines. The complete elliptic form of the 2-D, axisymmetric Navier-Stokes equations for compressible turbulent flow were solved. Included are the complete fluid and thermal effects of the hot mainstream gas interacting with the cooling cavity purge flow at actual engine flow conditions for generalized geometries. Additional flow conditions above and below those for engine nominal conditions are also considered. The relationships among the important flow parameters are investigated by examining the entire set of computations. The predictions reveal that a small recirculation zone in the stator shroud axial gap region is the primary mechanism for the considerable thermal transport from the mainstream to the turbine blade root/retainer region of the rotor.

Introduction

Modern gas turbine engines may be characterized by their extremely high cycle pressures and temperatures, increased reliability, reduced weight, and tight seal clearances. These characteristics have greatly increased the importance of understanding fluid flow and heat transfer phenomena in the engines. However, due to the wide range of flow conditions and the complex geometry of these engines, measurements and predictions have been made under simple, idealized conditions. Recently, developments in numerical algorithms, physical modeling, and computer capabilities have made Computational Fluid Dynamics (CFD) techniques applicable to the internal as well as external aerodynamics of the gas turbine engine.

The current work involves a numerical study of enclosed rotor-stator cavities with radial outward cooling flow induced by the rotor. The cooling flow rate supplied to the cavity must be high enough to prevent the rotor or the stator from being overheated, which is critical for the life of the materials. There has been a great deal of design effort to minimize the parasitic cooling flow rate in order to achieve high efficiency. There is presently considerable debate concerning how much parasitic cooling air must be sacrificed in order to achieve a reliable turbine blade root or retainer. Very little information is available for making these decisions, primarily because of the complex flow and heat transfer process in these rotating cavities.

Previous studies of these rotor-stator cavities have involved theoretical, experimental, or numerical work. Most of the theoretical studies are based on the momentum integral techniques of von Karman (1921). These techniques have the advantage of simplicity and ease of solution. However, they inherently lack the capability of predicting the presence and effect of the recirculation zone near the small axial clearance between the shroud and rotating disk. Owen et al. (1985) presented velocity measurements and integral momentum solutions for the axisymmetric flow inside a rotating cavity with either radial outflow or inflow of cooling fluid. Chew and Snell (1988) solved a problem of radial inflow between two plane co-rotating disks using the momentum integral methods. Compressibility of the flow was included in their analysis. Haaser et al. (1988) provided a simple analytical approach for determining the bulk temperature rise in the cavity due to the hot gas ingestion from the mainstream as well as the frictional heating. Farthing and Owen (1988) obtained flow visualization and heat transfer measurements in an idealized cavity comprising two disks with a shroud. The Nusselt numbers measured on the heated downstream disk of the cavity, were compared with theoretical solutions of the turbulent integral boundary-layer equations.

A more detailed investigation of the temperature and velocities in a rotating cavity requires solutions of the more complete Navier-Stokes equations. Chew (1984a, 1984b, 1985) developed such a computer model based on the TEACH code (Gosman and Pun, 1974) and predicted both laminar and turbulent flow in idealized rotating cavities. For turbulent flows, the *k-e* model and the mixing-length model were used. Morse (1988) used the modified Launder and Sharma (1974) low-Reynolds-number version of the *k-e* model to predict both radial inflow and outflow of cooling air for a rotating cavity. In addition, Louis and Salhi (1989) presented numerical solutions of the Navier-Stokes equations using a low-Reynolds-number *k-e* turbulence model developed from that of Lam and Bremhorst (1981).

These and other investigations generally report important progress toward obtaining useful predictions and measure-

---

Contributed by the International Gas Turbine Institute and presented at the 36th International Gas Turbine and Aeroengine Congress and Exposition, Orlando, Florida, June 3-6, 1991. Manuscript received at ASME Headquarters March 4, 1991. Paper No. 91-GT-275. Associate Editor: L. A. Riekert.

ments for a highly complex flow field. However, there are essentially no insightful data available illuminating the important axisymmetric case of thermal/momentum transport across the mainstream–cavity interface. Almost all of the previous work pertains to the extremely simplified flow fields of test rigs that do not include the turbine mainstream pass. In addition, previous adiabatic predictions and measurements are for incompressible flow fields, whereas at engine conditions very substantial pressure and density variations occur as the cavity purge air exits the cavity and enters the mainstream. One partial exception is the Vaughan and Turner (1987) recently showed that, at least for certain conditions, a laminar three-dimensional (nonaxisymmetric) solution indicates a sinusoidally varying ingress–egress cycle in the θ direction passing through the mainstream–cavity interface.

The present investigation includes the complete momentum and thermal effects of the mainstream gas interacting with the cooler cavity purge flow with an adiabatic rotor. That is, a full accounting is made of the compressibility and mechanical/thermal energy exchanges at the actual engine pressures, temperatures, and mass flow rates of both the mainstream and purge flow streams. The objective is to provide an enhanced physical understanding of the important fundamental mechanisms and relationships for the mainstream–cavity interface of a generalized geometry. The results presented include the important influence of the hot mainstream at actual engine nominal conditions.

Computational Method

The present predictions are solutions, under the assumptions of steady and axisymmetric flow, of the following continuity, momentum, and energy equations:

$$\frac{\partial(\rho U_i)}{\partial x_i}=0$$

$$\frac{\partial(\rho U_i U_j)}{\partial x_i}=-\frac{\partial p}{\partial x_j}+\frac{\partial \tau_{ij}}{\partial x_i}$$

$$\frac{\partial(\rho U_i H)}{\partial x_i}-\frac{\partial}{\partial x_j}\left(\Gamma_H\frac{\partial H}{\partial x_j}\right)=\frac{\partial}{\partial x_j}\left[U_l\tau_{lj}-\Gamma_H\frac{\partial}{\partial x_j}\left(\frac{V^2}{2}\right)\right]$$

The third equation is the stagnation enthalpy form of the energy equation. The computer code solves the complete elliptic form of the Reynolds-averaged, two-dimensional axisymmetric Navier–Stokes equations for compressible turbulent flow. Several approaches of the well-known TEACH code (Gosman and Pun, 1974) are utilized. The primitive variables are solved on a system of three staggered grids using the SIMPLER algorithm of Patankar (1980). The QUICK differencing scheme of Leonard (1979) was incorporated in a convergence-enhancing manner (Rhode et al., 1986) for all convective terms in order to reduce false diffusion. Each of the variables is computed in a sequential fashion using the Tri-Diagonal Matrix Algorithm.

Turbulence Modeling. In the second equation above, τ_{ij} is the effective stress tensor representing the sum of molecular and turbulent components. The effective stress is evaluated using the conventional eddy viscosity approach. There are many approaches to modeling the eddy viscosity, and several of these are briefly compared herein for rotating disk flows. The Prandtl mixing length model, for example, involves the ad hoc specification of a turbulence mixing length scale ℓ_m a priori. The turbulent eddy viscosity for this model is given as

$$\nu_t=\ell_m^2\left[\left(\frac{\partial U_i}{\partial x_j}+\frac{\partial U_j}{\partial x_i}\right)\frac{\partial U_i}{\partial x_j}\right]^{1/2}$$

The simplest category of turbulence models that close the Reynolds-averaged equations without ad hoc information are the two-equation models. The standard k-e model (Launder and Spalding, 1974) is the most popular for practical computations. For this model, the eddy viscosity is evaluated from the Kolmogorov–Prandtl formula as

$$\nu_t=c_\mu k^2/e$$

Note that it is proportional at each grid point to the product of the turbulent length scale and the inverse velocity scale, i.e., $k^{3/2}/e$ and $k^{1/2}$. The usage of a single length scale at each grid point implies that the turbulence is isotropic, which is a shortcoming of such models.

The turbulent kinetic energy k and turbulent energy dissipation rate s are evaluated from the following transport equations:

$$\frac{\partial(\rho U_i k)}{\partial x_i}=P-\rho e+Diff$$

$$\frac{\partial(\rho U_i e)}{\partial x_i}=\frac{e}{k}(C_{e1}P-C_{e2}\rho e)+Diff$$

where P is the production of turbulence kinetic energy. This

Nomenclature

a = radial width of inlet
c = stator shroud gap axial width
C_w = volumetric flow rate parameter $=Q/(\nu R)$
e = turbulent energy dissipation rate
h = modeled radial width of mainstream passage
H = stagnation enthalpy
k = total turbulent kinetic energy $=k^{(1)}+k^{(2)}$
$k^{(1)}, k^{(2)}$ = partial turbulence kinetic energies
K = turbulence energy wave number
L_e = characteristic length scale
P = static pressure
Q = volumetric throughflow rate
R = radius of rotor
R_i = radius of cooling air inlet slit to cavity
$\mathrm{Re}_{x,m}$ = axial Reynolds number of mainstream $=(2Uh)/\nu$
Re_θ = rotational Reynolds number of cavity $=(\Omega R^2)/\nu$
$\mathrm{Re}_{\theta,m}$ = rotational Reynolds number of mainstream $=(2Wh)/\nu$
s = axial width of cavity
T = temperature
T^* = normalized temperature $=(T-T_2)/(T_1-T_2)$
t = radial thickness of shroud
x, r, θ = axial, radial, and tangential coordinates
x_i = spatial coordinate in Cartesian tensor notation
U, V, W = mean velocities in x, r, θ directions
U_i = velocity denoted in Cartesian tensor notation
μ = absolute viscosity
ν = kinematic viscosity
ρ = fluid density
$\epsilon^{(1)}, \epsilon^{(2)}$ = turbulence energy fluxes
Ω = rotational velocity
κ = von Karman constant

Superscripts

$*$ = nondimensionalized
(1) = production zone of turbulent kinetic energy spectrum
(2) = transfer zone of turbulent kinetic energy spectrum

Subscripts

1 = mainstream
2 = cooling purge flow

model is for high-Reynolds-number flow regions where the turbulent viscosity is many times larger than the molecular viscosity. It utilizes a wall function expression to bridge over the low-Reynolds number region, which is between the wall and $y^+ \approx 12$. This model is thus invalid in the near wall region of a rotating disk where viscous pumping is an important mechanism. Thus it is quite reasonable to assume that a low-Reynolds-number version of the *k-e* model with integration completely to the wall is needed.

However, when rotating flow predictions from these two approaches for the *k-e* model were compared by Williams et al. (1991) and by Avva et al. (1990) with experimental data over a range of conditions, there was very little deviation found between these models. In fact, the high-Re version was slightly better in many cases. Further, Avva et al. (1989) also reached the same conclusion for a range of low-Re test cases for which the low-Re version was developed. It is noteworthy that Chew and Vaughan (1988) found that the velocity profiles from their mixing-length model solution near a rotating disk suggest that wall functions, i.e., high-Re models, can be used. Due to the well-known economic advantages of using wall functions to bridge the low-Re near-wall regions, it was decided to focus on the high-Re type of *k-e* model.

Shortcomings of the *e* equation, in addition to the single-scale assumption for the entire turbulence spectrum, are: (*a*) uncertainties in the physical reasoning in determining the source/sink terms, and (*b*) the absence of two-point correlation effects. Ko and Rhode (1989) discuss the derivation and assessment of a new two-scale dissipation equation, the derivation of which begins with a different fundamental equation than previous multiscale or single-scale models. The new approach constitutes a degree of progress in removing the above three weaknesses. That is, the requirement for modeling the source/sink terms using merely physical/dimensional arguments has been replaced with algebraic complexity in the derivation. Also, a new way of evaluating the source/sink coefficient functions, which incorporates new two-point correlation physics, is incorporated. Comparison of predictions with measurements over a wide range of test cases revealed the model's superiority over the standard *k-e* model. As expected, the improvement primarily occurs when there is an abrupt change in the shear field or when flowfield regions dominated by more than one length scale arise. Note that both of these situations are found when the purge air entering the rotor-stator cavity impinges on the rotor.

The new model is based on the assumption that the energy spectrum can be divided into two portions, each having its own length and velocity scales. The derivation of the new model began with the following dynamic equation for the anisotropic energy spectrum (Hinze, 1975):

$$\frac{\partial E(K,\,t)}{\partial t}=F(K,\,t)-2\nu K^2E(K,\,t)-\phi_{lm}(K,t)\frac{\partial \mathrm{U}_m}{\partial \mathrm{x}_l}$$

The term on the left is the rate of change of the energy spectrum. The term $F(K,\,t)$ represents the difference between the energy flux by inertial interaction from the eddies in the wavenumber range $[0,\,K]$ into the wavenumber K, and the flux to the smaller eddies in the wavenumber range $[K,\,\infty]$. The term $2\nu K^2E(K,\,t)$ represents the viscous dissipation of mechanical energy into heat. The final term $\phi_{lm}(K,\,t)\partial U_m/\partial x_l$ describes turbulence production and the transfer of energy between wavenumbers due to the interaction with the mean flow.

The resulting governing equations for $k^{(1)}$ and $k^{(2)}$ are

$$\frac{Dk^{(1)}}{Dt}=P^{(1)}-\epsilon^{(1)}+Diff$$

$$\frac{Dk^{(2)}}{Dt}=\epsilon^{(1)}-\epsilon^{(2)}+Diff$$

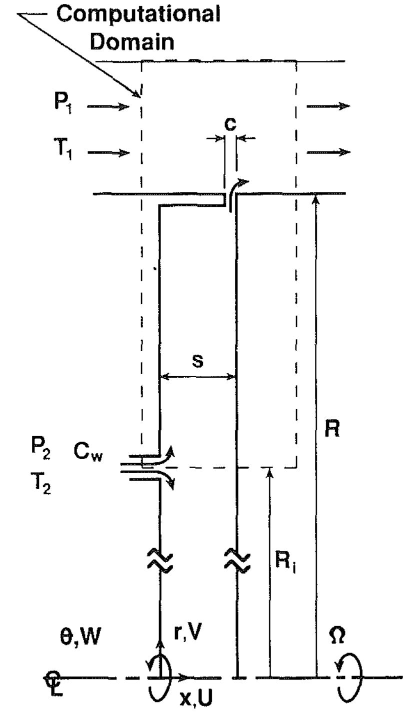

Fig. 1 Idealized configuration and computational domain for purge cavity-mainstream interaction

where $k^{(1)}$ and $k^{(2)}$ are the large and intermediate-eddy partial turbulence energies, which are found in the production and transfer zones of the turbulence energy spectrum, respectively. The governing equations for the energy transfer rates are:

$$\frac{D\epsilon^{(1)}}{Dt}=C_1^{(1)}\frac{\epsilon^{1}P}{k^{(1)}}-C_2^{(1)}\frac{\epsilon^{(1)^2}}{k^{(1)}}+Diff$$

$$\frac{D\epsilon^{(2)}}{Dt}=C_1^{(2)}\frac{\epsilon^{(2)^2}}{k^{(2)}}+C_2^{(2)}\frac{\epsilon^{(1)}\epsilon^{(2)}}{k^{(2)}}+C_3^{(2)}\frac{\epsilon^{(2)}P}{k^{(2)}}$$

$$-C_4^{(2)}\frac{\epsilon^{(2)}P}{k^{(1)}}-C_5^{(2)}\frac{\epsilon^{(1)}\epsilon^{(2)}}{k^{(1)}}+Diff$$

where $\epsilon^{(1)}$ and $\epsilon^{(2)}$ are the turbulence energy fluxes leaving the large- and intermediate-eddy zones, respectively. Note that $k=k^{(1)}+k^{(2)}$ and $e=\epsilon^{(2)}$. The turbulent viscosity is obtained from

$$\nu_t=\frac{C_\mu(k^{(1)}+k^{(2)})^2}{\epsilon^{(2)}}$$

Figures 2–4 are typical of a comparison study of three different turbulence models for predicting the type of flowfield under study. The measurements of Dailey et al. (1964) in a similar rotor-stator cavity with axial inlet and radial outlet flow were used. The new multiscale was compared to the standard high-Re *k-e* model and measurements over a very wide range of operating conditions. Radial and tangential velocities as well as the frictional moment coefficient and pressure have been examined. The comparisons shown here cover the range of throughflow parameter $C_w=Q/(\nu R)$ from 1450 to 3443 and the Re_θ range from 2.95×10^5 to 9.5×10^6. As shown in Fig. 2, the radial velocities predicted by the multiscale model (Ko and Rhode, 1990) are better than the others compared. This is particularly true near the disk surface located at $x/s=1.0$. Further, the standard *k-e* model shows better agreement with the measurements than the mixing-length model, which has previously been a popular approach for this test case. A comparison of tangential velocity is given in Fig. 3 for a lower C_w of 1708 and the same Re_θ of 6.95×10^5. Observe once again that the multiscale model is preferred. Moreover,

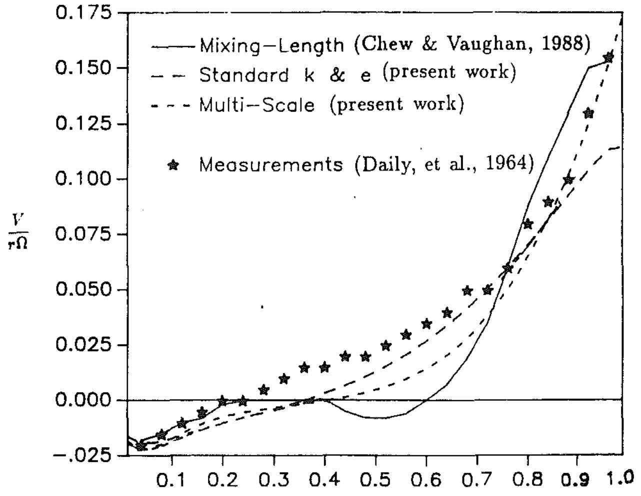

Fig. 2 Comparison of radial velocity for several turbulence models for an enclosed rotating disk with throughflow ($C_w = 3443$, $\mathrm{Re}_\theta = 6.95 \times 10^5$)

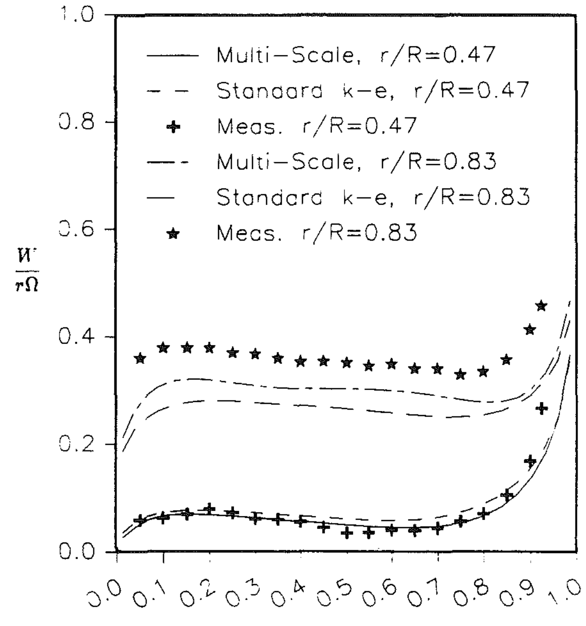

Fig. 3 Comparison of tangential velocity for two turbulence models for an enclosed rotating disk with throughflow ($C_w = 1708$, $\mathrm{Re}_\theta = 6.95 \times 10^5$)

note that the degree of improvement over the standard *k-e* model increases for more challenging conditions such as for $x/s > 0.9$ in Fig. 2 and for $r/R > 0.6$ in Fig. 3. The moment coefficient values, which are sensitive to solution discrepancies, are given in Fig. 4 for a lower C_w of 1450 and higher Re_θ values ranging from 2.5×10^6 to 9.5×10^6. Here again, a considerable improvement is found for the multiscale solution, which shows only approximately 7 percent disparity with measurements as compared to 27 percent for the standard *k-e* solution.

Perhaps most significant of all is the improvement for the historically defying simple test case of the free axisymmetric jet. Specifically, the spreading rate was recently overpredicted by 35 percent using the standard *k-e* model and only 18 percent using the Multiscale model. Note that this free jet is quite similar to that of free flow over a rotating disk in that turbulence quantities change very rapidly in the streamwise direction.

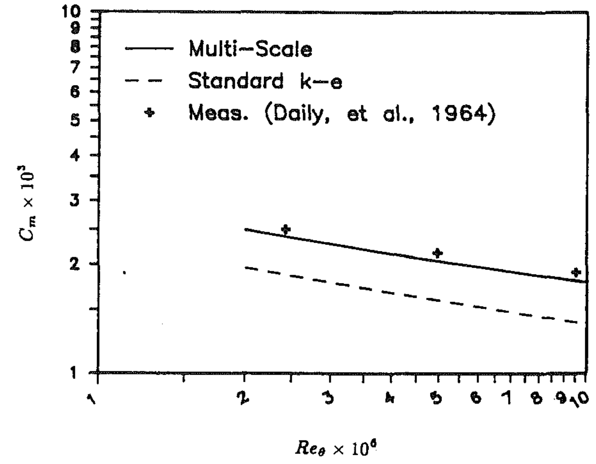

Fig. 4 Comparison of frictional moment coefficient for two turbulence models for an enclosed rotating disk with throughflow ($C_w = 1450$)

Domain and Boundary Conditions. It is only the cavity occupying the extremely narrow axial space between an upstream stator and a downstream rotor blade, and the corresponding length of mainstream duct, that has been modeled herein. Figure 1 illustrates the idealized cavity and mainstream duct showing the computational domain and geometry variables. A shroud was located on the (upstream) stator, and the radial width of the annular mainstream duct was decreased in order to reduce the considerable computing cost without affecting the computations. An experienced turbine designer (Baskharone, 1990) was consulted in modeling the mainstream duct. It was decided that for this short axial segment, approximating this passage as a straight annular duct is a good approximation. This results from the fact that the diverging effect of the flow is counterbalanced by the increasing boundary layer displacement thickness, which is caused by the high mainstream swirl velocity.

The mainstream inlet boundary values were chosen as those leaving an upstream stator vane. In the interest of providing generalized results, uniform radial distributions of each variable were assumed at both the mainstream and the cavity domain inlets. The inlet values for axial and tangential velocities as well as enthalpy, temperature, and pressure were obtained from actual engine nominal conditions. These were supplied by Ivey (1990), who is employed by a gas turbine manufacturer (see "The Cases Considered"). The radial velocity was assumed zero. The total inlet turbulence kinetic energy k was estimated as $k = 0.03U^2$. Next, k was divided into the partial kinetic energies $k^{(1)}$ and $k^{(2)}$ with a constant ratio of $k^{(1)}/k^{(2)} = 1.5$; $\epsilon^{(1)}$ and $\epsilon^{(2)}$ were estimated using

$$\epsilon^{(1)} = \epsilon^{(2)} = \frac{k^{1.5}}{L_e}$$

where L_e is the characteristic length scale of the flow. This relationship simply results from the fact that the characteristic turbulence length scale is $L_e = k^{1.5}/e$ and that $e = \epsilon^{(2)}$. For the present study, L_e was taken as 30 percent of the radial width of each inlet passage.

Along solid boundaries, the wall function was used for velocity components tangent to the wall, as well as for evaluating the turbulence production term in the $k^{(1)}$ equation. The standard wall function is derived from the log-law of the wall and is given by Launder and Spalding (1974) as

$$\frac{U}{(\tau/\rho)_w} C_\mu^{1/4} k^{1/2} = \frac{1}{\kappa} \ln\left[Ey\, \frac{(C_\mu^{1/2} k)^{1/2}}{\nu} \right]$$

The turbulent wall stress τ is evaluated in terms of constants $C_\mu = 0.09$, $\kappa = 0.41$, and $E = 9.793$, as well as U, k, and y values at the near-wall grid point. The modification incorporated for the rotating surface is based on swirling pipe flow measurements of Backshall and Landis (1969), for example. It entails replacing the near-wall grid point value of U with the corresponding value $V_r = \sqrt{U^2 + W^2}$ for walls parallel to the axial direction. The wall shear stress τ_ν is then the vector sum of the axial and tangential components. These components, which are what actually enters into the computations, are then evaluated from:

$$\tau_{r\theta} = \tau_\nu W / V_r$$

$$\tau_{rx} = \tau_\nu U / V_r$$

Walls parallel to the radial direction are treated analogously.

Further, $\epsilon^{(1)}$ and $\epsilon^{(2)}$ were evaluated at near-wall grid points from

$$\epsilon^{(1)} = \epsilon^{(2)} = \frac{C_\mu^{0.75} k^{1.5}}{\kappa y}$$

where y is the normal distance from the wall. Also, the zero normal gradient condition was specified along the wall for $k^{(1)}$ and $k^{(2)}$. The adiabatic condition was chosen for the energy equation along the rotor as well as other walls because: (*a*) It is the most general simplest case, and (*b*) there are no generalized wall temperature or heat flux data available for engine nominal conditions.

At the outlet, zero normal gradient of the flow properties has been specified while axial velocities are corrected at each iteration so that overall mass balance is achieved. The domain outlet was displaced far enough downstream from the cavity to allow zero normal gradient boundary conditions there, but not so far downstream as to require unnecessary computations. After examining several solutions with a different axial location of the outlet, it was placed at $x/s = 1.85$. During the examinations, special attention was given to the distribution of wall shear stresses along the mainstream surface of the rotor to ensure there was no flow reversal near the outlet plane. Such flow reversal would necessitate the specification of downstream boundary values.

Grid independence tests were conducted using 43×63, 60×117, and 104×144 grids. These are highly nonuniform grids, each with several rates of expansion and contraction in order to resolve fine details economically. Thus there is much greater difference in grid spacing that the numbers of grid lines above indicates. Further, the nearest-to-wall grid spacing was maintained constant for these grids so that all of the y^+ values along the wall were within the proper range $12 < y^+ < 250$ for using wall functions. The 104×144 grid was sufficient for the production computations.

Results

The Cases Considered. The flow in a rotor–stator cavity is very complex. Moreover, the addition of a mainstream makes the flow more complicated. When a disk rotates, there is a thin boundary layer (the Ekman layer) close to the rotor in which, due to the centrifugal forces, there is a pumping action causing fluid to move radially outward. It was noted (Greenspan, 1968) that the Coriolis force is balanced by the viscous shear and the pressure forces.

The presence of a hot mainstream strongly influences the flow and temperature fields inside the cavity. The turbine rim cavity shown in Fig. 1 has been generalized to provide an enhanced broad understanding of the thermal interaction between the cavity and the mainstream. Results from this idealized cavity configuration provide basic first-order characteristics of the flow and heat transfer applicable in a general way to actual engine cavities. The physical dimensions are: radius of the rotor $R = 0.308$ m, radial width of the mainstream passage $h/R = 0.0975$, $s/R = 0.0612$, $c/R = 0.00936$, $a/R = 0.00725$, $R_i/R = 0.795$, and radial thickness of the shroud $t/R = 0.00725$. The cooling flow enters the cavity axially through an annular slit in the stator at temperature T_2 and leaves radially through the gap between the rotor and the stator shroud.

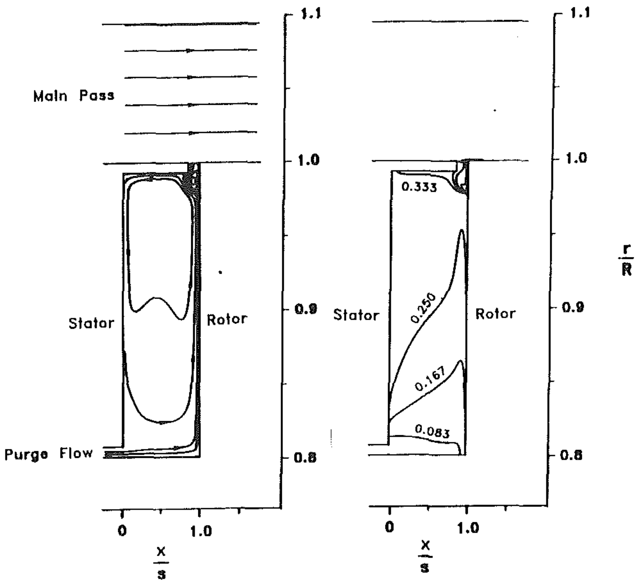

(a) Streamline pattern (b) Isotherm pattern

Fig. 5 (*a*) Streamlines and (*b*) isotherms for the turbine rim cavity at engine nominal conditions with $C_w = 7200$

Actual engine nominal conditions according to Ivey (1990) are: (*a*) axial Reynolds number in the main pass $\mathrm{Re}_{x,m} \equiv (2\rho U h)/\mu = 1.17 \times 10^6$; (*b*) rotational Reynolds number of the rotor $\mathrm{Re}_\theta \equiv (\rho \Omega R^2)/\mu = 7.62 \times 10^6$; (*c*) differential pressure $\Delta P^* \equiv [(P_2 - P_1)/P_1] \times 10^3 = -10$; (*d*) differential temperature $\Delta T^* \equiv 2C_p(T_2 - T_1)/(\Omega R)^2 = -4.6$; (*e*) swirl ratio at the main pass domain inlet $W/U = \tan(\pi/12)$; and (*f*) swirl ratio at the turbine cavity domain inlet $W/U = 0$. Subscripts 1 and 2 refer to the mainstream and the cooling purge flow, respectively. The fluid properties above are referenced at T_1 and P_1.

Turbine Blade Root or Retainer Heating. Detailed flow and thermal characteristics in the rim cavity are examined in this section for various values of the cooling flow rate parameter $C_w = 1500$, 7200, and 13,000 with other parameters maintained constant at engine nominal conditions. Recall that for generality and simplicity, all solid surfaces including the disk are modeled as adiabatic.

Figure 5 shows predicted streamlines and isotherms for the rim cavity flowfield with $C_w = 7200$ at engine nominal conditions. Due to the intense free shear action where the mainstream contacts the cavity fluid at $x/s = 0.9$ and $r/R = 1.0$, a small gap recirculation zone (GRZ) is formed in and below the shroud axial gap.

It is easily seen how this GRZ can transport thermal energy from the mainstream to: (*a*) the crucial turbine blade root and/or retainer location on the rotor near $r/R = 1.0$ and (*b*) the large cavity recirculation zone. The disk-pumped boundary layer (the Ekman layer) along the rotor has been deflected away by this GRZ, so the cooling flow never contacts the blade root/retainer location on the rotor as shown in Fig. 5(*a*). It is noticed that the thickness of the Ekman layer reaches a rather constant value quickly for $r/R > 0.8$. The isotherms shown in Fig. 5(*b*) and elsewhere have been normalized as $T^* = (T - T_2)/(T_1 - T_2)$ and have a uniform increment of 0.083 in this figure.

Figure 6 shows corresponding velocity vectors in a magnified

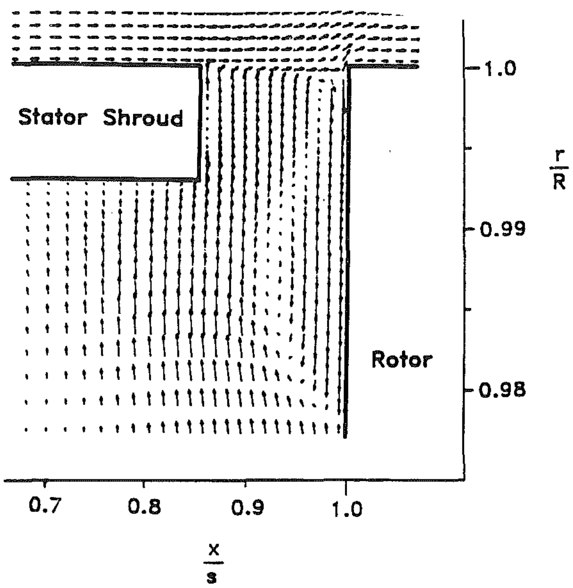

Fig. 6 Magnified view of velocity vectors near the gap region at engine nominal conditions with $C_w = 7200$ (the mainstream vectors for $r/R > 1.0$ have been scaled down by 50 percent for clarity)

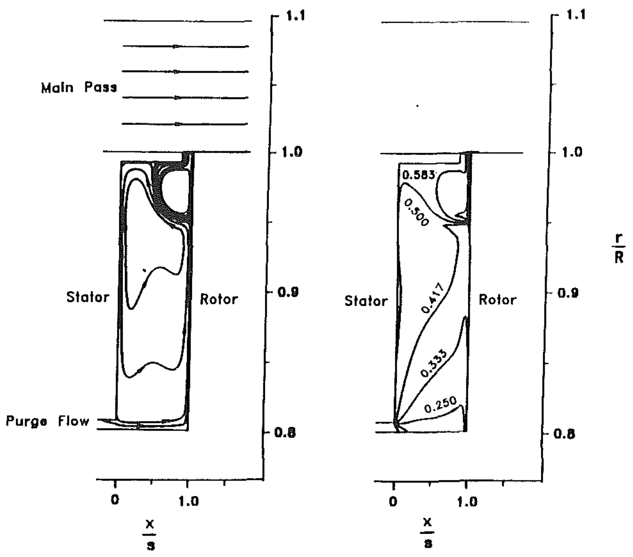

(a) Streamline pattern (b) Isotherm pattern

Fig. 8 (*a*) Streamlines and (*b*) isotherms for the turbine rim cavity at engine nominal conditions with $C_w = 1500$

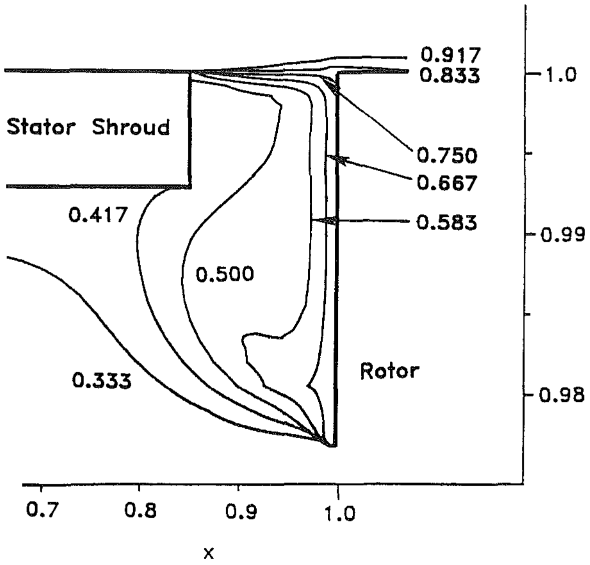

Fig. 7 Magnified view of isotherms near the gap region at engine nominal conditions with $C_w = 7200$

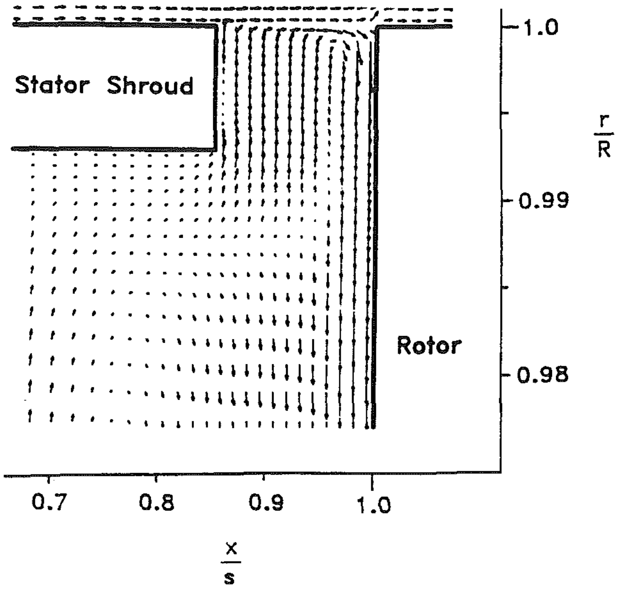

Fig. 9 Magnified view of velocity vectors near the gap region at engine nominal conditions with $C_w = 1500$ (the mainstream vectors for $r/R > 1.0$ have been scaled down by 50 percent for clarity)

view of the shroud axial gap region at engine nominal flow conditions. The length of the vectors in the main pass has been scaled down to half of the true length for clarity of the figure. Note from the vectors at $r/R = 1.0$ that the time-averaged turbulent flow exhibits no predicted ingress of the hot mainstream into the cavity. Figure 6 clearly shows that, at least for the present engine nominal conditions, the generalized axisymmetric flowfield exhibits no direct contact of the hot mainstream gas with the blade root/retainer area of the disk. Note that on the rotor there is a GRZ separation point at $r/R = 0.977$ where the outward flowing Ekman layer of cooling air and the inward flowing recirculating flow meet.

In Fig. 7 isotherms as normalized above are shown in a magnified view of the gap region when $C_w = 7200$. Notice that a steep temperature gradient occurs here and is confined to the GRZ. Also notice that T^* increases sharply from 0.333 to 0.667 from the inner to the outer edge of the GRZ separation point at $r/R = 0.977$. Further, the GRZ is also located at the position of the crucial turbine blade root/retainer, the thermal reliability of which is of major concern. Since there is clearly no mainstream ingress and no thermal convection along the rotor (adiabatic solid walls were specified), this thermal effect must result from rotor frictional heating or thermal transport from the mainstream to the GRZ and, in turn, to the outer disk region of the GRZ itself. It is believed that the GRZ diffusion/convection transport is the primary culprit for this heating because Figs. 5-7 show that the purge cooling flow reaches a temperature of only $T^* = 0.333$ before it is deflected away from the rotor at $r/R = 0.977$ and heated further as it passes outward through the shroud gap alongside the GRZ. In addition, the severe temperature gradient seen in Fig. 7 at $r/R = 1.0$ indicates an extremely high rate of turbulent thermal diffusion radially from the mainstream into the GRZ there.

The pressure field is not shown here. The expected abrupt

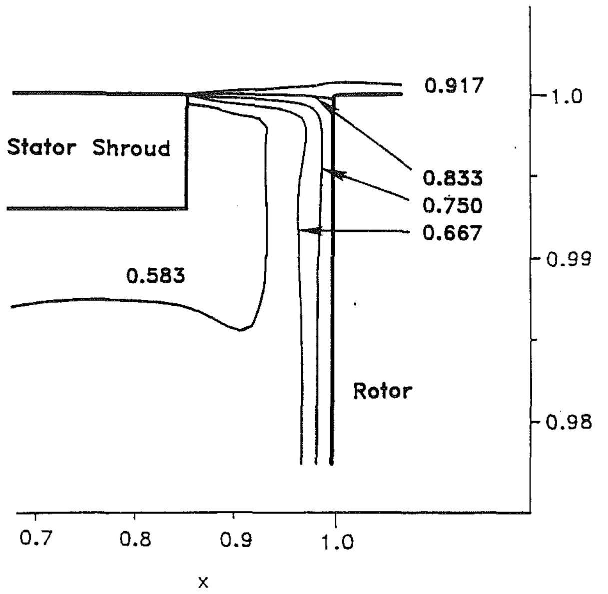

Fig. 10 Magnified view of isotherms near the gap region at engine nominal conditions with $C_w = 1500$

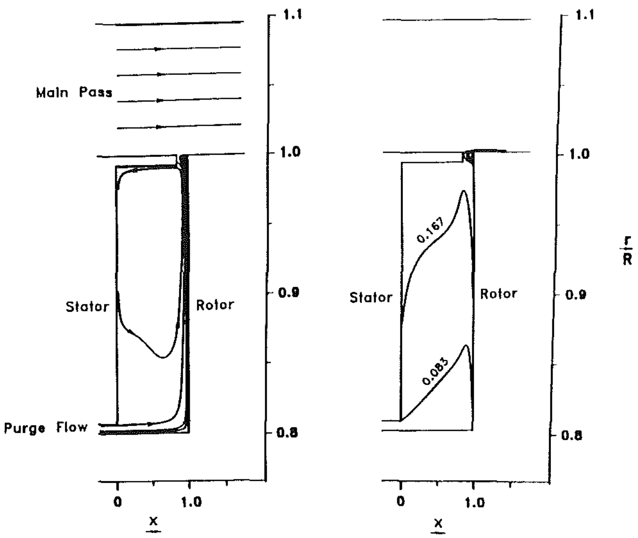

Fig. 11 (a) Streamlines and (b) isotherms for the turbine rim cavity at engine nominal conditions with $C_w = 13{,}000$

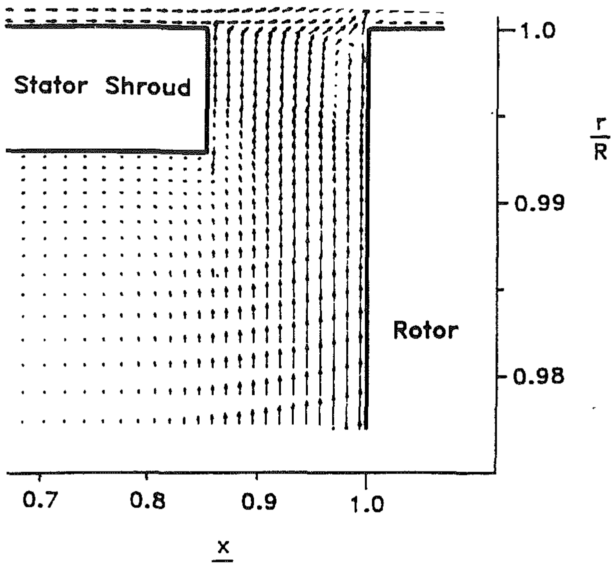

Fig. 12 Magnified view of velocity vectors near the gap region at engine nominal conditions with $C_w = 13{,}000$ (the mainstream vectors for $r/R = 1.0$ have been scaled down by 50 percent for clarity)

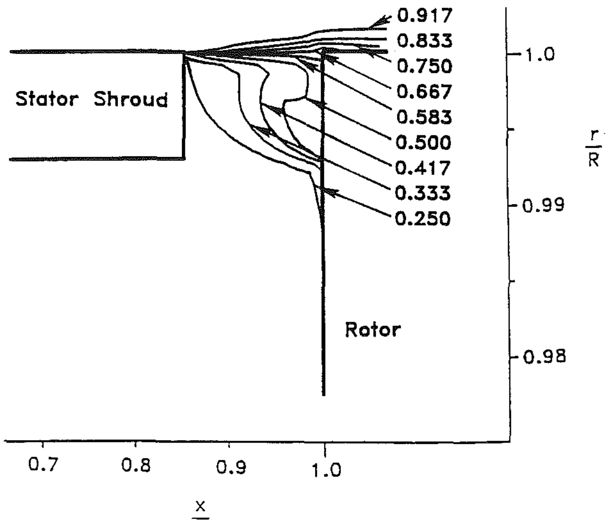

Fig. 13 Magnified view of isotherms near the gap region at engine nominal conditions with $C_w = 13{,}000$

change was found as cooling fluid passes outward through the shroud seal. From additional computer runs it was determined that the pressure difference ΔP^* (defined above) between the cavity and mainstream inlets increases in magnitude as Re_θ increases (for constant C_w, etc.). Specifically for the nominal C_w of 7200, $\Delta P^* = -3.16$ at $\mathrm{Re}_\theta = 3.18 \times 10^6$ and $\Delta P^* = -24.9$ at $\mathrm{Re}_\theta = 11.4 \times 10^6$. In addition, ΔP^* decreases in magnitude as C_w increases for a constant nominal $\mathrm{Re}_\theta = 7.62 \times 10^6$. That is, $\Delta P^* = -20$ when $C_w = 1522$ and $\Delta P^* = -9.27$ when $C_w = 7690$.

Figures 8–10 show momentum and heat details at the engine nominal conditions, except with $C_w = 1500$. The GRZ in Fig. 8 is much larger than that in Fig. 5. The separation point is observed here at $r/R = 0.95$. Due to the increased size of the GRZ, the hot zone extends farther inward along the disk and inside the cavity. It is easily seen that the radial extent of the Ekman layer and the size of the GRZ depend on several parameters such as Re_θ, C_w, and $\mathrm{Re}_{x,m}$. High Re_θ or high C_w indicates more intense centrifugal pumping, which reduces the size of the GRZ. On the other hand, higher $\mathrm{Re}_{x,m}$ increases the free shear stresses along the outer edge of the GRZ, which results in a larger GRZ. The gap region of Fig. 9 shows generally the same path of coolant flow outward through the gap along the shroud tip at $x/s \approx 0.85$. Figure 10 shows isotherms in the gap region corresponding to Fig. 8(*b*). Similar to Fig. 7, the isotherms adjacent to the disk inside the GRZ region shown in Fig. 10 are essentially parallel to the disk surface. The outer region of the GRZ is covered with hot thermal layers of almost constant thickness.

Figures 11–13 show momentum and heat transport in the cavity when C_w is increased to 13,000, which is almost twice as high as the nominal cooling flow rate. As shown in Fig. 11, the GRZ attached to the rotor is so small that it remains inside the gap region. When the axial temperature distribution at a radial location inside the cavity is examined, it should be noticed that the outer edge of the Ekman layer exhibits the lowest temperature at that radial location. Figure 12 shows the corresponding velocity vector plot in the gap region. Here a large portion of the gap axial width exhibits egress of the cooling flow. Isotherms in the gap region of Fig. 13 show that the cavity region where $r/R \leq 0.99$ remains cool with T^* less than 0.250 whereas the outer region is under rapid change of temperature from $T^* = 0.250$ to $T^* = 0.667$.

Conclusions

A finite difference code has been developed for the study of the momentum and thermal details of rotor-stator cavities at realistic gas turbine engine conditions. The computer code was used to solve the complete elliptic form of the two-dimensional, axisymmetric Navier-Stokes equations for compressible turbulent flow with adiabatic walls. It was shown that the multiscale *k-e* model is better than the mixing-length or the standard *k-e* model in predicting the closely related experiment of Daily et al. (1964).

Predictions were obtained for the flow in a generalized turbine rim cavity interacting with the mainstream flow. The velocity vectors and isotherms in the stator shroud axial gap region reveal: (*a*) that a gap recirculation zone is the primary mechanism for the axisymmetric transport of heat from the main pass to the blade root or retainer area, (*b*) detailed characteristics of the thermal/momentum behavior in the shroud gap region, and (*c*) the influence of halving and doubling the engine nominal cooling flow C_w on the size and shape of this hot recirculation zone region as well as the temperature and flow pattern in the cavity.

Acknowledgments

The technical information graciously supplied by Dr. P. Ivey and Dr. E. Baskharone is greatly appreciated. The financial support of the Turbomachinery Research Consortium of Texas A&M University is gratefully acknowledged. The authors are also indebted to the Supercomputer Center at the University for a grant of CRAY-YMP CPU time.

References

Avva, R. K., Ratcliff, M. L., and Leonard, A. D., 1989, "CFD Analysis of Rotating Disk Flows, in: *Recent Advances and Applications in Computational Fluid Dynamics*, ASME FED-Vol. 103, pp. 99–105.

Avva, R. K., Smith, C. E., and Singhal, A. K., 1990, "Comparative Study of High and Low Reynolds Number Versions of $k-\epsilon$ Models," AIAA Paper No. AIAA-90-0246.

Backshall, R. G., and Landis, F., 1969, "The Boundary-Layer Velocity Distribution in Turbulent Swirling Pipe Flow," ASME *Journal of Basic Engineering*, Vol. 91, pp. 728–733.

Baskharone, E., 1990, Personal Communication.

Chew, J. W., 1984a, "Development of a Computer Program for the Prediction of Flow and Heat Transfer in a Rotating Cavity," *International Journal of Numerical Methods in Fluids*, Vol. 4, p. 667.

Chew, J. W., 1984b, "Prediction of Flow in Rotating Disc Systems Using the k-ϵ Turbulence Model," ASME Paper No. 84-GT-229.

Chew, J. W., 1985, "Prediction of Flow in a Rotating Cavity With Radial Outflow Using a Mixing Length Turbulence Model," *Proceedings of the 4th International Conference on Numerical Methods in Laminar and Turbulent Flows*, Swansea, United Kingdom.

Chew, J. W., and Snell, R. J., 1988, "Prediction of the Pressure Distribution for Radial Inflow Between Co-rotating Discs," ASME Paper No. 88-GT-61.

Chew, J. W., and Vaughan, C. M., 1988, "Numerical Predictions for the Flow Induced by an Enclosed Rotating Disc," ASME Paper No. 88-GT-127.

Daily, J. W., Ernst, W. D., and Asbedian, V. V., 1964, "Enclosed Rotating Disks With Superposed Through Flow," Hydrodynamics Laboratory, MIT, Report No. 64.

Farthing, P. R., and Owen, J. M., 1988, "The Effect of Disk Geometry on Heat Transfer in a Rotating Cavity With a Radial Outflow of Fluid," ASME JOURNAL OF TURBOMACHINERY, Vol. 110, pp. 70–77.

Gosman, A. D., and Pun, W. M., 1974, "Calculations of Recirculating Flows," Research Report, Report No. HTS/74/2, Department of Mechanical Engineering, Imperial College, London, United Kingdom.

Greenspan, H. P., 1968, *The Theory of Rotating Fluids*, Cambridge University Press, United Kingdom.

Haaser, F., Jack, J., and McGreehan, W., 1988, "Windage Rise and Flowpath Gas Ingestion in Turbine Rim Cavities," ASME JOURNAL OF TURBOMACHINERY, Vol. 110, pp. 78–85.

Hinze, J. O., 1975, *Turbulence*, McGraw-Hill, New York.

Ivey, P. C., 1990, General Electric Aircraft Engines, Private Communication.

Karman, Th. von, 1921, "Über Laminare und Turbulente Reibung," *Z. Angew. Math. Mech.*, Vol. 1, p. 233.

Kim, S. W., and Chen, C. P., 1987, "A Multiple-Time-Scale Turbulence Model Based on Variable Partitioning of Turbulent Kinetic Energy Spectrum," NASA CR-179222.

Ko, S. H., and Rhode, D. L., 1989, "Development of a New Multiscale k-ϵ Model," Annual Report TRC-PERF-2-89, #510, Mechanical Engineering Department, Texas A&M University.

Ko, S. H., and Rhode, D. L., 1990, "Derivation and Testing of a New Multiscale k-ϵ Turbulence Model," AIAA Paper No. 90-0243.

Lam, G. K. G., and Bremhorst, K., 1981, "A Modified Form of k-ϵ Model for Predicting Wall Turbulence," ASME *Journal of Fluids Engineering*, Vol. 103, pp. 456–460.

Launder, B. E., and Sharma, B. I., 1974, "Application of the Energy-Dissipation Model of Turbulence to the Calculation of Flow Near a Spinning Disc," *Letters in Heat and Mass Transfer*, Vol. 1, p. 131.

Leonard, B. P., 1979, "A Stable and Accurate Convective Modeling Procedure Based on Quadratic Upstream Interpolation," *Computer Methods in Applied Mechanics and Engineering*, Vol. 19, pp. 59–98.

Louis, J. F., and Salhi, A., 1989, "Turbulent Flow Velocity Between Rotating Co-axial Disks of Finite Radius," ASME JOURNAL OF TURBOMACHINERY, Vol. 111, pp. 333–340.

Morse, A. P., 1988, "Numerical Prediction of Turbulent Flow in Rotating Cavities," ASME JOURNAL OF TURBOMACHINERY, Vol. 110, p. 202.

Owen, J. M., Pincombe, J. R., and Rogers, R. H., 1985, "Source-Sink Flow Inside a Rotating Cylindrical Cavity," *Journal of Fluid Mechanics*, Vol. 155, pp. 233–265.

Patankar, S. V., 1980, *Numerical Heat Transfer and Fluid Flow*, McGraw-Hill, New York.

Rhode, D. L., Demko, J. A., Traegner, U. K., Morrison, G. L., and Sobolik, S. R., 1986, "Prediction of Incompressible Flow in Labyrinth Seals," ASME *Journal of Fluids Engineering*, Vol. 108, pp. 19–25.

Vaughan, C. M., and Turner, A. B., 1987, "Numerical Prediction of Axisymmetric Flow in a Rotor-Stator System With an External Mainstream Flow," *Proceedings of 5th International Conference on Numerical Methods in Laminar and Turbulent Flow*, Swansea, United Kingdom, pp. 1640–1651.

Williams, M., Chen, W. C., Baché, G., and Eastland, A., 1991, "An Analysis Methodology for Internal Swirling Flow Systems With a Rotating Wall," ASME JOURNAL OF TURBOMACHINERY, Vol. 113, pp. 83–90.

An Experimental Study of Fluid Flow in Disk Cavities

S. H. Bhavnani
Mem. ASME

J. M. Khodadadi
Mem. ASME

J. S. Goodling
Mem. ASME

Department of Mechanical Engineering,
Auburn University,
Auburn, AL 36849-5341

J. Waggott
Advanced Engineering & Development,
Dresser-Rand Steam Turbine, Motor,
and Generator Division,
Wellsville, NY 14895

Results are presented for an experimental study of fluid flow in models of gas turbine disk cavities. Experiments were performed on 70-cm-dia disks for rotational Reynolds numbers up to 2.29×10^6. *Velocity and pressure distributions are presented and compared to previous theoretical and experimental studies for a free disk, and an unshrouded plane rotor-stator disk system. Minimum coolant flow rates for the prevention of ingress, determined for the case of a simple axial rim seal, compare well with previously published data.*

Introduction

As part of the design of modern gas turbines, coolant flows must be supplied to the cavities between the stator and rotor disks. These flows must be at least sufficient to prevent the ingestion or ingress of hot mainstream gases into the cavities. At the same time, excessive amounts of coolant flow beyond the minimum required to prevent ingress lead to overall turbine inefficiencies.

Analytical studies of minimum flow rates in real gas turbines are difficult because of the complex geometry involved. Most experimental studies have been directed toward obtaining data for simple geometries. There is a need to quantify the effects that various parameters have on the velocity and pressure fields within disk cavities. These include coolant mass flow rate, rotational speed, coolant thermophysical properties, geometry, and seal configurations. This paper presents results of an investigation on such simple geometries. Beyond this paper, we will present similar data for the geometry associated with a real gas turbine wherein the seal geometry is not simple.

Fluid flow near an open free rotating disk can be treated as the simplest case when considering complex flows of relevance to turbomachinery. A similarity solution to the laminar boundary-layer form of the equations of motion was obtained by Cochran (1934) for this case. Erian and Tong (1971) reported measured velocities for the turbulent free disk problem. Fluid flow around a disk rotating in a closed housing has been solved using approximate techniques (Schlichting, 1979). The results for both the laminar and turbulent cases indicate that an intermediate layer of fluid between the two boundary layers revolves with about half the angular velocity of the disk. The more complex case of plane disks with openings in the enclosure has been a subject of numerous computational and experimental studies. Owen (1984) in a review article discussed this case as a more complicated form of the free disk, showing that the outward flow entrained into the boundary layer on the rotor is supplied by radial inflow along the stator. The influence of throughflow on plane disk geometries has been discussed in the theoretical studies of Bayley and Owen (1969) and Uzkan (1981). The presence of throughflow gives rise to the establishment of a net radial outflow, and can be used to alter or eliminate the radial inflow along the stator. Attempts have been made to modify the cavity geometry in order to reduce ingress. For example, Uzkan and Lipstein (1986) have shown that the ingestion of external flow into the gap at the disk periphery can be modified markedly by providing a honeycombed pattern on the stator surface. Specifically, the minimum coolant flow rate was found to be 63 percent less for the honeycombed surface, when compared to that of the smooth plane surface.

Several studies have been performed as attempts to understand complex flow patterns in air-cooled gas turbines. These have concentrated on simple parallel flat disks with a variety of shroud geometries. Bayley and Owen (1970) showed that the static pressure distribution for a great portion of the disk was insensitive to the presence of the shroud. The minimum mass flow necessary to prevent ingress was determined to be proportional to the rotational Reynolds number and the shroud axial clearance ratio. Owen and Phadke (1980) reported an empirical correlation for the minimum mass flow based on pressure measurement and flow visualization. Phadke (1983) later reported laser-based flow visualization in a shrouded rotor–stator system with throughflow. Laminar flow structure and onset of instability were elucidated. Phadke and Owen (1983) concluded that the radial-clearance seals performed extremely well in inhibiting ingress when compared to axial-

---

Contributed by the International Gas Turbine Institute and presented at the 36th International Gas Turbine and Aeroengine Congress and Exposition, Orlando, Florida, June 3–6, 1991. Manuscript received at ASME Headquarters February 20, 1991. Paper No. 91-GT-137. Associate Editor: L. A. Riekert.

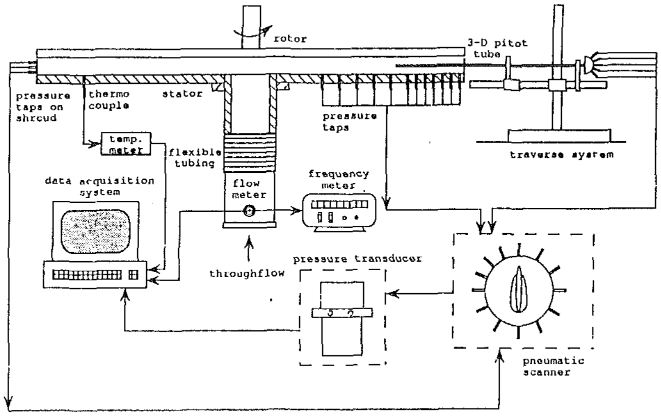

Fig. 1 Experimental setup

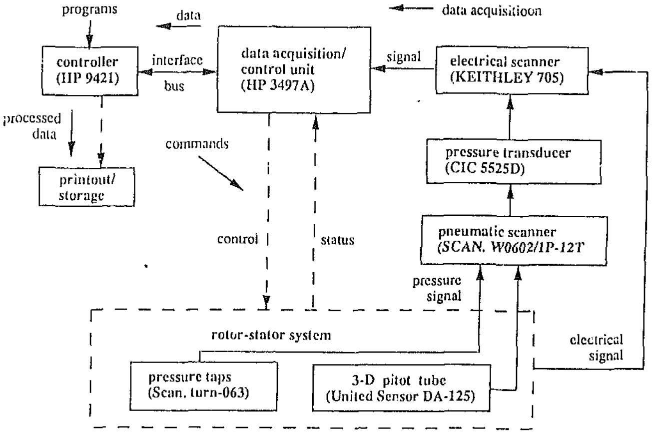

Fig. 2 Data acquisition and control (DAC) system block layout

clearance seals. In addition, the amount of coolant required to prevent ingress decreased with increasing overlap ratio. The complementary work on Phadke and Owen (1988) concentrated on using flow visualization, pressure, and concentration measurements in studying seven seal geometries. Empirical correlations for the minimum flow rate necessary to prevent ingress were obtained for individual seal designs. El-Oun et al. (1988) found that the minimum flow rate was independent of the location where the flow was fed into the rotor-stator system.

This paper reports experimental results obtained for the simple geometries of a free rotating disk, unshrouded parallel disks (one rotating and one stationary), and shrouded parallel disks.

Description of Experiments

All experiments were performed on disks mounted horizontally and spun in room air in the chuck of a Bridgeport milling machine, capable of discrete rotational speeds up to 2784 rpm set by a belt-pulley system. Figure 1 is a schematic of the components used. When throughflow was required, room air was supplied by a flow adjustable blower with an in-line filter. A turbine flowmeter (FTI FT-48N650-G8) with an accuracy of 1 percent was installed to sense throughflow volumetric flow rates. Static wall pressures were sensed by taps in the stator at radial locations of r/r_o = 0.3, 0.4, 0.5, 0.6, 0.7, 0.75, 0.80, 0.85, 0.9, 0.95, 0.97, and 0.99. Additionally, five pressure taps were located on the shroud at distances of 0.356 cm, 1.422 cm, 2.134 cm, 2.845 cm, and 3.200 cm, from the stator surface. These pressure taps were made by drilling holes of 0.254-mm diameter into the Plexiglas stator and countersinking them from the outside enough to insert a small-diameter steel tube upon which was fastened flexible plastic transmitting tubes. A Scanivalve 12 port pneumatic switch wafer (Model W1261/1P-12T) was used to send pressure signals to a calibrated diaphragm pressure transducer (CIC Model 5525D) with accuracy of 0.0025 cm of water. Ambient air temperature was monitored by a thermocouple located in the disk cavity. All instrumentation was connected to an HP Digital Acquisition and Control (DAC) system for monitoring, signal analysis and reduction, and display and storage. A block diagram of the DAC system is shown in Fig. 2.

Free disk data were obtained from a 0.703-m-dia disk made from 1.59-cm stock sheet aluminum. Shrouded disk data were obtained from that same disk with a matching Plexiglas disk mounted parallel, below and stationary to it, with and without a shroud at the outer periphery of that stator. The shroud was fabricated from thin metal and attached to the outer edge of the stator with screws and sealed. To ensure safety of operation, a heavy metal cage was built around the experimental setup and a clear plastic screen was constructed in front of the data acquisition station for further protection.

Velocity measurements were taken by use of a constant-temperature hot-wire anemometer (HWA) and/or a three-dimensional Pitot tube. The former was made by TSI, Model 1054B, with a Model 1210-T.15 tungsten single wire filament, 0.9525 cm in length and 0.0038 mm in diameter with a range of 1000 cm/s. Calibration data provided by TSI were corrected for local ambient temperature. Independent calibration data were obtained by use of a small wind tunnel and Pitot tube. The HWA was mounted to the traversing mechanism of the Bridgeport (i.e., longitudinal slide, cross slide, and the vertical slide) for precise positioning with respect to the disk (radial and axial distances, ±0.0025 cm). Rotor speed was set by a particular combination of pulleys and always measured by a digital stroboscope with an accuracy of ±1 rpm.

The movement of a 0.318-cm diameter, three-dimensional Pitot tube (United Sensor and Control Corporation model DA-125) was manually controlled by a traversing mechanism with an accuracy of ±0.13 cm. The yaw angle of the probe was determined with an adjustable disk dial graduated in intervals of 0.5 degrees. Static pressures along the stator were sensed

Nomenclature

C_w = dimensionless throughflow rate $= \dot{m}/\mu r_o$
G = gap ratio $= s/r_o$
G_{ca} = axial seal clearance ratio $= s_{ca}/r_o$
$\dot{m}$ = mass flow rate
P = pressure
P_{atm} = atmospheric pressure
P^* = dimensionless pressure ratio $= (P - P_{\text{atm}})/P_{\text{atm}}$
r = radial coordinate
r_o = outer radius of the disk
Re_ϕ = rotational Reynolds number $= r_o^2\omega/\nu$
Re_r = local rotational Reynolds number $= r^2\omega/\nu$
s = spacing between the rotor and stator
s_{ca} = axial seal clearance
V_r = radial component of velocity
V_t = tangential component of velocity
V_z = axial component of velocity
z = axial coordinate
μ = dynamic viscosity
ν = kinematic viscosity
ξ = dimensionless axial coordinate $= z\sqrt{\omega/\nu}$
ρ = fluid density
ω = rotational speed

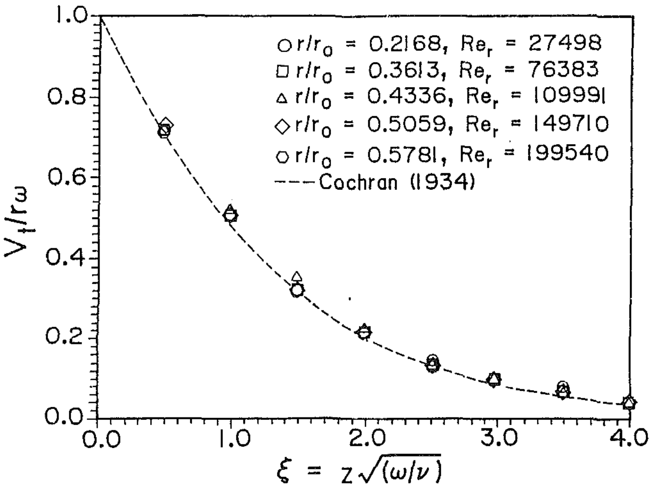

Fig. 3 Tangential velocity profiles (laminar flow) for the plane disk

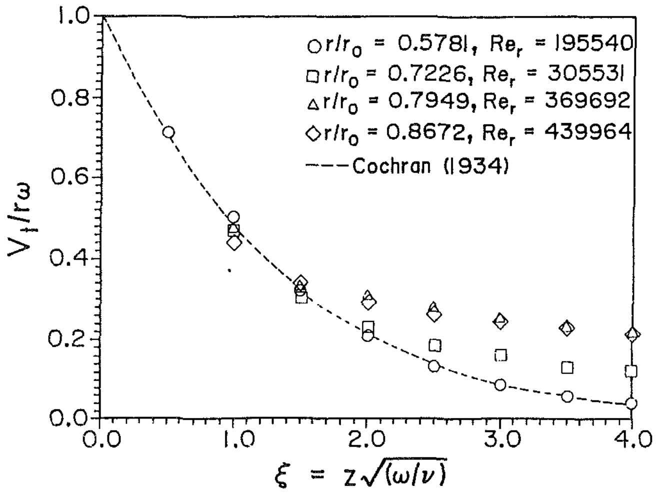

Fig. 5 Tangential velocity profiles (turbulent flow) for the plane disk

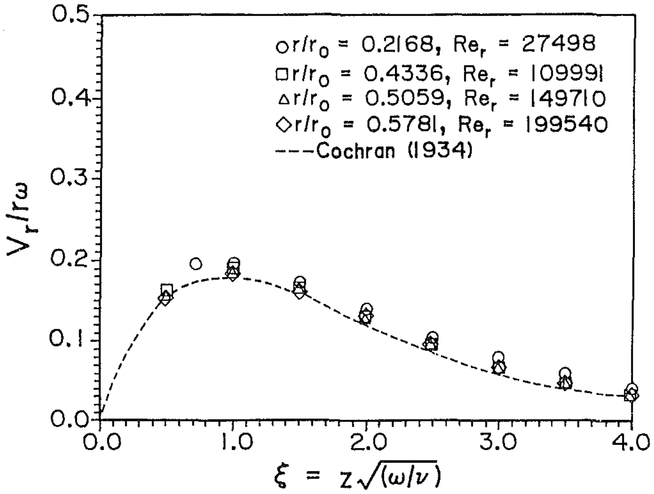

Fig. 4 Radial velocity profiles (laminar flow) for the plane disk

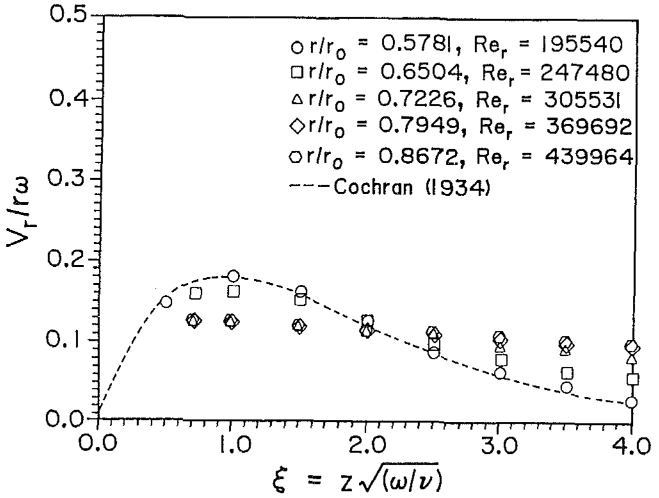

Fig. 6 Radial velocity profiles (turbulent flow) for the plane disk

by a pressure transducer with an accuracy of ±0.0025 cm of water and monitored by the DAC. Independent verification of the Pitot tube calibration against a one-dimensional Pitot tube was done also in the wind tunnel.

Results and Discussion

The disk configurations tested included plane disks with and without throughflow, and shrouded disks with and without throughflow. The primary aim of the study was to determine the minimum throughflow required to prevent ingress of main flow gases into the turbine disk cavities. The effects of several parameters on the velocity and pressure distributions within a disk cavity were therefore studied in order to provide a better understanding of the flow field.

The overall experimental method was calibrated using the 0.703 m diameter free disk. For this sized disk in air, the axial velocity component in the three-dimensional flow field around a free rotating disk is negligible compared to the tangential and radial components. Therefore, measurements were made of the tangential and radial components of velocity only, using the hot-wire anemometer described above. This technique permitted measurement within the boundary layer for both laminar and turbulent flow. Measured tangential and radial velocities for the laminar case are displayed in Figs. 3 and 4, respectively, in dimensionless form (data points). The dashed lines, corresponding to the similarity solution of Cochran (1934), indicate good agreement here between theory and experiment. Figures 5 and 6 show tangential and radial data, respectively, obtaining at higher values of local rotational Reynolds number. These data clearly show the transition from laminar to turbulent behavior with the resulting characteristic flat velocity profile associated with turbulent flow. The values of dimensionless velocity at $\xi = 4.0$ compare very well with similar data obtained by Erian and Tong (1971). It is to be noted that for aerodynamically smooth surfaces, the transition from laminar to turbulent flow usually occurs at a rotational Reynolds number of 300,000 for this flow geometry (Schlichting, 1979) and such is the case here.

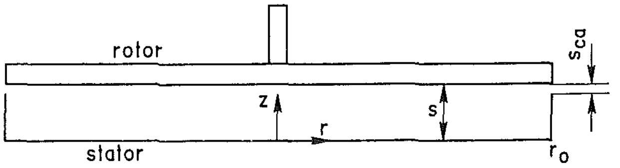

Fig. 7 Schematic of the plane disk geometry

Plane Disks

Velocity field. Fluid flow within a cavity formed by two plane disks with one rotating and the other held stationary presents a flow field that is truly three dimensional in nature. This geometry is shown in Fig. 7. Unlike the free disk discussed

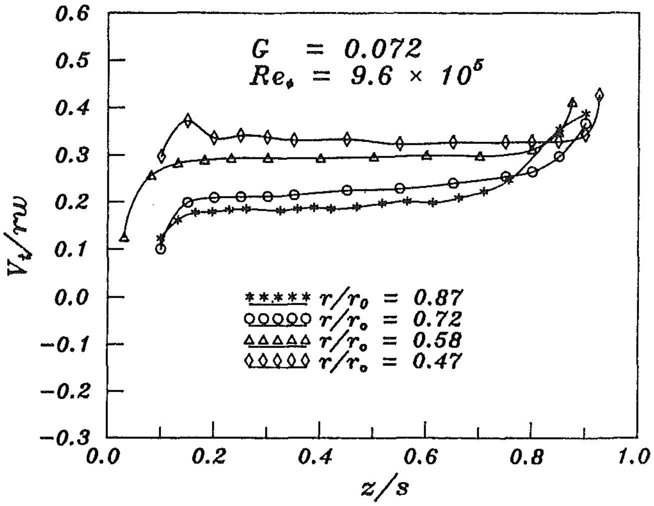

Fig. 8 Tangential velocity profiles for the unshrouded parallel disks (three-dimensional Pitot tube)

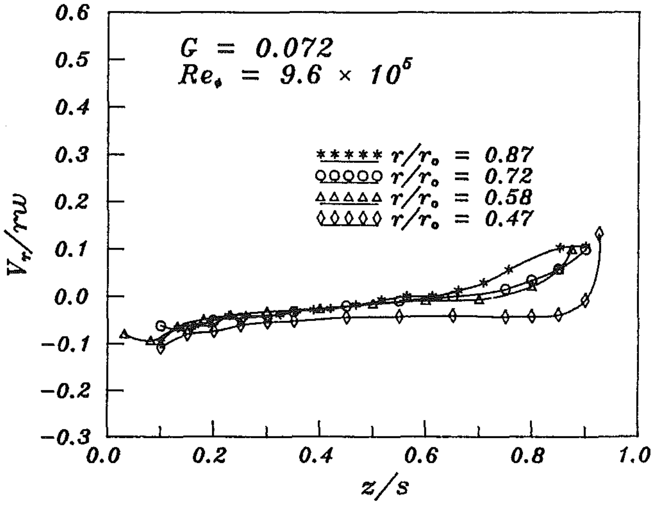

Fig. 9 Radial velocity profiles for the unshrouded parallel disks (three-dimensional Pitot tube)

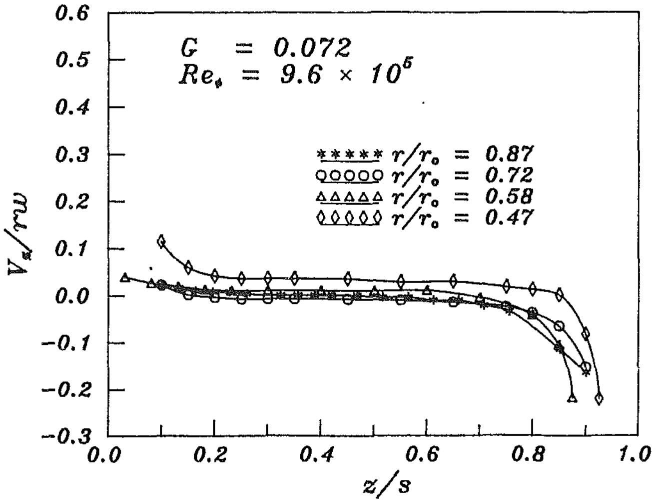

Fig. 10 Axial velocity profiles for the unshrouded parallel disks (three-dimensional Pitot tube)

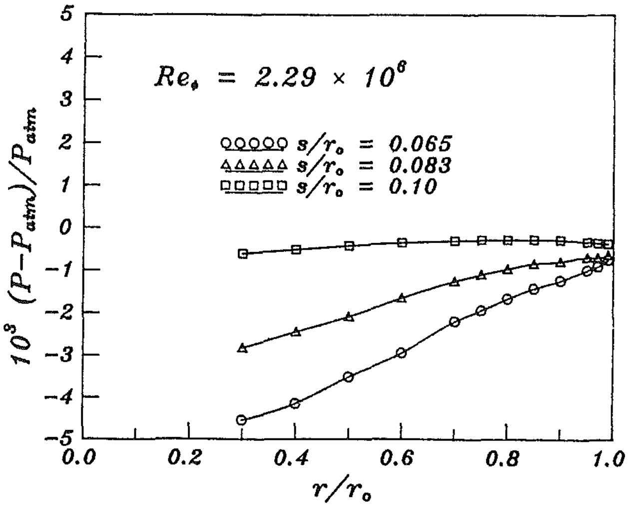

Fig. 11 Effect of gap variation on radial pressure distribution for unshrouded parallel disks

above, the axial component of velocity is not negligibly small in comparison with the radial and tangential velocities in a large portion of the flow field between the two disks. For these experiments only the three-dimensional pitot tube was used to measure velocities in the disk cavity. The reason for this is that it is extremely difficult to measure a three-dimensional velocity field with a single wire HWA with limited degrees of rotation as was the case in the confined space between the two disks. Unfortunately, the size of the three-dimensional Pitot tube (0.318 cm diameter) was such that it could not be used for measuring velocity in the boundary layer without disrupting it. Data in the boundary layers are still shown in the various plots but are intended to display qualitative trends only.

Figures 8, 9, and 10 show data for the dimensionless tangential, dimensionless radial, and dimensionless axial velocities for parallel plane disks with no throughflow plotted as a function of dimensionless axial distance from the stator ($z/s = 0$ and 1 represent the stator and the rotor surfaces, respectively). These three plots were obtained for fixed Reynolds number and fixed spacing between rotor and stator. Figure 8 indicates uniform tangential velocities in a region between the two boundary layers ($z/s = 0.2$ to 0.65). Since the data do not superimpose for various dimensionless radii, this core is not inviscid. Despite this, the value for dimensionless tangential velocity are near those predicted by Owen and Rogers (1989) under the a priori assumption of the presence of an inviscid core. Figure 9 shows both boundary layers with the one associated with the rotor gradually thickening as radius increases. Figure 9 also shows that the radial velocities are predominantly negative in the core (up to about z/s of 0.7) at radial locations indicating a slow inward radial velocity. Axial velocities, Fig. 10, in the core are close to zero. However, at a low radius ($r/r_0 = 0.47$), the axial velocity has a significant nonzero value. This is because of the interaction of the stator and rotor boundary layers and the turning of the fluid that is moving radially inward along the stator to an outward moving stream along the rotor. This is also evident in Fig. 9 for a radial location of 0.47 where there is a significant negative radial velocity, which changes rapidly to a positive value as the rotor is approached, without any large zero value plateau, unlike the curves for the other radial locations.

Static Pressure Measurements. Pressure measurements were made at several radial locations. Additionally, measurements made along four orthogonal radii confirmed that the flow was axisymmetric to within 3 percent.

Experiments were conducted at a rotational Reynolds number of 2.29 × 10^6 and at three different gap ratios. These measurements are shown in Fig. 11 with the pressure represented by a dimensionless pressure difference, $P^* = (P - P_{\text{atm}})/$

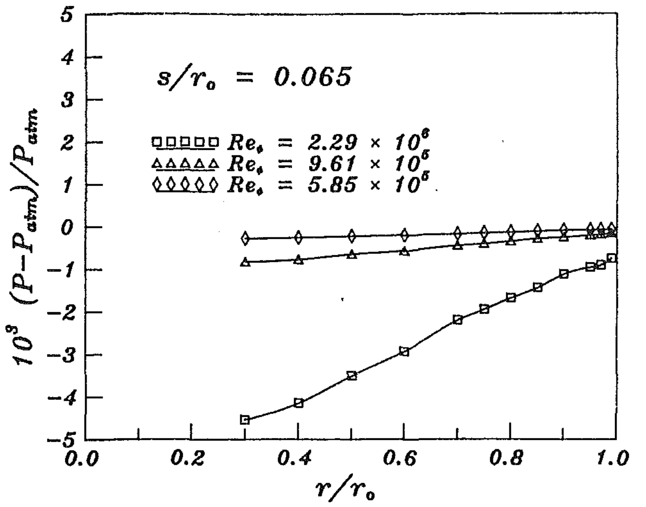

Fig. 12 Effect of the rotational Reynolds number on radial pressure distribution for unshrouded parallel disks

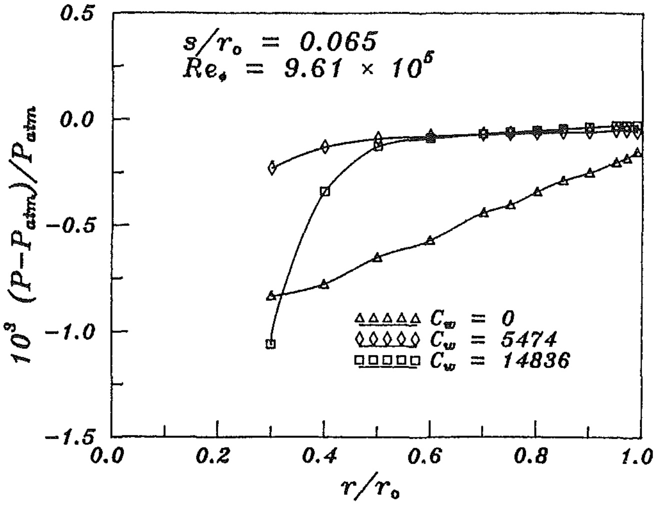

Fig. 13 Effect of throughflow rate on radial pressure distribution for unshrouded parallel disks

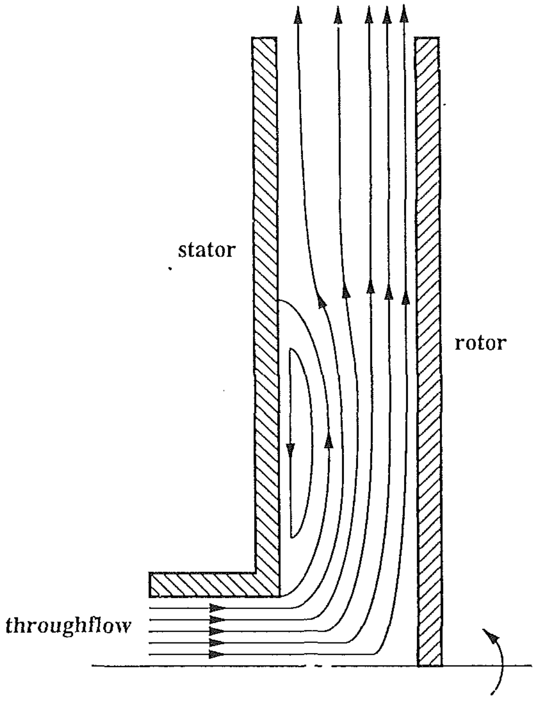

Fig. 14 Qualitative flow pattern for unshrouded parallel disks (G_{ca} = 0.005, G = 0.1, C_w = 5474)

P_{atm}, where P_{atm} is the atmospheric pressure outside the cavity. The pressure measurements were made differentially, with care being taken to locate the atmospheric pressure port sufficiently far from the experimental setup so that rotor windage effects were eliminated. It can be seen that the pressure decreases as the gap ratio decreases for all radial locations, and that the stator pressures are negative in all cases. The larger pressure gradients at lower gap ratios indicate larger magnitudes of the radial inward velocity components as the gap between the rotor and the stator is decreased.

The data shown in Fig. 12 were obtained for several different rotational Reynolds numbers at a constant gap ratio of 0.065. It is observed that the pressure decreases as the rotational Reynolds number increases. It can also be seen that the radial pressure gradient increases as the rotational Reynolds number increases, indicating a larger radial inflow along the stator, which in turn indicates a higher magnitude of disk pumping along the rotor, as expected.

When air is supplied at the centerline to produce a radially outward throughflow into the cavity between the two disks, the stator pressure distribution is altered considerably. This effect is shown in Fig. 13 for data measured at a gap ratio of 0.065 and a rotational Reynolds number of 9.61×10^5. Data for nondimensional flow rates of 5474 and 14,836 are compared with the no-throughflow data. It can be seen that at large radial locations pressure gradients and pressures both approach zero. At small radii, the local flow is dominated by the source flow. This suggests a recirculatory pattern at lower values of the radial coordinate as indicated qualitatively in Fig. 14.

Shrouded Disks

Static Pressure Measurements. In a recent review article, Owen (1988) suggests that, although some experimental work has been conducted to measure the effects of seal geometry and rotational speed on the sealing performance of simple rotor-stator systems, more corroborative investigations are necessary.

The plane disks discussed previously were shrouded to provide an axial seal gap that could be varied in size. Tests were conducted on axial clearance seals with gap ratio $G = 0.1$, and axial clearance ratios $G_{ca} = 0.005$, 0.01, and 0.0144. Pressure distributions at four values of rotational speeds and three values of coolant air flow rate were obtained in each case. Figures 15–17 show the effect of Reynolds number on dimensionless pressure difference, P^*, with the dimensionless radius, r/r_o, and variable G_{ca} and C_w.

The rotation of the disk creates a positive radial pressure gradient in the cavity. It is evident from the data that at a given flow rate C_w and axial gap ratio, G_{ca}, the pressure at any radius decreases with increasing rotational speed. Comparison of Figs. 15(*a*), 15(*b*), and 15(*c*) shows that at a given rotational Reynolds number and flow rate, C_w, the pressure level inside the cavity decreases with increase in G_{ca}. As observed by Owen (1988), negative values of P^* at r/r_0 values approaching unity indicate that there is ingress into the cavity through the seal. A set of data was also taken to determine the effect of change in gap ratio, G, on the variation of pressure level. It is seen from Figs. 15(*b*) and 18 that slight variation in gap ratio ($G = 0.113$) has no significant effect on the pressure inside the cavity. This confirms a similar observation made by Bayley and Owen (1970) that the rotor–stator gap was not a dominant factor in the range of gaps tested, which varied from 0.06 to 0.18.

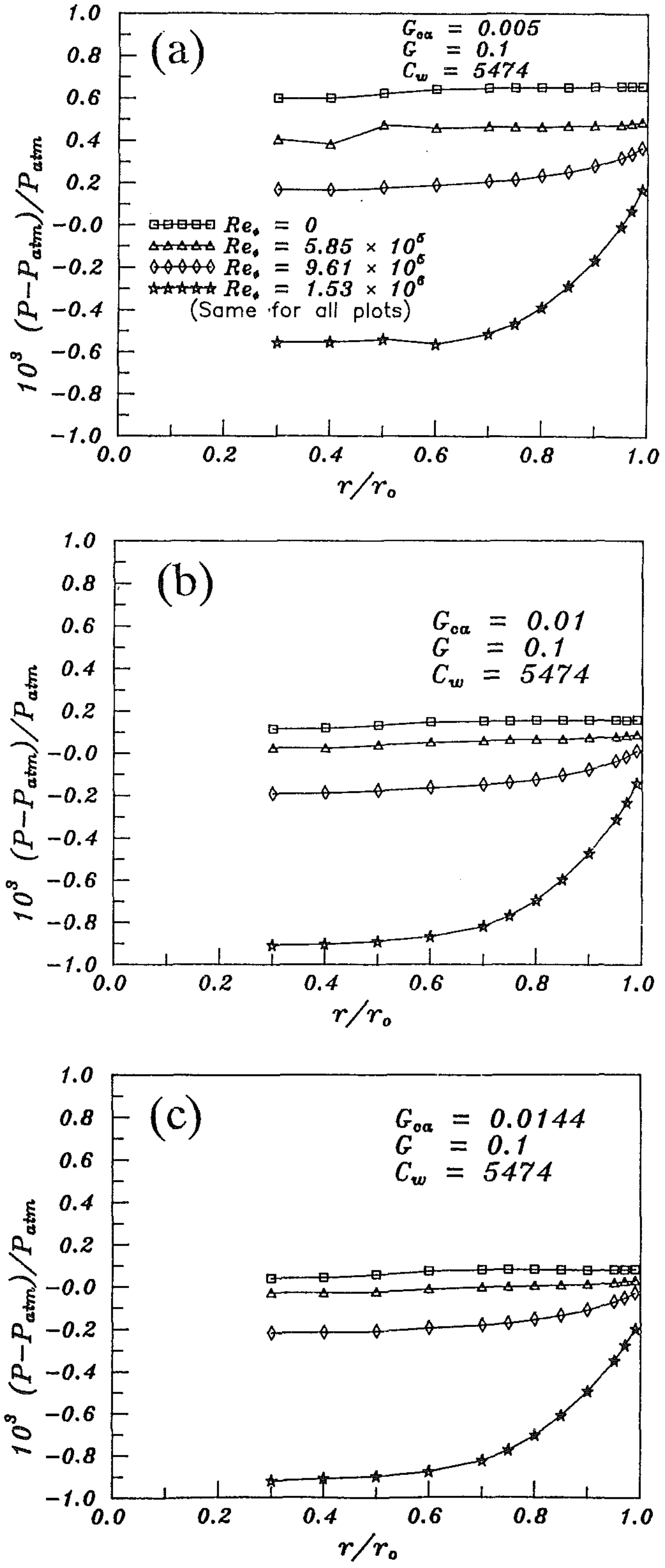

Fig. 15 Radial pressure variation with G = 0.1 and C_w = 5474: (*a*) G_{ca} = 0.005, (*b*) G_{ca} = 0.01, (*c*) G_{ca} = 0.0144

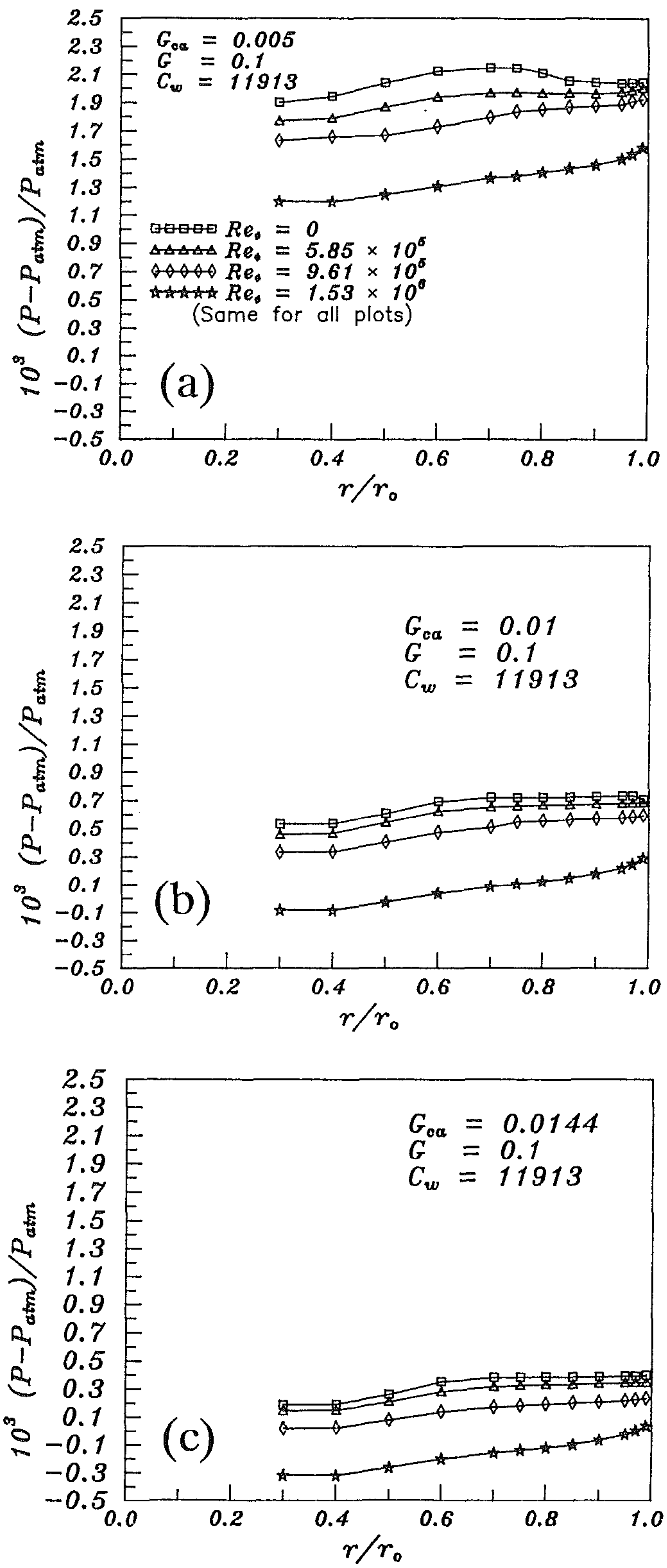

Fig. 16 Radial pressure variation with G = 0.1 and C_w = 11,913: (*a*) G_{ca} = 0.005, (*b*) G_{ca} = 0.01, (*c*) G_{ca} = 0.0144

Figure 19 presents a comparison of data obtained by Phadke and Owen (1983) for nearly identical geometric and flow conditions (G_{ca} and G were the same, but Re_ϕ differed by 2½ percent and C_w differed by 0.1 percent). It is seen that the Phadke and Owen data on pressure values are higher near the outer radius. Chew (1991) analyzed the Phadke and Owen data and concluded that a significant error had been made in the measurement of G_{ca} (0.005 in a value of 0.01). It is known that cavity pressures are very sensitive to the value of the seal gap. A comparison of Figs. 15(*a*) and 15(*b*) supports this.

Minimum Throughflow Rates. The minimum dimensionless throughflow, $C_{W\min}$, required to prevent ingress strongly depends on the pressure inside the cavity, which in turn depends on three parameters: rotational Reynolds number Re_ϕ, clear-

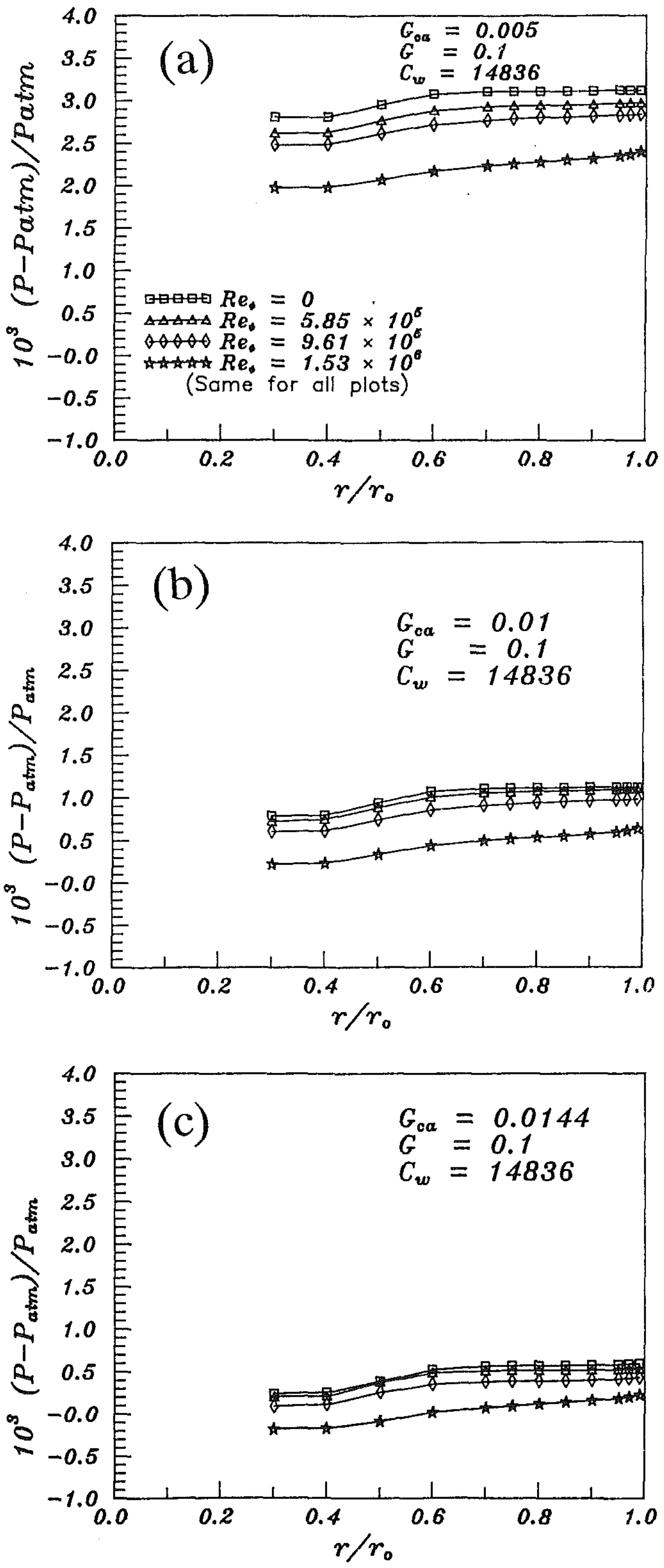

Fig. 17 Radial pressure variation with G = 0.1 and C_w = 14,836: (*a*) G_{ca} = 0.005, (*b*) G_{ca} = 0.01, (*c*) G_{ca} = 0.0144

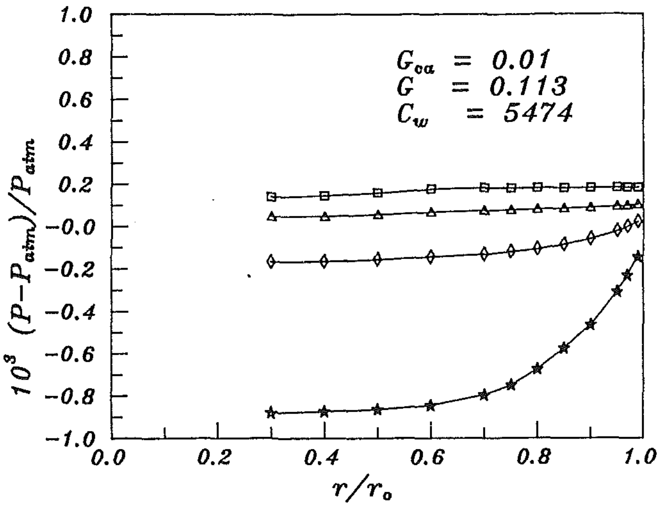

Fig. 18 Radial pressure variation with throughflow (G_{ca} = 0.01, G = 0.113, C_w = 5474)

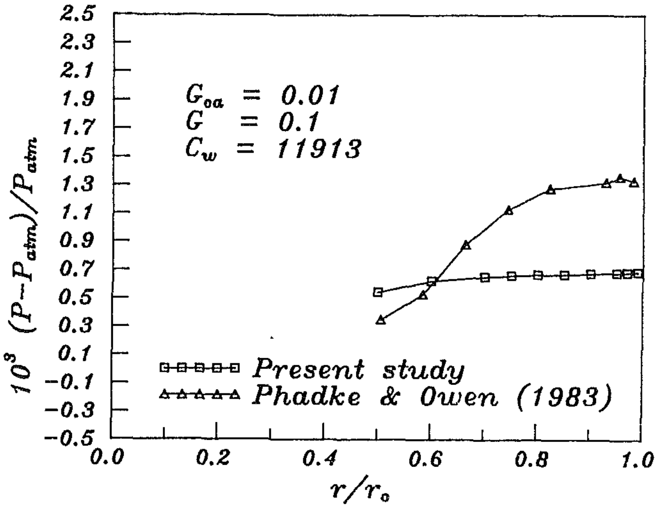

Fig. 19 Comparison of pressure variation with data of Phadke and Owen (1983)

ance ratio G_{ca}, and seal geometry. A generalized correlation for $C_{W\min}$ has been developed as a function of these parameters (Bayley and Owen, 1970). As indicated earlier, the gap ratio is not a strong parameter, when it is large enough to permit individual boundary layers to develop along both the rotating disk and the stationary disk.

Several different flow visualization techniques were employed in this study to identify the onset of ingress of exterior fluid into the cavity. Laser sheet illumination proved to be the most effective. The beam of a 5 mW He-Ne laser (Melles-Griot) was focused on a cylindrical lens (focal length of 5 mm) and the sheet of light was then directed at the clearance between the rotor and the shroud. Water vapor released adjacent to the shroud provided the necessary light scattering. The technique used to discern minimum flow rate was to increase the air supplied to the cavity incrementally while observing the flow pattern at the seal gap. Upon observing a flow reversal, $C_{W\min}$ was recorded.

Eleven data points were taken at three rotational Reynolds numbers and several different axial clearances as shown in Fig. 20. The data are well correlated by the expression

$$C_{W\min}=7.82\,G_{ca}^{0.677}\mathrm{Re}_{\phi}^{0.714}$$

Superimposed on this plot is the correlation obtained by Phadke and Owen (1988)

$$C_{W\min}=0.28G_{ca}^{0.677}\mathrm{Re}_{\phi}^{0.956}$$

The data conform well with the above prediction at $\mathrm{Re}_\phi = 10^6$ but the slopes are slightly lower than those of Phadke and Owen (1988). As can be seen, the dependence on the seal clearance is confirmed. Uncertainty bands on the present data are 1, 3, and 7 percent for Re_ϕ, $C_{W\min}$, and G_{ca}, respectively. The latter is primarily due to slight misalignment of the two disks and some offset in the radial direction of the shroud.

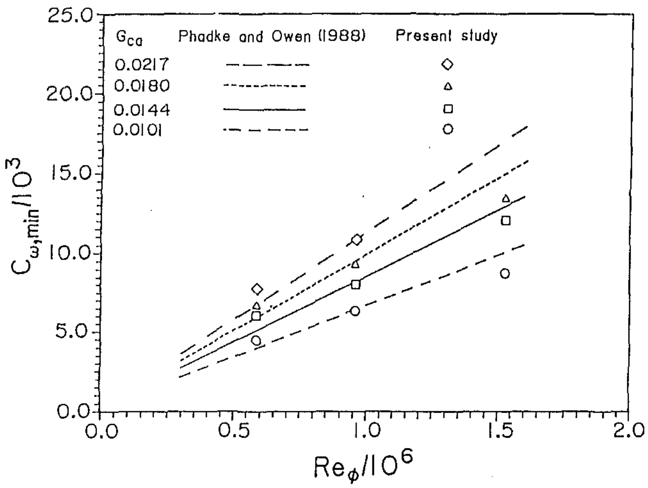

Fig. 20 Minimum throughflow rate as a function of the rotational Reynolds number for different axial clearance ratios

Conclusions

In summary, for the laminar free disk problem, theoretical solutions found by a similarity transformation were verified by experimental measurements. For the plane disk with no throughflow, the core of rotating fluid outside the boundary layers does not act like a rotating solid as in the case for an enclosed double sided disk. For this case, pressure measurements indicate a recirculatory zone at low values of the radial coordinate along the stator wall.

Some of the qualitative and quantitative results previously reported by Owen and his co-workers are verified by these experiments. The flow pattern between shrouded disks is a strong function of the seal clearance and the rotational Reynolds number, but is not strongly dependent on the gap between rotor and stator. Some pressure measurements obtained in an earlier study did not compare well with those obtained in the present study. It has been reported in the literature that the clearance measurements made in the earlier study may not have been correct. Measured minimum throughflow rates conform to previously published data at $Re_\phi = 10^6$ but differ somewhat at higher and lower Reynolds number.

Acknowledgments

Support for this contractual work provided by Alabama Electric Cooperative, Electric Power Research Institute, and the Dresser-Rand Corporation is gratefully acknowledged.

References

Bayley, F. J., and Owen, J. M., 1969, "Flow Between a Rotating and a Stationary Disc," *The Aeronautical Quarterly*, Vol. 20, pp. 333–354.

Bayley, F. J., and Owen, J. M., 1970, "The Fluid Dynamics of a Shrouded Disk System With a Radial Outflow of Coolant," ASME JOURNAL OF ENGINEERING FOR POWER, Vol. 92, pp. 335–341.

Chew, J. W., 1991, "A Theoretical Study of Ingress for Shrouded Rotating Disk Systems With Radial Outflow," ASME JOURNAL OF TURBOMACHINERY, Vol. 113, pp. 91–97.

Cochran, W. G., 1934, "The Flow Due to a Rotating Disk," *Proceedings of the Cambridge Philosophical Society*, Vol. 30, pp. 365–375.

Erian, F. F., and Tong, Y. H., 1971, "Turbulent Flow Due to a Rotating Disk," *Physics of Fluids*, Vol. 14, pp. 2588–2591.

El-Oun, Z. B., Neller, P. H., and Turner, A. B., 1988, "Sealing of a Shrouded Rotor-Stator System With Preswirl Coolant," ASME JOURNAL OF TURBOMACHINERY, Vol. 110, pp. 218–225.

Owen, J. M., and Phadke, U. P., 1980, "An Investigation of Ingress in a Simple Shrouded Rotating Disk System With a Radial Outflow of Coolant," ASME Paper No. 80-GT-49.

Owen, J. M., 1984, "Fluid Flow and Heat Transfer in Rotating Disc Systems," in: *Heat and Mass Transfer in Rotating Machinery*, D. E. Metzger and N. H. Afgan, eds., Hemisphere Publishing Co., Washington, DC, pp. 81–102.

Owen, J. M., 1988, "Air-Cooled Gas-Turbine Discs: a Review of Recent Research," *International Journal of Heat and Fluid Flow*, Vol. 9, No. 4, pp. 354–365.

Owen, J. M., and Rogers, R. H., 1989, *Flow and Heat Transfer in Rotating-Disc Systems, Vol. I, Rotor-Stator Systems*, Wiley, New York, pp. 125–136.

Phadke, U. P., 1983, "Flow Visualization in a Simple Rotor-Stator System With Throughflow," *Proceedings of the 3rd International Symposium on Flow Visualization*, Hemisphere Publishing Co., Washington, DC, pp. 728–732.

Phadke, U. P., and Owen, J. M., 1983, "An Investigation of Ingress for an 'Air-Cooled' Shrouded Rotating Disk System With Radial Clearance Seals," ASME *Journal of Engineering for Power*, Vol. 105, pp. 178–183.

Phadke, U. P., and Owen, J. M., 1988, "Aerodynamic Aspects of the Sealing of Gas Turbine Rotor-Stator System. Part 1: The Behavior of Simple Shrouded Rotating-Disc Systems in a Quiescent Environment," *International Journal of Heat and Fluid Flow*, Vol. 9, No. 2, pp. 98–105.

Schlichting, H., 1979, *Boundary Layer Theory*, 7th ed., McGraw-Hill Pub. Co., New York, pp. 102–107.

Uzkan, T., 1981, "Effects of Coolant Air Inlet Conditions on Turbulent Flow Between a Turbine Disk and Its Casing," ASME *Journal of Engineering for Power*, Vol. 103, pp. 637–644.

Uzkan, T., and Lipstein, N. J., 1986, "Effects of Honeycomb-Shaped Walls on the Flow Regime Between a Rotating Disk and a Stationary Wall," ASME *Journal of Engineering for Gas Turbines and Power*, Vol. 108, pp. 553–561.

W. Waschka

S. Wittig

S. Kim

Lehrstuhl und Institut für Thermische
Strömungsmaschinen,
Universität Karlsruhe (T.H.),
D-7500 Karlsruhe,
Federal Republic of Germany

Influence of High Rotational Speeds on the Heat Transfer and Discharge Coefficients in Labyrinth Seals

Heat transfer and leakage loss measurements were obtained for compressible flows in typical straight-through labyrinth seals with high rotational speeds. The experiments are an extension of our earlier measurements in a stationary test facility. In order to ensure direct comparisons to the original experiments, the principal dimensions of the test facility and gas dynamic parameters of the hot gas were kept similar. The new study encompasses a wide range of Taylor numbers, Reynolds numbers, and clearances between the rotating annular fins and the stationary shroud. Heat transfer coefficients are determined for the stator as well as for the rotor. Temperature measurements along the cooled rotor were performed utilizing a high-accuracy telemetric system. Continuous clearance control was achieved by employing specially designed gages. Detailed pressure and temperature measurements in the axial as well as in the circumferential direction were performed. Heat transfer coefficients and loss parameters are presented and compared with those obtained under steady-state conditions.

Introduction

Despite advanced techniques such as gas-film seals, labyrinths remain the most important and widely used sealing elements in turbomachinery since their introduction in steam turbines near the turn of the century. The main tasks of this contactless seal are to reduce the undesired leakage between the rotating and stationary components of the engine and to control the cooling air supply. A small clearance accommodates the differential thermal expansion between the rotating fins and the shroud as well as the centrifugal growth. Although this clearance allows parasitic losses, it guarantees a high durability of the seal. As the resulting leakage strongly influences the performance level of the engine, many theoretical and experimental studies have been done to understand the fluid mechanics of labyrinths. The earlier analytic and experimental attempts by Martin, Stodola, Egli, Komotori, and others are summarized in Trutnovsky's (1981) comprehensive book. Recent investigations are presented by Stocker (1978), Wittig (1982, 1987a, 1987b, 1988), Dörr (1985), Jacobsen (1987), and Schelling (1988). Wittig et al. (1987a, 1987b, 1988) and Schelling (1988) performed numerical computations of the flowfield inside the labyrinth seal, using a finite-volume computer code based on the time-averaged turbulent Navier-Stokes equations and the *k-e* turbulence model. In verifying the experimental results, Wittig et al. (1987a, 1987b, 1988) also solved the energy equation for the entire flowfield inside a straight-through and a stepped labyrinth seal. Utilizing the analogies between heat transfer and wall friction, local heat transfer coefficients could be derived. The heat transfer from the hot gas to the labyrinth components is another important aspect for seal design, especially for the thermal expansions and—if utilized— for the active clearance control. But there are also detrimental effects of the heat transfer on the required air cooling system in a blade that is in contact with the seal and also on the durability of the seal itself, caused by the high temperature gradients in the rotating fins. Heat transfer coefficients have been published only by a few authors, e.g., Sheinin (1961), Shvets et al. (1963), Kapinos and Gura (1970, 1973), Kuznezow and Zuravlov (1972), Metzger and Bunker (1985), Wittig et al. (1987a), Jacobsen (1987), and Schelling (1988).

However, most studies are based on the assumption that there is only a negligible effect of rotation on the leakage rate and heat transfer in labyrinth seals. Moreover, in most of the very few experiments including rotational effects, centrifugal growth and the thermal expansion was not measured and only in some cases considered theoretically. As the differential growth of rotor and stator often exceeds the cold stationary clearance, such a shortcoming results in significant uncertainties in the calculated characteristic values. Therefore, it is not surprising that some of the published results are not in good agreement. Becker (1907), apparently the first to consider this problem, found no rotational effects on the labyrinth flow. Friedrich (1933) measured a 20 percent leakage reduction in a straight-through labyrinth seal and Yamada (1962) observed

---

Contributed by the International Gas Turbine Institute and presented at the 35th International Gas Turbine and Aeroengine Congress and Exposition, Brussels, Belgium, June 11-14, 1990. Manuscript received by the International Gas Turbine Institute January 17, 1990. Paper No. 90-GT-330.

a maximum increase of the drag coefficient by a factor 10, if the flow was laminar; but rotation had little impact on the seal flow, as soon as the flow became turbulent. The leakage increased by 13 percent in Chi and Morrison's (1985) stepped seal but decreased by 9 percent in Stocker's (1978) seal toward higher rotational speeds.

The majority of the studies, examining the effect of rotation on the seal flow, have been done numerically. Stoff (1980) predicted the incompressible flow in a straight-through labyrinth seal, but the computed domain was restricted to a single cavity. The resulting data and the corresponding LDA measurements of mean swirl velocity in an enlarged water model differed by 7 percent. Demko et al. (1987) determined a second recirculating zone of the incompressible cavity flow at high rotational speeds. More details of the cavity flow were obtained by Demko et al. (1988) and Rhode et al. (1986, 1988). Their predictions are compared with hot-film measurements obtained in enlarged water models. The latest numerical and experimental work has been done by Wittig et al. (1989), examining rotational effects on the compressible flow as well as on heat transfer. Earlier heat transfer measurements were performed by the above mentioned authors, Sheinin, Shvets, Dyban, Khavin, Kapinos and Gura, but no significant effects of rotation were found. Recent studies by McGreehan et al. (1989) indicate a significant windage power dissipation for high speeds, which reduces the leakage mass due to the Raleigh line effect but augments the thermal load of the seal material.

Further, it is well known that in the absence of a dominant axial flow, rotation drastically augments the heat transfer (i.e., Patankar and Murthy, 1982) between the hot gas and the cooled labyrinth components.

Of course, the basic assumption that rotation has little impact on the seal flow is valid for many conditions, tested by numerous authors. However, despite the considerable quantitative differences in the measured rotational effects on the labyrinth flow and heat transfer, the studies have also demonstrated that rotation cannot be neglected at small axial Reynolds numbers and high Taylor numbers. While, in the past, there were few relevant applications, recent advances in seal design produce high-pressure labyrinth seals, which operate at high speed and low leakage rates. Furthermore, the shaft speed in modern turbomachinery becomes very high and the peripheral velocity of the tip of the fin reaches supersonic velocities in some cases. Active clearance control and special abradable coatings on the nonrotating stator allow tighter clearances and lead to lower leakage rates and higher ratios of axial to peripheral velocity. These developments require more accurate predictions for the design of modern engines, taking into account the geometry of the entire labyrinth. To verify numerical results and to improve available Navier-Stokes finite volume computer codes, detailed measurements under realistic conditions are required. The straight-through labyrinth seal was the first geometry studied in the present research; stepped and staggered labyrinths will follow.

Experimental Facility and Instrumentation

Our previously described test facility (Wittig et al., 1987a, 1987b, 1988), where plane configurations have been studied, was extended by a new test section for high rotational labyrinth seals. The test facility is shown schematically in Fig. 1. Air is supplied by compressors with a pressure ratio of 4.0 and a maximum mass flow of 0.5 kg/s. The supply pressure is kept constant at 3.5 bar by means of a bypass valve, which guarantees uniform conditions for mass flow measurements. The mass flow rate is determined by one of three orifice meters, applicable to the appropriate measurement range and connected to a precision water pressure gage. The electrical heater is designed for a maximum exit temperature of 400°C and can be controlled continuously from 0–150 kW. A specially designed settling chamber is used to obtain velocity and temperature profiles before entering the new test section, which is shown in Fig. 2. The thick-walled housing (position 5) of the test section is mounted directly behind the settling chamber. The flow exits via a large Carnot diffuser, which provides constant pressure conditions at the exit of the seal. The labyrinth seal in the test section consists of an inner rotating part (position 2) with six fins (diameter: 250 mm, pitch: 12 mm, thickness of the fins: 2.5 mm) and a stationary outer smooth part (position 4), the stator. Due to experimental requirements a scaled-up model (5:1) was used. Three stators with different inner diameters (251, 252, and 252.6 mm) were built to study clearance effects. The rotor consists of the shaft (position 1), the earlier mentioned inner part of the seal (position 2), and the seal supporters (position 3). Press-fittings are used to avoid small local displacements of the components after mounting. Also, a special rotor design was required to ensure a constant clearance distribution in the axial and azimuthal directions, during the diameter growth due to the centrifugal forces.

A "flying" rotor-support (both bearings are on the right-hand side of the seal) was chosen to provide undisturbed flow conditions at the entrance of the seal. The support also allows

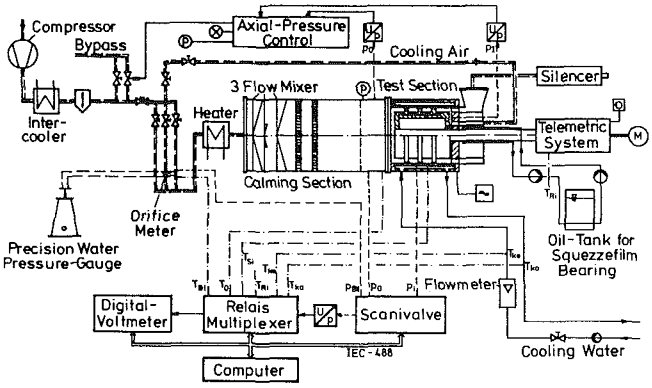

Fig. 1 Labyrinth seal test facility

Nomenclature

A = flow area, m^2
c = mass-averaged axial velocity, m/s
d = diameter of the fins, m
C_D = discharge coefficient
h = fin height, m
$\dot{m}_{\text{ideal}}$ = ideal mass flow rate
n = rotational speed, 1/min
p = pressure, N/m^2
$\dot{Q}_{\text{ideal}}$ = ideal flow function, $\sqrt{\text{kg K/kJ}}$

R = specific gas constant, kJ/kg K
r_w = radius of the cavity, m
s = gap width, m
t = pitch, m
u = peripheral velocity of the cavity, m/s
α = heat transfer coefficient, W/m^2

μ = dynamic viscosity, kg/m s
κ = isentropic coefficient
ρ = density, kg/m^3

Subscripts

crit = critical value
max = maximum value
meas = measured value
o = settling chamber
∞ = behind the seal

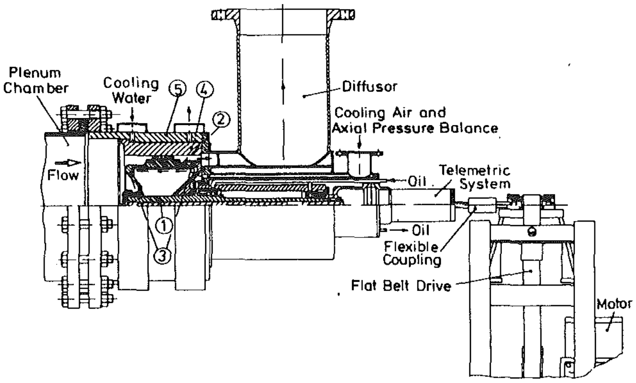

Fig. 2 Test section for rotating labyrinth seals

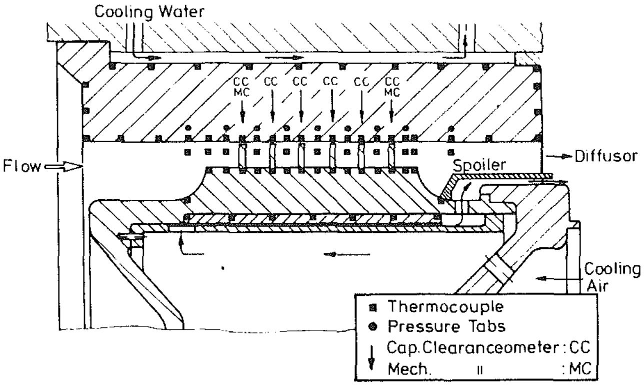

Fig. 3 Schematic instrumentation in one cross-sectional area

good exchangeability of the stators and there is no need for an extensive bearing cooling system, as both bearings are in the cold region of the test section. High-precision spindle bearings with an extremely small bearing play reduce rotor eccentricity and displacement to a minimum. Rotor dynamic vibrations are kept small, using an additional damping squeeze film between the outer bearing box and the housing (film thickness: 80 μm, damping coefficient: 2 Ns/mm). However, it should be mentioned that the squeeze film was built up only for speeds below the first critical speed (2500 rpm) while the outer bearing box is sitting on the housing. As a consequence, all measurements in this range of speed were done only with conventional bearing. To reduce the high axial pressure thrust on the bearings the air cooling system of the rotor, used for heat transfer measurements, was combined with a thrust balance. Therefore, the cooling air is led through channels in the housing to a chamber downstream of the rotor. Based on the measured pressures in the two opposing chambers and the relevant rotor regions, the rest load is calculated to adjust the pressure of the cooling air. Furthermore, the air flows into the rotor chamber and through the annular gap along the inner side of the rotating seal to the diffuser behind the seal. A spoiler is used to separate the cooling air and the leakage flow directly behind the seal.

Water was used as the cooling fluid for the heat transfer measurements on the stator. The annular gap for the water cooling is separated in several axial chambers. The water flow can be controlled by valves located at the exit of each chamber.

Instrumentation. Surface temperatures of the stator and rotor and the gas temperatures were measured by NiCr-Ni (Type J) thermocouples (diameter 0.5 mm). The stator was instrumented in three different cross sections, to provide information for the required water cooling and also about probable rotordynamic effects on heat transfer. The gas temperatures were also recorded at three different cross sections in the plenum chamber, in the center of each cavity and at the exit of the seal. The 27 thermocouples of the rotor are an integral to the rotating part of the telemetric system, which includes time-multiplexer, amplifier, temperature compensation, and frequency modulation of the signals. The modulated signals and a reference signal are sent to the stationary part of telemetric system demodulated and again separated. The uncertainty of the calibrated system is less than 1 K. The pressure distribution inside the seal was obtained in three different cross sections from pressure taps in the stator. All values, including the settling chamber pressure and the pressure behind the labyrinth seal, are determined by an absolute pressure gage in connection with a scanivalve. A precision water pressure gage was used in the case of small pressure differences over the seal. The principle instrumentation is shown in Fig. 3.

Clearance Measurements. A positive clearance measurement is one of the most critical elements for an accurate analysis and description of the measured heat transfer and the leakage losses, because centrifugal growth and thermal expansions reach at some cases 50 percent of the original clearance. Therefore, an extensive amount of work was done for exact clearance measurements. A total of ten capacitive clearanceometers and six mechanical gages are mounted in the stator above the fins of the rotor. Three mechanical and three capacitive clearanceometers are mounted above the first and the last fin, to compute in addition the eccentricity of the rotor. Above each of the other fins one further capacitive clearanceometer is available. The small fins (2.5 mm) and the relatively great gap (0.5, 1.0, and 1.3 mm) required a special, small designed sensitive area (0.8 mm–30 mm) of the clearanceometers. The operating temperature is limited by the isolation material to 250°C. The measurement frequency is 17 kHz. The mechanical gages are used only for control purposes. In Fig. 4 the entire fin-averaged gap width is presented as a function of the rotational speed for a cold gas and hot gas, for the pressure ratio 1.26. All pressure, temperature, and capacitive signals as well as the rotational speed are recorded by a data acquisition system and processed.

The rotor is driven by an electrical motor (maximum 3000 rpm) in connection with a flat belt drive (ratio 1:7). An extremely flexible coupling is located between the belt drive and the rotor. The entire facility and the data acquisition were tested, utilizing an annular gap geometry. The calculated discharge coefficients and heat transfer coefficients of the annular gab have been compared with literature values and excellent agreement obtained.

Experimental Results and Discussion

For direct comparisons with our earlier measurements in a stationary test facility (Wittig et al., 1987b), the same dimensionless mass flow parameter was used, to describe and analyze the labyrinth seal losses. The flow discharge coefficient is defined as

$$C_D = \frac{\dot{m}_{\text{meas}}}{\dot{m}_{\text{ideal}}} \tag{1}$$

where $\dot{m}_{\text{ideal}}$ is determined as the mass flow through an ideal nozzle, with the same cross-sectional flow area as in the gap of the labyrinth seal and same entire pressure ratio. $\dot{m}_{\text{ideal}}$ is calculated in the usual way:

$$\dot{m}_{\text{ideal}} = \frac{\dot{Q}_{\text{ideal}} \cdot p_o \cdot A}{\sqrt{T_o}} \tag{2}$$

with

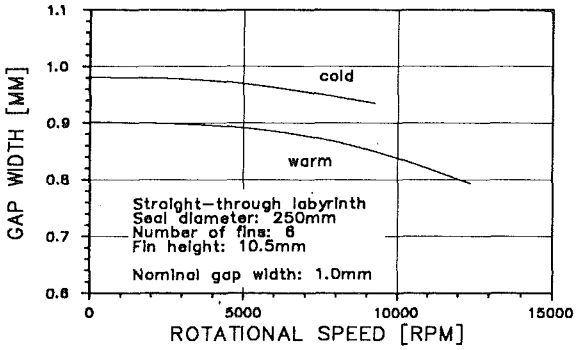

Fig. 4 The influence of rotational speed on the gap width

$$\dot{Q}_{\text{ideal}} = \left(\frac{p_\infty}{p_o}\right)^{\frac{1}{\kappa}} \sqrt{\frac{2\kappa}{R\cdot(\kappa-1)}\left[1-\left(\frac{p_\infty}{p_o}\right)^{\frac{\kappa-1}{\kappa}}\right]} \tag{3}$$

for subcritical pressure ratios. For supercritical pressure ratios the value of $\dot{Q}_{\text{ideal}}$ is equal to the maximum value at

$$\left(\frac{p_\infty}{p_o}\right)_{\text{crit}} = \left(\frac{2}{\kappa+1}\right)^{\frac{\kappa}{\kappa-1}} \tag{4}$$

The actual, speed-dependent cross-sectional area is determined by averaging the continuously measured clearances as described.

The local heat transfer coefficient is derived from

$$\alpha = \frac{d\dot{Q}}{dA\cdot(T_G - T_W)} \tag{5}$$

with

$$d\dot{Q} = -\lambda\cdot\nabla\cdot T|_{\text{wall}} \tag{6}$$

The local heat flux $d\dot{Q}$ is determined from the two-dimensional temperature distribution in the stator and the rotor. The temperature distribution is calculated from the wall temperatures, utilizing a finite-element program. The wall temperatures T_W at each boundary knot of the finite-element net are interpolated from local measured values by rational spline functions. The gas temperature T_G was also determined from local measurements. For the fin region, the calculated heat transfer coefficient is equivalent to a fin heat transfer coefficient, as the only fin temperature ($T_W = T_{Wr}$) was measured in the fin root. In addition, mean heat transfer coefficients were calculated by averaging the local values. The averaged coefficients for the stator refer to the total flow exposed surface, whereas the averaged coefficients for the rotor describe the total heat flux normalized to the rotor surface without fins. The reference gas and wall temperatures have been averaged from the local values. The rotational effect is described by the ratio of the Taylor number to the axial Reynolds number. These dimensionless numbers are defined as

$$Ta = \frac{u_w\cdot 2\cdot s}{\nu}\sqrt{\frac{s}{r_w}}; \qquad \text{Re} = \frac{\dot{m}_{\text{meas}}}{\bar{\mu}\cdot\pi\cdot r_w} \tag{7}$$

This combination can be regarded as the ratio of axial to peripheral momentum. However, it should be kept in mind that the application of the Taylor number as a criterion for stable operations is only valid for flows between rotating cylinders. While the well-known Taylor vortices in annular gaps are caused by hydrodynamic instabilities, the origin of a second recirculation zone in the labyrinth cavity is due to the boundary conditions at the rotating fins. As a consequence, it can be expected that the rotational effects are strongly dependent on the labyrinth seal geometry, especially the cavity design. For the experimental procedure discussed, the rotational speed was varied for each pressure ratio selected. In order to achieve comparability with our earlier experiments in flat models (scale 5:1), Fig. 5 presents the experimentally derived discharge coefficients without rotation as a function of the pressure ratio and the gap width. Considering side wall effects in the flat model, the agreement is excellent. The pressure distribution, geometry variations and scaling effects are discussed elsewhere by Wittig et al. (1982, 1987a, 1987b, 1988).

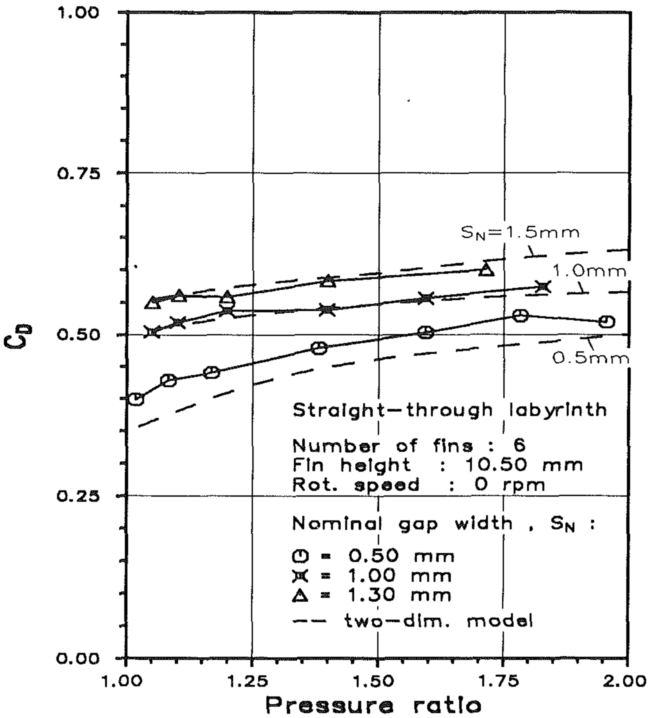

Fig. 5 Discharge coefficients without rotation; comparison with the two-dimensional models

Figures 6, 7, and 8 show the influence of rotational speeds on the discharge coefficients as a function of the Reynolds number. A large decrease of the discharge coefficients toward higher rotational speeds is evident at low Reynolds numbers. At the smallest Reynolds number (Re = 2000) and highest speed (10,000 rpm) a 25 percent reduction of the discharge coefficient was obtained. The comparison between Figs. 6, 7, and 8 reveals an upper limit of the rotational effects at Reynolds numbers of approximately 5000 to 10,000, depending on the clearance. The limiting Reynolds number seems to increase with increasing clearance. This behavior agrees with the results of Yamada (1962), who measured a strong dependence of the resistance coefficients from the ratio s/r_w. Another interesting observation, regarding the limiting Reynolds numbers, is that these values coincide fairly well with our earlier measurements with the stationary test facility, indicating a transition along the smooth stator wall from laminar to turbulent flow at Reynolds numbers of approximately 6000. This also confirms the results of Yamada for a flow between rotating coaxial cylinders with rectangular grooves, as far as his results show a dramatic increase of the resistance coefficient with increasing rotational speeds, when the flow was laminar, but only a negligible effect if the flow was already turbulent. It seems that, although in purely laminar flows, axial and peripheral flow components are first independent of each other leading only to an increase of the shaft torque, beyond a certain critical peripheral speed a second vortex originates, which drastically augments the flow resistance. Although, in turbulent flows, axial and peripheral flow components are no longer independent and there is a continuous increase of turbulence with higher rotational speeds, it should be noted that a high azimuthal velocity is required,

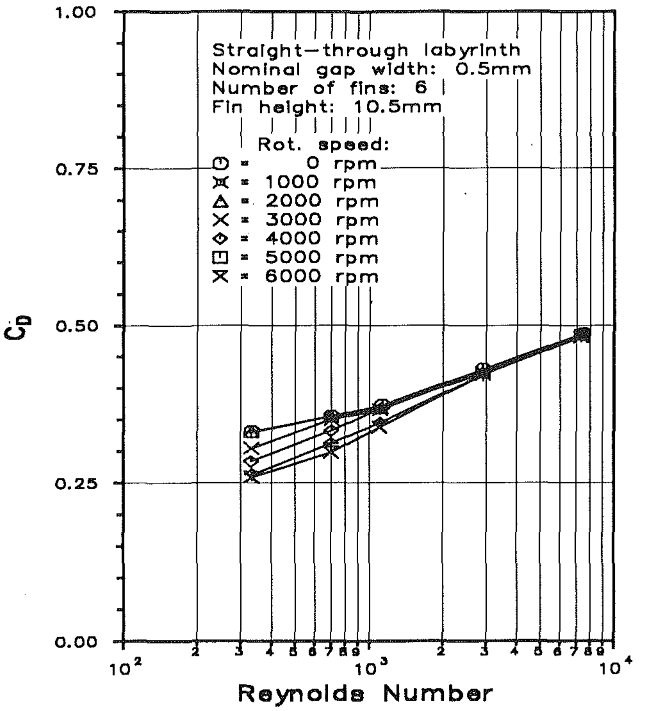

Fig. 6 Rotational effects as a function of Reynolds number ($s_N = 0.5$ mm)

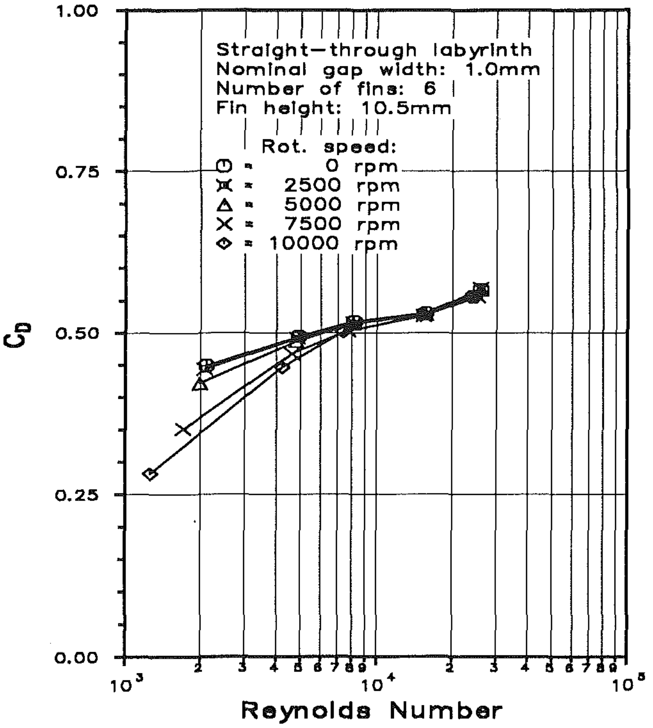

Fig. 7 Rotational effects as a function of the Reynolds number ($s_N = 1.0$ mm)

indicated by the peripheral-to-axial momentum, to obtain a domination of the swirl. Otherwise, the dividing stream line between the main stream and the cavity flow is shifted more and more outward due to the increasing centrifugal forces as shown by Demko et al. (1987), thus increasing the carry-over effect, as the stagnation point at the downstream cavity wall also shifts outward. However, if a second vortex is established at very high shaft speeds, an increase of flow resistance can be expected. This however is not in relevance in most technical applications. Figures 9, 10, and 11 indicate the influence of the momentum ratio, including the geometry-factor s/r_w for general physically similarity, on the discharge coefficients. A comparison between these figures reveals a critical ratio $Ta/\mathrm{Re}_{\mathrm{crit}}$ of approximately 0.2 for all clearances. Demko et al. (1987) computed a critical value of 0.9 for the incipience of a second vortex. Demko's prediction was based on measured inlet boundary conditions of a cavity. Although the ratio $s/r_w = 0.178$ mm/38.6 mm of Demko's seal is similar to our ratio $s/r_w = 0.5$ mm/114.5 mm, Demko's cavity is 75 percent tighter, which increases the resistance against an origination of a second recirculation flow. A final clarification of this problem is expected from our momentary numerical investigations, regarding rotational effects on the flow and the heat transfer in the same labyrinth geometries as used for the experimental part of our studies.

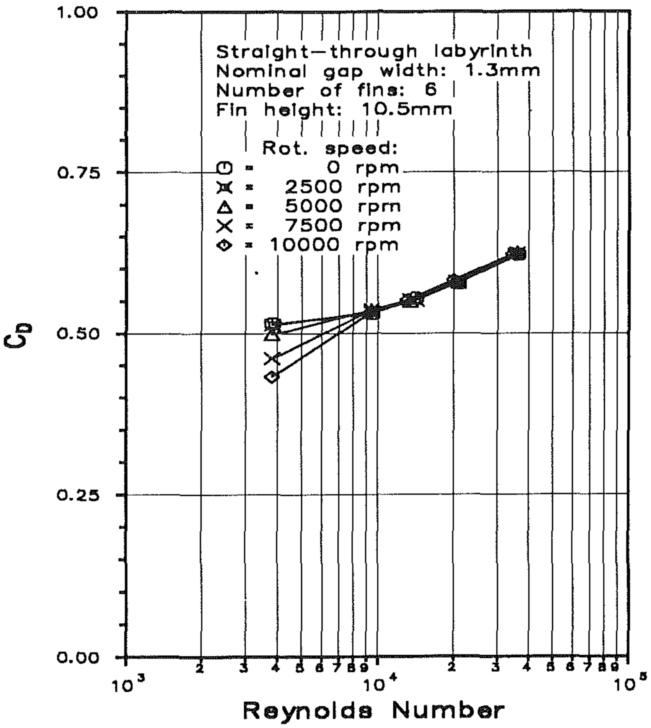

Fig. 8 Rotational effects as a function of the Reynolds number ($s_N = 1.3$ mm)

The influence of rotation on heat transfer is presented in Fig. 12, for the nominal clearance $s_N = 1.0$ mm. In Fig. 12(*a*), the determined global Nusselt numbers for the rotor and the stator, without rotation, are compared with our earlier measurements in a flat model. The data obtained from the three-dimensional model agree very well with those obtained from the two dimensional model. The relative increase of the Nusselt number, based on the Nusselt number achieved at no rotation, is shown in Fig. 12(*b*) as a function of the ratio Ta/Re. The increase of the Nusselt number starts approximately at a ratio $Ta/\mathrm{Re} = 0.1$ and reaches a factor of three at a maximum speed and the smallest Reynolds number. The rotational effects are slightly higher on the rotor than on the stator. The distributions of the local heat transfer coefficients on the labyrinth surface of the rotor and the stator are plotted in Figs. 13 and 14, respectively, for a pressure ratio of 1.26. It should be noted that the computed values at the fin root of the rotor (Fig. 13) are fin heat transfer coefficients as described earlier. Thus they are a good indication for rotational effects on the local heat flux and also on the global heat transfer. The local heat flux is highest at the root of the fins.

At the stator, the highest rise of the heat transfer is observed upstream of the labyrinth entrance. Here the axial velocity is

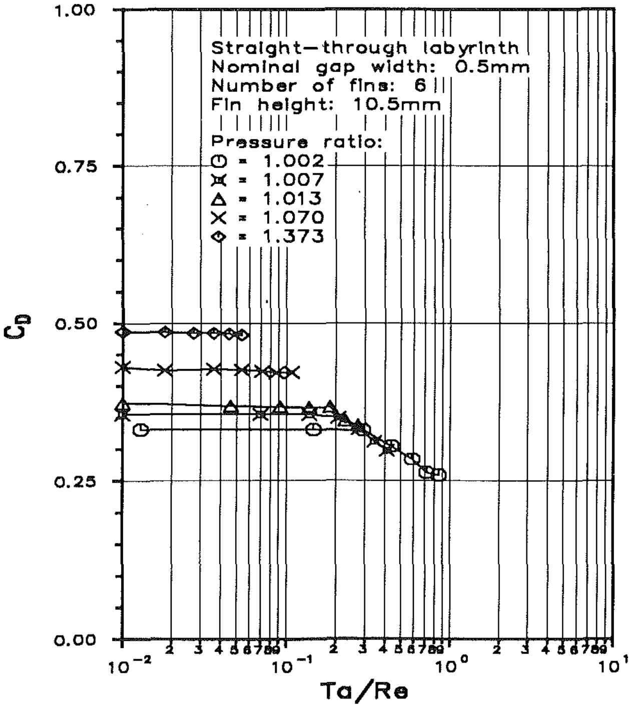

Fig. 9 Rotational effects on the discharge coefficients as a function of the ratio *Ta*/Re ($s_N = 0.5$ mm)

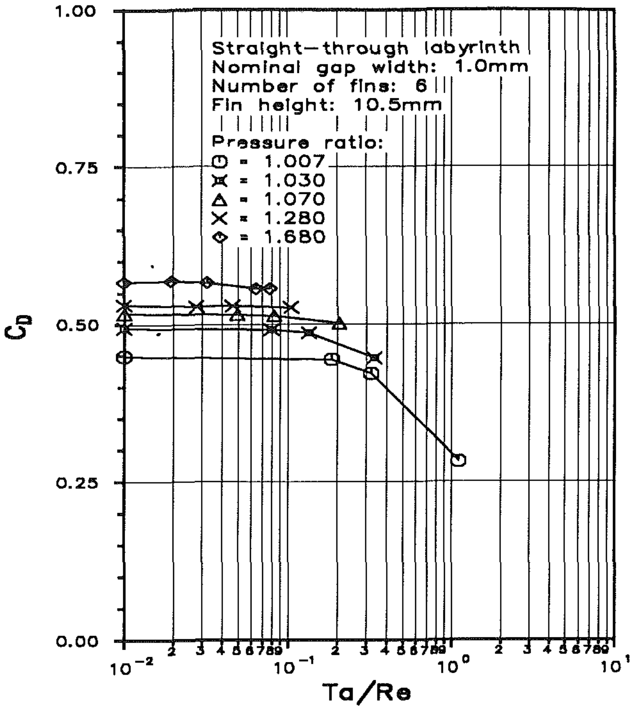

Fig. 10 Rotational effects on the discharge coefficients as a function of the ratio *Ta*/Re ($s_N = 1.0$ mm)

relatively small and thus, the heat transfer is dominated by the preswirl. Due to the high acceleration of the flow at the entrance of the first fin, the influence of the swirl decreases drastically. The heat transfer distribution indicates a maximum above the fins and an increase of 12,400 rpm, or about 10 percent, compared to the nonrotating case.

Summary

A new test facility was presented, where heat transfer and leakage rate measurements for compressible flows in a straight-through labyrinth seal with high rotational speeds have been performed. Heat transfer coefficients have been experimentally determined for the stator as well as for the rotor, utilizing a high-accuracy telemetric system. Specially designed capacitive clearance gages guarantee a detailed continuous clearance measurement.

Heat transfer and discharge coefficients under steady-state conditions agree very well with earlier measurements in a two-dimensional model. The results show a significant effect of the rotation beyond a ratio *Ta*/Re of approximately 0.2, which reduces the leakage rate and increases the heat transfer. Future work is directed toward experimental and numerical investigations of stepped and staggered labyrinth seals.

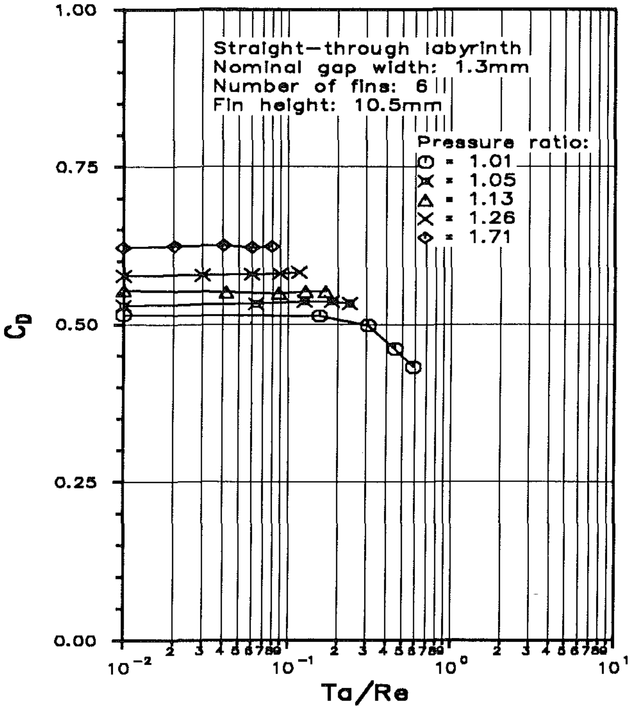

Fig. 11 Rotational effects on the discharge coefficients as a function of the ratio *Ta*/Re ($s_N = 1.3$ mm)

References

Becker, E., 1907, "Strömungsvorgänge in ringförmigen Spalten und ihre Beziehung zum Poiseuilleschen Gesetz," *VDI-Forschungsheft 48*, VDI-Verlag, Berlin, pp. 1–42.

Chi, D., and Morrison, G. L., 1985, "Incompressible Flow in Stepped Labyrinth Seals," ASME Paper No. 85-FE-4.

Demko, J. A., Morrison, G. L., and Rhode, D. L., 1987, "Effect of Shaft Rotation on the Incompressible Flow in a Labyrinth Seal," *Proc. of the 5th International Conference on Numerical Methods in Laminar and Turbulent Flow*, Canada.

Demko, J. A., Morrison, G. L., and Rhode, D. L., 1988, "Prediction and Measurement of Incompressible Flow in a Labyrinth Seal," 26th Aerospace Sciences Meeting, Paper No. AIAA-88-0190.

Dörr, L., 1985, "Modellmessungen und Berechnungen zum Durchflussverhalten von Durchblicklabyrinthen unter Berücksichtigung der Übertragbarkeit," Dissertation, Institut für Thermische Strömungsmaschinen der Universität Karlsruhe, Federal Republic of Germany.

Friedrich, H., 1933, "Untersuchungen über das Verhalten der Schaufelspaltdichtungen in Gegenlauf-Dampfturbinen," Dissertation, Institut für Thermische Strömungsmaschinen der Universität Karlsruhe, Federal Republic of Germany.

Jacobsen, K., 1987, "Experimentelle Untersuchungen zum Durchfluss und Wärmeübergang in Durchblick- und Stufen-labyrinthdichtungen," Dissertation, Institut für Thermische Strömungsmaschinen der Universität Karlsruhe, Federal Republic of Germany.

Kapinos, V. M., and Gura, L. A., 1970, "Investigation of Heat Transfer in Labyrinth Glands on Static Models," *Thermal Engineering*, Vol. 17, No. 11, pp. 53-56.

Kapinos, V. M., and Gura, L. A., 1973, "Heat Transfer in a Stepped Labyrinth Seal," *Teploenergetika*, Vol. 20, No. 6, pp. 22-25.

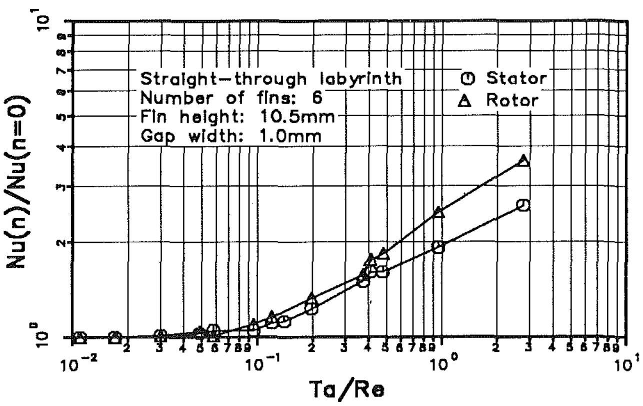

Fig. 12(*a*) Global Nusselt numbers; comparison with the results of the two-dimensional models

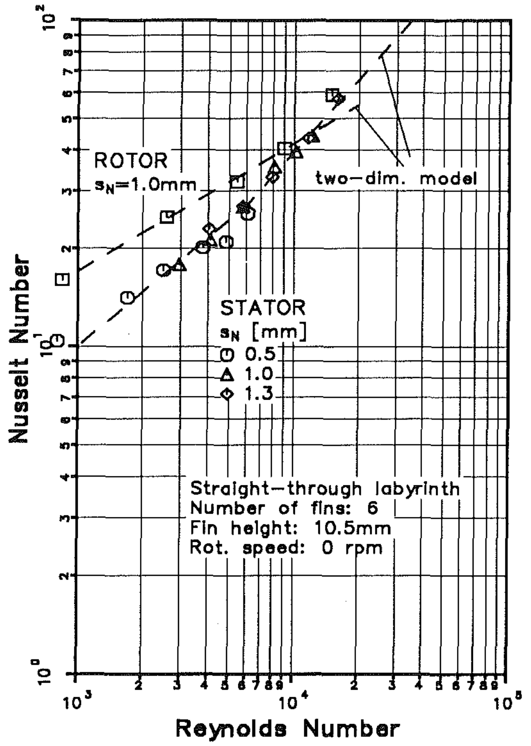

Fig. 12(*b*) Rotational effects on the global Nusselt numbers as a function of the ratio *Ta*/Re (s_N = 1.0 mm)

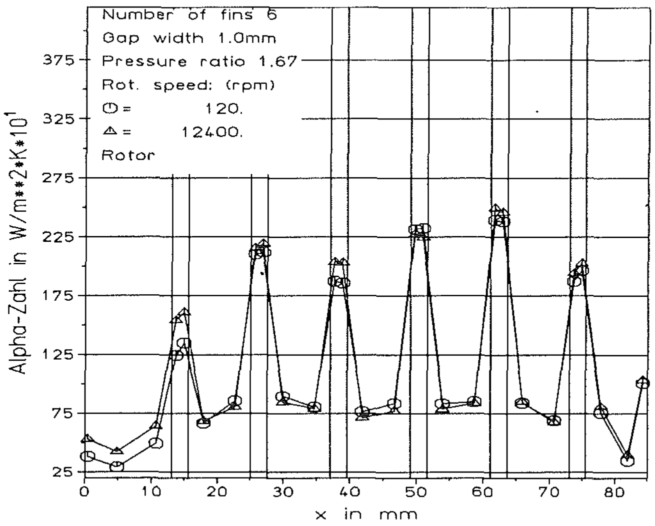

Fig. 13 Local heat transfer coefficients for the rotor (s_N = 1.0 mm)

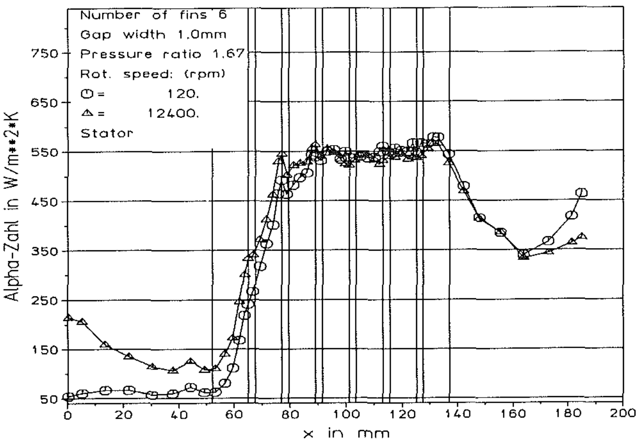

Fig. 14 Local heat transfer coefficients for the stator (s_N = 1.0 mm)

Kuznezov, A. L., and Zuravlov, O. A., 1972, "Wärmeübergang in den Labyrinthdictungen von Gasturbinen," *Energomashinostroenie*, No. 5, pp. 10–12 [in Russian].

McGreehan, W. F., and Ko, S. H., 1989, "Power Dissipation in Smooth and Honeycomb Labyrinth Seals," ASME Paper No. 89-GT-220.

Metzger, D. E., and Bunker, R. S., 1985, "Heat Transfer for Flow Through Simulated Labyrinth Seals," presented at the Symposium on Transport Phenomena in Rotating Machinery, USA.

Patankar, S. V., and Murthy, J. Y., 1982, "Analysis of Heat Transfer From a Rotating Cylinder With Circumferential Fins," presented at the Symposium on Heat and Mass Transfer in Rotating Machinery, Dubrovnik, Yugoslavia.

Rhode, D. L., and Hibbs, R. I., 1986, "A Comparative Investigation of Corresponding Annular and Labyrinth Seal Flowfields," ASME Paper No. 89-GT-195.

Rhode, D. L., Demko, S. H., and Morrison, G. L., 1988, "Numerical and Experimental Evaluation of a New Low-Leakage Labyrinth Seal," 24th Joint Propulsion Conference, Boston, Paper No. AIAA/ASME 88-2884.

Schelling, U., 1988, "Numerische Berechnung kompressibler Strömungen mit Wärmeübergang in Labyrinthdichtungen," Dissertation, Institut für Thermische Strömungsmaschinen der Universität Karlsruhe, Federal Republic of Germany.

Sheinin, E. I., 1961, "Experimentelle Untersuchung des Wärmeübergangs in der Zone der Endabdichtung der Gasturbinen," *Energomashinostroenie*, No. 1, pp. 25–27 [in Russian].

Shvets, I. T., Khavin, V. Y., and Dyban, E. P., 1963, "Heat Exchange in Labyrinth Seals of Turbine Rotor," *Energomashinostroenie*, Vol. 12, pp. 8–12 [in Russian].

Stocker, H. L., 1978, "Determining and Improving Labyrinth Seal Performance in Current and Advanced High Performance Gas Turbines," AGARD-CP-237.

Stoff, H., 1980, "Incompressible Flow in a Labyrinth Seal," *Journal of Fluid Mechanics*, Vol. 100, Part 4, pp. 817–829.

Trutnovsky, K., 1981, *Berührungsfreie Dichtungen*, VDI-Verlag, Düsseldorf, Federal Republic of Germany.

Wittig, S. L. K., Dörr, L., and Kim, S., 1982, "Scaling Effects on Leakage Losses in Labyrinth Seals," ASME *Journal of Engineering for Power*, Vol. 104, pp. XX–00.

Wittig, S. L. K., Jacobsen, K., Schelling, U., and Kim, S., 1987a, "Experimentelle und theoretische Untersuchungen zum Durchflussverhalten und Wärmeübergang in Labyrinthen," *Abschlussbericht FVV*, Vorhaben No. 293, Vol. 391, p. 343.

Wittig, S. L. K., Schelling, U., Kim, S., and Jacobsen, K., 1987b, "Numerical Predictions and Measurements of Discharge Coefficients in Labyrinth Seals," ASME Paper No. 87-GT-188.

Wittig, S. L. K., Jacobsen, K., Schelling, U., and Kim, S., 1988, "Heat Transfer in Stepped Labyrinth Seals," ASME *Journal of Engineering for Gas Turbines and Power*, Vol. 110, pp. 63–69.

Wittig, S. L. K., Waschka, W., and Scherer, T., 1989, "Einfluss der Rotation auf das Durchflussverhalten und den Wärmeübergang in Labyrinthdichtungen," *FVV-Informationstagung*, Bad Orb.

Yamada, Y., 1962, "On the Pressure Loss of Flow Between Rotating Coaxial Cylinders With Rectangular Grooves," *Bull. of JSME*, Vol. 5, No. 20, pp. 642–651.

An Experimental Investigation of Nozzle-Exit Boundary Layers of Highly Heated Free Jets

J. Lepicovsky
Senior Supervisor,
Sverdrup Technology, Inc.,
NASA Lewis Research Center Group,
Brook Park, OH 44142

An experimental investigation of the effects of nozzle operating conditions on the development of nozzle-exit boundary layers of highly heated air free jets is reported in this paper. The total pressure measurements in the nozzle-exit boundary layer were obtained at a range of jet Mach numbers from 0.1 to 0.97 and jet total temperatures up to 900 K. The analysis of results shows that the nozzle-exit laminar boundary-layer development depends only on the nozzle-exit Reynolds number. For the nozzle-exit turbulent boundary layer, however, it appears that the effects of the jet total temperature on the boundary-layer integral characteristics are independent from the effect of the nozzle-exit Reynolds number. This surprising finding has not yet been reported. Further, laminar boundary-layer profiles were compared with the Pohlhausen solution for a flat-wall converging channel and an acceptable agreement was found only for low Reynolds numbers. For turbulent boundary layers, the dependence of the shape factor on relative Mach numbers at a distance of one momentum thickness from the nozzle wall resembles Spence's prediction. Finally, the calculated total pressure loss coefficient was found to depend on the nozzle-exit Reynolds number for the laminar nozzle-exit boundary layer, while for the turbulent exit boundary layer this coefficient appears to be constant.

1 Study Objective

Boundary layer development along a solid surface has a decisive effect on local heat transfer rate to the solid body. In nozzle flows, the jet development and jet plume spreading and mixing rates are strongly affected by the nozzle-exit boundary layer state and parameters [1]. In spite of wide engineering application of nozzle flow and heat transfer processes, there is a lack of experimental data in the available literature on boundary layer development in highly heated flows, contrary to the preponderance of data on boundary layer development in flows with nonelevated temperatures.

An objective of this experimental study was to investigate the effects of jet operating conditions on the nozzle-exit boundary-layer development. Investigation of nozzle-exit boundary-layer characteristics was a separate subtask of a large NASA funded research effort on control and enhancement of hot jet mixing [1, 2]. The author hopes that the presented results will contribute to the public domain database on nozzle-exit boundary-layer characteristics of highly heated air free jets.

2 Experimental Configuration

2.1 Test Facility. The reported experiments were conducted in Lockheed's Jet Flow Facility, shown in Fig. 1. The facility consists of a 256-mm-dia plenum, followed by an initial contraction to a 102-mm-dia, 690-mm-long supply duct. The stainless steel converging nozzle with a sharp nozzle lip is mounted to the supply duct. The nozzle exit diameter is 50.8 mm, its length is 178 mm, and the nozzle "sink" distance is also 178 mm. The nozzle "sink" distance is defined as the distance from the nozzle exit plane to a vertex of a cone determined by the nozzle length and inlet and exit diameters (Fig. 2). Coordinates of the nozzle inner contour are given in Table 1. The plenum-to-nozzle contraction ratio is 25.

The flow facility is supplied by compressed air and may be heated by a throughflow propane burner up to 1000 K at pressure ratios up to 4. To minimize the wall heat flux, the plenum is lined with 25-mm-thick Kaowool insulation. The supply duct and test nozzle, however, are not thermally insulated.

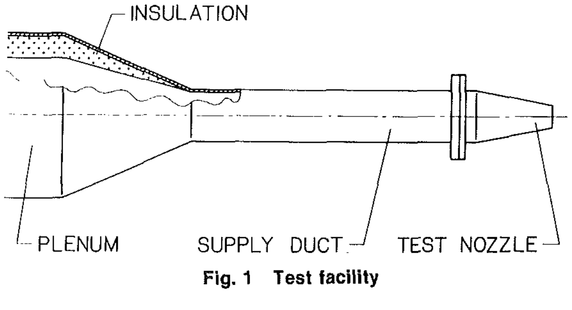

Fig. 1 Test facility

Contributed by the International Gas Turbine Institute and presented at the 35th International Gas Turbine and Aeroengine Congress and Exposition, Brussels, Belgium, June 11-14, 1990. Manuscript received by the International Gas Turbine Institute January 15, 1990. Paper No. 90-GT-255.

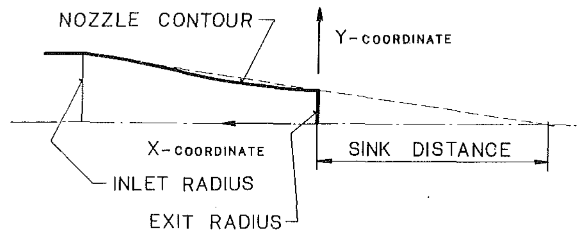

Fig. 2 Test nozzle geometry

Table 1 Nozzle inner contour coordinates

x (mm)	0	9	25	37	45	64	76
y (mm)	25.4	25.4	25.9	26.9	27.8	30.8	32.9
x (mm)	89	101	121	140	155	165	178
y (mm)	35.2	37.3	41.0	44.4	47.0	48.7	50.8

x - distance from the nozzle exit plane

y - radius of the nozzle inner surface

2.2 Jet Operating Conditions. During the experiments, the jet was operated at a broad range of exit velocities and flow total temperatures. The Mach number range was varied from 0.1 to 0.97 and the total temperature ranged from unheated jets (285 K) to jets heated up to 900 K. The jet was discharged into still air at ambient temperature. During the boundary-layer traversing, the jet operating conditions were kept as steady as possible. However, a slow drift was sometimes experienced; the maximum standard deviations of plenum total pressure and total temperature from the nominal values during the entire program are shown in Table 2.

Throughout this paper, the nozzle operating conditions are expressed as a jet Reynolds number, Re_S, which is based on the jet core velocity, kinematic viscosity based on the jet static temperature, and nozzle sink distance, which is based on the analogy between the converging nozzle flow and the flow in a flat-wall converging channel [3]. The author believes that for the nozzle boundary layer development, the sink distance is a more suitable geometric characteristic than the nozzle exit diameter, because it allows a comparison among nozzles of various shapes and diameters.

2.3 Instrumentation. Three pressures and two temperatures were continuously monitored during the experiments. They were plenum total pressure, static pressure upstream of the test nozzle, the boundary-layer local total pressure, the plenum total temperature, and ambient temperature. In addition, the ambient pressure was read before each test set.

United Sensor probes were used for the total pressure measurements; a PAC-12-KL probe for the plenum total pressure and a BR-020-12-C-11 probe for the boundary-layer total pressure. The boundary layer probe has a hook-shaped sensing stem of 0.5-mm diameter with a flattened tip to minimize the shift in the effective center. The tip is 0.7 mm wide and 0.25 mm high. The height of the inner sensing slit is 0.05 mm. A wall tap was used to measure the static pressure in front of the test nozzle. Validyne pressure transducers P305D, rated ±220 kPa and ±86 kPa, were used in connection with the probes for jet exit Mach numbers above 0.4. For the nozzle operating conditions below Mach number 0.4, transducers rated at ±8.6 kPa and ±3.5 kPa were used.

Table 2 Maximum standard deviations of total pressures and total temperatures from nominal nozzle operating conditions

Jet Mach number	< 0.3	0.3 - 0.7	> 0.7
Total pressure	135 Pa	300 Pa	430 Pa
Total temperature	3.2 K	2.2 K	1.9 K

The plenum total temperature and ambient temperature were measured by Omega thermocouple probes CAIN-18U-12. The thermocouple readings were converted to the Kelvin scale using the multi-input process monitor Digi-Link (model LK-S) from Kaye Instruments.

A two-component positioner, attached to the nozzle flange, moved the boundary layer probe in axial and radial directions. The positioner utilizes two Velmex metric traversers (Unislide) driven by electric stepper motors (200 steps/rev). Driving electronics for the steppers consisted of Superior Electric Modulynx motion control system interfaced to a Digital Equipment VAX 11/750 computer.

The entire data acquisition process, including probe traversing, was fully automated and controlled by the facility dedicated VAX 11/750 computer. The acquired pressure and temperature data were reduced on line and converted to engineering units. Nozzle exit conditions, Mach number, jet exit velocity, and flow temperature were continuously displayed on a computer terminal. All the acquired data were also stored in a raw, unreduced form for eventual future off-line data correction procedures.

2.4 Measurement Uncertainty. Extreme care was exercised to ensure the highest possible reliability and accuracy of the acquired data. Each test point in every boundary-layer survey represents an average of five repetitive pressure and temperature readings. The time between successive readings was 8 s. Each time a probe was moved to a new position, there was a settling time period of 20 s allowed before the data reading procedure continued.

Nomenclature

a = jet flow speed of sound
D = nozzle exit diameter
$H_{\delta\theta}$ = displacement-momentum shape factor $= \delta/\theta$
$H_{\epsilon\theta}$ = energy-momentum shape factor $= \epsilon/\theta$
M = Mach number $= U/a$ or u/a
p = pressure
Re = Reynolds number $= U \cdot S/\nu$ or $U \cdot D/\nu$
S = nozzle sink distance
T = temperature
U, u = velocity
y^* = radial distance from nozzle wall
δ = displacement thickness
ϵ = energy thickness
η_s = dimensionless distance $= y^* \cdot \sqrt{U/(S \cdot \nu)}$
θ = momentum thickness
λ = boundary layer thickness
ν = jet flow kinematic viscosity
ρ = jet flow density
σ = total pressure loss coefficient

Subscripts

A = ambient
J = jet
P = probe
S = nozzle sink
T = total
λ = boundary layer edge
0.995 = 99.5 percent of boundary layer thickness

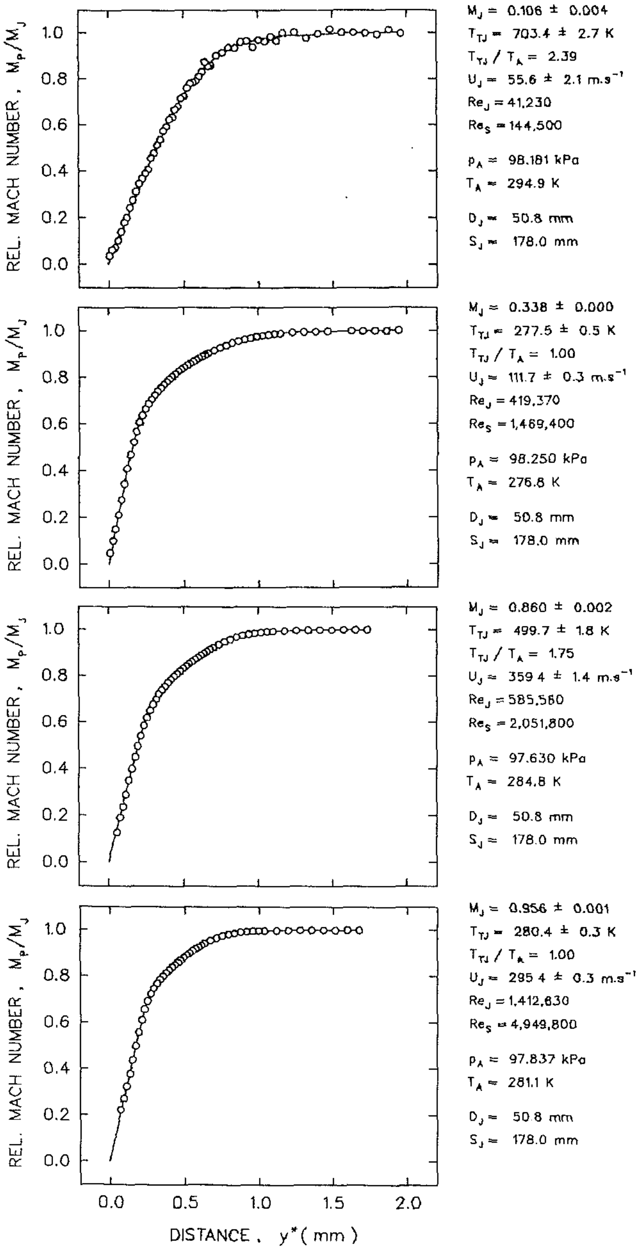

Fig. 3 Nozzle-exit boundary-layer profiles

All pressure transducers were carefully calibrated and the calibration data stored in the computer memory. Slope calibration data points for each transducer were curve fitted with a cubic-parabola curve to improve the pressure conversion accuracy. Standard deviations of calibration points from the best cubic-parabola fits were on average 50 percent smaller than those for the best straight-line fits. The largest standard deviations of calibration points from the best cubic-parabola fits were 13 Pa for a 3.5 kPa transducer and 110 Pa for a 220 kPa transducer.

The temperature conversion accuracy of the Digi-Link processor in the range from 140 K to 1660 K was ±0.003 percent of the reading plus 0.25 K; it is ±3 K at 900 K and ±1.5 K at 300 K. No temperature recovery corrections were applied to the thermocouple readings; the temperature probe recovery fators were assumed to be 1.

The boundary layer probe was positioned by a two-directional traversing mechanism with the smallest reliable step of 0.01 mm. All the probe moves during a boundary layer survey were made in the same direction to eliminate any possible backlash in the traversing mechanism. Also, before each boundary-layer survey, the probe was aligned with the nozzle lip using an electric buzzer to determine the probe/nozzle contact.

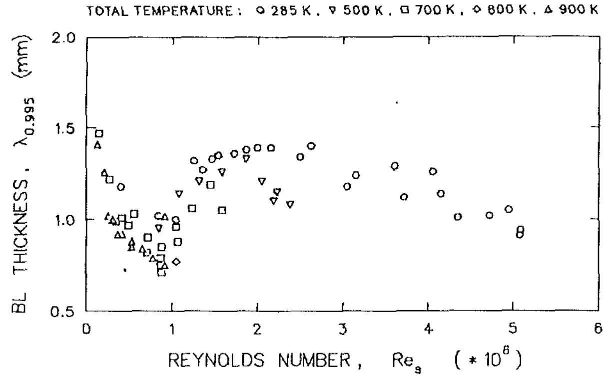

Fig. 4 Nozzle-exit boundary-layer thickness distribution

The exact location of the probe sensing slit also depends on probe stem deflections due to the stem aerodynamic loading and thermal expansion. Both these factors increase the actual radial distance between the probe tip and the nozzle inner wall. From the observed probe stem angle deflection at Mach number 0.9, it was estimated that the maximum radial shift of the probe head at the outer edge of the nozzle-exit boundary layer is less than 0.02 mm. A calculated maximum shift due to thermal expansion is less than 0.01 mm. Because the probe head deviation from the "correct" position decreases rapidly as the probe head approaches the nozzle wall, no corrections were applied to the recorded positions.

No corrections have been applied to the boundary-layer probe readings either due to the viscous effects at low velocities or for the shift of the probe effective center due to the velocity gradients in the measured boundary layers.

3 Test Results

3.1 Boundary-Layer Mach Number Profiles. Boundary-layer Mach-number profiles were calculated from total-pressure distributions measured across the nozzle-exit boundary layers. Local velocities were calculated assuming a flow with static temperature constant and equal to the core static temperature. The reason for this simple approach was the unknown temperature distribution across the investigated heated-flow boundary layers.

For a given survey profile, all the calculated discrete velocity values were fitted with an analytical curve based on parametric cubic spline fitting subroutine ICFSKU from the IMSL Library [4]. As examples, four velocity profiles depicting the experimental points as well as the fitted curves are shown in Fig. 3.

Boundary layer thickness $\lambda_{0.995}$ was calculated from the fitted analytical curve as a distance from the nozzle inner wall where the local velocity reaches 99.5 percent of the velocity value in the jet core. A distribution of the boundary layer thickness $\lambda_{0.995}$ as a function of the nozzle operating conditions, expressed in terms of the jet-exit Reynolds numbers, is shown in Fig. 4. As seen in this figure, the boundary layer thickness decreases rapidly from its low Reynolds number value with an increasing jet Reynolds number and reaches its minimum for a critical Reynolds number of $1 * 10^6$. After that, the boundary layer thickness increases rapidly, reaches a local maximum, and then decreases again. A noticeable scatter of the boundary-layer thickness values, however, does not allow formulation of firm conclusions about the effects of the flow temperature on the boundary layer development. These effects are discussed in the following subsection on boundary-layer integral characteristics.

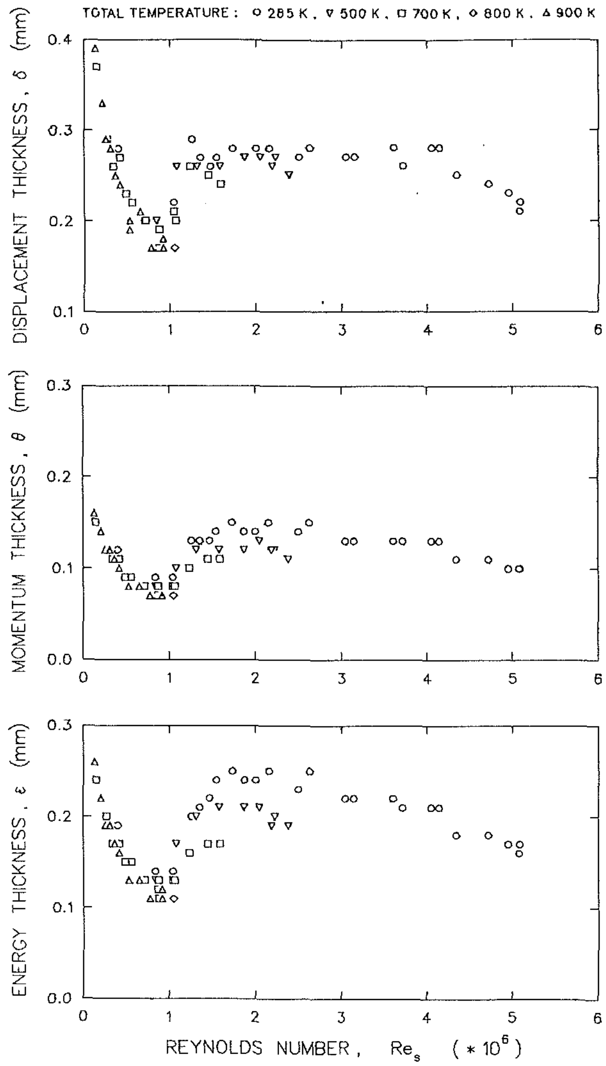

Fig. 5 Boundary-layer integral characteristics

3.2 Integral Characteristics. Boundary-layer integral characteristics provide a basic description of the velocity distribution behavior in a particular boundary layer. The three commonly used integral characteristics are displacement, momentum, and energy thicknesses (δ, θ, ϵ). For axisymmetric or plane flows, these characteristics are defined as follows [3]:

$$\delta = \int_0^\lambda \left(1 - \frac{\rho}{\rho_\lambda}\frac{u}{U_\lambda}\right) dy$$

$$\theta = \int_0^\lambda \frac{\rho}{\rho_\lambda}\frac{u}{U_\lambda}\left(1 - \frac{u}{U_\lambda}\right) dy$$

$$\epsilon = \int_0^\lambda \frac{\rho}{\rho_\lambda}\frac{u}{U_\lambda}\left(1 - \frac{u^2}{U_\lambda^2}\right) dy$$

where λ is the boundary-layer total thickness (the radial distance where a local velocity reaches the core-flow velocity) and the subscript λ denotes values at the outer edge of the boundary layer. The presented integral characteristics were calculated using the assumption of a constant-property fluid (T_J = const, ρ = const). The integral characteristics were calculated from fitted analytical curves using numerical integration utilizing the IMSL subroutine DCADRE [4].

The dependence of the integral characteristics on nozzle operating conditions is shown in Fig. 5. As seen here, the jet exit Reynolds number has a dramatic effect on these characteristics, resembling the behavior of the boundary-layer thickness distribution shown in Fig. 4. The data scatter in these plots appear to be smaller than that for the boundary-layer thickness distribution.

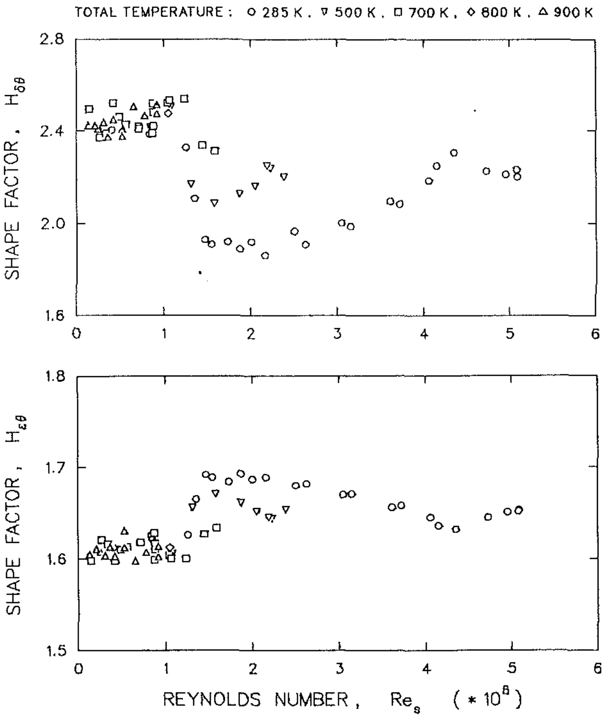

Fig. 6 Shape factor distributions

The displacement thickness, in Fig. 5, decreases rapidly with an increasing jet Reynolds number and reaches its minimum for a critical Reynolds number of $1 * 10^6$. Beyond the critical Reynolds number, the displacement thickness suddenly increases and then remains more or less constant until the nozzle-exit velocity approaches the transonic region where the displacement thickness starts slowly to drop off ($Re_S \cong 4.5 * 10^6$ for $T_T = 285$ K). It appears that above the critical Reynolds number the displacement thickness always drops off when the jet exit velocity approaches the sonic region ($Re_S \cong 2.2 * 10^6$ for $T_T = 500$ K and $Re_S \cong 1.5 * 10^6$ for $T_T = 700$ K). A similar trend exists in the two remaining plots in Fig. 5 for the momentum and energy thickness development. After reaching their maxima beyond the critical Reynolds number, both the momentum and energy thicknesses gradually decrease with an increasing jet-exit Reynolds number.

A closer inspection of these plots, namely of the energy-thickness distribution, reveals that the flow temperature does not play any significant role for the nozzle operating conditions below the critical Reynolds number. Above the critical Reynolds number ($Re_S = 1 * 10^6$), however, the effects of the elevated flow temperatures are clearly traceable. Three separate branches appear to emerge for the nozzle operating conditions above the critical Reynolds number, each associated with a certain jet total temperature (285 K, 500 K, and 700 K). Thus, in this region, the flow temperature should be considered as an additional parameter to the jet Reynolds number, influencing the nozzle-exit boundary-layer development.

3.3 Shape Factors. Shape factors characterize the shape of the boundary-layer velocity profile. The displacement-momentum and energy-momentum shape factors are defined as [3]:

$$H_{\delta\theta} = \delta/\theta$$

and

$$H_{\epsilon\theta} = \epsilon/\theta$$

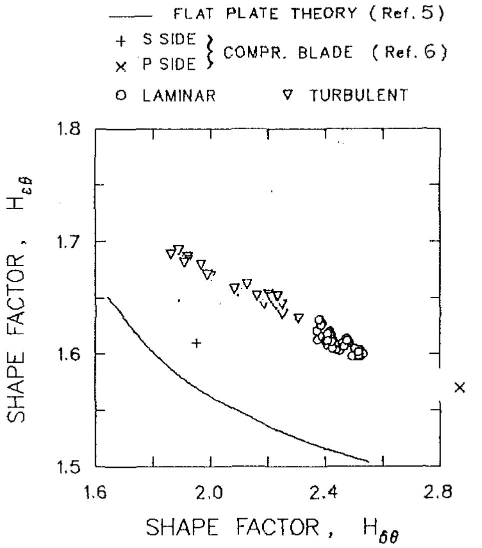

Fig. 7 Relationship between boundary-layer shape factors

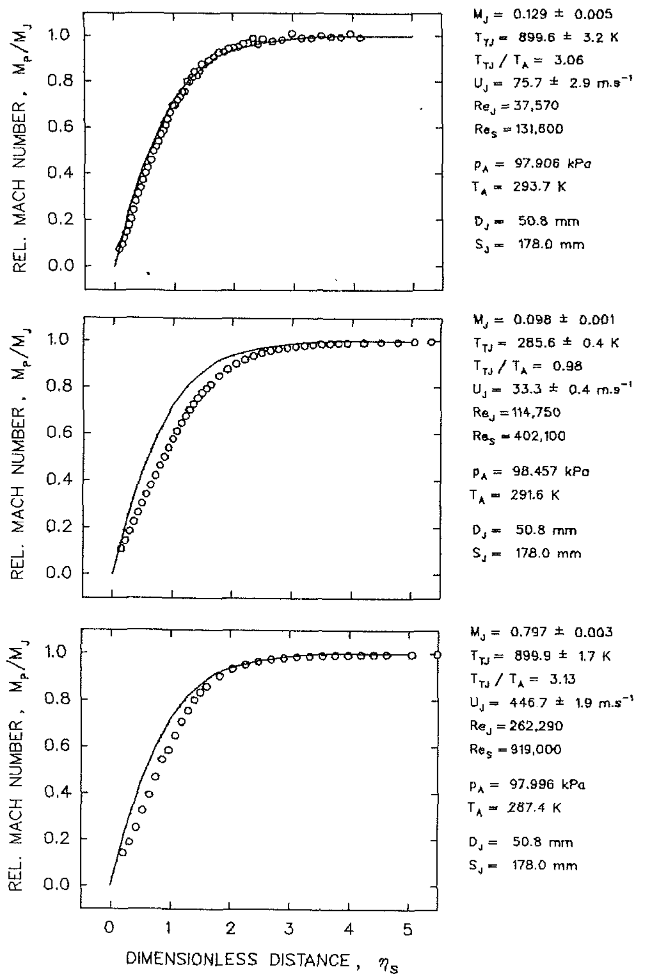

Fig. 8 Comparison of measured laminar boundary-layer profiles with Pohlhausen solution for flat wall converging channel

The significance of the boundary-layer shape factors lies in detection of boundary-layer transition from laminar to turbulent. For example, it is well established that for a flat plate boundary layer, the displacement-momentum shape factor exhibits a sudden drop from a value of 2.6 for the laminar layer to a value of about 1.4 for the turbulent boundary layer [3].

As seen in Fig. 6, at the jet Reynolds number of $Re_S = 1 * 10^6$, the displacement-momentum shape factor $H_{\delta\theta}$ drops from 2.5 to 1.9 for the unheated flow ($T_T = 285$ K), to 2.1 for the flow heated to 500 K, and only to 2.3 for the flow heated to 700 K. Thus, the jet Reynolds number $1 * 10^6$ marks the end of the laminar regime of the nozzle-exit boundary layer. In the transitional and turbulent regions, the value of the displacement-momentum shape factor depends strongly on the flow total temperature, as was already noticed in the case of the integral characteristics. The momentum-displacement shape factor exhibits higher values for higher flow temperatures. After the boundary layer transition, the value of the displacement-momentum shape factor increases with an increasing jet Reynolds number.

Analogous behavior can be observed also for the second shape factor $H_{\epsilon\theta}$. In this case, however, the value of the energy-momentum shape factor increases for the laminar/turbulent transition. The increasing flow total temperature diminishes the rise of this factor during transition in comparison with the laminar boundary-layer value.

As the nozzle-exit velocity approaches the sonic region, both shape factors exhibit a reversal in their trends. This is obvious at least for the unheated flow ($Re_S \cong 4.5 * 10^6$, $T_T = 285$ K). For the heated flows ($Re_S \cong 2.2 * 10^6$, $T_T = 500$ K and $Re_S \cong 1.5 * 10^6$, $T_T = 700$ K), the experimental scatter prevents drawing a similar conclusion with sufficient confidence. The reasons for this trend reversal are not apparent.

An important conclusion about similarity of boundary-layer velocity profiles can be drawn from the mutual relation between displacement-momentum and energy-momentum shape factors. This relation is plotted in Fig. 7. As this figure indicates, the shape factors $H_{\delta\theta}$ and $H_{\epsilon\theta}$ are uniquely related to each other. This means that the boundary-layer velocity profiles exhibit a high degree of similarity. Exact similarity of the laminar boundary-layer profiles is, in fact, a base for a mathematical solution of the boundary-layer equations [3]. For the exactly similar laminar boundary layers, the relation between shape factors in Fig. 7 would be represented by a single point. Acutally, all the experimental data for the nozzle-exit laminar boundary layers are clustered very closely together, thus indicating only minor deviations from the mutual similarity. For the turbulent boundary layers, the relation between these two shape factors has a linear form. This indicates that the turbulent velocity profiles can be described approximately by a one-parameter family of curves, which simplifies the mathematical solution of the boundary-layer equations.

The experimentally determined relation between $H_{\delta\theta}$ and $H_{\epsilon\theta}$ shape factors for the nozzle-exit boundary layer does not agree quantitatively very well either with experimental data for a flat plate [5] or with Weighardt's theoretical prediction [3]. To illustrate a possible range of data for "non-flat-plate" experiments, recent data from boundary-layer measurements on a compressor blade in a cascade are also shown in Fig. 7 [6].

4 Discussion

4.1 Laminar Nozzle-Exit Boundary Layer. As already indicated in Fig. 7, the laminar boundary layer velocity profiles exhibit a high degree of similarity for various nozzle operating conditions. The measured laminar boundary-layer profiles were also compared with an available analytical solution of the boundary layer equation obtained by K. Pohlhausen [3]. This was derived for flow in a flat-wall convergent channel.

The comparison of three laminar boundary-layer profiles with the Pohlhausen solution is shown in Fig. 8. Dimensionless distance η_s in the Pohlhausen approach relates the boundary-layer thickness to the nozzle sink distance. The selected nozzle operating conditions for the three profiles cover the Reynolds number range from $0.13 * 10^6$ to $0.92 * 10^6$. As seen in this figure, the measured profile at the lowest Reynolds number agrees very well with the Pohlhausen solution. At higher Reyn-

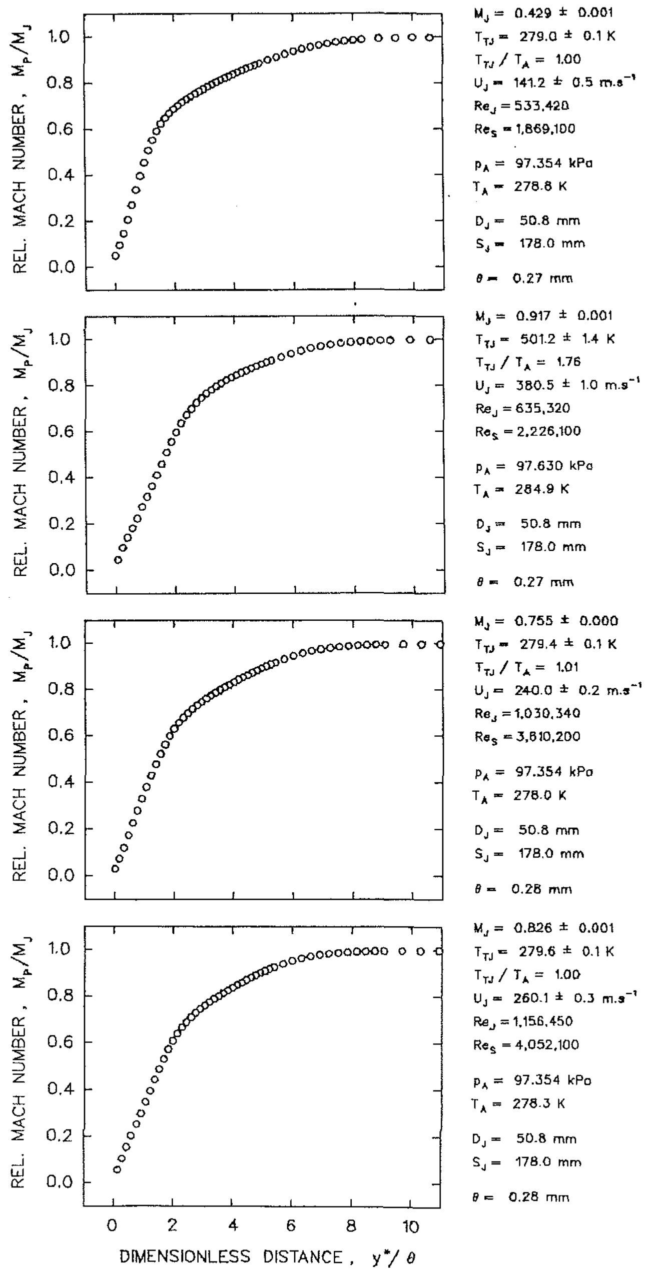

Fig. 9 Normalized turbulent boundary-layer profiles

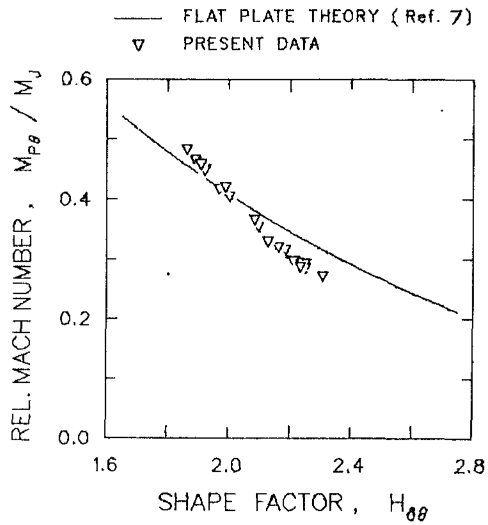

Fig. 10 Comparison of measured and predicted local Mach numbers for turbulent boundary-layer profiles

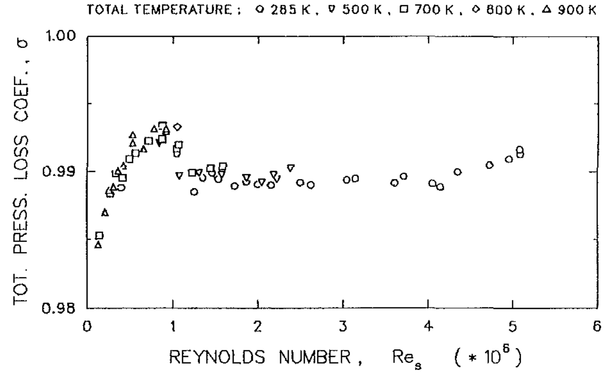

Fig. 11 Total-pressure loss coefficient as a function of nozzle operating conditions

olds numbers, however, there is an observable deviation of the experimental data from the theoretical profiles. Reasons for this deviation are not clear.

4.2 Turbulent Nozzle-Exit Boundary Layer. Some of the measured turbulent nozzle-exit boundary-layer profiles, normalized with the corresponding momentum thickness, are shown in Fig. 9. As seen in this figure, the turbulent boundary-layer profiles show a sharp rise close to the nozzle wall, which gives way abruptly to a more gradual rise through the rest of the boundary layer. Based on the relation between boundary-layer shape factors (Fig. 7), it has already been pointed out that turbulent boundary-layer profiles also exhibit a high degree of similarity. Due to this similarity, the turbulent boundary-layer profiles may be approximated by a one-parameter family of curves. The displacement-momentum shape factor $H_{\delta\theta}$ is often used as such a parameter [7]. Based on this similarity assumption, the following relation between the turbulent boundary-layer velocity and the shape factor $H_{\delta\theta}$, at a distance from a wall equal to the momentum thickness, was derived by Spence [7]:

$$\left(\frac{u}{U_\lambda}\right)_{y*=\theta} = \left[\frac{H_{\delta\theta}-1}{H_{\delta\theta}(1+H_{\delta\theta})}\right]^{\frac{H_{\delta\theta}-1}{2}}$$

A comparison between this prediction and measured data for the nozzle-exit boundary layer is given in Fig. 10. The plotted experimental data cover the range of Reynolds numbers from $1*10^6$ to $5*10^6$. The data for three flow total temperatures of 285 K, 500 K, and 700 K are included in this plot. There is no indication of any difference between heated and unheated jets; however, the experimental data exhibit a stronger dependence of the boundary-layer local velocity on the shape factor $H_{\delta\theta}$ than shown by the prediction.

4.3 Total-Pressure Loss Coefficient. The total-pressure loss coefficient is usually defined as a ratio of the average total pressure and isentropic total pressure for a given flow cross area. The measured total-pressure nozzle-exit boundary-layer profiles were utilized to calculate the total-pressure loss coefficient for a given circular nozzle as a function of the nozzle operating conditions. The resulting data are shown in Fig. 11. For the laminar boundary layer, the total-pressure loss coefficient depends on the nozzle operating conditions. The coefficient value rises rapidly from 0.985 at the lowest test Reynolds number to the value of 0.995 at the Reynolds number of $1*10^6$, which marks the boundary layer transition. For the turbulent boundary layer conditions, the value of the total-pressure loss coefficient is nearly constant and equal to 0.99. A detailed inspection of this plot may reveal a very slight increase of the coefficient value for the jet exit velocity reaching the transonic region for both heated and unheated jets.

5 Conclusions

During the course of this study, several conclusions and observations have been found as listed below:

- For the laminar nozzle-exit boundary layer, the boundary layer thickness and integral characteristics are functions of the jet Reynolds number only. Shape factors, for the laminar boundary layer, are constant. No difference between heated and unheated jets was observed.
- For the turbulent nozzle-exit boundary layer, the boundary layer thickness and shape factors appear to be functions of the jet exit Reynolds number and flow temperature. The results show that the flow temperature, for turbulent exit-boundary layer, should be considered as an independent parameter.
- Laminar nozzle-exit boundary layer profiles, for the given nozzle geometry, agree acceptably with the Pohlhausen solution for flat-wall converging channels only at low jet Reynolds numbers.
- For the turbulent exit boundary layers, at a wall distance equal to the momentum thickness, the dependence of the relative local Mach number on the shape factor resembles Spence's prediction. However, the experimental data exhibit a stronger dependence than that shown by the prediction.
- The total-pressure loss coefficient depends on the nozzle operating conditions for the laminar nozzle-exit boundary layer. For the turbulent nozzle-exit boundary layer, for all practical purposes, the total-pressure loss coefficient is constant and independent of the nozzle operating conditions for both heated and unheated jets.

The presented results pointed out some differences in the turbulent nozzle-exit boundary-layer development between heated and unheated jets. Of course, the validity of the conclusions reached here may be restricted to the range of investigated nozzle operating conditions and test nozzle geometry.

Acknowledgments

The work was performed at the Research Center of the Georgia Division of the Lockheed Aeronautical Systems Company and was sponsored by the NASA-Lewis Research Center under Contract NAS3-23708.

References

1 Lepicovsky, J., Ahuja, K. K., Brown, W. H., Salikkudin, M., and Morris, P. J., "Acoustically Excited Heated Jets," NASA CR-4129, 1988.

2 Ahuja, K. K., Lepicovsky, J., Tam, C. K. W., Morris, P. J., and Burrin, R. H., "Tone-Excited Jets, Theory and Experiments," NASA CR-3538, 1982.

3 Schlichting, H., *Boundary-Layer Theory*, 7th ed., McGraw-Hill, New York, 1979, pp. 152, 168, 354, 455, 673, 675.

4 IMSL Library, Edition 9, International Mathematical & Statistical Libraries, Inc., Houston, 1981.

5 Rotta, J. C., "Critical Review of Existing Methods for Calculating the Development of Turbulent Boundary Layers," in: *Fluid Mechanics of Internal Flow*, G. Sovran, ed., Elsevier Publishing Company, 1967, New York, pp. 84–90.

6 Deutsch, P., and Zierke, W. C., "The Measurement of Boundary Layers on a Compressor Blade in a Cascade at High Positive Incidence Angle," NASA CR-179492, 1986.

7 Spence, D. A., "The Development of Turbulent Boundary Layers," *Journal of the Aeronautical Sciences*, Vol. 23, 1956, pp. 3-15.